Studies on NET4B and associated proteins

DAVID ANTHONY MENTLAK

Studies on NET4B and associated proteins

David Anthony Mentlak

Submitted in accordance with the requirements for the degree of Doctor of Philosophy

School of Biological and Biomedical Sciences
Durham University

September 2015

Abstract

The cytoskeleton is an essential component of the eukaryotic cell, determining both the cellular architecture and function. In plant cells, the cytoskeleton is composed of two distinct networks of filamentous proteins; microtubules and actin microfilaments, as well as a plethora of associated proteins that organise or regulate the network. Metazoans use a range of adaptor proteins, such as spectrin, α-actinin, filamin, and the FERM-domain proteins, that link actin to membrane structures. However these protein families are absent in plants, despite the predominance of the actin cytoskeleton in organelle and endomembrane trafficking. Recently a novel plant-specific superfamily of actin-binding proteins has been identified, termed the Networked (NET) family. The NET family is composed of thirteen members in *Arabidopsis thaliana*, divided into four phylogenetic clades, with members of each subclade associating with specific membrane compartments (Deeks et al. 2012; Wang et al. 2014). The NET4s are the only NET subfamily that can be found universally throughout the genomes of the Tracheophytes, and in *A. thaliana* NET4A associates with actin surrounding the vacuole. NET4B remains a relatively uncharacterised member of the NET family and was thus the focus of this project. Through live cell imaging and an actin cosedimentation assay, NET4B was shown to bind actin filaments *in vivo* and *in vitro*. The expression pattern of NET4B in plants was investigated using *NET4Bpromoter*::GUS lines, demonstrating a high expression in roots and guard cells. Immunogold labelling of plant roots with a NET4B specific antibody revealed its preferential localisation to the tonoplast. The NET4s therefore represent novel actin-vacuole adaptors in plants, and this project investigates the role of these proteins in plant cell growth and identifies key interacting partners that implicate the NET4s in signalling events.

Work described within this thesis has been submitted for publication:

Deeks, M.J., Calcutt, J.R., Ingle, E.S., Hawkins, T.J., Chapman, S., Richardson, A.C., **Mentlak, D.A.,** Dixon, M.R., Cartwright, F., Smertenko, A.P., Oparka, K, Hussey, P.J. (2012). A superfamily of actin-binding proteins at the actin-membrane nexus of higher plants. *Current Biology*, **22**: 1595-1600.

Declaration

I can confirm that this thesis and the original research described therein are my work. Wherever the contributions of others are involved, appropriate credit has been given, with due reference to the literature and acknowledgement of collaborative research.

No material contained in this thesis has been submitted for the award of a higher degree elsewhere.

Statement of Copyright

Acknowledgements

There are many people whom I wish to thank for their encouragement and support throughout my PhD. Firstly, I would like to thank Professor Patrick Hussey who has supervised this project and provided a great deal of advice and encouragement throughout my studies. I would like to thank Dr. Ian Moore and his group for identifying the interaction between RabG3f and NET4B, and his advice concerning this project. Thank you to the Functional Interactomics Group at Ghent University for the service they provided with the NET4A TAP-tagging screen. I would also like to thank the BBSRC for their generous funding of this project.

Thanks go to all the members of the Hussey lab who have made it a great environment to work in over the past four years. Special thanks go to Dr. Tim Hawkins for helping to supervise and mentor me throughout this project; I have really appreciated all your generous support and I cannot thank you enough for the help you provided in proofreading and critiquing this thesis. I would also like to thank Dr. Pengwei Wang and Dr. Andrei Smertenko for their technical advice regarding during my time in the lab. Thanks go to Dr. Mike Deeks for his support in co-sedimentation assays. I would also like to thank Dr. Johan Kroon for introducing me to different experimental techniques within the lab; as well as having some great stories to tell and I will always remember how you met someone. Pat, Greg, Rita and Simon, thank you for the many good times we have shared.

I would also like to thank several members of the Biology department for their involvement in various aspects of this project. Thank you to all the staff at the Durham Life Sciences Support Unit (and the two rabbits) for generating the polyclonal antibodies which opened up the possibility of performing a range of immunological experiments. Thank you to Christine Richardson and Helen Grindley for their contribution to the immunogold labelling experiments. I would also like to thank Dr. Ian Cummins for his advice in all biochemical aspects of this project.

Many thanks go to my Mum, Dad, Tom, Nick and Sheila for their love, encouragement and support throughout my PhD. I would like to thank Nick for his wise words and musings on life, as well as the occasional game of poetry tennis. Thank you to my

housemates Jack and James for getting me through my PhD, I really appreciated the countless cracking walks to Tesco that we had. Martin, Anna and Liv, thank you for being great friends and listening to my stories regarding the aforementioned Tesco trips. I would like to thank James, Martin and Liv for their additional help in proofreading this thesis. Finally, I would like to thank Philippa for always being there for me; you are truly amazing and I could not have completed this thesis without you!

Table of Contents

List of Figures

List of Tables

List of Abbreviations

3AT	3-Amino-1,2,4-triazole
A	Adenine
aa	Amino acid
ABP	Actin Binding protein
AD	Activation domain
ADP	Adenosine diphosphate
AF	Actin Filament
ANOVA	Analysis of variance
APM	Amiprophosmethyl
ATP	Adenosine triphosphate
BCECF-AM	2',7'-Bis-(2-carboxyethyl)-5-(6)-carboxyfluorescein, acetoxymethyl ester
BD	Binding domain
bp	Base pair
CA	Constitutively active
CaMV	Cauliflower mosaic virus
CBB	Coomasie Brilliant Blue
cDNA	Complimentary DNA
CDS	Coding DNA sequence
CH	Calponin homology
CLSM	Confocal laser scanning microscopy
co-IP	Co-immunoprecipitation
Ct	Carboxyl-terminus
DAG	Days after germination
df	Degrees of freedom
DMSO	Dimethyl sulphoxide
DN	Dominant negative
DNA	Deoxyribonucleic acid
dsDNA	Double-stranded DNA
eFP	Electronic fluorescent pictograph browser
EMBOSS	European Molecular Biology Open Software Suite
ER	Endoplasmic reticulum
ERM	Ezrin/radixin/moesin

ETI	Effector triggered immunity
FABD2	Second actin-binding domain of Arabidopsis FIMBRIN1
F-actin	Filamentous actin
FERM	Four-point-one/ezrin/radixin/moesin
FRET	Fluorescence resonance energy transfer
Fw	Forward primer
G-actin	Globular monomeric actin
GAP	GTPase activating protein
GDF	GDP-dissociation factor
GDI	GDP-dissociation inhibitor
GDP	Guanosine diphosphate
GEF	Guanine exchange factor
GFP	Green fluorescent protein
GTP	Guanosine triphosphate
GTPase	Guanosine triphosphatases
GUS	β-Glucuronidase
GV3	Genevestigator version 3
H	Histidine
HPFFS	High pressure freezing and freeze substitution
HRP	Horse radish peroxidase
IRQ	Isoleucine arginine glutamine domain/protein
kb	Kilobase
kDa	Kilodalton
KMD	Kinesin motor domain
L	Leucine
LD	Labelling density
LV	Lytic vacuole
M	Molar
mg	Milligram
ml	Millilitre
mM	Millimolar
mRNA	Messenger RNA
MT	Microtubule
MVB	Multivesicular body
NAB	NET-Actin Binding domain

NET	Networked family protein
ng	Nanogram
Ni-NTA	Nickel-nitrilotriacetic acid
nm	Nanometre
nos	Nopaline synthase terminator
ORF	Open reading frame
PCR	Polymerase chain reaction
PI(3)P	Phosphatidylinositol 3-phosphate
PI3K	Phosphatidylinositol 3-kinase
PM	Plasma membrane
PSV	Protein storage vacuole
PTI	Pattern triggered immunity
PVC	Prevacuolar compartment
qPCR	Quantitative polymerase chain reaction
RLI	Relative labelling index
RNA	Ribonucleic acid
RT-PCR	Reverse-transcription polymerase chain reaction
Rv	Reverse primer
SAIL	Syngenta Arabidopsis insertion library
SAZ	Stamen abscission zone
sdH2O	Sterilised distilled water
SDS-PAGE	Sodium dodecyl sulfate - Polyacrylamide gel electrophoresis
SMART	Simple Modular Architecture Research tool
SNARE	Soluble NSF Attachment Protein Receptor
TAIR	The Arabidopsis information Resource
TAP	Tandem affinity purification
T-DNA	Transfer-DNA
TEM	Transmission electron microscopy
TGN	Trans-Golgi network
TMV	Tobacco mosaic virus
TVS	Transvacuolar strand
TWC	Total water content
W	Tryptophan
WT	Wild-type
X-Gluc	5-bromo-4-chloro-3-indolyl-beta- D-glucuronic acid

Y2H	Yeast-2-hybrid
µg	Microgram
µl	Microlitre
µM	Micromolar

Chapter 1 - Introduction

1.1 Overview

The cytoskeleton is an essential component of the eukaryotic cell, determining both its cellular architecture and function. The plant cell cytoskeleton is composed of two distinct networks of filamentous proteins; microtubules (MTs) and actin microfilaments (AFs). The actin cytoskeleton is a highly dynamic network involved in a range of cellular processes including cell development and division (Barrero et al. 2002; Deeks et al. 2007), vesicle and organelle transport (Mathur et al. 2002; Peremyslov et al. 2012), and responding to biotic and abiotic stresses (Henty-Ridilla et al. 2014; Oikawa et al. 2008). The actin cytoskeleton interacts with a range of actin-binding proteins (ABPs) that can modulate AF dynamics, mediate transport activity, organise higher-order actin structures, and link the actin cytoskeleton to membrane structures. The coordination and control of the network through these ABPs allows the actin cytoskeleton to function in such a broad range of cellular processes. Insights into how the actin cytoskeleton works in conjunction with these accessory proteins will further our understanding of its function in plant cell growth and development.

Various ABPs that link the actin cytoskeleton to membrane systems can be found in metazoans and fungi. However in plant cells there are few functional homologues of these proteins (Hussey et al. 2002), despite the importance of actin-membrane interactions in plant cell signalling (Pleskot et al. 2014), and vesicular transport (Boevink et al. 1998; Sheahan et al. 2004; Higaki et al. 2006). Characterising novel plant-specific ABPs that link the actin cytoskeleton to membranes will greatly increase our knowledge of how these two systems are uniquely coordinated in the plant cell.

This thesis focuses on characterising a novel plant-specific ABP known as NET4B. This protein is a member of the recently discovered NETWORKED (NET) superfamily of actin-binding proteins, characterised by the presence of a conserved N-terminal NET actin-binding (NAB) domain (Deeks et al. 2012). There are thirteen members of this family, that divide into four phylogenetically distinct subclades (Deeks et al. 2012; Hawkins et al. 2014). Representative members of each subclade have been shown to associate with the actin cytoskeleton and different membrane compartments. Characterising NET4B would therefore greatly increase our knowledge of the actin-membrane interface in plant cells.

In order to demonstrate the role of ABPs in plant cells, this chapter begins by describing the structure and function of the plant actin cytoskeleton. The different categories of ABPs in the eukaryotic cell will be discussed, with a focus on the actin-membrane adaptors. Furthermore, the control of membrane trafficking through Rab GTPases in plant cells shall be introduced. Finally, this chapter presents an overview of the NET family, and its evolution in land plants, and concludes with the strategy for characterising NET4B.

1.2 Structure and function of the actin cytoskeleton in plant cells

Actin exists in two forms in the cell; monomeric globular actin (G-actin) and filamentous actin (F-actin; Steinmetz et al. 1997). The actin cytoskeleton is a highly dynamic structure as F-actin undergoes polymerisation and depolymerisation events (Welch et al. 1997). Actin polymerisation occurs through a process of nucleation and elongation. Actin dimers and trimers are thermodynamically unstable structures, however they can act as a 'seed' for rapid elongation of F-actin through the addition of G-actin monomers (Pollard & Borisy 2003). Additional actin nucleation factors, such as the Arp2/3 complex, can stabilise these actin 'seeds' to enable polymerisation (Hussey et al. 2006).

F-actin is composed of two protofilaments that form a right-handed double helix. Monomeric actin is asymmetrical in structure, and each monomer aligns in the same orientation along the filament. This therefore creates a polar filament with 'barbed' and 'pointed' ends (Pollard & Borisy 2003). These two ends exhibit differences in their rate of polymerisation and depolymerisation; assembly occurs faster at the barbed end and disassembly occurs primarily at the pointed end (Pollard & Borisy 2003).

Actin is a nucleotide binding protein, and associates with both adenosine triphosphate (ATP) and adenosine diphosphate (ADP). Monomers being added to the elongating filament are bound to ATP, and once integrated into the filament the ATP is hydrolysed to ADP. The hydrolysis of ATP reduces the affinity that neighbouring actin subunits have for each other and allows subunits to dissociate more readily (Orlova & Egelman 1992).

Filamentous actin forms various different arrays in plant cells. During interphase, F-actin can be found at different locations within the cell including a dense meshwork at the cell cortex, subcortical actin bundles, actin cables in transvacuolar strands, and an

actin meshwork surrounding the nucleus (Figure 1.1; Valster et al. 1997; Nick 1999). The actin cytoskeleton is also utilised during cell division where F-actin associates with the pre-prophase band, the phragmoplast and forms a cage around the mitotic spindle (Yu et al. 2006).

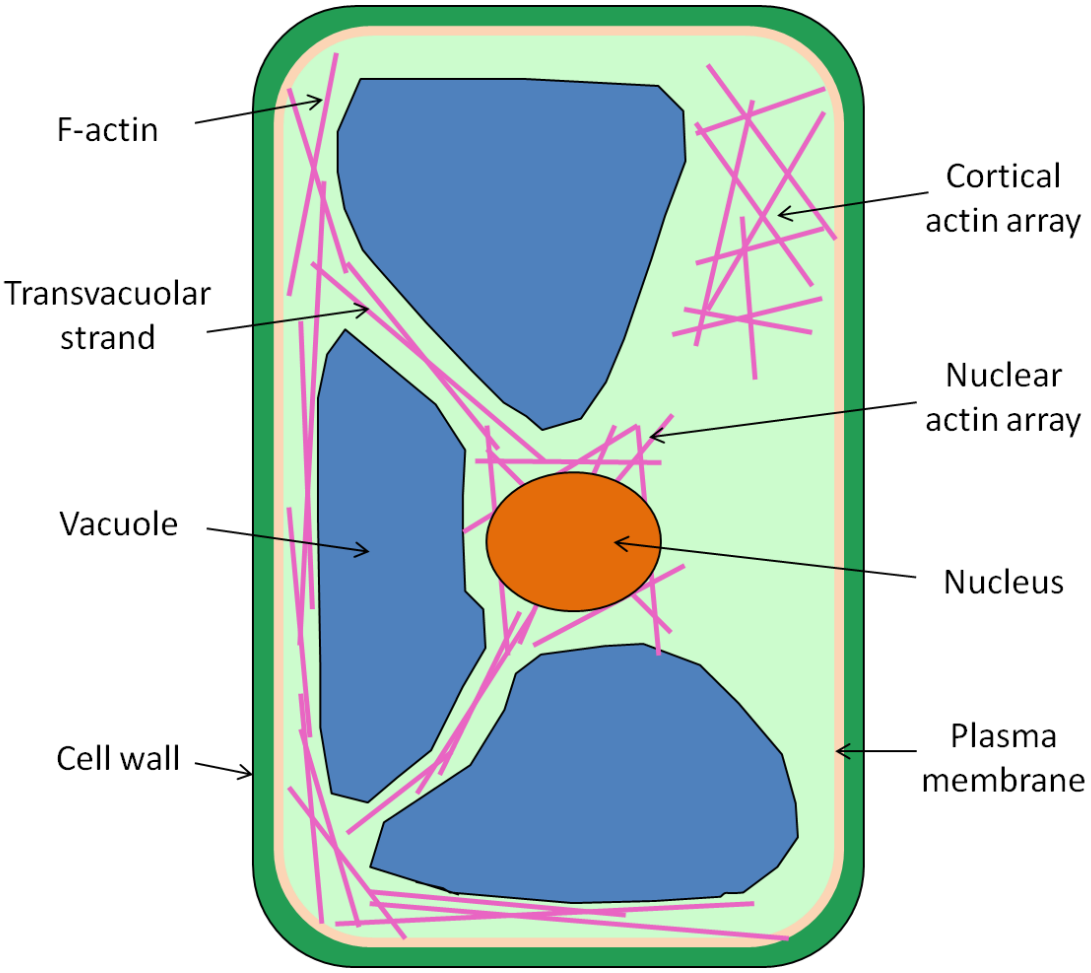

Figure 1.1: F-actin arrays in plant interphase cells. Schematic diagram of a plant interphase cell showing three F-actin arrays: dense F-actin at the cortex, AFs forming a basket around the nucleus, and actin filaments connecting the cell periphery to the nucleus through transvacuolar strands. Diagram modified from Calcutt (2009).

The actin cytoskeleton is involved in a range of processes in plant cells including cell division, cell growth and morphogenesis, transport of membrane structures, responding to the environment and signal transduction. The actin cytoskeleton is crucial during plant cell growth (Hussey et al. 2006); fine actin filaments are required for the expansion of interdigitating lobes in leaf epidermal cells (Fu et al. 2002; Mathur 2006);

and the actin cytoskeleton is also important in the delivery of Golgi-derived vesicles to areas of cell wall growth during polarised cell growth in root hairs and pollen tubes (Peremyslov et al. 2008; Rounds et al. 2014). Disruption to the actin cytoskeleton can lead to dramatic changes in plant morphology. This is exemplified by the defects in plant growth observed in mutants of ABPs that regulate actin dynamics, such as ACTIN INTERACTING PROTEIN 1 (AIP1) and villin proteins (Ketelaar et al. 2004; van der Honing et al. 2012).

The trafficking of vesicles, through the acto-myosin network in plant cell results in the continuous flow of the cytosol and is termed cytoplasmic streaming (Verchot-Lubicz & Goldstein 2010). This process is important for the transport of cytosolic molecules that could not be achieved through diffusion alone (Esseling-Ozdoba et al. 2008). The interaction between actin and myosin motors also mediates the transport of various organelles including Golgi, mitochondria, transport vesicles and peroxisomes (Hashimoto et al. 2005; Avisar et al. 2009; Peremyslov et al. 2013).

Organelle movement can also occur through rearrangements to the actin cytoskeleton in response to environmental signals. Chloroplasts need to be positioned to receive maximal light, and avoid photodamage when light intensity is too high. The actin cytoskeleton is important in the photorelocation of chloroplasts, and chloroplast associated actin filaments are reorganised in response to changing light conditions (Kadota et al. 2009). The physical link between AFs and chloroplasts is mediated through the anchoring protein, CHLOROPLAST OUTER ENVELOPE PROTEIN 1 (CHUP1; Oikawa et al. 2003). The level of blue light in the cell is perceived by phototropins, which initiate downstream signalling events, resulting in the reorganisation of the actin cytoskeleton and chloroplast movement (Kadota et al. 2009).

The plant actin cytoskeleton also dynamically responds to biotic stress such as pathogen attack. The actin cytoskeleton, endoplasmic reticulum (ER) and Golgi bodies localise to attempted sites of fungal pathogen penetration, and are important in the delivery of defence components (Takemoto et al. 2003; Hardham et al. 2007). Perception of bacterial microbe-associated molecular patterns (MAMPs) at the plasma membrane, through receptor kinases (such as FLS2), results in downstream changes to the actin cytoskeleton and an increase in F-actin abundance (Henty-Ridilla et al. 2013; Li et al. 2015). Changes to the actin cytoskeleton are crucial in the defence response and pharmacologically disrupting actin filaments leads to an increased susceptibility to

pathogen attack (Henty-Ridilla et al. 2013). Recent studies have also demonstrated that two ABPs, Capping Protein (CP) and ACTIN DEPOLYMERISING FACTOR 4 (ADF4), are important for callose deposition at the site of attack and transcriptional reprogramming during pathogen defence (Henty-Ridilla et al. 2014; Li et al. 2015). These studies therefore demonstrate the central importance of the actin cytoskeleton in the response and transmission of signals during biotic stress.

1.3 Actin-binding proteins

The dynamic nature of the actin cytoskeleton, and the range of activities that it participates in, are orchestrated through the association of a variety of spatially distributed and temporally activated ABPs (Hussey 2004). Some of these proteins can associate with monomeric G-actin whilst others interact with F-actin. ABPs can be categorised into three groups; ABPs affecting aspects of actin dynamics, ABPs that mediate transport activity and ABPs that organise higher-order structures (Hussey et al. 2006). Figure 1.2 illustrates the range of ABPs used in the plant cell. This section shall introduce these different categories of ABPs with a focus on those that cross-link and anchor actin filaments to membrane structures.

1.3.1 Actin-binding proteins that regulate actin dynamics

As mentioned previously, the actin cytoskeleton is highly dynamic and undergoes continuous cycles of polymerisation and depolymerisation of F-actin. The dynamic nature of the actin cytoskeleton is governed by a range of ABPs that influence these changes to F-actin. ABPs that regulate actin dynamics do so through various strategies including; regulating the availability of G-actin, acting as F-actin nucleators, and capping or severing AFs (Hussey et al. 2006). Profilins are an example of conserved ABPs that sequester G-actin monomers and appear to have a dual role in regulating actin dynamics. When actin filaments are capped, profilin can act to sequester actin monomers, thus preventing polymerisation (Staiger et al. 1997). However, in animal cells when filaments are uncapped, profilin can promote polymerisation at the barbed end by acting as a nucleotide exchange factor, converting actin monomers into their polymerisable form (Pantaloni & Carlier 1993).

Actin nucleators include the Arp2/3 complex and the formins. The Arp2/3 complex is a conserved seven subunit complex that promotes actin barbed-end polymerisation and additionally caps the pointed end (Hussey et al. 2006). This complex binds to existing

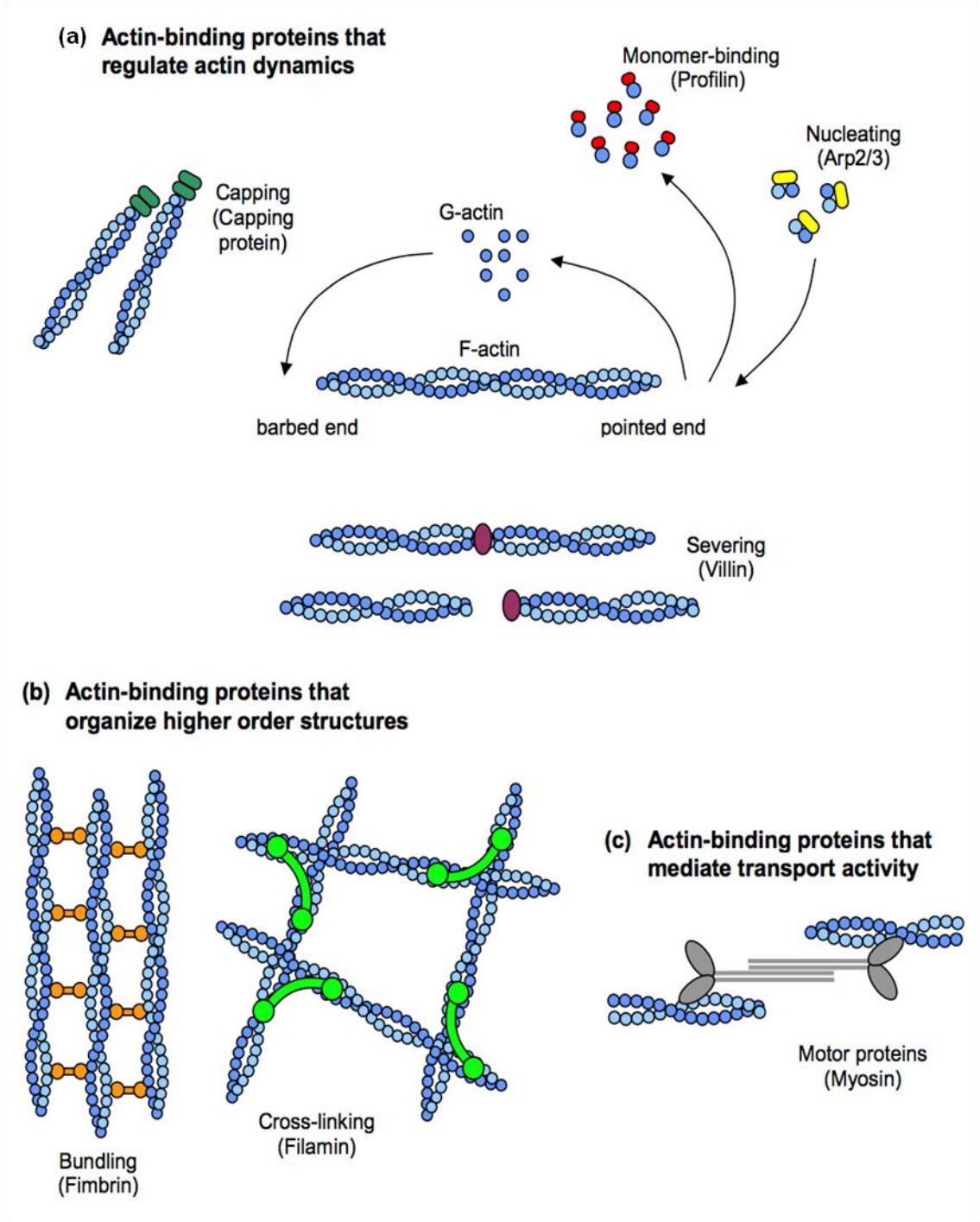

Figure 1.2: Actin-binding proteins. Diagram shows three main classes of ABPs including: (a) ABPs that regulate the dynamics of the actin cytoskeleton, (b) ABPs that cross-link AFs into higher order structures, (c) ABPs that mediate transport activity. Figure from Calcutt (2009).

actin filaments and polymerises a new AF branch at an angle of 70° to the primary filament. *Arabidopsis thaliana* (referred to as Arabidopsis) homologues of the Arp2/3 complex are crucial in maintaining plant cell expansion, and can also affect guard cell responses (Mathur et al. 2003; Jiang et al. 2012; Li et al. 2013). The formins are a conserved class of multifunctional ABPs that can act as actin nucleators. In Arabidopsis there are 21 formins that are subdivided into two subfamilies based on their N-terminal domains (Deeks et al. 2002). Formins are capable of nucleating unbranched actin filaments as well as acting as actin bundling proteins (Michelot et al. 2005).

Finally, ABPs can also affect actin dynamics by capping F-actin or severing actin filaments. Capping proteins bind to the end of filaments and therefore control actin polymerisation or depolymerisation. An example of these proteins is the conserved heterodimeric capping protein (CP; Huang et al. 2003). This protein is able to bind to the barbed end of filaments and thus prevents actin polymerisation (Huang et al. 2003). ABPs can also regulate actin dynamics through severing actin filaments. These include the conserved ADF/cofilin proteins that sever AFs to promote actin turnover (Zheng et al. 2013; Henty-Ridilla et al. 2013). Recent studies have demonstrated that actin turnover in plant cells is governed by AF severing, as opposed to complete depolymerisation of F-actin (Staiger et al. 2009; Smertenko et al. 2010).

1.3.2 Actin-binding proteins that mediate transport activity

The second group of ABPs are those that mediate transport activity, the myosins, which transport cargo along actin filaments using the energy derived from ATP hydrolysis (Sellers 2000). Myosins are molecular motors that typically consist of three domains; the head domain interacts with actin and binds ATP, the neck domain can interact with calmodulin family members, and the tail domain is specific to each class and can include coiled-coil domains and cargo binding regions (Hammer & Sellers 2012). Myosins can move along AFs as changes to their bound nucleotide status (ATP/ADP) alters the conformation of the motor domain, which exerts a force along the actin filament and results in the movement of cargo (Schliwa & Woehlke 2003). The Arabidopsis myosin family is composed of 17 proteins; 13 class XI variants and 4 class VIII variants (Reddy & Day 2001; Peremyslov et al. 2011).

1.3.3 Actin-binding proteins that mediate higher-order actin structures

Another class of ABPs are those that organise actin filaments into higher-order structures through either bundling actin filaments, cross-linking AFs into a loose meshwork array or anchoring the actin cytoskeleton to membrane structures (Winder & Ayscough 2005). Of particular interest to this project are ABPs that cross-link AFs and those that anchor AFs to membranes, and these shall be discussed in relation to animal and plant cells.

1.3.4 Actin-binding proteins that cross-link and anchor actin filaments to membranes in animals

The association between the actin cytoskeleton and membrane systems is crucial in mediating signal transduction and maintaining cellular structure (Sechi & Wehland 2000; Winder & Ayscough 2005). Animal cells contain many different proteins that act as actin-membrane adaptors including the calponin-homology (CH) domain proteins and certain FERM (four-point-one/ezrin/radixin/moesin) domain proteins.

The CH domain superfamily are a major group of structural ABPs that are defined by the presence of a conserved actin-binding domain, consisting of a pair of CH domains, and includes α-actinin, spectrin, filamin, fimbrin, dystrophin and utrophin (Gimona et al. 2002). Most of these proteins contain a single actin-binding domain (ABD), and dimerisation of the proteins enables cross-linking and bundling of actin filaments. However fimbrin contains two ABDs and can thus interconnect filaments into tight bundles (Bañuelos et al. 1998). The size of these proteins, and the separation of their ABD can affect whether they bundle or cross-link AFs, with smaller proteins typically forming bundles and larger proteins with more separated ABDs creating a meshwork of filaments (Djinovic-Carugo et al. 2002). However it should be noted that this is not necessarily the case in all actin organising ABPs. For example the recently discovered plant-specific actin-binding protein CROLIN1, is a short 37kDa protein that dimerises and can bundle and cross-link actin filaments (Jia et al. 2013).

Spectrin is a member of the CH domain proteins that links the actin cytoskeleton to membrane structures. This protein tethers actin filaments to membranes by interacting with peripheral membrane proteins that in turn associate with integral membrane proteins (Bennett & Lambert 1991). The ability of spectrin to dimerise and cross-link creates a two-dimensional meshwork at membrane structures that is then linked to the

actin cytoskeleton (Bennett & Lambert 1991). The spectrin 'skeleton' can associate with the plasma membrane and internal membrane structures including the Golgi, and is important in maintaining their structure (De Matteis & Morrow 2000). Additional CH domain proteins that anchor the actin cytoskeleton to membrane structures are dystrophin and utrophin. These proteins associate with various membrane bound proteins, thus linking the actin cytoskeleton to the extracellular matrix (Keep 2000).

Another member of the CH domain superfamily that functions as an actin cross-linker and membrane adaptor is α-actinin. This protein forms anti-parallel dimers that can bundle oppositely orientated filaments in striated muscle cells, and bundles similarly orientated filaments at focal adhesion sites (Sjöblom et al. 2008). The actin bundles created by α-actinin are anchored to focal adhesion sites through interactions with integrins (Otey et al. 1990), and through the adaptor proteins; vinculin and talin (Bois et al. 2006). Filamin is another CH domain protein that cross-links AFs into a loose orthogonal meshwork that can be anchored to the plasma membrane via peripheral and integral membrane receptor proteins including integrins (van der Flier & Sonnenberg 2001; Popowicz et al. 2006). Figure 1.3 shows how α-actinin and filamin can organise and anchor the actin cytoskeleton to the plasma membrane.

The FERM proteins are a family of proteins that are characterised by the presence of an N-terminal FERM domain (Moleirinho et al. 2013). There are approximately 50 proteins that contain this domain, and of interest to this project are the ERM (ezrin/radixin/moesin) proteins. These proteins provide a regulated linkage between the actin cytoskeleton and the plasma membrane, and are important in maintaining specific plasma membrane domains such as microvilli (Berryman et al. 1993; Bretscher et al. 2002). The ERM proteins can interact with integral membrane proteins at the plasma membrane through their N-terminal FERM domain, and can bind F-actin through a C-terminal domain (McClatchey & Fehon 2010). Studies have shown that the ERM proteins can exist in an inactive closed conformation, with the membrane and actin-binding domains self-associating and thus masking their activity (Pearson et al. 2000). Phosphorylation of the ERM proteins opens up these proteins and enables interactions between F-actin and membrane structures. The attachment of actin to membrane systems can thus be regulated through the ERM proteins and these proteins have been implicated in a range of cellular processes including cell shape determination, membrane-protein localisation and signal transduction (Bretscher et al. 2002).

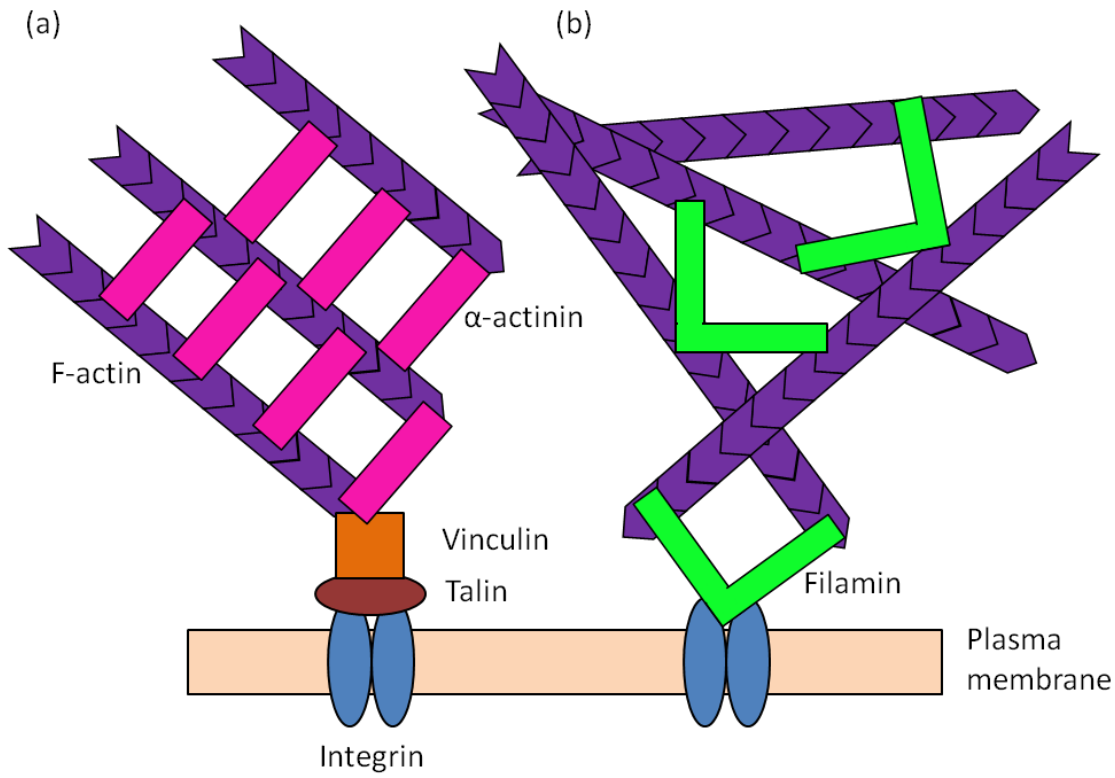

Figure 1.3: Actin cross-linking and anchoring proteins, α-actinin and filamin. (a) α-Actinin can bundle actin filaments and anchor them to focal adhesion sites through interactions with vinculin and talin. (b) Filamin cross-links actin filaments into a loose meshwork and can anchor these structures to the plasma membrane through association with integrin receptors. Diagram modified from Calcutt (2009).

1.3.5 Actin-membrane adaptors in plants

Bioinformatics analysis has revealed that many of the CH domain proteins, including spectrin, filamin, dystrophin and α-actinin, as well as the ERM proteins are not present in the Arabidopsis genome (Hussey et al. 2002; Meagher & Fechheimer 2003; Drøbak et al. 2004). Fimbrin is the only member of the CH domain superfamily for which an Arabidopsis homologue (AtFim1) has been identified and characterised (Kovar et al. 2000). Although plants lack these large families of actin-membrane adaptors, plants still possess a variety of ABPs that link the actin cytoskeleton to membrane structures.

Several ABPs that associate with membranes in plants are not plant-specific and can be found across the eukaryotes and many of these are multifunctional proteins. Examples of these multifunctional proteins are the formins. Arabidopsis formin8 is important for actin bundling and nucleation, and can associate with the nuclear envelope in interphase

cells (Xue et al. 2011). Several Arabidopsis formins have also been shown to associate with the plasma membrane, through either transmembrane domains, interaction with phospholipids or additional proteins (Favery et al. 2004; Cheung & Wu 2004; Deeks et al. 2005; Martinière et al. 2011; van Gisbergen et al. 2012; Cvrčková 2013). In addition, it has recently been discovered that the Arabidopsis heterodimeric capping protein associates with the ER and Golgi (Jimenez-Lopez et al. 2014), and its activity can be regulated by phosphatidic acid levels (Huang et al. 2006; Li et al. 2012). The presence of these proteins at membranes suggests that they could be important in facilitating cross-talk between actin dynamics and signal transduction (Jimenez-Lopez et al. 2014; Wang & Hussey 2015).

The nuclear envelope also forms important links with the actin cytoskeleton through interactions between the SUN (SAD1/UNC84) and KASH (Klarsicht/Anc/Syne-1 homology) domain proteins; a complex which is conserved across the eukaryotes (Zhou & Meier 2013). SUN proteins are localised to the inner nuclear membrane and interact with KASH domain proteins at the outer nuclear membrane. The Arabidopsis genome contains two SUN domain proteins (Graumann et al. 2010), as well as plant-specific KASH proteins, WPP-DOMAIN-INTERACTING PROTEINS (WIPs) and SUN-INTERACTING NUCLEAR ENVELOPE (SINE) proteins (Zhou et al. 2012; Zhou et al. 2014). Recently, myosin XI-i has been shown to interact with a WIP interacting protien (WPP DOMAIN-INTERACTING TAIL-ANCHORED PROTEIN 2; WIT2), and this interaction is crucial for controlling nuclear movement and morphology (Tamura et al. 2013). In addition, SINE1 can associate with F-actin and is important in positioning nuclei in guard cells (Zhou et al. 2014).

Plant specific actin-membrane adaptors have also been described and one of these is the previously mentioned CHUP1 (Oikawa et al. 2003). This protein links chloroplasts to the actin cytoskeleton and the plasma membrane, and is important in the photorelocation of chloroplasts (Oikawa et al. 2003; Oikawa et al. 2008; Kadota et al. 2009). In addition, a recent family of plant-specific myosin receptors have also been identified that link the myosin XI class proteins to vesicles (Peremyslov et al. 2013). Although these proteins do not interact directly with the actin cytoskeleton, they will be important for our understanding of actin-vesicle dynamics in plants.

The NET superfamily is a recently discovered plant-specific family of actin-binding proteins that associate with different membrane systems in plant cells. The

characterisation of this family will greatly increase our knowledge of the link between the actin cytoskeleton and membranes in plants. Before further discussion of the NET family in section 1.5, the role of Rab GTPases in membrane trafficking shall be introduced.

1.4 Rab GTPases and membrane trafficking

1.4.1 Regulation of membrane trafficking

The eukaryotic endomembrane system is crucial in controlling the movement of macromolecules with the cell, and functions in their synthesis, targeting, delivery and degradation (Contento & Bassham 2012). The endomembrane system is composed of a range of biochemically distinct membrane bound organelles that are functionally linked through membrane trafficking (Rutherford & Moore 2002). Vesicle trafficking is needed in order to transport cargo and maintain the structural integrity and properties of each particular compartment. Regulation of membrane trafficking is crucial in the eukaryotic cell and in plants targeted vesicle transport is necessary for plant development as well as responses to the environment (Cui et al. 2014; Ellinger et al. 2014; Antignani et al. 2015).

The main organelles within the endomembrane system are the ER, the Golgi complex, the trans-Golgi network (TGN), multivesicular bodies/prevacuolar compartments (MVBs/PVCs), the plasma membrane and the vacuole (Jürgens 2004). Two main membrane trafficking pathways exist in the cell, the biosynthetic pathway and the endocytic pathway (Figure 1.4). The entry point to the endomembrane system starts with the biosynthetic pathway. Soluble and membrane bound proteins are synthesised in the ER, which can then be trafficked through the Golgi complex to the TGN. Cargo can then be transported to either the plasma membrane or the vacuole depending on its function. In the endocytic pathway, cargo is internalised from the plasma membrane to the TGN, which represents the convergence point of the two pathways (Dettmer et al. 2006; Lam et al. 2007; Viotti et al. 2010). Endocytosed cargo is subsequently either recycled back to the plasma membrane or targeted to the vacuole for degradation. Traffic to the vacuole has been shown to occur through MVBs which represent prevacuolar compartments (PVCs; Tse et al. 2004; Scheuring et al. 2011).

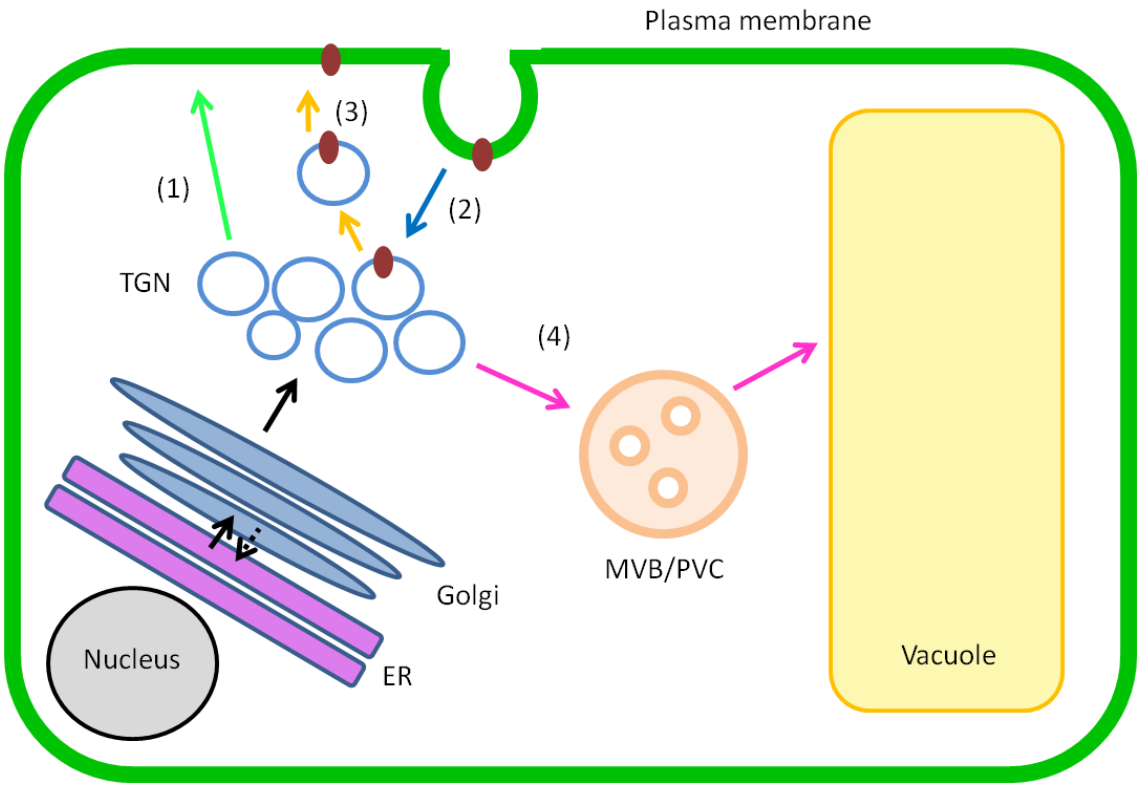

Figure 1.4: Endomembrane trafficking in plant cells. Diagram shows the main trafficking pathways along the biosynthetic and endocytic trafficking pathways. Soluble and membrane cargo is synthesised in the endoplasmic reticulum (ER) and is transported through the Golgi to the trans-Golgi network (TGN). Cargo is then either trafficked to the plasma membrane (PM) (1) or to the vacuole (4). Endocytosis occurs at the plasma membrane (2), and cargo can either be recycled back to the PM (3) or trafficked to the vacuole for degradation through multivesicular bodies/prevacuolar compartments (MVBs/PVCs) (4). The TGN represents the convergence point of the biosynthetic and endocytic trafficking pathways. Diagram modified from Contento & Bassham (2012).

The flux of membrane systems within the cell is tightly controlled and one of the major regulators of the eukaryotic endomembrane system are the Rab GTPases (Rutherford & Moore 2002). The Rabs are part of the Ras superfamily of small guanosine triphosphatases (GTPases), that function as GDP/GTP regulated molecular switches (Wennerberg et al. 2005). Rab GTPases cycle between an inactive cytosolic-GDP bound form and an activated GTP-bound form on the target membrane (Behnia & Munro 2005). This regulated switch acts as a signal to recruit effector proteins that can mediate the downstream processes in membrane trafficking, such as transportation and tethering of vesicles.

Eukaryotic cells contain a range of different Rab GTPases that mediate distinct steps in membrane trafficking, and different kingdoms contain a diversified range of Rabs (Hutagalung & Novick 2011). The total number of Rab proteins in different kingdoms, appears to reflect the evolution of complex multicellular systems, with *Saccharomyces cerevesiae*, *Homo sapiens*, and *A. thaliana* containing 11, 60 and 57 Rabs respectively (Pereira-Leal & Seabra 2001). However, despite this diversification, the evolution of the Rab proteins across the eukaryotes shows a phylogeny of functional groups as opposed to a phylogeny of species, and different Rab orthologs across the eukaryotes perform similar functions (Pereira-Leal & Seabra 2001; Stenmark 2012). In Arabidopsis, there are 57 Rab GTPases that group into 8 different subfamilies, termed Rabs A-G (Pereira-Leal & Seabra 2001; Rutherford & Moore 2002). Members of the different subfamilies have been shown to mediate distinct steps in membrane trafficking for example the RabA1 subfamily are important in transport between the TGN and the plasma membrane (Asaoka et al. 2013).

Of interest to this project are the Arabidopsis RabG members. Sequence analysis of the RabG members has provisionally divided this group into three subgroups; RabG1, RabG2 and RabG3a-f (Pereira-Leal & Seabra 2001; Rutherford & Moore 2002). The RabG3 subfamily is most closely related to the mammalian Rab7 and yeast Ypt7p proteins (Pereira-Leal & Seabra 2001; Rutherford & Moore 2002), and these Rabs have both been implicated in traffic to the lysosome/vacuole (Schimmöller & Riezman 1993; Méresse et al. 1995; Vitelli et al. 1997), as well as homotypic vacuole fusion in yeast (Haas et al. 1995). Studies on Arabidopsis RabG3c have demonstrated that this Rab localises to the tonoplast (Saito et al. 2002; Bottanelli et al. 2011; Bottanelli et al. 2012); a localisation shared by RabG3f, which has recently been shown to localise to the tonoplast as well as PVCs (Cui et al. 2014; Ebine et al. 2014).

The role of the RabG3s in membrane trafficking has recently been revealed through overexpression of dominant-negative (DN) mutant Rabs that have a reduced affinity for GTP (Cui et al. 2014). Overexpression of an inactive DN-RabG3f in Arabidopsis resulted in fragmented vacuoles, enlarged PVCs, altered trafficking to the vacuole and severe growth defects in the plant (Cui et al. 2014). These results demonstrated the central importance of RabG3f in the trafficking of PVCs to the vacuole and in controlling vacuole morphology. In addition, genetic studies of multiple RabG3 members results in semi-dwarfism and affects vacuolar morphology of the protein storage vacuoles and lytic vacuoles (Ebine et al. 2014).

Rab GTPases are essential regulators of membrane trafficking events. Central to their role in trafficking is their ability to cycle between an inactive GDP-bound form and an active GTP-bound form. Once activated, the Rabs can then recruit specific effectors that mediate downstream processes. The section below shall describe the mechanisms regulating this molecular switch.

1.4.2 Rab GTPases as molecular switches

Rab GTPases cycle between the cytosol and the target membrane, and the nucleotide bound to the Rab (GDP or GTP) influences both its localisation and activity (Figure 1.5; Hutagalung & Novick 2011). Rabs are irreversibly modified with the addition of isoprenyl lipid (geranylgeranyl) moieties at their C-terminal cysteine residues, which enables their association with membranes (Kinsella & Maltese 1992). Inactive GDP-bound Rabs are maintained in the cytosol as they interact with a GDP-dissociation inhibitor (GDI) protein that masks these lipid moieties and prevents GDP dissociation (Sasaki et al. 1990; Shisheva et al. 1999; Rak et al. 2003). Prior to membrane insertion, the GDI needs to be removed to expose the lipid anchors. GDI displacement factors (GDF) have been identified that are associated with membranes, and promote the release of GDI and thus enable Rab insertion (Dirac-Svejstrup et al. 1997; Hutt et al. 2000; Sivars et al. 2003). Once dissociated from GDI and inserted into the membrane, Rabs can then be activated by a guanine exchange factor (GEF), which exchanges GDP for GTP (Allaire et al. 2010; Nordmann et al. 2010). Binding of GTP to the Rab induces a conformational change in the switch I and switch II regions, which become highly ordered upon GTP binding (Dumas et al. 1999; Stroupe & Brunger 2000). This conformational change permits the interaction with Rab effectors that can stabilise the Rab at their membrane site (Grosshans et al. 2006). Finally, Rabs are inactivated by GTPase activating proteins (GAP) that hydrolyse GTP for GDP and therefore allow membrane extraction via GDI (Xiao et al. 1997; Haas et al. 2005).

Fundamental to the role of Rab GTPases in membrane trafficking is their association with specific membrane compartments. Recent studies, have demonstrated that specific membrane targeting of Rabs can be determined through the action of their cognate GEF (Gerondopoulos et al. 2012; Blümer et al. 2013). These studies added a mitochondrial targeting sequence to specific Rab GEFs, which resulted in the mislocalisation of their associated Rabs to this organelle. In addition, Rabs were not properly targeted when mutant GEFs were expressed that had a reduced nucleotide exchange

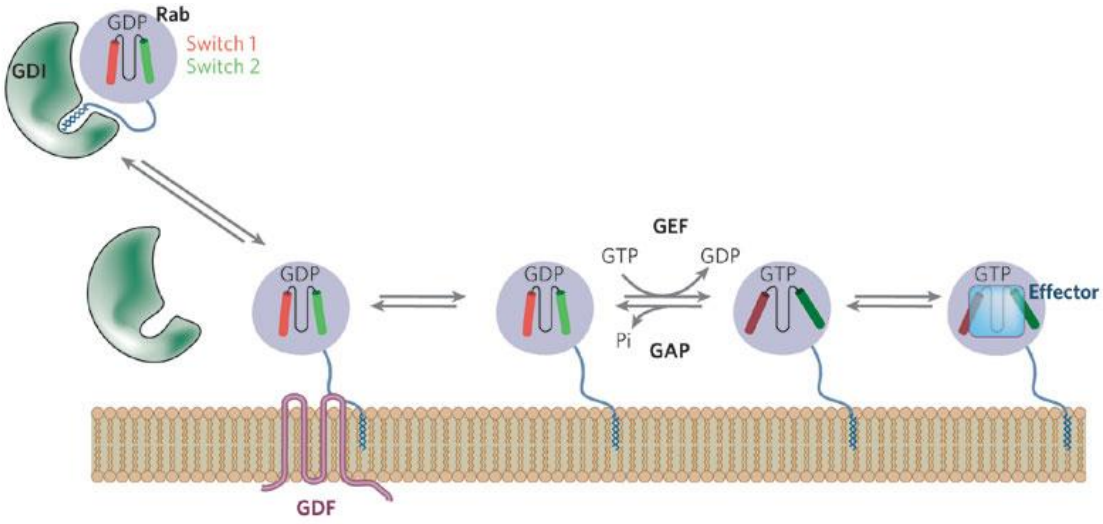

Figure 1.5: The Rab GTPase cycle. The localisation and activity of Rabs is governed by their nucleotide bound state. In the cytosol, GDP-bound inactive Rabs are in a complex with a GDP-dissociation inhibitor (GDI) that masks the isoprenyl lipid anchors and prevents GDP dissociation. GDP-dissociation factors (GDFs) can be present at the target membrane, and these function to displace GDI, allowing membrane insertion. Once anchored at the membrane Rabs can be activated by guanine exchange factors (GEFs) that exchange GDP for GTP. The presence of GTP causes a conformational change in the switch I and II regions and allows the recruitment of effector proteins involved in downstream processes. The interaction between Rabs and effectors stabilises their localisation at the membrane. Rabs are inactivated by GTPase activating proteins (GAPs) that promote GTP hydrolysis. Once inactivated GDP-bound Rabs can be subsequently extracted from the membrane by GDI. Figure used with permission from Behnia & Munro (2005).

activity (Blümer et al. 2013). Various Rab GEFs have been shown to localise to the same compartment as their Rabs which could therefore permit the precise activation of Rabs at their specific target membrane (Barr 2013). Indeed, the RabG3f GEF, the MON1-CCZ1 (MONENSIN SENSITIVITY1 - CALCIUM CAFFEINE ZINC SENSITIVITY1) complex, has recently been shown to localise to PVCs which activates RabG3f at this compartment, and so mediates transport to the tonoplast (Cui et al. 2014; Singh et al. 2014; Ebine et al. 2014).

The specific nature of the Rab GTPases as molecular switches means that they are rapidly switched off once the particular membrane recognition event is over (Barr 2013). Rab GAPs are critical in terminating these events by activating the hydrolysis of GTP and inactivating the Rab. Recently, it has been observed that Rab GAPs are

recruited in a 'Rab cascade' (Figure 1.6; Rivera-Molina & Novick 2009; Nottingham et al. 2011; Nottingham et al. 2012). This occurs where GTP-bound Rabs recruit GAPs as effectors, and these GAPs then specifically terminate the activity of the Rab from the previous compartment. Similarly, Rab GEFs can function in these 'Rab cascades' and GEFs can be recruited as effectors that then activate the Rab in the following trafficking pathway (Ortiz et al. 2002; Zhu et al. 2009; Cui et al. 2014). The ordered recruitment of GEFs and GAPs ensures the spatio-temporal activation of Rabs along distinct trafficking pathways (Hutagalung & Novick 2011).

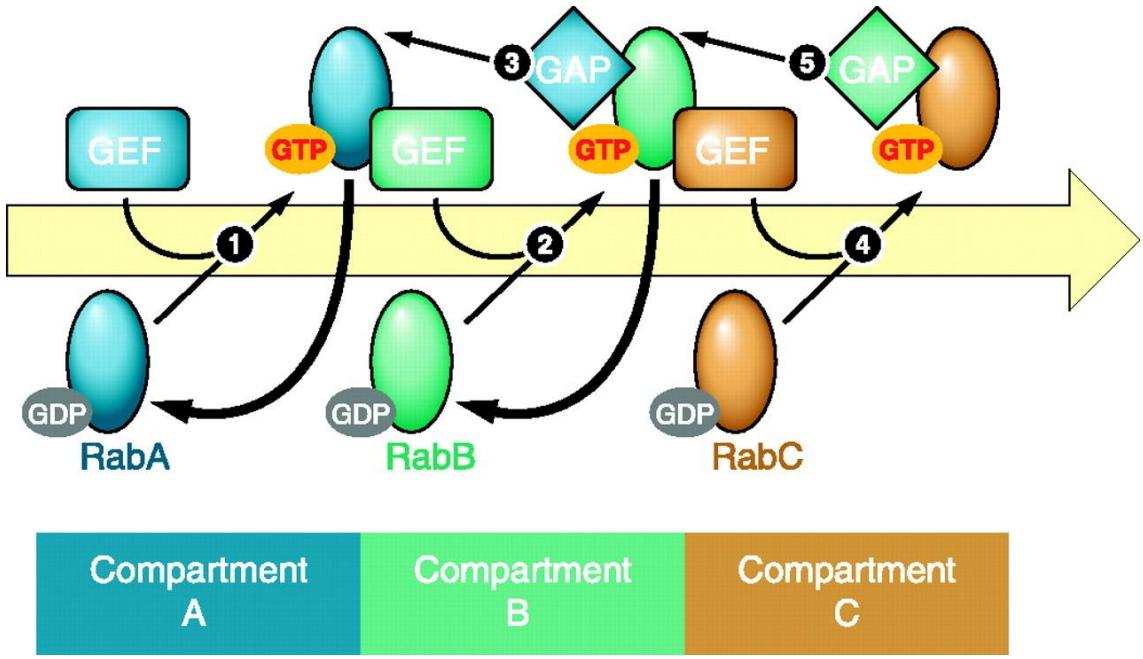

Figure 1.6: Rab cascades ensure ordered recruitment of Rabs along a trafficking pathway. Diagram showing how specific Rabs recruit Rab GEFs and GAPs as effector proteins to regulate the transition between Rab labelled membrane compartments. RabA reaches its target membrane and is activated by its cognate GEF (1). Once activated, RabA then recruits the RabB GEF to the membrane (2), and therefore ensures activation of RabB at the correct compartment. Active RabB subsequently recruits the GAP for RabA (3), which results in RabA inactivation and establishes the RabB labelled compartment. This cascade can continue down the trafficking pathway to regulate the spatio-temporal activation of Rabs. Figure from Hutagalung & Novick (2011).

1.4.3 Rab GTPases and their effectors in vesicle trafficking

Effector proteins are generally defined as interacting with the active GTP-bound Rab and mediating downstream processes (Grosshans et al. 2006). However effectors have been characterised that bind preferentially to GDP-bound Rabs, for example protrudin, a

Rab9 effector (Shirane & Nakayama 2006). Rab effectors mediate the different stages of vesicle transport (Figure 1.7); vesicle budding, movement, tethering and fusion, and specific effectors can be recruited for each Rab-defined trafficking pathway. Currently our knowledge of Rab effectors in plants is very limited, therefore examples of effectors shown here predominantly relate to metazoan systems.

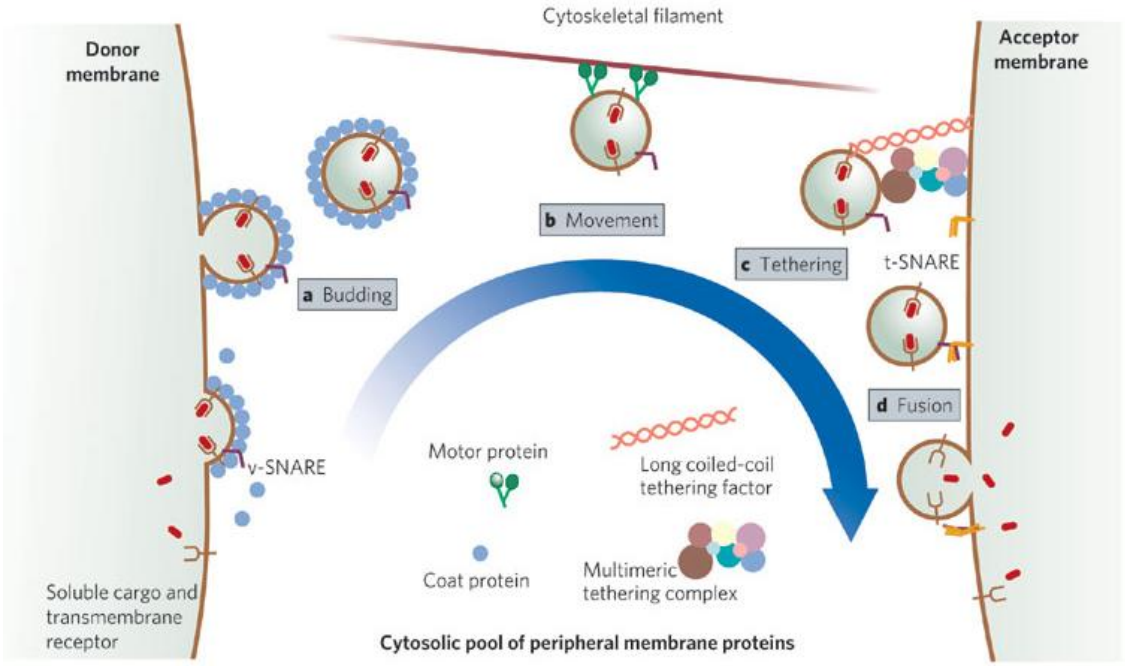

Figure 1.7: Stages of vesicle transport. Diagram shows the different stages of vesicle transport from donor to acceptor membranes, and the range of proteins that can mediate these processes. (a) Cargo is first selected and vesicles are budded from the donor membrane. (b) Vesicles are transported along cytoskeletal filaments through interactions with motor proteins. (c) Prior to fusion, vesicles are tethered at the acceptor membrane through long coiled-coil proteins and multisubunit tethering complexes. (d) SNARE proteins mediate the fusion of vesicles at the acceptor membrane, which releases the cargo. Rab GTPases can recruit effector proteins that are involved in these different steps along the trafficking pathway. Figure used with permission from Behnia & Munro (2005).

The first stage in vesicle trafficking involves cargo selection and formation of the vesicle. A large proportion of intracellular trafficking utilises coated vesicles for transport (Hutagalung & Novick 2011). Coat proteins, including clathrin and coat protein complex I and II (COPI and COPII), are important in cargo selection, vesicle budding and fission (Gürkan et al. 2006). Sorting of cargo into specific vesicles is

determined by the interaction of transmembrane receptors with coat proteins (Stenmark 2009). However additional factors can influence coat protein recruitment including Rab GTPases. For example, the Rab9 effector, TIP47 (TAIL INTERACTING PROTEIN OF 47 kDa) interacts with the cytosolic tail of two mannose 6-phosphate receptors (MPRs), and this Rab9-TIP47-MPR interaction facilitates in the recycling of MPRs from late endosomes to the TGN (Carroll et al. 2001).

The directional targeting of vesicles can be achieved through movement along cytoskeletal 'tracks'. Metazoans utilise microtubules and AFs for vesicle transport through interactions with kinesin/dynein and myosin motors, respectively (Stenmark 2009). Rab GTPases are important signals that provide specificity to this transport and can recruit motor proteins directly or indirectly through adaptor proteins. Rab6 regulates the membrane dynamics of Golgi derived vesicles and recruits a kinesin-like protein (rabkinesin-6) as an effector for plus-end motility along microtubules (Echard et al. 1998; Fontijn et al. 2001). Rab GTPases can also recruit motor proteins through adaptor proteins. Melanophilin/Slac2a is a Rab27a effector that acts as an adaptor for a myosin Va motor and is important for melanosome transport (Fukuda et al. 2002; Strom et al. 2002; Nagashima et al. 2002).

Prior to membrane fusion, vesicles can be tethered to their destination membrane which ensures their accurate targeting (Hutagalung & Novick 2011). Rab GTPases can recruit effectors that form long-range contacts between vesicles, and these tethering factors fall into two main categories; multisubunit tethering complexes and long coiled-coil proteins (Behnia & Munro 2005). There are eight known multisubunit tethering complexes in eukaryotes which includes the Exocyst complex (Golgi-PM), the Conserved Oligomeric Golgi (COG) complex (endosome-Golgi, intra-Golgi) and the homotypic fusion and vacuole protein sorting (HOPS) tethering complex (vacuole-vacuole, endosome-vacuole) (Hutagalung & Novick 2011). The HOPS complex is a Ypt7p/Rab7 effector that has two Rab-binding sites at either end, and can thus bridge two Rab-labelled vacuolar compartments prior to fusion (Bröcker et al. 2012).

In addition to the multisubunit tethering complexes, various long coiled-coil tethers have also been identified. Coiled-coil domains are formed of α-helices that wrap around each other to form a supercoil (Mason & Arndt 2004). This feature is determined by a heptad repeat in the amino acid primary structure, with residues in the first and fourth positions being hydrophobic and the fifth and seventh positions being polar or charged

(Mason & Arndt 2004). This pattern forms a helix with hydrophobic residues in the helix core and charged residues forming electrostatic interactions between the helices. One of the key features of the coiled-coil domain is that it permits the dimerisation/oligomerisation of proteins (Rose & Meier 2004). The formation of a coiled-coil protein can create rod-like structures with specific functional domains (Rose & Meier 2004). This feature is crucial for fulfilling their function as tethering proteins, as they can protrude into the cytosol and capture trafficking vesicles. Several long coiled-coil proteins have been found to act as tethering factors, including the golgins and EARLY ENDOSOMAL ANTIGEN 1 (EEA1). Their association with membrane systems varies, and these proteins can contain transmembrane domains, interact with specific lipids and interact with Rab GTPases at the membrane (Gillingham & Munro 2003; Osterrieder 2012). The golgins are a large group of conserved coiled-coil tethers that function at the Golgi and many of these proteins contain multiple Rab-binding sites that are thought to form a matrix that tethers vesicles through the Golgi (Sinka et al. 2008; Hayes et al. 2009). EEA1 is a Rab5 effector that is important in endosome tethering in metazoans, and can bind active Rab5 on one membrane and phosphatidylinositol 3-phosphate (PI(3)P) on the opposing membrane (Christoforidis et al. 1999; Lawe et al. 2000; Mishra et al. 2010).

In addition to bridging two opposing membranes, tethers can also regulate the fusion event mediated by SNARE proteins. The exocyst, HOPS and COG complexes, as well as EEA1, have all been implicated in regulating SNARE proteins (Simonsen et al. 1999; Wiederkehr et al. 2004; Starai et al. 2008; Laufman et al. 2009). Therefore tethering proteins appear to have a dual role in capturing oncoming vesicles as well as ensuring the fidelity in membrane fusion (Hutagalung & Novick 2011).

The final stage of vesicle trafficking involves vesicular fusion with the destination membrane. Fusion is mediated by SNARE (Soluble NSF Attachment Protein Receptor) proteins that are found on opposing membranes, which are referred to as vesicle- and target-SNARES (v- and t-SNAREs). Interaction of these proteins forms a four-helix bundle that can overcome the energy needed for vesicle fusion (Chen & Scheller 2001; Whyte & Munro 2002). As mentioned previously, Rab proteins mostly regulate this fusion process indirectly through effector proteins such as tethering factors (Grosshans et al. 2006).

The activation of Rabs at membranes acts as a signal to recruit specific effector proteins that mediate these different trafficking steps. As well as motor proteins and tethering factors, various additional Rab effectors have been characterised. As mentioned previously, Rab GEFs and GAPs can act as effector proteins in 'Rab cascades'. Signalling proteins, examples of which include phosphatidylinositol kinases, can also be recruited as Rab effectors. These proteins generate specific lipid species in the membrane which can additionally act as a signal for protein interactions involved in membrane trafficking (Behnia & Munro 2005). For example, the Rab5 effector VPS34 (VACUOLAR PROTEIN SORTING 34) is a phosphatidylinositol-3-OH kinase, that generates PI(3)P lipids in early endosomes (Gillooly et al. 2000; Murray et al. 2002). The presence of these lipids and GTP-Rab5 on early endosomes then recruits EEA1 that can subsequently mediate endosomal tethering (Christoforidis et al. 1999; Gaullier et al. 2000). In addition, Rabs have also been shown to interact with ABPs. For example in animals, fascin, an actin-bundling protein, has been shown to be an effector of Rab35 and this interaction is important in filopodia formation in cell culture and bristle development in *Drosophila melanogaster* (Zhang et al. 2009).

Importantly, there are very few Rab effector proteins that have currently been described in plants. Those characterised include golgin proteins (Osterrieder et al. 2009), phosphatidylinositol kinases (Preuss et al. 2006; Camacho et al. 2009), and an E3 ubiquitin ligase (Antignani et al. 2015). Therefore identifying novel Rab effectors will increase our knowledge of how Rabs mediate distinct trafficking events in plants.

1.5 The NET superfamily

1.5.1 Introduction to the NET family

Recently the NETWORKED (NET) family of actin-binding proteins was discovered that could bridge the gap in our knowledge between plant actin and membrane structures (Deeks et al. 2012). Initially a high-throughput screen to identify the subcellular localisation of novel plant proteins was conducted by Escobar et al. (2003). This screen used an Arabidopsis cDNA library, created using randomized primers, that was later cloned into a tobacco mosaic virus (TMV) GFP expression vector and transiently transfected into *Nicotiana tabacum* leaf epidermal cells. The subcellular localisation of these cDNA-GFP fragments were then manually screened using confocal laser scanning microscopy (CLSM). One such fragment highlighted a striking

filamentous array, and was later identified to encode for the N-terminal 288 amino acids of a previously uncharacterised protein, located at gene locus At3g22790, which we later termed NETWORKED 1A (NET1A; Deeks et al. 2012).

Further studies then focussed on characterising the nature of this filamentous array. The same NET1A$^{1-288}$ fragment was fused to GFP and transiently transformed into *Nicotiana benthamiana* leaf epidermal cells under the expression of a cauliflower mosaic virus (CaMV) 35S promoter. Cytoskeletal disrupting drugs were applied to these NET1A$^{1-288}$-GFP expressing leaf sections, which demonstrated that actin depolymerising drugs, but not microtubule depolymerising drugs, could disrupt this network, suggesting that it decorates the actin cytoskeleton. This finding was further supported by colocalising the NET1A fragment with a known actin-binding marker mCherry-FABD2, which encompasses the second actin-binding domain of AtFim1 (Voigt et al. 2005). These studies therefore demonstrated that this fragment was capable of associating with the actin cytoskeleton (Calcutt 2009; Deeks et al. 2012).

Within this N-terminal NET1A fragment, residues 10-85 share a 73% homology to the N-terminal region of the previously characterised *Petunia inflata* KINASE INTERACTING PROTEIN 1 (KIP1; Skirpan et al. 2001). This domain (Pfam07765) was previously uncharacterised, however it was distinct from the central coiled-coil domain of KIP1 that was shown to specifically interact with the cytosolic domain of POLLEN RECEPTOR KINASE 1 (PRK1; Skirpan et al. 2001). It was therefore hypothesised that this conserved domain could be a direct actin-binding domain. Further studies using the first 94 amino acids of NET1A (NET1A$^{1-94}$) revealed that it could associate with actin filaments *in vivo* and bind directly to actin filaments *in vitro* using a high speed co-sedimentation assay. This minimal actin-binding region was termed the NET actin-binding (NAB) domain, which represents a novel plant-specific actin-binding motif, with no apparent primary sequence homology to known actin-binding domains (Deeks et al. 2012).

Through bioinformatics analysis, a total of thirteen sequences in the Arabidopsis proteome were identified that share this conserved N-terminal NAB domain, and were together termed the NET superfamily (Deeks et al. 2012). These proteins range in predicted size from 25 to 199 kDa. The family divides into four distinct subfamilies, defined by the sequence comparisons of the NAB domain as well as structural organisation of the C-terminal domains and protein length (Figure 1.8; Deeks et al.

2012; Hawkins et al. 2014). Each of these proteins share the conserved N-terminal NAB domain, and stretches of predicted coiled-coil domains in the C-terminus. The NAB domain of representative members of each subfamily have been shown to associate with actin filaments *in vivo,* through GFP fusion proteins and the transient *N. benthamiana* system (Deeks et al. 2012).

Having established that the NET family represents a novel family of actin-binding proteins, the subcellular localisation of the full-length proteins was subsequently investigated. Representative members of each subfamily have been shown to associate with different membrane systems in plant cells, as shown by the schematic diagram in Figure 1.9. GFP fusions to NET1A, expressed under its endogenous promoter, localised to the plasma membrane in the root, and showed an enrichment to the apical and basal membranes (Calcutt 2009; Deeks et al. 2012). NET1A was also shown to be enriched at the plasmodesmata, which was confirmed through immunogold labelling using an anti-NET1A antibody (Deeks et al. 2012). Publicly available microarray data suggests that the NET2 subfamily are mostly expressed in pollen (Dixon 2013; Hawkins et al. 2014). Expressing a NET2A-GFP fusion in Arabidopsis, under the control of the *NET2A* promoter, showed a localisation to distinct submicron foci at the plasma membrane of the growing pollen tube (Dixon 2013; Deeks et al. 2012). These punctae were arranged on actin filaments and represent a 'beads on a string' pattern that is characteristic of the NET proteins (Dixon 2013; Deeks et al. 2012). Similarly, transiently expressing full-length NET1A-GFP in *N. benthamiana* leaf epidermal cells labelled a 'beads on a string pattern', with discrete immobile punctae being observed on actin filaments (Deeks et al. 2012). Expressing a NET3A-GFP fusion protein in tobacco BY2 cells, under the control of a CaMV 35S promoter, labelled foci at the nuclear membrane and showed a 'beads on a string' pattern on cytosolic filaments. NET3C has recently been shown to associate with the ER-PM anchoring sites in *N. benthamiana* and Arabidopsis (Wang et al. 2014). Further studies have also demonstrated that NET3B can associate with the ER when expressed in *N. benthamiana* leaf epidermal cells (Wang & Hussey unpublished). Finally, NET4A localises to actin filaments surrounding the tonoplast in the Arabidopsis root, when expressed as a GFP fusion protein under the control of the *NET4A* promoter (Deeks et al. 2012). These studies therefore demonstrate that the NET family represents a novel family of actin-binding partners that associate with membrane systems in plants cells.

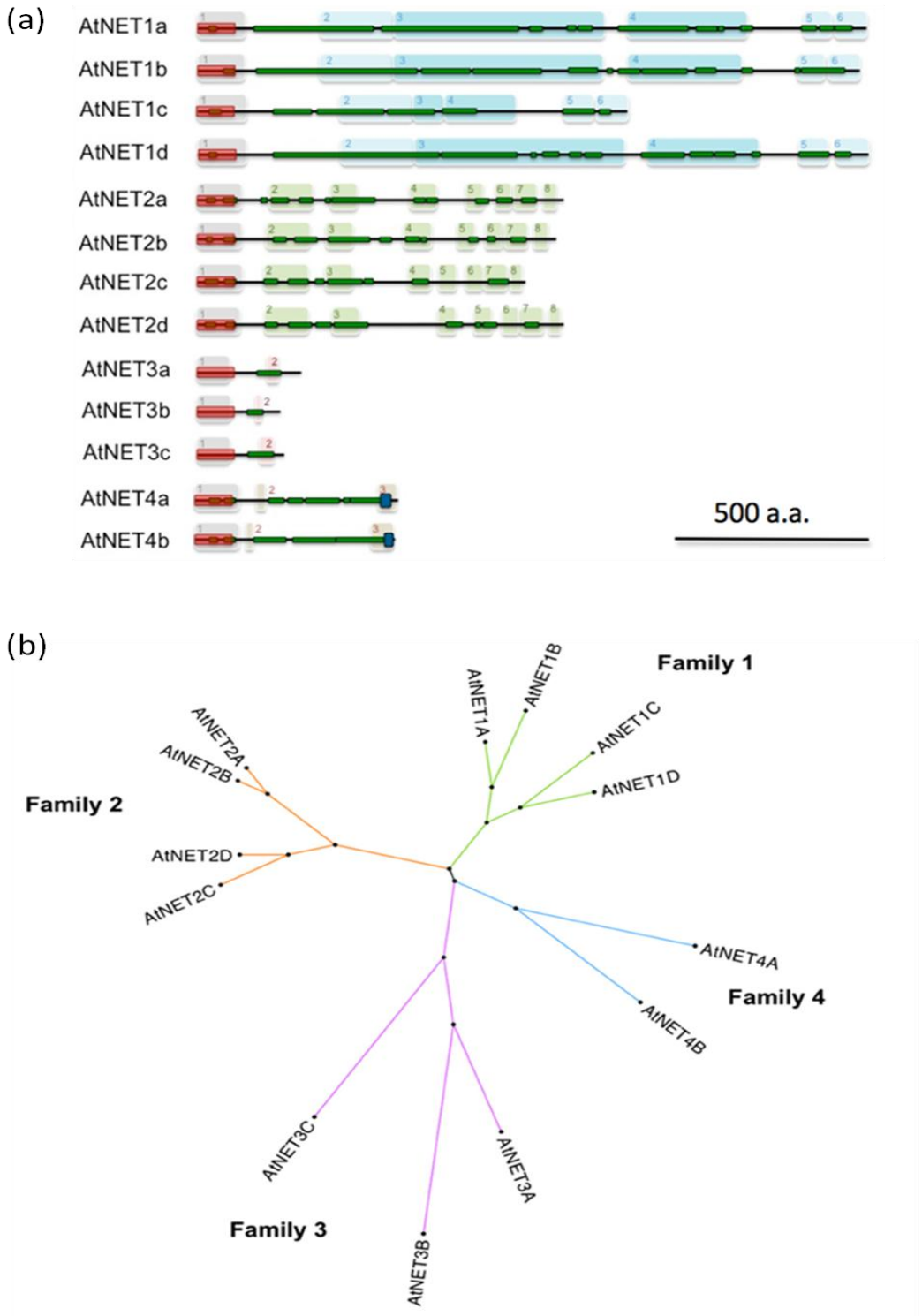

Figure 1.8: The Arabidopsis NET family. The thirteen proteins of the Arabidopsis NET family form four phylogenetically different subclades, based on sequence homology of the NAB domains and C-terminal structure. (a) Protein structure of the NET proteins; the NAB domain is shown in red and the coiled-coil domains are shown in green. Regions of homology that are shared within each subfamily are shown with numbered tiles. Figure used with permission from Deeks et al. (2012). (b) Cladogram showing the thirteen proteins of the NET family form four distinct subfamilies based on amino acid sequence comparisons of the NAB domain. Figure from Hawkins et al. (2014).

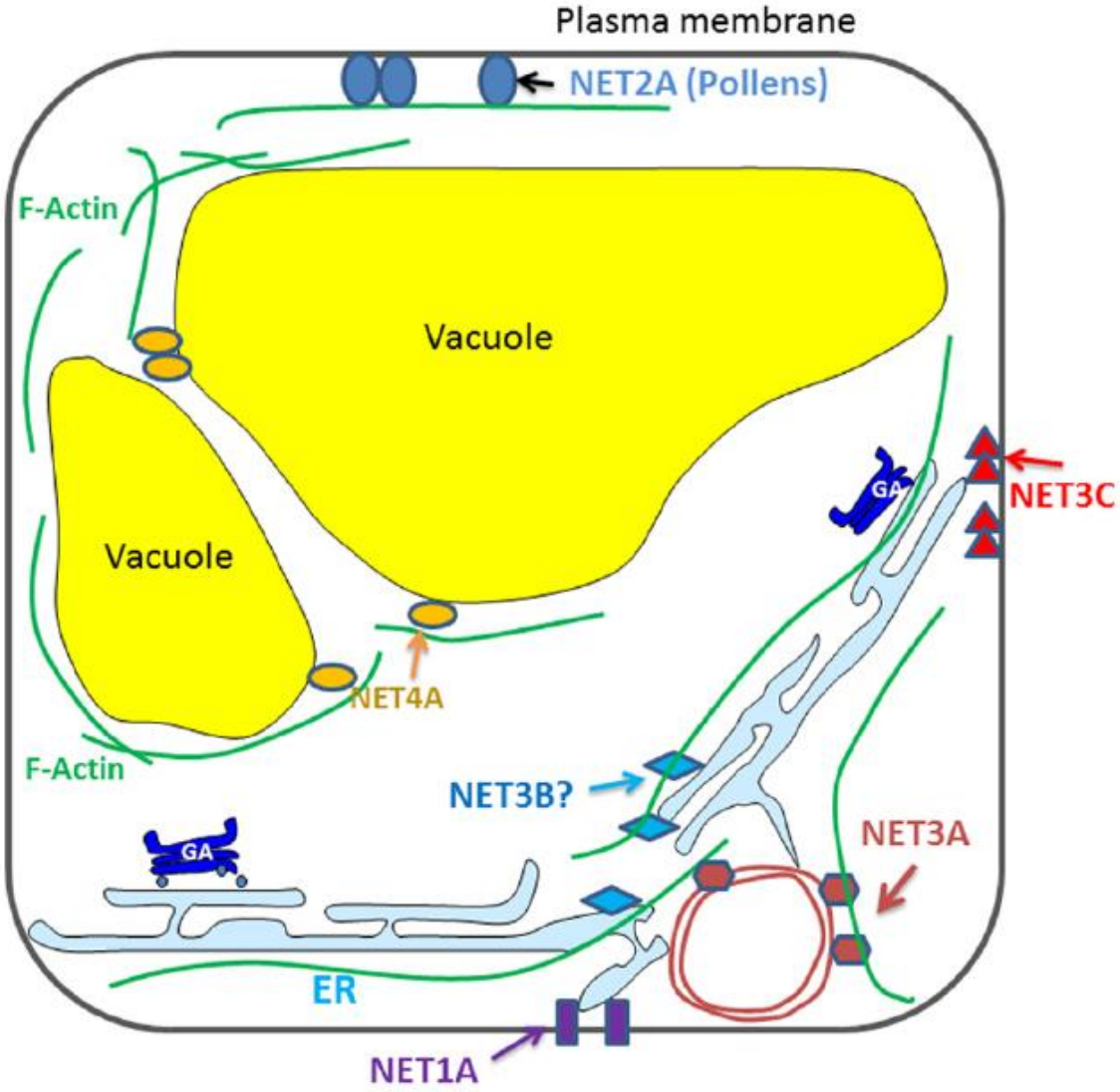

Figure 1.9: Subcellular localisation of the full-length NET proteins. Schematic diagram showing the subcellular localisation of various members of the NET family. Figure from Wang & Hussey (2015).

1.5.2 The evolution of the NET family

Having established that the NET family is composed of thirteen proteins in Arabidopsis, it was of interest to study the evolutionary history of the NET family. Bioinformatics analysis was performed to assess whether the NAB domain could be found in any additional genomes. Interestingly, the NAB domain could only be found in Tracheophyte genomes, and was not present in the Bryophytes or more ancient extant plant clades (Figure 1.10; Deeks et al. 2013; Hawkins et al. 2014). In addition, *NET* genes in the angiosperm genomes consistently group into the same four subfamilies, which therefore represent four phylogenetically distinct subclades.

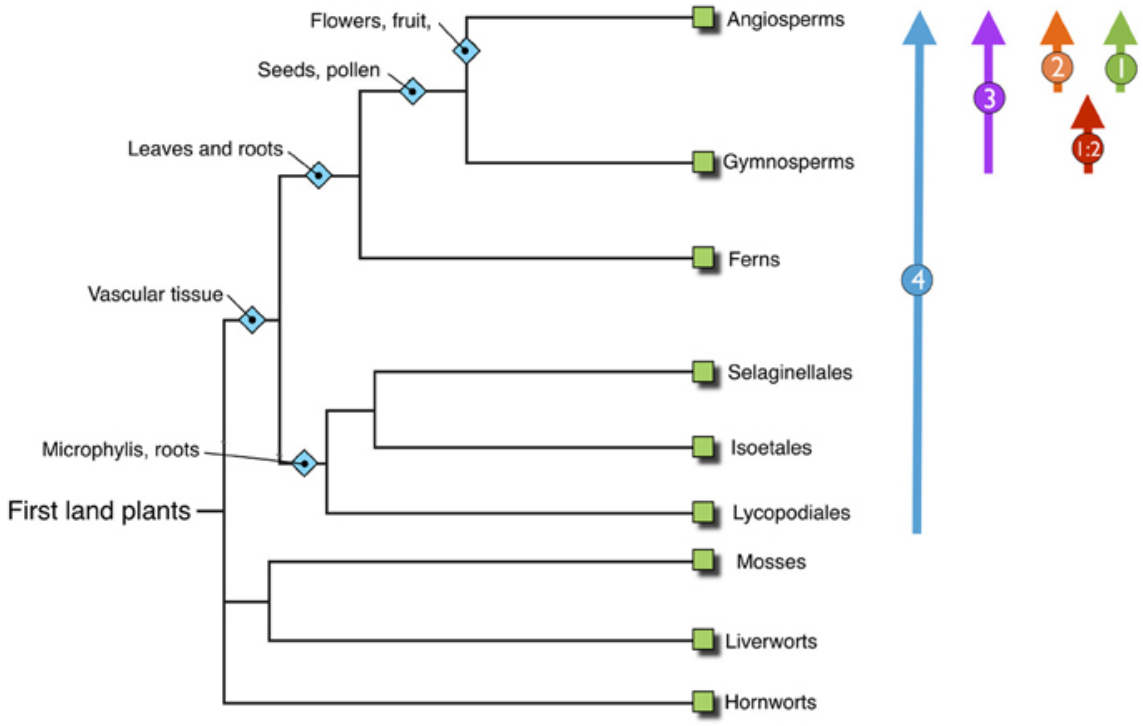

Figure 1.10: The emergence of the NET family during land plant evolution. Figure shows the results of recent bioinformatics analysis of the NET proteins, and depicts the appearance of the NET subfamilies in relation to the evolution of land plants. The phylogenetic tree on the left shows the relationship of extant land plants and highlights key innovations in plant evolution. Coloured arrows indicate the NET subfamilies identified within these plant genomes; NET4 (blue), NET3 (purple), NET2 (orange), NET1/2 hybrid (red), NET1 (green). Figure adapted from Hawkins et al. (2014).

The first NET gene can be found in the genomes of *Selaginella moellendorffii*, a clubmoss (Lycophyte) which is an extant species of the earliest vascular plant (Deeks et al. 2012; Hawkins et al. 2014). Phylogenetic analysis revealed that the *S. moellendorffi* genome contains two NET proteins that are homologues of the NET4s. The emergence of the NET family in the Lycophytes, marks a significant point in land plant evolution, as it marks the onset of vascular development in plants (Banks 2009). This development enabled plants to transport water and nutrients through the vascular tissue, and permitted increased growth associated with mechanical stiffness provided by the lignified tissue. As NET4A associates with the tonoplast in the epidermis of the root, it is tempting to speculate that the earliest NET4 protein could have supported the vacuole against increased turgor pressure associated with vertical growth (Hawkins et al. 2014).

Bryophytes and Tracheophytes also differ in their cytoskeletal control of membrane dynamics. Higher plants predominantly utilise the actin cytoskeleton for regulating endomembrane and organelle dynamics, including the control of vacuole morphology (Boevink et al. 1998; Sheahan et al. 2004; Higaki et al. 2006). However, *Physcomitrella patens*, a Bryophyte, regulates vacuole dynamics through microtubules and not the actin cytoskeleton (Oda et al. 2009). Therefore there appears to be a divergence in the cytoskeletal control of vacuole dynamics during land plant evolution. The emergence of the NETs during Tracheophyte evolution correlates with this switch to actin based membrane dynamics (Hawkins et al 2014).

During land plant evolution, the NET family diversified and three NAB isoforms can be found in the genomes of the Gymnosperms, which represent NET4, NET3 and a unique NET1/2 hybrid (Hawkins et al. 2014). The NET1/2 hybrid shares several unique characteristics that are found in the NET1 and NET2 NAB domains. However, in the angiosperm genomes, the NET1 and 2 subfamilies diverge into distinct subfamilies, with the NET2s representing a predominantly pollen expressed subfamily (Dixon 2013; Hawkins et al. 2014). The diversification of the NET family appears to correlate with major developments in land plant evolution.

1.5.3 NET4A: an actin-vacuole adaptor

The NET4s were the first NET proteins to emerge during land plant evolution, and in Arabidopsis the NET4 subfamily is composed of two proteins; NET4A and NET4B. Previous studies on NET4A, using a NET4A-GFP fusion protein under the control of the endogenous *NET4A* promoter, revealed that it localised to actin filaments surrounding the tonoplast membrane in the root (Figure 1.11, Deeks et al. 2012). This therefore suggests that it could have an important role in linking the actin cytoskeleton to the vacuole membrane.

The vacuole can occupy up to 90% of the total volume of plant cells (Taiz 1992). Water can flow into the vacuole, generating turgor pressure in connection with the plant cell walls, which allows plant cell wall expansion (Zouhar & Rojo 2009; Zhang et al. 2014). As discussed previously, the vacuole is also part of both the biosynthetic and endocytic pathways. Proteins can be targeted to the vacuole for degradation; for example the PIN1 auxin efflux carrier is targeted to the vacuole in response to cytokinin signalling (Marhavý et al. 2011). Hydrolytic enzymes and the acidity of the lytic vacuole lumen govern the degradative properties of this compartment (Marty 1999). Plants also contain

protein storage vacuoles (PSVs), that are mainly found in the embryo and these vacuoles provide a source of nitrogen during seed germination (Frigerio et al. 2008; Feeney et al. 2013).

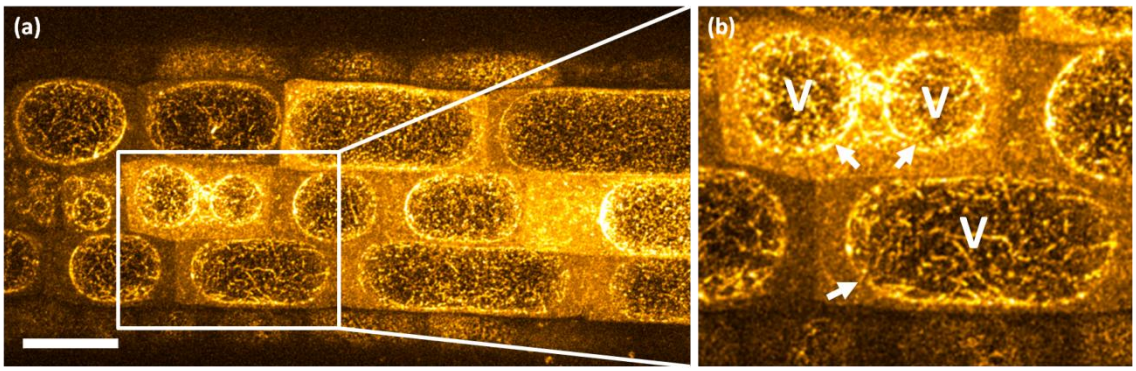

Figure 1.11: Subcellular localisation of NET4A-GFP. (a) Image shows a z-projection of the localisation of NET4A-GFP expressed under the *NET4A* promoter in stably transformed Arabidopsis. (b) Digital zoom was used to demonstrate NET4A-GFP localisation in the white boxed area. NET4A-GFP localises to filaments surrounding the vacuole in the epidermis of Arabidopsis roots. Figure used with permission from Deeks et al. (2012). V = vacuole, arrowhead = tonoplast, scale bar: 20 μm.

The vacuole is a very dynamic organelle and can undergo major morphological changes during development and responses to the environment. During root development, vacuole biogenesis occurs in the root tip, and the vacuole changes from a highly convoluted structure in the dividing cells of the meristem, into the large central vacuole observed in differentiated cells (Viotti et al. 2013). Dramatic changes to vacuole morphology are also observed during guard cell opening and closing. These highly specialised cells sense and respond to environmental changes through altering their volume and turgor pressure, thus regulating stomatal aperture and gaseous exchange with the environment (Gao et al. 2009). During guard cell closure, the vacuole changes from a large central turgid structure and decreases in volume and becomes highly convoluted (Gao et al. 2005; Tanaka et al. 2007; Andrés et al. 2014). Similarly, the actin cytoskeleton rearranges from a radial array of actin filaments, in open guard cells, to a more randomly orientated longitudinal array during guard cell closure (Hwang & Lee 2001; Gao et al. 2008; Higaki et al. 2010). It is currently unclear whether the actin cytoskeleton determines these dynamic vacuole changes, however one study has demonstrated that pharmacologically disrupting actin filaments prevented the reformation of the vacuole during guard cell opening (Li et al. 2013). Similarly, a

mutant of the Arp2/3 complex prevented vacuole reformation during guard cell opening (Li et al. 2013). Although these studies suggest that the actin cytoskeleton could regulate vacuole dynamics in guard cells, there is no currently characterised molecular adaptor between these two systems.

The actin cytoskeleton has been shown to be in close association with the tonoplast (Higaki et al. 2006), and numerous studies have demonstrated that the actin cytoskeleton is important in maintaining the morphology of the vacuole. Various studies have shown that transvacuolar strands (TVS), that are important for the movement of organelles within the cell (Nebenführ et al. 1999; van Gestel et al. 2002; Ruthardt et al. 2005), depend on an intact cytoskeleton. Pharmacologically disrupting the actin cytoskeleton in tobacco BY2 cells results in the loss of these vacuolar structures (van Gestel et al. 2002; Higaki et al. 2006; Sheahan et al. 2007). In addition, mutants of the Arp2/3 complex have been shown to cause defects in trichome development, associated with a disrupted actin cytoskeleton and vacuole morphology (Mathur et al. 2003). These studies therefore demonstrate that the link between the actin cytoskeleton and the vacuole is crucial in maintaining vacuole morphology.

Currently our knowledge on the molecular mechanism by which these systems are linked remains poorly understood. However two proteins have been recently characterised that could link these two structures; the vacuolar H^+-ATPase (V-ATPase) B subunits (Ma et al. 2012); and NET4A (Deeks et al. 2012). The conserved V-ATPase is a multisubunit proton pump that is important for the acidification of intracellular compartments, and associates with the TGN and tonoplast in plants (Futai et al. 2000; Dettmer et al. 2006; Ma et al. 2012). In animals and yeast, the V-ATPase B and C subunits have been shown to bind directly to F-actin with high affinity (Holliday et al. 2000; Vitavska et al. 2005; Zuo et al. 2008). The recent study on the three Arabidopsis V-ATPase B subunits demonstrated that they can indeed bind, bundle and stabilise actin filaments *in vitro* (Ma et al. 2012). However the functional importance of this association *in planta* remains to be tested experimentally.

Significantly, NET4A is currently the only other known actin-binding protein that associates with the tonoplast in plants (Figure 1.11; Deeks et al. 2012). The localisation of NET4A to the actin cytoskeleton surrounding the tonoplast suggests that it could have a role in regulating vacuole dynamics. Although NET4A has been shown to associate at this membrane-actin interface, very little is currently known about NET4B.

This project therefore focussed on characterising this novel plant-specific protein as it could greatly increase our knowledge of actin-membrane associations in plant cells.

1.6 Characterisation strategy for NET4B

Numerous different experimental approaches were utilised during this project in order to characterise NET4B. Firstly, bioinformatics analysis was used to predict its secondary structure and identify additional conserved domains with other NET proteins, namely the conserved C-terminal IRQ domain shared with NET4A, NET4B, NET3A and NET3C. Publicly available microarray data was then examined in order to identify the tissue expression profile of *NET4B* as well as gene changes in response to different stresses. These analyses are described in Chapter 3.

As NET4B is a member of the NET superfamily of actin-binding proteins, it was therefore imperative to establish whether NET4B similarly associates with the actin cytoskeleton. Chapter 4 studies the *in vivo* localisation of NET4B and focuses on establishing whether this protein, and the NET4B-NAB domain, associates with the actin cytoskeleton *in vivo*. This was achieved through transiently transforming *N. benthamiana* leaf epidermal cells with NET4B-GFP and NET4B-NAB-GFP fusion constructs and imaging their localisation. The nature of the filamentous arrays decorated by these constructs was investigated through the application of cytoskeleton disrupting drugs and colocalisation studies with a known actin marker. Furthermore, the subcellular localisation of NET4B truncations was studied in an attempt to identify additional functional domains. Finally, an *in vitro* F-actin binding assay was performed to determine the nature of the actin association with the NET4B-NAB domain.

The *in situ* expression pattern and subcellular localisation of NET4B in Arabidopsis was investigated using four different experimental approaches and these are described in Chapter 5. Firstly, the transcriptional expression profile of *NET4B* was established by expressing the GUS reporter gene under the control of the *NET4B* promoter in stably transformed Arabidopsis plants. Secondly, specific anti-NET4B polyclonal antibodies were generated and used to test the translational profile of NET4B in various Arabidopsis tissues through Western blot analysis. Thirdly, a NET4B-GFP fusion protein was expressed in transgenic Arabidopsis plants under the control of the endogenous *NET4B* promoter. Finally, the subcellular localisation of NET4B was

investigated *in planta* through immunogold labelling and transmission electron microscopy using the anti-NET4B antibodies.

Chapter six describes the experiments that were performed to identify potential interacting partners of NET4B. The first aspect of this analysis involved using the yeast-2-hybrid (Y2H) system to study whether NET4B is capable of interacting with itself and NET4A. Secondly, two Y2H screens were performed using either NET4B or the conserved C-terminal IRQ domain as bait. The potential interactors from this screen were then validated using the Y2H system. In addition to this screen, results from a Tandem Affinity Purification (TAP)-tagging screen using NET4A as bait, as well as results from a collaborative project with Dr. Ian Moore, demonstrated that the NET4s could interact with two vacuole associated Rab GTPases. The interaction between the NET4s and these Rabs was explored further using the Y2H system.

Chapter Seven outlines the experiments that were designed to discern a function for the *NET4s*. T-DNA insertion mutant lines in *NET4A* and *NET4B* were used to knock-out or knock-down the expression of these genes respectively. Genetic crosses were used to generate a double mutant of the two *NET4* genes, as there could be functional redundancy in this subfamily. These mutant lines were then studied for an observable phenotype relating to the *NET4s* expression pattern and subcellular localisation.

The final results chapter, Chapter 8, describes the identification of a novel family of Arabidopsis proteins that contain the C-terminal IRQ domain. Bioinformatics analysis was subsequently used to study the predicted secondary structure of these proteins, as well as their gene expression profiles, potential interacting partners, and predicted subcellular localisations.

The concluding chapter, Chapter 9, finishes with a discussion on the reported experimental findings and explores the potential role of the NET4s and the associated novel family of IRQ proteins.

Chapter 2 - Materials & Methods

2.1 Materials

2.1.1 Plant material

Nicotiana benthamiana plants were used for the transient transformation of GFP-fusion constructs in leaf epidermal cells and protein extraction followed by western blot analysis. *Arabidopsis thaliana* Columbia (Col-0) ecotype were used as the background line for immunogold labelling with the anti-NET4B antibody, protein extraction and western blot analysis, and creation of the stably transformed *NET4Bpro*::NET4B-GFP lines. The Col-0 seeds were originally obtained from Lehle seeds.

The *NET4Bpro*::GUS lines were created by Dr. Tim Hawkins through the *Agrobacterium tumefaciens* (referred to as Agrobacterium) floral dipping method of Arabidopsis (Col-0).

The SALK and SAIL T-DNA insertion lines were obtained from NASC and were used for the creation of the *net4b* and *net4a* homozygous lines as well as the subsequent double mutant line. The SALK_056957 line was used for *NET4B*, and the SALK_083604 and SAIL_116_C08 lines were used for *NET4A*.

2.1.2 Bacterial strains

Agrobacterium GV3101 strain was used for transient transformation of *N. benthamiana* leaf epidermal cells as well as stable transformation of Arabidopsis through the floral dipping method. The following *Escherichia coli* strains were used: DB3.1 for amplifying the empty Gateway vectors, DH5α for cloning, and Rosetta 2 for protein expression.

2.1.3 Yeast strains

Two strains of *Saccharomyces cerevisiae* were used: AH109 was used for autoactivation tests and for transformation with the bait constructs (pGBKT7) and the Y187 strain was used for the prey constructs and the cDNA library.

2.1.4 Vectors and constructs

All vectors used were commercially available, with the exception of: (1) pGAT4 that was developed by Dr. Tijs Ketelaar (Wageningen University) to create a Gateway compatible protein expression vector, (2) pBI101G vector that was developed by Dr. Martin Kieffer (University of Leeds) in order to create a Gateway compatible version of the pBI101 vector (Clontech). Table 2.1 summarises the vectors used in this project.

Vector name	Vector function	Vector size (bp)	Resistance	Supplier
pDONR207	Gateway entry vector	5585	Gentamicin (bacteria)	Invitrogen
pBI101G	Gateway β-glucuronidase expression vector under endogenous promoter	12200	Kanamycin (bacteria & plants)	University of Leeds
pGAT4	Gateway protein expression vector with N-terminal 6xHis-tag	5256	Ampicilin (bacteria)	Durham University
pMDC43	Gateway expression vector for N-terminal GFP fusion under 2x35S promoter	12460	Kanamycin (bacteria) Hygromycin (plants)	University of Zurich via ABRC
pMDC83	Gateway expression vector for C-terminal GFP fusion under 2x35S promoter	12513	Kanamycin (bacteria) Hygromycin (plants)	University of Zurich via ABRC
pMDC107	Gateway expression vector for C-terminal GFP fusion under endogenous promoter	11738	Kanamycin (bacteria) Hygromycin (plants)	University of Zurich via ABRC
pGBKT7	Gateway bait vector for Y2H studies. N-terminal GAL4 DNA binding domain fusion	9715	Kanamycin (bacteria) Tryptophan (yeast)	Durham University

pGADT7	Gateway prey vector for Y2H studies. N-terminal GAL4 activation domain fusion	10399	Kanamycin (bacteria) Leucine (yeast)	Durham University

Table 2.1: List of cloning and expression vectors

Dr. Tim Hawkins originally amplified and cloned the full length NET4B coding DNA sequence (CDS) from *Arabidopsis thaliana* 7-day old whole seedling tissue first strand cDNA and cloned it into the Gateway entry vector pDONR207. This clone was then used as a template for further cloning reactions performed in this project. Furthermore, Dr. Tim Hawkins previously cloned the NET4B-NAB domain (for N- and C-terminal fusions) into the pDONR207 construct, which was used for further cloning reactions during this project.

In addition, the *NET4Bpro*::NET4B-GFP construct in the pMDC107 vector was originally cloned by Dr. Tim Hawkins using genomic DNA derived from Arabidopsis (Col-0). This construct comprised the 1742 bp *NET4B* open reading frame (ORF) and an approximately 2 kb upstream region, as was used to create the *NET4Bpro*::GUS lines.

2.2 Molecular biology methods

2.2.1 Preparation of chemically-competent cells

2.2.1.1 *E. coli* strains

Glycerol stocks of DH5α were streaked onto solid LB media plates (5g/l yeast extract (Melford), 10 g/l peptone (Melford), 10 g/l NaCl (Fisher), 20 g/l agar (Melford), pH 7.0) and grown overnight for approximately 14-16 hours at 37 °C. Single colonies were used to inoculate a liquid culture of 100 ml SOB medium (2% tryptone (Melford), 0.5% yeast extract, 0.05% NaCl, 2.5 mM KCl, 10 mM $MgCl_2$ (BDH)) in a 1L conical flask, which was grown on a rotary shaker overnight at room temperature (~22 °C). The culture was grown to an OD_{600} of 0.4-0.6, and then incubated on ice for 10 minutes prior to pelleting the cells through centrifugation at 2,500 *g* for 5 minutes at 4 °C. The pellet was resuspended in 32 ml ice-cold TB buffer (10 mM PIPES (Melford) pH 6.7, 15 mM $CaCl_2.H_2O$, 250 mM KCl, 55 mM $MnCl_2.4H_2O$ (Sigma)) and incubated for a further 10 minutes on ice. The resuspended cells were centrifuged at 2500 *g* for 5 minutes at 4°C. The resultant pellet was resuspended in 8 ml ice-cold TB buffer,

supplemented with 0.7% DMSO (Sigma) after full resuspension, and the cells were incubated on ice for 10 minutes. Aliquots of the cells (~200µl) were made in microcentrifuge tubes, snap frozen in liquid nitrogen and stored permanently at -80°C.

2.2.1.2 Agrobacterium GV3101 strains

Glycerol stocks of GV3101 cells were streaked onto solid YEB media plates (1 g/l yeast extract, 5 g/l meat extract (Merck), 5 g/l peptone, 5 g/l sucrose (Melford), 0.5 g/l $MgSO_4.7H_2O$ (BDH), 20 g/l agar (Melford), pH 7.0; 25 µg/ml gentamicin (Melford), 25 µg/ml rifampicin (Melford)) and grown for 2 days at 30 °C. Single colonies were used to grow an overnight YEB culture (containing 25 µg/ml gentamicin, 25 µg/ml rifampicin) for 14-16 hours at 30 °C. 1ml of the overnight culture was used to inoculate 50 ml YEB (containing 25 µg/ml gentamicin, 25 µg/ml rifampicin), which was grown for approximately 4-5 hours until the cells reached an OD_{600} of 0.5-0.6. The culture was centrifuged at 3000 x g for 5 minutes at 4°C, and the pellet was resuspended in 50 ml ice-cold 0.15 M NaCl. Cells were incubated for 15 minutes on ice before a final centrifugation at 3,000 *g* for 5 minutes at 4°C. The resultant pellet was resuspended in 5 ml ice-cold 20 mM $CaCl_2$ (BDH), and aliquots of 200 µl were flash frozen in liquid nitrogen and stored at -80 °C.

2.2.2 Transformation of chemically competent cells using the heat shock method

2.2.2.1 *E. coli* strains

Approximately 100 ng plasmid DNA was added to 100-200 µl competent *E. coli* cells and incubated on ice for 15 minutes. Cells were placed on a heat block at 42 °C for 45 seconds and immediately transferred to ice for 2 minutes. 400 µl LB liquid medium was subsequently added to the cells and they were left to recover shaking at 37 °C for 1 hour. Cells were centrifuged at 3,000 *g* for 2 minutes and resuspended in approximately 100 µl LB liquid medium before being spread out on solid LB selective plates, and grown for 14-16 hours at 37 °C.

2.2.2.2 Agrobacterium strains

Approximately 100 ng plasmid DNA was added to 100-200 µl competent Agrobacterium cells on ice. Cells were flash frozen in liquid nitrogen then transferred to a water bath at 37 °C for 5 minutes. 400 µl YEB liquid medium was added to the cells and they were left to recover shaking at 30 °C for 2-3 hours. Cells were centrifuged at 3,000 *g* for 2 minutes and resuspended in approximately 100 µl YEB liquid medium

before being spread out on solid YEB selective plates (25 μg/ml gentamicin, 25 μg/ml rifampicin plus plasmid selection), and grown for 2 days at 30 °C.

2.2.3 Plasmid DNA purification

Plasmid DNA was purified using the Promega Wizard Plus SV Miniprep DNA Purification System. Single colonies were used to inoculate an overnight liquid medium culture. Cells were then centrifuged at 3,000 *g* for 5 minutes and the resulting pellet was resuspended and lysed to break open the cells. Lysis was terminated using a neutralising solution, and alkaline phosphatase was added to inactivate released bacterial proteins that could affect DNA purity. The lysate was cleared through centrifugation and transferred into a customised spin column containing a DNA binding matrix. The spin column was washed with buffer and the DNA was eluted in 50-100 μl nuclease-free water and stored at -20 °C.

2.2.4 Restriction digests

Restriction digests of the transformed plasmids were routinely used as a diagnostic technique to confirm the presence of the inserted sequence. Digests typically contained: 2 μl of the appropriate 10x reaction buffer, 1 μl restriction enzyme, 2 μl purified plasmid DNA (as described in 2.2.3), 15 μl sterilised distilled H_2O (sdH_2O). Digest reactions were incubated at 37 °C for 2 hours and resolved using agarose gel electrophoresis (see 2.2.8).

2.2.5 RNA purification

Total RNA was purified from 15-day old vertically grown Arabidopsis seedlings of the *net4b.1*, *net4a.1*, *net4b.1/net4a.1* and azygous homozygous F_3 generation, using the Qiagen RNeasy Mini kit. Approximately 100 mg of tissue was weighed and transferred into microcentrifuge tubes. Tissue was flash frozen in liquid nitrogen and ground using a liquid nitrogen cooled micropestle. Cells were lysed using 450 μl of RLT buffer (containing 10 μl/ml ß-mercaptopethanol (Sigma)) and the lysate was centrifuged through a QIAshredder spin column at 8,000 *g* for 2 minutes, which removes plant debris and homogenises the lysate. The cleared lysate was mixed with a 0.5x volume of 96-100% ethanol (Riedel-de-Häen) and applied to an RNeasy spin column, which contains an RNA-binding silica-based membrane, and the sample was centrifuged at 8,000 *g* for 15 seconds.

An optional on-column DNase digestion step was then performed to remove any genomic DNA contamination using the RNase-Free DNase Set (Qiagen). The RNA-binding membrane was first washed with 350 µl buffer RW1, before DNase I was applied to the membrane and incubated for 15 minutes at room temperature. The digested DNA was removed through two subsequent wash steps with buffer RPE. RNA was eluted in RNase-free water and stored at -80 °C.

2.2.6 cDNA synthesis

cDNA was synthesised from Arabidopsis total RNA extractions (according to 2.2.5), using the GoScript Reverse transcription system (Promega) using oligo$(dT)_{15}$ primers and a reverse transcriptase enzyme (GoScript reverse transcriptase). Heating steps were performed using a G-Storm (GRI) PCR machine.

Firstly, the following components were mixed in a PCR tube: 1 µl oligo$(dT)_{15}$ primer (0.5 µg/reaction), 3 µg RNA and nuclease-free water was added to a final volume of 10.2 µl. Samples were initially heated to 70 °C for 5 minutes and then transferred to ice for 5 minutes. The reverse transcription mix was added to the PCR tube, and consisted of: 4 µl GoScript 5x Reaction buffer, 1.8 µl $MgCl_2$ (final concentration 2.25 mM), 1 µl PCR nucleotide mix (final concentration of 0.5 mM for each dNTP), 1 µl recombinant RNasin ribonuclease inhibitor, 1 µl GoScript reverse transcriptase. The reverse transcription mix and RNA/primer mix were combined and mixed with gentle pipetting to give a total volume of 20 µl. Primers were annealed at 25 °C for 5 minutes before an extension step at 42 °C for 1 hour for first-strand cDNA synthesis. The reverse transcriptase reaction was terminated through a final inactivation step at 70 °C for 15 minutes and cDNA was stored at -20 °C.

2.2.7 Genomic DNA extraction using the Edwards prep method

Genomic DNA was extracted from leaf tissue as described in (Edwards et al. 1991). Rosette leaves of approximately 2 cm in length were excised from 4-week old Arabidopsis plants and flash frozen in liquid nitrogen. Frozen leaf tissue was ground using a liquid nitrogen cooled micropestle and 400 µl extraction buffer (250 mM NaCl, 200 mM TrisHCl (Fisher) pH 7.5, 25 mM EDTA (Ethylenediaminetetraacetic acid (Sigma)), 0.5% (w/v) sodium dodecyl sulphate (SDS, (BDH)) was added and the samples were vortexed for 5 seconds. Leaf debris was pelleted through centrifugation at 16,100 *g* for 10 minutes, and 200 µl of the resultant supernatant was removed and

combined with an equal volume of isopropanol (BDH) in order to precipitate the genomic DNA. Samples were incubated at room temperature for 2 minutes before centrifugation at 16,100 *g* for 5 minutes. The supernatant was removed, and the resulting pellet was washed with 70% (v/v) ethanol, before a final centrifugation at 16,100 *g* for 5 minutes. The ethanol was carefully removed and the sample was left to dry at 37 °C for 30 minutes. The pellet was then resuspended in 30 µl nuclease-free water and stored at -20 °C.

2.2.8 Agarose gel electrophoresis

Agarose gels were typically prepared by dissolving 1% or 3% (w/v) Agarose Low EEO (Melford) in 1x TAE buffer (40 mM Tris acetate, 1 mM EDTA (Ethylenediaminetetraacetic acid)) through heating. Once cooled to room temperature, ethidium bromide (BDH) was added (5 µl per 200 ml 1 x TAE), and the liquid gel mixture was poured into trays to set. DNA loading buffer blue (Bioline; 5x stock) was added to DNA samples prior to loading into the wells. Hyperladder I and V (Bioline) and 2-Log DNA Ladder (NEB) were typically used as molecular weight standards. Gels were run in an electrophoresis tank containing 1x TAE. 1% were run at 100V for 20-30 minutes, 3% gels were run at 70V for 50-90 minutes. Gels were imaged using a Bio-Rad Gel-Doc 1000 system.

2.2.9 Amplification of fragments of interest using the Polymerase Chain Reaction

The polymerase chain reaction (PCR) was used to amplify fragments of interest from cDNA, gDNA or purified plasmid DNA. When high fidelity of replication was needed, the Phusion (NEB) DNA polymerase was used.

For reactions using the Phusion DNA polymerase, the following PCR reaction was set up (for a 20 µl total reaction): 12.4 µl sdH_2O, 4 µl 5xPhusion HF or GC buffer (NEB), 0.4 µl 10 mM dNTPs (made from 100 mM stocks of dATP, dGTP, dCTP, dTTP), 1 µl forward primer (10 µM stock; Eurofins/IDT), 1 µl reverse primer (10 µM stock; Eurofins/IDT), 1 µl template DNA and finally 0.2 µl Phusion DNA polymerase. The typical PCR programme consisted of the following stages:

Stage	Temperature (°C)	Time	Cycles
Initial Denaturing	98	30 s	1
Denaturing	98	10 s	35
Annealing	55-65	15 s	
Extension	72	30 s/kb	
Final extension	72	10 mins	1

Table 2.2: Standard PCR conditions using Phusion DNA polymerase

Annealing temperature and extension time was varied depending on the base composition and size of the fragment. Annealing temperature was typically set at 5 °C below the predicted melting temperature of the primers.

The Phusion DNA polymerase was used for amplification of all genes and fragments used for cloning reactions. All NET4B truncations were amplified using the full-length NET4B in the pMDC83 vector as the template DNA. DEP1, RabG3a, RabG3f, RabD2a, RabA5c and RabF2a were amplified from first-strand cDNA synthesised from 5-day old Arabidopsis seedling RNA. Gene-specific primers are listed in Appendix 1.

When high-fidelity of replication was not essential, for example genotyping PCR reactions, the Biotaq DNA polymerase (Bioline) or MyTaq DNA polymerase (Bioline) were used. For reactions using the Biotaq DNA polymerase, the following typical PCR reaction was set up (for a 25 µl total reaction): 17.85 µl sdH_2O, 2.5 µl 10xNH_4 buffer (Bioline), 1 µl 50 mM $MgCl_2$ (Bioline), 0.5 µl 10 mM dNTPs (made from 100 mM stocks of dATP, dGTP, dCTP, dTTP), 1 µl forward primer (10 µM stock; Eurofins/IDT), 1 µl reverse primer (10 µM stock; Eurofins/IDT), 1 µl template DNA and finally 0.15 µl Biotaq DNA polymerase. The typical PCR programme for Biotaq DNA polymerase consisted of the following stages:

Stage	Temperature (°C)	Time	Cycles
Initial Denaturing	95	1 min	1
Denaturing	95	30 s	35
Annealing	55-65	30 s	
Extension	72	30 s/kb	
Final extension	72	10 mins	1

Table 2.3: Standard PCR conditions using Biotaq DNA polymerase

As well as Biotaq DNA polymerase, MyTaq DNA polymerase was used as it has a much faster extension time. For reactions using the Mytaq DNA polymerase, the

following typical PCR reaction was set up (total volume: 25 µl): 16.85 µl sdH_2O, 5 µl 5x MyTaq Reaction Buffer (contains 5 mM dNTPS, 15 mM $MgCl_2$, stabilisers and enhancers), 1 µl forward primer (10 µM stock; Eurofins/IDT), 1 µl reverse primer (10 µM stock; Eurofins/IDT), 1 µl template DNA and finally 0.15 µl MyTaq DNA polymerase. The typical PCR programme for MyTaq DNA polymerase consisted of the following stages:

Stage	Temperature (°C)	Time	Cycles
Initial Denaturing	95	1 min	1
Denaturing	95	15 s	35
Annealing	55-65	15 s	
Extension	72	15 s*	

Table 2.4: Standard PCR conditions using MyTaq DNA polymerase.

Similarly to the Phusion DNA polymerase PCR reactions, annealing temperatures and extension times were varied when using Biotaq and MyTaq DNA polymerase. The extension time for MyTaq DNA polymerase was typically set at 15 seconds as this is sufficient to amplify 1-5 kb. Annealing temperature was typically set at 5 °C below the predicted melting temperature of the primers.

2.2.10 Cloning using the Gateway cloning system

The Gateway cloning system (Invitrogen) was used for all cloning reactions.

2.2.10.1 BP reaction

The BP reaction was used to insert PCR amplified fragments (as described in 2.2.9) into the entry vector pDONR207. The BP reaction was set up as follows: 1-7 µl PCR product, 1 µl pDONR207 (150 ng/µl), made up to a total volume of 8 µl with 1x TE buffer (10mM Tris.HCl pH 8.0, 1mM EDTA), 2 µl BP Clonase II enzyme mix was then added and the reaction was incubated at 25 °C for 1 hour. The reactions were terminated with the addition of 1 µl Proteinase K followed by a 10 minute incubation at 37 °C.

The recombinant entry vector was transformed into competent DH5α *E. coli* cells (as described in 2.2.2.1) and the transformed cells were streaked onto LB agar plates (25 µg/ml gentamicin). Restriction digests (according to 2.2.4) were used to confirm the presence of the insert in the clones, followed by DNA sequencing of the insert fragment (as described in 2.2.11).

2.2.10.2 LR reaction

The LR reaction was used to transfer fragments of interest from the entry vector to the destination vector. Several destination vectors were used during this project as listed in Table 2.1. The LR reaction mix was set up as follows: 1 µl pDON207 entry vector containing insert fragment (150 ng/µl), 1 µl of the appropriate destination vector (150 ng/µl), 6 µl 1x TE buffer (pH 8.0), finally 2 µl LR Clonase II enzyme mix was added and the reaction was incubated at 25 °C for 1 hour. The reactions were terminated with the addition of 1 µl Proteinase K followed by a 10 minute incubation at 37 °C.

The recombinant destination vector was transformed into competent DH5α *E. coli* cells (as described in 2.2.2.1) and the transformed cells were streaked onto LB agar plates containing the appropriate selection described in Table 2.1. Restriction digests (see 2.2.4) were used to confirm the presence of the insert in the clones, followed by DNA sequencing of the insert fragment (according to 2.2.11).

2.2.11 DNA sequencing

Durham University Biological Sciences (DBS) Genomics performed all DNA sequencing reactions using an Applied Biosystems 3730 DNA Analyser.

2.2.12 Site-directed mutagenesis

Site-directed mutagenesis was used to generate constitutively-active or dominant-negative mutations of RabG3a and RabG3f, and was performed using the QuikChange Lightning Site-Directed Mutagenesis Kit (Agilent Technologies). RabG3a and RabG3f clones in pDONR207 were used as the dsDNA templates for the reaction. Primers were designed to have a length of 25-45 bp, with a melting temperature (T_m) ≥78 °C according to the following formula:

$$T_m = 81.5 + 0.41(\%GC) - (675/\text{number of bases}) - \%\ \text{mismatch}$$

Desired mutations were designed to be in the centre of the primer. For the T22N mutation in both RabG3a and RabG3f, the 'ACC' sequence (threonine) was mutated to 'AAT' or 'AAC', respectively, which codes for an asparagine residue. For the Q67L mutation; the 'CAA' and 'CAG' sequences in RabG3a and RabG3f, respectively, were mutated to 'CTT', changing glutamine for leucine. The mutagenesis reactions were set up in microcentrifuge tubes and included: 5 µl 10x reaction buffer, 1 µl dsDNA template (100 ng), 1 µl each of the forward/reverse mutagenesis primer (10 pmol stock,

see Appendix 1.6 for primer sequences), 1 µl dNTP mix, 1.5 µl QuikSolution reagent, sdH_2O to a final volume of 50 µl and 1 µl QuikChange Lightning enzyme (*Pfu*-based DNA polymerase). Reactions were then run using a thermal cycler using the following protocol:

Stage	Temperature (°C)	Time	Cycles
Initial Denaturing	95	1 min	1
Denaturing	95	30 s	18
Annealing	60	30 s	
Extension	68	3 mins	
Final extension	68	5 mins	1

Table 2.5: Thermal cycler programme for the mutagenesis PCRs

Following thermal cycling, the parental methylated and hemimethylated DNA was digested with the addition of 2 µl *Dpn* I enzyme and incubation at 37 °C for 5 minutes. Mutated samples were then transformed into chemically competent *E. coli* (as described in 2.2.2.1), and grown overnight on LB agar plates (containing 25 µg/ml gentamicin). Plasmids were subsequently purified (according to 2.2.4) and mutations were confirmed through DNA sequencing (see 2.2.11).

2.2.13 Agrobacterium-mediated transient transformation of *N. benthamiana* leaf epidermal cells

The protocol for transient *N. benthamiana* transformation was based on the method described in Sparkes et al. (2006). Agrobacterium GV3101 cells transformed with the plasmid of interest (as described in 2.2.1.2) were used to start a 5 ml overnight YEB culture (containing 25 µg/ml gentamicin/rifampicin plus plasmid selection). Additionally, overnight cultures of GV3101 cells containing the p19 protein were prepared (25 µg/ml gentamicin/rifampicin, 50 µg/ml kanamycin), in order to suppress gene silencing. Both cultures were grown at 30 °C for 14-16 hours, and were then centrifuged at 3,000 *g* for 5 minutes. Pelleted cells were resuspended in 2 ml infiltration buffer (50 mM MES (2-(*N*-morpholino) ethanesulfonic acid (Sigma)) pH 6.5, 28 mM D-glucose (Melford), 2 mM $Na_3PO_4.12H_2O$ (trisodium orthophosphate), 100 µM acetosyringone (3',5'-Dimethoxy-4'-hydroxyacetophone (Fluka), 200 mM stocks in DMSO). Cells were washed twice and finally resuspended in 1 ml infiltration buffer. The OD_{600} of the cells was measured using a 1:10 dilution of the resuspended cells and the cells were diluted in 2 ml infiltration buffer to an OD_{600} of 0.01-0.05. The constructs

and p19 were mixed in 1:1 ratios, or 1:1:2 ratios when two constructs were simultaneously infiltrated.

N. benthamiana leaves were infiltrated by making three small cuts on the lower epidermis, and the infiltration solution was injected using a needless syringe. The area of total leaf infiltration was then marked with a pen. Infiltrated plants were approximately 5-6 weeks old, and infiltrated leaves were 3-5 cm in length, with 3-4 leaves being infiltrated per plant.

2.2.14 Agrobacterium-mediated stable transformation of Arabidopsis through floral dipping

Arabidopsis plants that were approximately 5-6 weeks old were used for floral dipping. In the weeks prior to floral dipping, the stems were cut back to the base to promote bushier plant growth with more inflorescences. Prior to floral dipping, siliques and open flowers were removed.

The floral dipping method was based on the protocol in Clough & Bent (1998) and adapted by Calcutt (2009). Chemically competent Agrobacterium GV3101 cells were transformed with the plasmid of interest (as described in section 2.2.1.2) and single colonies were used to inoculate a 5 ml liquid YEB culture (containing 25 μg/ml gentamicin, 25 μg/ml rifampicin and plasmid selection) that were grown at 30 °C for 24 hours. This culture was added to a fresh 500 ml YEB culture (containing the same antibiotics) and was grown for 24 hours at 30 °C on a shaker. Finally, the culture was centrifuged at 6,000 *g* for 15 minutes using a Beckman Coulter Avanti J-20 XP centrifuge fitted with a JLA 10.500 rotor, and the pellet was resuspended in a 1l 5% (v/v) sucrose solution. Prior to dipping, 0.05% (v/v) Silwett L-77 (Lehle seeds) was added to this solution, in order to break the surface tension and increase the efficiency of the floral dip.

The pruned Arabidopsis plants were dipped into the above solution for 15 seconds with gentle stirring. The dipped plants were then placed into a plastic bag and kept in a shaded environment overnight to maintain humidity. Dipped plants were removed from the bag after 24 hours and were returned to normal greenhouse conditions. The same dipping procedure (omitting the pruning step) was repeated one week later. Plants were then allowed to mature and seed was collected when the plants were dry.

2.2.15 Genotyping of the T-DNA insertion line plants using PCR

The T-DNA insertion lines were genotyped by using Biotaq (Bioline) PCR reactions (as described in 2.2.9) using genomic DNA (extracted according to 2.2.7) as a template for the reaction. Typically two PCR reactions were used to genotype each plant. The first reaction used gene-specific forward and reverse primers (see Appendix 1.7) that were designed to be approximately 500 bp at either side of the T-DNA insertion. These primers would amplify a band in the wild-type allele. The second reaction used T-DNA-specific left border primers (LBa1 or LB3 for SALK and SAIL lines respectively; see Appendix 1.7 for sequences) together with the gene-specific forward or reverse primer, depending on the orientation of the T-DNA insertion. These primers would amplify a band in the T-DNA insert allele. In azygous plants, a band would only be amplified in the wild-type reaction, heterozygous plants would produce bands in both reactions, and plants that were homozygous for the insert would only amplify a band in the insert reaction. As a positive control that the PCR reaction had worked, *mago* forward and reverse primers were used in all reactions to amplify a 1868 bp fragment from *MAGO NASHI* (At1g02140; see Appendix 1.7).

2.2.16 Genotyping of the *NET4Bpro*::NET4B-GFP transformed lines

Genotyping PCR reactions were used to confirm the presence of the *NET4Bpro*::NET4B-GFP (NET4B107) transgene in several selected T_2 generation plants. Genomic DNA (as described in 2.2.7) was used as template DNA in the genotyping PCR reaction. Only one PCR reaction was performed which used two NET4B107 specific primers: IRQ Fw and GFP Rv (see Appendix 1.2 and 1.9 for sequences). These would only detect a band if the transgene had been transformed into the plant. As a positive control, the *mago* forward and reverse primers were used to amplify a 1868 bp fragment of the *MAGO NASHI* gene (At1g02140). Genomic DNA extracted from untransformed Arabidopsis Col-0 was used as a template in additional reactions and acted as a negative control. As a positive control for this fragment, the NET4B107 vector was used as a template DNA.

2.2.17 Reverse transcription-PCR analysis of the T-DNA insertion lines

Reverse transcription-PCR was used to analyse the disruption of the *NET4B* and *NET4A* transcripts in the homozygous *net4b.1*, *net4a.1* and *net4b.1/net4a.1* T-DNA insertion lines. RNA was extracted from 15-day old vertically grown seedlings of the mutant

lines (see 2.2.5) and was used as a template for cDNA synthesis (as described in 2.2.6) Gene specific primers were used to amplify fragments upstream, downstream and overlapping the T-DNA insertion for the *net4a.1* mutant, and only one fragment was amplified for the *net4b.1* mutant as the insert is in the promoter. As a positive control, gene specific primers were used that amplified a fragment of the Arabidopsis *ELONGATION FACTOR 1-α* (*EF1α*, At5g60390). All primer sequences are listed in Appendix 1.8. DNA amplification was performed using the MyTaq (Bioline) DNA polymerase (according to 2.2.9). PCR products were run on either a 1% or 3% (w/v) agarose gel, depending on fragment size (as described in 2.2.8).

2.2.18 qPCR analysis of the homozygous *net4b* T-DNA insertion lines

qPCR analysis was performed to analyse the gene expression levels of *NET4B* in the *net4* T-DNA insertion lines: *net4b.1*, *net4a.1*, *net4b.1/net4a.1* and the azygous control. RNA was extracted from 15-day old vertically grown seedlings of the mutant lines and used as a template for cDNA synthesis (see sections 2.2.5 and 2.2.6). Each genotype had three biological replicates, using RNA extracted from tissue grown at different time points.

Two sets of primers were used in the qPCR reaction (see Appendix 1.8 for sequences). *NET4B* specific primers, q4BFw/Rv, were used to amplify a band of 186 bp. For normalisation of relative expression levels, gene specific primers (EF1α Fw/Rv) were used that amplified a 187 bp fragment of the Arabidopsis *EF1α* (At5g60390). *EF1α* was used as it has previously been shown to be a consistent reference gene (Czechowski et al. 2005). All qPCR reactions used the SensiFAST SYBR DNA polymerase No-ROX Kit, which contains dNTPs, an antibody-mediated hot-start DNA polymerase and the SYBR Green I dye. In order to reduce pipetting errors, template and primer mixes were made for each individual cDNA template and primer pair combination. The following generic template and primer mixes were used, which show the quantities required for one reaction:

Template master mix:

- 2x SensiFAST SYBR DNA polymerase No-ROX -10 µl
- sdH_20 - 4.5 µl
- cDNA - 0.5 µl (diluted 1:4 with nuclease-free water)

Primer master mix:

- Primer 1 (10 pmol/µl) - 0.5 µl
- Primer 2 (10 pmol/µl) - 0.5 µl
- sdH_20 - 4.5 µl

These two master mixes were combined in 100 µl capacity strip tubes (Qiagen) to give a total volume of 20 µl. Several different reactions were set up for each qPCR run. Firstly each cDNA template mixes (*net4b.1*, *net4a.1*, *net4b.1/net4a.1* and the azygous control) were used in reactions to amplify either *NET4B* or *EF1α.* Secondly two negative control reactions were used. Firstly, each cDNA mix (as stated above) were used in a reaction without the addition of primers, and the primer mix was replaced with 5 µl sdH_20. Secondly, each primer pair was used in a reaction without the addition of a cDNA template, and the template mix was replaced with 15 µl sdH_20. All qPCR reactions were run in triplicate using a Rotor-gene Q PCR machine (Qiagen) using the following programme:

Stage	Temperature (°C)	Time	Cycles
Initial denaturing step	95	3 mins	1
Denaturing	95	20 s	40
Annealing	55	20 s	
Extension	72	30 s	

Table 2.6: Thermal cycler programme for qPCR reactions.

Following the qPCR reaction, melt curve analysis was performed by raising the temperature in increments of 1 °C from 55 °C to 99 °C, pausing for 30 seconds after the first step, followed by 5 seconds for each subsequent temperature increment. Expression of each gene was analysed using the Rotorgene Q Series software v1.7 using the ΔCT method. The expression of *NET4B* was calculated against a 'normalised control' (the *EF1α* fragment) and was calculated as a mean average across the three biological replicates.

2.3 Yeast-2-Hybrid

2.3.1 Yeast transformation

Glycerol stocks of the AH109 and Y187 yeast strains were streaked onto solid YPDA plates (20 g/l peptone, 10 g/l yeast extract, 0.003% (w/v) adenine hemisulphate (Sigma), 2% (w/v) D-glucose, 20 g/l agar, pH 6.5) and grown for 2 days at 30 °C. Single colonies were used to inoculate a 10 ml YPDA culture that was grown for 12-14 hours at 30 °C. The OD_{600} of this culture was checked using a spectrophotometer, and the cells were diluted to an OD_{600} of 0.2 in 100 ml YPDA and grown for a further 4 hours at 30 °C. The culture was centrifuged at 1,800 *g* for 5 minutes, and the resultant pellet was resuspended in 50 ml sdH_2O. The cells were centrifuged as before and resuspended in 1.5 ml 1x Li/TE buffer (10mM Tris.HCl pH 7.5, 1mM EDTA, 100mM lithium acetate (Sigma)) and transferred to microcentrifuge tubes. Cells were centrifuged at 16,000 *g* for 15 seconds and resuspended in 1.2 ml 1x Li/TE buffer and were now ready for transformation.

Deoxribonucleic acid sodium salt (ssDNA (Sigma)) acted as the carried DNA for yeast transformation and was resuspended in sdH2O and shredded by forcing through a 19-gauge syringe needle. Prior to use, ssDNA was denatured by heating at 95 °C for 5 minutes and rapidly cooling in an ice bath.

For yeast transformations, the following components were combined in a pre-chilled microcentrifuge tube: 1µ g plasmid DNA (100-300 ng/µl) containing the fragment of interest, 160 µg denatured ssDNA (2 mg/ml), 100 µl competent yeast cells and 600 µl PEG/Li/TE buffer (40% (w/v) PEG-4000 (polyethylene glycol 4000 (BDH)), 100 mM lithium acetate, 10 mM Tris.HCl, 1 mM EDTA, pH 7.5). Cells were gently mixed by pipetting and incubated at 30 °C for 30 minutes. 10 µl DMSO was then added and the cells were incubated at 42 °C for 15 minutes. The cells were centrifuged at 16,000 *g* for 15 seconds and the pellet was resuspended in 1 ml sdH_2O. Centrifugation was repeated and the cells resuspended in 1 ml 0.9% (w/v) NaCl solution. 100 µl of 1/10 and 1/100 dilutions (made in 0.9% NaCl solution) were spread onto solid SD minimal growth media (SD media; 6.9 g/l yeast nitrogen base without amino acids (Formedium), 20 g/l agar, 2% (w/v) D-glucose, pH 5.8, plus 100 ml/l of appropriate 10x dropout solution) containing 50 µg/ml kanamycin, and plates were incubated for 2-3 days at 30 °C.

For the 10x dropout solution, the dropout mix (-WHLA) was first made and consisted of: 3 g L-isoleucine, 15 g L-valine, 2 g L-arginine HCl, 3 g L-lysine, 2 g L-methionine, 5 g L-phenylaline, 20 g L-threonine, 3 g L-tyrosine, 2 g L-uracil. 10x Dropout solutions (400 ml) were made by combining 2.2 g of the dropout mix with the following amino acids depending on the dropout required: 80 mg L-adenine hemisulphate (A), 80 mg L-histidine HCl monohydrate (H), 400 mg L-leucine (L), 80 mg L-tryptophan (W). All amino acids were obtained from Sigma.

2.3.2 Autoactivation tests

Autoactivation tests were used to ensure growth did not occur on selective media in the absence of mating. Autoactivation tests were performed for NET4B (pGBKT7/pGADT7), NET4A (pGBKT7/pGADT7) and NET4B IRQ + Ct (pGBKT7), which were all transformed into the AH109 strain (according to 2.3.1). Three colonies of each strain were resuspended in 100 µl sdH2O and 10 µl of each colony was dropped onto selective SD dropout plates (containing 50 µg/ml kanamycin). For the autoactivation tests for NET4B/NET4A in pGBKT7 and pGADT7, colonies were dropped onto selective media lacking either leucine or tryptophan with the addition of 2.5 mM 3AT (3-Amino-1,2,4-triazole, Sigma). Colonies were also dropped onto -L and -W plates as a control for colony growth. For NET4B and IRQ + CT fragments in pGBKT7, seven plates were used (-WH, -WH + 2.5 mM 3AT, -WH + 5 mM 3AT, -WH + 10 mM 3AT, -WA, -WHA, -W + 100 µM X-α-Gal (5-Bromo-4-chloro-3-indolyl-α-D-galactopyranoside; Sigma). Colonies were allowed to dry and the plates were incubated for 5-7 days at 30 °C. Plates were imaged using a Bio-Rad Gel-Doc 1000 system or an Epson Perfection 4490 Photo flatbed scanner.

2.3.3 Yeast-2-hybrid library screen

Two separate yeast-2-hybrid screens were performed for each bait construct (NET4B and IRQ + Ct). Firstly, an 80 ml overnight SD (-W) culture of the bait construct in Y187 was grown for 24 hours until they reached an OD_{600} of 2.0 and the cells were counted using a haemocytometer. 2 ml of random primed cDNA-prey library cells and 2 ml of oligodT cDNA-prey library cells (both from whole seedling), were mixed with the relevant volume of bait culture containing 1.0 x 10^9 bait cells (40-60 mls). The mixed culture was centrifuged at 1000 *g* for 5 minutes and resuspended in 10 mls YPDA which was poured onto solid YPDA plates and incubated overnight at 30 °C. The mated cells were washed off the plates in 10 mls ½YPDA, centrifuged as above and

resuspended in 10 mls fresh ½YPDA. 100 µl of these cells were used for the mating efficiency tests as described in 2.3.4. The remainder of the cells were plated onto 15 cm plates, containing SD media with -WLHA + 10 mM 3AT dropout (with the addition of 50 µg/ml kanamycin). 500 µl of cells were used per plate and the plates were incubated at 30 °C for 10 days. Colonies that started to appear after 5 days incubation were streaked onto identical SD dropout plates (50 µg/ml kanamycin), and grown for a further 5 days at 30 °C. The colonies that could survive on the second selection plate were used to inoculate liquid cultures and the cDNA-prey plasmid clone was rescued (according to 2.3.5).

The protocol for the second library screen was very similar and included two changes to the method. After overnight mating the cells were washed in 30 ml sdH_2O, which was centrifuged as above and resuspended in 5 ml sdH_2O which was subsequently spread onto selective plates using 200 µl per plate.

2.3.4 Mating efficiency test

Prior to spreading the mated cells on the SD selection plates, 100 µl of the cells were aliquoted for mating efficiency tests. Serial dilutions of the cells were made using sdH_2O, dilutions were made at 1:1000, 1:10,000, 1:100,000, and 100 µl of the dilutions were plated onto SD -L (to select for prey library) and -LW (to select for diploids) plates (containing 50 µg/ml kanamycin) and cells were counted after 3 days growth at 30 °C. The number of diploid colonies screened was calculated by multiplying the number of colonies on the 1:100,000 dilution by the plating volume (100 µl) and total resuspension volume for the mated cells (5 or 10ml). Mating efficiency (% of diploids) was calculated as: (Number of diploid colonies / Number of library colonies) x 100.

2.3.5 Plasmid rescue

Colonies that successfully grew after being restreaked onto fresh SD dropout media plates (-WLHA + 10 mM 3AT) were taken forward for plasmid rescue. Colonies were inoculated into 5 ml liquid cultures of SD -WHLA +10 mM 3AT (containing 50 µg/ml kanamycin) and grown for 48 hours at 30 °C. Cultures were centrifuged at 5,000 *g* for 5 minutes and resuspended in 50 µl yeast lysis buffer (YLB; 50 mM Tris.HCl pH 7.5, 0.85 M Sorbitol (BDH), 10 mM EDTA, containing a few grains of Lyticase (Sigma) per ml YLB). Cells were incubated at 37 °C for 1 hour before being flash frozen in liquid nitrogen and thawed at 37 °C. The Promega Wizard Plus SV Miniprep DNA

Purification System was subsequently used to purify plasmid DNA (as described in 2.2.3) starting with the addition of the resuspension buffer. Purified plasmid DNA was then sequenced, (according to 2.2.11) using the T7 promoter primer (see Appendix 1.9 for sequence). Prey plasmids that were used for further one-on-one testing were transformed into *E. coli* DH5α (according to 2.2.1.1) to amplify the DNA before being transformed into the yeast Y187 strain (as described in 2.3.1)

2.3.6 Yeast one-on-one mating tests to confirm interactions

Several different yeast one-on-one mating tests were used to confirm potential protein-protein interactions. Bait and prey vectors (pGBKT7 and pGADT7) were transformed into the yeast strains AH109 and Y187 respectively. Single colonies of the bait vector (AH109) were first resuspended in 100 µl sdH_2O and 10 µl of this suspension was dropped onto solid YPDA plates. Once the drop had dried, single colonies of the prey vector (Y187) were similarly resuspended and 10 µl was placed on top of the dried drop containing the bait vector. The drops were allowed to dry and were then incubated at room temperature for 24-48 hours to allow the yeast to mate. As a negative control for autoactivation, the bait and prey vectors containing the plasmids of interest were also mated with the respective empty vectors. Typically, each one-on-one test mated three individual colonies for each bait-prey vector combination.

Once the yeast had grown, the mated cells were resuspended in 100 µl sdH2O and 10 µl was dropped onto solid SD -WL dropout media (containing 50 µg/ml kanamycin) to select for diploid mated cells. Plates were incubated at 30 °C for 3-4 days until colonies started to appear.

Diploid colonies were resuspended in 100 µl sdH_2O and 10 µl of this suspension was dropped onto selective SD dropout media (containing 50 µg/ml kanamycin) to test for potential interactions. Various different dropout selections were used during this project including: -WLA, -WLH + 2.5 mM 3AT, -WLH + 10 mM 3AT, -WLHA + 2.5 mM 3AT, -WLHA + 10 mM 3AT. As a positive control for yeast growth, diploid colonies were also dropped onto -WL SD plates (containing 50 µg/ml kanamycin). Once the drops had dried, the plates were sealed with Parafilm and incubated at 30 °C for 5-7 days. Yeast growth was imaged using an Epson Perfection 4490 Photo flatbed scanner.

2.4 *In vitro* protein methods

2.4.1 Expression and purification of 6xHis-tagged proteins

Competent Rosetta 2 cells were transformed (as described in 2.2.1.1) with pGAT4, the Gateway protein expression vector, containing the fragment of interest. Overnight cultures were prepared and used to inoculate 1L LB (100 μg/ml ampicillin (Melford) and 30 μg/ml chloramphenicol (Duchefa)), which was subsequently grown to at 37 °C until it reached an OD_{600} of 0.5-0.6. Protein expression was induced with the addition of 1 mM IPTG (Melford) and the cultures were incubated at 30 °C for 3 hours. Cultures were centrifuged at 6,000 *g* for 10 minutes at 4 °C using a Beckman Coulter Avanti J-20 XP centrifuge fitted with a JLA 10.500 rotor. The resultant pellet was resuspended in protein extraction buffer (1 M HEPES (N-(2-hydroxyethyl)piperazine-N'-(2-ethanesulfonic acid, Sigma) pH 7.0, 5 M NaCl, 5 mM ß-mercaptoethanol, 8 M Urea (BDH)), containing proteinase inhibitors (10 μg/ml leupeptin (Sigma), 1 mM PMSF (Sigma), 10 μg/ml TAME (Nα-p-Tosyl-L-arginine methyl ester hydrochloride, Sigma) 1 μg/ml pepstatin A (Sigma)). The bacterial cells were lysed by flash freezing in liquid nitrogen and thawing in a 37 °C water bath. The lysed cells were ultracentrifuged at 350,000 *g* for 15 minutes at 4°C using a Beckman Optima TLX ultracentrifuge fitted with a TLA 100.4 rotor.

The resultant supernatant containing the protein extract was removed and filtered through a 0.45 μm filter. The filtered extract was added to a column containing nickel nitrilotriacetic acid (Ni-NTA) agarose beads (Qiagen), which had been previously equilibrated with protein extraction buffer. The protein extract and Ni-NTA beads were incubated for 15 minutes on a rotary shaker at room temperature. The extraction buffer was pulled through the column, using a syringe attached to the base, and the beads were subsequently washed using 20 mM, 40 mM and 60 mM imidazole wash buffer (1 M HEPES pH 7.0, 5 M NaCl; 20 mM, 40 mM and 60 mM respectively imidazole (Sigma), and 6M, 4M and 3M respectively urea). Finally the His-tagged protein was eluted from the column using elution buffer (50mM HEPES pH 7.0, 300mM NaCl, 250mM imidazole, 2M Urea). Protein concentration was analysed with the Bradford assay (Bio-Rad Protein Assay), using a spectrophotometer set at a wavelength of 595 nm.

2.4.2 Dialysis of purified protein into phosphate buffer for antibody production

After purification of the 6xHis-tagged NET4B antigen fragment ($NET4B^{121-220}$), the urea was removed through buffer exchange. The eluted protein was dialysed overnight at 4 °C in 1x PBS buffer (137 mM NaCl, 2.7 mM KCl, 10 mM Na_2HPO_4 (di-sodium hydrogen orthophosphate dihydrate (BDH)), 1.8 mM KH_2PO_4 (potassium phosphate monobasic (Sigma), pH 7.4) using dialysis tubing. Purified protein was analysed using SDS-PAGE gel electrophoresis (according to 2.4.9) and was flash frozen in liquid nitrogen and stored at -80°C.

2.4.3 Dialysis of purified protein for the cosedimentation assay

Following purification of the 6xHis-tagged NET4B NAB domain ($NET4B^{1-105}$) and antigen fragment ($NET4B^{121-220}$), buffer exchange was performed to remove the urea. For dialysis of the purified NET4B-NAB domain and antigen fragment using dialysis tubing, the purified protein was dialysed overnight at 4 °C into KME buffer (50 mM KCl, 1 mM $MgSO_4$ (Sigma), 1 mM EGTA (ethylene glycol tetraacetic acid (Melford)), 10 mM imidazole, pH 6.5) containing 10% (v/v) glycerol. Dialysed protein was analysed through SDS-PAGE gel electrophoresis (according to 2.4.9) and was subsequently flash frozen in liquid nitrogen and stored at -80°C. Aliquots of the dialysis buffer (KME buffer containing 10% glycerol) were frozen for future use in the cosedimentation assay.

2.4.4 MALDI-TOF analysis of SDS-PAGE protein gel bands

MALDI-TOF-MS analysis was used to confirm the sequence of the purified proteins produced during this project. Protein samples were run on SDS-PAGE gels (according to 2.4.9) and sent to the Durham School of Biological and Biomedical Sciences (SBBS) Proteomics service for protein band digestion and subsequent analysis using a 4800 Plus MALDI TOF/TOF Analyzer (Sciex). Data-files were processed using GPS Explorer (3.6) software (Sciex) for protein identification from the SwissProt database (September 2013 release).

2.4.5 Production of polyclonal antibodies

Polyclonal antibodies were raised in rabbits against a fragment of NET4B ($NET4B^{121-220}$), purified from *E. coli* and dialysed into PBS buffer (as described in sections 2.4.1 and 2.4.2). Approximately 90 μg of the purified NET4B antigen fragment was used per

injection, and was mixed 1:1 with Freund's complete adjuvant (FCA) for the first inoculation and Freund's incomplete adjuvant (FIA) for all subsequent injections. Test-bleeds were taken prior to the first injection. Two rabbits were inoculated a total of 6 times at day 0, 14, 28, 42, 56 and 70. At day 77, the terminal bleed was collected and the serum was separated. Test-bleeds and terminal bleeds were used for Western blot analysis and immunogold labelling. Antibody production (including animal care, injections, test-bleeds and serum collection) was performed in-house by the Durham University Life Science Support Unit (LSSU).

2.4.6 Total protein extraction for initial antibody tests

Protein was extracted from 15-day old vertically grown Arabidopsis Col-0 plants for initial assessment of the rabbit terminal bleeds used in the production of the NET4B polyclonal antibodies. Plant tissue was ground to a fine powder in liquid nitrogen using a pestle and mortar. Homogenised tissue was then added to 2x protein extraction buffer (250 mM Tris-HCl pH 6.8, 4% (w/v) SDS, 20% (v/v) glycerol, 100 mM ß-mercaptoethanol, 0.02% Bromophenol blue (Sigma)) that was preheated to 95 °C. Samples were heated at 95 °C for 5 minutes and centrifuged at 16,000 *g* for 2 minutes and supernatants were stored at -80 °C until required.

2.4.7 Total protein extraction for quantitative analysis

Total protein extractions that were used for subsequent Western blot analysis required protein quantification prior to loading and followed the protocol described in Martinéz-García et al. (1999). This method utilises an extraction buffer that is compatible with commercial protein quantification assays, as it contains a low concentration of SDS and uses sodium metabisulfate ($Na_2S_2O_5$) as a reducing agent instead of dithriothreitol (DTT) or ß-mercaptoethanol.

Protein was extracted from various sources including Arabidopsis Col-0 tissues (seedlings, roots, leaves, inflorescence stems, flowers, siliques), 15-day old vertically grown Arabidopsis *net4* T-DNA mutant plants, and transformed *N. benthamiana* leaf tissue. Plant tissue was collected in microcentrifuge tubes, flash frozen in liquid nitrogen and subsequently homogenised using a liquid nitrogen cooled micropestle. Protein extraction buffer (125 mM Tris-HCl pH 8.8, 1% (w/v) SDS, 10% (v/v) glycerol, 50 mM $Na_2S_2O_5$ (Sigma)) was added to the homogenised tissue in the microcentrifuge tubes which were subsequently warmed to room temperature to resolubilise the SDS.

Samples were centrifuged at 16,000 *g* for 10 minutes and the supernatant decanted into a fresh tube. A small aliquot (approximately 10-20 µl) of the supernatant was used for calculating protein concentration using a spectrophotometer set at 750 nm and the Bio-Rad Detergent-compatible (Dc) Protein Assay (Bio-Rad). The remaining supernatant was diluted 4:1 using 5x Laemmli sample buffer (312 mM Tris-HCl, pH 6.8, 10% (w/v) SDS, 50% (v/v) glycerol, 25% (v/v) ß-mercaptoethanol, 0.05% (w/v) bromophenol blue) and samples were heated at 95 °C for 5 minutes. Samples were then centrifuged at 16,000 *g* for 2 minutes and supernatants were stored at -80 °C until required. Quantity of plant material varied from 100-300 mg and typically 2 µl protein extraction buffer was used per mg of plant material.

2.4.8 Total protein extraction from the *net4* mutant seeds

For analysis of protein trafficking in the embryos, total protein was extracted from dry seeds of the F_3 generation *net4b.1*, *net4a.1*, *net4b.1/net4a.1,* and azygous lines. Ten dry seeds from each line were ground in 20 µl of 1x Laemmli sample buffer (63 mM Tris.HCl pH 6.8, 2% (w/v) SDS, 10% (v/v) glycerol, 5% (v/v) ß-mercaptoethanol, 0.01% (w/v) bromophenol blue) and samples were heated at 95 °C for 5 minutes. 10 µl of each protein sample was separated using a 15% SDS-PAGE gel according to 2.4.9.

2.4.9 SDS-polyacrylamide gel electrophoresis

SDS-PAGE gel electrophoresis was used to separate proteins based on their size. The Bio-Rad Mini Protean II system was used to cast and run all gels. The resolving gel was first cast, which typically contained 7.5-15% (v/v) acrylamide (Protogel, 30% (w/v acrylamide, 0.8% (w/v) bisacrylamide), depending on the size of expected protein fragments, being added to the resolving buffer (0.1% (w/v) SDS, 375 mM Tris pH 8.8, 0.1% (w/v) ammonium persulphate (APS; Melford), 0.04% TEMED (N,N,N',N'-Tetramethylethylenediamine (Fluka)). Stacking gels were prepared using: 4% acrylamide, 125 mM Tris pH 6.8, 0.1% (w/v) SDS, 0.1% (w/v) APS, 0.002% (v/v) TEMED.

Prior to loading, protein was diluted 4:1 using 5x Laemmli sample buffer (312 mM Tris-HCl, pH 6.8, 10% (w/v) SDS, 50% (v/v) glycerol, 25% ß-mercaptoethanol, 0.05% bromophenol blue) and heated for 5 minutes at 95 °C. Electrophoresis was performed at 100-150V in a tank filled with 1x running buffer (25 mM Tris, 192 mM glycine (Sigma), 0.1% SDS).

2.4.10 Semi-native SDS-polyacrylamide gel electrophoresis

Semi-native SDS-PAGE gel electrophoresis was used to investigate the oligomerisation of NET4B *in planta* and was based on the protocol in Voulhoux et al. (2003). Total protein was extracted from Arabidopsis Col-0 15-day old vertically grown seedlings (according to 2.4.7) and the supernatant was diluted 4:1 with 5x Laemmli loading buffer. At this point the protein sample was divided into two aliquots; one was heated at 95 °C for 5 minutes (standard SDS-PAGE) and the other was heated at 65 °C for 5 minutes (semi-native SDS-PAGE). SDS-PAGE Electrophoresis was then carried out as described in 2.4.9.

2.4.11 Coomassie Brilliant Blue staining

For visualisation of protein in SDS-PAGE gels, gels were stained with Coomassie Brilliant Blue stain (CBB) (7% (v/v) glacial acetic acid, 35% ethanol, 0.125% (w/v) Coomassie Brilliant Blue R-250 (BDH)) for 20 minutes and destained for approximately 2 hours using destaining solution (10% methanol (Fisher), 10% glacial acetic acid).

2.4.12 Western blot analysis

SDS-PAGE gels used for immunological detection of protein through Western blotting were transferred onto nitrocellulose membranes (Whatman) using the Bio-Rad Mini-Protean II system. Transfer onto the membrane was performed overnight at 20V in a tank containing transfer buffer (48 mM Tris, 39 mM glycine, 0.375% (w/v) SDS, 20% (v/v) methanol). Following overnight transfer, the membrane was washed in dH_2O and protein bands were visualised using a 1:100 dilution of amido black staining solution (45% (v/v) methanol, 2% (v/v) acetic acid, 0.1% (w/v) Naphthol blue black (amido black; Sigma)). Membranes were stained for 5 minutes and imaged using a Bio-Rad Gel-Doc 1000 system, before being washed in dH_2O for 5 minutes.

Similar probing conditions were used throughout this project. Firstly, nitrocellulose membranes were blocked for 30 minutes in 2x TBST (20 mM Tris pH 7.4, 300 mM NaCl, 0.1% (v/v) Tween 20 (Sigma)) containing 5% (w/v) dried skimmed milk powder (Tesco). Membranes were then incubated with the primary antibody diluted in 2x TBST containing 5% milk, for one hour at room temperature. Primary antibody dilutions varied, but typically 1:500 was used for the anti-NET4B polyclonal antibodies.

The membrane was then washed three times for 5 minutes using 2x TBST, before being probed for 30 minutes with the secondary antibody diluted 1:3000 in 2x TBST containing 5% milk. Secondary antibodies used were conjugated to horseradish peroxidase (HRP). Anti-rabbit IgG/HRP antibodies (Dako, raised in pigs) were used for detection of anti-NET4B and anti-GFP (Invitrogen). Anti-mouse IgG/HRP antibodies (Amersham) were used to detect the monoclonal C4 anti-Actin antibody.

Following secondary antibody incubation, the membranes were washed as before and antibody binding was visualised with the application of ECL Western Blotting Detection Reagent (Amersham Biosciences). ECL was incubated for 1 minute before being visualised using a Fujifilm Intelligent Dark Box II and Fujifilm film image reader system, or being exposed to X-ray film (SLS) which was developed and fixed in a dark room. X-ray films were scanned using an Epson Perfection 4490 Photo flatbed scanner.

2.4.13 Co-sedimentation assay

All ultracentrifugation steps of the co-sedimentation assay were performed using a Beckman Optima TLX ultracentrifuge fitted with a TLA 120.1 rotor. Desiccated actin (rabbit skeletal muscle actin, Cytoskeleton Inc) was rehydrated with 100 µl sdH_2O to give a final protein concentration of 10 mg/ml (233 µM). Rehydrated actin was incubated on ice for 30 minutes before being diluted to a concentration of 25 µM using G-buffer (2 mM Tris pH 8, 0.5 mM DTT, 0.2 mM $CaCl_2$, 0.2 mM ATP (adenosine triphosphate (Sigma)), and incubated on ice for one hour. The actin was then ultracentrifuged at 350,000 *g* for 20 minutes at 4ºC and the top 75% of the supernatant was removed containing the soluble G-actin. 10 x KME (500 mM KCl, 10 mM $MgSO_4$, 10 mM EGTA, 100 mM imidazole, pH6.5) was then added to the actin, which promotes polymerisation of F-actin, and the sample was left for 2 hours at room temperature. Prior to the cosedimentation assay, the purified recombinant proteins were ultracentrifuged at 350,000 *g* for 20 minutes at 4ºC and the top 75% of the supernatant removed for use in the assay.

All reactions were set up using ultracentrifuge tubes kept on ice and contained the following components (total reaction volume of 100µl): 30µl reaction buffer (2 mM Tris pH 8, 50 mM KCl, 1 mM $MgSO_4$, 1 mM EGTA, 10 mM imidazole, 0.5 mM DTT, 0.2 mM $CaCl_2$, 0.2 mM ATP), 16 µl (10 µM) recombinant protein (where lower concentrations of protein was used, dialysis buffer was used up to 16 µl), 19 µl (5 µM) F-actin (or 19 µl reaction buffer where F-actin was omitted).

Seven different reactions were set up and F-actin was kept at 5 μM when used. The reactions included: NET4B-NAB alone (10 μM), F-actin alone, NET4B-NAB (10 μM) + F-actin, NET4B-NAB (5 μM) + F-actin, NET4B-NAB (2 μM) + F-actin, NET4B$^{121-220}$ fragment (10 μM) alone, NET4B$^{121-220}$ fragment (10 μM) + F-actin. The reactions were incubated at room temperature for 1 hour and were then ultracentrifuged at 350,000 *g* for 15 minutes at 22 °C. The supernatant was removed and diluted 4:1 in 5x Laemmli loading buffer. The pellet was resuspended in 100 μl G-buffer and diluted 4:1 in 5x Laemmli loading buffer. Samples were heated at 95 °C for 5 minutes before being separated on an SDS-PAGE gel (according to 2.4.9).

2.5 Cell Biology

2.5.1 High pressure freezing and freeze substitution of Arabidopsis root tips

Preparation of samples for immunogold labelling including fixation, embedding, sectioning and immunogold labelling, was performed by the SBBS Electron Microscopy team.

Root tips were prepared for immunogold labelling through high-pressure freezing and freeze substitution (HPFFS). Arabidopsis (Col-0) seedlings were grown vertically on ½MS agar plates for 7 days (as described in 2.6.2), and the distal 1-2 mm root tips were excised using a razor blade and immersed in 20% (w/v) BSA (bovine serum album). Samples were immediately transferred onto membrane carriers (Leica Microscystems Gmbh) and high-pressure freezing was performed using a Leica EMPACT high-pressure freezer.

Following high-pressure freezing, samples were fixed through freeze substitution using a Leica EM automated freeze substitution (AFS) device (Leica Microsystems GmbH). Samples were freeze-substituted slowly and at low temperatures using anyhdrous acetone containing 0.25% (v/v) glutaraldehyde and 0.1% (w/v) uranyl acetate. Firstly, the frozen samples were incubated in this solution for 48 hours at -80 °C, before the temperature was raised by hourly 1 °C increments until it reached -50 °C. Once the temperature had reached 50 °C, the sample was washed several times in anhydrous acetone and the sample was removed from the membrane carrier using a fine needle. Infiltration then continued into Monostep Lowicryl HM20 (Agar Scientific) at -50 °C by increasing the ratio of resin to acetone. Three step changes (12 hours each) of resin/acetone were made with increasing concentrations of resin (22, 33, and 66%

resin). After the final change, samples were incubated in 100% resin for 96 hours, with a fresh change of resin every 24 hours. Final resin embedding and UV polymerisation was performed at -50 °C for 48 hours and the temperature was then slowly raised to 20 °C, and maintained at this temperature for 24 hours. Once polymerisation was complete, ultrathin sections (50-70 nm) were prepared using a diamond knife and collected onto formvar coated nickel grids.

2.5.2 Immunogold labelling and transmission electron microscopy

For immunogold labelling, ultrathin sections were first rinsed with 0.1% (v/v) glycine in phosphate buffer saline (PBS). Samples were subsequently blocked for 30 minutes in 1% (w/v) BSA in PBS. Three five minute incubations were then performed using PBS containing 0.1% (w/v) BSA-c (Aurion), pH 7.4. BSA-c is a modified version of BSA, where lysine and arginine residues have been acetylated which results in an increased negative charge of the protein, and therefore linearisation and increased hydrophobicity. This blocking agent was used to improve the signal-to-noise ratio of the labelling.

Following the blocking steps the sections were incubated for 30 minutes with the primary antibody (rabbit anti-NET4B (A88)) diluted 1:100 in 0.1% BSA-c. In addition to the anti-NET4B antibody, grids were incubated with the anti-NET4B pre-bleed sera as a negative control.

Following primary antibody incubation, the grids were washed in 0.1% BSA-c using three 5-minute incubations. Sections were then incubated for 30 minutes with the 5 nm colloidal gold-conjugated goat anti-rabbit secondary antibody (British Biocell International, Cardiff, UK), diluted 1:20 in 0.1% BSA-c. Sections were also incubated without the secondary antibody as a negative control for immunogold labelling (secondary omission control). The grids were then rinsed using three 5-second washes of PBS, followed by four 2-minute washes with PBS. The antigen-antibody-gold complex was then stabilised with a 5 minute incubation using 1% (v/v) glutaraldehyde in PBS.

For transmission electron microscopy (TEM), the samples were stained for 5 minutes using 2% (w/v) aqueous uranyl acetate, followed by incubation in Reynolds lead citrate for 5 minutes. Sections were imaged using a Hitachi H-7600 TEM operating at 100 kV fitted with an AMT Orca-ER digital camera (Advanced Microscopy Techniques, Danvers, USA).

2.5.3 Confocal Laser Scanning Microscopy (CLSM)

GFP- and mCherry-tagged proteins were expressed in *N. benthamiana* leaf epidermal cells using the Agrobacterium-mediated transient transformation method (see 2.2.13). Imaging of the fusion proteins, including drug treatments, was performed 2-3 days post-infiltration. Leaf sections were prepared (distal to the wound site) and mounted on glass slides in dH_2O under a coverslip, with the lower epidermis of the leaf being imaged. For the *NET4Bpro*::NET4B-GFP lines, seedlings were grown vertically on ½MS agar plates (as described in 2.6.2) for 7 days and were subsequently mounted on a glass slide in dH_2O under a coverslip.

CLSM was performed using a Leica SP5 confocal laser scanning microscope, using x40 or x63 oil immersion lenses. GFP was imaged using the 488nm 20mW argon laser and emission was detected at 500-560nm. 488nm laser settings typically ranged between 3-6.6% total laser power, and a smart gain of 800-1000mV was used for PMT detectors, and 70-100% for the HyD detector, depending on signal strength. To image mCherry, the fluorophore was excited using a HeNe 594 nm laser and emission was detected at 600-650 nm. Laser settings for excitation of mCherry were typically between 50-60%, with similar detector settings as used for GFP. Sequential scans were used for the colocalisation experiments using the 488 nm and 594 nm laser, and images were overlaid using the Leica LAS AF software.

2.5.4 Cytoskeleton disrupting drug treatments on *N. benthamiana* leaves

For disruption of the actin cytoskeleton leaf sections were incubated for 30 minutes in 50 μM Latrunculin B (Sigma, prepared from 10 mM stock in DMSO) or 40 μM Cytochalasin D (Calbiochem, prepared from 10 mM stock in DMSO). As a negative control, leaf sections were incubated in sdH_2O containing 0.5% DMSO which represents the highest concentration used in these treatments.

For disruption of the microtubule cytoskeleton leaf sections were incubated for 1 hour in 40 μM Amiprophosmethyl (Fluka, prepared from 20 mM stock in DMSO). As a control, leaf sections were incubated in sdH_2O containing 0.2% DMSO.

2.5.5 Histochemical staining of the vacuole in the Arabidopsis root

The lytic vacuole in the roots of the *net4* mutant lines was visualised using the pH sensitive dye BCECF-AM (2',7'-Bis-(2-carboxyethyl)-5-(6)-carboxyfluorescein,

acetoxymethyl ester), which accumulates in the acidic compartments of the cell and labels the lytic vacuole (Swanson & Jones 1996). The protocol for vacuolar staining in the roots was adapted from (Feraru et al. 2010) and (Kolb et al. 2015).

The F_3 generation *net4b.1*, *net4a.1*, *net4b.1/net4a.1*, and azygous plants were grown vertically for 5 days (according to 2.6.2). Seedlings were transferred from the ½MS plates into liquid ½MS media containing 10 µM BCECF-AM (1.24 mM stock in DMSO (Sigma)), and incubated for one hour in the dark on an orbital shaker. Seedlings were then mounted in liquid ½MS media before imaging using CLSM (as described in 2.5.3). BCECF-AM was excited at 488 nm and emission was detected between 500-570 nm. A minimum of 7 seedlings were imaged for each genotype.

2.5.6 Imaging protein storage vacuoles in Arabidopsis embryos

The protocol for imaging the autofluorescence of protein storage vacuoles (PSVs) in Arabidopsis embryos was adapted from Shimada et al. (2003). Dry seeds of the F_3 generation *net4b.1*, *net4a.1*, *net4b.1/net4a.1*, and azygous lines were imbibed on damp filter paper and kept in the dark at 4°C for one hour. Seeds were then mounted in a drop of glycerol and the embryos were squeezed out from the seeds by applying pressure to the coverslip. The autofluorescence of PSVs was imaged using CLSM (see 2.5.3). Autofluorescence was excited at 488 nm and emission was detected between 500-630 nm. A minimum of five embryos were imaged for each genetic line.

2.5.7 GUS histochemical staining

NET4Bpro::GUS transformed plant tissue was incubated in GUS staining solution (100 mM phosphate buffer (61 mM Na_2HPO_4 and 39 mM NaH_2PO_4 (Sigma)), 10 mM EDTA pH 8, 0.1% (v/v) Triton X-100, 0.5 mM potassium ferricyanide, 0.5 mM potassium ferrocyanide, pH 7, 1 mM X-Gluc (20 mM stock in DMSO (Sigma)). To stain 7-day old seedlings, samples were incubated at room temperature in GUS buffer for 30-60 minutes, depending on signal strength. Preliminary experiments revealed severe dehydration of the roots during ethanol washes. Therefore the roots were excised from the cotyledons, and mounted immediately in GUS buffer (without potassium ferricyanide/ferrocyanide or X-Gluc). Cotyledons were cleared with several washes of 70% ethanol before being mounted on glass slides in 2.5% glycerol.

For staining floral tissue and siliques, open flowers or siliques of 5-6 week old plants were immersed in GUS staining solution and vacuum infiltrated for 5 minutes using an Eppendorf Concentrator 5301. Samples were then incubated at 37 ºC for 1-3 hours depending on signal strength. Stained plant tissue was washed repeatedly in 70% ethanol (v/v) to clear the samples of chlorophyll. When all the chlorophyll was cleared the samples were mounted on slides with a drop of 2.5% glycerol.

For staining of embryos, siliques from 5-6 week old plants were removed and gently opened with a razor blade thus allowing the GUS staining solution to penetrate the ovules. Ovules were incubated in the GUS staining solution whilst still attached to the siliques. Ovules were first vacuum infiltrated and then incubated at 37 °C for 1-3 hours, depending on signal strength. Plant tissue was washed repeatedly in 70% ethanol (v/v) to clear the samples of chlorophyll. Stained ovules were mounted on a slide with a drop of 2.5% glycerol and embryos were removed from the ovules by applying pressure to the coverslip.

Samples were imaged using a Zeiss Axioskop light microscope using x10 and x20 magnification, and an Olympus Research Stereo SZH10 microscope using x0.7 to x10 magnification. Images were captured using a Photometrics Coolsnap cf video camera and Openlab 3.1.1. software.

2.6 Plant growth conditions and phenotypic assays

2.6.1 *Nicotiana benthamiana* growth conditions

N. benthamiana plants were grown centrally by Durham University SBBS. Seeds were sown directly onto compost (seed and modular compost plus sand; F2 + S (Levington)), and were covered with a plastic propagator lid until they became established. Once the seedlings had grown approximately 1-2 cm tall they were transplanted into individual 10 cm pots and until they were 5-6 weeks old. Plants were grown in a growth chamber under a 16/8 hour photoperiod, with temperatures of 24 °C and 21 °C during the day and night respectively.

2.6.2 Arabidopsis growth conditions

Seeds were surface sterilised in 6% sodium hypochlorite (BDH) for 15 minutes, and washed 5 times in sdH_2O. Sterilised seeds were sown in 9 cm Petri dishes onto half-strength Murashige and Skoog (½MS) basal salt mixture (pH 5.7) containing 0.8%

(w/v) plant agar (Duchefa). During root growth assays, 12 cm square Petri dishes were used to ensure uniform growth across the plate. Plates were sealed with micropore tape (3M) and stratified for 3 days at 4°C in darkness. Plants were grown vertically in a temperature controlled Sanyo growth cabinet with a 16/8 hour photoperiod, and temperatures of 22 °C and 16° C during the day and night respectively.

After two weeks growth, plants were transferred into plastic trays containing compost (seed and modular compost plus sand; F2 + S (Levington)) that had been treated with Intercept insecticide (0.2 g/l, Bayer). Plants were grown in the Sanyo growth cabinet or a walk-in growth chamber using the same settings. Trays were covered with a propagator lid for approximately 1-2 weeks until the plants had become established.

2.6.3 Cross-pollination of Arabidopsis plants

Cross-pollination of Arabidopsis plants was used to generate the double *net4* T-DNA insertion lines, and was performed using forceps under a dissecting microscope. Unopened flowers from one genetic line were dissected; all floral whorls apart from the carpels were removed to prevent self-pollination. The papillae were then brushed using anthers from the other genetic line, thus covering them in pollen. Successful pollination resulted in swelling and growth of the silique. Mature siliques were removed and left to dry in a microcentrifuge tube prior to seed release through pod shattering.

2.6.4 Selection of transgenic Arabidopsis plants

During this project, Arabidopsis plants were stably transformed through the floral dipping method (as described in 2.2.14) with the *NET4Bpro*::NET4B-GFP construct, which is in the pMDC107 expression vector. The seed from the dipped plants was collected and selected on ½MS media plates containing 50 μg/ml Hygromycin B (Sigma) to select for transformed plants, and 200 μg/ml augmentin (GSK) which prevents growth of residual Agrobacterium. Seeds were first surface sterilised (according to 2.6.2) and spread on approximately 15-20 selective ½MS media plates. The plates were sealed and stratified for 3 days at 4°C in darkness, and were then grown horizontally in a Sanyo growth chamber. Seedlings transformed with the plasmid were resistant to the hygromycin and could survive on the plates, these plants were then transferred to soil and the seed was then collected.

2.6.5 Arabidopsis seed collection

Arabidopsis seeds were collected using the ARACON container system (Betatech). ARACON bases and tubes were placed over rosettes once floral bolting had occurred. Plants were grown to maturity in the Sanyo growth chambers or growth room, before being transferred to a seed collection room. Plants were left to senesce and dry for one month. Collected seeds were stored in microcentrifuge tubes kept at room temperature.

2.6.6 Root growth assays in unstressed conditions

The F_3 generation *net4b.1*, *net4a.1*, *net4b.1/net4a.1*, and azygous plants were grown as described in 2.6.2 on 12 cm square ½MS agar plates. Plates were first stratified for 3 days before being transferred to a Sanyo growth chamber. Plants were grown vertically and the primary root length of the seedlings was marked with a fine tip at days 4, 6, 8, 10. At day 12, the plates were scanned using an Epson 1680 Pro flatbed scanner. Root lengths were measured from the base of the hypocotyl to the tip of the primary root or the midpoint of the pen mark. Measurements were made using ImageJ FIJI software (Schindelin et al. 2012).

2.6.7 Root growth assays under stress conditions

The F_3 generation *net4b.1*, *net4a.1*, *net4b.1/net4a.1*, and azygous plants were grown as described in 2.6.2 on 12 cm square ½MS agar plates. Plates were first stratified for 3 days before being transferred to a Sanyo growth chamber. Plants were grown vertically for 5 days on ½MS agar plates before being transferred onto the stress treatment plates. Seedlings of a similar developmental stage (approximately 1 cm in root length) were selected and transferred using sterile forceps onto three plates; untreated ½MS agar plates, high salt treatment plates (½MS agar plates + 125 mM NaCl), drought stress plates (½MS agar plates + 200 mM sorbitol). The tip of the primary root tip was marked using a fine tip pen and the plants were grown vertically until they were 11-days old, and the plates were scanned using an Epson 1680 Pro flatbed scanner. Root lengths were measured from the base of the hypocotyl to the tip of the primary root (11 days after germination) or the midpoint of the pen mark (5 days after germination). Measurements were made using ImageJ FIJI software (Schindelin et al. 2012).

2.6.8 Transpirational water loss assay

The transpirational water loss assay was adapted from the protocol used in Jiang et al. (2012). The F_3 generation *net4b.1*, *net4a.1*, *net4b.1/net4a.1*, and azygous plants were grown for vertically for two weeks before being transferred to soil and grown until they were 5-weeks old (according to 2.6.2). All plants were well-watered 2 days prior to the transpirational water loss assay. Three fully expanded rosette leaves at a similar developmental stage were detached from the plant using forceps and placed in a plastic weighing boat. The leaves and weighing boat were weighed immediately to provide the fresh weight. Detached leaves were incubated at room temperature in the plastic weighing boats. The leaves were weighed at regular intervals: 30, 60, 90, 120, 180, 240 and 300 minutes after detachment. After the final measurement, the leaves were dried in a 70 °C incubator overnight and the dry weights of the leaves were recorded the following day. Subtracting the dry weight from the fresh weight provided the total water content (TWC) of the leaf. Water lost (ΔW) at each time point was calculated as a percentage loss of the total water content of the leaf using the following formula:

$$\% \text{ Water loss} = 100 - [(TWC - \Delta W) / TWC) \times 100]$$

2.7 Statistical and Image analysis

2.7.1 Statistical analysis software

Statistical analysis of *NET4B* expression levels and plant phenotypes was performed through ANOVA and post-hoc tests using SPSS software (version 17.0; SPSS).

2.7.2 Densitometry analysis

Densitometry analysis was used to quantitatively measure band density in CBB stained SDS-PAGE gels or Western blots. Band density is measured in terms of pixel intensity (e.g. darker and bigger bands give a higher intensity). The method for this analysis was based on the protocol created by Miller (2010). SDS-PAGE gels were imaged using a Bio-Rad Gel-Doc 1000 system, and Western blots on X-ray film were scanned using an Epson Perfection 4490 Photo flatbed scanner. Analysis of gels and blots was performed using the ImageJ FIJI software (Schindelin et al. 2012).

Images needed to be processed in gray-scale and so were first converted to 8-bit files. The rectangular tool was used to select a vertical area surrounding the lane of interest,

including all bands in that lane. This was repeated for each lane and then the intensity plot for the image was calculated. Protein bands appear as peaks on this blot, and the total area of the peaks depends on band intensity and size. The line tool was subsequently used to enclose the peak by drawing a line across the base of each peak, from the baseline level of background intensity. Finally the wand tool was used to measure the area of each peak in terms of relative arbitrary units.

For the analysis of the co-sedimentation assay, the band intensity for the NET4B-NAB protein in the supernatant and pellet lanes was calculated. The relative proportion of NET4B-NAB found in the pellet was then calculated as a percentage of the total band intensity observed in the supernatant and pellet. Three technical repeats of the SDS-PAGE gels were run and analysed to provide an average percentage intensity of the NAB domain in the pellet.

For analysis of the reduction of NET4B in the *net4* mutant lines, calculation of the relative intensity of each band (anti-NET4B and anti-actin) was performed according to the method described by Miller (2010). Firstly, the intensity of each anti-actin band in the mutant lanes were calculated as a percentage relative to the anti-actin band in the azygous control. This therefore normalised differences in loading across the mutant lines. Secondly, the intensity of each anti-NET4B band in the mutant lanes was calculated as a percentage of the anti-NET4B intensity relative to the azygous control. Finally, the relative intensity of the anti-NET4B bands was adjusted to account for differences in loading (as determined by the anti-actin band). This analysis therefore normalised the anti-NET4B band intensity across the samples and provided a value of band intensity relative to the density observed in the azygous control. Three biological replicates were used for this analysis to provide an average level of anti-NET4B band intensity in the different mutants (in terms of relative arbitrary units).

2.7.3 Quantitative analysis of anti-NET4B immunogold labelling

Quantitative analysis of the anti-NET4B immunogold labelling was performed according to the relative labelling index (RLI) method described in (Mayhew et al. 2002; Mayhew & Lucocq 2008; Mayhew 2011). This method provides a way of quantifying observed-counts on a subcellular compartment relative to an expected particle count through the use of stereological test-point counts. In addition, statistical analysis can be used to test whether the observed gold particle distribution differs from a random distribution.

Firstly, 82 images of the anti-NET4B labelled Arabidopsis root tip were captured at high magnification (x40,000) using TEM (see 2.5.2). Images were then selected for quantification using a random number generator. All images were processed using ImageJ FIJI software (Schindelin et al. 2012).

Prior to immunogold counting, the tonoplast and plasma membrane traces were converted to a cross-sectional area through the application of an acceptance zone. Applying the acceptance zone allowed the comparison of labelling across different subcellular compartments. Using ImageJ, the line tool was used to draw along the membrane traces. The width of the line was set to 30 nm which creates an acceptance zone of 15 nm at either side of the membrane. The 'Grid' plug-in was then used to superimpose a test-point lattice onto the image using squares of equal size (40,000 nm^2).

Observed gold particles (G_o) and test-point counts (P, counted as the bottom right corner of the grid) were then counted for each compartment. Gold particles that were directly on top of the acceptance zone line were included in that compartment. Gold particles and test-points were counted for the: tonoplast, plasma membrane, cell wall, mitochondria, endoplasmic reticulum (ER), Golgi, multivesicular bodies (MVB), cytosol and the nucleus. 502 gold particles were counted from 8 images, and additional counts were made for MVBs (G_o = 6, P = 21, from 16 additional images) as their expected gold count was not compatible with the Chi-squared analysis.

The expected gold count (G_e) for each subcellular compartment was calculated as (total sum of G_o x P) / total sum of P. The RLI for each compartment was calculated as RLI = G_o / G_e. Chi-squared analysis was performed for each subcellular compartment to test whether the observed distribution differed from random (expected distribution); $\chi^2 = (G_o - G_e)^2 / G_e$. The total Chi-squared value for all compartments was used to test whether observed gold particle distribution differed from random. Chi-squared values for each compartment were also expressed as a percentage of the total Chi-squared value (χ^2 as %). Preferential labelling at a particular compartment was determined based on two criteria: an RLI > 1, and a partial χ^2 value > 10% of the total.

Chapter 3 - Bioinformatics analysis of NET4B

3.1 Introduction

The NET1A-cDNA fragment, the first 288 amino acids of NET1A, was originally identified to localise to a filamentous network through a high-throughput screen carried out by Karl Oparka's lab (Escobar et al. 2003). Further characterisation of this fragment by the Hussey group, revealed that this fragment associates with actin filaments *in vivo* and that the first 94 amino acids (the NAB domain) could bind actin filaments directly *in vitro* (Calcutt 2009; Deeks et al. 2012). Bioinformatics analysis was fundamental in finding proteins that shared this domain and therefore in the discovery of the NETWORKED (NET) family (Calcutt 2009; Deeks et al. 2012).

The NET family was discovered through bioinformatics by searching the protein databases for proteins containing the NAB domain. Furthermore, bioinformatics analysis has been used to show that the NET proteins contain predicted coiled-coil domains, as well as showing the potential expression pattern of the NET genes (Calcutt 2009; Deeks et al. 2012; Hawkins et al. 2014).

This chapter documents several different bioinformatics approaches that have been used to gain further insight into NET4B. This analysis was used to discover the NET4B nucleotide and protein sequences, as well as the predicted secondary structure and tissue expression pattern of NET4B.

3.2 Identification of NET4B nucleotide and protein sequences

Preliminary information regarding NET4B was gathered from The Arabidopsis Information Resource (TAIR; Huala et al. 2001). The TAIR database maintains genetic and molecular biology data for the model plant *Arabidopsis thaliana*, as well as links to other bioinformatics resources and access to seed and DNA stocks. The information held on the TAIR database revealed that *NET4B* has an open reading frame (ORF) of 1742 base pairs (bp), which contains three exons (bp 1-15, 115-226 and 318-1742) as depicted in Figure 3.1. This gene encodes a 517 amino acid long protein with a predicted molecular weight of 60 kDa.

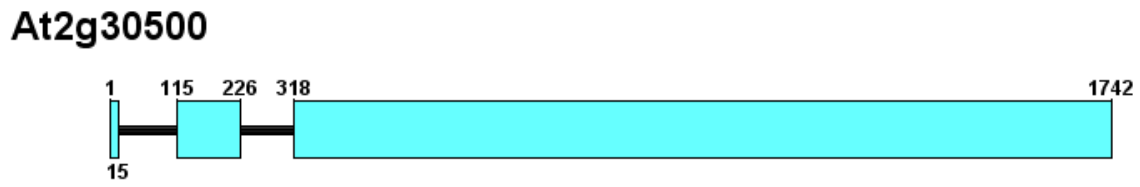

Figure 3.1: Schematic representation of the gene structure of *NET4B*. Diagram shows exons in blue and introns with a black line. Numbers represent base pair positions from the start codon. Diagram created using the Illustrator of Biological Sequences (IBS) software (Liu et al. 2015).

3.3 Predicted protein structure of NET4B

The predicted secondary structure of the NET4B protein was analysed through the SMART (Simple Modular Architecture Research Tool) web resource that allows users to detect protein domains within their protein of interest (Schultz et al. 1998; Letunic et al. 2014). Querying the SMART database with the NET4B amino acid sequence revealed two main features; the KIP1 domain (now termed the NAB domain) at the N-terminus and two coiled-coil domains. This domain architecture of the N-terminal NAB domain and C-terminal coiled-coil domains is consistent with all other members of the NET family (Deeks et al. 2012).

The KIP1 domain was identified by the SMART programme from the Database of Protein Families (Pfam), which identifies protein families using sequence alignments of conserved domains (Finn et al. 2014). The KIP1 domain or Pfam 07765, was identified as a domain present in the *Petunia inflata* KINASE-INTERACTING PROTEIN 1 (PiKIP1), however this domain did not have a characterised function prior to the discovery of the NET superfamily. The KIP1/NAB domain is structurally different from the central kinase interacting domain of KIP1 that was shown to directly interact with the cytosolic kinase domain of the POLLEN RECEPTOR-LIKE KINASE 1 (PRK1; Skirpan et al. 2001). Therefore, it should be noted that the NAB domain does not define a family of kinase interacting proteins.

The SMART resource identified two coiled-coil domains within NET4B running from amino acids 156-221 and 256-486 respectively. Coiled-coil domains are typically formed by two to five α-helices wrapping around each other to form a left-handed helix and supercoil (Mason & Arndt 2004). The basic sequence structure of these domains is

composed of a heptad repeat, where there is a seven-residue periodicity in the properties of the amino acids (Burkhard et al. 2001). The helices are formed by non-polar residues fitting inside the helix and polar residues residing outside the helix which gives rise to interactions between the two helices via electrostatic interactions (Mason & Arndt 2004).

The prediction of the coiled-coil domains on the SMART database uses the COILS programme (Lupas et al. 1991). This programme compares an amino acid sequence to a database of known two-stranded parallel coiled-coil containing proteins and creates a similarity score. The similarity score is then compared to globular and coiled-coil proteins and the programme generates a probability value that the sequence will adopt a coiled-coil. This programme uses a scoring matrix based on the amino acid sequences of myosins, paramyosins, tropomyosins, intermediate filaments, desmosomal proteins and kinesins (MTIDK matrix). The results of the coiled-coil prediction for NET4B using the COILs programme (MTIDK matrix, 28-residue window, and cut-off probability of > 0.9) are shown in Table 3.1.

COILS was the first described programme to predict the potential of proteins to form coiled-coils. Further developments on coiled-coil prediction programmes have demonstrated that the COILS programme can be prone to false positives as it can incorrectly predict coiled-coil domains in alpha-helical regions (Berger et al. 1995). Paircoil, is a coiled-coil prediction programme that uses pairwise residue correlations within the heptad repeat to predict whether a protein will form a coiled-coil. This programme has been shown to produce fewer false positives than the COILS programme, and it was the programme used originally to predict the coiled-coil domains of the NET proteins (Berger et al. 1995; Deeks et al. 2012). Paircoil2 has recently been developed which applies the same Paircoil algorithm to a larger database of coiled-coil domain containing proteins for comparison (McDonnell et al. 2006). The results of the coiled-coil prediction for NET4B using the Paircoil2 programme (28 residue window, cut-off value < 0.025) are shown in Table 3.1.

Both programmes predicted three coiled-coil domains occupying approximately 60% of the total NET4B protein length, however the position of the second coiled-coil differed between the two predictions (Table 3.1). As the Paircoil2 programme produces fewer false positives, it was used to generate the predicted secondary structure model for NET4B used throughout this project (Figure 3.2).

Programme	Start and end position of coiled-coil domains (amino acids)	% sequence predicted to be coiled-coils
COILS	153-233	57.6
	255-353	
	366-486	
Paircoil2	160-234	59.2
	248-264	
	266-482	

Table 3.1: Predicted coiled-coil domains from the COILS and Paircoil2 programme. Paircoil2 was used for the predicted coiled-coil domains as it has been shown to produce fewer false positives (Berger et al. 1995; McDonnell et al. 2006).

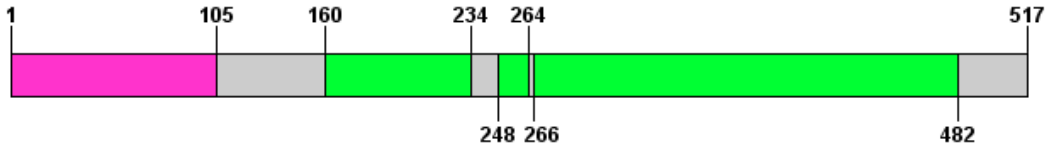

Figure 3.2: Model showing the secondary structure of NET4B. Schematic diagram of the secondary structure of NET4B protein showing the NAB domain in magenta and coiled-coil domains in green (based upon the Paircoil2 prediction). Numbers denote amino acids residues. This schematic diagram was generated using the IBS software (Liu et al. 2015).

3.4 Sequence similarity between NET4B and NET4A

As well as consulting the SMART database to identify potential functional domains of NET4B, a sequence alignment between NET4A and NET4B was performed to identify any conserved regions that could be functionally important. Previous bioinformatics analysis grouped these two proteins within the same Arabidopsis subfamily based on the sequence similarity in the NAB domain, structural organisation of the C-terminus and sequence length (Deeks et al. 2012). In order to identify potential conserved domains between NET4B and NET4A a global pairwise alignment was performed using The European Molecular Biology Open Software Suite (EMBOSS) Needle programme (Rice et al. 2000). This tool uses the Needleman-Wunsch algorithm to create an optimal alignment between two proteins along their entire length.

The alignment between NET4B and NET4A was performed using the default settings for protein alignments (Protein weighting matrix: EBLOSUM62, Gap opening penalty:

10, Gap extension penalty: 0.5). The result of this full-length alignment is shown in Figure 3.4. Overall, the two NET4 proteins share 40.6% identity and 58.5% similarity in amino acid composition. Within the two sequences, three areas of high similarity were manually detected; the NAB domain, conserved domain 2 (CD2) and conserved domain 3 (CD3). These three domains were then aligned separately using the EMBOSS Needle programme (using the previous settings) to give a percentage identity/similarity score for the individual region, and the results are shown in Figure 3.3 (c) and Table 3.2.

The conserved domain 2 was shown to be specific to the NET4 proteins through a BLAST (Basic Local Alignment Search Tool) search against the Arabidopsis proteome using the amino acid sequence of CD2 as an input. Recent bioinformatics research into the post-translational modification of the NET proteins has suggested that there could be a possible conserved serine phosphorylation site within this domain in the following conserved motif: RALKTAV**S**DAEQKIF (Simon Bush, personal communication). Therefore this domain could potentially be important in regulating the activity of the NET4 proteins and further work needs to be done to confirm this hypothesis.

Previous analysis by Dr. Tim Hawkins revealed that CD3 is also highly conserved in two other NET proteins; NET3A and NET3C (Hawkins, personal communication). The position of CD3 in all four NET proteins is at the C-terminus of the protein. Figure 3.4 (a) shows an alignment of the C-terminal 130 amino acids of the four NET proteins containing this domain. This alignment was made using the default settings on Clustal Omega (Sievers et al. 2011) and the output was visualised using Jalview (Waterhouse et al. 2009).

All four proteins have a highly conserved stretch of amino acids running from E474 - G496 on NET4B, as indicated by the red line in Figure 3.4 (a). Each of the four NET proteins have a conserved isoleucine (I), arginine (R) and glutamine (Q) residue in this stretch and this domain was therefore named the IRQ domain. Conserved residues also exist outside of this highly conserved stretch and the area they cover is indicated by the blue line in Figure 3.4 (a). As these amino acids were conserved at specific sites in each protein, they could potentially be important for any function that this domain might have. Therefore from this study the IRQ domain was defined as covering the area of the highlighted by the blue line, from the glutamate (E) at residue 464 to the isoleucine (I) at residue 502 on NET4B.

(a)

(b)

Colour	Residue at position	(Threshold, residue group)
BLUE	A, I, L, M, F, W, V	(60% WLVIMAFCHP)
	C	(60% WLVIMAFCHP)
RED	R, K	(60% KR) (85% K, R, Q)
GREEN	N	(50% N) (85% N, Y)
	Q	(60% KR) (50% QE) (85% Q, K, E, R)
	S, T	(60% WLVIMAFCHP) (50% TS) (85% S, T)
PINK	C	(100% C)
MAGENTA	E	(60% KR) (50% QE) (85% E, Q, D)
	D	(60% KR), (85% K,R,Q) (50% ED)
ORANGE	G	(0% G)
CYAN	H, Y	(60% WLVIMAFCHP) (85% W,Y,A,C,P,Q,F,H,I,L,M,V)
YELLOW	P	(0% P)

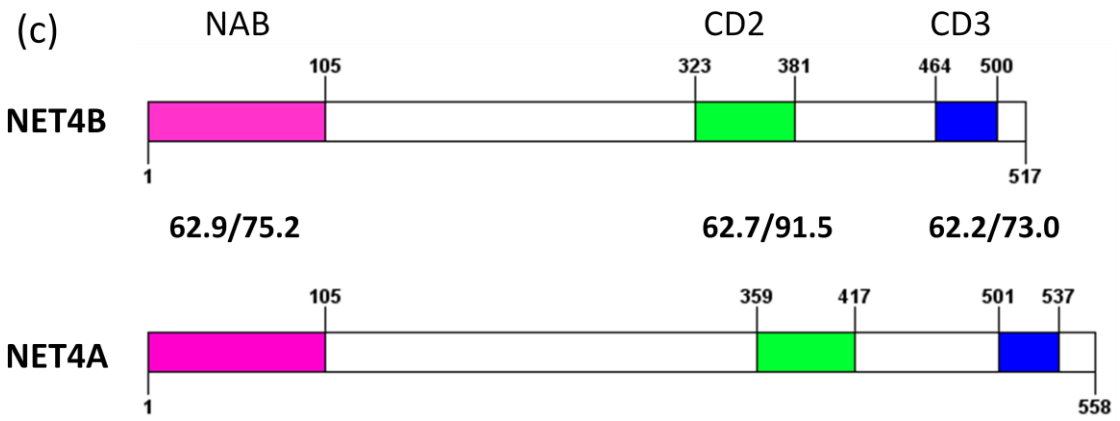

Figure 3.3: Amino acid sequence alignment between NET4B and NET4A. (a) The EMBOSS Needle programme was used to create a global pairwise alignment. The alignment was imaged using Jalview using the ClustalX default colours. Three areas of particular conservation are highlighted with a black line underneath the sequence. The first represents the NAB, followed by conserved domain (CD) 2 and 3. (b) ClustalX colour scheme key which is defined by the amino acid characteristics and conservation in the alignment. The key works as follows: the colour for the column is generated if the threshold value is met or exceeded. The minimum percentage is shown with the amino acids that must meet or exceed this threshold value. If the residues are grouped together such as 'KR' then the colour is applied if any combination of these residues meets or exceeds the threshold percentage. If the residues are separated by commas then the colour is applied when one of these residues individually meets or exceeds the threshold value. (c) Schematic diagram depicting the comparison between NET4B and NET4A, NAB domain is depicted in magenta, CD2 in green and CD3 in blue. Amino acid identities and similarity percentages are shown in bold between the domains. This diagram was created using the IBS software (Liu et al. 2015).

Alignment	NET4A amino acid locations	NET4B amino acid locations	Length	% Identity	% Similarity	% Gaps	Score
Full-length	1-558	1-517	576	40.6	58.5	13.0	991
NAB	1-105	1-105	105	62.9	75.2	0.0	345
CD2	359-417	323-381	59	62.7	91.5	0.0	198
CD3	501-537	464-500	37	62.2	73.0	0.0	113

Table 3.2: Results of the NET4B and NET4B amino acid sequence alignments using the EMBOSS Needle programme.

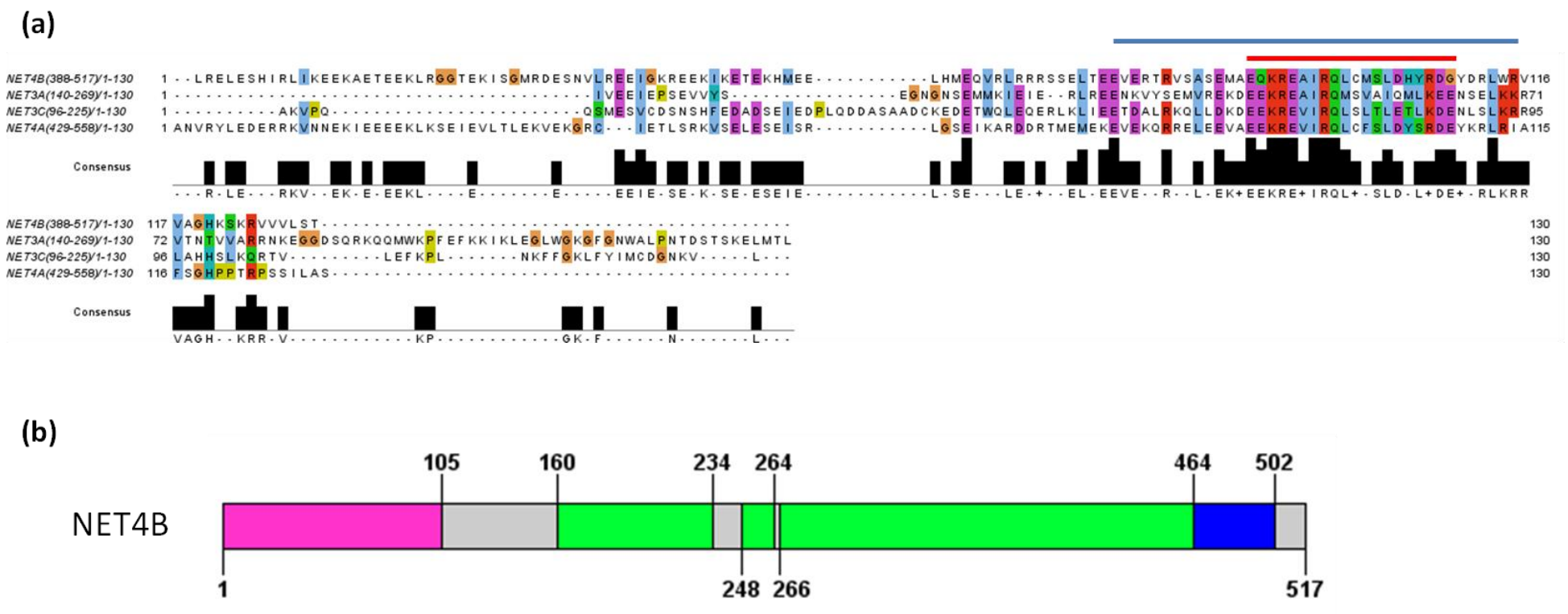

Figure 3.4: Defining the IRQ domain. (a) The last 130 aa residues of NET4A/4B/3A/3C were aligned using Clustal Omega and visualised using Jalview with the default ClustalX colour scheme as explained in Figure 3.4. The red line indicates the highly conserved stretch of amino acids from NET4B$^{E474\text{-}G496}$, the blue line indicates the area initially defined as the IRQ domain from NET4B$^{E464\text{-}I502}$. (b) Modified protein structure of NET4B created using the IBS software (Liu et al. 2015). NAB domain is shown in magenta, coiled-coils in green, and the IRQ domain in blue.

The actual position of the IRQ domain relative to the C-terminus, slightly differed between the four NET proteins and the C-terminal amino acids after this domain appeared to be relatively less conserved between the four proteins. Figure 3.4 (b) shows an amended model of the predicted secondary structure of NET4B that includes the C-terminal IRQ domain.

3.5 Gene expression analysis

Studying the expression pattern of a gene through bioinformatics analysis can provide information on a genes tissue localisation and response to stresses. This information can be valuable in discovering the function of a gene as it could suggest involvement in tissue-specific processes or adaptation to stresses.

Gene expression data, generated from DNA microarrays or RNAseq data for example, can be easily interpreted through the use of computer programmes such as Genevestigator and the Arabidopsis electronic Fluorescent Pictograph (eFP) Browser. Genevestigator Version 3 (GV3) compiles manually curated data from several different Affymetrix GeneChips as well as RNAseq data (Hruz et al. 2008). The Arabidopsis eFP browser compiles data from the Affymetrix ATH1 GeneChip and provides a very intuitive method of visualising gene expression data (Winter et al. 2007). Both of these programmes were used to investigate the publicly available gene expression data for *NET4B*, in terms of both tissue expression pattern and response to stresses.

3.5.1 Tissue expression pattern

Both Genevestigator and the Arabidopsis eFP browser were used to study the developmental and tissue specific pattern of *NET4B*. Figure 3.5 shows the expression of *NET4B* during various different stages of plant development. This analysis shows that *NET4B* has a relatively high level of expression and that the highest level of expression is seen at the germinating seed, seedling, young rosette and senescence stage. However it should be noted that the senescence stage data was compiled from significantly fewer experiments.

This developmental map indicates the specific stages that *NET4B* is expressed in but it does not distinguish which specific tissues show the highest levels of expression. Figure 3.6 shows a heatmap of *NET4B* expression levels as a percentage of the highest potential expression. Therefore, in this figure a darker shade indicates a tissue that has a

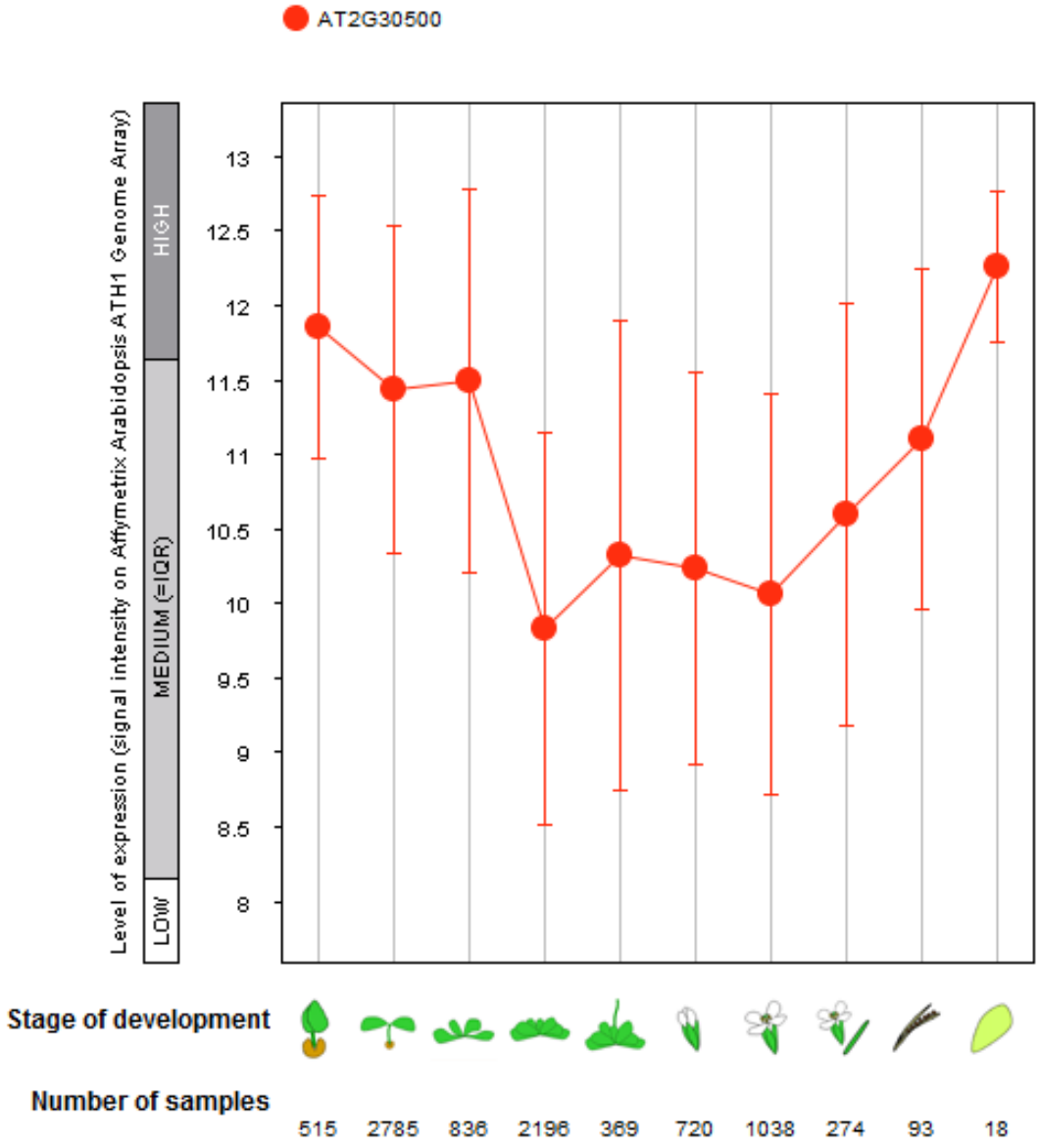

Figure 3.5: Genevestigator developmental map for *NET4B*. The Genevestigator tool was used to analyse the expression of *NET4B* during development. The level of expression is shown as the $\log_2$ value and the stages of development are pictorially represented from left to right as follows; germinated seed, seedling, young rosette, developed rosette, bolting, young flower, developed flower, flowers and siliques, mature siliques and senescence. Data is compiled and visualised using Genevestigator (Hruz et al. 2008).

proportionately higher level of *NET4B* expression rather than showing absolute values. This figure shows that *NET4B* is most highly expressed in guard cells and guard cell protoplasts. In addition, high levels of *NET4B* expression could be seen in the root protoplasts, with a slightly lower level of expression in the roots, seedlings and siliques. It should also be noted that there is limited *NET4B* expression in the mesophyll protoplasts, which could suggest that *NET4B* expression is specific to the guard cells of the leaf.

As a secondary source of expression data, the Arabidopsis eFP browser was also consulted for information on the expression pattern of *NET4B*. This tool allows the visualisation of expression data in both absolute and relative terms. Figure 3.7 shows the expression of NET4B in many different organs and stages of development. This figure uses data from a global analysis of Arabidopsis gene expression that was obtained from 79 different stages, using three technical repeats for most stages (Schmid et al. 2005). From this data set, expression for *NET4B* was shown to be highest in the developing embryo at stages 6, 8, 9 and 10, which correspond to the torpedo through to the green cotyledons stage. Slightly lower levels of expression were also found in the root and shoot apex inflorescence, and relatively low expression was seen in the rosette leaves. These results largely corroborate with the data compiled from Genevestigator, with expression being seen in the root, siliques and embryo. However this experiment demonstrates a higher level of expression in the shoot apex inflorescence that was not obvious using Genevestigator. Similarly, Genevestigator suggested a higher expression of *NET4B* during senescence that was not shown during this assay.

The Arabidopsis eFP browser also demonstrated that the highest level of *NET4B* expression level was observed in the root and therefore the tissue-specific pattern of *NET4B* in this organ was investigated. Figure 3.8 (a) shows the tissue-specific *NET4B* expression pattern that was generated using data from a high resolution spatio-temporal map of root expression, that collected both radial and longitudinal expression data in the Arabidopsis root (Brady et al. 2007). When studying the cross section of the root, *NET4B* was most highly expressed in the epidermis and cortex of the root, with the lowest levels in the endodermis. On the longitudinal axis, this study demonstrated that *NET4B* was most highly expressed in the maturation zone and the early elongation zones.

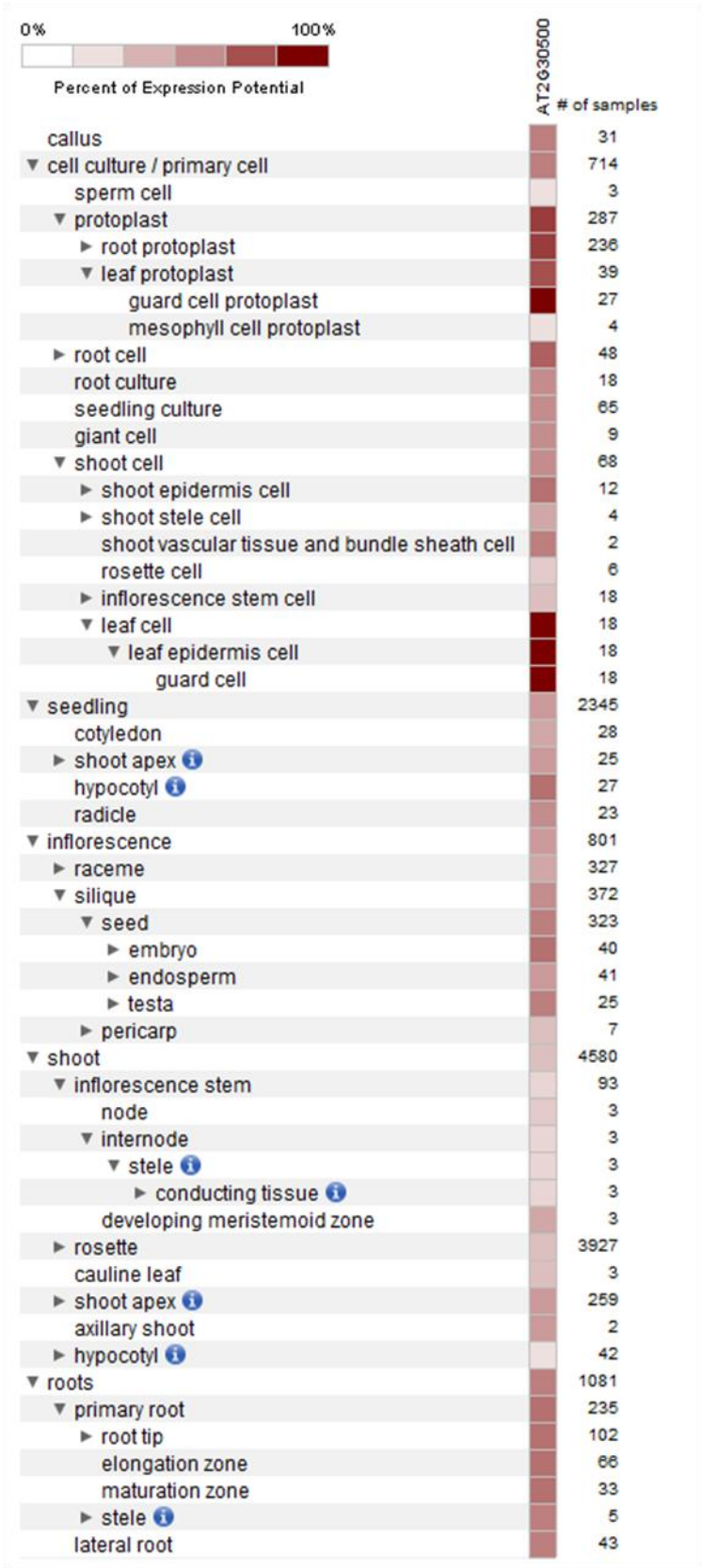

Figure 3.6: Expression pattern of *NET4B* using the Genevestigator database. Shown here is a heatmap of expression levels using the log2 values, with darker shades indicating higher levels of expression potential. Expression of *NET4B* is highest in the guard cells, roots, seedlings and siliques. Data is compiled and visualised using Genevestigator (Hruz et al. 2008).

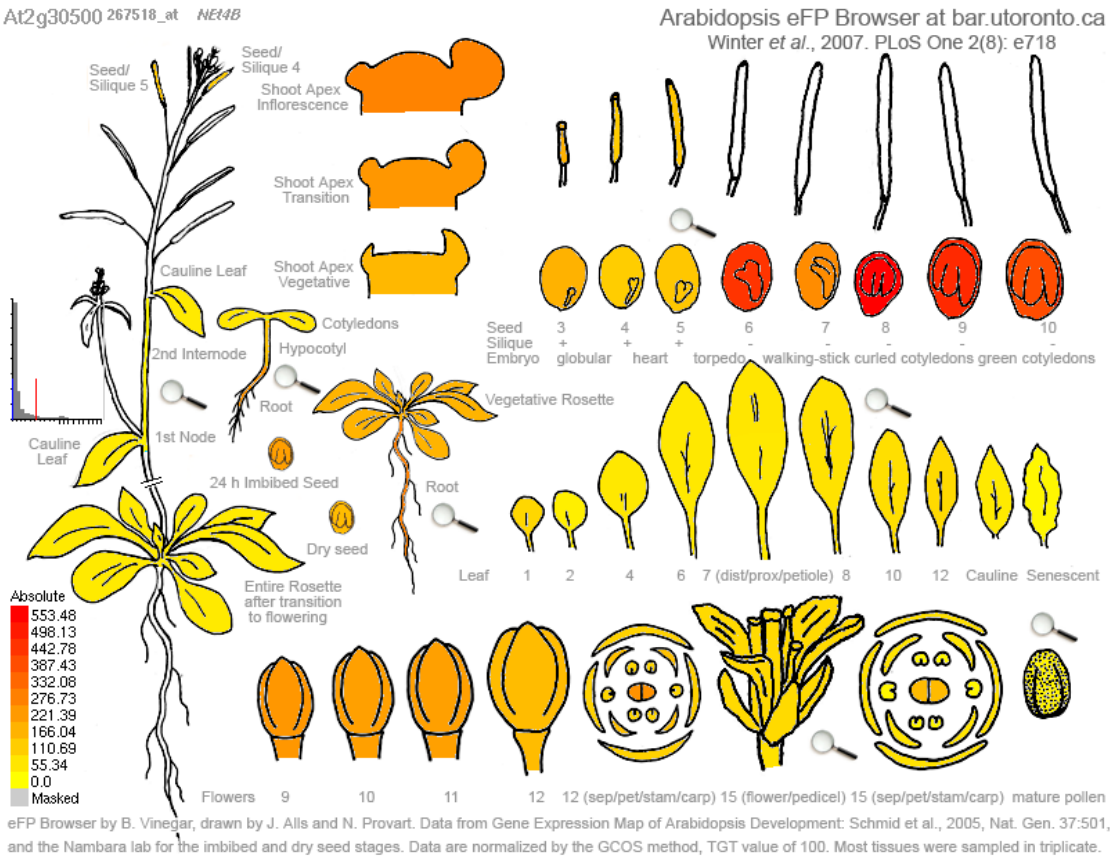

Figure 3.7: Developmental map of *NET4B* expression derived from Arabidopsis eFP browser database. Visualisation of absolute values of *NET4B* expression from the dataset of global Arabidopsis gene expression pattern in different tissues (Schmid et al. 2005). Shown here is the absolute levels of expression, and shows the range of expression values with low levels in yellow and high levels in red. Highest levels of *NET4B* expression from this data set are seen in the developing embryo at stages 6, 8, 9, 10. High levels of expression are also found in the root and shoot apex inflorescence. Relatively low levels of expression are found in the rosette leaf. Data is compiled and visualised using the Arabidopsis eFP browser (Winter et al. 2007).

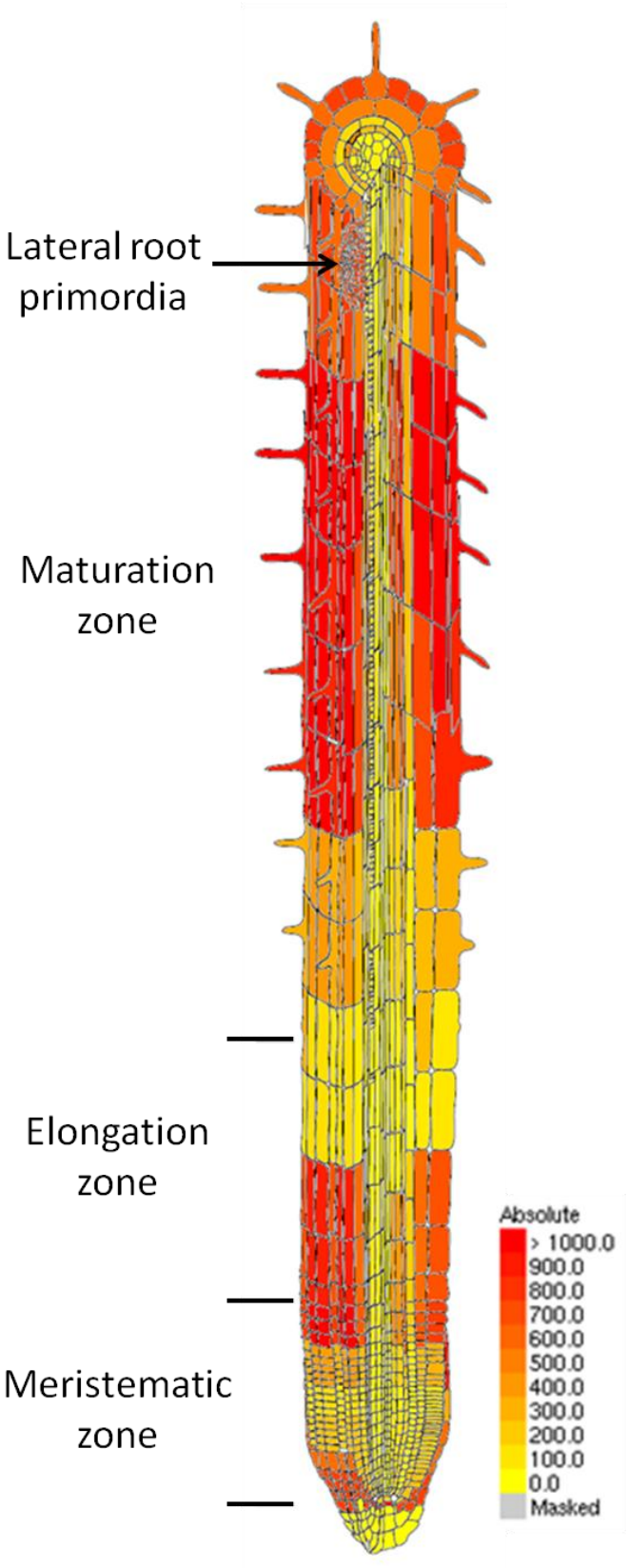

Figure 3.8: Expression map of *NET4B* in the root. The Arabidopsis eFP browser was used to visualise the absolute expression values of NET4B from the spatio-temporal map of root expression data (Winter et al. 2007; Brady et al. 2007). Shown here is the absolute levels of expression, and shows the range of expression values with low levels in yellow and high levels in red. *NET4B* is highly expressed in the epidermis and cortex of the root, and shows higher expression in the maturation and elongation zones.

Although microarray data does not exist for NET4A, the *NET4Apro*::NET4A-GFP lines demonstrated that NET4A was expressed in the epidermis of the root and localised to the tonoplast in this tissue (Deeks et al. 2012). Therefore the bioinformatics data for *NET4B* suggest that it could similarly be expressed in this tissue, as well as in the guard cells, siliques and embryos.

3.5.2 Perturbations

In addition to studying the developmental and tissue-specific expression pattern of *NET4B*, it was also important to study whether *NET4B* expression changes in response to certain stimuli. The Arabidopsis eFP browser was used to analyse the response of *NET4B* to various perturbations as this programme provides a very convenient method of visualisation. Three different perturbations were examined; hormone treatments, abiotic stress and biotic stress.

For hormone responses, the Arabidopsis eFP browser visualises data compiled from the AtGenExpress data set for hormone treatments (Goda et al. 2008). This dataset examined the gene responses in 7-day old Arabidopsis wild-type Col0 seedlings to seven phytohormones; auxin, cytokinin, gibberellin, brassionsteroid, abscissic acid, jasmonate and ethylene. Out of all these different hormone treatments only abscissic acid (ABA) induced a change in *NET4B* expression that was greater than a 1.5 fold-change. This study showed that incubation of 7 day old seedlings in 10 μM ABA for 3 hours induced a 1.6 fold change in *NET4B* expression levels. ABA is an important regulator of plant growth during water stress (Hoth et al. 2002), and therefore the upregulation of *NET4B* in response to this phytohormone could suggest a possible role for this protein during osmotic stress.

The changes to *NET4B* expression during abiotic stress was analysed using data visualised from an experiment studying the global stress responses of Arabidopsis. This assay is part of the AtGenExpress data set and investigated the gene expression changes in shoots and roots of 18-day old plants in response to various different stresses including; heat, cold, high osmolarity, drought, UV-B light and wounding (Kilian et al. 2007). Plants were grown in a customised growth chamber, where the plants grew on top of a polypropylene raft on liquid MS medium. This chamber enabled the plants to grow in a uniform environment and allowed the controlled application of stress and harvesting of tissue at the different time points.

The Arabidopsis eFP browser demonstrated that out of the stresses examined, only cold, osmotic, salt, drought and wounding elicited a fold-change in *NET4B* expression that was greater than 1.5. Table 3.3 shows how these different treatments were carried out and Figure 3.9 (a) and (b) shows the fold-change in *NET4B* expression in shoot and root tissue respectively. It should be noted that these graphs show the fold change of *NET4B* expression, but the absolute values of *NET4B* expression were consistently higher in the roots.

In the shoot, *NET4B* showed a very dramatic rapid change in expression in response to wounding which peaked at a 2.8 fold-change 1 hour after treatment. This transient expression in response to wounding was characteristic of most upregulated genes in this assay, and could be a reflection of the transient nature of this stress (Kilian et al. 2007). Cold treatment also lead to a change in *NET4B* expression in the shoots, and resulted in a 3.06 fold-change 6 hours after the treatment, which then dropped back down after 12 hours. However most genes that were upregulated in response to cold exhibited a continuous increase in expression after this stress treatment (Kilian et al. 2007). Osmotic, salt and drought stress did not induce any dramatic change in *NET4B* expression in the shoots.

In the roots, *NET4B* expression changed rapidly in response to drought, salt and osmotic stress and these stresses all resulted in a *NET4B* fold-change greater than 1.5 after 1 hour. Osmotic stress resulted in a consistently higher level of *NET4B* expression, whereas *NET4B* expression in response to salt and drought stress decreased after one hour. This pattern of response to these stresses, is similar to that observed by most upregulated genes in this assay and could be a reflection on the nature of the stresses, with osmotic being more continuous and salt/drought being more transient (Kilian et al. 2007). Cold and wounding did not elicit a dramatic change in *NET4B* expression in the root at any time point.

The Arabidopsis eFP browser also compiles data from different assays looking at gene expression changes in response to biotic stresses including; fungal, bacterial, oomycete, elicitors and aphids. Examining the response of *NET4B* to the various different biotic stresses revealed that expression only dramatically changed in response to infiltration of different strains of the bacterial pathogen, *Pseudomonas syringae*. This experiment was performed by the Nürnberger lab as part of the AtGenExpress project and is compiled on the Arabidopsis eFP browser (Winter et al. 2007). Global gene expression responses

Stress	Treatment
Cold	Growth chambers were transferred onto ice and kept at 4°C until harvest
Osmotic	300 mM mannitol was added to the MS medium
Salt	150 mM NaCl was added to the MS medium
Drought	The growth chamber lids were removed for 15 minutes, exposing the plants to a stream of air and resulted in a 10% loss in fresh weight.
Wounding	Leaves were punctured with a customised pin-tool, resulting in an average of three to four punctures per leaf.

Table 3.3: Description of the abioitic stress treatments performed by Kilian et al. (2007).

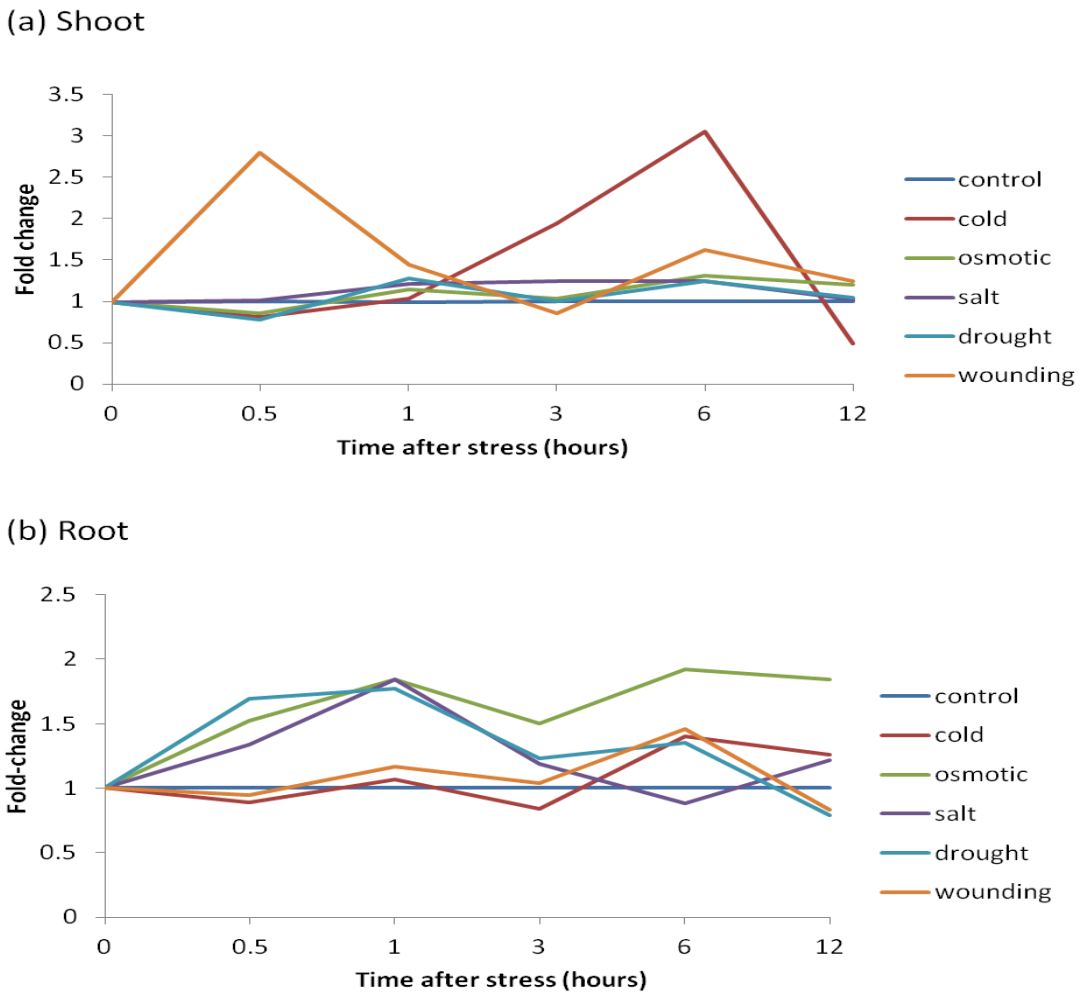

Figure 3.9: *NET4B* expression change during abiotic stress. *NET4B* expression changes under abiotic stress was obtained from the Arabidopsis eFP browser which compiled data from a global Arabidopsis stress response assay (Kilian et al. 2007). (a) and (b) and *NET4B* fold-change in response to the different stresses in shoot and root tissue respectively.

were analysed in response to the infiltration of four different *P. syringae* strains: virulent (pv. tomato DC3000), avirulent (pv. avrRpm1), Type III-Secretion system deficient (deficient; pv. tomato DC3000 hrcC-), nonhost (pv. *phaseolicola*).

These different strains were chosen as they elicit different responses in the plant. The virulent strain is compatible with Arabidopsis and is able to overcome the plants defences and cause disease (Katagiri et al. 2002). The avirulent strain induces effector triggered immunity (ETI) in the plant and causes a rapid response to prevent bacterial invasion, and leads to the hypersensitive response and localised cell death (Lewis et al. 2009). The deficient strain cannot secrete effectors into the apoplast of the plant cell. Therefore the bacteria cannot effectively suppress basal plant immunity, and the plant can therefore recognise the invariant microbe-associated molecular patterns (MAMPs) such as flagellin. Infiltration of this strain induces pattern triggered immunity (PTI) which leads to downstream defence signalling (Henty-Ridilla et al. 2013). The non-host pathovar is incompatible with Arabidopsis and cannot infect the plant and cause disease symptoms. The molecular mechanism of non-host resistance is poorly understood but it has been hypothesised that the bacteria cannot generate effective infection structures or that it cannot overcome the plants basal immunity in response to the pathogen (Mishina & Zeier 2007).

Figure 3.10 and Table 3.4 shows the change in *NET4B* expression after infiltration with these various different bacterial strains. This assay showed that a dramatic increase in *NET4B* expression was seen when leaves were infiltrated with the non-host pathovar, and this could be observed 6 hours post infection (hpi) and increased to a 5.34 fold-change 24 hpi. The avirulent and deficient strains also caused an increase in *NET4B* expression that was detectable 24 hpi, which lead to a 2.42 and 1.72 fold-change in expression respectively. The virulent strain did not cause any change in *NET4B* expression in this assay. The results from this experiment suggest that *NET4B* could be important in the response to non-host bacterial pathogens, as well as in the PTI and ETI responses of Arabidopsis.

3.6 Conclusion

Results from bioinformatics analysis presented here have shown that *NET4B* encodes a gene with an ORF of 1742 bp, which contains three exons. The *NET4B* gene was shown

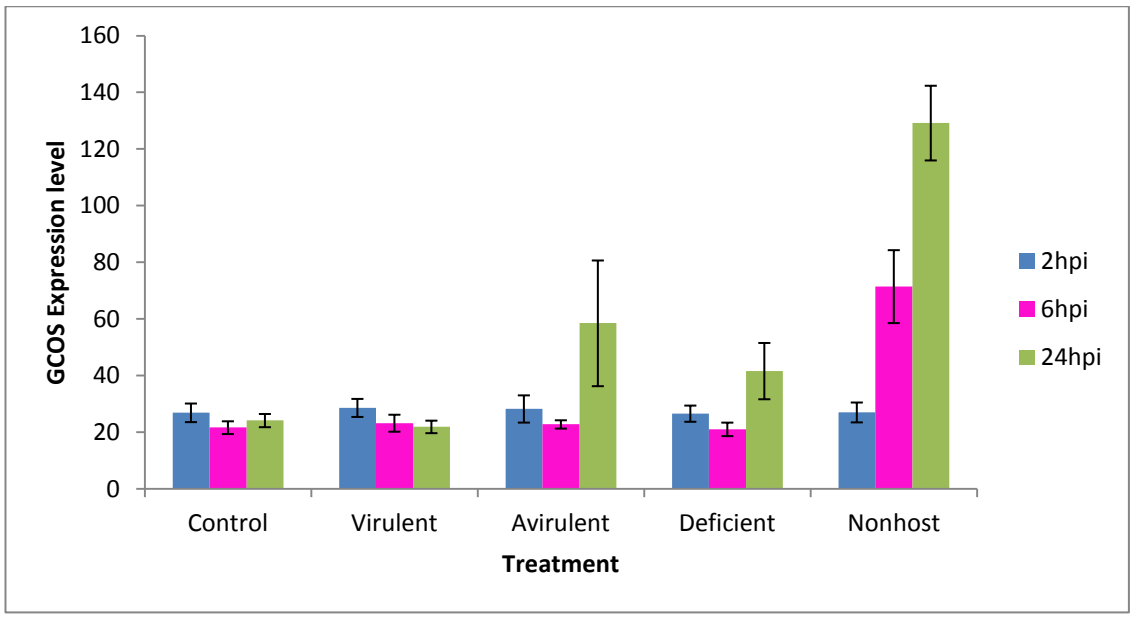

Figure 3.10: *NET4B* expression change during biotic stress. *NET4B* expression changes in response to several strains of *Pseudomonas syringae* was compiled from the Arabidopsis eFP browser using data generated from the Nürnberger lab (Winter et al. 2007). Shown here is a graph showing the absolute expression level of *NET4B* during the time course using the different bacterial strains. Error bars represent standard deviation of the mean expression signal. Control = 10mM MgCl2, Virulent = *Pseudomonas syringae* pv. tomato DC3000, Avirulent = pv. avrRpm1, Deficient = pv. tomato DC3000 hrcC-, Nonhost = pv. *phaseolicola*. SD = standard deviation of the mean expression signal. hpi= hours post infection. GCOS = GeneChip Operating Software.

	2hpi				6hpi				24hpi			
Strain	Expression level	SD	log2 value	Fold-change	Expression level	SD	log2 value	Fold-change	Expression level	SD	log2 value	Fold-change
Control	26.90	3.28	0.00	1.00	21.66	2.25	-0.01	0.99	24.16	2.33	-0.01	0.99
Virulent	28.63	3.18	0.09	1.06	23.23	3.00	0.10	1.07	21.93	2.21	-0.14	0.90
Avirulent	28.26	4.81	0.07	1.05	22.80	1.47	0.07	1.05	58.50	22.19	1.27	2.42
Deficient	26.60	2.86	-0.02	0.98	21.06	2.38	-0.05	0.97	41.63	9.94	0.78	1.72
Nonhost	27.03	3.51	0.00	1.00	71.46	12.88	1.72	3.29	129.20	13.19	2.41	5.34

Table 3.4: Values of *NET4B* expression change during biotic stress. Shown here are the values of NET4B expression change in response to pathogen infection. Data was obtained from the Arabidopsis eFP browser (Winter et al. 2007). Expression levels are those obtained from the GeneChip Operating software. SD = standard deviation, HPI = hours post infection. Bacterial strains are described in Figure 3.10.

to encode a protein that is 517 amino acids in length with a predicted molecular weight of 60 kDa.

The secondary structure of NET4B was investigated using online software which demonstrated that it contains the N-terminal NAB domain and three predicted C-terminal coiled-coil domains. Aligning the NET4B and NET4A amino acid sequences revealed that three conserved domains could be found between the two proteins; the NAB domain and two other conserved domains towards the C-terminus of the proteins. One of these domains was specific to the NET4s, and could potentially be involved in their post-translational modification and regulation through phosphorylation, however this remains to be confirmed experimentally. The third conserved domain, which was termed the IRQ domain, could be found in both NET4 proteins as well as NET3A and NET3C and could represent an important functional domain of these proteins. This domain was very close to the C-terminus of these proteins, however the relative position of this domain differed slightly between these NETs. The role of this conserved IRQ domain was investigated further in this project through analysis of its subcellular localisation (Chapter 4), identification of its potential interacting partners (Chapter 6) and further bioinformatics research into the presence of the IRQ domain in other proteins (Chapter 8).

The gene expression profile of *NET4B* was investigated in terms of tissue-expression pattern and response to different stresses. This analysis was performed using the Arabidopsis eFP browser and Genevestigator computer programmes that compile and visualise gene expression data largely derived from DNA microarray experiments.

During development, *NET4B* expression was shown to be highly expressed in the germinating seed, seedling, young rosette and senescence. In addition, *NET4B* was shown to be strongly expressed in the roots, developing embryo and guard cells. Furthermore, this analysis demonstrated that *NET4B* was predominantly expressed in the outer layers of the root, with expression being highest in the epidermis and cortex.

The expression pattern of *NET4B* in the roots similarly matches the expression of NET4A, which has been shown to be expressed in the epidermis of the root through *NET4Apro*::NET4A-GFP lines (Deeks et al. 2012). The tissue expression pattern of *NET4B* in Arabidopsis was investigated further in this project through the GUS reporter system, as described in Chapter 5.

The change in *NET4B* expression in response to different stimuli, including hormone treatment, abiotic and biotic stress was also investigated through bioinformatics analysis. For the hormone treatments, *NET4B* was shown to be upregulated in seedlings in response to the application of ABA. This phytohormone is important in regulating growth in response to the water status of the plant (Hoth et al. 2002), therefore *NET4B* could be important in the plants response to osmotic stress.

Investigating the response of *NET4B* to abiotic stresses showed differential expression changes in the shoot and roots. Wounding induced a very dramatic and transient increase in *NET4B* expression in the shoots. Cold treatment also lead to an increase in *NET4B* expression, however this only became apparent after 6 hours and the level of *NET4B* expression returned to normal after 12 hours of cold treatment. Drought, salt, and high osmolarity induced an increase in *NET4B* expression in the roots. Drought and salt stress both lead to transient changes in gene expression, however high osmolarity lead to a continuous upregulation of *NET4B*. Similarly to the ABA treatment, the upregulation of *NET4B* in the root during these stresses suggests that it could be important in the plants response to osmotic stress. The importance of the *NET4s* during osmotic stress was investigated further in this project through phenotypic analysis of the *net4* mutants and is discussed in Chapter 7.

Finally, the response of *NET4B* to biotic stress was also investigated using the Arabidopsis eFP browser. This analysis demonstrated that *NET4B* expression was upregulated in Arabidopsis rosette leaves infiltrated with different strains of the bacterial phytopathogen, *Pseudomonas syringae*. The non-host variety of *P. syringae* induced the largest fold-change in *NET4B* expression, although changes in expression were also seen in avirulent and typeIII- secretion system deficient mutants. *NET4B* expression did not change when leaves were infiltrated with the virulent *P. syringae* strain.

The strains that did show an increase in *NET4B* expression cannot effectively cause disease in Arabidopsis as the plant recognises these strains during pathogen attack, which leads to downstream defence signalling. Therefore, it is possible that the upregulation of *NET4B* is important in the defence response to these pathogens, and that the virulent strain is able to prevent this upregulation to promote invasion. The role of *NET4B* in the defence response could also encompass the wounding response as well as pathogen attack, as wounding similarly caused an upregulation of *NET4B*.

This chapter has described the initial *in silico* characterisation of *NET4B*, and has demonstrated the predicted secondary structure of NET4B as well as the tissue-expression pattern and stress responses of this gene. The following chapters describe the experiments used to further characterise NET4B in terms of its subcellular localisation, *in situ* expression pattern, interacting partners and potential function in plant growth and development.

Chapter 4 - *In vivo* and *in vitro* analysis of NET4B localisation and association with actin filaments

4.1 Introduction

The NET family is composed of thirteen proteins in Arabidopsis that all contain a conserved N-terminal NET actin binding (NAB) domain (Deeks et al. 2012). Since the initial identification of this family, representative members of each subclade have been shown to associate with the actin cytoskeleton (Deeks et al. 2012). This chapter describes the experiments used to characterise the association of NET4B with actin both *in vivo* and *in vitro*. Additionally, the subcellular localisation of various NET4B truncations were studied in order to identify additional functional domains within this protein.

4.1.1 Previous work studying the *in vivo* localisation of NET4A

Initial subcellular localisation studies of the NET proteins utilised the same GFP fusion protein strategy as used in Karl Oparka's screen (Escobar et al. 2003), however Agrobacterium was used to infect *Nicotiana benthamiana* leaf epidermal cells rather than the TMV based infection of *N. tabacum* leaves.

Agrobacterium naturally infect higher plants and they induce the formation of tumours through integration of their transfer-DNA (T-DNA) into the host genome. The integration of Agrobacterium T-DNA into the plant genome has been adopted by the plant science community as an efficient method to genetically engineer plants. The Agrobacterium T-DNA plasmid has been genetically modified to prevent tumour formation, which therefore enables DNA insertion without the associated disease symptoms. Genes of interest (with a specific tag if required) are transformed into the modified T-DNA plasmid of Agrobacterium, which can then be syringe-injected into the lower epidermis of *N. benthamiana* leaves. This method leads to the transient transformation of leaf epidermal cells and allows the visualisation of GFP fusion proteins *in vivo* (according to Kapila et al. 1997).

Previous studies on NET4A, using the Agrobacterium-mediated transformation system have revealed that it can associate with actin filaments when expressed in *N. benthamiana* leaf epidermal cells (Figure 4.1). Ectopic overexpression of the NET4A-NAB domain fused to GFP in leaf epidermal cells, under the control of a dual-CaMV

35S promoter, labelled a filamentous network (Figure 4.1 a). These filaments have been confirmed to be the actin cytoskeleton through drug studies and colocalisation with known actin-binding markers (Hawkins and Hussey, unpublished). Interestingly, overexpressing the full-length NET4A fused to GFP in this system, under the same dual-CaMV 35S promoter, localised to a 'beads on a string pattern' that has been observed for many members of the NET family (Figure 4.1 b and c; Hawkins and Hussey unpublished). The localisation of the NET4A-GFP fusion protein labels fine filaments, as well as discrete foci that decorate the filaments. In addition, the NET4A-GFP construct labels elongated structures, associated with actin filaments, which have been termed 'actin staples'.

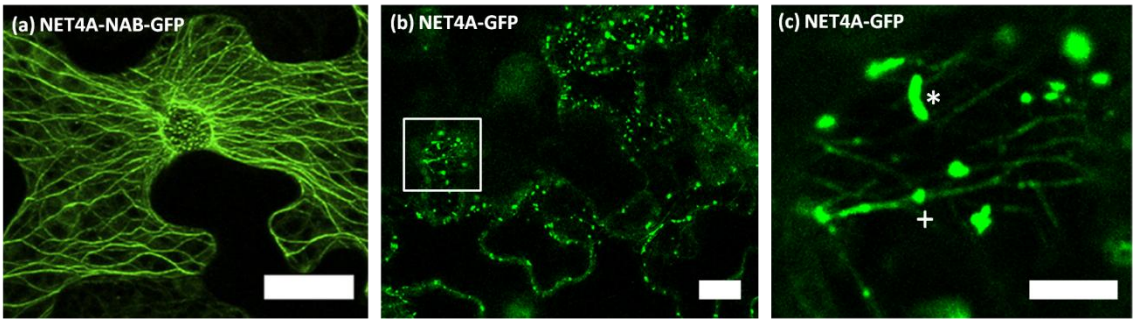

Figure 4.1: Transient expression of the NET4A-NAB-GFP and NET4A-GFP fusion proteins in *N. benthamiana* leaf epidermal cells. Previous studies on NET4A using the Agrobacterium-mediated transformation system have demonstrated its association with the actin cytoskeleton. (a) NET4A-NAB-GFP localises to actin filaments (Image from Deeks et al. (2012)). (b and c) NET4A-GFP localises to fine filaments, as well as filamentous punctae (+) and elongated structures termed 'actin staples' (*) (Images provided by Dr. Tim Hawkins, unpublished). Scale bars: (a and b) 20 μm, (c) 5 μm.

4.2 *In vivo* analysis of the NET4B-NAB domain and the full-length NET4B protein

NET4B remains a relatively uncharacterised member of the NET family and initial characterisation of this protein focussed on studying its association with actin filaments *in vivo*. The subcellular localisation of both the conserved NAB domain and the full-length NET4B, fused to GFP, were studied using the Agrobacterium-mediated transient expression system. Both constructs were used to demonstrate whether the putative NET4B-NAB domain could associate with actin, and also whether the full-length NET4B protein had a similar filamentous localisation.

4.2.1 Initial cloning of the NET4B-NAB domain and the full-length NET4B

The NET4B-NAB domain (aa 1-105) and the full-length NET4B protein (aa 1-517) were initially cloned by Dr. Tim Hawkins (Durham University). These constructs were subsequently cloned into the pMDC83 Gateway expression vector which fuses these constructs to a C-terminal GFP tag and enables their constitutive expression under the control of a dual CaMV 35S promoter (Curtis & Grossniklaus 2003, see Figure 4.2). Both NET4B fusion proteins were expressed in *N. benthamiana* leaf epidermal cells using the Agrobacterium-mediated transient transformation system (as described in 2.2.13). After a 2-3 day incubation period the subcellular localisation of these fusion proteins was imaged using CLSM.

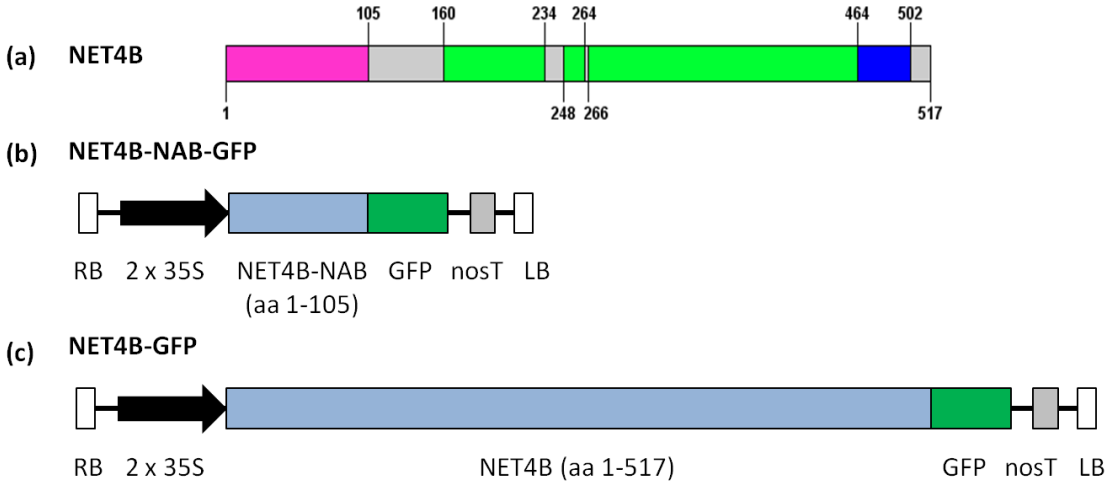

Figure 4.2: Schematic representation of the NET4B-GFP fusion proteins used in the transient expression studies. (a) Predicted protein structure of NET4B. The NAB domain is shown in magenta, coiled-coil domains are shown in green, the IRQ domain is shown in blue, and numbers denote amino acid residues. (b) and (c) NET4B-NAB-GFP and NET4B-GFP constructs generated using the pMDC83 vector. RB = right border, 2 x 35S = dual CaMV 35S promoter, GFP = green fluorescent protein, nosT = Nopaline synthase (nos) terminator, LB = left border.

4.2.2 Localisation of NET4B and the NET4B-NAB domain in *N. Benthamiana* leaf epidermal cells

The subcellular localisation of the NET4B-NAB-GFP and the NET4B-GFP fusion proteins were studied in *N. benthamiana* leaf epidermal cells using the Agrobacterium-mediated transient transformation system. As a negative control, free GFP was expressed under the control of the same dual CaMV promoter using the pMDC43 vector. The known actin-binding marker GFP-FABD2 was also expressed as a positive control for actin filaments. This construct encodes the C-terminal half of AtFIMBRIN1, which encompasses the second actin-binding domain of this protein (Voigt et al. 2005).

Figure 4.3 shows the initial images of the NET4B-NAB-GFP and NET4B-GFP fusion protein constructs when transiently expressed in *N. benthamiana* leaf epidermal cells. Both the NAB domain and full-length NET4B fusion proteins highlighted a filamentous network in the cell, showing both thick and fine filaments.

The NAB domain predominantly decorated a few highly bundled filaments within the cell (Figure 4.3. c and d). High expression could also be seen in the nucleus, and fluorescence was mostly uniform within this organelle, however distinct fluorescent foci were observed (Figure 4.4). The localisation of the NET4B-NAB-GFP to the nucleus could be due to the overexpression of the GFP construct coupled with the ability of GFP to translocate into the nucleus (Seibel et al. 2007). Indeed, free GFP alone also localised to the nucleus as well as the cytoplasm (Figure 4.3 a). The localisation of the NAB domain was similar in both high and low expressing cells, with fluorescence being observed on thick filaments and in the nucleus under both conditions. However in the highly expressing cells, there was an increased abundance of protein aggregates (Figure 4.3 d).

The *in vivo* localisation of the NET4B-NAB domain is very similar to what has been observed previously for the minimal NET1A-NAB (aa 1-94) domain (Calcutt 2009). The NET1A-NAB domain also showed an increased abundance of thicker filament bundles as well as fluorescence being seen in the nucleus. Furthermore, the presence of protein aggregates has been observed when NET1C and NET1D are expressed in this system (Ingle 2011). The formation of these aggregates could be due to the dimerisation of the NAB domain, but they could also be simply due to the constitutive overexpression of these proteins in this system.

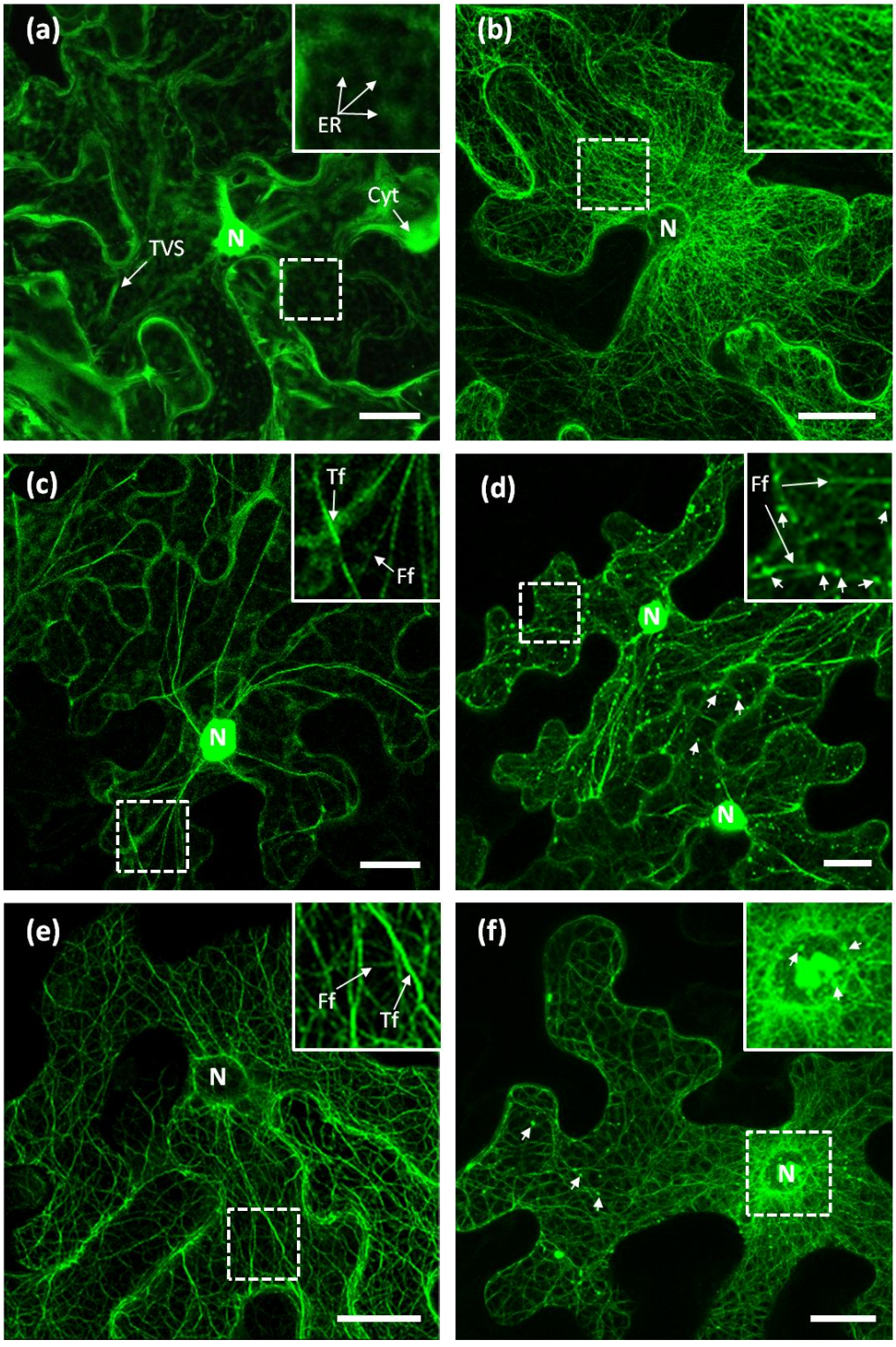

Figure 4.3: Transient expression of the NET4B-NAB-GFP and NET4B-GFP fusion proteins in *N. benthamiana* leaf epidermal cells. (a) Free GFP expression using the pMDC43 vector. (b) Actin filaments labelled with the GFP-FABD2 construct. (c-d) NET4B-NAB-GFP expression showing low and high expression respectively. (e-f) NET4B-GFP expression showing low and high expression respectively. Regions outlined with the white dashed line are magnified in the associated insets. Cyt = cytoplasmic signal, TVS = transvacuolar strand, ER = endoplasmic reticulum, N = nucleus, Tf = thick F-actin, Ff = fine F-actin, arrowheads indicate protein aggregates. Scale bar: 20 μm.

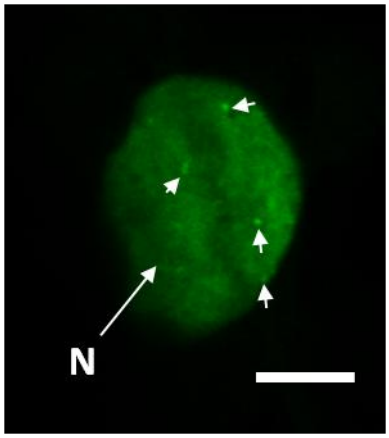

Figure 4.4: Localisation of the NET4B-NAB-GFP fusion protein in the nucleus. Lower intensity image showing the predominantly uniform fluorescence distribution in the nucleus of cells expressing the NET4B-NAB-GFP construct. N = nucleus, arrowheads indicate distinct fluorescent foci within the nucleus. Scale bar: 5 μm.

The full-length NET4B-GFP construct labelled a more distinctive mesh-like network of filaments and showed a more even distribution of filaments throughout the cell when compared to the NAB domain. NET4B-GFP decorated filaments were observed at the cell cortex and surrounding the nucleus (Figure 4.3 e). Cells with a higher expression of NET4B showed an increased number of aggregates localised throughout the cell and enriched around the nucleus (Figure 4.3 f). These aggregates were only observed outside of the nuclear envelope and were associated with thicker bundles surrounding the nucleus.

Interestingly, the NET4B labelled filaments differed from other full-length NET proteins as punctae were not observed along the filaments. This "beads on a string" like pattern has been seen for NET1A, NET2A and NET3A (Deeks et al. 2012; Duckney & Hussey, unpublished). NET4A also labels a filamentous punctae pattern, as well as elongated 'actin staples' (Figure 4.1). NET4B only appeared to decorate a filamentous pattern in this system with no obvious punctae pattern. However, subtle differences in NET4B localisation along the filament could be masked by the high expression levels within this system.

Both the NAB domain and full-length NET4B decorated filaments were clearly different from the free GFP negative control, which only localised to the cytosol and the nucleus (Figure 4.3 a). This therefore suggests that the presence of the GFP tag does not influence the filamentous localisation of the NET4B constructs. However it is possible

that the GFP tag could cause the translocation of the NET4B-NAB-GFP fusion protein into the nucleus. In addition, both NET4B constructs decorated a filamentous network that was significantly more bundled than the actin arrays labelled by GFP-FABD2 (Figure 4.3 b). This has also been observed with the NET1 and NET2 subfamily members and could be due to a potential bundling or cross linking activity of the NET proteins (Calcutt 2009; Dixon 2013).

The presence of the characterised NAB domain in NET4B and the localisation of the NET4B fusion proteins to a filamentous network would suggest that these constructs are associating with the actin cytoskeleton. However it could be possible that the filaments are microtubules or a network of self-assembled proteins. Therefore drug studies were performed to determine the nature of the NET4B-NAB and full-length NET4B decorated filaments and these experiments are described below.

4.2.3 Effect of cytoskeletal disrupting drugs on the localisation of NET4B-NAB-GFP and NET4B-GFP decorated filaments

The results from the initial infiltration studies suggest that the NAB domain and the full-length NET4B decorate filaments in this transient system. In plant cells, the two major filamentous networks of the cytoskeleton are actin microfilaments (AFs) and microtubules (MTs). Application of specific anti-actin or anti-microtubule drugs to the leaf sections expressing the NET4B-NAB-GFP and NET4B-GFP fusion proteins would distinguish which cytoskeletal system they are decorating.

Latrunculin B and Cytochalasin D, were both used to disrupt the actin cytoskeleton, and these drugs were applied to *N. benthamiana* leaf sections expressing the NET4B-NAB-GFP/NET4B-GFP fusion constructs, as well as the GFP-FABD2 construct as a positive control for actin depolymerisation. These two drugs use two different modes of action to depolymerise actin filaments; Latrunculin B complexes with and therefore sequesters G-actin monomers whereas Cytochalasin D binds to the barbed ends of actin filaments to prevent polymerisation (Wakatsuki et al. 2001).

The application of 50 μM Latrunculin B or 40 μM Cytochalasin D for 30 minutes was sufficient to breakdown actin filaments labelled by GFP-FABD2 (Figure 4.5 b and c). The extent of this breakdown varied from cell to cell due to differences in construct expression levels and drug uptake, however application of the drugs largely resulted in the disruption of the actin filament system. Both drugs were dissolved in dimethyl

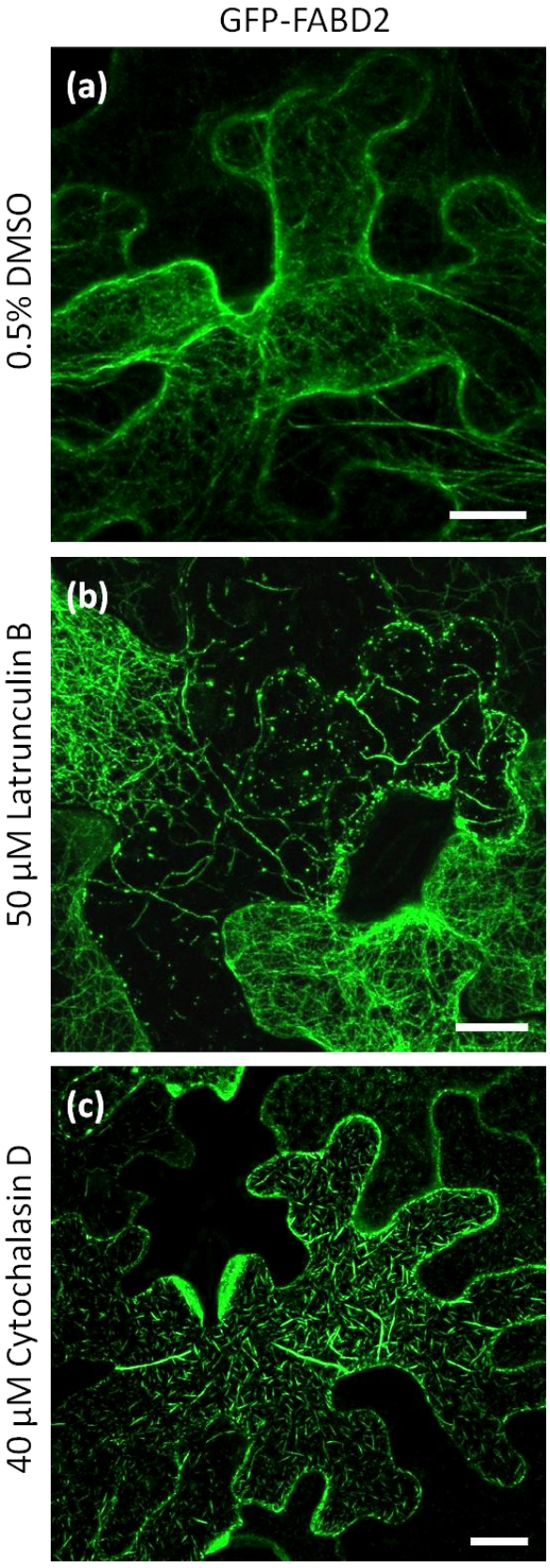

Figure 4.5: Effect of actin disrupting drugs on cells expressing the actin marker GFP-FABD2. Leaf sections expressing the GFP-FABD2 actin marker construct were incubated for 30 minutes in 50 µM Latrunculin B (b), 40 µM Cytochalasin D (c) or 0.5% DMSO as a negative control (a). Scale bar: 20 µm.

sulphoxide (DMSO), therefore as a negative control leaf sections were incubated for 30 minutes in the highest concentration of DMSO used (0.5%). This control showed that the presence of DMSO alone did not cause the disruption of actin filaments (Figure 4.5 a).

Figure 4.6 shows that the application of Latrunculin B and Cytochalasin D to leaf sections expressing the NET4B-NAB-GFP/NET4B-GFP constructs. Both drugs similarly led to the disruption of the filamentous network decorated by these fusion proteins. The extent of this disruption appeared to be more severe when the drugs were applied to the full-length NET4B-GFP construct, and both drugs led to the complete breakdown of the NET4B-GFP labelled filaments into small aggregates (Figure 4.6 e and f). Disruption of the NET4B-NAB-GFP or NET4B-GFP decorated filaments was not observed in the 0.5% DMSO control (Figure 4.6 a and d).

Application of these drugs to the NET4B-NAB-GFP expressing cells also resulted in the breakdown of filaments and small aggregates started to form, however larger filaments still remained (Figure 4.6 b and c). The persistence of NAB-GFP decorated filaments could be explained by the increased filament bundling seen in cells expressing this construct. These thicker filaments could be relatively more stable and resilient to the anti-actin drugs. Indeed, actin bundling proteins have been shown to reduce the sensitivity of actin filaments to actin depolymerising drugs (Winder et al. 2003; Jia et al. 2013).

To test whether the NET4B-NAB-GFP or NET4B-GFP constructs localised to the microtubule cytoskeleton, leaf sections expressing these constructs were incubated in the microtubule depolymerising drug Amiprophosmethyl (APM). APM is a herbicide that disrupts the microtubule cytoskeleton, and has been shown to specifically depolymerise plant microtubules (Morejohn & Fosket 1984; Murthy et al. 1994). As a positive control for microtubule depolymerisation, the kinesin motor domain of kinesin-7 fused to GFP (KMD-GFP; Deeks et al. 2010), was used as a microtubule marker.

The application of 40 μM APM for one hour was sufficient to breakdown the KMD-GFP decorated microtubule cytoskeleton (Figure 4.7 b). As APM was dissolved in DMSO, leaf sections were also incubated in 0.2% DMSO as a negative control, however this did not disrupt the KMD-GFP labelled filaments (Figure 4.7 a). In contrast

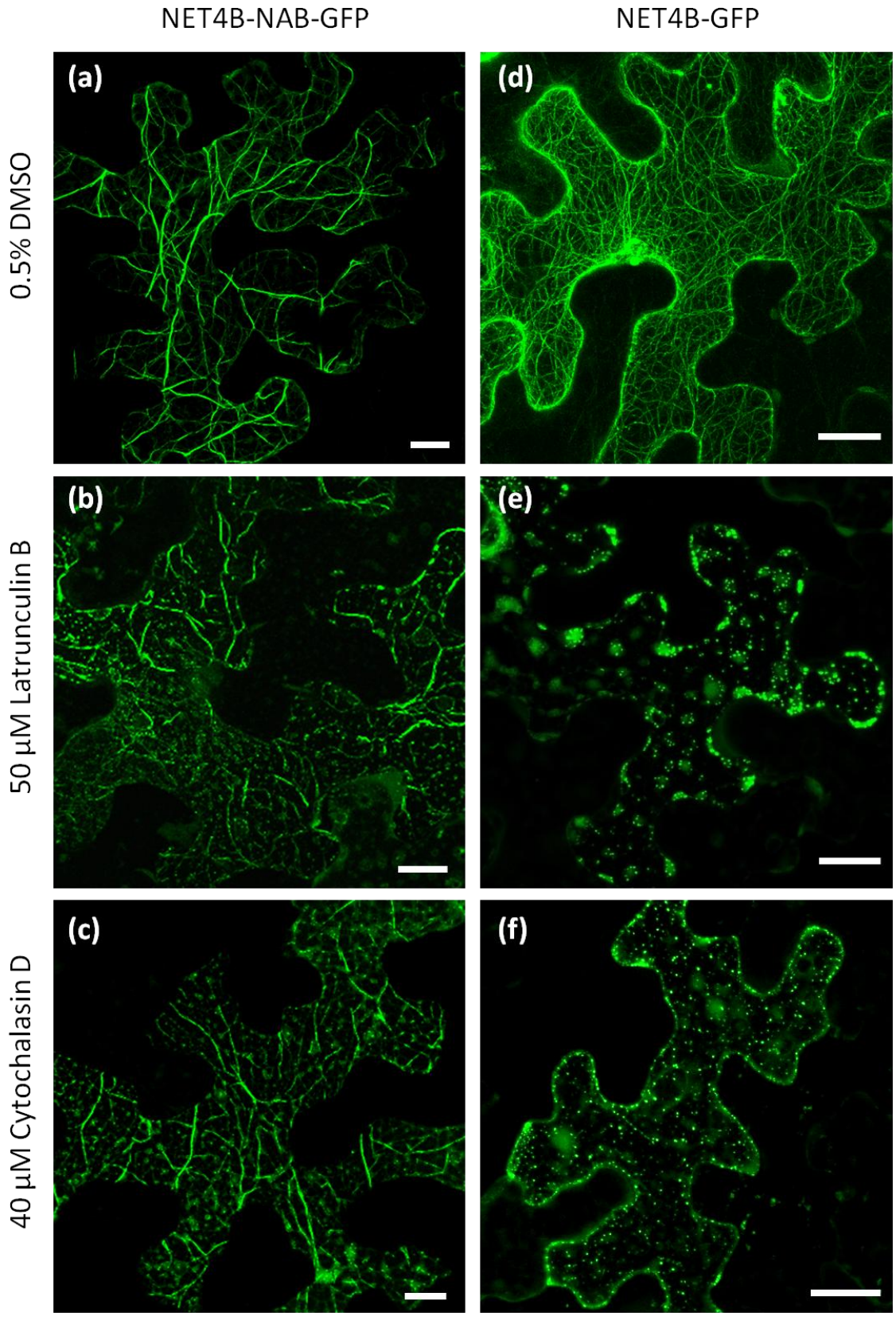

Figure 4.6: Effect of actin disrupting drugs on the NET4B-NAB-GFP and NET4B-GFP decorated filaments. *N. benthamiana* leaf sections expressing NET4B-NAB-GFP (a-c) or NET4B-GFP (d-f) were incubated for 30 minutes in 50 µM Latrunculin B (b and e), 40 µM Cytochalasin D (c and f) or 0.5% DMSO as a negative control (a and d). Scale bar: 20 µm.

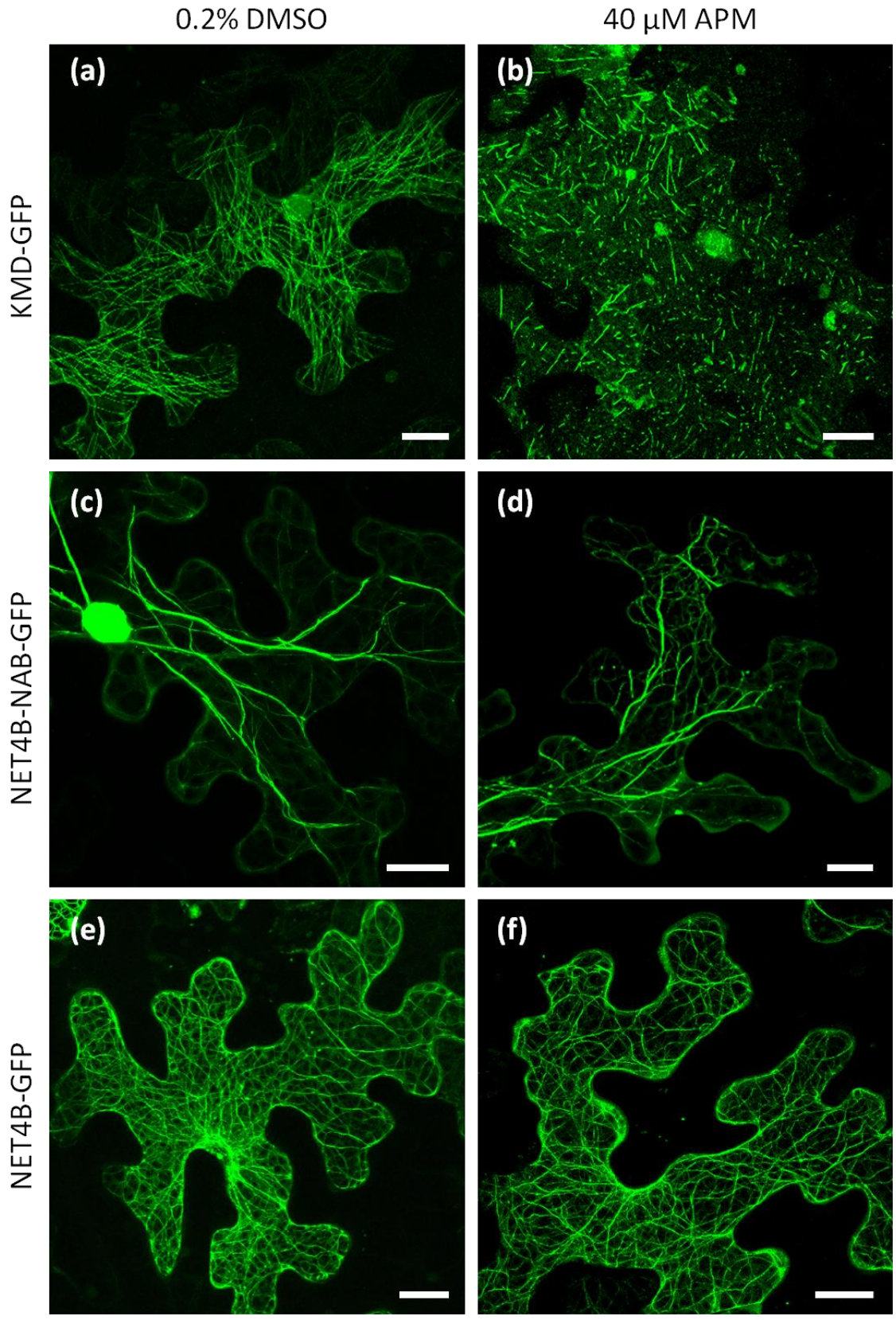

Figure 4.7: Effect of microtubule disrupting drugs on KMD-GFP, NET4B-NAB-GFP and NET4B-GFP decorated filaments. *N. benthamiana* leaf sections expressing the microtubule marker KMD-GFP (a and b), NAB-GFP (c and d) or NET4B-GFP (e and f) were incubated for one hour in 40 µM APM (b, d, f) or 0.2% DMSO as a negative control (a, c, e). Scale bar: 20 µm.

to KMD-GFP, the NET4B-NAB-GFP and the NET4B-GFP decorated filaments did not breakdown when incubated with APM (Figure 4.7 d and f).

The results from these experiments demonstrated that the NET4B-NAB-GFP and NET4B-GFP decorated filaments were sensitive to anti-actin drugs but not the anti-microtubule drug APM. This therefore suggests that NET4B can associate with the actin cytoskeleton *in vivo*, and that this association could be mediated through the NAB domain.

4.2.4 Colocalisation of the NAB domain and full-length NET4B with actin

The results from the drug studies experiments suggested that the NET4B-NAB domain and the full-length NET4B associate with the actin cytoskeleton *in vivo*. To add further evidence for this association, both constructs were co-infiltrated with the known actin-binding marker FABD2 fused to an N-terminal mCherry fluorescent tag (mCherry-FABD2). This construct was chosen as the spectral profiles of GFP/mCherry are more distinct than the traditional GFP/RFP fusion proteins, which reduces the likelihood of observing spectral bleed-through artefacts. Co-expression of either NET4B-NAB-GFP or NET4B-GFP with mCherry-FABD2 in the same cell would allow the concomitant visualisation of FABD2 labelled actin filaments with the NET4B decorated filaments. The sequential scanning function of the Leica SP5 confocal microscope was used for excitation and detection of the fluorescent proteins, using both the 488 nm and 594 nm laser for GFP and mCherry excitation respectively. Overlaying the two scans enables the observation of filament colocalisation.

The expression levels of the NET4B and FABD2 constructs varied throughout the transformed leaf, with some epidermal cells only expressing one of the constructs, however in cells that were expressing both markers, the NAB domain and the full-length NET4B decorated filaments were shown to colocalise with actin filaments (Figure 4.8 and 4.9). Some cells only expressed one of the fusion constructs and these provided an internal control and demonstrated that colocalisation was not caused by bleed-through between the different channels on the microscope.

Taken together, the results from the colocalisation and drug studies have demonstrated that the full-length NET4B protein is able to associate with actin *in vivo* and that this could be mediated through the conserved NAB domain.

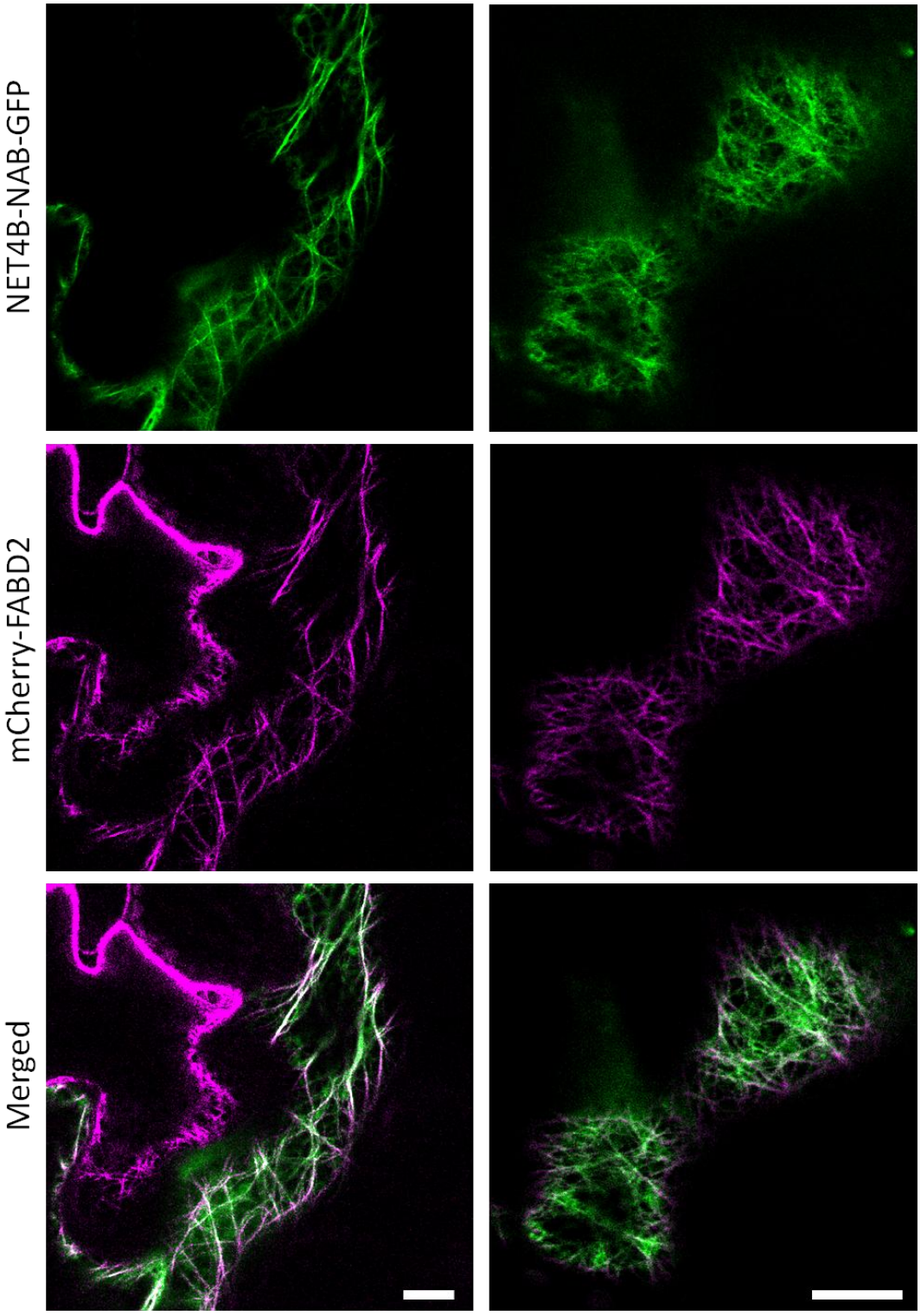

Figure 4.8: Colocalisation of NET4B-NAB-GFP decorated filaments with F-actin. *N. benthamiana* leaves were co-infiltrated with the known actin-binding marker mCherry-FABD2 and NET4B-NAB-GFP. The samples were excited with the 488 nm laser to visualise the NET4B-NAB:GFP filaments, and the 594 nm laser to excite and visualise actin filaments labelled with mCherry-FABD2. NET4B-NAB-GFP filaments are shown in green, mCherry-FABD2 labelled actin filaments are shown in magenta, colocalised filaments in the merged image appear white. Shown here are two representative leaf sections. Scale bar: 20 μm.

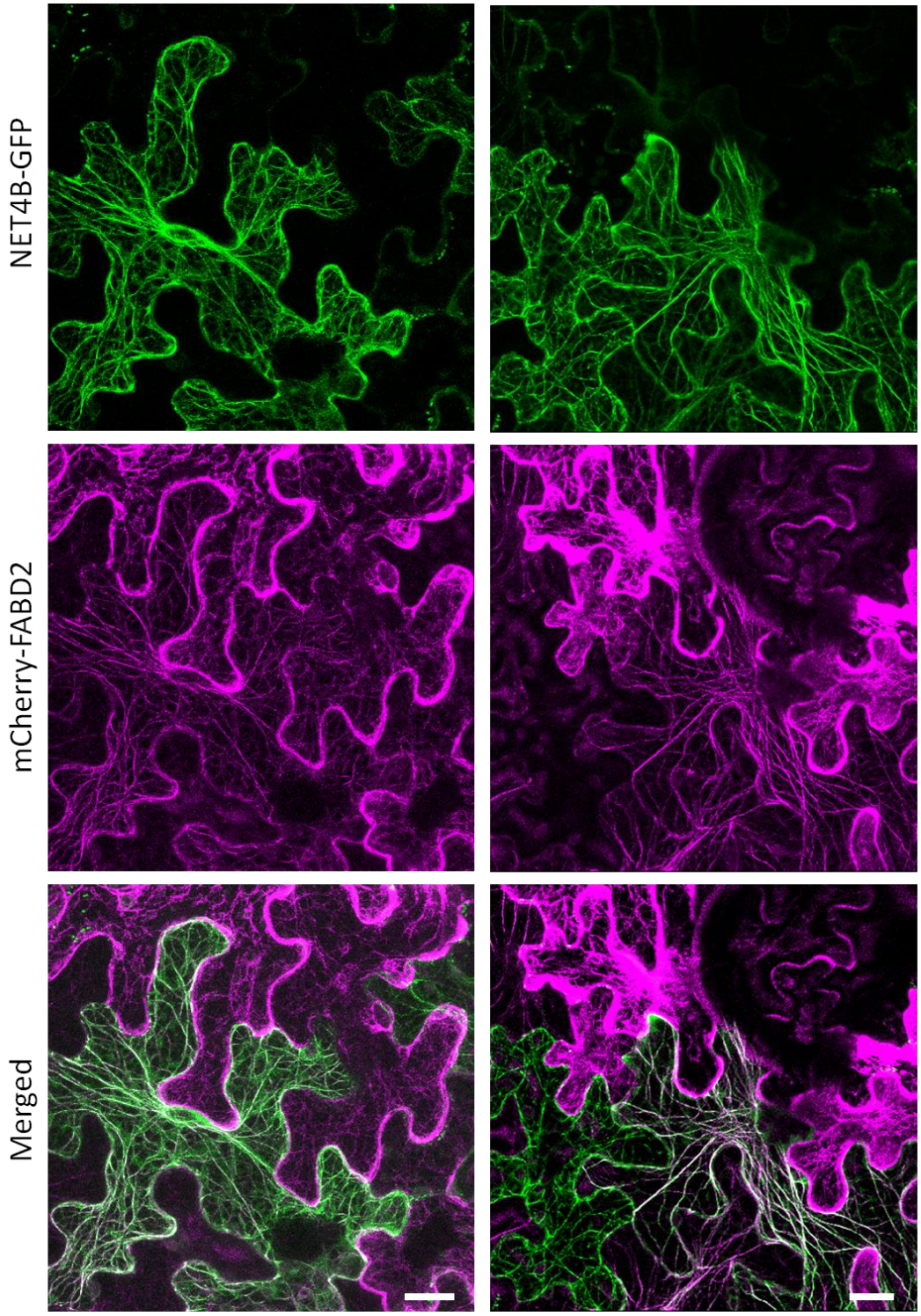

Figure 4.9: Colocalisation of NET4B-GFP decorated filaments with F-actin. *N. benthamiana* leaves were co-infiltrated with the known actin-binding marker mCherry-FABD2 and NET4B-GFP. The samples were excited with the 488 nm laser to visualise the NET4B-GFP filaments, and the 594 nm laser to excite and visualise actin filaments labelled with mCherry-FABD2. NET4B-GFP decorated filaments are shown in green, mCherry-FABD2 labelled filaments are shown in magenta, colocalised filaments in the merged image appear white. Shown here are two representative leaf sections. Scale bar: 20 μm.

4.3 *In vivo* localisation of NET4B truncations

The results from the previous section have established that the full-length NET4B protein and the NET4B-NAB domain can associate with actin *in vivo*, however little is known about the C-terminus of NET4B. Therefore GFP fusions to several NET4B truncations were created and subsequently expressed in *N. benthamiana* leaf epidermal cells using the Agrobacterium-mediated transient transformation system. This analysis would demonstrate whether the NAB domain was solely responsible for the association of NET4B with actin. In addition, this investigation would reveal whether the C-terminus of the protein could localise to a specific subcellular compartment.

4.3.1 Cloning and expression of the NET4B truncations

Five different truncations of the NET4B gene were created and subsequently fused to GFP for transient expression in *N. benthamiana* leaves (Figure 4.10). These truncations were designed to overlap with each other and covered the full-length of the NET4B protein. The truncations were also made with consideration of the previously identified C-terminal IRQ domain. This domain, described in Chapter 3.4, is highly conserved between NET4B, NET4A, NET3A and NET3C. All four proteins share this domain at their C-terminus, and in NET4B the IRQ domain was defined as being from amino acid residues 464-502.

Figure 4.10 demonstrates how the different truncations correspond to the full-length NET4B protein. The -IRQ:GFP construct (aa 1- 463), lacks the IRQ domain and encompasses the NAB domain and the majority of the coiled-coil domains. The -NAB-IRQ:GFP construct (aa 106-463) lacks the N-terminal NAB domain and the C-terminal IRQ domain, and contains the central coiled-coil domains. The -NAB construct (aa 106-517) encoded the full-length protein without the NAB domain and was generated with both N- and C-terminal GFP fusions. This construct would assess whether the rest of NET4B could associate with actin, therefore GFP was fused to both ends to prevent any artefacts caused by the presence of the GFP. The IRQ:GFP construct (aa 464-502) encoded the IRQ domain. Finally, the IRQ + Ct:GFP construct (aa 464-517), encoded the IRQ domain and the relatively less conserved amino acid residues to the C-terminus of NET4B. The Gateway cloning system was used to clone these fragments as described in section 2.2.10.

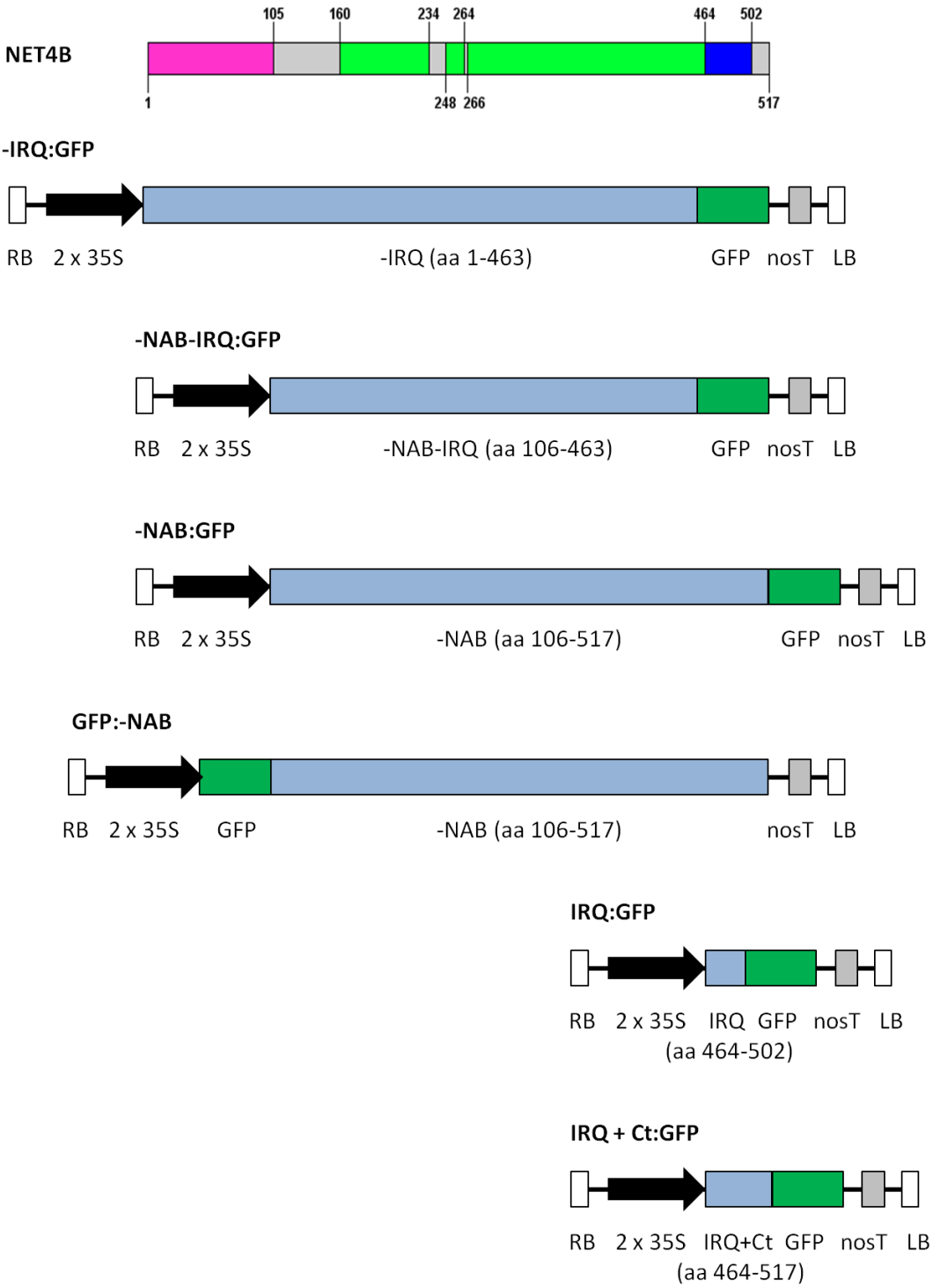

Figure 4.10: Diagram showing the GFP fusions to various NET4B truncations. Various truncations of NET4B were amplified and fused to GFP using either the pMDC43 or the pMDC83 vector, for N- and C-terminal GFP fusions respectively. These truncations are shown with reference to the predicted protein structure of NET4B, showing the NAB domain in magenta, coiled-coil domains in green and the IRQ domain in blue, numbers denote amino acid residues. RB = right border, 2 x 35S = dual CaMV 35S promoter, GFP = green fluorescent protein, nosT = Nopaline synthase (nos) terminator, LB = left border.

4.3.2 *In vivo* localisation of the NET4B fragments

Figure 4.11 shows a representative image of each of these truncation-fusion proteins expressed in *N. benthamiana* leaf epidermal cells. The "glow" colour palette was utilised on the Leica LAS-AF software, as it allows intensity variations to be more easily perceived.

The -IRQ:GFP construct labelled a filamentous system, analogous to that of the full-length NET4B-GFP, with a very defined mesh of filaments being decorated throughout the cortex and surrounding the nucleus (Figure 4.11 a).

The -NAB-IRQ:GFP, -NAB:GFP and GFP:-NAB constructs all appeared to be largely cytosolic (Figure 4.11 b, c and d, respectively). These constructs all showed fluorescence localised to the cytosol, transvacuolar strands and endoplasmic reticulum (ER). This localisation did not appear to be drastically different to that observed previously with free GFP expressed using the pMDC43 vector (Figure 4.3 a).

Similarly, the localisation of the IRQ:GFP construct showed a cytosolic localisation, with fluorescence in the cytosol, ER, transvacuolar strands and also a uniform distribution of fluorescence in the nucleus (Figure 4.11 e). As mentioned previously, GFP can be translocated into the nucleus (Seibel et al. 2007), which could therefore result in the nuclear localisation of IRQ:GFP.

The localisation of the IRQ + Ct:GFP construct was remarkably different to the other truncations and showed a punctate appearance in the cell, as well as the cytosolic and nuclear localisation seen with the IRQ:GFP construct (Figure 4.11 f). These punctae were in general localised to the cortex of the cell and were roughly uniform in size and shape, and typically had a submicron diameter. The mean average diameter of these punctae was 581 nm (n = 46, from 3 different cells, SD ± 123 nm). Performing a time-lapse of cells expressing the IRQ + Ct:GFP construct showed that the punctae grouped into three categories of movement; motile punctae, stop/start movement, and stationary/relatively immobile punctae (Figure 4.12). The motile punctae all appeared to flow in a uniform direction which correlated with the flow of the cytosolic background signal, which suggests they were moving in the cytoplasmic stream. As these punctae are relatively uniform in shape, they are unlikely to represent protein aggregates. It is possible that they are labelling vesicle compartments within the cell and the size of the punctae correlates with the typical size of Golgi vesicles and endosomes

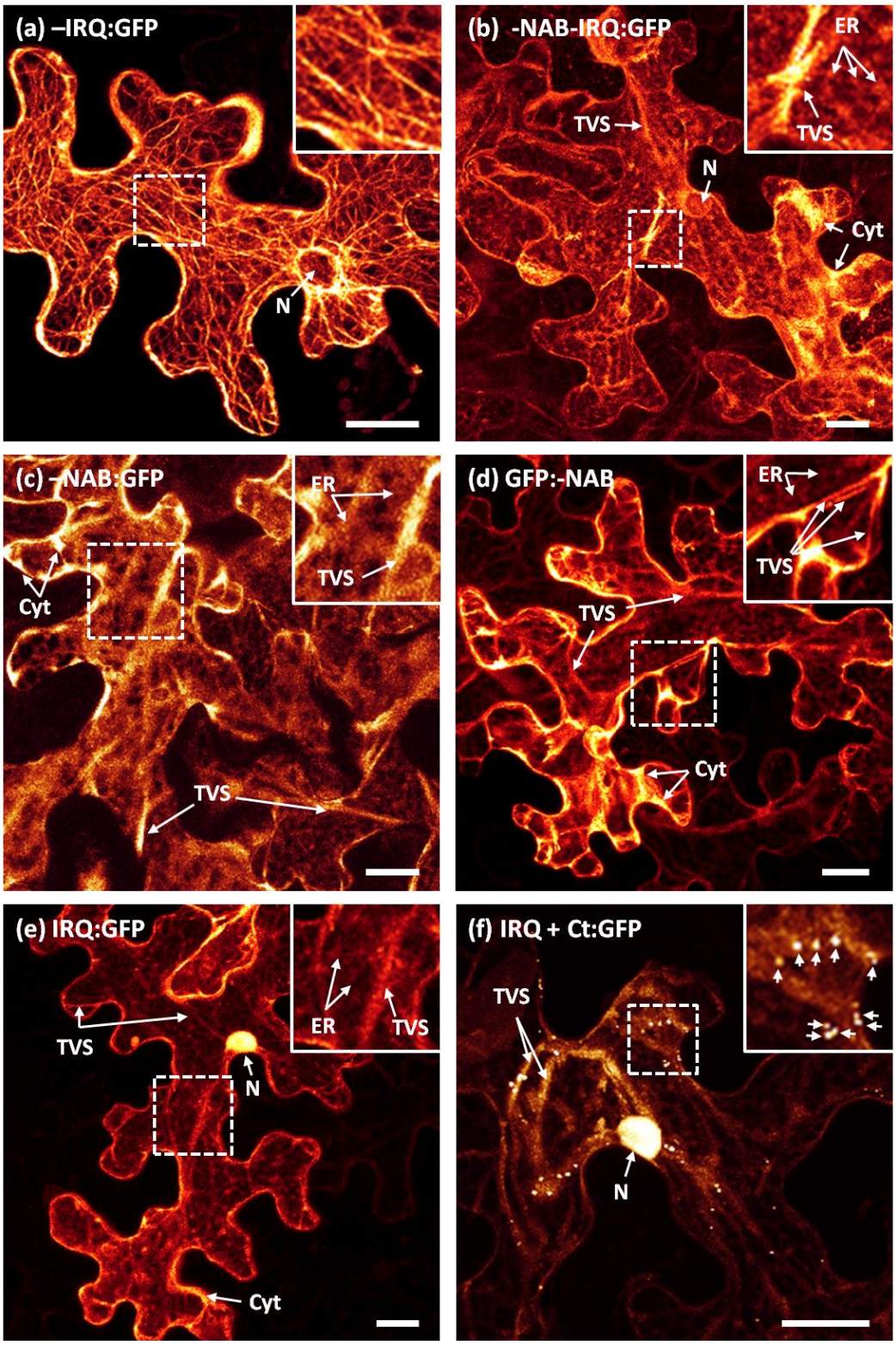

Figure 4.11: *In vivo* analysis of the NET4B truncations expressed in *N. benthamiana* leaves. The NET4B truncations were transiently expressed in *N. benthamiana* leaf epidermal cells using the pMDC83 or pMDC43 vectors. (a) -IRQ:GFP (pMDC83), (b) –NAB-IRQ:GFP (pMDC83), (c) –NAB:GFP, (pMDC83), (d) GFP:-NAB (pMDC43), (e) IRQ:GFP (pMDC83), (f) IRQ + Ct:GFP, (pMDC83). Regions outlined with the white dashed line are magnified in the associated insets. Cyt = cytoplasmic signal, TVS = transvacuolar strand, N = nucleus, ER = endoplasmic reticulum, arrowheads indicate fluorescent punctae. Scale bar: 20 μm.

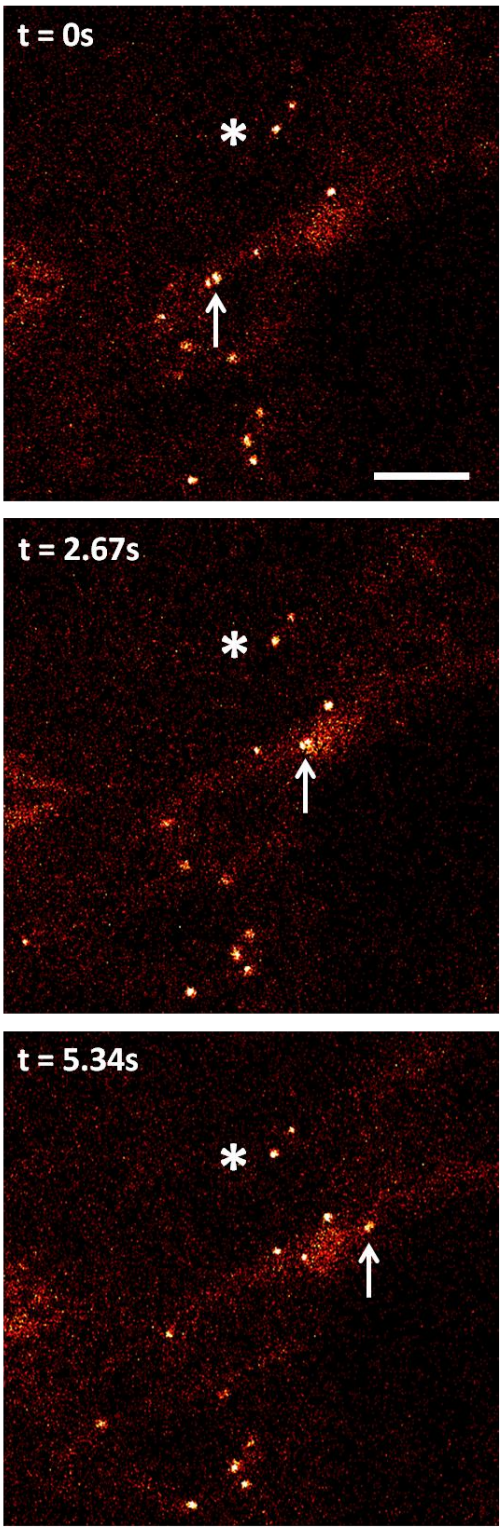

Figure 4.12: Time series of the moving IRQ + Ct:GFP labelled punctae. *N. benthamiana* leaf epidermal cells expressing the IRQ + Ct:GFP construct were imaged over time and shown here are three static images of a representative time lapse movie. The white arrow denotes a moving punctae and the asterix highlights a static punctae. The relative time period is shown in the top left. Scale bar: 10 μm.

(Dupree & Sherrier 1998; Jürgens 2004). Furthermore previous studies on the movement of Golgi stacks have shown that they exhibit similar categories of movement, from stationary to rapid movement (Boevink et al. 1998; Nebenführ et al. 1999).

The results from these experiments have suggested that the NAB domain is the only actin-binding domain that can be found on NET4B. Both the -NAB:GFP and GFP:-NAB constructs were cytosolic which suggests that the association of NET4B with actin is mediated through the NAB domain alone. Furthermore these experiments have demonstrated that the C-terminal 54 amino acids of NET4B (IRQ + Ct:GFP) could associate with moving punctae, however the identity of these punctae remains currently unknown.

4.4 *In vitro* F-actin binding assay

The experiments described in this chapter so far have described how NET4B can associate with the actin cytoskeleton *in vivo* and that the minimal N-terminal NAB domain could mediate this association. However these studies did not distinguish whether the association with actin is direct or indirect through intermediary proteins. Previous studies on NET1A have demonstrated that the NAB domain can bind directly to actin filaments *in vitro* using an F-actin co-sedimentation assay, which led to the characterisation of the NAB domain as an actin-binding domain (Calcutt 2009; Deeks et al. 2012). To establish whether the NET4B-NAB domain could also bind directly to F-actin, a similar actin co-sedimentation assay was performed as was used for NET1A.

The F-actin co-sedimentation assay works through differential sedimentation of proteins during ultracentrifugation. After ultracentrifugation, the insoluble pellet fraction and the soluble supernatant fraction can be analysed to see where the proteins are localised. The protein of interest (NAB) is soluble and will therefore be present in the supernatant. Polymerised actin filaments are insoluble and will therefore be found in the pellet fraction. If the protein of interest directly binds to actin filaments then it will co-sediment with F-actin, when the two are incubated together prior to ultracentrifugation, and will subsequently be found in the pellet.

4.4.1 Cloning and expression of the NET4B-NAB domain and antigen fragment

The NET4B-NAB domain (aa 1-105) was chosen for the F-actin co-sedimentation assay as this minimal domain was shown to associate with actin *in vivo*. A fragment of

NET4B that was later utilised as an antigen during antibody production, NET4B$^{121-220}$, was used as a negative control in this experiment. Chapter 5 discusses further detail about how this antigen fragment was chosen. However, for the purposes of this experiment, this fragment was chosen as a control as it does not overlap with the NAB domain and they are both of a similar size (Figure 4.13). Both the NET4B-NAB domain and the NET4B$^{121-220}$ fragment were cloned into the pGAT4 destination vector (as described in 2.2.10) for protein expression in *Escherichia coli*.

Figure 4.13 (b) and (c), shows the fusions of the two expressed constructs. Both constructs were expressed in *E. coli* Rosetta 2 cells as histidine-tagged fusion proteins according to the methods described in 2.4.1. Both of these constructs were purified from the insoluble bacterial pellet in the presence of urea, and subsequently dialysed into KME buffer for the co-sedimentation assay (according to 2.4.3). The Bradford's assay (Bio-Rad) was used to quantify the purified protein.

The purified NET4B-NAB and NET4B$^{121-220}$ fragment are shown in Figure 4.13 (d) and (e). Both fragments could be effectively purified using the Ni-NTA beads; a single band was purified for the NAB domain, and two bands were present after the purification of the NET4B$^{121-220}$ fragment. MALDI-TOF performed by the School of Biological and Biomedical Sciences (SBBS) Proteomics centre, confirmed the correct expression of both constructs, however the lower molecular weight band observed with NET4B$^{121-220}$ did not give a clear result and could represent contamination.

4.4.2 F-actin binding assay

The F-actin co-sedimentation assay was performed according to the methods described in 2.4.11. Desiccated rabbit skeletal muscle actin was used as the source of actin in this assay, and was initially rehydrated and then polymerised to F-actin by increasing the salt concentration in the buffer. Five different reactions were set up in the ultracentrifuge tubes; NET4B-NAB alone, F-actin alone, NET4B-NAB and F-actin, NET4B$^{121-220}$ alone, NET4B$^{121-220}$ and F-actin. The concentration of F-actin was kept at 5 μM throughout the experiments, whereas the concentration of the NAB domain was varied for the different reactions. The NAB alone, and all the reactions using NET4B$^{121-220}$ were kept at 10 μM.

Incubating actin with a range of NAB concentrations would determine the concentration-dependent nature of this association. Using a higher concentration of the

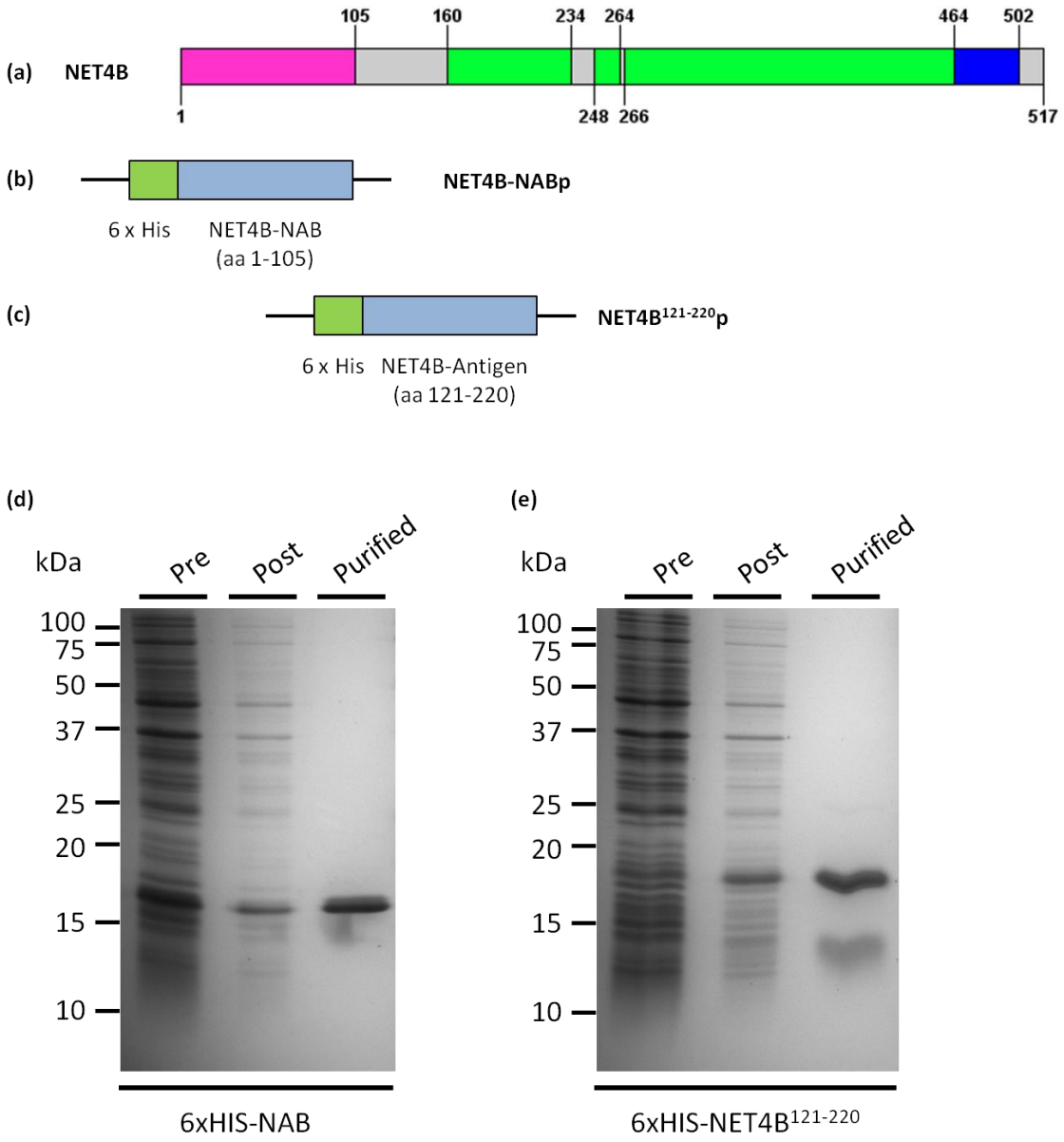

Figure 4.13: Purification of the NET4B-NAB domain and the NET4B$^{121-220}$ protein fragment. (a) Schematic diagram of NET4B showing the NAB domain in magenta, coiled-coil domains in green, and the IRQ domain in blue. Numbers denote amino acid residues. (b) and (c) Expression constructs for the purification of the NET4B-NAB domain and NET4B$^{121-220}$ protein fragments using a 6xHistidine tag. (d) and (e) Coomassie Brilliant Blue stained SDS-PAGE gel showing the purification of these constructs. Pre = bacterial pellet before induction with IPTG, post = bacterial pellet three hours after IPTG induction, purified = purified protein using Ni-NTA beads (after overnight dialysis).

NAB domain could saturate the actin-binding sites, therefore a larger proportion of the NAB would be unable to bind actin and would remain in the supernatant. As the concentration of the NAB domain is lowered, the ratio of the NAB domain that is bound or unbound to F-actin would increase as the level of saturation is reduced, and therefore a larger proportion of the NAB would be found in the pellet.

Figure 4.14 shows the results of the F-actin co-sedimentation assays. Separation of the supernatant and pellet fractions on an SDS-PAGE gel revealed that the NAB domain alone was predominantly soluble and could largely be observed in the supernatant fraction, with a relatively small amount being found in the pellet (Figure 4.14 a). Polymerised F-actin was insoluble and the majority could be found in the pellet fraction, with a small amount present in the supernatant. Incubation of the NAB domain with F-actin resulted in a larger proportion of the NAB domain being observed in the pellet fraction, suggesting that the NAB is binding directly to F-actin. Decreasing the concentration of NAB domain in the reaction to 2 μM resulted in a larger proportion of the NAB domain found in the pellet relative to the supernatant.

The SDS-PAGE gels of the reactions used in Figures 4.14 (a) were repeated to give three technical repeats and the intensity of the NAB domain in the supernatant and pellet fractions were subsequently quantified through densitometry analysis (as described in 2.7.2). Figure 4.14 (b) and (c) shows the results of this analysis. At the lowest concentration of NAB domain (2 μM) the proportion of the NAB domain found in the pellet increased dramatically compared to higher concentrations, when incubated with F-actin. These results suggest that at the higher concentration of NAB domain, the NAB/F-actin binding site is saturated and a large proportion of the NAB is unable to bind F-actin and thus remains in the supernatant. Reducing the concentration of the NAB domain increases the ratio of the NAB domain that is bound/unbound to F-actin, therefore resulting in a larger proportion of the purified NAB protein in the pellet fraction.

The NET4B$^{121\text{-}220}$ fragment was used as a negative control for actin binding (Figure 4.14 d). This fragment alone was soluble and was present in the supernatant after ultracentrifugation. Incubating this fragment with F-actin did not influence its distribution, and it remained in the supernatant. Therefore the co-sedimentation of the NAB domain with F-actin is dependent on its ability to bind actin, as evidenced by the

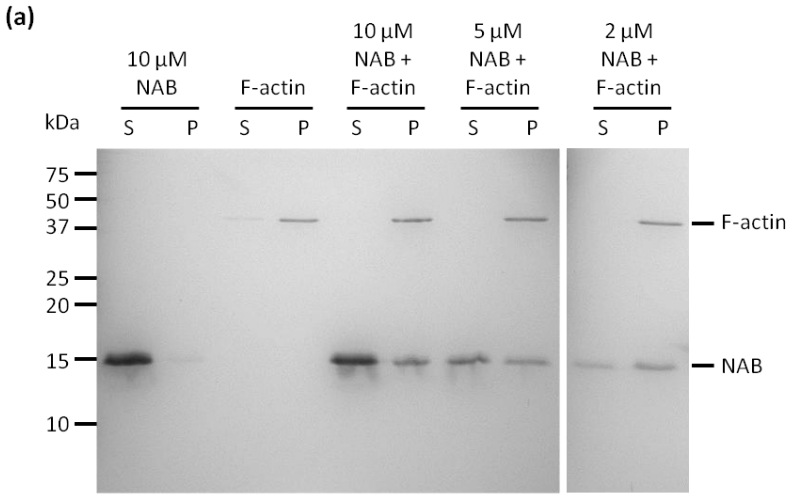

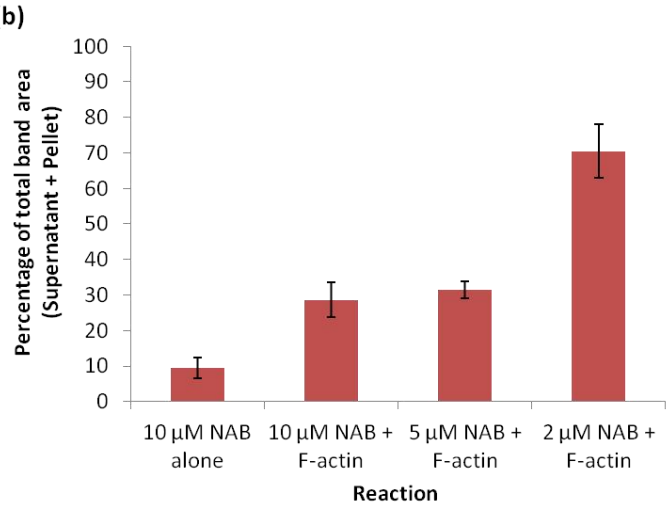

(c)

Reaction	Pellet (%)
10 µM NAB alone	9.52
10 µM NAB + F-actin	28.57
5 µM NAB + F-actin	31.48
2 µM NAB + F-actin	70.50

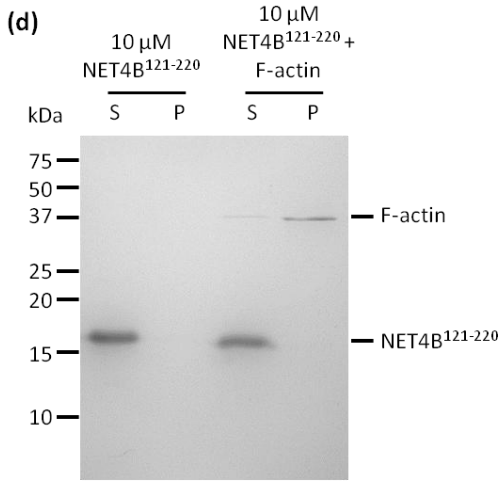

Figure 4.14: *In vitro* F-actin binding assay. After ultracentrifugation of the reactions, the supernatant (S) and pellet (P) fractions were separated on 15% SDS-PAGE gels, using the Precision Plus Dual Colour protein ladder as a molecular weight standard. (a) Co-sedimentation assay using the purified NET4B-NAB and F-actin at 5 µM. (b) and (c) The NAB band intensity in the supernatant and pellet fractions from (a) were quantified using densitometry. The results of this analysis are illustrated with a bar chart (b) and summarised in a table (c). Shown here is the mean percentage of NAB protein in the pellet from three technical repeats of the SDS-PAGE gel. Error bars represent standard error of the mean. (d) Co-sedimentation assay using the purified NET4B$^{121-220}$ protein fragment with 5 µM actin.

fact that a similar sized soluble fragment of NET4B was unable to co-sediment with F-actin in this assay.

The results of these experiments have demonstrated that the NET4B-NAB domain can bind directly to F-actin *in vitro*. The conditions used in this experiment did not enable the calculation of the dissociation coefficients (K_d) for the NET4B-NAB domain, however for the purpose of this study it was deemed sufficient to demonstrate actin binding.

4.5 Conclusion

This chapter has demonstrated the *in vivo* association of the NET4B-NAB domain and the full-length NET4B protein with actin filaments, as well as the direct *in vitro* interaction between the NET4B-NAB domain and F-actin.

The *in vivo* association was demonstrated using two different experimental approaches; application of three different cytoskeleton disrupting drugs, and colocalisation of the NET4B constructs with a known actin-binding marker. Latrunculin B and Cytochalasin D were both used to depolymerise actin filaments and led to the breakdown of the NET4B-NAB-GFP and full-length NET4B-GFP decorated filaments. Application of the microtubule depolymerising drug Amiprophosmethyl did not affect the NET4B-NAB-GFP or NET4B-GFP decorated filaments, and taken together these drug studies suggest that NET4B associates with actin filaments. Further evidence for this association was provided through colocalisation of the NET4B-NAB-GFP and NET4B-GFP decorated filaments with a known actin-binding marker mCherry-FABD2. These results therefore established that the full-length NET4B and the NET4B-NAB domain are both able to associate with the actin cytoskeleton *in vivo*.

The *in vivo* localisation of various truncations of the NET4B protein were then studied using the transient *N. benthamiana* system. These experiments demonstrated that the NAB domain represents the only actin-binding domain of NET4B, as truncations lacking this domain appeared cytosolic and were unable to bind filaments. Furthermore, these truncation studies demonstrated that the C-terminal 54 amino acids of NET4B, which encompassed the IRQ domain, labelled moving punctae in the cell. Parallel *in vivo* studies using the IRQ + Ct:GFP truncations of NET4A and NET3A, performed by Dr. Tim Hawkins, have also shown a similar localisation to moving punctae, suggesting that this localisation is conserved across these different proteins. The identity of these

punctae could be further explored through colocalisation studies using known endosomal markers. As an alternative strategy to elucidate the function of this domain, a yeast-2-hybrid screen was performed during this project using the IRQ + Ct domain as bait, with the aim of identifying potential interacting partners. The results of this analysis are discussed in Chapter 6.

Interestingly, the IRQ:GFP construct alone (aa 464-502), which contains the conserved IRQ domain, did not label these punctae. It is possible that the relatively less conserved C-terminal amino acids 503-517 could be important for the punctate localisation. However as the C-terminus of NET4A, NET4B, and NET3A differ, it is unlikely that the conserved punctate pattern could be mediated by these residues. Alternatively, the secondary structure of the 54 amino acids at the C-terminus could be important in conveying the punctate localisation. Truncating this region could affect this secondary structure and subsequently influence the subcellular localisation. Another explanation could be that the proximity of the GFP tag to the IRQ domain in the IRQ:GFP construct could cause steric hindrance that interferes with its localisation. The additional amino acids between the GFP tag and the IRQ domain in the IRQ + Ct:GFP construct could provide a flexible linker that allows the IRQ domain to localise to discrete foci.

The final experiment in this chapter utilised an *in vitro* approach to study whether the NET4B-NAB domain could interact directly with actin filaments. Previous studies using a co-sedimentation assay have demonstrated that the NET1A-NAB domain can interact directly with F-actin (Calcutt 2009; Deeks et al. 2012). Therefore, a similar approach was used to test whether the NET4B-NAB domain could interact directly with F-actin *in vitro*. The purified NET4B-NAB domain protein alone is soluble and was found in the supernatant after ultracentrifugation. However incubating the NET4B-NAB domain with polymerised F-actin caused the NAB domain to co-sediment with F-actin and was found in the pellet fraction. This result therefore suggests that the NET4B-NAB domain can bind directly to F-actin *in vitro*.

Chapter 5 - *In situ* expression and localisation of NET4B in *Arabidopsis thaliana*

5.1 Introduction

The previous chapter demonstrated that NET4B associates with actin filaments *in vivo* when ectopically overexpressed (CaMV 35S) in *Nicotiana benthamiana* leaf epidermal cells. In this chapter the experiments used to elucidate the subcellular localisation and *in situ* expression pattern of the native NET4B protein will be described.

The transcriptional profile of *NET4B* was investigated through the GUS reporter system, using transgenic plants that expressed the GUS reporter gene under the control of the *NET4B* promoter. In addition to the gene expression pattern, the translational profile of NET4B was investigated in Arabidopsis. This was achieved through Western blot analysis, by probing protein extracted from different plant tissues with an anti-NET4B polyclonal antibody.

Two different experimental approaches were used to investigate the *in situ* subcellular localisation of NET4B. The first approach involved creating transgenic Arabidopsis lines that expressed a NET4B-GFP fusion protein under the control of the *NET4B* promoter. The second approach was achieved through immunogold labelling of Arabidopsis root tips using the anti-NET4B antibody and transmission electron microscopy (TEM).

5.2 Analysis of the *NET4B* transcriptional expression pattern in Arabidopsis using the GUS reporter system

The first approach to study the *in situ* expression of *NET4B* involved studying its gene expression pattern in Arabidopsis. In order to study the transcriptional expression profile of *NET4B*, transgenic Arabidopsis plants expressing the GUS reporter gene under the control of the *NET4B* promoter were created. The GUS gene encodes the *Escherichia coli* ß-glucuronidase enzyme which catalyses the cleavage of ß-glucuronides. Importantly, this enzyme uses X-Gluc (5-bromo-4-chloro-3-indolyl-beta-D-glucuronic acid) as a substrate and cleaves it into two products; a colourless glucuronic acid and chloro-bromoindigo which produces a blue precipitate.

The GUS reporter system is widely used as a tool to study gene expression patterns, as transgenic plants expressing a *promoter*::GUS construct will only transcribe the GUS gene in tissues where the promoter is active. The activity of the GUS enzyme, and therefore the activity of the promoter, can be investigated histochemically by analysing the localisation of the blue precipitate after incubation with X-Gluc (Jefferson et al. 1987).

In this study, the expression profile of *NET4B* was studied using stably transformed Arabidopsis lines containing the *NET4Bpro*::GUS construct, which were previously generated by Dr. Tim Hawkins. These lines were created by amplifying an approximately 2 kb promoter region of *NET4B,* upstream of the *NET4B* gene, which was subsequently cloned into the Gateway modified GUS expression vector pBI101G (Jefferson et al. 1987). Figure 5.1 (a) shows a schematic diagram of the *NET4Bpro*::GUS construct. Wild-type Arabidopsis (Col-0) plants were transformed with this construct using the floral dip method (as described in 2.2.14), and the T_1 generation of transformed plants were selected on media containing kanamycin. Positively selected plants were then further tested for the activity of the GUS gene by incubating a section of root and leaf tissue in the GUS buffer (as described in 2.5.5). After antibiotic selection and the observation of GUS activity, eleven transformed (T_1) plants were identified. These plants were allowed to self-pollinate to produce a T_2 generation of seed that were used to study the transcriptional profile of *NET4B* in different Arabidopsis tissues and at different developmental stages.

5.2.1 Expression pattern in 7-day old seedlings

The transcriptional profile of *NET4B* in the roots and cotyledons of young seedlings was assessed by incubating whole seedlings in the GUS buffer for approximately 30-60 minutes at room temperature, without vacuum infiltration. Preliminary experiments revealed that placing the roots through a series of ethanol washes rapidly dehydrated the roots. To overcome this issue, the roots were excised from the cotyledons and were mounted directly in GUS buffer (lacking X-Gluc, potassium ferricyanide and potassium ferrocyanide) before imaging. The excised cotyledons were washed repeatedly in 70% ethanol to clear the tissue, before studying the expression pattern.

Lines 1-10 were used to assess the expression profile of *NET4B* in young seedlings and representative examples of *NET4B* expression are shown in Figure 5.1. Line 11 was not

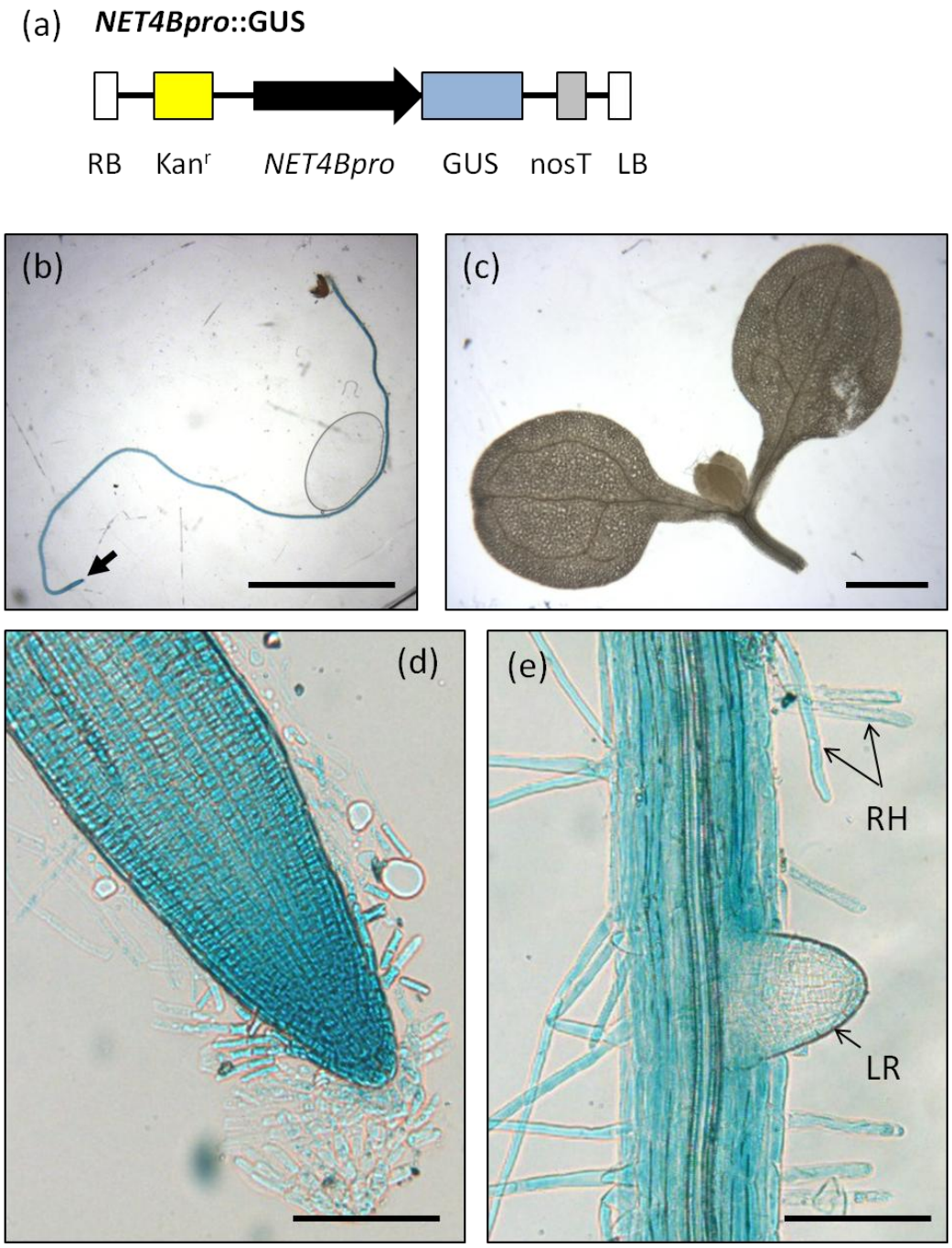

Figure 5.1: Expression profile of *NET4B* in 7-day old seedlings. (a) *NET4Bpro*::GUS construct created using the pBI101G expression vector. RB = right border, Kan^r = kanamycin resistance, *NET4Bpro* = 2kb NET4B promoter, GUS = ß-glucuronidase enzyme, nosT = nos terminator, LB = left border. (b)-(e) Whole 7-day old seedlings were stained for approximately 30-60 minutes. Roots were excised and mounted in GUS buffer without X-Gluc and imaged under the microscope. Cotyledons were washed repeatedly in 70% ethanol before being imaged. (b) Whole root showing expression throughout the root, particularly at the root tip (black arrow). (c) Cotyledons stained for the same amount of time showed no expression. (d) Expression of *NET4B* was highest at the primary root tip. (e) GUS activity is found at a lower level in the rest of the root, and is present in the root hairs (RH) but absent from the emerging lateral roots (LR). Scale bars: (b) 500 µm, (c-e) 100 µm.

analysed during these experiments due to problems in germination. All the analysed lines showed a similar expression pattern with the highest level of GUS activity in the root tip (Figure 5.1 d), and the rest of the root showing a lower level of GUS staining. Additionally, these ten lines showed expression in the root hairs (Figure 5.1 e). Within the root, expression did not appear to be confined to a particular cell layer as has been seen for the vasculature localised expression of *NET1A* (Calcutt 2009). However, sectioned GUS stained samples would be needed to discern the cross-sectional expression profile of *NET4B* in the roots. GUS activity was not observed in the cotyledons of any of the analysed lines (Figure 5.2 c).

Interestingly, expression appeared to be absent from the emerging lateral root in lines 1-10 (Figure 5.1 e). The differing expression of *NET4B* within the primary and lateral roots tips could be due to the different nature of their development. The primary root apical meristem is established during embryogenesis, whereas the lateral roots are derived from founder cells in the pericycle of the root (Tian et al. 2014). Furthermore, lateral roots do not initially demonstrate positive gravitropism which could be due to their lack of statoliths and vascular connections with the primary root, as well as differences in auxin transport (Guyomarc'h et al. 2012; Rosquete et al. 2013).

5.2.2 Expression pattern in floral tissue

The expression profile of *NET4B* in floral tissue was determined by incubating detached open flowers from 5-6 week old plants in the GUS buffer. The samples were vacuum infiltrated to allow penetration of the solution into the tissue, followed by an incubation of 1-3 hours at 37 °C. After incubation in the GUS buffer the floral tissue was cleared through several washes in 70% ethanol. All eleven *NET4Bpro*::GUS lines were used to study the transcriptional profile of *NET4B* in floral tissue.

Figure 5.2 shows the results of this analysis and Appendix 2.1 shows the breakdown of expression in the different lines. GUS activity was seen in the: sepals (eleven lines); papillae (nine lines); and the filaments (five lines). Furthermore when the incubation time was reduced, GUS activity was detectible in the guard cells in a range of different floral tissues. GUS staining was observed in the guard cells of: sepals (Figure 5.2 c; all 11 lines), along the inflorescence stem (Figure 5.2 d; 8 lines), and in the anthers (Figure 5.2 e; nine lines). The expression of *NET4B* in the guard cells has been previously demonstrated through microarray data as described in Chapter 3.5. Therefore this

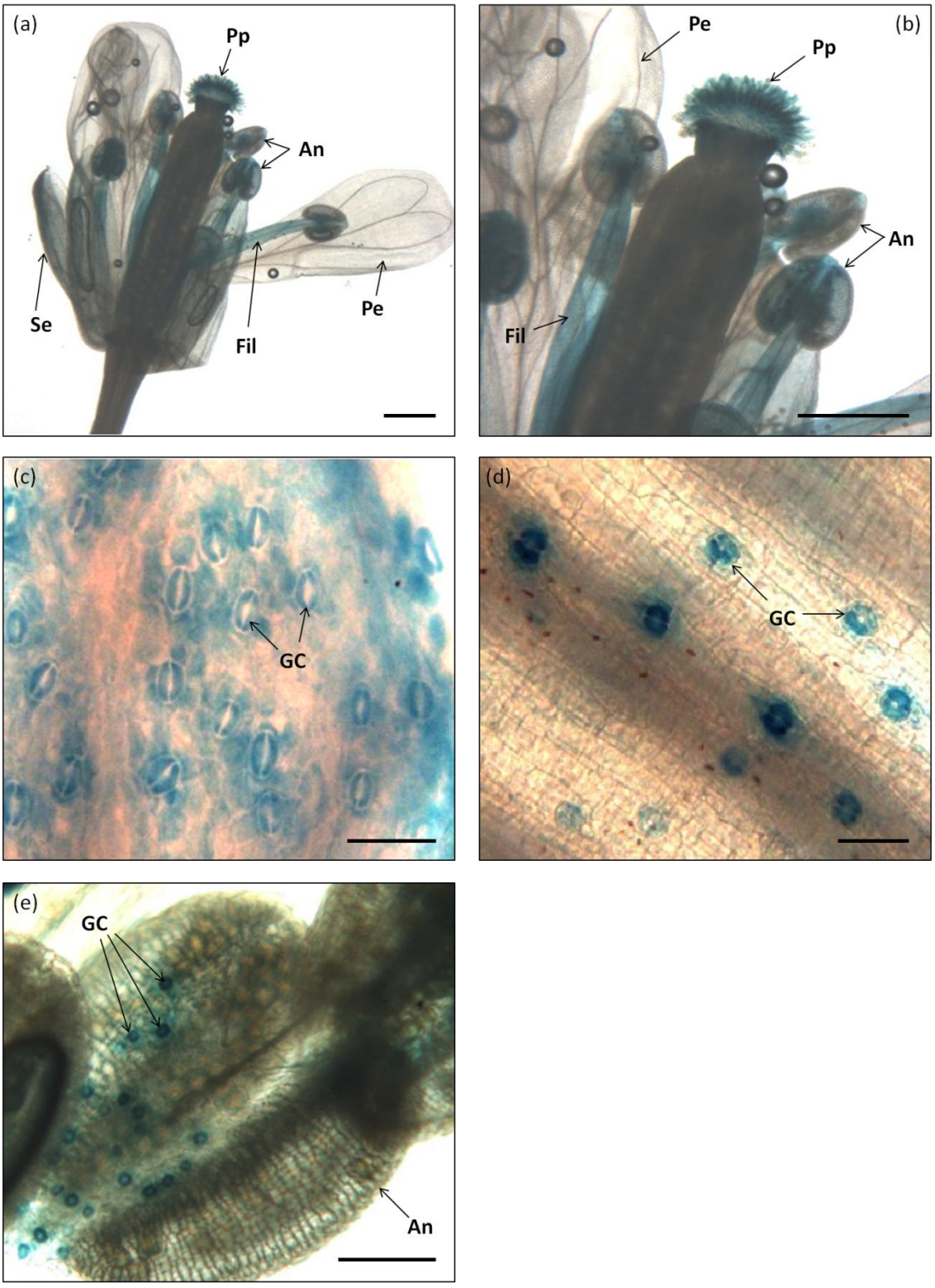

Figure 5.2: Expression pattern of *NET4B* in floral tissue. Opened flowers from 5-6 week old plants of the *NET4Bpro*::GUS lines were stained for GUS activity. (a) and (b) opened flowers showing expression in the sepals, papillae and filaments. (c)-(e) Expression in the guard cells; (c) sepals, (d) inflorescence stem, (e) anther. An = anther, Fil = filament, GC = guard cell, Pe = petal, Pp = papillae, Pe = petal, Se = sepal. Scale bars: (a and b) 500 μm, (c) 50 μm, (d) 20 μm, (e) 100 μm.

NET4Bpro::GUS analysis provides further evidence for the expression of *NET4B* in these highly specialised cells.

5.2.3 Expression pattern in siliques and embryos

The final GUS assays involved studying *NET4B* expression pattern in the siliques and developing embryo. GUS activity in the siliques was assessed by detaching siliques from 5-6 week old plants, and incubating them in the GUS buffer followed by vacuum infiltration and incubation at 37 °C for 1-3 hours. The tissue was then cleared through several washes of 70% ethanol. GUS activity in the developing embryo was examined by staining siliques of 5-6 week old plants that had been carefully opened using a razor blade. Ovules were stained in the GUS buffer, as above, whilst still attached to the siliques. The ovules were subsequently mounted on a slide and gentle pressure was applied to the cover slip to separate the embryo from the ovule.

All eleven lines were used to assess the expression profile in the siliques. The expression profile in the developing embryos was examined using five randomly selected lines (lines 1, 5, 7, 10 and 11). However only a low number of stained embryos were observable after separation from the ovules, and all embryos observed were from later stages of development.

Figure 5.3 shows the results of this analysis in both siliques and the developing embryo. In all eleven lines expression of *NET4B* was confined to the stamen abscission zone (SAZ, Figure 5.3 b). In addition to staining at the SAZ, guard cell localised GUS activity could also be observed in close proximity to the SAZ in some stained siliques, as seen in Figure 5.3 (b).

The expression pattern of *NET4B* observed in the embryos of the different transformed lines showed more variation than was observed in other tissues. In addition, embryos within the same line had slightly varying patterns of GUS staining. The full list of observed expression patterns is listed in Appendix 2.2. Generally, GUS activity could be observed throughout the developing embryos with a particular enrichment at the root tip (Figure 5.3 c). However in some stained embryos, GUS activity appeared to be more restricted to the root tip (Figure 5.3 d). This is similar to observations in the seedling root tip and floral guard cells where areas of maximal expression appear before areas of lower expression, depending on the incubation time. In addition, some embryos only

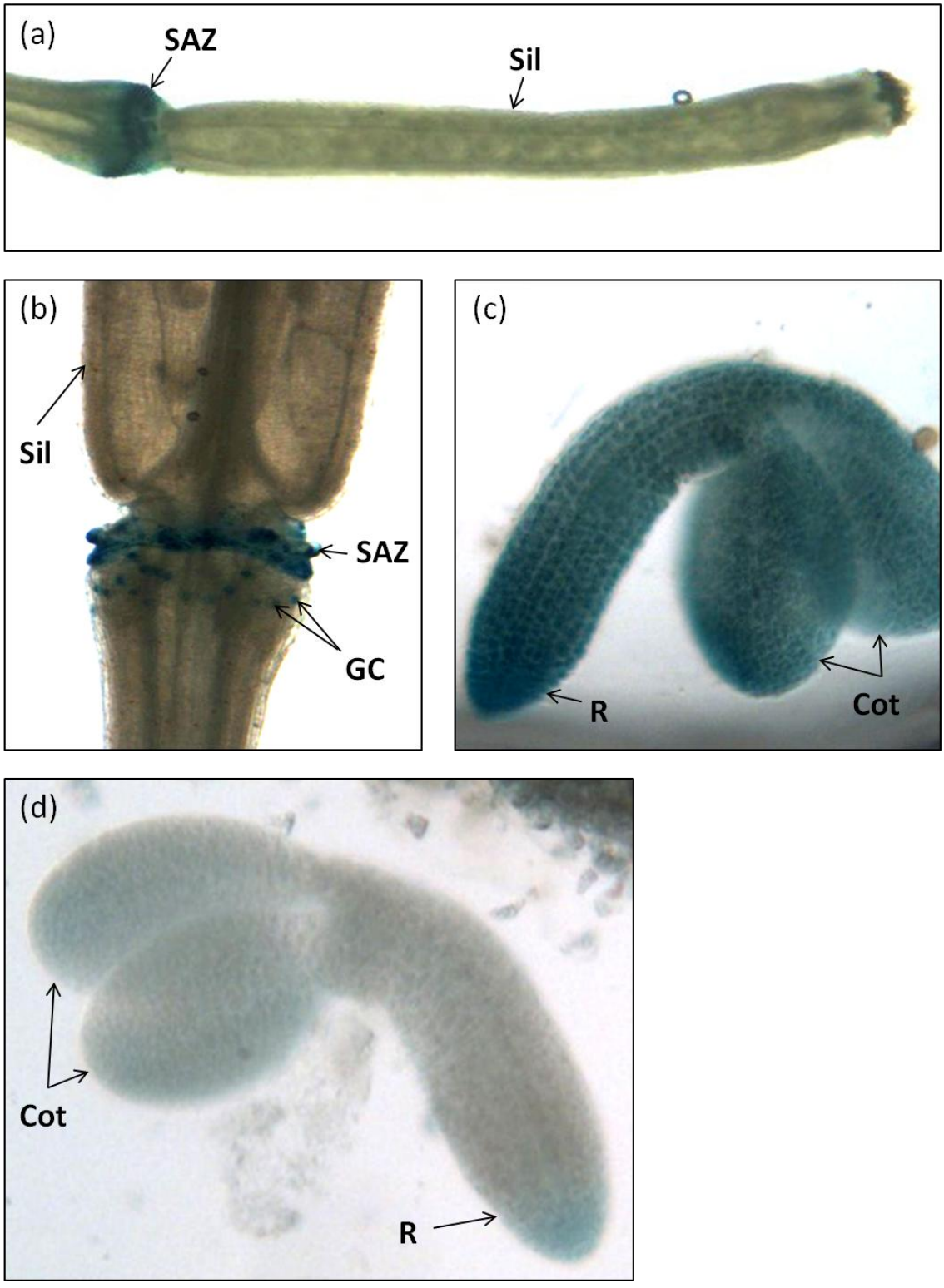

Figure 5.3: Expression of *NET4B* in the siliques and embryos. Siliques and embryos from 5-6 week old plants of the *NET4Bpro*::GUS lines were stained for GUS activity. (a) silique, (b) stamen abscission zone of the silique, (c) GUS activity shown throughout the embryo, (d) embryo displaying particular *NET4B* expression in the root tip. Cot = cotyledon, GC = guard cell, R = root, SAZ = stamen abscission zone, Sil = silique. Scale bar: (a) 1 mm, (b) 500 μm, (c and d) 50 μm.

showed expression restricted to the side of one cotyledon, which suggests that the GUS buffer was not able to penetrate sufficiently into the ovule and could account for the variation observed within embryos of the same line.

From this analysis, it is clear that *NET4B* is expressed in the developing embryo. Using a larger sample size consisting of different embryo developmental stages would enable the temporal expression changes of *NET4B* to be characterised during embryo development.

5.3 Analysis of NET4B expression in Arabidopsis

The *NET4Bpro*::GUS studies demonstrated the transcriptional profile of *NET4B* in Arabidopsis. To study the translational profile, polyclonal antibodies were raised against NET4B, which were used to test its tissue translation profile through Western blot analysis. In addition, these anti-NET4B antibodies were also used to investigate the subcellular localisation of NET4B through immunogold labelling as discussed in section 5.5.

5.3.1 Identification of the NET4B antigen fragment

In order to generate polyclonal antibodies, mice or rabbits are typically inoculated with an antigen against a target protein. The inoculated animals will then raise antibodies against the particular antigen fragment and at the end of the inoculation period the blood serum is harvested. This serum will contain the antibodies raised against the antigen fragment, and it can therefore be used for the immunological detection of the target protein. Specificity of the antibody is crucial when studying the localisation of a target protein as non-specific antibodies could detect additional non-target proteins.

As NET4B is highly homologous to NET4A, the NET4B antigen fragment was chosen as a region with the least conservation between the two proteins. Figure 5.4 (c) shows an alignment of the two NET4 proteins with the region of the least similarity being highlighted. This 100 amino acid fragment ($NET4B^{aa121\text{-}220}$; Figure 5.4 b) was chosen as it was distinct from the two highly conserved regions of the two NET4 proteins; the N-terminal NAB domain and the C-terminal IRQ domain.

In addition, this fragment was also chosen as it has a low hydrophobicity. Figure 5.5 shows a Kyte & Doolittle hydrophobicity plot of the NET4B antigen fragment that was

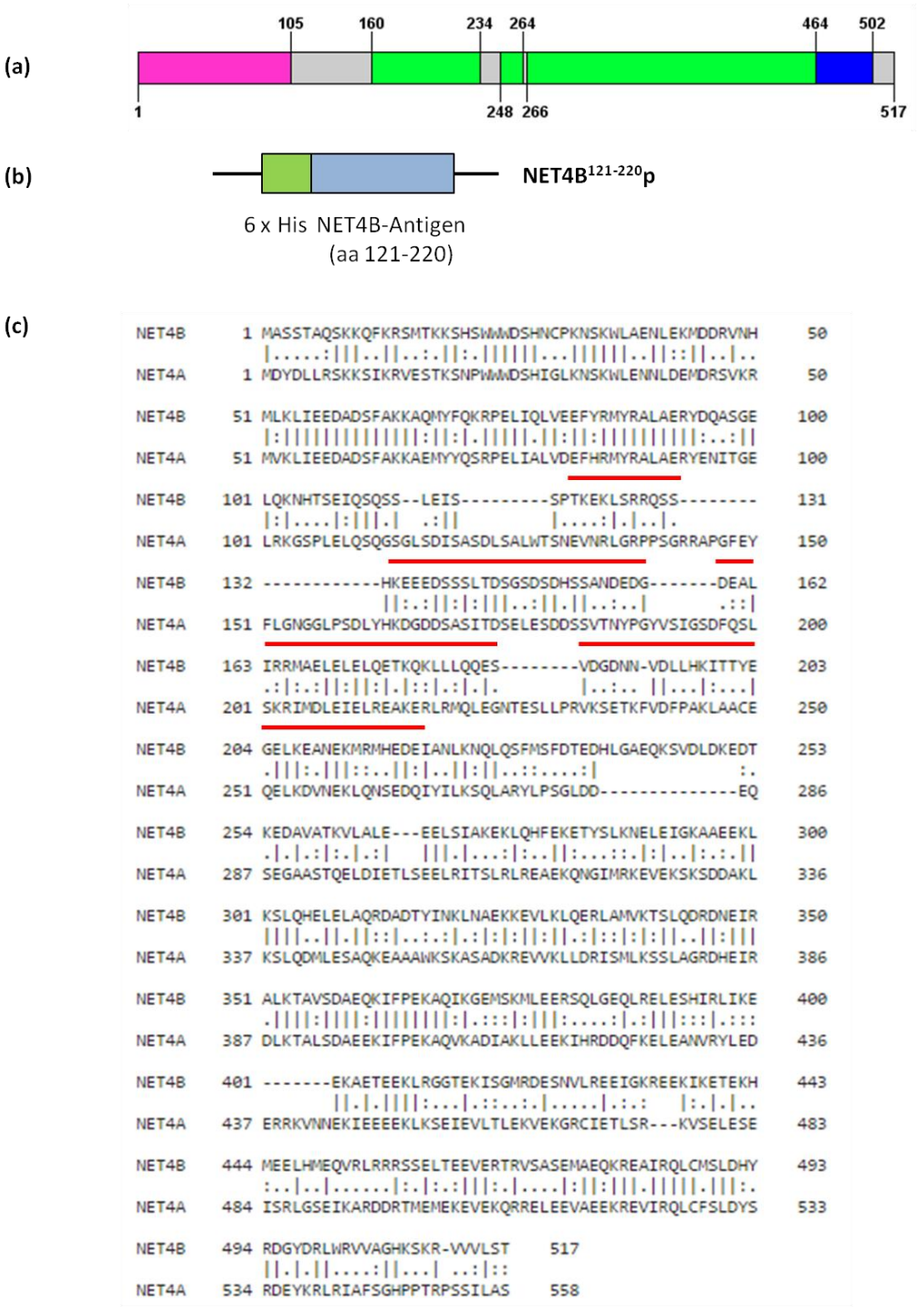

Figure 5.4: Identification of the NET4B antigen fragment. (a) Schematic diagram showing the secondary structure of NET4B, created using the Illustrator of Biological Sequences (IBS) software (Liu et al. 2015). NAB domain is shown in magenta, coiled-coil domains are shown in green, and the IRQ domain is shown in blue, numbers denote amino acid residues. (b) Expression construct for the purification of the NET4B$^{121-220}$ protein fragment using a 6xHistidine tag. (c) Alignment of the amino acid sequences of NET4B and NET4A using the EMBOSS Needle programme (Rice et al. 2000). Connecting lines between the sequence indicate identical residues and dots indicate similar residues. The region chosen as the NET4B antigen fragment is highlighted with a red line above the NET4B sequence.

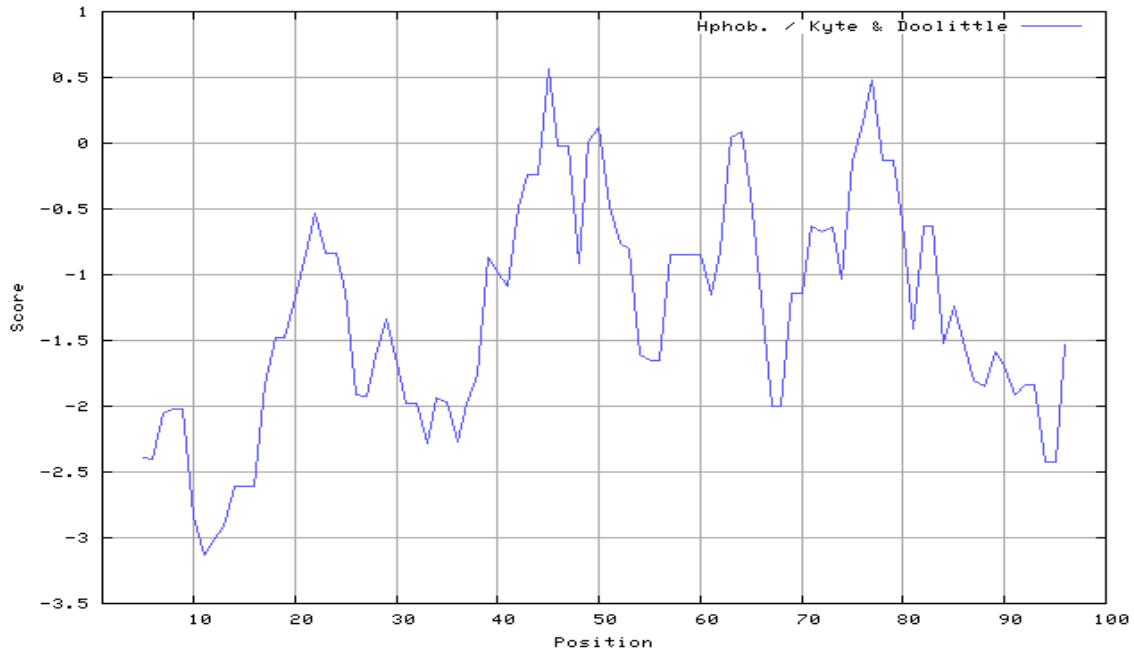

Figure 5.5: Hydrophobicity plot for the NET4B antigen fragment (NET4B$^{121-220}$). Kyte & Doolittle hydrophobicity plot of the NET4B antigen fragment, generated using the ProtScale programme on the ExPASy server (Kyte & Doolittle 1982; Artimo et al. 2012). Scores greater than zero indicate hydrophobic regions. The NET4B$^{121-220}$ antigen fragment is not very hydrophobic and would be suitable for host inoculation.

generated using the ProtScale programme on the ExPASy server (Kyte & Doolittle 1982; Artimo et al. 2012). The Kyte & Doolittle algorithm calculates the average hydropathy of a fragment based on the hydrophilic and hydrophobic nature of the amino acid sequence, with more hydrophobic amino acids generating a more positive score. The low hydrophobicity of this fragment would allow it to remain soluble during inoculation, and it would therefore be more likely to elicit an immune response in the host organism.

The cloning and purification of this fragment is described in section 2.2.10 and 2.4.1 respectively. Following dialysis, the purified protein was separated on a 15% SDS-PAGE gel to determine the molecular weight of the purified protein (Figure 5.6). The predicted molecular weight of this fragment was 11.4 kDa, however the purified protein produced three strong bands during separation on the SDS-PAGE gel, which appeared to be between 20- and 10- kDa. These bands were confirmed to correspond to the NET4B antigen fragment through MALDI-TOF mass spectrometry performed by the Durham University Proteomics service (as described in 2.4.4). The smaller bands are therefore likely to represent breakdown products of the full-length fragment. As this

protein fragment remained soluble after purification, it was used to generate anti-NET4B polyclonal antibodies as discussed below.

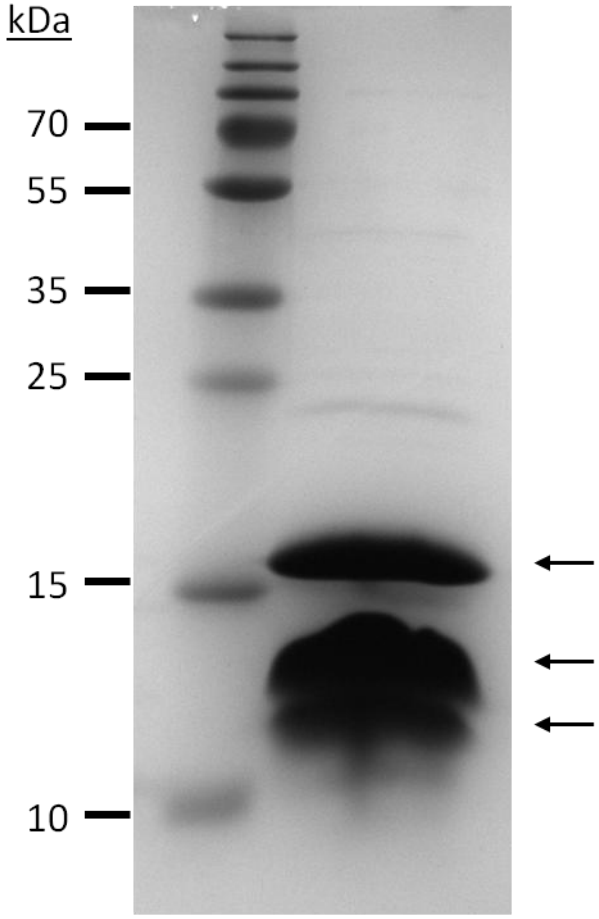

Figure 5.6: Purification of the NET4B antigen fragment (6xHis-NET4B$^{121-220}$). The NET4B antigen fragment was expressed as a 6xHistidine tagged fusion protein and purified from *E. coli* Rosetta 2 cells using a nickel-nitrilotriacetic acid column, followed by overnight dialysis into PBS. Shown here is the purified protein that has been separated on a 15% SDS-PAGE gel and subsequently stained with Coomassie Brilliant Blue. Three strong bands were visible (labelled by the black arrows), and these were confirmed to correspond to NET4B through MALDI-TOF analysis. PageRuler Plus Prestained Protein ladder (Thermo Scientific) was used as a molecular weight marker.

5.3.2 Production of the anti-NET4B polyclonal antibodies

Polyclonal antibodies to the NET4B antigen fragment were raised in rabbits. As variation can occur in the individual immune response of each host organism, two different rabbits (A88 & A89) were inoculated with the same protein fragment (as described in 2.4.5). The specificity of the antibodies raised in these rabbits was assessed using Western blot analysis. Total protein extracted from 15-day old vertically grown

wild-type Arabidopsis plants was separated on a 10% SDS-PAGE gel and transferred to a nitrocellulose membrane (according to 2.4.6 and 2.4.9) The sera derived from the terminal bleeds were initially used to probe the membrane at dilutions of 1:500, 1:1000 and 1:2000 (Figure 5.7). Sera from both rabbits detected a band at approximately 60 kDa which corresponds with the predicted molecular weight of NET4B. However the A89 sera also produced a prominent lower molecular weight band at around 40 kDa. Furthermore, the dilution series also demonstrated that this 40 kDa band was preferentially detected over the 60 kDa band. The sera derived from this rabbit was therefore deemed likely to be none-specific and was not used for further experiments.

In order to further validate that the specificity of the A88 sera for NET4B, Western blot analysis was performed with the A88 pre-bleed sera obtained prior to inoculation with the purified NET4B antigen fragment (Figure 5.8). Equal amounts of total protein (50 µg) extracted from 15-day old vertically grown wild-type Arabidopsis plants (as described in 2.4.7) were separated on a 10% SDS-PAGE gel and subsequently transferred onto a nitrocellulose membrane for Western blot analysis (as described in 2.4.9 and 2.4.12). Equal loading of the sample was confirmed through staining the membrane with Amido black. Probing the membrane with the A88 pre- and terminal-bleed at a dilution of 1:500 revealed that, under the same conditions, a single prominent band at approximately 60 kDa could only be detected in the A88 terminal bleed. This therefore demonstrates that this band is detected by polyclonal antibodies produced in response to the NET4B antigen fragment.

The size of the A88 band corresponds to the predicted molecular weight of NET4B (60 kDa) but is also very close to the predicted molecular weight of NET4A (64 kDa). Therefore the specificity of the A88 derived antibodies in detecting NET4B was tested further as described below.

5.3.3 Determining the specificity of the anti-NET4B antibody

The specificity of the A88 derived antibodies for NET4B was tested further through Western blot analysis on protein extracts derived from *N. benthamiana* leaf epidermal cells overexpressing either NET4B-GFP or NET4A-GFP.

The two NET4-GFP constructs in the pMDC83 vector (as discussed in Chapter 4) were transiently transformed into *N. benthamiana* leaf epidermal cells, using separate plants for each construct, through the Agrobacterium mediated transformation method (as

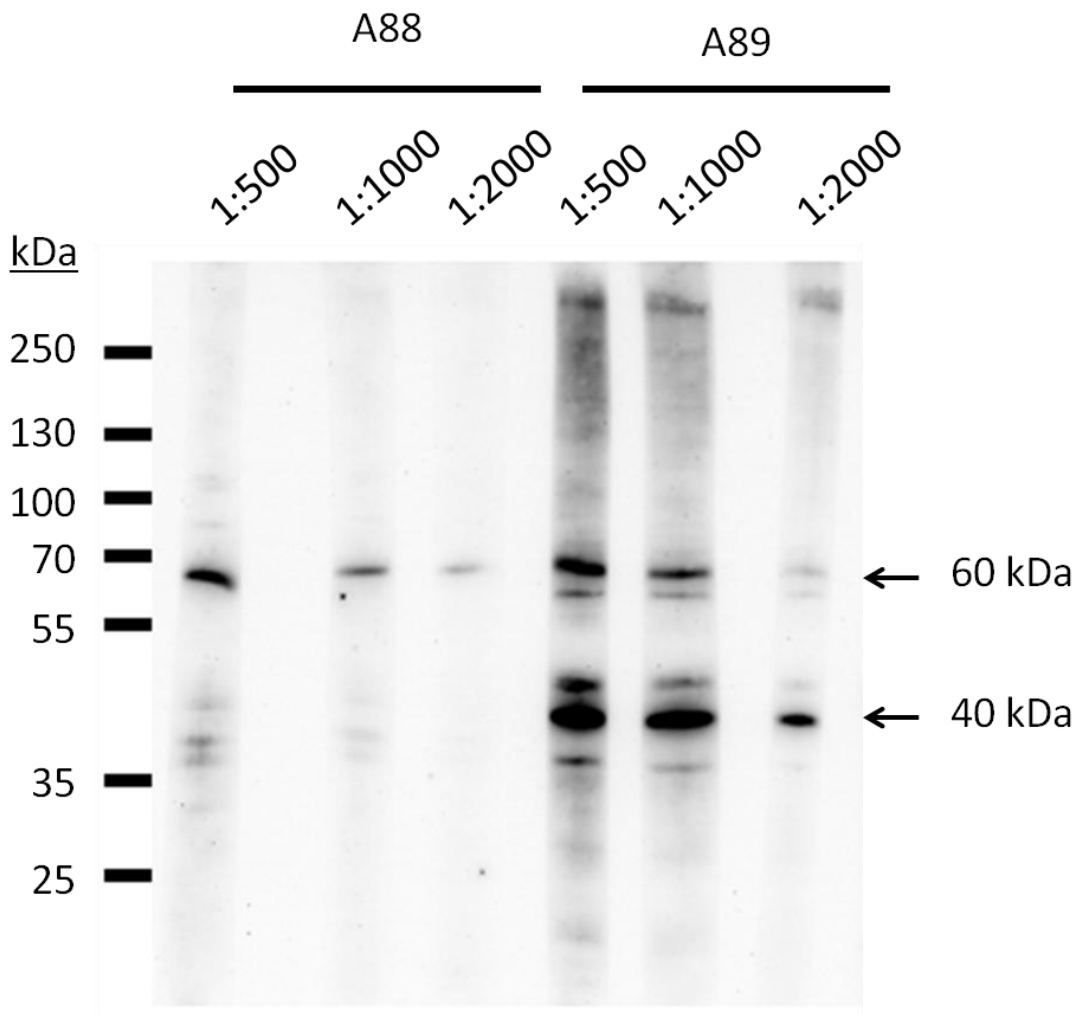

Figure 5.7: Western blot analysis of the rabbit terminal bleeds. Total protein extracted from 15-day old wild-type Arabidopsis plants was separated on a 10% SDS-PAGE gel and transferred to a nitrocellulose membrane for Western blot analysis. The membrane was cut into strips and probed with various dilutions (1:500, 1:1000, 1:2000) of the A88 and A89 rabbit terminal bleeds, followed by a secondary anti-Rabbit/HRP antibody (1:2000; Dako). The A88 sera produced only one prominent band at 60 kDa which corresponds to the predicted molecular weight of NET4B. Whereas, the A89 sera produced two bands at 60- and 40- kDa, with the lower molecular weight band appearing stronger during the dilution series. The A89 sera was therefore deemed to be none-specific and was not used for further experiments. The Precision Plus Protein Dual Colour (Bio-Rad) was used as a molecular weight standard.

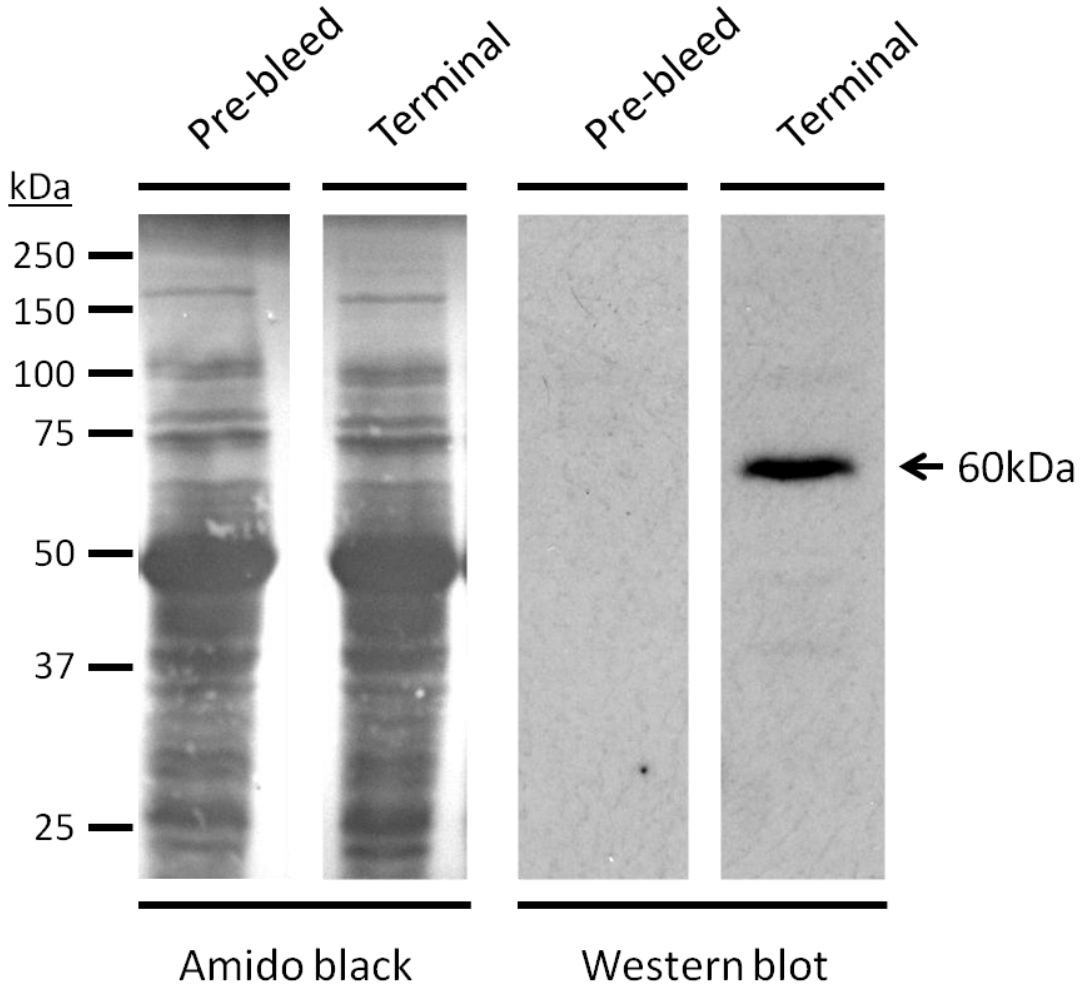

Figure 5.8: Western blot analysis of the A88 rabbit pre- and terminal-bleeds. Equal amounts of total protein (50 µg) extracted from 15-day old wild-type Arabidopsis plants were separated on a 10% SDS-PAGE gel and transferred to a nitrocellulose membrane for Western blot analysis. Amido black staining of the nitrocellulose membrane confirmed equal loading of the protein. Western blot analysis was performed with the A88 pre- or terminal bleeds (1:500), followed by a secondary anti-Rabbit/HRP antibody (1:2000; Dako). The previously detected 60 kDa band could only be detected using the A88 terminal bleed and not the pre-bleed. This therefore demonstrates that this band was due to the inoculation of the rabbit with the NET4B antigen fragment. The Precision Plus Protein Dual Colour (Bio-Rad) was used as a molecular weight standard.

described in 2.2.13). After a two-day incubation period, the expression of the two constructs was confirmed through confocal laser scanning microscopy (CLSM), and total protein extracts were prepared from the transformed leaf sections (as described in 2.4.7). Total protein concentration was quantified using the Detergent Compatible (Dc) Bradford assay (Bio-Rad). Equal amounts of total protein (50 μg) derived from transformed leaf tissue were separated on a 10% SDS-PAGE gel before being transferred onto a nitrocellulose membrane for Western blotting. The membrane was probed with the A88 sera at a 1:20,000 dilution. As a positive control, the same extracts were probed with an anti-GFP antibody (1:1000; Invitrogen).

The result of this Western blot demonstrated that the A88 derived sera detected a single band at around 100 kDa in total protein extracts derived from the NET4B-GFP transformed leaf but not the NET4A-GFP transformed leaf sections (Figure 5.9). The size of this band is similar to the predicted size of the NET4B-GFP fusion protein (60 kDa NET4B + 27 kDa GFP). An identically loaded nitrocellulose membrane probed with the anti-GFP antibody revealed that the same sized band could be detected in protein extracts from both the NET4B-GFP and the NET4A-GFP transformed tissue. This demonstrates that the polyclonal antibodies derived from the A88 rabbit sera cannot cross-react with NET4A. The A88 sera was therefore described as containing anti-NET4B polyclonal antibodies.

5.3.4 Analysis of NET4B expression in different Arabidopsis tissue using Western blots analysis

Having established the specificity of the anti-NET4B antibodies, they could therefore be used to immunologically detect which tissues NET4B is expressed in through Western blot analysis. Total protein was extracted from 7-day old whole seedlings, 15-day old roots, 15-day old young leaves, mature rosette leaves, cauline leaves, inflorescence stems, flowers and siliques. Seedling and 15-day old tissue were derived from plants grown vertically on ½MS agar plates. Mature Arabidopsis tissue was derived from 6-week old plants that had been transferred to soil after two weeks of vertical growth on ½MS plates. Total protein was extracted according to the methods described in 2.4.7, and was quantified using the Bradford Detergent Compatible (Dc) Protein Assay (Bio-Rad). Equal amounts of total protein (50 μg) from each tissue were separated on a 10% SDS-PAGE gel and subsequently transferred to a nitrocellulose membrane for Western

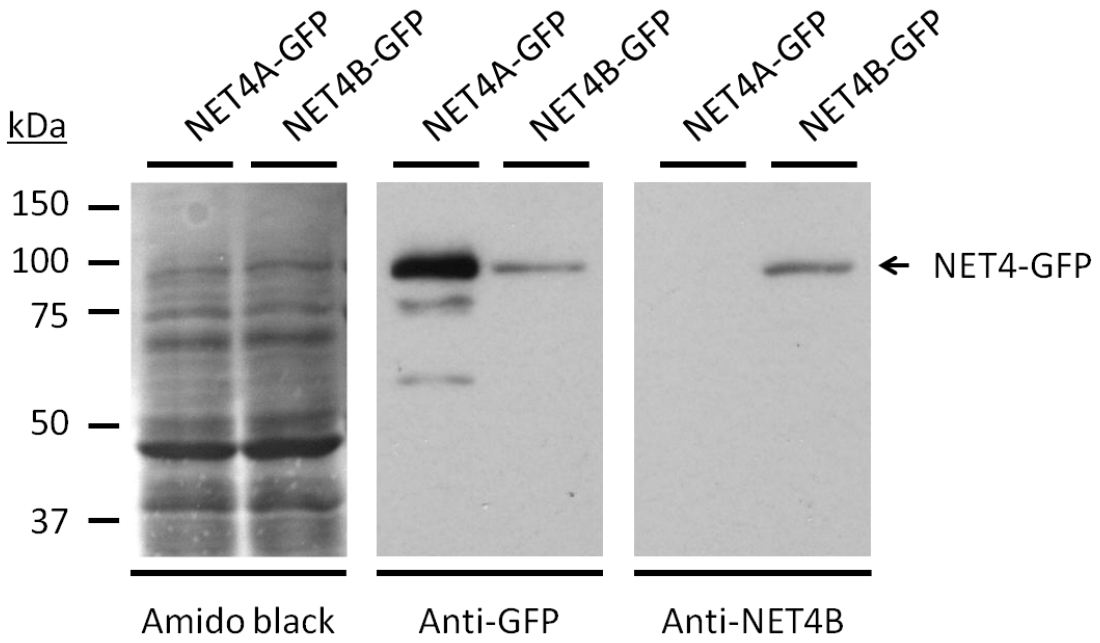

Figure 5.9: Testing the specificity of the anti-NET4B antibody. Total protein was extracted from *N. benthamiana* leaves that were transiently transformed with either NET4B-GFP or NET4A-GFP (expressed using the CaMV 35S promoter in the pMDC83 vector). Equal amounts of NET4B-GFP and NET4A-GFP (50 μg) total protein extracts were separated on two identically loaded 10% SDS-PAGE gels and transferred to nitrocellulose membranes. Amido black was used to confirm equal loading of the protein (shown here is one representative membrane). The two membranes were probed concomitantly with either anti-NET4B or anti-GFP. The anti-NET4B antibody only detected a band in the NET4B-GFP lane whereas the ant-GFP antibody detected a band in both NET4B-GFP and NET4A-GFP protein extracts, thus proving the specificity of the anti-NET4B antibody for NET4B. The Precision Plus Protein Dual Colour (Bio-Rad) was used as a molecular weight standard.

blotting using the anti-NET4B antibody (1:500). Transfer of protein onto the membrane was confirmed through Amido black staining.

Probing this membrane with the anti-NET4B antibody revealed that it detected a very prominent band in protein extracts from the root, as well as slightly less intense bands in the seedling, young leaf and flowers (Figure 5.10). No band was detected in the lanes containing mature leaf, cauline leaf, inflorescence stem or silique protein extracts. The results of this Western blot corroborate with the *NET4Bpro*::GUS data that demonstrated that a very high level of GUS activity could be found in the roots, and in particular at the root tip. This Western blot analysis also supports the GUS data which showed that *NET4B* could be expressed in flowers, with higher levels of GUS activity being observed in the guard cells. The lack of a detectible band in the mature leaves, inflorescence stems or siliques does not necessarily indicate a complete absence of NET4B within these tissues, as it is possible that NET4B is expressed at a lower level within these tissues which was not detected during this assay. Indeed, the *NET4Bpro*::GUS data demonstrated guard cell expression of *NET4B* in the stem, and also expression in the developing embryo. The transcript levels of *NET4B* throughout the different Arabidopsis tissues could be quantified through qPCR.

5.4 *In vivo* analysis of the NET4B-GFP fusion protein expressed under the control of the *NET4B* promoter in Arabidopsis roots

Having demonstrated the transcriptional and translational profile of NET4B in Arabidopsis, it was imperative to study the *in situ* subcellular localisation of this protein. The first experimental approach used was to create transgenic Arabidopsis plants that expressed a NET4B-GFP fusion protein under the control of the *NET4B* promoter. Previous subcellular studies of NET4B-GFP in Chapter 4 relied upon an ectopic overexpression system in *N. benthamiana* leaf epidermal cells. Creating transgenic *NET4Bpro*::NET4B-GFP Arabidopsis lines, however, would permit the visualisation of NET4B in the specific tissues where the promoter is active and at endogenous levels.

5.4.1 Creation of the *NET4Bpro*::NET4B-GFP construct

The Gateway pMDC107 vector was used to create the *NET4Bpro*::NET4B-GFP lines (Curtis & Grossniklaus 2003). This promoterless vector can be used to fuse a C-terminal GFP tag to a full-length gene with its respective upstream promoter. Creation,

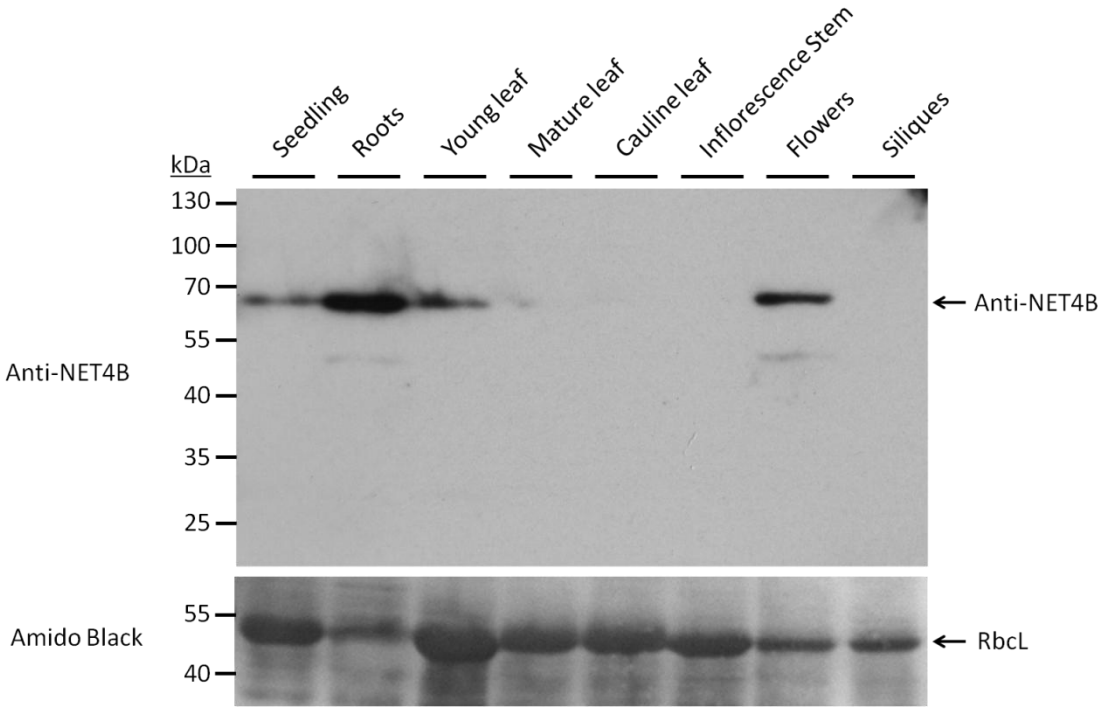

Figure 5.10: NET4B protein expression in different Arabidopsis tissue examined through Western blot analysis. Total protein was extracted from different tissues of Arabidopsis and quantified using the Bradford Detergent Compatible (Dc) Protein Assay (Bio-Rad). Equal amounts of total protein (50 µg) from each sample were separated on a 10% SDS-PAGE gel and transferred to a nitrocellulose membrane, before being probed with the anti-NET4B antibody (1:500). Amido black staining confirmed the transfer of protein, shown here is the Rubisco large chain (RbcL). Page Ruler Prestained was used as molecular weight marker.

and initial floral dipping, of the *NET4Bpro*::NET4B-GFP construct was performed by Dr. Tim Hawkins (Durham University; described in section 2.1.4) and Figure 5.11 (b) shows a schematic diagram of this construct.

The floral dipping method was used to transform wild-type Arabidopsis (Col-0) plants (as described in 2.2.14). The T_1 generation of seed were selected on ½MS plates containing hygromycin. The floral dipping of this construct was repeated twice, by myself and Dr. Tim Hawkins, and produced 29 primary transformants that were allowed to self-pollinate to produce the T_2 generation. Plants from the individual T_2 generation lines were grown vertically on ½MS plates and were manually screened for GFP fluorescence in the roots as the *NET4Bpro*::GUS studies revealed that this tissue showed the highest levels of expression. Screening was initially performed using the Leica M165FC Fluorescent Stereo microscope and further analysis was performed using the Leica SP5 confocal microscope. Initial screening of the plants revealed that only very weak fluorescence could be observed in the roots of 11 plants and this fluorescence was almost indistinguishable from autofluorescence found in control roots. Detectible fluorescence could not be observed in above ground tissue of the transformed plants.

Genotypic PCRs were performed to confirm the presence of the *NET4B107* construct in these T_2 generation plants (according to 2.2.16). Genomic DNA (gDNA) was extracted from the leaves using the Edwards prep method (as described in 2.2.7) and was subsequently used as a template in the genotyping PCR reaction. Two sets of primers were used in this genotyping PCR reaction; *NET4B107* specific primers and a set of primers that would amplify a control band. The *NET4B107* specific primers (IRQ Fw + GFP Rv) would amplify a 231 bp fragment and the position of these primers are shown in Figure 5.11 (b). As a positive control, the *mago* forward and reverse primers were used to amplify a 1868 bp fragment of the *MAGO NASHI* gene (At1g02140). Genomic DNA extracted from the leaves of untransformed Arabidopsis Col-0 was also used as a template in additional reactions that served as a negative control for the presence of the *NET4B107* specific fragment. As a positive control for this fragment, the *NET4B107* vector was used as a template DNA.

The results of this genotypic PCR are shown in Figure 5.11 (c), which showed that one plant from each line, apart from line 15, produced a *NET4B107* specific band. Due to the segregating nature of the T_2 generation not every plant will be homozygous for this

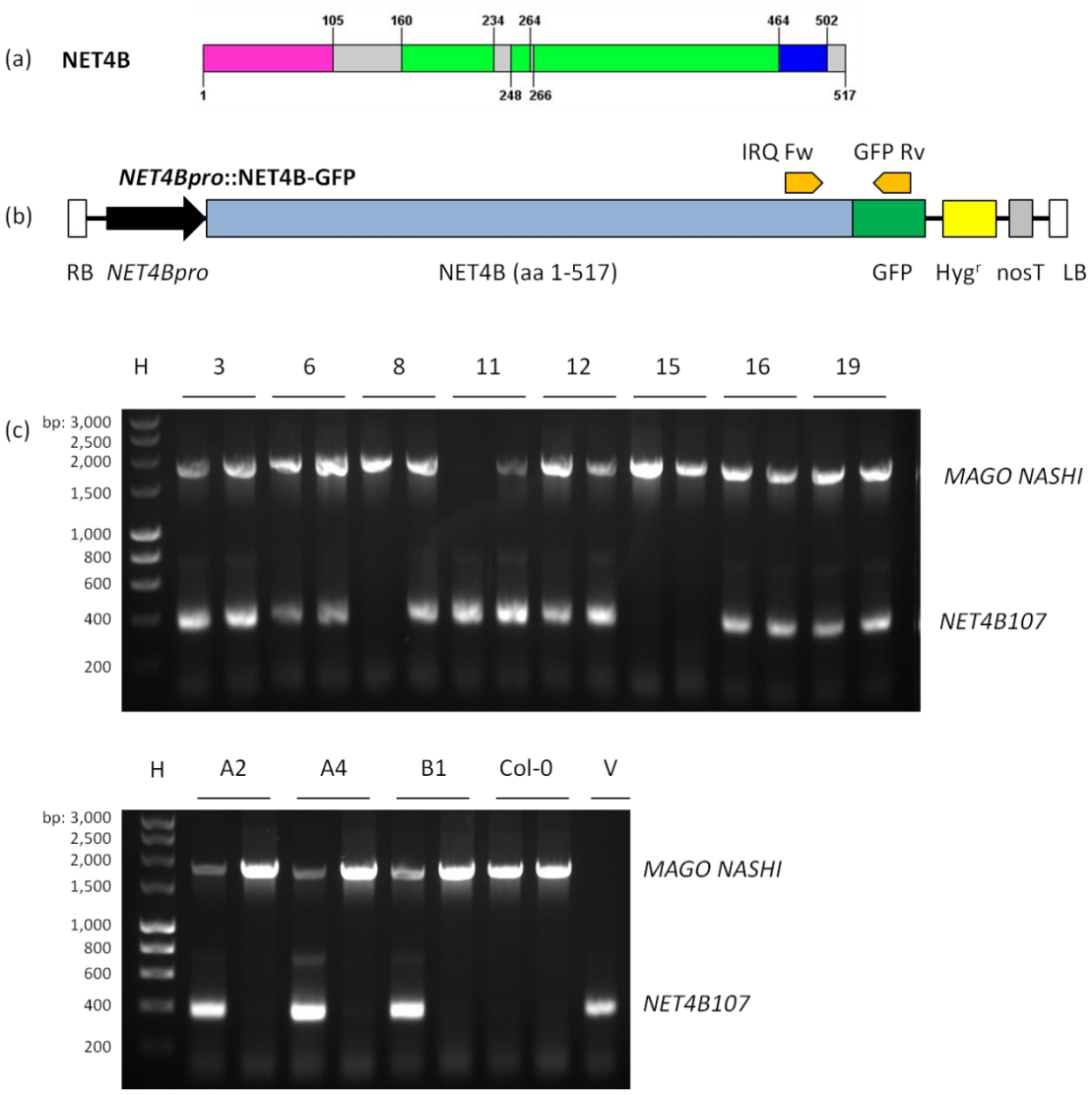

Figure 5.11: Genotyping of the *NET4Bpro*::NET4B-GFP stably transformed lines. (a) Schematic diagram showing the structure of NET4B created using the IBS software (Liu et al. 2015). The NAB domain is shown in magenta, coiled-coil domains are shown in green, IRQ domain is shown in blue and the numbers denote amino acid residues. (b) Schematic diagram of the *NET4Bpro*::NET4B-GFP construct using the pMDC107 expression vector. Shown above the construct are the position of the two primers, IRQ Fw and GFP Rv, used to genotype the NET4B107 stably transformed lines (orange arrows). RB = right border, *NET4Bpro* = 2kb NET4B promoter, GFP = green fluorescent protein, Hyg^r = hygromycin resistance, nosT = nos terminator, LB = left border. (c) Genotyping PCR used to confirm the presence of the *NET4B107* transgene in the transformed lines using the NET4B107 specific primers to amplify a 231 bp fragment. *MAGO NASHI* Fw and Rv primers were also used to amplify a control band of 1868 bp. Genomic DNA, extracted from two plants of the T_2 generation, was used as the template in the genotyping PCR reactions. Untransformed Col-0 was also used as a negative control and the NET4B107 Vector (V) was used as a positive control. Hyperladder I was used as a molecular weight marker.

construct and 25% of the plants should be azygous for the transgene. This therefore explains why some plants did not successfully produce a *NET4B107* specific band in each genotyped plant. Consequently, it is possible that the two genotyped plants in line 15 were azygous for the transgene and therefore produced no *NET4B107* specific band. However from this genotyping analysis the 10 lines that were evidently transformed with the *NET4Bpro*::NET4B-GFP transgene were taken forward for further analysis using CLSM.

5.4.2 Localisation of the NET4B-GFP fusion construct in Arabidopsis roots

Having established that 10 lines contained the *NET4Bpro*::NET4B-GFP transgene and showed very weak fluorescence in the root, it was imperative to study the subcellular localisation of the NET4B-GFP fusion protein through CLSM in these plants. The T_2 generation of transformed seeds were grown vertically on ½MS plates for 7 days before being imaged using the Leica SP5, using the 488 nm laser to excite GFP. A minimum of ten roots were examined for each line.

From this analysis only three lines; lines 3, 19 and A4 demonstrated a pattern of fluorescence that could be distinguished from the autofluorescence detected in untransformed Arabidopsis roots. As observed previously using the stereo fluorescence microscope, the fluorescence from these lines was very weak. Figure 5.12 shows the pattern of fluorescence that was seen in these three transformed lines as well as autofluorescence from an untransformed root. The Leica 'glow' palette was used to visualise the GFP fluorescence as this colour scheme makes areas of particularly intense fluorescence easier to distinguish from the background signal. The fluorescence observed in all three lines was largely cytosolic and areas of intense fluorescence could not be distinguished. In the untransformed root only a punctate pattern of nuclear autofluorescence could be observed in the root tip.

The lack of a conclusive *in situ* localisation for NET4B through this experimental approach could represent an incompatibility of NET4B with this system. It is possible that the level of NET4B in the Arabidopsis root is under tight regulation and introducing further copies of NET4B results in its subsequent degradation. In addition, the presence of the C-terminal GFP tag could interfere with the endogenous function of NET4B and could lead to the fusion protein being degraded. As this experimental approach could not definitively demonstrate a subcellular localisation for NET4B, a

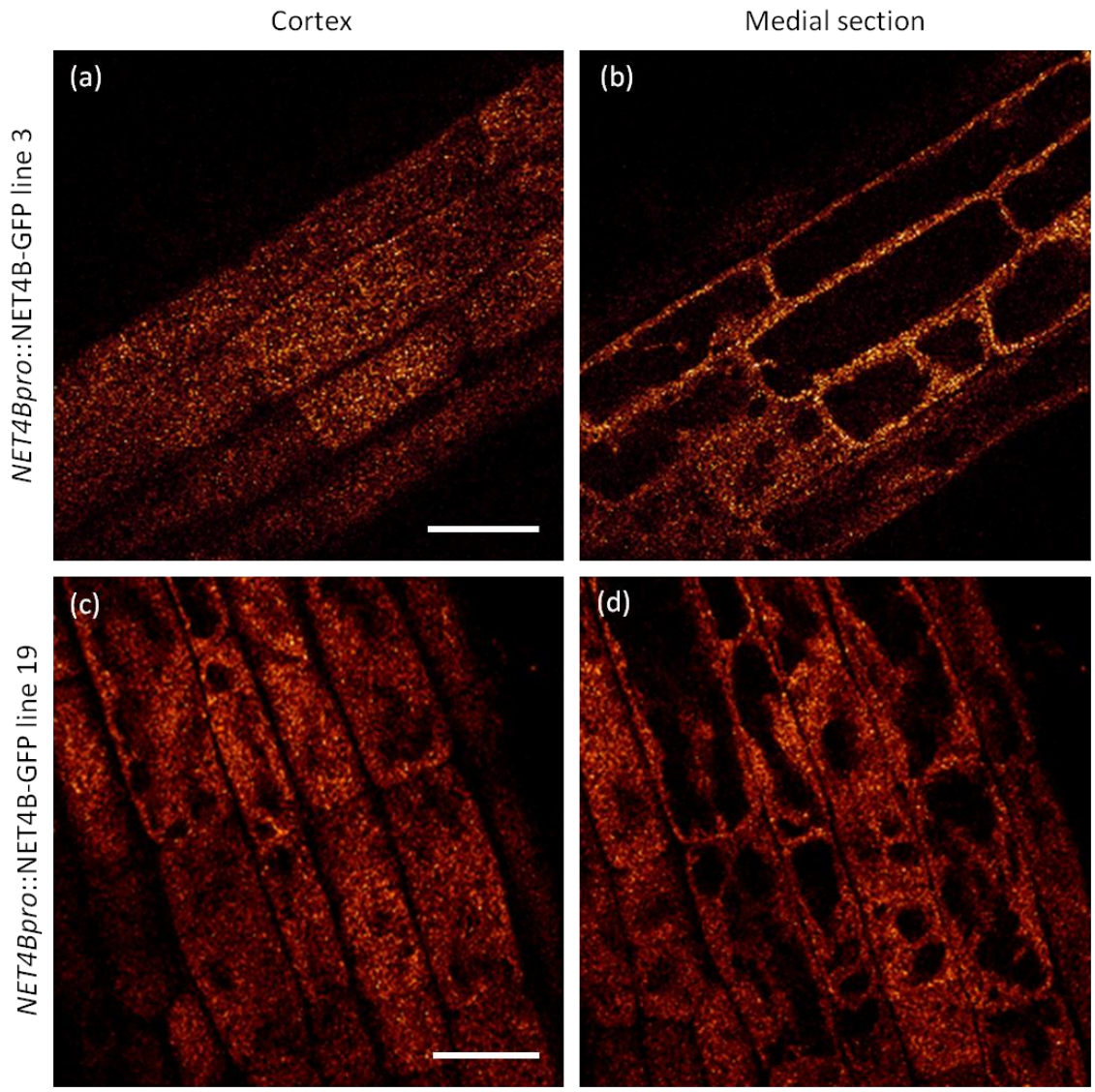

Figure 5.12 continued overleaf.

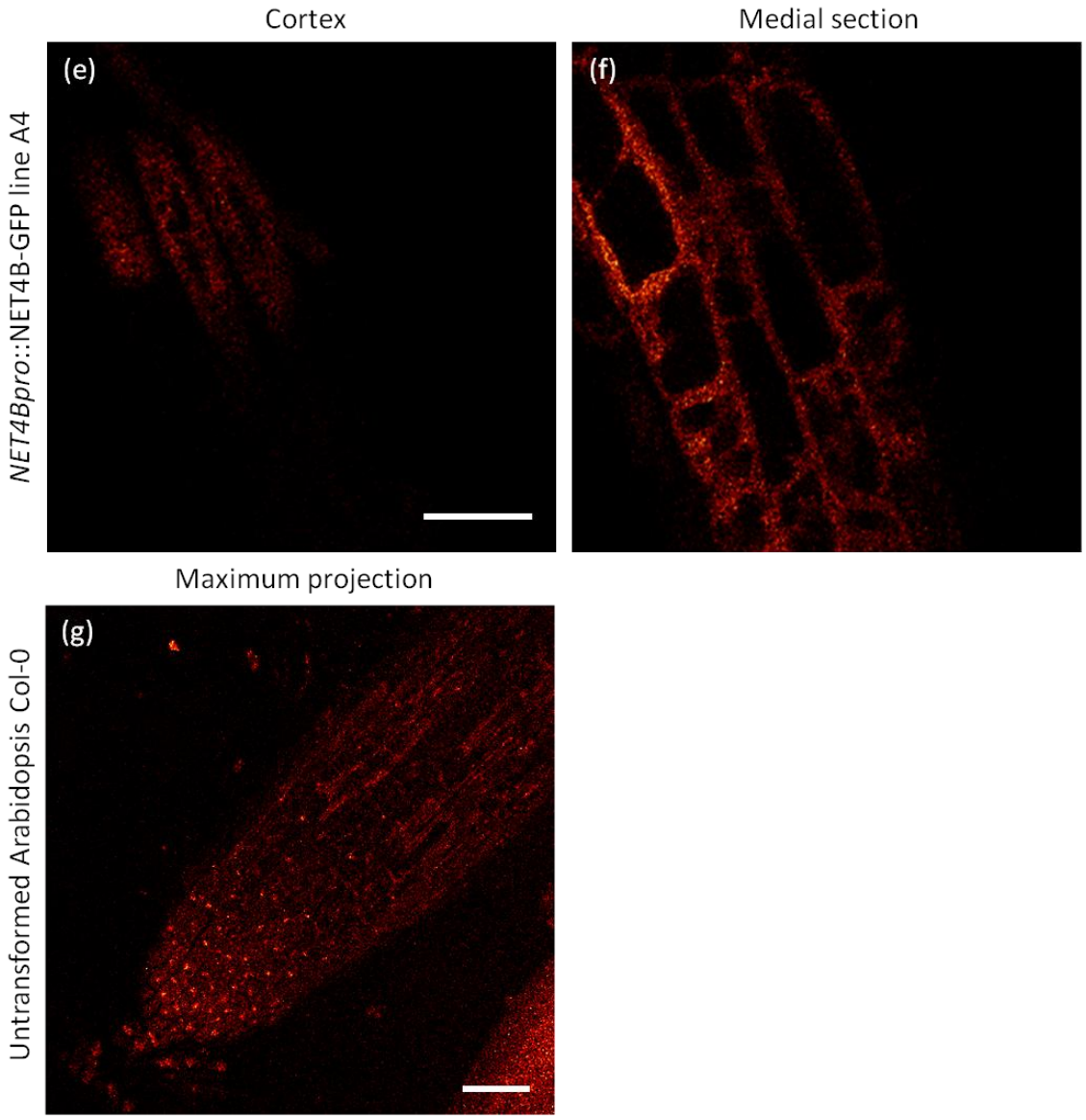

Figure 5.12: Localisation of the *NET4Bpro*::NET4B-GFP fusion protein in stably transformed Arabidopsis. Only three lines showed a level of fluorescence that could be discerned from the autofluorescence of wild-type Arabidopsis roots. Line 3 (a-b), line 19 (c-d) and line A4 (e-f) all exhibited cytosolic GFP fluorescence and no areas of particularly intense signal could be observed. Shown here is the expression in 7-day old T_2 generation roots at the cortex and medial section of root cells from the elongation zone. (g) The wild-type Arabidopsis (Col-0) root only showed autofluorescence in the nucleus. Scale bars: (a, c, e) 20 μm. (s) 50 μm.

different approach was undertaken using immunogold labelling with the anti-NET4B antibody, as described below.

5.5 Localisation of NET4B in Arabidopsis root tips using immunogold labelling and transmission electron microscopy

Immunological detection and imaging of a target protein within a fixed sample, either through immunofluorescence or immunogold labelling, enables the visualisation of its native localisation. Primary antibodies, raised against the target protein, bind to the antigenic site within the tissue sample. The location of the primary antibody, and therefore the antigen, can then be detected through the application of a secondary antibody that is conjugated to a fluorochrome (for use in immunofluorescence) or a gold particle (for immunogold labelling and electron microscopy).

In this study, immunogold labelling and transmission electron microscopy (TEM) was used to detect the native subcellular localisation of NET4B within the root. The anti-NET4B antibody (as described in section 5.3), was used to detect endogenous NET4B in ultrathin sections of high pressure frozen and freeze substituted (HPFFS) sections of Arabidopsis root tips. The primary antibody was then detected using 5 nm colloidal gold-conjugated goat anti-rabbit antibodies.

Cryofixation of the samples was chosen over traditional chemical fixation, as aldehyde fixatives have been shown to rupture the tonoplast membrane, releasing vacuolar contents and reducing the ultrastructure detail that can be observed (Wilson & Bacic 2012). The rapid immobilisation of tissues using HPFFS results in the preservation of fine cellular structure as well as maintaining the integrity of antigenic sites for antibody recognition.

5.5.1 Immunogold labelling of TEM sections of Arabidopsis root tips using the anti-NET4B antibody

Immunogold labelling was performed on the root tips of 7-day old Arabidopsis seedlings (as described in 2.5.1 and 2.5.2), as the *NET4Bpro*::GUS studies demonstrated that the *NET4B* promoter was active within this tissue at this developmental stage. In this analysis, only one anti-NET4B labelled Arabidopsis root tip exhibited a high quality of preservation (Figure 5.13 a). Imaging of this section focussed on the deeper cell files of the root and did not include the outer edge of cells, as seen in Figure 5.13 (a).

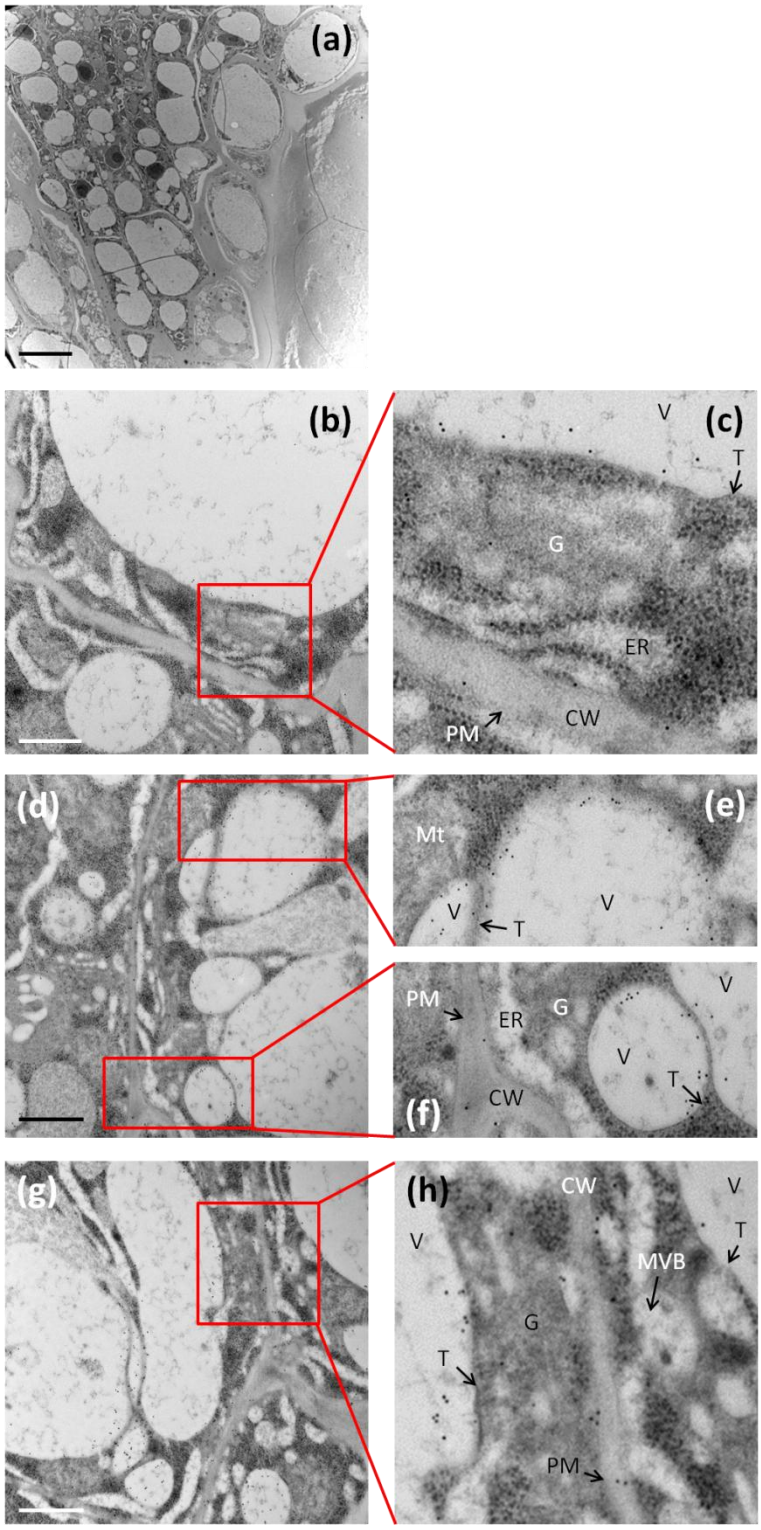

Figure 5.13: *In situ* localisation of NET4B in Arabidopsis root tips using immunogold labelling and TEM. High pressure frozen and freeze substituted sections of the Arabidopsis root tip were labelled with the anti-NET4B antibody and imaged using TEM (a; x4000 magnification). Examples of several labelled cells (b, d, g) of the Arabidopsis root tip were imaged at high magnification (x 40,000). Digital zoom was used to demonstrate labelling of the red-boxed area (c, e, f, g). V = vacuole, T = tonoplast, G = Golgi, ER = endoplasmic reticulum, PM = plasma membrane, CW = cell wall, MVB = multivesicular body, Mt = mitochondria. Scale bars: (a) 5 µm, (b, d, g) 500 nm.

Labelling of the sample with the anti-NET4B antibody showed a particular enrichment to the tonoplast surrounding the lytic vacuole, including the large central vacuole and smaller vacuolar compartments (Figure 5.13). As well as the tonoplast, labelling was consistently observed at the plasma membrane, however the density of gold particles at this membrane appeared to be lower than that of the tonoplast. In both cases, labelling appeared to be evenly distributed across the different membranes and was not localised to discrete foci. Very little labelling could be consistently observed outside of these two compartments.

In addition to the tonoplast and the plasma membrane, double-membrane structures that could potentially represent autophagosomes were labelled with the anti-NET4B antibody (Figure 5.14). Five similar structures were observed which were labelled with the anti-NET4B antibody. These double-membrane structures could be viewed in the cytosol, as well as in association with the plasma membrane.

No gold particle labelling was observed with the primary antibody omission control from this experiment (Figure 5.15). The A88 pre-bleed sera control did not show labelling to the tonoplast, however limited labelling was observed at the plasma membrane (Figure. 5.16). Therefore the labelling at the plasma membrane observed with the anti-NET4B antibody was deemed to be non-specific and could represent background signal from the rabbit sera. Only one double-membrane structure was observed in each of the pre-bleed and primary omission controls, however these structures were not labelled in both cases.

Initial observation of the immunogold labelling using the anti-NET4B antibody, after consideration of the pre-bleed control, demonstrated that NET4B localises to the tonoplast in the Arabidopsis root tip. In order to ascertain whether NET4B preferentially localises to this compartment, quantitative analysis of the anti-NET4B immunogold labelling was performed as described below.

5.5.2 Quantification of the observed anti-NET4B immunogold labelling

Quantification of immunogold labelling enables the interpretation of antigen site density across different subcellular compartments. One of the most commonly used quantitative assessments of immunogold labelling involves calculating the labelling density (LD) of a particular compartment (Mayhew et al. 2002). This method calculates the number of gold particles per unit length of membrane or per unit area of organelle, and provides an

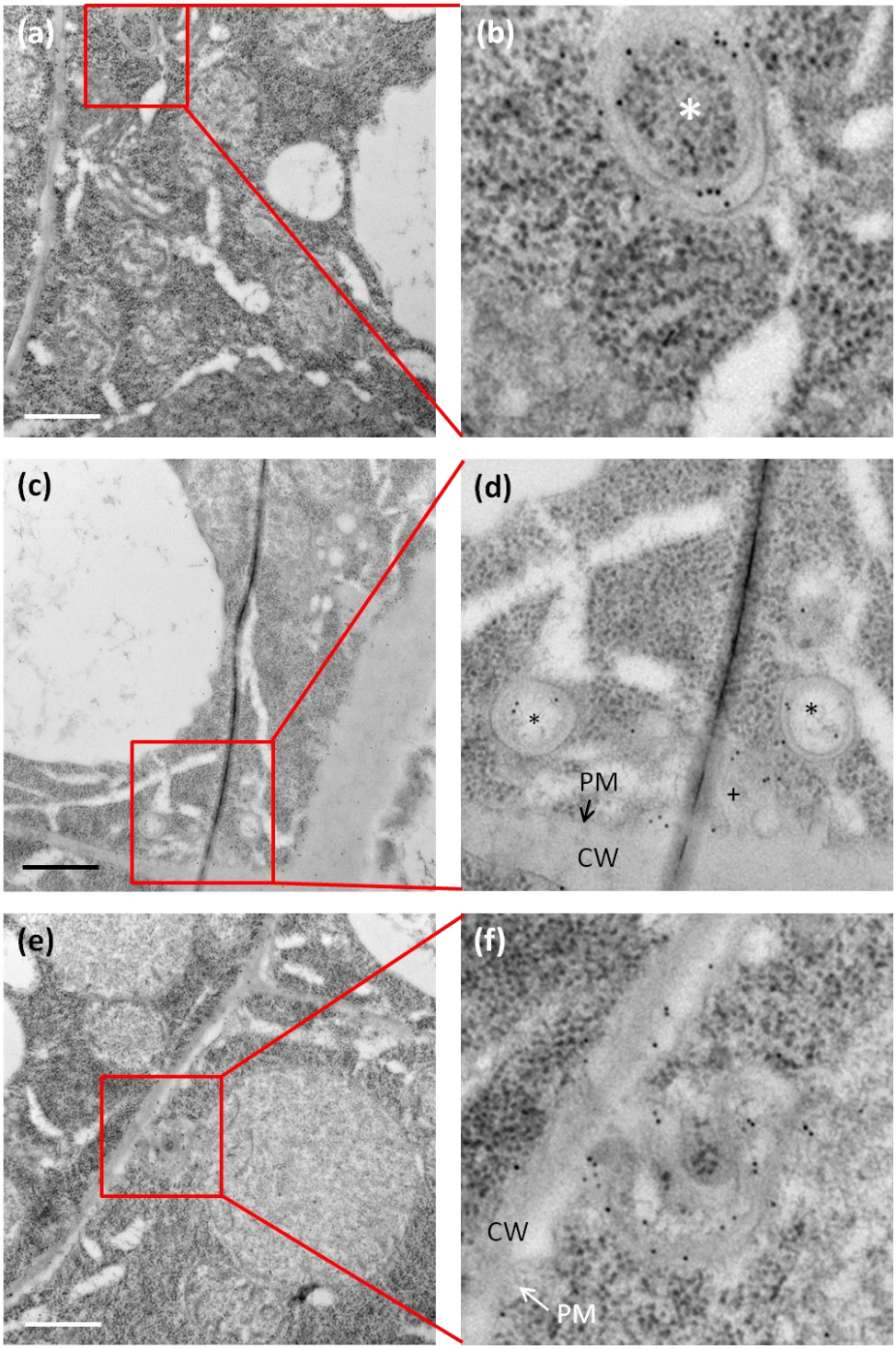

Figure 5.14: *In situ* localisation of NET4B to double-membrane structures in the Arabidopsis root tip through immunogold labelling and TEM. Several cells contained anti-NET4B labelled double-membrane structures that could represent autophagosomes. Cells were imaged at high magnification (a, c, e; x40,000) and digital zoom was used to show localisation within the respective red boxed areas (b, d, f). (a and b) double-membrane structure (white asterix) which appears to enclose cytoplasmic material. (c and d) two double-membrane structures (black astrerix) in close proximity to the plasma membrane and labelling of another double-membrane structure in association with the plasma membrane (black cross). (e) and (f) Double-membrane structure that appears to be continuous with the plasma membrane. Scale bars: 500 nm.

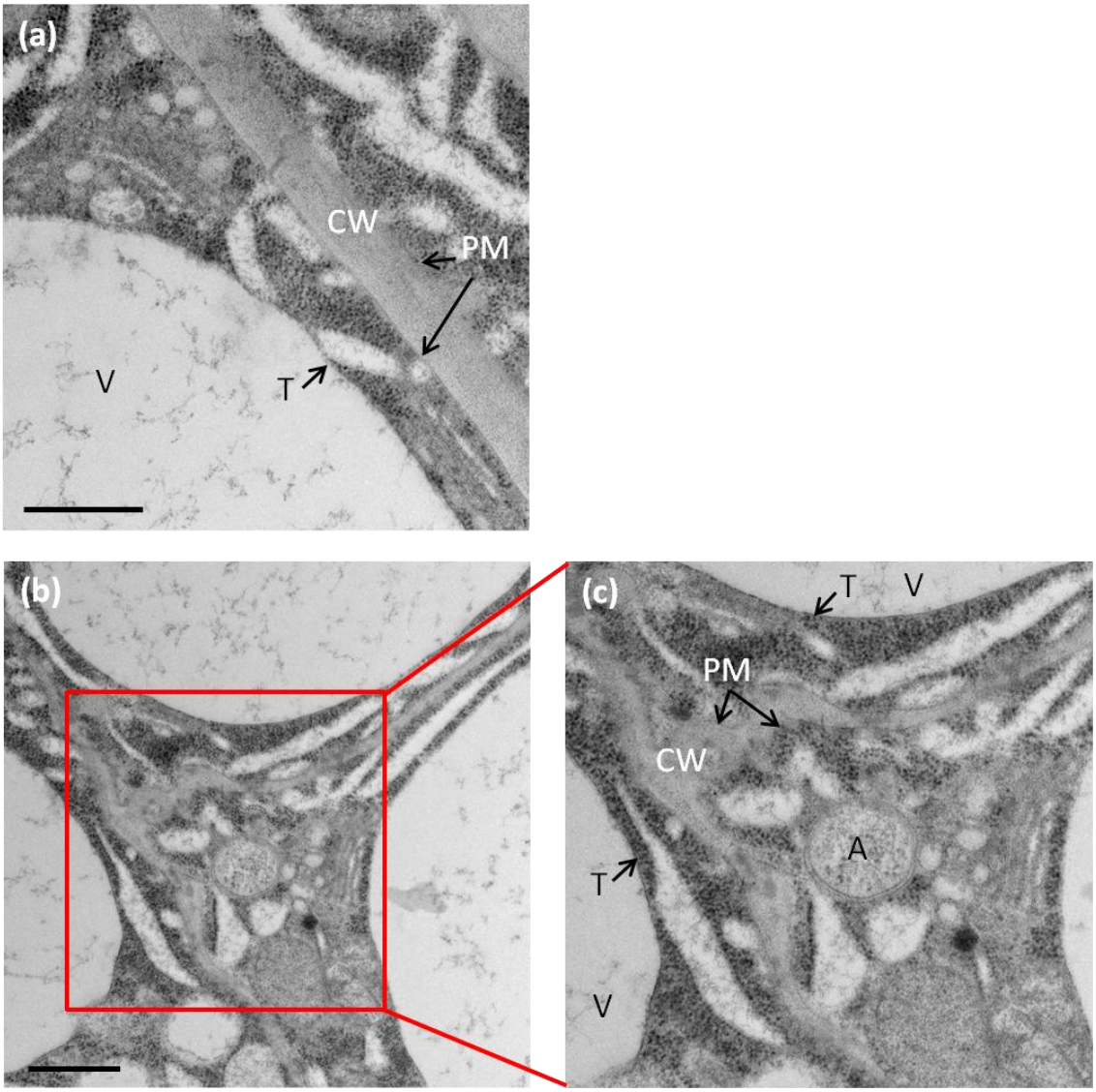

Figure 5.15: Primary antibody omission control for the anti-NET4B immunogold labelling. Primary omission control was performed concomitantly with the anti-NET4B immunogold labelling and on sections from the same Arabidopsis root tip. (a and b) Examples of cells of the Arabidopsis root tip were imaged at high magnification (x60,000 and x40,000 respectively). Digital zoom was used in (c) to show localisation of the red-boxed area in (c). No labelling was observed throughout the sample. V = vacuole, T = tonoplast, PM = plasma membrane, CW = cell wall, A = potential autophagosome. Scale bars: (a) 20 µm, (b and c) 500 nm.

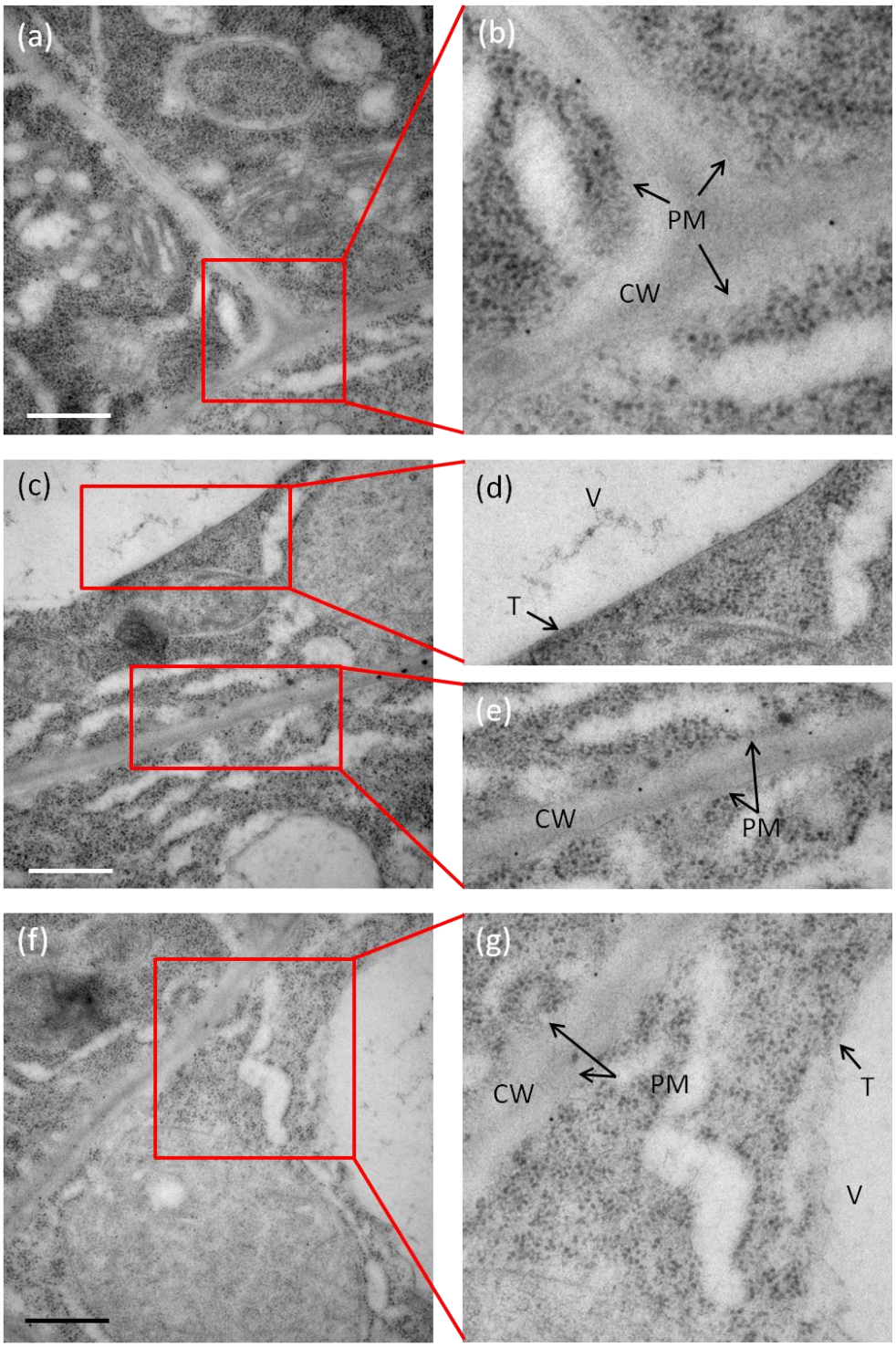

Figure 5.16: Immunogold labelling of Arabidopsis root tips using the A88 pre-bleed sera. Immunogold labelling, of the Arabidopsis root tip, performed with the A88 pre-bleed sera at the same concentration as the anti-NET4B antibody (1:100) and on sections from the same Arabidopsis root tip. (a, c, f) Examples of cells of the Arabidopsis root tip imaged at high magnification (x50,000). Digital zoom was used in (b, d, e, g) to show localisation of the respective red boxed areas. (a-e). Limited labelling with the pre-bleed sera could be seen at the plasma membrane (b, e, g) but not at the tonoplast (d and g). V = vacuole, T = tonoplast, PM = plasma membrane, CW = cell wall. Scale bars: 500 nm

estimation of the antigen concentration in a particular organelle. Although this method can be useful in providing an indication of differential localisation of an antigen to a specific organelle, it does not provide statistical evidence to suggest whether the observed gold pattern differs from a random distribution (Mayhew et al. 2002).

Furthermore, this method does not permit the direct comparison of LD between membrane structures (such as the plasma membrane and tonoplast) with volume-occupying organelles (such as the Golgi or mitochondria; Mayhew et al. 2002). For membrane structures, LD density can be calculated as gold counts per unit length (gold counts μm^{-1}) whereas LD density of volume-occupying organelles is calculated as gold counts per unit area (gold counts μm^{-2}). As these two labelling densities are described in different units, the LD for organelles and membranes cannot be directly compared using this method.

Further advances in quantitative analysis of immunogold labelling have utilised stereological based techniques to determine whether the observed gold particle distribution differs from an expected distribution due to random chance (Mayhew et al. 2002). Firstly, the number of observed gold particles (G_o) for a particular organelle are counted. Secondly, a test-point lattice is randomly superimposed over the TEM section to derive point counts for the different subcellular compartments (Figure 5.17). The number of lattice "points" that occur on a particular organelle are counted and provide an "expected" particle count (G_e; after normalisation to the total number of observed gold counts). As the number of expected point counts that occur on a particular organelle depends upon its size, it is possible to derive a relative labelling index (RLI) for each subcellular compartment. The RLI is calculated as the number of observed gold particles per expected particle. Chi-squared (χ^2) analysis can then be used to compare whether the observed gold counts are statistically different from the expected distributions. Several studies have demonstrated the utility of this method, and it has been used to investigate phagosome fusion (Rittig et al. 2003), effector secretion systems in host-bacteria interactions (Abdallah et al. 2008), glycosyltransferase (AtMUR3) localisation in the plant Golgi apparatus (Chevalier et al. 2010; Mayhew 2011), and mitochondrial ATPase subunit localisation (Šubrtová et al. 2015).

In addition to the statistical analysis of gold particle distributions, recent advancements to this method have been described that allow for the direct comparison of RLI between membranes and organelles. Mayhew & Lucocq (2008) demonstrated that surface-

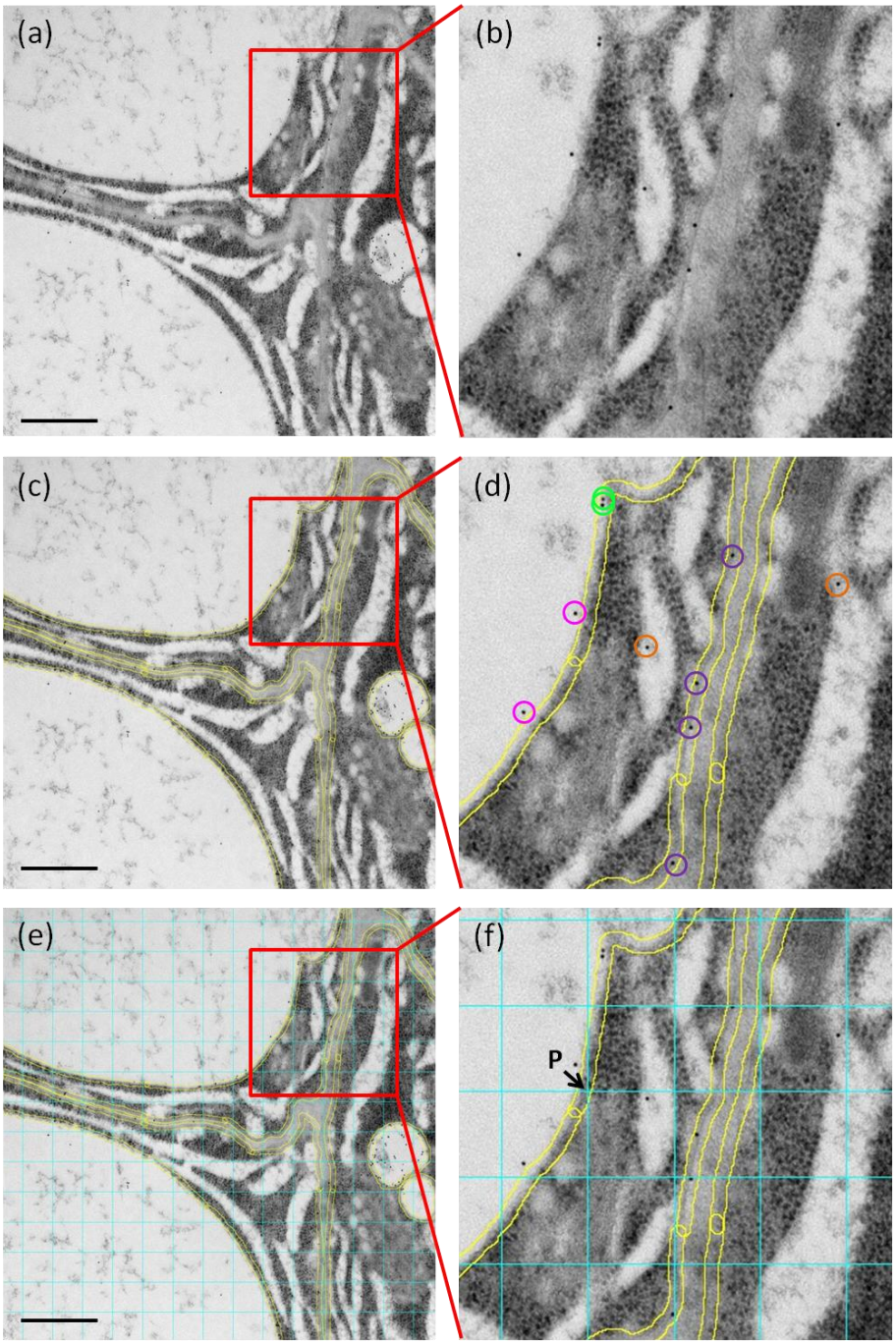

Figure 5.17: Processing of the anti-NET4B labelled samples for immunogold quantification. Figure showing the process of quantification of immunogold particles using the RLI method. (a) and (b) show the unprocessed anti-NET4B immunogold labelled TEM image. (c) and (d) The tonoplast and plasma membrane were processed from surface-occupying compartments into volume-occupying compartments, by creating an acceptance zone of 30 nm spanning the membrane trace. Gold particles were counted if they resided within or on the yellow lines. In (d) various different gold particle localisation can be seen, green = tonoplast, purple = plasma membrane, orange = endoplasmic reticulum, magenta = vacuole outside of acceptance zone. (e) and (f) show the random superimposition of a lattice of test points (*P*; cyan) on the TEM section. Test points are counted at the bottom right corner of the grid. A test point at the tonoplast is labelled in (f). Scale bar: 500nm.

occupying membrane structures could be converted into volume-occupying structures, through the application of an "acceptance zone" at a fixed distance at either side of the membrane. Using this method, it is therefore possible to compare the RLI of all compartments within the cell by using the same test-point lattice system (Figure 5.17).

As the RLI method of quantification has two clear advantages over the LD method, namely statistical evaluation of labelling and enabling the comparison of membrane/organelle compartments, it was chosen for quantification of the anti-NET4B immunogold labelled TEM sections. The sections below describe the calculation of the appropriate "acceptance zone" for these samples and the subsequent quantification of the observed anti-NET4B labelled gold particle distribution.

5.5.3 Calculation of the appropriate "acceptance zone"

The "acceptance zone", described by Mayhew & Lucocq (2008), takes into account the orientation of the primary and gold-conjugated secondary antibody in relation to the antigen site (Figure 5.18 a). Therefore, in order to calculate an appropriate acceptance zone, it is important to measure the dispersion of gold particles from the membrane trace. When deciding on the final size of the acceptance zone, it is important that it encompasses the majority of membrane labelling without being too large to reduce labelling density (Mayhew & Lucocq 2008).

Figure 5.18 (b) shows the results of the observed anti-NET4B labelled gold particle distribution from the tonoplast, measured using the FIJI ImageJ software (Schindelin et al. 2012). The median gold particle distance from the tonoplast was 14.3 nm (n = 239). From this data, it was determined that an acceptance zone of 15 nm at either side of the tonoplast and plasma membrane would be sufficient to record a large proportion of gold particles at these membranes. An example of the applied acceptance zones to the TEM sections of the Arabidopsis roots was previously shown in Figure 5.17.

5.5.4 Quantification of the anti-NET4B immunogold labelling distribution in Arabidopsis root tips

For quantification of the anti-NET4B immunogold labelling, the previously discussed relative labelling index (RLI) method of quantification was used (Mayhew et al. 2002; Mayhew & Lucocq 2008). Firstly, 82 images at high magnification (x40,000) were taken of the anti-NET4B labelled Arabidopsis root tip and individual images were then selected for quantification using a random number generator. Image analysis was

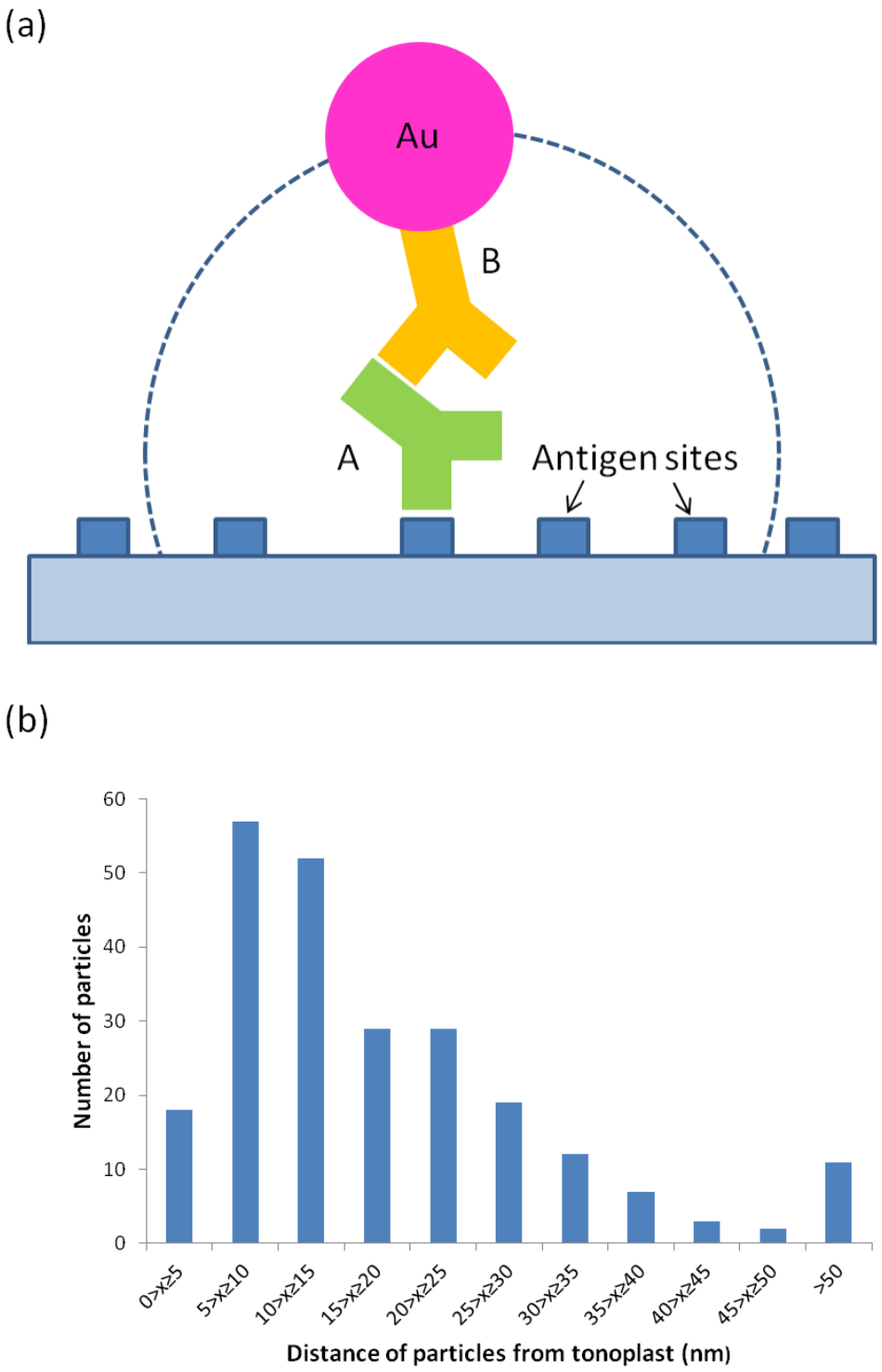

Figure 5.18: Calculation of the acceptance zone for the anti-NET4B labelling at the tonoplast. (a) Schematic diagram showing the potential positions of the gold particle relative to the antigen site. The gold particle is separated from the antigen site by two immunoglobulin molecules (A and B), and the radial distance of the gold particle is shown by the dotted blue line. Diagram modified from Amiry-Moghaddam & Ottersen (2013). (b) Histogram showing the distribution of anti-NET4B labelled gold particles from the tonoplast membrane. The median distance of gold particles from the tonoplast was 14.3 nm (n = 239).

undertaken using the FIJI ImageJ software (Schindelin et al. 2012). The vacuoles of each image were identified due to similar morphology and staining, and their respective tonoplast membrane traces were converted to sectional-profile areas by applying an acceptance zone of 15 nm at either side of the membrane. An identically sized acceptance zone was applied to all plasma membrane in the field of view. The test-point lattice grid, consisting of squares of equal size (40,000 nm^2), was randomly superimposed over the electron micrographs. Observed gold particles (G_o) and test-points (P) were counted for the tonoplast, plasma membrane, cell wall, mitochondria,endoplasmic reticulum (ER), Golgi, multivesicular bodies (MVB), cytosol and the nucleus. In total, 502 gold particles were counted from 8 images. As only a small number of MVBs were encountered in these 8 images, the resultant expected count was incompatible with the Chi-squared analysis. Therefore further gold particle and test-point counts were made for MVBs from the total set of images, which brought the total observed gold particle count to 508. As the occurrence of autophagosomes within the section was very rare, they were not included in this analysis.

The expected gold count (G_e) for each subcellular compartment was calculated as (total sum of G_o x P) / total sum of P. The RLI for each compartment was calculated as RLI = G_o / G_e. In order to statistically analyse whether the observed gold distributions differed from the expected, Chi-squared analysis was performed for each subcellular compartment: $\chi^2 = (G_o - G_e)^2 / G_e$. The partial Chi-squared values for each compartment were also expressed as a percentage of the total Chi-squared value (χ^2 as %).

Table 5.1 shows the results of this analysis. The results of the Chi-squared test showed that the observed gold particle distribution significantly differed from a random distribution ($\chi^2 = 594.47$, df = 8, $P < 0.001$). Two criteria were then used to determine whether the anti-NET4B labelling showed a preferential labelling to a particular compartment (Mayhew et al. 2002; Mayhew 2011). Random labelling of a compartment is expected to give an RLI value of 1, therefore for a compartment to be considered as preferentially labelled the corresponding RLI needs to be greater than this value. Secondly, the partial χ^2 value of a compartment should account for a substantial proportion of the total χ^2 value (χ^2 > 10% of the total).

From this analysis only the tonoplast satisfied the two criteria for being preferential labelled with the anti-NET4B antibody (RLI > 1, χ^2 value > 10% of total). The tonoplast

Compartment	Observed gold count, G_o	Point count, P	Expected gold count, G_e	RLI, G_o / G_e	χ^2 value	χ^2 as %
Tonoplast	225	87	62.87	3.58	418.13	70.34
PM	82	51	36.85	2.23	55.31	9.30
Cell wall	88	158	114.17	0.77	6.00	1.01
Mitochondria	5	52	37.58	0.13	28.24	4.75
ER	33	119	85.99	0.38	32.66	5.49
Golgi	16	59	42.63	0.38	16.64	2.80
MVB	8	21	15.17	0.53	3.39	0.57
Cytosol	35	115	83.10	0.42	27.84	4.68
Nucleus	16	41	29.63	0.54	6.27	1.05
Column total	508	703	508.00		594.47	100.00

Table 5.1: Quantification of the anti-NET4B immunogold labelling in Arabidopsis root tips. Quantification of the anti-NET4B labelling was performed according to the methods of (Mayhew et al. 2002; Mayhew & Lucocq 2008). Observed gold particle counts (G_o) and point counts (P) were recorded for each compartment. The expected gold count (G_e) for each compartment was calculated by normalising the point counts to the total observed gold counts. For $\chi^2 = 594.47$, df = 8, $P < 0.001$ (χ^2 analysis), there is sufficient evidence to suggest that the observed gold particle distribution differs significantly from a random distribution. Only the anti-NET4B labelling at the tonoplast (RLI = 3.58, χ^2 = 70.34% of total), meets the two criteria for being preferentially labelled (RLI > 1, χ^2 value > 10% of total). PM = plasma membrane, ER = endoplasmic reticulum, MVB = multivesicular body.

demonstrated the most abundant anti-NET4B labelling (RLI = 3.58, χ^2 = 70.34% of total). Labelling at this compartment is almost four times greater than what is predicted for a random distribution of gold particles. Furthermore the partial χ^2 value of the tonoplast contributed the vast majority of the total χ^2 value.

Localisation of gold particles to the plasma membrane only satisfied one of the two criteria for preferential labelling (RLI = 2.23, χ^2 = 9.30% of total). The observed gold particle distribution at the plasma membrane is greater than would be expected for a random distribution, however it's corresponding partial χ^2 value contributes significantly less to the total value in comparison with the tonoplast. Although the partial χ^2 value is still greater than the other compartments, it was not greater than the 10% threshold value. In addition, the A88 pre-bleed sera control also demonstrated limited labelling of the plasma membrane. Therefore the gold particles observed at this compartment could represent labelling due to antibodies present from the rabbit prior to inoculation with the NET4B antigen.

Observed gold labelling from the other subcellular compartments did not satisfy either of the two criteria for preferential labelling, and for all compartments the observed labelling distribution was lower than is predicted for a random distribution (RLI < 1). The results from this *in situ* immunogold analysis have therefore demonstrated that the anti-NET4B antibody preferentially localises to the tonoplast in the Arabidopsis root tip.

5.6 Conclusion

This chapter has described several different experimental approaches designed to study the *in situ* expression and subcellular localisation of NET4B in Arabidopsis.

Firstly, the transcriptional expression pattern of *NET4B* was studied by creating stably transformed Arabidopsis lines expressing the GUS reporter gene under the control of the *NET4B* promoter. Histochemical staining revealed that *NET4B* was expressed in the roots, particularly in the root tip, as well as the guard cells, papillae, filaments and stamen abscission zone. Initial observations also demonstrated that *NET4B* is expressed in the developing embryo. The expression of *NET4B* in the roots, guard cells and embryos is further supported by publicly available microarray data described in Chapter 3.5.

The translational profile of NET4B in Arabidopsis was also investigated through Western blot analysis. Polyclonal antibodies were generated in rabbits against a recombinant NET4B protein fragment. These antibodies were confirmed to be specific to NET4B and did not cross-react with NET4A. Western blot analysis of different Arabidopsis tissue using the anti-NET4B antibodies revealed that NET4B was highly expressed in the roots, seedlings, young leaves and flowers. This experiment therefore compliments the GUS transcriptional profile, and confirms that NET4B is highly expressed in the roots.

Having established the transcriptional and translational profile of NET4B in Arabidopsis, the subcellular localisation of NET4B was investigated using two methods. Firstly, a NET4B-GFP fusion protein was expressed in Arabidopsis under the control of the endogenous *NET4B* promoter. Several stably transformed lines were identified however only very weak cytosolic expression of the NET4B-GFP fusion protein could be observed.

As this method did not provide a very conclusive subcellular localisation for NET4B, immunogold labelling of the Arabidopsis root tip was performed using the anti-NET4B antibody. Gold particle distribution in the root tip was shown to be confined to the tonoplast and plasma membrane. However the plasma membrane localisation was deemed likely to be non-specific as the pre-bleed sera also showed limited labelling of this compartment. Quantification of the immunogold labelled sections confirmed that NET4B preferentially labels the tonoplast membrane. In addition to the tonoplast membrane, initial observations revealed that the anti-NET4B antibody labelled double-membrane structures that could potentially represent autophagosomes.

The results of this chapter, combined with previous data from the Hussey lab (Deeks et al. 2012), have therefore demonstrated that the NET4s are a tonoplast associated subfamily of the NET proteins. The next chapter describes experiments performed to investigate the interacting partners of NET4B, as this could suggest the potential processes that it might be involved with at the tonoplast.

Chapter 6 - Investigating the interacting partners of NET4B and the IRQ + Ct domain

6.1 Introduction

The previous chapters have demonstrated that NET4B is able to bind actin *in vivo* and *in vitro* via the NAB domain. Studying the expression pattern and subcellular localisation of NET4B showed that it is highly expressed in roots and guard cells, and can associate with the tonoplast in the root. Similarly, NET4A associates with actin surrounding the vacuole in the root (Deeks et al. 2012). Taken together, this suggests that the NET4s could represent important actin-vacuole linkers in plants.

As well as sharing the conserved NAB domain, the NET4s also share another highly conserved domain termed the IRQ domain. This domain is a short C-terminal domain that is also found in NET3A and NET3C. Results from Chapter 4 demonstrated that the last 54 amino acids of NET4B, which contained the IRQ domain plus a short C-terminal extension (IRQ + Ct), localised to moving punctae when fused to GFP and transiently expressed in *Nicotiana benthamiana* leaf epidermal cells. However, the identity of these punctae remains unknown.

This chapter describes various experiments used to identify potential interacting partners of NET4B and the IRQ domain. Studying the interacting partners of the full-length NET4B and the IRQ domain, will increase our knowledge of the function of this protein and the IRQ domain in particular, and will help us to understand the role of NET4B in the plant. Three different approaches are described in this chapter, that were used to investigate the NET4B interacting partners.

Firstly, the oligomerisation of NET4B was investigated through "semi-native" SDS-PAGE gels and yeast-2-hybrid (Y2H) studies. Full-length NET4B and the IRQ + Ct domain were also used as bait in a Y2H screen to identify potential interacting partners. Finally, a possible link between the NET4s and two vacuolar Rab GTPases was discovered and the nature of this interaction was investigated further using the Y2H system. The experiments described in this chapter were performed in collaboration with Dr. Tim Hawkins (Durham University). Experiments in this chapter have predominantly used the Y2H system, therefore a short introduction to this method will be given prior to describing the experimental results.

6.1.1 Introduction to the Y2H system

The Y2H system is a powerful tool to study potential protein-protein interactions. This system is based on the reconstruction of a functional transcription factor that activates downstream reporter genes when an interaction occurs (Fields & Song 1989). The presence of this interaction can be monitored as the downstream reporter genes are required for growth on selective media. This method uses a split GAL4 transcription factor from *Saccharomyces cerevisiae*, where the "DNA binding domain" (BD) of GAL4 is fused to a protein of interest (bait) and the "GAL4 activation domain" (AD) is fused to another protein of interest or a protein encoded by a cDNA library fragment (prey). Figure 6.1 shows how this system works; when two proteins interact they are able to form a functional GAL4 transcription factor that activates the transcription of downstream reporter genes through the recruitment of RNA polymerase.

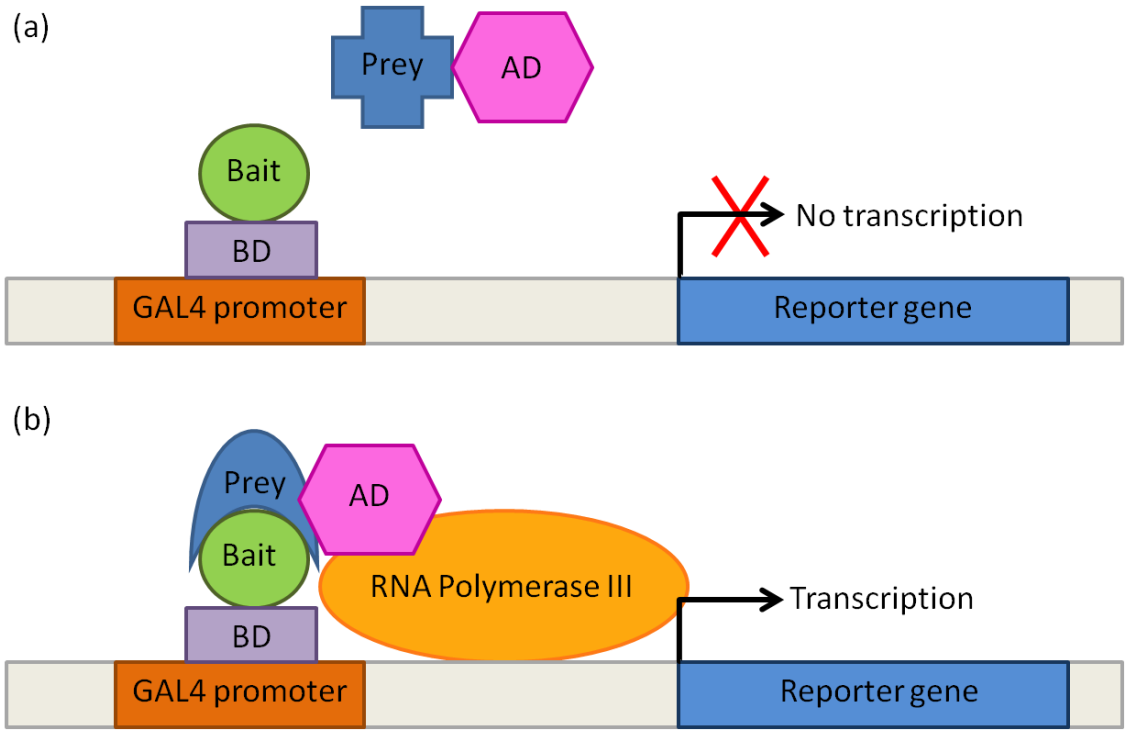

Figure 6.1: Diagram of the Y2H system. Bait plasmids are fused to the DNA-binding domain (BD) and prey plasmids are fused to the activation domain (AD). (a) If the bait and prey do not interact then a functional transcriptional factor is not formed and transcription does not occur. (b) If the bait and prey construct interact, then a functional GAL4 transcription factor is formed that can bind to GAL4 promoter regions and activate the transcription of downstream reporter genes such as *HIS3*, *ADE3* and *LacZ*, through the recruitment of RNA polymerase III. Diagram modified from Brückner et al. (2009).

The Clontech Matchmaker Y2H system, which uses the GAL4 transcription factor, was used for all the experiments described in this chapter. This system uses two different vectors, pGBKT7 and pGADT7, which respectively create DNA-binding domain and activation-domain fusions. Both vectors contain selectable marker genes that enable the selection of successfully transformed yeast cells. pGBKT7 contains a gene for the production of tryptophan and pGADT7 contains a gene to produce leucine. After transforming yeast with these vectors, the yeast are plated onto media lacking either of these amino acids and only transformed cells can survive.

For the mating tests, these vectors are transformed into two different strains of *S. cerevisiae*; AH109 and Y187. These yeast strains contain three reporter genes under the control of the GAL4 upstream activating sequence; *HIS3* which encodes a gene to produce histidine, *ADE2* which encodes a gene to produce adenine, and *LacZ* which encodes a gene to produce ß-galactosidase.

To test for protein-protein interactions the bait and prey constructs are transformed into the two different yeast strains. The two yeast strains are mated and diploids are subsequently grown on selective media to test for an interaction. This selective media will lack tryptophan (to select for the bait) and leucine (to select for the prey), and also lack either histidine or adenine (to select for the reporter genes).

If the bait and prey proteins interact then this forms a functional GAL4 transcription factor that can activate the *HIS3* and *ADE3* genes, and therefore the yeast can survive on media lacking these amino acids. The *HIS3* and *ADE3* reporter genes can be used individually or together to alter the stringency of the screen. It is also possible to select colonies on the basis of ß-galactosidase expression, which is turned on by the *LacZ* reporter. The expression of this enzyme, through successful protein-protein interactions, turns the diploid colony blue when grown on media containing X-α-Gal.

6.2 NET4B dimerisation analysis

The NET family proteins are characterised by the presence of the NAB domain at the N-terminus of the protein, and are predicted to form long coiled-coil domains in the C-terminus of the protein (Deeks et al. 2012). Coiled-coil domains can mediate protein-protein interactions and lead to the oligomerisation of proteins to form higher-order structures (Rose & Meier 2004). This intrinsic ability can be important for the function

of many coiled-coil proteins that serve as structural or organisational proteins (Rose & Meier 2004).

The ability of NET4B to form dimers or oligomers, with itself and also NET4A was investigated using two experimental techniques. Firstly, total protein extracted from Arabidopsis seedlings was separated using "semi-native" SDS-PAGE gel electrophoresis, followed by Western blot analysis with the anti-NET4B antibody. Secondly, the oligomerisation of NET4B and NET4A was tested specifically using the Y2H system.

6.2.1 Western blot analysis of NET4B oligomer formation through "semi-native" SDS-PAGE gels and Western blot analysis

Polyacrylamide gel electrophoresis (PAGE) is used to separate proteins on a gel based on their size, and is usually performed in the presence of a detergent (e.g. sodium dodecyl sulfate; SDS) and proteins are denatured prior to loading, through boiling and reducing conditions of the loading buffer (Zewert & Harrington 1993). The presence of SDS shields the respective charge of the protein, and provides each protein with a negative charge, allowing proteins to be separated according to their molecular weight. SDS-PAGE gels provide great resolution and separation of individual proteins, however protein complexes cannot be distinguished due to the denaturing conditions used prior to loading.

Several studies have used "semi-native" SDS-PAGE gels to examine the oligomerisation status of proteins (Voulhoux et al. 2003; Bos et al. 2007; Snyers et al. 2007; Gucciardo et al. 2007). These semi-native conditions have been defined in various ways; omission of sample boiling prior to loading, omission of SDS from the polyacrylamide gel and loading buffer, and omission of reducing agents from the loading buffer. Semi-native SDS-PAGE gels allow the observation of higher-order complexes with the advantages of standard SDS-PAGE gels, but without the problems associated with optimisation of truly native PAGE gels (Zewert & Harrington 1993).

Semi-native SDS-PAGE was used to test whether NET4B could form part of a higher-order complex in Arabidopsis. Total protein was extracted from 15-day old Arabidopsis seedlings grown vertically on ½MS plates (as described in 2.4.7). The extracted protein was then aliquoted into two microcentrifuge tubes; one was heated at 95 °C and the other was heated at 65 °C for five minutes to retain the integrity of protein complexes.

Both samples were separated on a 7.5% SDS-PAGE gel which was then transferred to a nitrocellulose membrane for Western blot analysis using the anti-NET4B antibody.

Figure 6.2 shows a representative Western blot of total Arabidopsis protein probed with anti-NET4B under denaturing (95 °C) and semi-native conditions (65 °C). Denaturing the protein complexes in Arabidopsis protein extracts through heat treatment led to the previously observed single band at approximately 60 kDa, which represents monomeric NET4B. Under semi-native conditions, the band at 60 kDa was still detected as well as three additional higher molecular weight bands. A faint band was seen at around 100-120 kDa and two intense bands could be seen between 150-250 kDa. The sizes of these additional bands indicate that NET4B could oligomerise, as they roughly correspond to the predicted sizes of NET4B dimers, trimers and tetramers (120-, 180- and 240- kDa respectively). However as this Western blot is performed on total protein extract, it is also possible that the higher molecular weight bands represent complexes of other proteins interacting with NET4B. The experiments described below describe how the Y2H system was used in order to further examine the possibility of NET4 oligomerisation.

6.2.2 Testing homo- and hetero-oligomerisation of the NET4s using the Y2H system

The results of the semi-native SDS-PAGE gel and Western blot analysis with the anti-NET4B antibody showed that NET4B forms higher-order complexes. However this experiment did not conclusively show whether these complexes are formed by oligomerisation of NET4B either as homo-oligomers or as hetero-oligomers with NET4A. The Y2H system was therefore used to examine the oligomerisation of the NET4s *in vivo*.

Full-length NET4B and NET4A were cloned into the pGBKT7 and pGADT7 vectors to create the binding domain and activation domain fusion proteins. Prior to testing interactions between the NET4s, an autoactivation test was performed to assess whether these constructs were able to activate the downstream *HIS3* reporter gene. The *HIS3* reporter gene is known to have a "leaky" expression and basal levels of the gene can give rise to false positives (Van Criekinge & Beyaert 1999). 3-amino-triazole (3AT) can be used to inhibit the intrinsic activity of the *HIS3* gene product and therefore minimise false positives (Van Criekinge & Beyaert 1999).

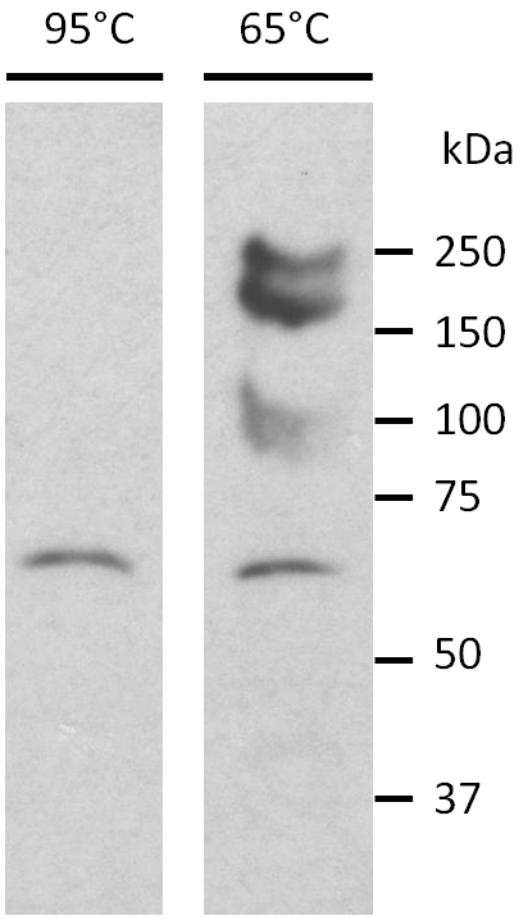

Figure 6.2: NET4B forms higher-order complexes *in planta*. Protein was extracted from 15-day old Arabidopsis seedlings and either heated at 95 °C or 65 °C for 5 minutes. Protein was subsequently separated on a 7.5% SDS-PAGE gel and analysed through Western blotting using the anti-NET4B antibody (1:500). Under semi-native conditions (65 °C) the integrity of higher-order complexes formed with NET4B are retained. PageRuler Prestained Plus was used as a molecular weight marker.

The four clones (both NET4s in both vectors) were transformed into the AH109 yeast strain (which contains the *HIS3* reporter gene) and were selected on media lacking tryptophan (-W) or leucine (-L). Transformed cells were resuspended in water and dropped onto selective media lacking histidine with the addition of 2.5 mM 3AT (-WH/-LH +2.5 mM 3AT). Previous results by Dr. Pengwei Wang, using the NET3 proteins in the yeast vectors, showed that this level of 3AT was sufficient to inhibit autoactivation of these proteins. As a positive control for colony growth, the cells were dropped onto either -W or -L. Figure 6.3 shows the results of the autoactivation test.

The positive control showed that growth could occur on media containing histidine (-W/-L) but no growth was observed on the selection plates lacking histidine (-WH/-LH + 2.5 mM 3AT). This concentration of 3AT was therefore sufficient to suppress autoactivity of the *HIS3* reporter gene and was used throughout the Y2H experiments.

The ability of NET4B to form homo-oligomers was first tested by cloning the full-length NET4B into both the pGBKT7 and pGADT7 vectors, to produce BD-NET4B and AD-NET4B fusion proteins. The BD-NET4B was then transformed into AH109, and the AD-NET4B was transformed into Y187, which were selected on either media lacking tryptophan (-W) or media lacking leucine (-L). The two strains were then mated (as described in 2.3.6), and diploids were selected on media lacking tryptophan and leucine (-WL). As a negative control for autoactivation, the BD-NET4B and AD-NET4B constructs were mated with the complimentary empty vector. After diploid colonies of each pair were successfully selected, they were resuspended in water and dropped onto three selective media plates lacking tryptophan and leucine, and either lacked histidine (-WLH) or adenine (-WLA) or both (-WLHA). 2.5 mM 3AT was used for all media lacking histidine to suppress autoactivation. As a positive control for colony growth, the cells were dropped onto media lacking leucine and tryptophan (-WL) to select for the diploids.

Figure 6.4 shows the results from this experiment, one colony was selected from each mate that represented the general growth pattern seen across the different experiments. Growth was observed on all the positive controls for diploid selection, and no growth was observed on the negative empty vector controls. Growth could occur on selective media lacking histidine when NET4B was mated with itself, however this growth was not observed on the -WLA or -WLHA plates. This suggests that NET4B can form homo-oligomers through the Y2H system, however this interaction might be relatively weak as growth was only observed using one reporter gene.

As NET4B and NET4A share a higher degree of similarity (41% amino acid identities and 59% similarities; see Chapter 3.4) and they both associate with the tonoplast in the root, they could potentially form hetero-oligomers and this interaction was tested using the Y2H system. The NET4B and NET4A pGBKT7 constructs were transformed into AH109 cells, and the NET4B and NET4A pGADT7 constructs were transformed into Y187 cells. Several mates were performed; BD-NET4B and AD-NET4B were mated to confirm NET4B homodimerisation; BD-NET4A and AD-NET4A were mated to test

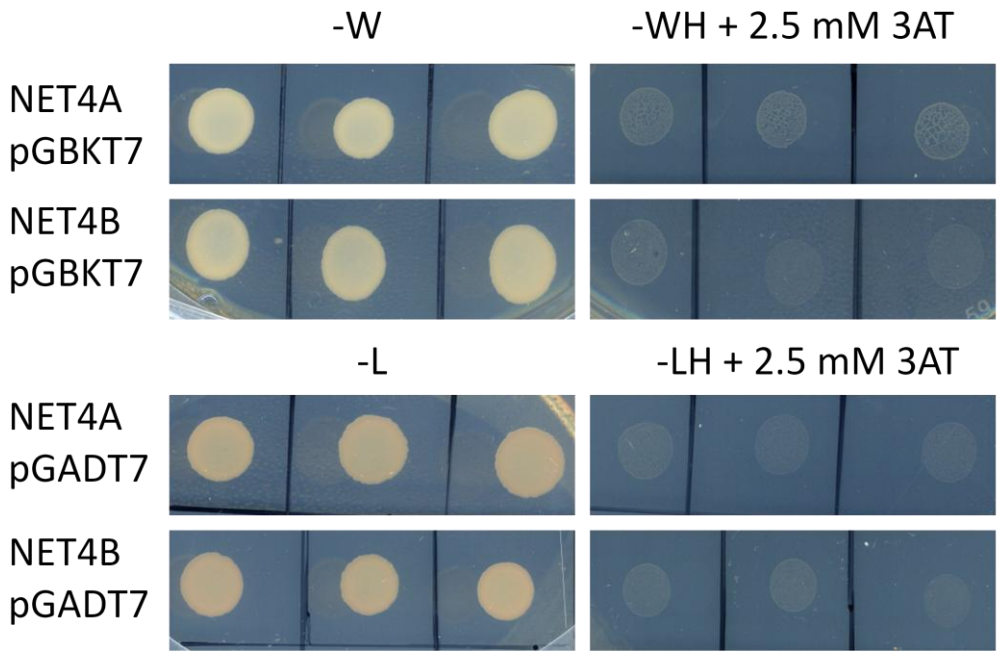

Figure 6.3: Autoactivation test of NET4A and NET4B in pGBKT7 and pGADT7. NET4A and NET4B in the pGBKT7 and pGADT7 vectors were transformed into AH109 cells for the autoactivation tests. Three transformed colonies of each construct were resuspended in water and dropped onto -W or -L plates, and media lacking histidine with the addition of 2.5 mM 3AT (-WH/-LH + 2.5 mM 3AT). Growth occurred on -W or -L but not on media lacking histidine showing that these constructs do not autoactivate under these conditions.

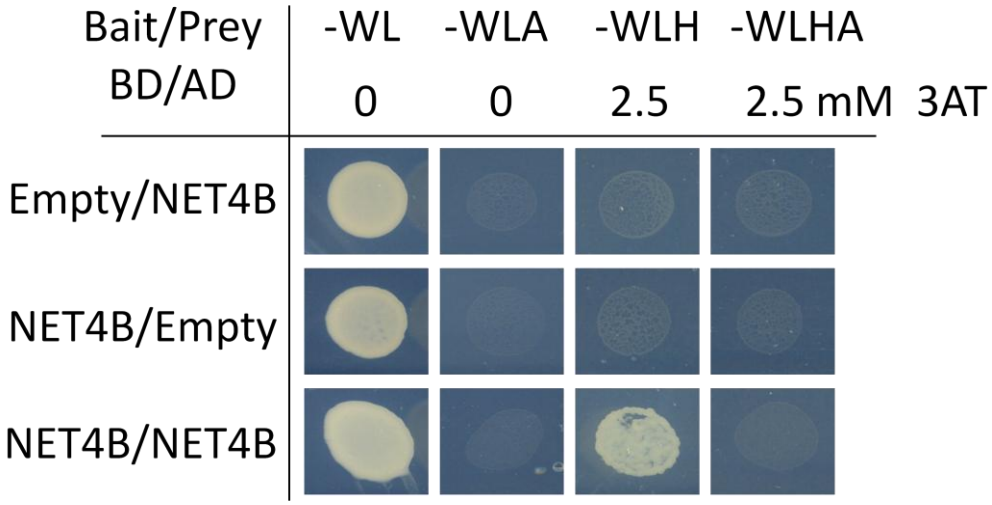

Figure 6.4: Homo-oligomerisation of NET4B using the Y2H system. Yeast cells transformed with NET4B in pGBKT7 (BD) and pGADT7 (AD) were mated together or with the reciprocal empty vector as a negative control. Mated diploid colonies were resuspended and dropped onto the selective media plates and the -WL to control for diploid growth. Growth could occur in the NET4B/NET4B mate when grown on media lacking tryptophan, leucine and histidine (-WLH + 2.5 mM 3AT). Shown here is the growth of one representative diploid colony after seven days growth.

NET4A homodimerisation. To test for heterodimerisation, BD-NET4B was mated with AD-NET4A and the reciprocal mate was also performed. For a negative control against autoactivation, each construct was mated with the respective empty vector. After diploids were selected, colonies were resuspended in water and dropped on -WL and -WLH + 2.5 mM 3AT plates. In this experiment -WLA and -WLHA were excluded as the *ADE3* reporter gene was not activated in the NET4B homodimerisation test.

Figure 6.5 shows the results of the NET4 hetero-oligomerisation test, showing the growth of one representative colony after five days growth. Autoactivation did not occur as growth was not observed on the negative control plates. Similar to NET4B, NET4A was able to grow on selective media lacking histidine (+ 2.5 mM 3AT) when mated with itself, suggesting that it can form homo-oligomers. The yeast mates containing NET4B and NET4A were also able to grow on selective media suggesting that they could form hetero-oligomers. Growth from the AD-NET4B/BD-NET4A mate was very clear on selective media, however only a few small colonies could be seen on the BD-NET4B/AD-NET4A mate. The difference between these two mating directions could be due to the functionality of the fusion protein pairs in yeast.

6.3 Investigating the interacting partners of full-length NET4B and the IRQ + Ct domain using the Y2H system

The previous section demonstrated the potential of the NET4 proteins to interact with themselves and each other to form higher-order complexes. Following on from this experiment, the Y2H system was used to screen a cDNA library to identify additional interacting partners of NET4B. Two different baits were used for the screen; the full-length NET4B and the highly conserved C-terminal IRQ + Ct domain. Relatively little is currently known about the IRQ + Ct domain and this screen could potentially shed light on its function.

To perform a cDNA library screen, the full-length NET4B and the IRQ + Ct domain (the last 54 amino acids of NET4B) were cloned into the pGBKT7 bait vectors, as the cDNA library is cloned into pGADT7. Prior to screening, an autoactivation test of these constructs was performed to ensure colony growth was only seen for true protein-protein interactions. Both constructs were cloned into the AH109 cells and colonies were resuspended in water and dropped onto media lacking tryptophan (to select for the bait vector) and either histidine or adenine to assess reporter genes autoactivity. Three colonies of each construct were resuspended and dropped onto the following plates;

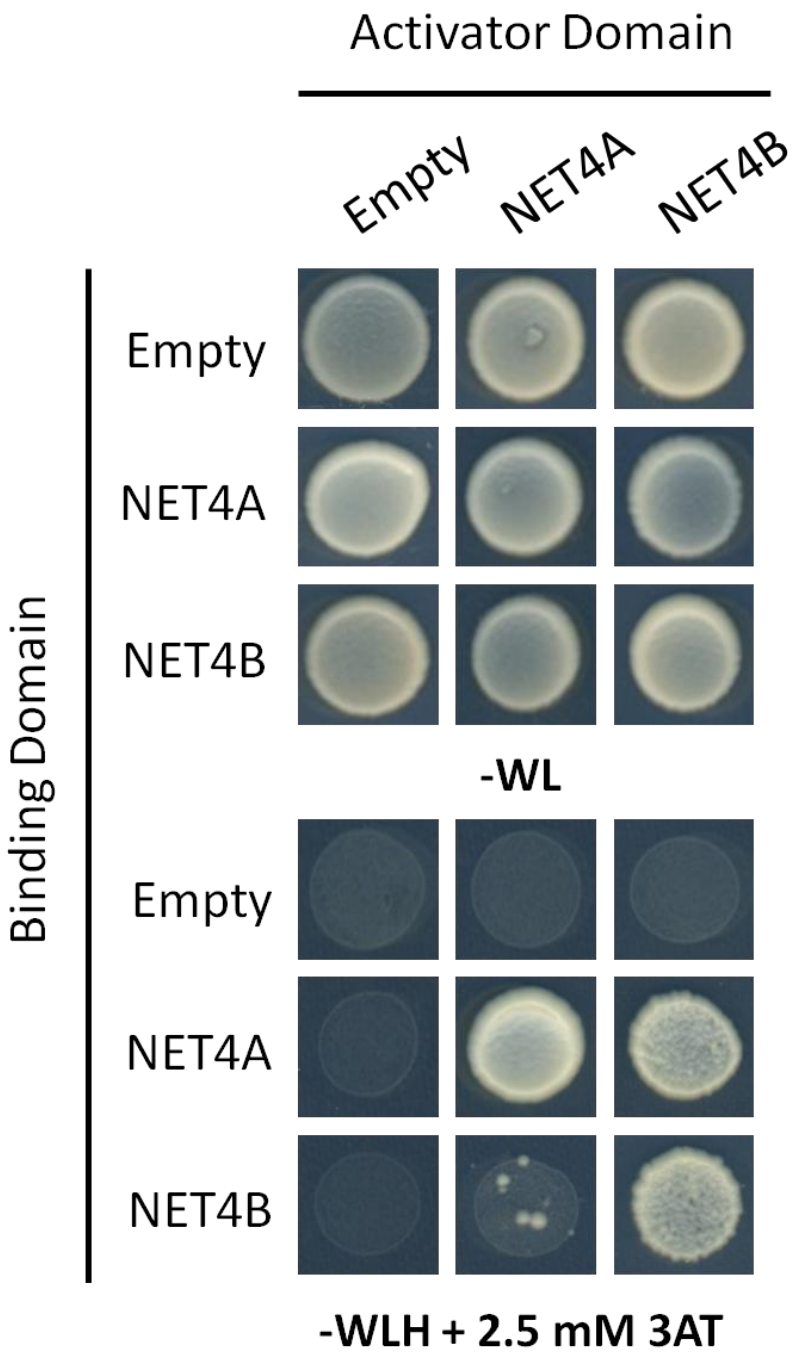

Figure 6.5 Hetero-oligomerisation of the NET4 proteins using the Y2H system. NET4B and NET4A in the pGBKT7 (binding domain) and pGADT7 (activation domain) vectors were mated together, and with the reciprocal empty vectors as a negative control. Diploids were dropped onto -WL plates (as a positive control for growth), and media lacking tryptophan, leucine and histidine (-WLH + 2.5 mM 3AT, to test for an interaction). NET4A and NET4B could both form homo-dimers. Additionally, NET4B and NET4A could also form hetero-dimers, however fewer colonies grew in the BD-NET4B/AD-NET4B direction. Shown in this figure is the representative growth of one colony after five days growth.

-WH (media lacking tryptophan and histidine) -WH plus 3AT at 2.5, 5 and 10 mM, -WA (media lacking tryptophan and adenine), -WHA (media lacking tryptophan, histidine and adenine) and finally -W + X-α-Gal (media lacking tryptophan, with the addition of 100 μM 5-Bromo-4-chloro-3-indolyl-α-Dgalactopyranoside).

Figure 6.6 shows the results of these tests after seven days growth. The -WH plate shows clear colony growth for both constructs, showing that autoactivation occurs without the addition of 3AT. Growth on the -WH plus 3AT plates was significantly reduced suggesting that the 3AT can suppress the autoactivation of the *HIS3* reporter gene. The addition of 10 mM 3AT was chosen to suppress the autoactivity of the *HIS3* reporter in the screen, although later tests revealed that 2.5 mM 3AT was sufficient for both constructs. Growth was not observed on the -WA or -WHA plates, showing that screening on these reporter genes would not lead to false-positives due to autoactivation of the *ADE3* reporter. Finally, when the colonies were dropped onto the -W + X-α-Gal plates, a blue colour was seen almost immediately with the NET4B construct. The IRQ + Ct domain produced a less intense blue, however autoactivation still occurred on the *LacZ* reporter gene and so it was omitted from further experiments.

As the -WHA plate showed minimal autoactivation, this combination of reporter genes was used for screening the Y2H library in combination with the addition of 10 mM 3AT to suppress the autoactivation of the *HIS3* reporter. Using the two reporter genes would increase the stringency of the screen and potentially pull back strong interactors with reduced false positives. The final Y2H screening plates also lacked leucine to select for the prey construct, which therefore only allowed the growth of mated diploid cells.

The full-length NET4B and IRQ + Ct domain were then used to screen a combination of an oligodT and a random primer cDNA library from Arabidopsis seedlings. This library was selected as both *NET4B* and *NET4A* are expressed in this tissue and would therefore provide more relevant interactors. Two independent screens were performed for both full-length NET4B and the IRQ + Ct domain according to the methods described in section 2.3.3. The mating efficiency and approximate number of diploids screened from these mates are listed in Table 6.1 (section 2.3.4 describes how these were calculated). The second screen used a slightly different protocol, with the cells being washed in sterile distilled water after mating as well as being resuspended in a smaller volume of water prior to selection. These changes could account for the increased mating efficiencies achieved with the second screen.

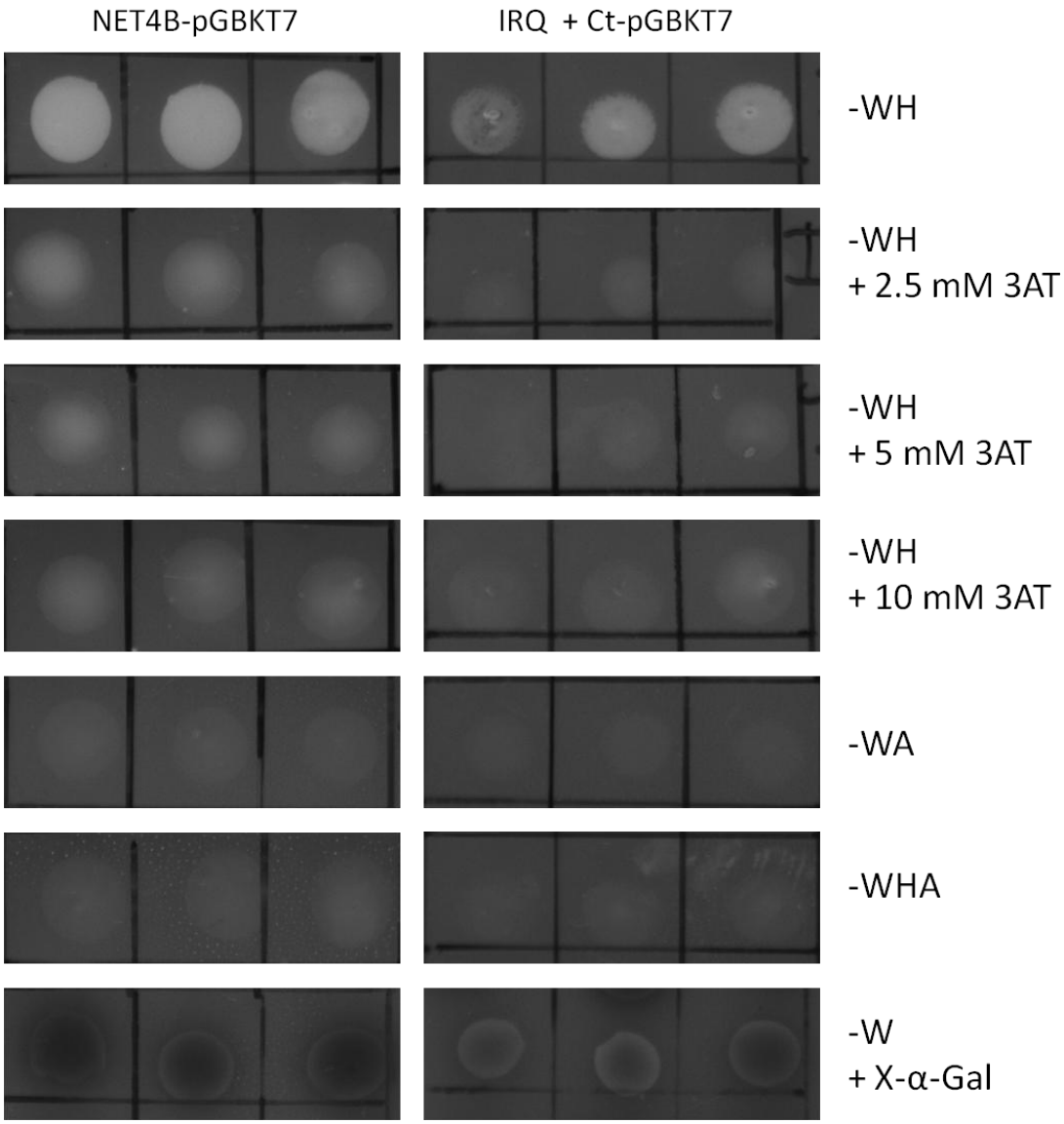

Figure 6.6: Autoactivation tests of NET4B and the IRQ + Ct domain in pGBKT7. The NET4B and IRQ + Ct domain were cloned into the bait pGBKT7 vector and transformed into AH109 yeast cells. Autoactivation of these constructs was tested on media lacking tryptophan (to select for pGBKT7), and either histidine (H) or adenine (A). 3AT was used at various concentrations to suppress the *HIS3* gene product. X-α-Gal was used to assess autoactivation of the *LacZ* reporter through blue/white selection. Three colonies of each construct were grown on the selection plates for seven days. Both constructs grew on media lacking histidine without 3AT (-WH), thus demonstrating autoactivation. The addition of 3AT suppressed this autoactivation. Growth was not observed on media lacking adenine (-WA/-WHA). However autoactivation did occur on X-α-Gal as both NET4B and IRQ + Ct colonies turned blue. The final selection plate chosen for the Y2H screen used the highest stringency conditions; media lacking tryptophan, leucine, histidine and adenine plus 10 mM 3AT (-WLHA + 10 mM 3AT).

Bait	Approximate mating efficiency (% of diploids)	Approximate number of diploid clones screened
NET4B (Screen 1)	6.02	5.25E+07
NET4B (Screen 2)	16.96	1.95E+08
IRQ + Ct (Screen 1)	8.00	1.68E+08
IRQ + Ct (Screen 2)	33.33	3.30E+08

Table 6.1: Table showing the mating efficiencies and number of diploids screened in the different Y2H cDNA library screens.

Once the yeast were mated, they were selected on the -WLHA + 10 mM 3AT dropout plates. After 4 days growth colonies started to appear, which were then restreaked onto fresh -WLHA + 10 mM 3AT plates. If these colonies could resume growth then they were presumed to be potential interactors and the corresponding cDNA clone was rescued (see 2.3.5) and the plasmids were sequenced using pGADT7 sequencing primers (according to 2.2.11; see Appendix 1.9 for primer sequence).

6.3.1 Results of the Y2H screen using NET4B and the IRQ + Ct domain as bait

Across both screens, a total of 33 clones were selected using NET4B as bait, and 6 clones were selected using the IRQ + Ct domain and a full list of these fragments are listed in Appendix 3.1. The open reading frame of these clones were checked to be in frame with the activation domain.

As these screens pulled back a lot of potential interactors for NET4B, it was decided to select only a few likely candidates for further tests. Many clones that were pulled back were either ribosomal subunits, heat shock proteins and proteosome subunits which can frequently represent false positives in Y2H screens (Serebriiskii et al. 2000). Therefore these clones were discounted from further tests.

The criteria for selecting potential interactors was based on; the number of colonies found; association of the clone with a membrane compartment; and whether it had a role in guard cells or biotic stress responses as Affymetrix data showed an up-regulation of *NET4B* in these conditions (see Chapter 3.5.2). Table 6.2 lists the potential interactors that were taken forward. Some of these clones were pulled back more than once, however they only represented identical cDNA fragments.

Locus	Description	Number of colonies	Screen
NET4B			
AT3G02230	RGP1, REVERSIBLY GLYCOSYLATED POLYPEPTIDE 1,	3	1 and 2
AT5G15650	RGP2, REVERSIBLY GLYCOSYLATED POLYPEPTIDE 2,	3	1 and 2
AT3G07195	RIN4L, RPM1-INTERACTING PROTEIN 4 (RIN4)-LIKE PROTEIN,	2	1 and 2
AT2G43130	RABA5c, ARABIDOPSIS RAB GTPASE HOMOLOG A5C,	1	2
AT1G70300	KUP6, K+ UPTAKE PERMEASE 6	1	2
IRQ + Ct			
AT1G21690	RFC4, REPLICATION FACTOR C 4	5	1 and 2
AT5G53850	DEP1, DEHYDRATASE-ENOLASE-PHOSPHATASE-COMPLEX 1	4	1 and 2

Table 6.2: Table showing the prey plasmids that were selected for one-on-one mating.

At3g02230 and At5g15650 encode REVERSIBLY GLYCOSYLATED PROTEINS (RGP) 1 and 2 respectively. RGPs are a highly conserved protein family and in Arabidopsis there are five proteins that share between 50 and 95% amino acid sequence similarity (Rautengarten et al. 2011). Early work on RGP1 established that it could be reversibly glycosylated and that it is a soluble protein that can peripherally attach to membranes (Delgado et al. 1998). Recent studies on RGP1 and RGP2 have shown that they are both expressed throughout the plant and show high expression in the root apical meristem (Rautengarten et al. 2011). This study also demonstrated that both proteins localise to Golgi vesicles as well as to the cytosol. Furthermore they were shown to encode UDP-L-mutases that interconvert UDP-Ara*f* and UDP-Ara*p* sugars, and this activity was shown to be essential for plant cell wall establishment and plant development. Previous studies into the function of these proteins have shown that a *rgp1/rgp2* double mutant is lethal and that mutant pollen have enlarged vacuoles and have defects in cell division during pollen mitosis (Drakakaki et al. 2006). The association of these proteins with the Golgi and their potential role in vacuole integrity made them a promising interactor of NET4B.

At3g07195 encodes an RPM1-INTERACTING 4-LIKE (RIN4L) protein and is a parolog of RIN4. RIN4 is an important regulator of pattern triggered immunity (PTI) and effector triggered immunity (ETI), and is targeted by many pathogenic effectors (Dodds & Rathjen 2010). RIN4 is expressed in guard cells and can regulate the activity of a plasma membrane H^+-ATPase, which affects guard cell opening and closure in response to pathogens (Liu et al. 2009). Affymetrix data for *NET4B* showed that it is expressed in guard cells and is highly up-regulated in response to pathogens (see Chapter 3). Therefore RIN4L could represent an interesting interacting protein that could suggest a possible functional link for NET4B in plant defence.

At2g43130 encodes a Rab GTPase, RabA5c or ARA4, that has been shown to localise to Golgi cisternae, trans-Golgi network and Golgi derived vesicles (Ueda et al. 1996). Rab GTPases are important in recruiting effector proteins that drive the different steps of membrane trafficking (Zerial & McBride 2001). As the NET proteins associate different membrane systems with the cytoskeleton, it is possible that they are involved in membrane trafficking events and are recruited by Rab GTPases.

At1g70300 encodes K^+ UPTAKE TRANSPORTER 6 (KUP6) which is a potassium transporter protein. A recent study that generated a triple mutant in several KUP genes (*KUP6*, *KUP8* and guard cell rectifying K+ channel (*GORK*)) showed that these genes are important for plant cell growth and the response to drought stress through controlling potassium homeostasis (Osakabe et al. 2013). This study also demonstrated that KUP6 is localised to the plasma membrane. The expression of *NET4B* in the root and guard cells could suggest a possible role for this gene in the drought response, which could be mediated through interactions with potassium transporters such as KUP6.

REPLICATION FACTOR C 4 (RFC4) is a subunit of the conserved replication factor C complex, and was pulled back as an interactor of the IRQ + Ct domain. This complex is conserved across eukaryotes and is important in loading the proliferating cell nuclear antigen (PCNA) onto DNA which then increases the processivity of DNA polymerase δ during DNA replication (Shultz et al. 2007). The second interactor for the IRQ + Ct domain was a cDNA clone of At5g53850 which encodes a trifunctional enzyme, DEHYDRATASE-ENOLASE-PHOSPHATASE COMPLEX 1 (DEP1). A recent study on this gene has shown that it is highly expressed in the vasculature and is involved in the Yang cycle that recycles 5-methylthioadenosine to methionine (Pommerrenig et al.

2011). It is possible that RFC4 and DEP1 are multifunctional proteins that could have uncharacterised roles associated with the cytoskeleton.

6.3.2 Confirming potential interactors from the screen using one-on-one Y2H mating

To validate these potential interactors, further one-on-one mating tests were performed between these clones and either full-length NET4B or the IRQ + Ct domain. The rescued prey plasmids were transformed into *E. coli* DH5α cells and further purified from these cells (as described in section 2.2.2.1 and 2.2.3) before being transformed back into the Y187 yeast mating strain (according to 2.3.1).

These recovered clones were then ready for one-on-one mating tests to confirm whether the results from the screen could be reproduced. The yeast containing the prey plasmids were mated with either the NET4B or IRQ + Ct domain bait constructs in the AH109 cells. The rescued prey plasmids were also mated with the empty pGBKT7 vector as a negative control for autoactivation. Similarly, full-length NET4B and the IRQ + Ct domain were also mated with the empty pGADT7 vector.

Diploids mated cells were resuspended in water and dropped onto several different selection plates; -WL (lacking in tryptophan and leucine, as a positive control for diploid growth), -WLA (lacking tryptophan, leucine and adenine), -WLH + 2.5 or 10 mM 3AT (lacking tryptophan, leucine and histidine with the addition of 3AT) and finally -WLHA + 2.5 or 10 mM 3AT (lacking tryptophan, leucine, adenine and histidine plus 3AT). The different dropout medias were used to test the stringency of the interactors even though they were selected on high stringency plates (-WLHA + 10 mM 3AT).

Figure 6.7 shows the results of the mate between NET4B and the prey plasmids that were recovered using NET4B as bait. Shown here is a representative colony after seven days growth. These tests showed that RGP1 and RGP2 did not show any growth on the selective media, suggesting that they do not interact with NET4B. Growth was observed on -WLA and -WLH + 2.5 mM 3AT when NET4B was mated with RIN4L, and growth was also observed on -WLH + 2.5 mM 3AT when NET4B was mated with KUP6. However the plasmids for RIN4L, RabA5c and KUP6 all showed growth on the selective media when they were mated with the empty vector which suggests that they

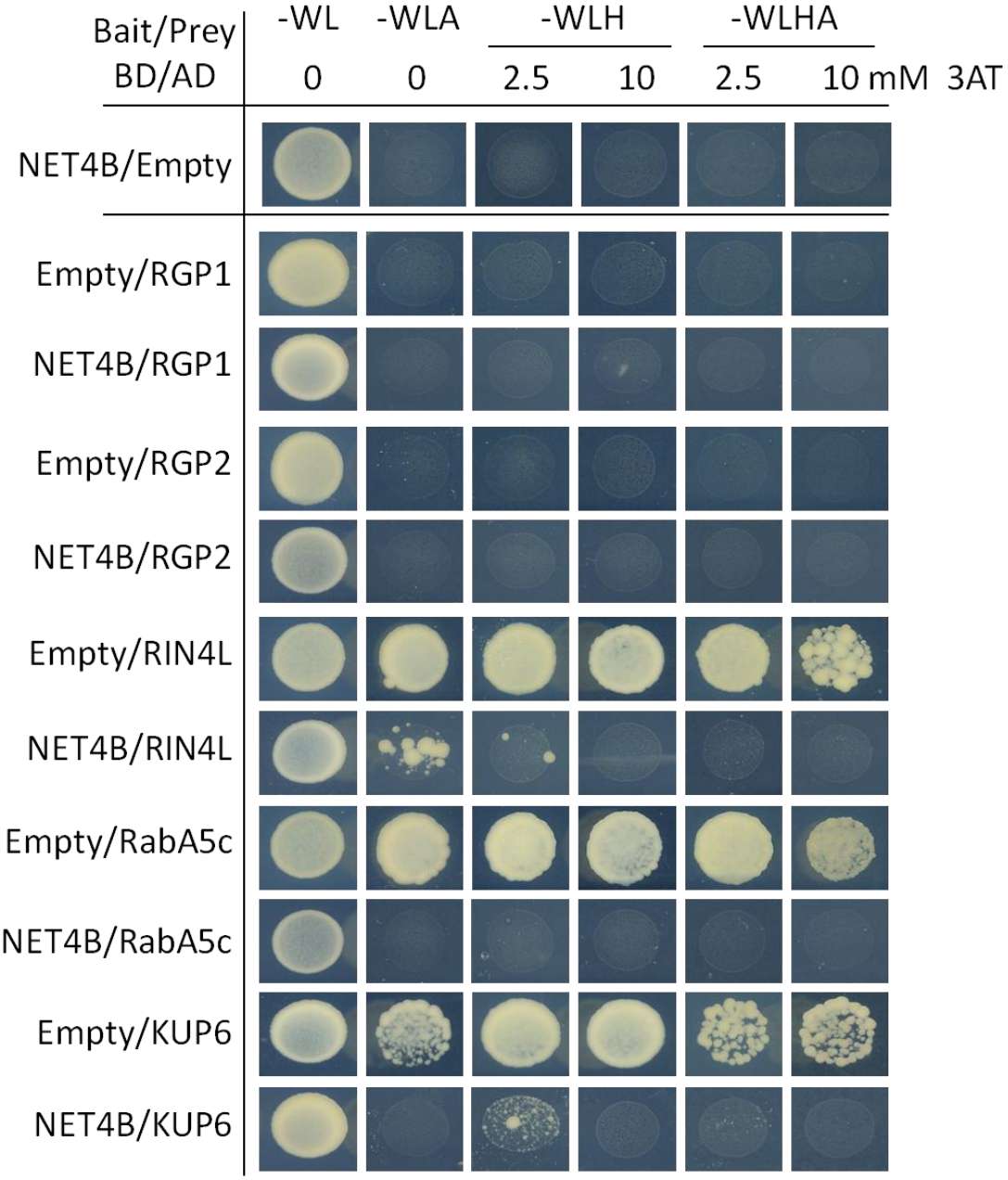

Figure 6.7: One-on-one mating tests with NET4B and the recovered prey from the NET4B Y2H screen. Recovered prey constructs (pGADT7) were mated with the empty bait vector (pGBKT7, as a negative control for autoactivation) or NET4B (to test for an interaction). NET4B was also mated with the empty pGADT7 vector as a negative control for autoactivation. Diploids of these mates were dropped onto media lacking tryptophan and leucine (-WL, as a positive control for diploid growth) and the various selective media to test for an interaction (-WLA, -WLH, -WLHA, with the addition of 3AT on media lacking histidine). RGP1 and RGP2 did not grow on selective media, demonstrating that an interaction had not occurred. RIN4L, RabA5c and KUP6 all autoactivated as they grew on selective media when mated with the empty vector. This suggests that they are therefore not true interactors of NET4B. This figure shows the growth of one representative diploid colony after seven days growth.

represent false positives. The results from this experiment therefore suggest that the selected NET4B prey plasmids do not represent true interactors.

The one-on-one mating tests for the potential interactors of the IRQ + Ct domain were performed in a similar way as those of NET4B. The prey plasmids were mated with both the IRQ + Ct domain and the full-length NET4B as bait, as well as the empty pGBKT7 vector as a negative control. The NET4B constructs were also mated with the pGADT7 empty vector as a negative control for autoactivation. The diploid cells were dropped onto the selection plates as described above.

Figure 6.8 shows the results of this experiment showing the growth of one representative diploid colony after seven days. This experiment showed autoactivation did not occur with RFC4 or DEP1, as growth was not observed with the empty vector mates. Growth of RFC4 was seen on the -WLH plates when mated with either the IRQ + Ct domain or the full-length NET4B. This therefore suggests a positive interaction between RFC4 and NET4B which could be mediated through the IRQ + Ct domain. Although growth was seen on -WLH these mates were not able to grow on the more stringent -WLHA plates which was used for selection during the screen.

The interaction of the DEP1 prey plasmid and the IRQ + Ct domain, as well as the full-length NET4B, could represent a true interaction. The negative control of DEP1 and the empty bait vector mate did not grow on the selective dropout plates. However growth was observed on all dropout plates when DEP1 was mated with the IRQ + Ct domain and the full-length NET4B. Therefore, the results of this test show that DEP1 could strongly interact with the full-length NET4B and the IRQ + Ct domain.

The results of these one-on-one mating tests suggested that the selected prey plasmids from the NET4B screen represented false positives. However, the tests using the IRQ + Ct prey plasmids suggested that both RFC4 and DEP1 could be true interactors and further tests were performed to examine this possibility, as described below.

6.3.3 One-on-one mating of full-length DEP1 with NET4B

In order to verify RFC4 and DEP1 as true interactors of NET4B, it was imperative to test whether the full-length coding sequences of these proteins could interact with NET4B rather than just the cDNA fragment. Both genes were therefore cloned from Arabidopsis for further one-on-one mating tests using the Y2H system.

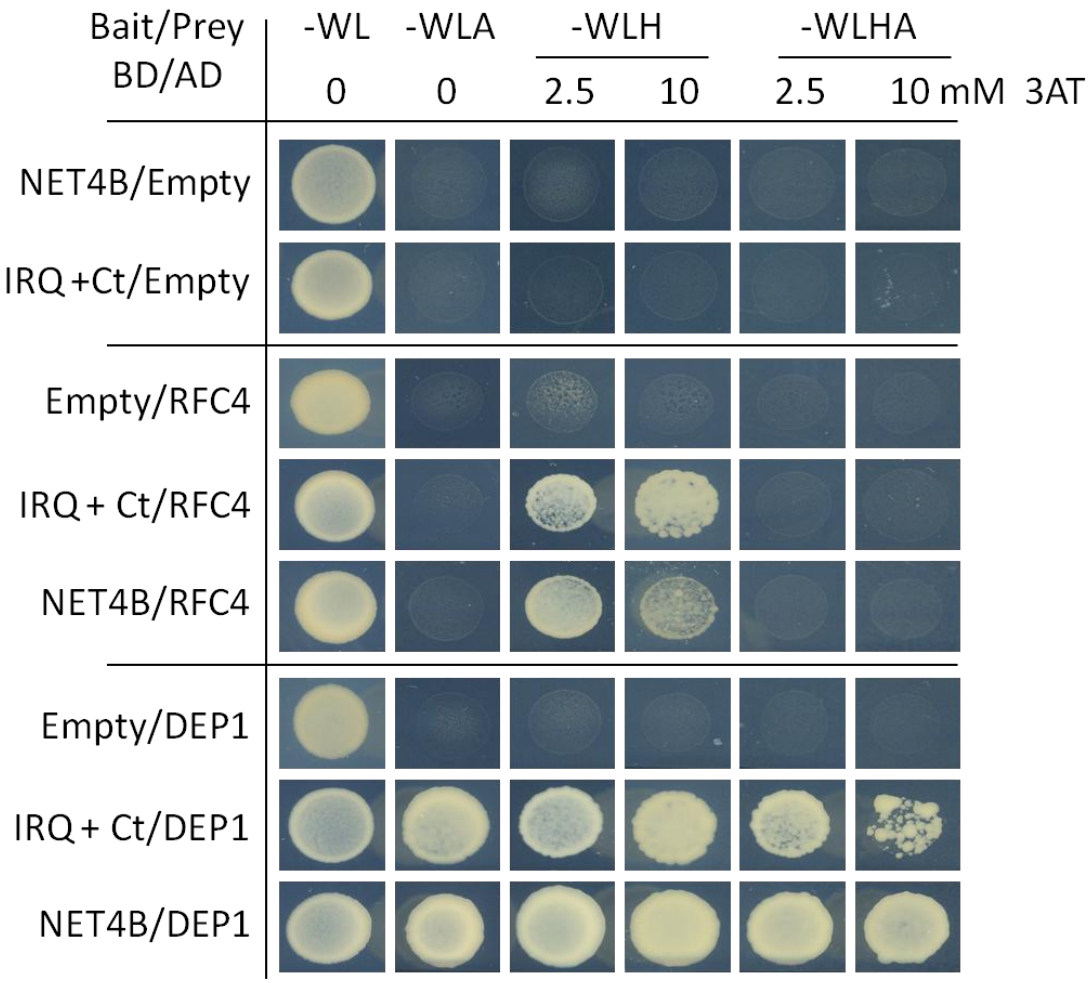

Figure 6.8: One-on-one mating tests between NET4B, the IRQ + Ct domain and the prey from the IRQ + Ct Y2H screen. Rescued prey constructs (pGADT7) were mated with the empty bait vector (pGBKT7, to control for autoactivation) or NET4B/IRQ + Ct (to test for an interaction). NET4B and the IRQ + Ct domain constructs were also mated with the pGADT7 empty vector as a negative control for autoactivation. Diploids of these mates were dropped onto media lacking tryptophan and leucine (-WL, as a control for diploid growth) and the various selective media to test for an interaction (-WLA, -WLH, -WLHA, with the addition of 3AT on media lacking histidine). Autoactivation did not occur for either RFC4 or DEP1. Growth on selective media lacking histidine occurred when the full-length NET4B and the IRQ + Ct domain were mated with the RFC4 prey plasmid. Diploids from the mates between DEP1 and full-length NET4B or the IRQ + Ct could grew on all selective media. This suggests a possible interaction for both RFC4 and DEP1 with NET4B and the IRQ + Ct domain. This figure shows the growth of one representative colony after seven days growth.

The amino acid sequence of the cDNA fragments were first searched against the Arabidopsis proteome to assess which gene models they were derived from. This revealed that the RFC4 fragment could only be found in the At1g21690.3 splice variant (four splice variants exist for this gene), and the cDNA fragment aligned with the last 33 amino acids (aa) of this 341 aa protein. The amino acid sequence of the DEP1 cDNA fragment was similar to all three splice variants of the gene, however the At5g53850.2 splice variant gave the highest alignment score. Aligning the cDNA amino acid sequence with the full-length protein showed that this fragment aligned with the last 156 aa of this protein.

The domain architecture of the amino acid sequence of RFC4 and DEP1 was investigated through the SMART programme (a Simple Modular Architecture Research Tool) and is shown in Figure 6.9 (Schultz et al. 1998; Letunic et al. 2014). This analysis showed that the full-length RFC4 protein contained two major domains; an N-terminal AAA-type ATPase and a C-terminal Replication factor C domain, however the cDNA fragment did not overlap with either of these domains. Studying the domain architecture of DEP1 and the cDNA fragment using the SMART programme revealed that DEP1 contains two major domains; an N-terminal Aldolase II domain and a C-terminal haloacid dehalogenase-like hydrolase domain (Pfam: HAD2). The cDNA fragment was shown to overlap extensively with the HAD2 domain.

Gene specific primers were designed to both the full-length At5g53850.2 and At1g21690.3, as well as primers for cloning the aligned cDNA prey fragment (see Appendix 1.5 for sequences). The expression profiles of these genes were examined using the Arabidopsis eFP-browser (Winter et al. 2007), which showed DEP1 and RFC4 are expressed ubiquitously throughout the plant (see Appendix 4). At5g53850.2 was amplified from cDNA derived from 5-day old Arabidopsis seedlings (provided by Dr. Pengwei Wang, Durham University). However the At1g21690.3 splice variant of RFC4 could not be cloned from cDNA derived from either Arabidopsis seedlings or flowers. As the representative gene model containing the initial cDNA library fragment could not be cloned, RFC4 was no longer continued with one-on-one testing.

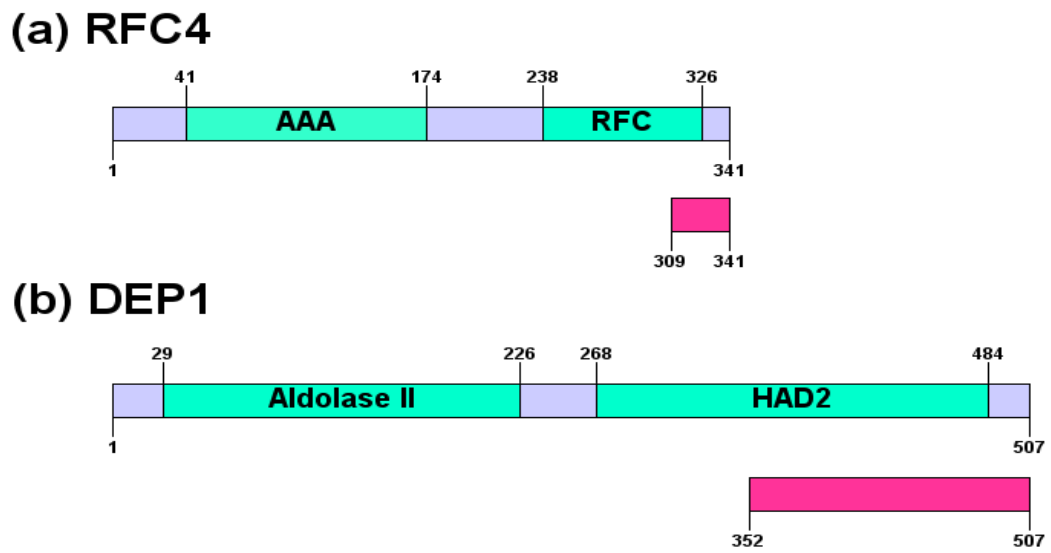

Figure 6.9: Protein domain structures of RFC4 and DEP1. Domain architectures of RFC4 and DEP1 were analysed using the SMART database tool. Protein length is in grey, specific domains are in blue, the recoved cDNA fragments are shown in magenta. Numbers denote the amino acid positions. (a) RFC contains an AAA-type ATPase domain, and a Replication factor C C-terminal domain (RFC). (b) DEP1 has two domains; Aldolase II and the HAD2 domain. The Illustrator of Biological Sequences (IBS) software was used to create this diagram (Liu et al. 2015).

The full-length DEP1 and the last 156 aa fragment, termed DEP1$^{352\text{-}507}$, were successfully amplified from Arabidopsis cDNA and were cloned into the pGBKT7 and pGADT7 vectors using the Gateway system (according to 2.2.10). Cloning into both bait and prey vectors enabled the interaction between DEP1 and NET4B / the IRQ + Ct domain to be tested in both mating directions.

To test these interactions, DEP1 and DEP1$^{352\text{-}507}$ in the bait pGBKT7 vector were transformed into AH109, and were subsequently mated with NET4B and the IRQ + Ct domain in the prey pGADT7 vector in Y187 cells. Both the DEP1 and NET4B constructs were mated with the reciprocal empty vector to ensure no autoactivation occurred. For the other mating direction; DEP1, DEP1$^{352\text{-}507}$ and the original DEP1 cDNA library fragment (DEP1^{cDNA}) in the prey pGADT7 vector (Y187 cells) were mated with NET4B and the IRQ + Ct domain in the bait pGBKT7 vectors (AH109 cells). The empty vector mates were also performed for these constructs as a negative control for autoactivation. Once diploids for each of these mates were selected they were resuspended in water and dropped onto selective media lacking tryptophan, leucine and histidine with 2.5mM 3AT (-WLH + 2.5 mM 3AT). This dropout media

was selected as it was the least stringent and so would increase the likelihood of observing an interaction.

Figure 6.10 shows the results of the one-on-one mating tests with DEP1 and NET4B showing the growth of one representative colony. The results of this experiment again showed that the $DEP1^{cDNA}$ fragment could interact with NET4B and the IRQ + Ct domain. Similarly the cloned DEP1 fragment, $DEP1^{351-507}$, could also interact with NET4B and the IRQ + Ct domain, when mated in both directions which therefore replicates the result from the library screen. However in this system the full-length DEP1 protein did not show evidence for an interaction when mated with NET4B. It is possible that the tertiary structure of the full-length protein may abolish or diminish the availability of this domain ($DEP1^{351-507}$) for NET4B interaction *in planta*. Alternatively, the full-length DEP1 might not be compatible with the Y2H system. This could be due to steric hindrance interfering with the association of the binding/activation domains. To successfully resolve this, an additional method for studying interactions could be used for example co-immunoprecipitation or FRET-FLIM (fluorescence energy transfer - fluorescence lifetime imaging microscopy).

6.4 The interaction between NET4s and Rab GTPases

To further explore interaction partners of the NETWORKED family proteins, several members of the NET family, including NET4A, were sent for TAP-Tag analysis (Ghent University). TAP-tagging utilises two different tags, for example protein G and the streptavidin-binding peptide, to isolate protein complexes *in planta* using two sequential purification steps. The identity of the purified proteins can then be determined through mass spectrometry techniques. Using the double affinity tag reduces the presence of contaminating proteins in the sample and provides an effective method to determine *in planta* protein complexes (Van Leene et al. 2015). TAP-MS of NET4A was performed by the Functional Interactomics group at VIB, Ghent University. Here NET4A, fused to the TAP-tag, was expressed in Arabidopsis cell culture and protein complexes were purified out from these cells. The major interactor identified was RabG3a, which was consistently pulled back through multiple detergent treatments (Hawkins and Hussey, unpublished). Rab GTPases are key regulators of membrane transport and the Arabidopsis RabG3 subfamily control trafficking steps to the vacuole (Rutherford & Moore 2002; Bottanelli et al. 2011; Bottanelli et al. 2012; Cui et al. 2014).

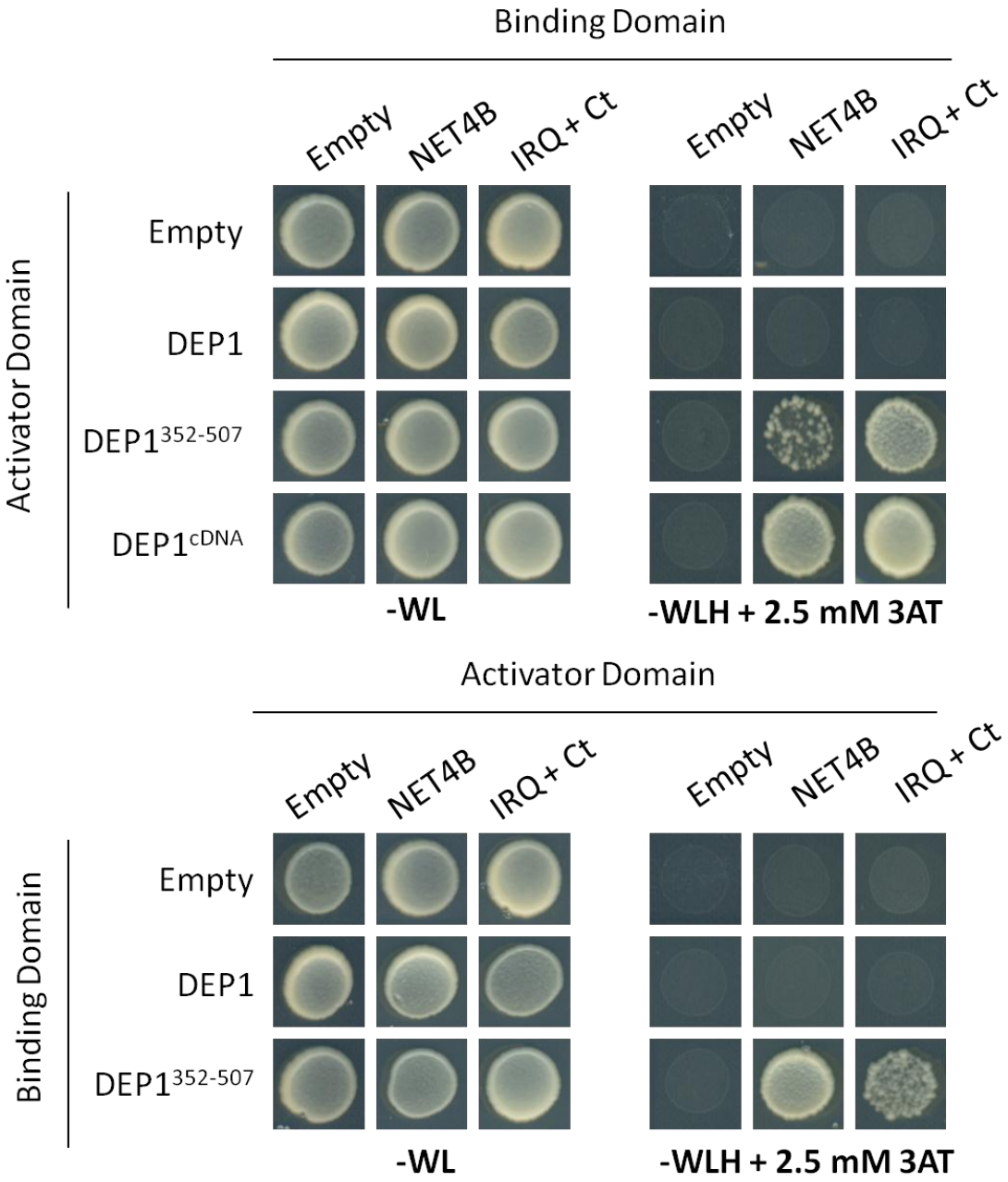

Figure 6.10: One-on-one mating test of NET4B with DEP1. Full-length DEP1, and the short interacting fragment DEP1$^{352\text{-}507}$, were cloned into the bait and prey vectors (pGBKT7 and pGADT7). These were then mated with the reciprocal empty vector (to control against autoactivation) and the full-length NET4B and the IRQ + Ct domain, in both mating orientations. The original rescued prey plasmid in pGADT7, DEP1^{cDNA}, was also used in these mates as a positive control for growth on the selective media. Diploids were dropped onto media lacking tryptophan and leucine (-WL, as a control for diploid growth) and media lacking tryptophan, leucine and histidine with 2.5 mM 3AT (-WLH + 2.5 mM 3AT, to test for a positive interaction). Only the DEP fragments, DEP1$^{352\text{-}507}$ and DEP1^{cDNA}, could grow on selective media when mated with NET4B or the IRQ + Ct domain. Full-length DEP1 could not interact with NET4B or the IRQ + Ct in either orientation. Shown in this figure is the growth of one representative diploid colony after five days growth.

Furthermore in collaboration with Dr. Ian Moore, the interaction between NET4B and RabG3f was also identified. Using co-immunoprecipitation with anti-GFP antibodies followed by label-free mass spectrometry, NET4B was consistently detected in triplicate immunoprecipitates from plants expressing YFP-RabG3f, but not from wild-type plants or plants expressing YFP-RabA2a which belongs to a distinct group of Rab GTPases that localise to the trans-Golgi network (Monika Kalde and Ian Moore, personal communication).

Taken together, these two screens provide evidence for an interaction between the NET4s and the RabG3 GTPases. The nature of these interactions was explored further using the Y2H system.

6.4.1 Cloning and creation of dominant-negative and constitutively-active mutants of the RabG3 GTPases

Arabidopsis *RabG3f* is encoded by a gene at the locus At3g18820 and only has the one splice variant. *RabG3a* has four splice variants, as annotated by the Arabidopsis information resource (TAIR) database, and is encoded by a gene at the At4g09720 locus. Three of the *RabG3a* splice variants utilise the same start and stop codon with different splicing of the mRNA, whereas the fourth splice variant represents a truncated form of the gene.

To clone these two genes, gene specific primers were designed for the representative *RabG3f* gene. For *RabG3a*, primers were designed to At4g09720.1 as this was annotated as the representative gene model and is one of the larger splice variants (see Appendix 2.4 for sequences of both Rabs). First strand cDNA synthesised from 5-day old Arabidopsis seedling RNA was used as the DNA template when cloning these genes. Both genes were successfully amplified by PCR and were cloned into pDONR207 by the Gateway system (according to 2.2.10). These clones were then sequenced (according to 2.2.11), which confirmed that both genes, and specifically the At4g09720.1 splice variant, were cloned.

As well as testing whether the NET4s could interact with the RabG3 GTPases in their native state, it was also essential to test whether the NET4s interact with these Rabs in their inactive GDP-bound or activated GTP-bound state. As discussed in Chapter 1.4, Rab GTPases are activated at their target membrane through action of a guanine nucleotide exchange factor (GEF) that exchanges GDP for GTP. Active GTP-bound

Rabs are then able to recruit effector proteins that mediate the different steps in membrane trafficking. Studies on the interactions between Rab GTPases and their effector proteins have made use of site-directed mutagenesis to generate Rabs that are locked into a GDP- or GTP-bound state. By creating these mutants, it can then be assessed whether the interactor of interest represents an effector protein of the Rab, as effectors typically bind Rabs in their active GTP-bound form. Various studies have utilised three main mutations in conserved G box regions (GDP/GTP binding motif elements) of the Rabs to generate dominant-negative (DN; GDP-bound) and constitutively-active (CA; GTP-bound) versions of the Rabs as shown in Figure 6.11 (Rutherford & Moore 2002; Wennerberg et al. 2005).

In order to generate DN mutations several studies have converted the conserved serine (S)/threonine (T) in the phosphate interaction site (G1 region) to an asparagine residue (N) (Nassar et al. 2010). In the RabG3 Rab GTPases this mutation resembles a threonine to asparagine mutation at amino acid 22 (T22N). The serine/threonine in this region coordinates a magnesium ion that is important for GTP binding, but changing this to an asparagine residue prevents the occupation of this magnesium ion through steric hindrance (Nassar et al. 2010). This mutation causes a reduction in the Rabs' affinity for GTP without affecting the affinity for GDP (Feig & Cooper 1988). This mutation therefore creates a dominant-negative mutation as the Rab preferentially interacts with GDP.

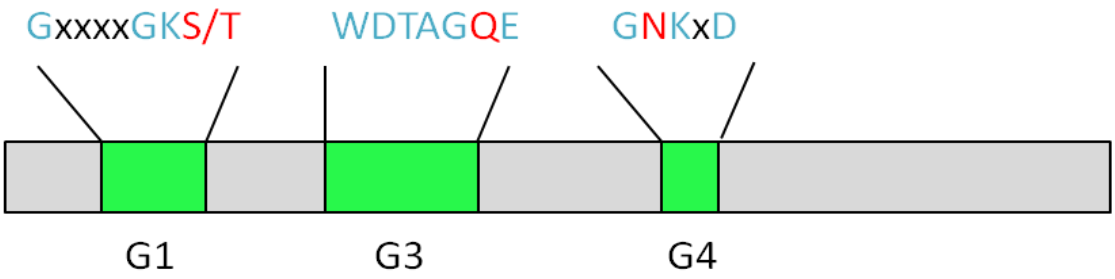

Figure 6.11: Diagram of a typical Rab GTPase with conserved sites used for site-directed mutagenesis. Schematic diagram of a representative 200 amino acid Rab GTPase. Shown in green are three conserved G box domains that can be mutated to create dominant-negative and constitutively-active Rabs. The conserved motifs are shown above each box and represent single amino acid codes. Letters in blue are conserved non-mutated amino acids, black letters vary between sequences, and letters in red can be mutated to create various mutations. Diagram modified from Rutherford & Moore (2002).

In addition to this mutation, dominant-negative mutations can also be created by mutating an asparagine (N) to an isoleucine (I) residue in the nucleotide binding domain (G4 region). For the RabG3 Rab GTPases this mutation would be an asparagine to isoleucine mutation at amino acid 125 (N125I). This creates a nucleotide-free Rab GTPase, similar to that seen with the N116I mutation of Ras^{H}, that has been shown to have a dominant-negative effect in membrane trafficking (Walter et al. 1986; Chow et al. 2008; Bottanelli et al. 2011; Choi et al. 2013).

The commonly used mutation for generating a constitutively-active Rab GTPase involves mutating a conserved glutamine (Q) in the G3 region to a leucine (L) residue (Gabe Lee et al. 2009). For the RabG3 proteins this represents a glutamine to leucine mutation at amino acid 67 (Q67L). This glutamine has been shown to coordinate an active site water molecule that is important for the hydrolysis of GTP to GDP (Langemeyer et al. 2014). Mutating glutamine to a hydrophobic leucine residue, dramatically lowers the intrinsic GTP hydrolysis rate and therefore these mutants remain bound to GTP and are termed constitutively-active (Langemeyer et al. 2014).

In this study, only the T22N and the Q67L mutation were made for each RabG3 as they have recently been used to successfully create dominant-negative and constitutively-active versions of RabG3f (Cui et al. 2014). Both dominant-negative (T22N) and constitutively-active (Q67L) mutations were generated for both RabG3a and RabG3f using the QuikChange lightning site-directed mutagenesis kit (Agilent technologies; as described in 2.2.12). The wild-type, T22N and Q67L versions of each Rab in pDONR207 were subsequently cloned into the yeast bait and prey vectors, pGBKT7 and pGADT7, for one-on-one mating tests with the NET4s.

6.4.2 One-on-one mating tests between NET4B and RabG3a

The initial one-on-one mating tests were performed with NET4B and the wild-type and mutated RabG3a. Testing the NET4B and RabG3a interaction was performed in both directions, e.g. BD-NET4B/AD-RabG3a and AD-NET4B/BD-RabG3a. The constructs in the bait vector were transformed into the AH109 cells and the prey vectors were transformed into the Y187 cells. NET4B in the bait vector was mated with all three versions of RabG3a in the prey vector, and the reciprocal mates were also performed. All constructs were mated with their reciprocal empty vectors as a negative control for autoactivation. Diploids were resuspended in water and dropped onto the following selective media; -WL (lacking in tryptophan and leucine, as a positive control for

diploid growth), -WLA (lacking tryptophan, leucine and adenine), -WLH + 2.5 mM 3AT (lacking tryptophan, leucine and histidine with the addition of 3AT) and finally -WLHA + 2.5 mM 3AT (lacking tryptophan, leucine, adenine and histidine plus 3AT).

Figure 6.12 shows the growth of one representative colony for this one-on-one mating test between NET4B and the different mutations of RabG3a. Growth was not observed on selective media for the empty vector control tests, showing that autoactivation did not occur. Mating BD-NET4B with AD-RabG3a produced no growth on any of the selective media. However growth was consistently observed on the -WLH plate, in the other mating orientation when AD-NET4B was mated with BD-RabG3a and BD-RabG3a^{Q67L}. Growth did not occur when AD-NET4B was mated with BD-RabG3a^{T22N}. This therefore suggests that NET4B can interact with the wild-type version of RabG3a and the constitutively-active, GTP-bound RabG3a^{Q67L} version but not the dominant-negative GDP-bound RabG3a^{T22N} version. This suggests that NET4B could be a potential effector protein of this Rab, as it interacts specifically with the activated GTP-bound version.

Although this result was not seen in both mating directions, this could be due to the functionality of these constructs in the Y2H system. Furthermore, as growth was only seen using the *HIS3* reporter which is the lowest stringency, this suggests a relatively weak interaction between NET4B and the Rab.

6.4.3 One-on-one mating between the NET4s and both RabG3 GTPases

The one-on-one mating test with NET4B and RabG3a showed that a positive interaction could occur with both the wild-type and constitutively-active version. The breadth of this NET4/RabG3 interaction was investigated further and the ability of both NET4s to interact with RabG3a and RabG3f was examined.

These interaction tests were only performed with the NET4s in the prey vector and the Rabs in the bait vector, as this was the only orientation that showed a positive interaction in the previous experiment. The multiple RabG3a and RabG3f constructs in the bait vectors were transformed into the AH109 cells and the NET4B and NET4A prey vectors were transformed into the Y187 strains. AD-NET4B and AD-NET4A were then mated with the different versions of the BD-RabG3a and BD-RabG3f constructs. Reciprocal empty vector mates were also performed as a negative control for autoactivation. Diploids were resuspended in water and dropped onto -WL plates (as a

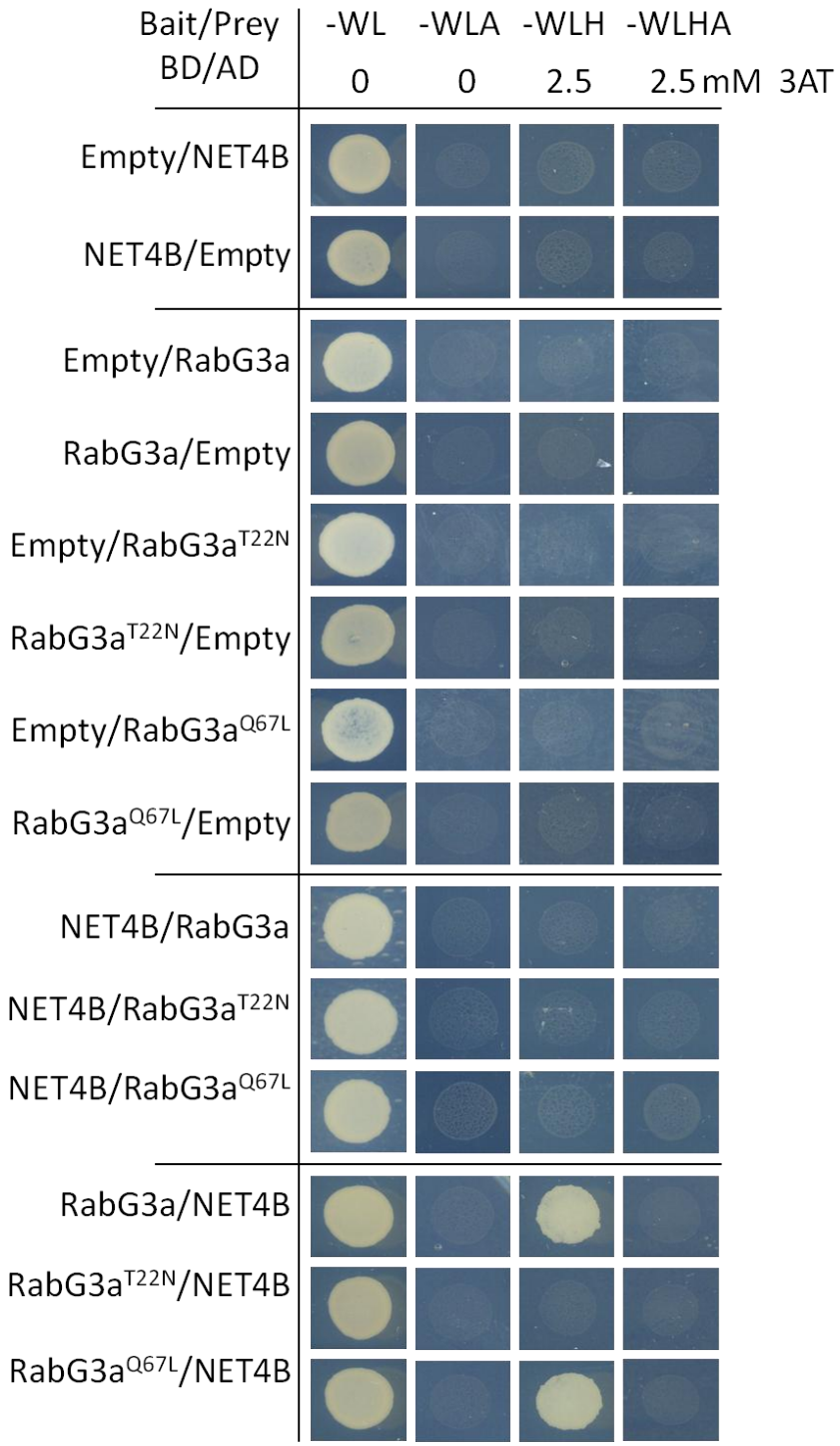

Figure 6.12: One-on-one mating test between NET4B and RabG3a using the Y2H system. One-on-one mating tests were performed with NET4B and the different RabG3a mutations using both mating directions. Each construct was mated with the reciprocal empty vector as a negative control for autoactivation. Diploids were dropped onto -WL plates (to control for diploid growth), and various selective dropout media to test for an interaction (-WLA, -WLH, -WLHA, with 2.5 mM 3AT on media lacking histidine). AD-NET4B and BD-RabG3a/RabG3a^{Q67L} could grow on selective media lacking histidine, suggesting they interact. This interaction was not observed with the dominant-negative RabG3a^{T22N}. Shown here is the growth of one representative diploid colony for each mate after seven days growth.

positive control for diploid growth) and media lacking tryptophan, leucine and histidine with 2.5 mM 3AT (-WLH + 2.5 mM 3AT, to test for an interaction).

Figure 6.13 shows the growth of one representative colony after seven days. The negative control empty vector mates again showed no growth on the selective media. NET4B and NET4A were both shown to produce viable colonies on the selective media when mated with the wild-type RabG3a and constitutively-active RabG3a^{Q67L} version, but not with the dominant-negative RabG3a^{T22N}. Similarly, both NET4s were shown to interact with the wild-type RabG3f and constitutively-active RabG3f^{Q67L} version, and growth was not observed when the NET4s were mated with the dominant-negative RabG3f^{T22N} version. However, growth on the NET4B/wild-type-RabG3f diploid mate was consistently slower than the other positive interactions.

The results of this experiment suggest that both NET4 proteins could interact with two different RabG3 Rab GTPases in their wild-type and activated GTP-bound state. Therefore both NET4 proteins could represent effector proteins of the RabG3s and be recruited in membrane trafficking events at the vacuole. However, it is possible that the NET4s interact with additional classes of Rab GTPases and the experiments described below, were designed to test the specificity of NET4B to the vacuolar RabG3 GTPases.

6.4.4 Testing the interaction of NET4B with other Rabs

Different classes of Rab GTPases are responsible for recruiting effector proteins and regulating membrane trafficking events in discrete steps of the endomembrane system (Rutherford & Moore 2002). Therefore, the specificity of the NET4s to the Arabidopsis subclass of vacuolar Rab GTPases was tested using the Y2H system. These experiments could elucidate whether the potential role of the NET4s in membrane trafficking is restricted to the vacuole. Several Rab GTPases, involved in distinct membrane trafficking events were selected to test whether they interact with NET4B. These included Rab GTPases from the RabD, RabA and RabF subclasses.

RabD2a (Rab1b; ARA5; At1g02130) is a member of the RabD2 class. This class closely resemble mammalian Rab1 and yeast Ypt1 Rab GTPases that have been shown to be important in ER to Golgi transport (Rutherford & Moore 2002). RabD2a has also been shown to mediate ER to Golgi transport using a GFP-based assay for membrane trafficking in tobacco leaf epidermal cells (Batoko et al. 2000).

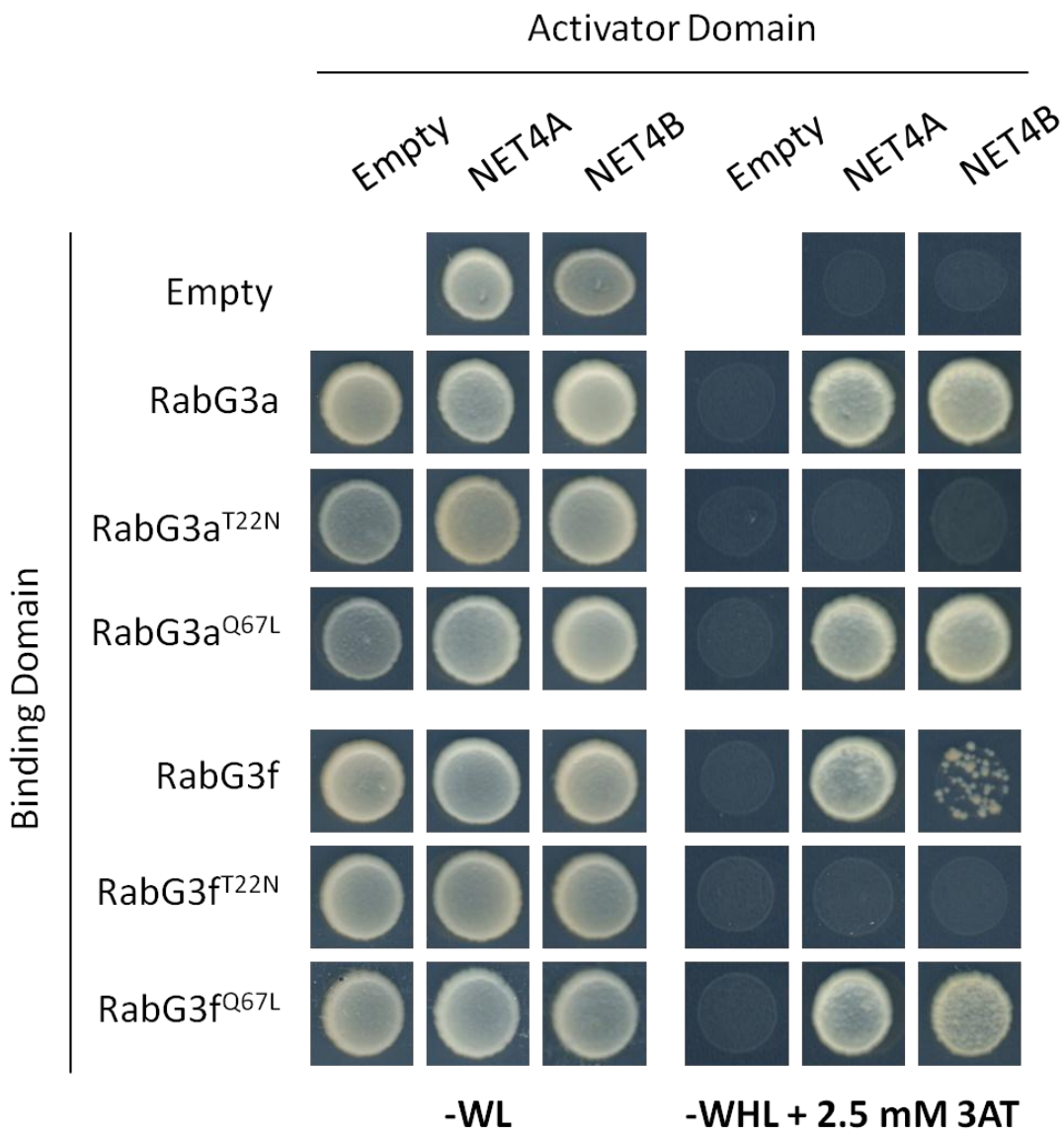

Figure 6.13: One-on-one mating test between the NET4s and the RabG3s using the Y2H system.. NET4B and NET4A in pGADT7 (activation domain) were mated with the different mutations of RabG3a and RabG3f in the pGBKT7 vector (binding domain). Each construct was also mated with their reciprocal empty vector as a negative control for autoactivation. Diploids were dropped onto -WL plates (to control for diploid growth), and media lacking tryptophan, leucine and histidine with 2.5 mM 3AT (-WLH + 2.5 mM 3AT, to select for positive interactions). Growth occurred on media lacking histidine when the NET4 proteins were mated with the wild-type and constitutively-active (Q67L) versions of the RabG3 proteins, suggesting a positive interaction. Growth was not observed when the NET4 proteins were mated with the dominant-negative (T22N) mutation of either RabG3. Shown in this figure is the growth of one representative diploid colony for each mate after five days growth.

RabA5c (ARA4, At2g43130) is a member of the Arabidopsis RabA subfamily, which is subdivided into 6 subclasses (RabA1-6). The RabA subclass is most closely related to mammalian Rab11a, Rab11b and Rab25 which localise to recycling endosomes (Rutherford & Moore 2002). RabA5c was selected for investigation as a fragment of this protein was pulled back in the Y2H screen using NET4B as bait. As discussed previously, RabA5c has been shown to associate with the Golgi cisternae, trans-Golgi network and Golgi derived network (Ueda et al. 1996).

Finally, RabF2a (RHA1; Rab5a; At5g45130) is a member of the RabF subclass, which is composed of three members in Arabidopsis (Rutherford & Moore 2002). These proteins are homologues of the mammalian Rab5/Rab22, and the yeast Ypt51/Ypt52/Ypt53 which are involved in endocytosis (Rutherford & Moore 2002). RabF2a localises to the prevacuolar compartments (PVCs) and is important in mediating transport from the PVC to the vacuole (Sohn et al. 2003; Lee et al. 2004). RabF2a could represent a potential interactor as the NET4s could be important in trafficking RabF labelled endosomes as they convert to RabG labelled endosomes on the trafficking route to the vacuole.

These three Rabs were amplified from cDNA derived from Arabidopsis 5-day old seedling RNA, using a PCR reaction with gene-specific primers (listed in Appendix 1.5). The Gateway system was used to clone these genes first into pDONR207 and then into the bait pGBKT7 vector (as described in 2.2.10). Once cloned into the bait vector, the BD-Rabs were transformed into the yeast AH109 strain and were subsequently mated with NET4B in the prey vector in Y187 cells. As a positive control for interaction, NET4B was also mated with RabG3a which was shown to positively interact in previous experiments. As a negative control for autoactivation, all constructs were mated with the reciprocal empty vector. Diploids were resuspended in water and dropped onto two plates; one plate lacking tryptophan and leucine (-WL, as a positive control for diploid growth) and one plate lacking tryptophan, leucine and histidine with 2.5 mM 3AT (-WLH + 2.5 mM 3AT, to test for an interaction).

Figure 6.14 shows the results of this experiment, showing the growth of one representative colony after five days growth. Growth was not observed for RabD2a, RabA5c or RabF2a, however it could be observed for the RabG3a acting as the positive control. This suggests that the interaction between NET4B and Rab GTPases is specific to the RabG3 subclade.

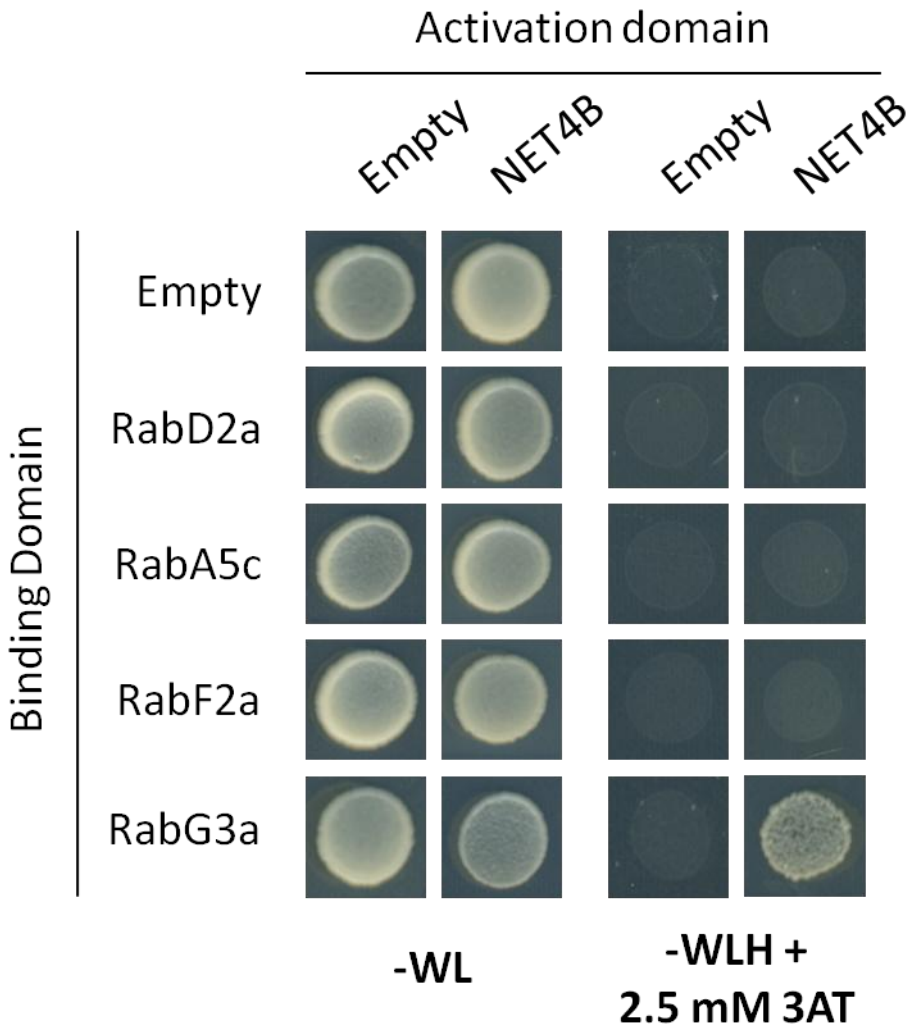

Figure 6.14: One-on-one mating test between NET4B and RabD2a, RabA5c, and RabF2a. NET4B in pGADT7 (activation domain) was mated with three non-vacuolar Rab GTPases in pGBKT7 (binding domain); RabD2a, RabA5c and RabF2a. As a positive control for growth on selective media, NET4B was also mated with RabG3a. As a negative control, all constructs were mated with the reciprocal empty vector. Successfully mated diploids were dropped onto media lacking tryptophan and leucine (-WL, as a positive control for diploid growth) and media lacking tryptophan, leucine and histidine with 2.5 mM 3AT (-WLH + 2.5 mM 3AT, to test for positive interactions). Only diploids from the mate between NET4B and RabG3a could grew on media lacking histidine, suggesting that NET4B is specific to this subclade of Rab GTPases. Shown in this figure is the representative growth of one diploid colony from each mate after five days growth.

6.4.5 Identification of the active Rab-binding site on NET4B using the Y2H system

Having established that both NET4 proteins interact with the constitutively-active versions of the RabG3s, it was imperative to identify the domain responsible for this interaction. To identify the Rab interactor domain, the Y2H system was used to mate various truncations of NET4B with the constitutively-active RabG3a^{Q67L} GTPase. Only the constitutively-active version was used as this would identify which part of NET4B interacted with the Rab specifically when it was activated and bound to GTP.

The Y2H system has been used frequently in the past to identify the Rab-binding domain of Rab effector proteins (Camacho et al. 2009; Miller et al. 2013; Antignani et al. 2015). By using various overlapping truncations of a protein, it is possible to locate the region responsible for Rab interaction. In order to find the Rab-binding domain of NET4B, the truncations used in Chapter 4.3 for the subcellular localisation studies were employed in this experiment.

Figure 6.15 shows the different truncations that were used to identify the Rab-binding domain. Seven different forms of NET4B were tested; full-length NET4B (NET4B; aa 1-517), the NAB domain alone (NAB; aa 1-105), NET4B without the IRQ domain (-IRQ; aa 1-463), NET4B without the NAB or IRQ domain (-NAB-IRQ; aa 106-463), NET4B without the NAB domain (-NAB; aa 106-517), the IRQ domain (IRQ; aa 464-502), and the IRQ domain to the C-terminal end of the protein (IRQ + Ct; 464-517). As the Y2H vectors use N-terminal binding/activation domain fusions, these truncations were all cloned with a stop codon using the primers listed in Appendix 1.2. These truncations were then cloned into pDONR207 and finally the prey pGADT7 vector using the Gateway system (see 2.2.10). The truncations were not cloned into pGBKT7 as the full-length NET4B only interacted with RabG3a when NET4B was in the prey vector.

The different truncations of NET4B in the pGADT7 vector were transformed into the yeast Y187 strain and mated with the constitutively-active RabG3a^{Q67L} mutation in the bait pGBKT7 vector. Each construct was also mated with the reciprocal empty vector as a negative control for autoactivation. Successfully mated diploids were resuspended in water and dropped onto two plates; one plate lacked tryptophan and leucine (-WL, as a positive control for diploid growth) and the selective plate lacked tryptophan, leucine

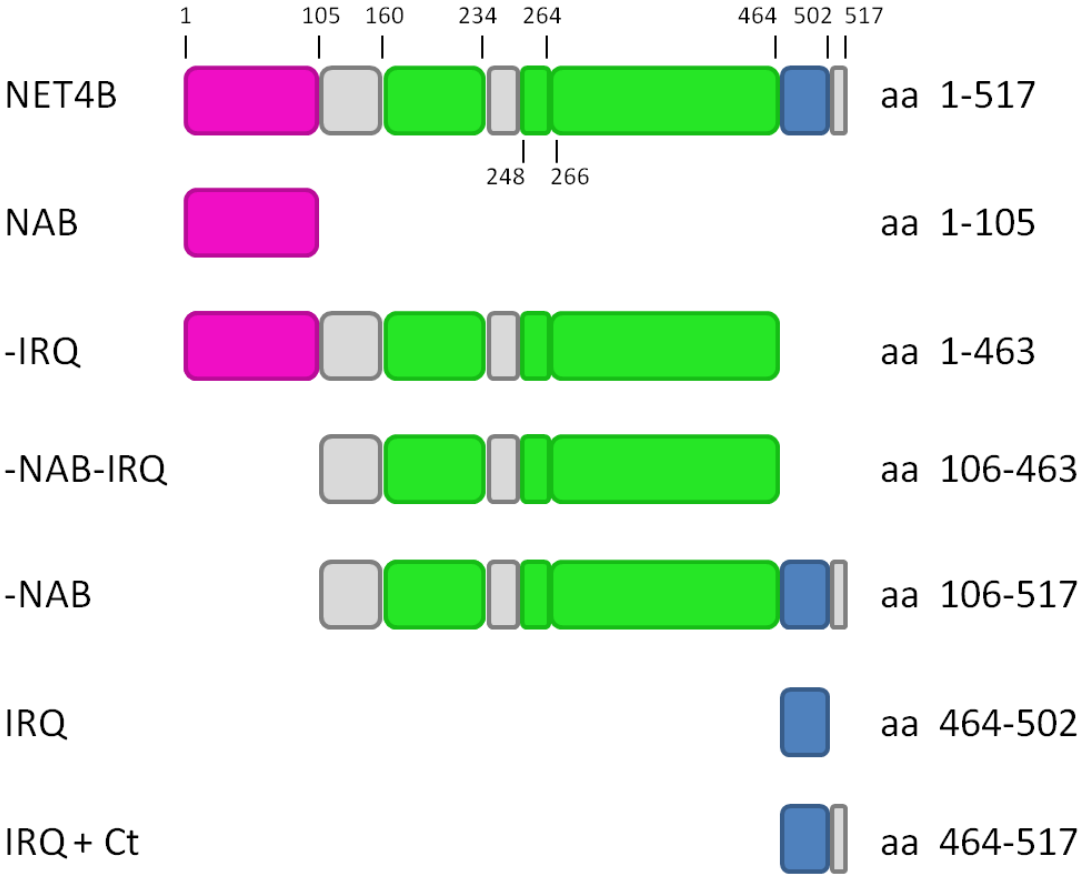

Figure 6.15: Diagram of the truncations used for finding the active Rab-binding domain of NET4B. Shown here is a schematic representation of the six truncations of NET4B that were used to find the Rab-binding domain using the Y2H system. The NAB domain is shown in magenta, coiled-coil domains in green, IRQ domain in blue and amino acids not belonging to a specific domain shown in grey. Numbers denote amino acid residues.

and histidine with the addition of 3AT (-WLH + 2.5mM 3AT, to test for positive interactions).

Figure 6.16 shows the result of this experiment showing the representative growth of one colony after five days growth. The empty vector control showed that autoactivation did not occur on the selective plate lacking histidine, and the full-length NET4B/ RabG3a^{Q67L} mate successfully grew on the selective media. The results of this experiment showed that the IRQ + Ct domain (aa 464-517) was sufficient to mediate the interaction between NET4B and the constitutively-active RabG3a. Growth was also observed when the -NAB truncation, which contained the IRQ + Ct domain, was mated with the active Rab. However the NAB alone, -IRQ and -NAB-IRQ truncations could not grow on the selective media. These three truncations all lacked the IRQ + Ct domain which provides further evidence that this domain forms the interaction site with the constitutively-active RabG3a. Interestingly, the interaction between the active Rab and the IRQ + Ct was lost when this fragment was truncated to the 39 amino acids (NET4B$^{464-502}$) of the IRQ fragment.

As growth on selective media was observed when the RabG3a^{Q67L} was mated with the C-terminal 54 amino acids (IRQ + Ct), but growth did not occur when NET4B lacking this domain (the -IRQ fragment) was mated with the constitutively-active RabG3a, this suggests that there is only one Rab-binding domain on NET4B, located at the C-terminus of the protein. Truncating the IRQ + Ct domain, resulted in the loss of an interaction with the active-Rab. The results of this experiment show that the last 54 amino acids, which contain the IRQ domain, are capable of interacting with the active RabG3a. Further truncations of the IRQ + Ct domain were generated and used to find the minimal Rab-binding domain of NET4B through the Y2H system, as described below.

6.4.6 Finding the minimal Rab-binding domain of NET4B

Seven further truncations of the C-terminal 54 amino acids of NET4B were made in order to identify the minimal Rab-binding domain. As the IRQ + Ct is already relatively small, the truncations were designed to progressively reduce this domain by approximately 10 amino acids with each truncation. These truncations were also made with consideration to the most highly conserved amino acids of this domain, as demonstrated from an alignment of NET4B, NET4A, NET3A and NET3C (see Figure

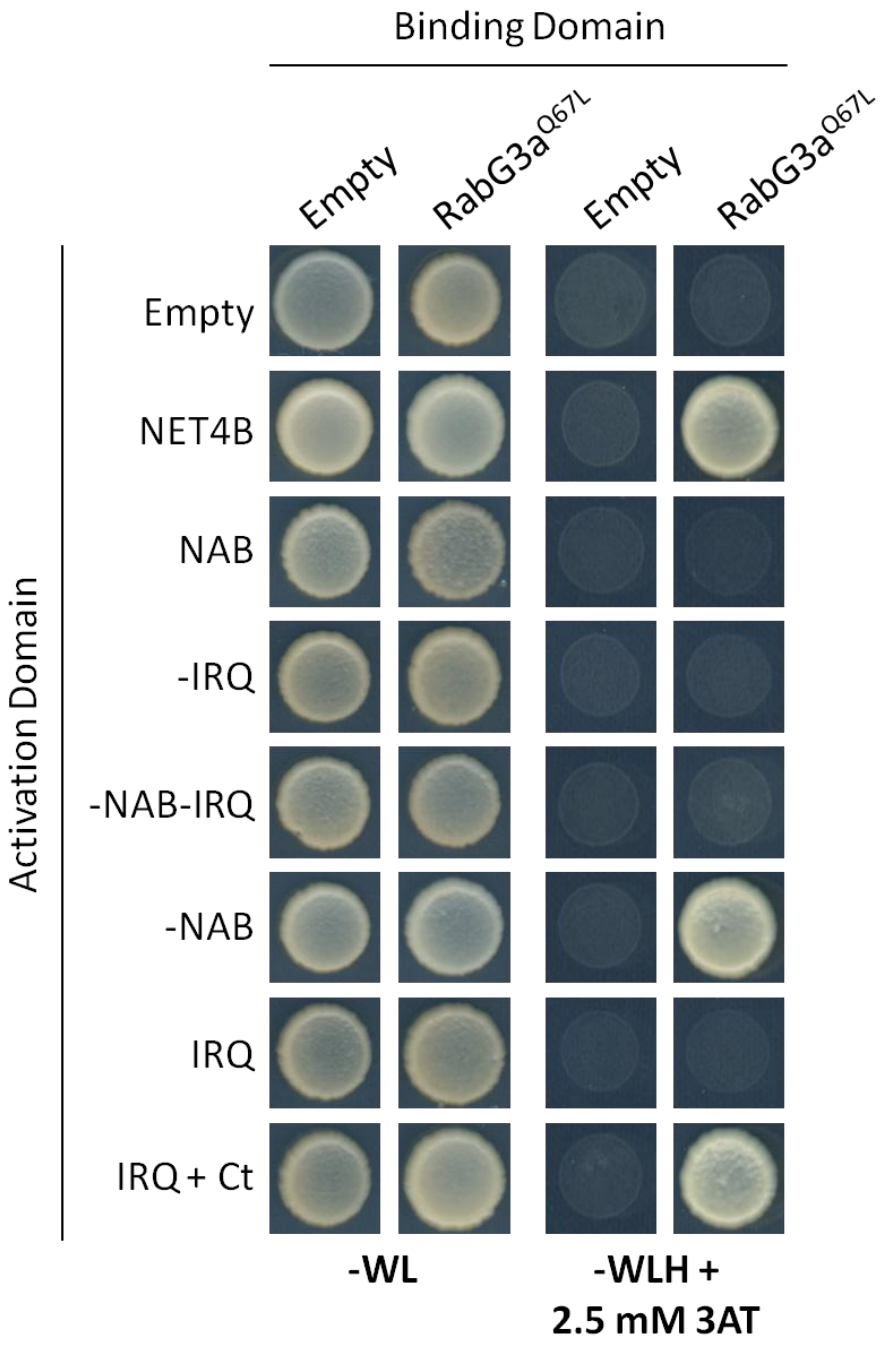

Figure 6.16: One-on-one Y2H mating tests with the NET4B truncations and the constitutively-active RabG3a^{Q67L}. The various truncations of NET4B were fused to the activation domain (pGADT7) and mated with RabG3a^{Q67L} fused to the DNA binding domain vector (pGBKT7). These constructs were also mated with the reciprocal empty vector as a negative control for autoactivation. Successfully mated diploids were dropped onto media lacking tryptophan and leucine (-WL, as a positive control for diploid growth) or media lacking tryptophan, leucine and histidine with 2.5 mM 3AT (-WLH + 2.5 mM 3AT, to test for an interaction). Growth on selective media only occurred when RabG3a^{Q67L} was mated with NET4B, -NAB or the IRQ + Ct, which suggests the last 54 amino acids mediates the interaction with the active RabG3a. Shown in this figure is the growth of one representative diploid colony from each mate after five days growth.

6.17 a). Further truncations of the IRQ domain (aa 464-502) were not made as this fragment did not demonstrate an interaction with the active Rab in the previous experiment. Figure 6.17 shows the truncations of the C-terminal 54 amino acids that were generated, and termed IRQΔ1-7. Primers were designed for each of these additional truncations and are listed in Appendix 1.3. PCR fragments of these truncations were cloned into pDONR207 and then pGADT7 using the Gateway system (according to 2.2.10), and subsequently transformed into the yeast Y187 cells (as described in 2.3.1).

The IRQΔ1-7 constructs, and the previously used IRQ + Ct and IRQ in pGADT7 were mated with the constitutively-active RabG3a^{Q67L} in pGBKT7. Each construct was mated with the reciprocal empty vector as a negative control for autoactivation. Successfully mated diploids were resuspended in water and dropped onto one plate lacking tryptophan and leucine (-WL, as a positive control for diploid colony growth) and one selection plate lacking tryptophan, leucine and histidine with the addition of 2.5 mM 3AT (-WLH + 2.5 mM 3AT).

Figure 6.18 shows the result of this experiment, showing the representative growth of one colony after five days growth. Diploids from the negative control mates did not grow on the selection plate lacking histidine, demonstrating that autoactivation did not occur. The results from this experiment showed that only IRQΔ7 showed a similar level of growth as the IRQ + Ct domain. This truncation has a reduction of the last six amino acids of the IRQ + Ct domain, and terminates this truncation at an arginine (R) residue that is conserved in both NET4B and NET4A. To a lesser extent, IRQΔ1 was able to grow on the selection plate lacking histidine, suggesting an interaction still occurred with the active Rab. This domain has a truncation of ten amino acids from the N-terminal end of the IRQ + Ct domain. IRQΔ6, which is a combination of these two truncations (10aa from the N-terminus and 6aa from the C-terminus of the IRQ + Ct domain), still showed detectable growth on the selection plate lacking histidine. However the growth of IRQΔ6 on the selection plate was drastically reduced compared with IRQΔ1 and IRQΔ7, and only a thin layer of yeast colonies grew. Further truncations from the N-terminus end alone (IRQΔ2/3) or in combination with the truncation from the C-terminus end (IRQΔ4/5) failed to produce any growth on the selection plate suggesting that these truncations prevent the IRQ + Ct from interacting with the active RabG3a. These IRQΔ2-5 truncations all have reductions in the stretch of

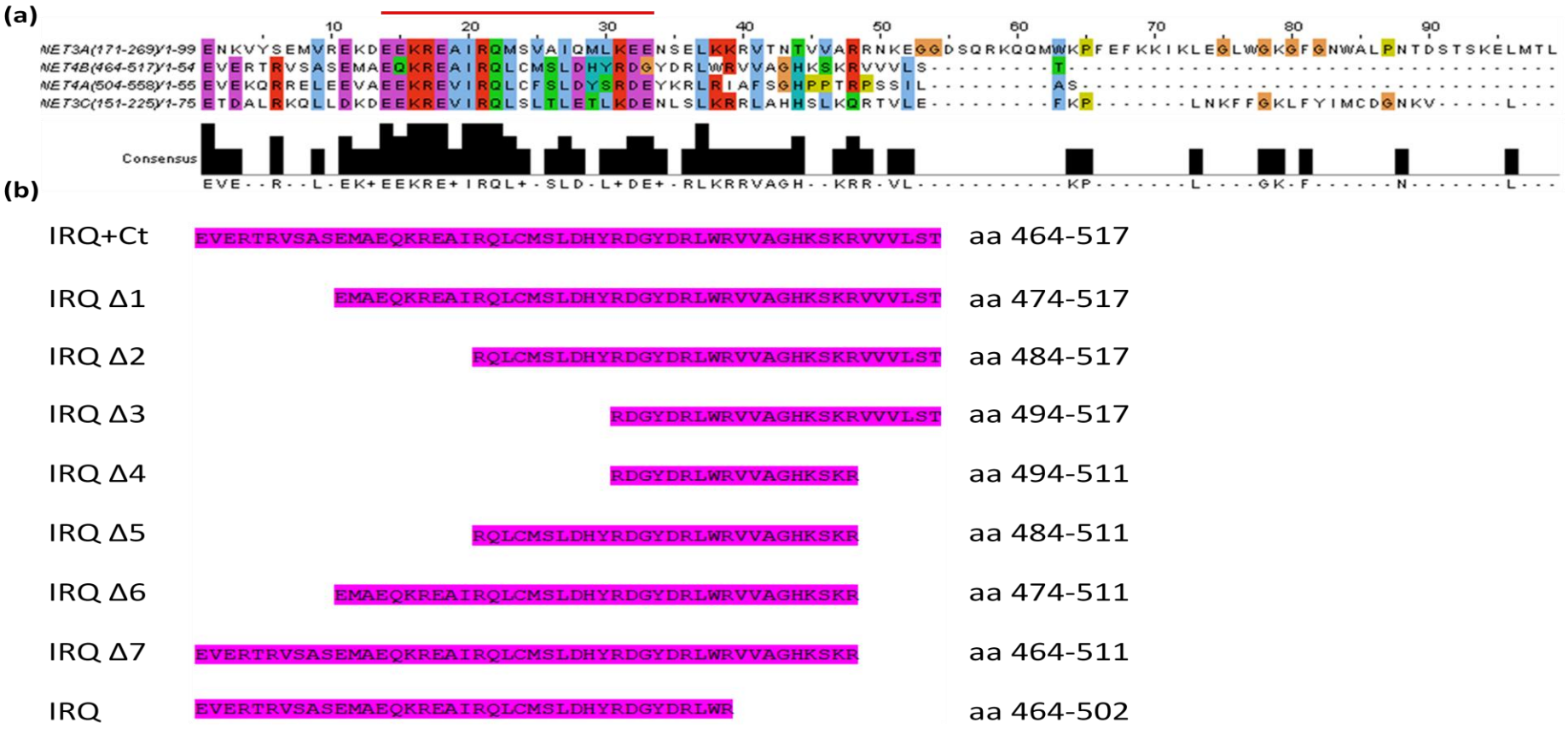

Figure: 6.17: Diagram of the IRQ truncations used to find the minimal active Rab-binding domain. (a) Alignment of the NET IRQ sequences (NET3A$^{171\text{-}269}$, NET3C$^{151\text{-}225}$, NET4A$^{504\text{-}558}$, NET4B$^{464\text{-}517}$) generated using Clustal Omega (Sievers et al. 2011) and visualised using Jalview (Waterhouse et al. 2009), using the ClustalX default colour scheme which corresponds to the amino acid residue type and conservation in the column (see Chapter 3.4; Thompson et al. 1997). The red line above the alignment depicts the stretch of conserved amino acids from the glutamate (E) at NET4B^{474} to the glycine (G) at NET4B^{496}. (b) Diagram of NET4B IRQ truncations used for finding the minimal Rab-binding domain.

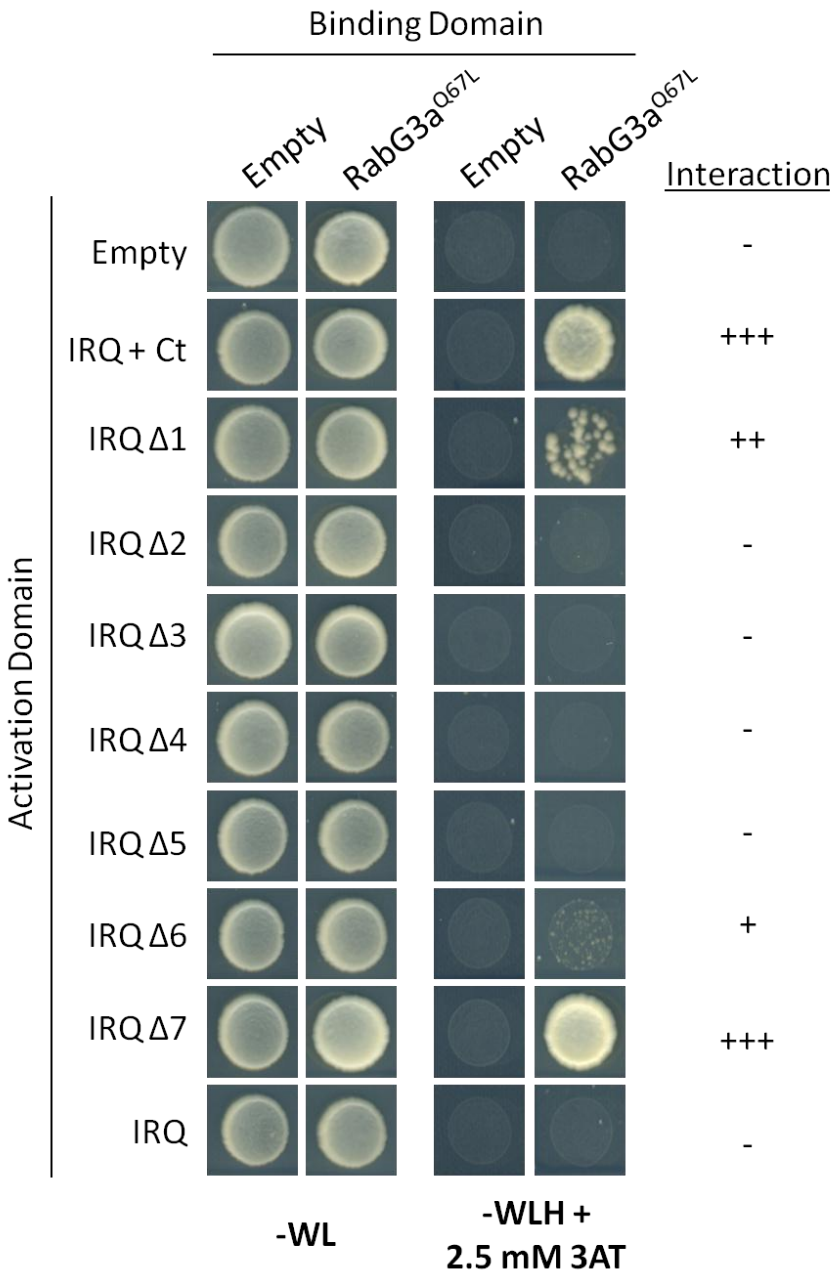

Figure 6.18: One-on-one Y2H mating tests of the IRQ truncations with the constitutively-active RabG3a^{Q67L}. The various IRQ truncations fused to the activation domain (pGADT7) were mated with RabG3a^{Q67L} fused to the DNA binding domain vector (pGBKT7). These constructs were also mated with the empty vector as a negative control for autoactivation. Successfully mated diploids were dropped onto media lacking tryptophan and leucine (-WL, as a positive control for diploid growth) or media lacking tryptophan, leucine and histidine with 2.5 mM 3AT (-WLH + 2.5 mM 3AT, to test for an interaction). Depicted on the right of the yeast colonies is a scale of yeast growth; - = no growth, + = minimal growth, ++ = growth that is still less than the -WL plate, +++ = maximum growth achieved. Maximum growth on selective media occurred when RabG3a^{Q67L} was mated with the IRQ + Ct and IRQΔ7, growth was reduced when RabG3a^{Q67L} was mated with IRQΔ1 and only minimal growth occurred with IRQΔ6. Shown in this figure is the growth of one representative diploid colony from each mate after five days growth.

highly conserved residues that starts at the glutamate (E) at residue 474, to the glycine (G) at residue 496 (NET4B$^{474-496}$).

The results from this experiment suggest that the IRQ domain of NET4B could be responsible for mediating the interaction with the constitutively-active RabG3a. This experiment has shown that the NET4B$^{464-511}$ fragment is able to effectively grow on selective media when mated with the active Rab. Any further truncations of this domain reduce the effectiveness of this growth. However very minimal growth can be seen when the IRQΔ6 truncation was used in this mate. This suggests that the stretch of conserved amino acids (NET4B$^{474-496}$) could be critical in mediating the interaction with NET4B. Furthermore, as growth was stronger when the NET4B$^{464-511}$ fragment was not truncated, this suggests that residues outside of the conserved stretch (NET4B$^{474-496}$) could be important in maintaining the interaction with the active RabG3a. This could be due to the importance of secondary structure across this domain in mediating the Rab interaction. Truncating the NET4B$^{464-511}$ fragment could compromise the secondary structure of this domain and therefore prevent an interaction with the active Rab.

6.5 Conclusion

This chapter has described several different experimental approaches to study the potential interacting proteins of NET4B. The experiments used in this chapter aimed at studying three main themes; the oligomerisation of the NET4 proteins, screening for interactors of NET4B and the IRQ + Ct domain, and characterising the interaction between the NET4 proteins and two vacuolar Rab GTPases. The main experimental approach that was used throughout involved using the Y2H system to test for possible interactions.

The NET family is characterised by the presence of the conserved N-terminal NET actin-binding (NAB) domain, and also stretches of predicted coiled-coil domains in the C-terminus of the protein (Deeks et al. 2012). Coiled-coil domains are known to mediate protein-protein interactions and lead to the oligomerisation of proteins; a feature which can be important for their structure and function (Rose & Meier 2004). Through the use of a "semi-native" SDS-PAGE gel of total protein extracted from Arabidopsis, and subsequent probing with an anti-NET4B antibody, it was shown that NET4B could form part of higher molecular weight complexes. This experiment showed that the anti-NET4B detected the monomeric NET4B band at 60kDa and three

other bands under "semi-native" conditions, which included one band between 100-120kDa and two bands between 150-250kDa. The bands seen in this semi-native SDS-PAGE gel roughly correlated with the sizes of dimeric, trimeric and tetrameric NET4B, which suggests that NET4B could interact with itself to form oligomers.

The ability of the NET4 proteins to form homo- and hetero-oligomers *in vivo* was demonstrated using the Y2H system. The potential for NET4A homo-oligomerisation *in planta*, was also recently confirmed in the TAP-tagging screen as NET4A pulled back itself (Hawkins and Hussey, unpublished). NET4B was not detected as an interactor of NET4A in this screen, however this could be due to the overexpression of NET4A in this system leading to the preferential formation of NET4A homo-oligomers.

As well as testing whether the NET4 proteins could interact with themselves, it was also essential to identify additional binding partners of NET4B. To do this a Y2H screen of an Arabidopsis seedling cDNA library was performed using the full-length NET4B and the IRQ + Ct domain as bait. The IRQ + Ct fragment was selected as bait as relatively little is known about the function of this highly conserved domain. Two independent screens were performed for each bait construct and potential candidates were tested further using one-on-one Y2H mating tests.

Five clones were selected from the NET4B-bait screen for further one-on-one testing; RGP1, RGP2, RIN4L, RabA5c and KUP6. However these further tests showed that the selected clones either did not interact or they autoactivated. The prey plasmids that were rescued using the IRQ + Ct domain as bait yielded two main candidates, RFC4 and DEP1, that are respectively involved in DNA replication and the enzymatic recycling of methionine. Both of these plasmids were shown to interact with the IRQ + Ct domain and full-length NET4B in the one-on-one tests.

Further tests were then performed to reproduce the results from the screen. The splice variant of RFC4 detected in the screen could not be cloned from Arabidopsis and therefore further experiments focussed on DEP1. During these tests, DEP1 and the same interacting fragment identified in the screen, were cloned from Arabidopsis and mated with NET4B and the IRQ + Ct domain. The results from this mating test demonstrated that the DEP1 fragment could interact with NET4B, however the full-length DEP1 did not show evidence for an interaction with NET4B. It is possible that the full-length DEP1 protein is not compatible with the Y2H system. Therefore further *in planta*

experiments, for example FRET-FLIM and co-immunoprecipitation, could be used to examine the NET4B/DEP1 interaction.

Distinct from the Y2H screen performed in this project, two additional screens identified an interaction between the NET4s and a class of Arabidopsis vacuolar Rab GTPases (RabG3s). Firstly, NET4A was sent for TAP-tagging analysis which revealed an interaction with RabG3a. Secondly, through collaboration with Dr. Ian Moore (University of Oxford), NET4B was detected in a pulldown assay using RabG3f as bait. The Rabs identified here belong to the RabG3 subclass that are important in vacuolar trafficking and maintaining vacuole morphology (Rutherford & Moore 2002; Cui et al. 2014; Ebine et al. 2014).

The ability of the NET4s to interact with these proteins was examined further using the Y2H system. As well as using the Rabs in their native state, dominant-negative and constitutively-active mutations of these proteins were created to study whether the NET4 proteins interacted with the GDP- or GTP-bound Rabs. Performing one-on-one mating tests revealed that the NET4s could interact with both RabG3s in their wild-type state and specifically in the constitutively-active (GTP-bound) state. This therefore suggests that the NET4 proteins could be recruited by two vacuolar Rab GTPases and be effectors involved in membrane trafficking events at the tonoplast.

The specificity of the interaction between NET4B and the vacuolar RabG3s was tested further using the Y2H system. NET4B was mated with three additional Arabidopsis Rab GTPases; RabD2a, RabA5c and RabF2a. These Rabs were chosen as they function at distinct membrane trafficking steps and are important at the ER-Golgi interface, Golgi, and PVCs respectively (Rutherford & Moore 2002). The results from this mating test showed that these Rabs could not interact with NET4B, which suggests that NET4B is specific to the RabG3 subclade.

Having established that the NET4s interact specifically with the RabG3 GTPases, it was imperative to identify the NET4 domain that mediates this interaction. To identify the Rab-binding domain, various truncations of NET4B were mated with the constitutively-active RabG3a^{Q67L}. This experiment showed that the last 54 amino acids (the IRQ + Ct domain) of NET4B could mediate the interaction with the active Rab. Conversely, NET4B lacking this domain (-IRQ) could not interact with the active Rab. The results

from this experiment showed that NET4B contains only one Rab-binding domain that is found in the IRQ + Ct domain.

The IRQ + Ct domain of NET4B contains within it the IRQ domain as defined in Chapter 3.4, which is conserved between the NET4s, NET3A and NET3C. Therefore it was important to examine whether the conserved IRQ domain, or the less conserved C-terminal amino acid residues of NET4B, could mediate the interaction with the Rab. Several truncations of the IRQ domain were created and mated with the active RabG3a^{Q67L} which showed that the last six amino acid residues were not essential for Rab interaction. Further truncations of the IRQ then started to impede the growth on selective media. Very minimal growth was still observed for the IRQΔ6 truncation (NET4B$^{474-511}$) suggesting that this could be the smallest truncation that is still able to interact with the Rab. However, the IRQΔ7 truncation (NET4B$^{464-511}$) was the smallest truncation that did not cause a visible disruption to the interaction, in terms of growth on selective media. Both these truncations (IRQΔ6 and Δ7) maintain an intact IRQ domain and therefore it could be suggested that the IRQ domain is the Rab-binding domain of NET4B. As this domain is highly conserved with NET4A, it is likely that this domain represents the Rab-binding domain of both NET4 proteins.

This chapter has resulted in four main findings; the NET4 proteins could hetero-oligomerise to form higher-order structures, NET4B could interact with DEP1, the NET4 proteins can interact with two active GTP-bound vacuolar Rab GTPases, and that the NET4B IRQ domain is responsible for mediating this interaction. This chapter has shown the potential of NET4B to be involved in membrane trafficking events at the vacuole membrane, and the next chapter will focus on describing a potential function for the NET4 proteins at the vacuole in roots, embryos and guard cells.

Chapter 7 - Phenotypic analysis of the *net4* mutant lines

7.1 Introduction

The results from Chapters 4, 5 and 6 have described the subcellular localisation, tissue expression pattern and interacting partners of NET4B. The experiments used in Chapter 4 showed that NET4B can associate with actin *in vivo* and bind to actin directly *in vitro* via the NAB domain. Using *promoter*::GUS analysis, the expression of *NET4B* in the roots, guard cells, floral tissue and embryos was revealed. Through immunogold labeling, using a NET4B specific antibody, NET4B was shown to preferentially localise to the tonoplast in the root. NET4A has also been previously described to associate with actin surrounding the vacuole in the root (Deeks et al. 2012), which suggests that both NET4 proteins have a similar role in the plant. Yeast-2-hybrid studies in Chapter 6 demonstrated that both NET4 proteins could interact with active-RabG3 GTPases, RabG3a and RabG3f, that control membrane trafficking events at the vacuole (Mazel et al. 2004; Cui et al. 2014). As the NET4s interacted with these Rabs specifically in their activated GTP-bound form, it is likely that the NET4s are recruited as effector proteins and are involved in mediating downstream membrane transport at the tonoplast.

Although the results of the previous chapter have shown the subcellular localisation and interacting partners of the NET4s, the precise cellular processes that these proteins are involved in have yet to be determined. In this chapter, several experiments were performed in an attempt to elucidate the potential role of the NET4s. These experiments were based on disrupting the expression profile of the *NET4* genes and subsequently analysing the phenotypic effect this had on the plant.

As there could be potential functional redundancy between *NET4B* and *NET4A*, transgenic lines with alterations to the transcripts of both genes were created and crossed together to produce a double *net4b/net4a* mutant. This mutant was analysed in parallel with the single *net4* mutants for the presence of an observable phenotype. Phenotypic analysis of these mutants focussed on examining primary root growth, vacuole morphology, protein trafficking and rosette leaf transpirational water loss. Generation of the mutant lines and subsequent experiments were performed in tandem with Dr. Tim Hawkins (Durham University).

7.2 Creating the double homozygous *net4b/net4a* mutant lines

7.2.1 Analysis of the *net4b* and *net4a* T-DNA insertion lines

Insertional mutagenesis through Agrobacterium mediated T-DNA insertion is a commonly used tool for reverse genetics in Arabidopsis. T-DNA, on the order of 5-25 kb, is randomly inserted into plant chromosomes and can result in the dramatic disruption of gene function at, or in close proximity, to the insertion site (Bhatt et al. 1996). The site of T-DNA insertion can be mapped through PCR and sequencing-based analysis, which allows the identification of T-DNA insertions in specific genes of interest.

The Salk Institute Genomic Analysis Laboratory (SIGnAL) have catalogued a collection of Arabidopsis genome wide T-DNA insertion events (Alonso et al. 2003), which at the time of publication had determined the location of 88,000 insertions that resulted in the mutation of 21,700 genes. Seed from these lines and other T-DNA insertion lines, including the Syngenta Arabidopsis Insertion Library (SAIL) lines, are publicly available and can be ordered from the Nottingham Arabidopsis Stock Centre (NASC).

The SIGnAL T-DNA Express Arabidopsis Gene Mapping Tool was used to identify T-DNA insertion sites in *NET4B* and *NET4A*. Only one T-DNA insertion line was available for *NET4B* (SALK_056957), and four insertions were catalogued for *NET4A* (SALK_017623, SALK_017630, SALK_083604, SAIL_116_C08). The *NET4B* T-DNA insertion was predicted to be within the first intron, however sequencing of the *NET4B* specific T-DNA insert PCR fragment (as described in 7.2.2) revealed the actual location of this insertion to be in the *NET4B* promoter region (Table 7.1). The location of the insert within the gene can have a dramatic effect on transcript disruption. T-DNA insertions that occur in introns can be spliced out, whereas insertions before the start codon typically reduce transcript levels rather than completely "knock-out" the gene (Wang 2008). All of the *NET4A* insertions were located in exon 3, and could therefore lead to an effective knock-out of the protein coding transcript. The line SAIL_116_C08 has an insertion that is closer to the start codon whereas the other insertions are located further downstream and in close proximity to each other. Lines SAIL_116_C08 and SALK_083604 were selected for crossing with the *net4b* insertion. Using two

independent mutant lines would allow more confidence when ascribing a phenotype to the *net4s*. Table 7.1 shows the insertions sites of the selected lines.

Line	Insertion point in gene	Insertion location	Primers for WT PCR	WT fragment (bp)	Primers for insert PCR	Insert fragment (≈ bp)
NET4B						
SALK_056957	promoter	-172	957 Fw + 957 Rv	1110	Lba1 + 957 Rv	542
NET4A						
SAIL_116_ C08	exon 3	419	C08 Fw + C08 Rv	972	LB3 + C08 Rv	520
SALK_083604	exon 3	1489	604 Fw + 604 Rv	1186	Lba1 + 604 Fw	766

Table 7.1: T-DNA insertion lines for *NET4B* and *NET4A*. Shown here are the confirmed locations of the T-DNA insertion sites. Numbers denote insertion positions relative to the translational start site.

7.2.2 Identification of the homozygous *net4b* and *net4a* T-DNA insertion lines

Before crossing the *net4b* and *net4a* mutant alleles, it was essential to confirm that the insertion lines were homozygous for the intended mutation. Genomic DNA (gDNA) was extracted from the rosette leaves of the mutant lines (SALK_056957, SAIL_116_C08 and SALK_083604) and was used as a template DNA for two genotyping PCR reactions (as described in 2.2.15). Figure 7.1 shows the specific primers used for these genotyping PCR reactions (see Appendix 1.7 for primer sequences). As well as these specific primer pairs, the *mago* forward and reverse primers were used to amplify a 1868 bp fragment of the *MAGO NASHI* gene (At1g02140), which acted as a positive control for the PCR reactions.

The first PCR reaction, termed the wild-type PCR, amplified a band using gene specific primers at either side of the T-DNA insertion site. These primers were designed to be roughly 500 bp away from the insertion site in both directions and would therefore amplify a band of around 1 kb if the wild-type allele was present. The size of the wild-type bands ranged from 972 to 1186 bp in length (see Table 7.1).

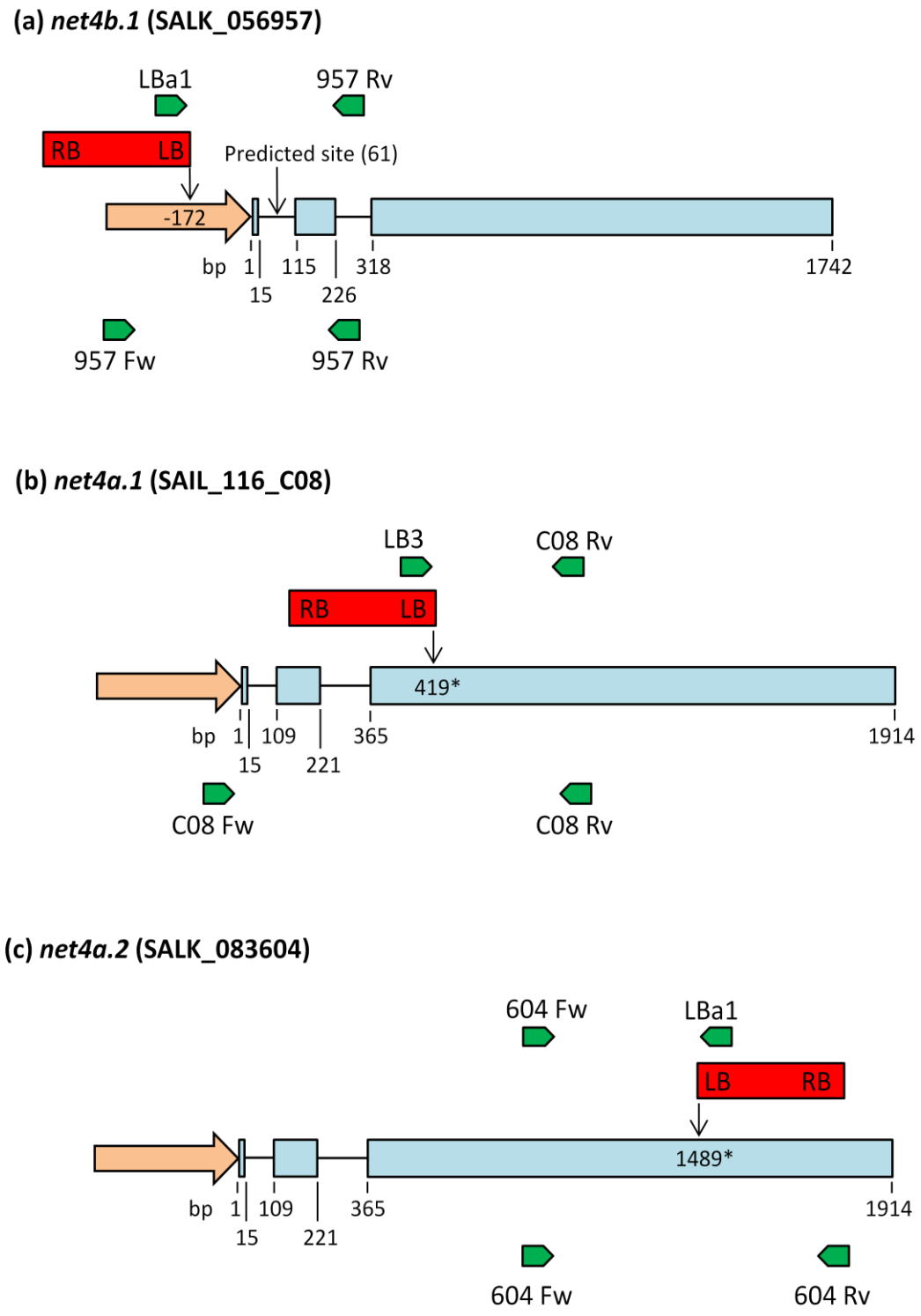

Figure 7.1: Positions of the T-DNA insertion lines and the primers used for genotyping. Diagram shows the T-DNA position and primers used for the (a) SALK_056957, (b) SAIL_116_C08 and (c) SALK_083604 lines. Exons are depicted in blue, introns in black and promoter region with the orange arrow. The T-DNA insertion is shown by the red box, and the direction of the insert is shown by the orientation of the left border (LB) and right border (RB). Primers used are shown by the green arrows. Gene specific primers (shown below the gene) were used to detect the wild-type allele, and the left border primer with the corresponding gene specific primer (above the gene) detected the mutant allele.

The second PCR reaction, termed the insert reaction, amplified a band using the T-DNA left border specific primer (either LBa1 for SALK lines, or LB3 for SAIL lines) and the gene specific forward or reverse primer, depending on the direction of the T-DNA insert. This band would be detected if the T-DNA was present in the gene and represents the mutant allele. The size of these bands ranged between 520 to 766 bp.

Azygous plants would produce a band in the wild-type PCR but not the insert PCR. Plants that were heterozygous for the mutant allele would produce a band in both the wild-type PCR and the insert reaction, whereas homozygous plants would only produce a band in the insert reaction. Figure 7.2 shows a representative genotyping gel for the SAIL_116_C08 line, showing all three identified genotypes.

Once homozygous plants for each T-DNA insertion line were identified, the precise location of the T-DNA insert was determined. This was achieved by amplifying the insert PCR fragment, using either LB3 or LBa1 and the respective gene specific primer, and then sequencing this fragment using a primer that was more proximal to the left border (LB3 for SAIL and LBb1 for SALK, see Appendix 1.9 for primer sequences). The resultant sequence was aligned to the known *NET4A* and *NET4B* sequences, allowing the left-border T-DNA insertion site to be determined. This confirmed the location of SALK_056957 in the promoter, and the two *NET4A* mutant lines in exon 3 (see Table 7.1).

The plants that were confirmed as homozygous through the genotyping PCRs were allowed to self-pollinate, leading to a homozygous T_4 generation that could be used for subsequent crossing. The seed for each homozygous line was pooled and the different lines were designated as follows: *net4b.1* for SALK_056957, *net4a.1* for SAIL_116_C08, and *net4a.2* for SALK_083604.

7.2.3 Strategy for creating the double homozygous *net4b/net4a* lines

Genes that share high homology can exhibit functional redundancy, where the absence of one gene is compensated by the other. Therefore a phenotype may not be identified in a single mutant but could be observed when two or more closely related genes are mutated. As the *NET4s* are closely related and belong to the same subfamily of the NETs, a double mutant in both genes was created which was analysed for an observable phenotype alongside the single mutants that were generated in the cross.

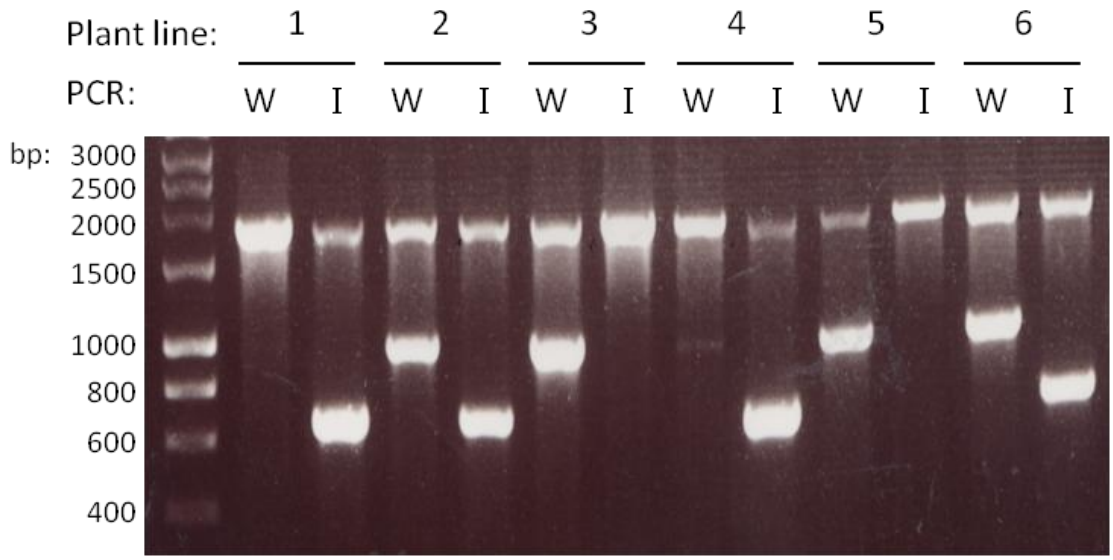

Figure 7.2: Example of the PCRs used to genotype the single T-DNA insertion lines. Two PCRs were run using gDNA from the *net4* mutant alleles to confirm the presence of the T-DNA insertion. Shown here is a representative genotyping PCR for *net4a.1* (SAIL_116_C08). The wild-type PCR (W) used the C08 Fw/Rv primers to amplify a band at either side of the insert (972 bp). The insert (I) PCR used the C08 Rv and LB3 primers to amplify a band if the insertion was present (520 bp). As a control, the *mago* Fw/Rv primers were used to ensure the PCR reaction had worked (1868 bp). Azygous plants produced a band in the wild-type PCR but not the insert PCR (plants 3 and 5). Heterozygous plants amplified a band in both PCR reactions (plants 2, 4 and 6). Homozygous plants only produced a band in the insert PCR (plant 1). Hyperladder I was used as a molecular weight marker.

Creating the double *net4b/net4a* mutant homozygous lines involved various different stages as depicted in Figure 7.3. Firstly, the homozygous *net4b.1*, *net4a.1* and *net4a.2* lines were grown up to the flowering stage for crossing. Two crosses were made which would generate *net4b.1/net4a.1* and *net4b.1/net4a.2* double mutant lines. In order to prevent self-pollination, the flowers from the *net4b.1* lines were dissected to remove any anthers; leaving the *net4b.1* stigma which was pollinated with pollen from the *net4a.1* or *net4a.2* lines. The reciprocal cross was also generated, pollinating either the *net4a.1* or *net4a.2* stigmas using anthers from *net4b.1*.

The seed from these cross-pollinated plants were collected and grown under normal conditions. The F_1 generation should be heterozygous for each insertion and this was confirmed through two genotyping PCR reactions. Genomic DNA was extracted from the leaves and used as a template for the insert PCR reactions of the respective crosses (e.g. *net4b* insert and *net4a* C08 insert PCR for the *net4b.1/net4a.1* cross). These reactions used the same primers as used to find the single homozygous lines (shown in Figure 7.1). Heterozygous plants were found in both genetic crosses and these plants were allowed to self-pollinate to produce the F_2 generation.

The F_2 generation represents a segregating population and 1 in 16 plants should be azygous, single homozygous *net4b*, single homozygous *net4a* and double homozygous *net4b/ne4a*. To identify these different genotypes, genomic DNA was extracted from rosette leaves of the different plants and used as a template for four genotypic PCR reactions. All the PCR reactions used the same primer pairs as used to genotype the single homozygous lines as shown in Figure 7.1, as well as the *mago* primers to produce a positive control band of 1868 bp in all reactions.

The first two reactions were the wild-type PCR reactions and used gene specific primers at either side of the T-DNA insert, and would amplify a band of 1110 bp for *NET4B.1*, and either a 972 bp fragment for *NET4A.1* or a 1186 bp band for *NET4A.2*, depending on the genetic cross that was made. This band would only be amplified if the wild-type allele was present. The other two PCR reactions were the insert PCR reactions and used the gene specific primer with the T-DNA left border primer (LBa1 or LB3); this would amplify fragments of 542 bp for *net4b.1*, 520 bp for *net4a.1* and 766 bp for *net4a.2*. This insert band would only be amplified if the mutant allele was present. Using these four different PCR reactions, it was possible to determine the genotypes of the F_2 generation.

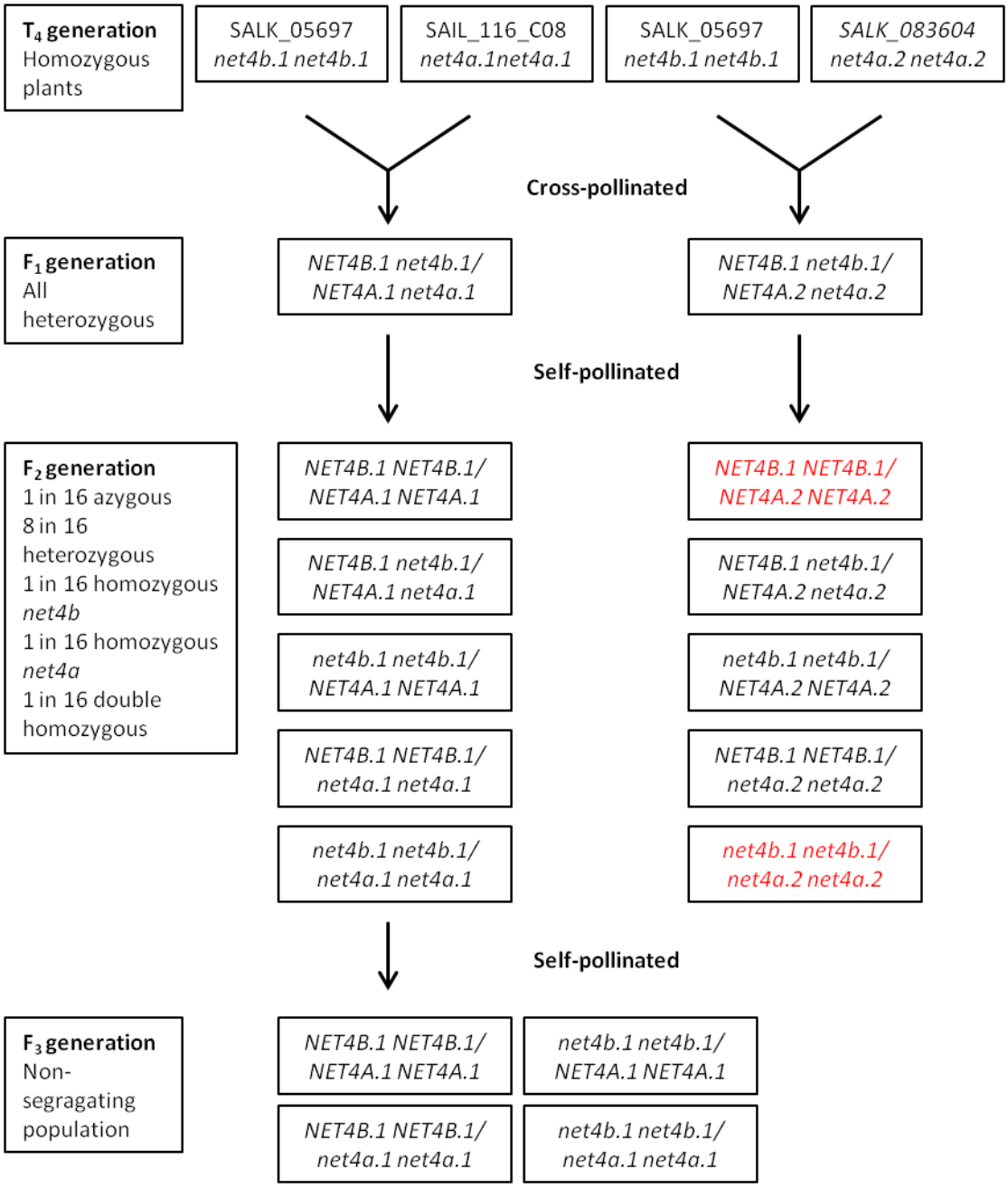

Figure 7.3: Strategy for generating the homozygous *net4b.1/net4a.1* double mutant lines. Anthers from the homozygous line of *net4b.1* were used to cross-pollinate both *net4a.1* and *net4a.2* homozygous lines, and the reciprocal cross was also performed. The F_1 generation were confirmed to be heterozygous for both insertions through genotyping PCR reactions. In the F_2 generation only the *net4b.1/net4a.1* cross produced azygous, single homozygous mutants and the double homozygous mutants. These plants were allowed to self-pollinate producing the non-segregating lines in the F_3 generation which were used for phenotypic analysis. The *net4b.1/net4a.2* did not produce azygous or double homozygous plants (shown in red), and this cross was not continued for further experiments. Diagram adapted from Calcutt (2009).

Azygous plants would only produce bands in the wild-type PCR reactions and not the insert reactions, whereas the double homozygous mutants would only produce bands in the insert PCR reactions. The single *net4b* homozygous mutants would produce bands in the *net4b* insert reaction and the *NET4A* wild-type reaction, and would not amplify bands in the *NET4B* wild-type reaction or the *net4a* insert reaction. Similarly, the single *net4a* homozygous mutants would amplify bands in the *net4a* insertion reaction and the *NET4B* wild-type reaction, and would not produce bands in the *net4b* insertion reaction or the *NET4A* wild-type reaction.

For the *net4b.1/net4a.1* cross, 42 plants were genotyped in the F_2 generation, which included: three ayzgous plants, two homozygous *net4b.1*, three homozygous *net4a.1* and six double *net4b.1/net4a.1* homozygous plants. Table 7.2 (a) shows the full range of genotypes that were observed from this cross. Segregation analysis was performed on the different genotypes to assess whether they segregated according to Mendelian inheritance of a dihybrid cross. Table 7.2 (b) shows the Chi-squared analysis that was performed to analysed whether the observed genotype segregation differed from the expected ratios. As only a small number of plants were genotyped, several genotypes were grouped together as they produced low expectation values. The results of this analysis suggest that the genotypes observed did not significantly differ from the expected ratios, which suggests that the genotypes segregated according to Mendelian inheritance ($\chi^2 = 2.25$, df = 4, $P > 0.5$).

A total of 125 plants were genotyped for the *net4b.1/net4a.2* cross in the F_2 generation, however the genotyped plants appeared to segregate differently to the expected ratios. Out of the 125 plants, no azygous or double homozygous *netb.1/net4a.2* plants were found, however all the other possible genotypes were observed. Table 7.2 (c) shows the different genotypes that were observed and the associated Chi-squared analysis for this cross. From this analysis, there was strong evidence to suggest that the observed ratios differed significantly from the expected ratios and that this difference could not be due to chance alone ($\chi^2 = 87.13$, df = 8, $P < 0.005$).

There are several possible reasons why this cross did not segregate according to Mendelian inheritance. Genetic linkage can affect the inheritance of genes, as genes that are located close to each other on the same chromosome could be inherited together. However, as *NET4B* is located on chromosome 2 and *NET4A* is located on chromosome 5, genetic linkage could not be responsible for the observed segregation pattern. It is

(a) Observed F_2 generation genotypes of the *net4b.1/net4a.1* cross

										Total
EXPECTED RATIO	1	2	1	2	4	2	1	2	1	16
GENOTYPE	AABB	AABb	AAbb	AaBB	AaBb	Aabb	aaBB	aaBb	aabb	
OBSERVED	3	5	2	5	14	3	3	1	6	42

(b) Chi-squared analysis of the *net4b.1/net4a.1* F_2 generation

						Total
EXPECTED RATIO	3	3	2	4	4	
GENOTYPE	AABB + AABb	AAbb +Aabb	AaBb	AaBb	aaBB +aaBb + aabb	
OBSERVED (O)	8	5	5	14	10	42
EXPECTED (E)	7.88	7.88	5.25	10.50	10.50	42.00
O-E	0.13	-2.88	-0.25	3.50	-0.50	
(O-E)2	0.02	8.27	0.06	12.25	0.25	
(O-E)2/E	0.002	1.05	0.01	1.17	0.02	**2.25**

(c) Chi-squared analysis of the *net4b.1/net4a.2* F_2 generation

										TOTAL
EXPECTED RATIO	1	2	1	2	4	2	1	2	1	16
GENOTYPE	AABB	AABb	AAbb	AaBB	AaBb	Aabb	aaBB	aaBb	aabb	
OBSERVED	0	7	18	11	57	6	20	6	0	125
EXPECTED	7.8	15.6	7.8	15.6	31.3	15.6	7.8	15.6	7.8	125
O-E	-7.8	-8.6	10.2	-4.6	25.8	-9.6	12.2	-9.6	-7.8	
(O-E)2	61.0	74.4	103.8	21.4	663.1	92.6	148.5	92.6	61.0	
(O-E)2/E	7.8	4.8	13.3	1.4	21.2	5.9	19.0	5.9	7.8	**87.13**

Table 7.2: Genotypes of the F_2 generation from the *net4b.1/net4a.1* and *net4b.1/net4a.2* crosses. The results of the genotyping PCR reactions were used to determine the different genotypes of the F_2 generation and whether they matched the expected ratio of Mendelian inheritance from a dihybrid cross. A= wild-type NET4A, a = mutant *net4a*, B = wild-type NET4B, b = mutant *net4b*. (a) Observed genotype ratios of the *net4b.1/net4a.1* cross. (b) Chi-squared analysis of the *net4b.1/net4a.1* cross. Several genotypes were grouped together as the small sample size created expected values that are incompatible with the Chi-squared test. The observed genotypes did not significantly differ from the expected ratios of Mendelian inheritance ($\chi^2 = 2.25$, df = 4, $P > 0.5$). (c) Chi-squared analysis on the observed genotype ratios of the *net4b.1/net4a.2* cross. No azygous or double homozygous plants were found and there was sufficient evidence to suggest that the observed genotypes significantly differed from the expected ratios and that this difference was not due to chance alone ($\chi^2 = 87.13$, df = 8, $P < 0.005$).

feasible that there are additional T-DNA insertions in the two genetic lines that are not being genotyped and could therefore influence the segregation patterns. It is possible that another T-DNA insertion has a lethal affect on plant viability and that the *net4b.1* or *net4a.2* mutations repress this other mutation from showing its phenotype. Therefore when neither of the *net4* insertions are present a non-viable embryo would be produced, which would account for the observed lack of azygous plants. Furthermore it is possible that the double homozygous *net4b.1/net4a.2* mutation could be embryonically lethal, which would therefore prevent the double mutant being produced in the F_2 generation.

As the *net4b.1/net4a.1* cross produced all desired genotypes, this cross was continued for further analysis. Figure 7.4 shows the genotyping PCR reactions that were used to identify the azygous (A1), *net4b.1* homozygous (B1), *net4a.1* homozygous (E1) and *net4b.1/net4a.1* double homozygous plants (B3). These plants were allowed to self-pollinate to produce the non-segregating F_3 generation of plants which were used for subsequent phenotypic analysis.

Before starting the phenotypic analysis of these lines, it was essential to assess the effect the T-DNA insertion mutants have on the transcripts of the *NET4B* and *NET4A* genes. Reverse-transcription-PCR (RT-PCR) was used to assess the transcripts levels of both *NET4* genes in all the genotypes. In addition, quantitative PCR (qPCR) was used to quantify the level of *NET4B* transcript in the mutant lines and the protein level of NET4B was assessed through Western blot analysis with an anti-NET4B antibody.

7.2.4 Confirming the disruption of the *NET4B* and *NET4A* transcripts using RT-PCR

RT-PCR was used to assess whether the *NET4B* and *NET4A* transcripts had been disrupted by the T-DNA insertions. RNA was extracted from the mutant plant tissue and used to synthesise cDNA using a reverse-transcriptase enzyme (as described in 2.2.5 and 2.2.6). This cDNA would therefore represent the mRNA produced by the mutant plant. The cDNA was used as a template in a PCR reaction with gene specific primers and if a band was less intense or absent in the mutant then this would suggest that the T-DNA insertion had disrupted gene transcription.

RNA was extracted from 15-day old vertically grown seedlings as both *NET4* genes are highly expressed in the roots. The total amount of RNA was normalised to 3 μg, and was used to synthesise cDNA using oligo(dT)15 primers and the GoScript Reverse

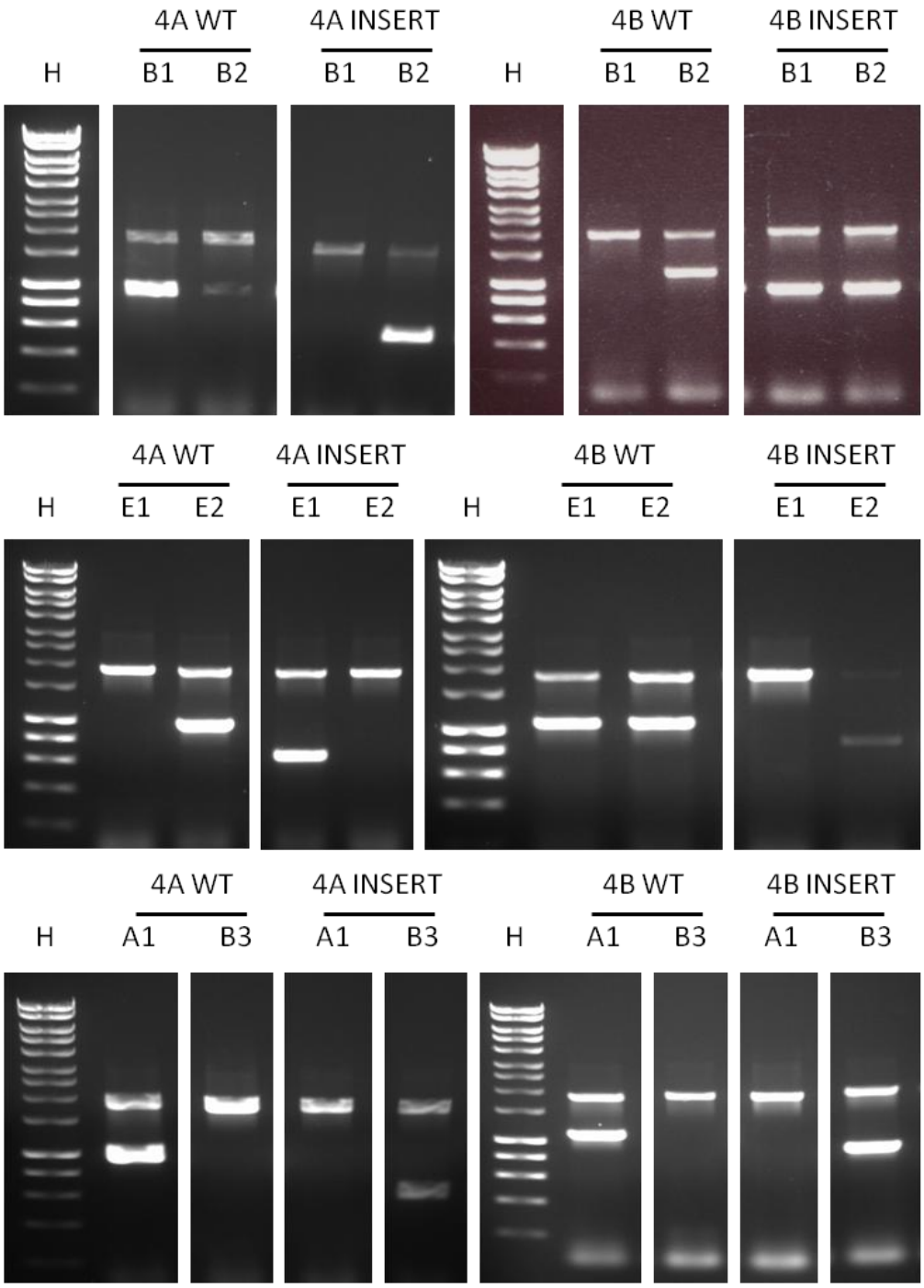

Figure 7.4: Identification of *net4* mutants used for phenotypic analysis. Genomic DNA was extracted from leaves of the F_2 generation and used as a template for four genotyping PCR reactions. 4A Wild-type (WT) and 4B WT PCR reactions used the C08 Fw/Rv and 957 Fw/Rv primers, respectively, to amplify a band spanning the T-DNA insertion site (972 and 1110 bp respectively). For the insert PCR reactions, C08 Rv and LB3 were used for *net4a.1*, and 957 Rv and LBa1 primers were used for *net4b.1* (band size of 520 and 542 bp respectively). B1 represents a single *net4b.1* homozygote line (4B insert and 4A WT band present, 4B WT and 4A insert absent), E1 represents a single homozygote *net4a.1* line (4A insert and 4B WT band present, 4A WT and 4B insert absent), A1 represents an azygous line (only WT bands), B3 represents a double homozygote (only insert bands). B2 and E2 were included as they act as internal controls for the PCR reactions. The 1868 bp band represents the *mago* F/R primers used as a control for the PCR reaction. Hyperladder I was used as a molecular weight marker.

Transcription System. This cDNA was then used as a template for a PCR reaction using various different primer combinations, as shown in Figure 7.5 (see Appendix 1.8 for primer sequences). As the *net4b.1* T-DNA insertion is in the promoter region only one primer pair was used, q4B Fw/Rv (amplifying a 186 bp fragment). For the *net4a.1* mutation, three different primer combinations were used; q4A.1 Fw and q4A.2 Rv amplified a band that spanned the T-DNA insertion (697 bp fragment); q4A.1 Fw/Rv (166 bp fragment) and q4A.3 Fw/Rv (148 bp fragment) amplified fragments upstream and downstream of the insertion respectively. As a positive control, gene specific primers were used that amplified a fragment 187 bp of the Arabidopsis *ELONGATION FACTOR 1-α* (*EF1α*, At5g60390), as this has been previously shown to be a consistent reference gene (Czechowski et al. 2005). In these PCR reactions, cDNA from two different double mutant parent lines, B3 and C3, were used to ensure that the double mutant was correctly identified. As a negative control dH_2O was used as a template to ensure that a band was not amplified without cDNA.

The results of the RT-PCR are shown in Figure 7.6. Using the q4B Fw/Rv primers, a band was amplified in each genetic background. However the band appeared slightly fainter in the *net4b.1* and *net4b.1/net4a.1* lines, suggesting that the transcript level is reduced in these mutants compared to the azygous and *net4a.1* lines. Therefore it is likely that the *net4b.1* allele is a "knock-down" mutant rather than a "knock-out", which is consistent with the T-DNA insertion being in the promoter region (Wang 2008).

For the *net4a.1* allele, using primers at either side of the T-DNA insertion could produce a band in the azygous and *net4b.1* PCR reactions but not in the *net4a.1* or the double mutant PCR reactions. However using primers both upstream and downstream of the T-DNA insertion could produce a band in all genotypes. This suggests that the *net4a.1* T-DNA insertion cannot produce a fully functional *NET4A* transcript as it is disrupted by the presence of the T-DNA. As upstream and downstream fragments were amplified, this suggests that transcription could continue through the T-DNA insertion in the *NET4* gene, producing a non-functional transcript. The extension time during this PCR was sufficient to amplify bands of up to 5 kb therefore if transcription continues through the T-DNA insert then the total NET4A-TDNA transcript must be greater than 5 kb. Although NET4A transcripts are expressed both upstream and downstream of the insertion, protein translation could be stopped or disrupted by the T-DNA insert (Wang 2008). Future work is currently underway to study whether the NET4A protein levels are altered in the mutant backgrounds using a NET4A specific antibody.

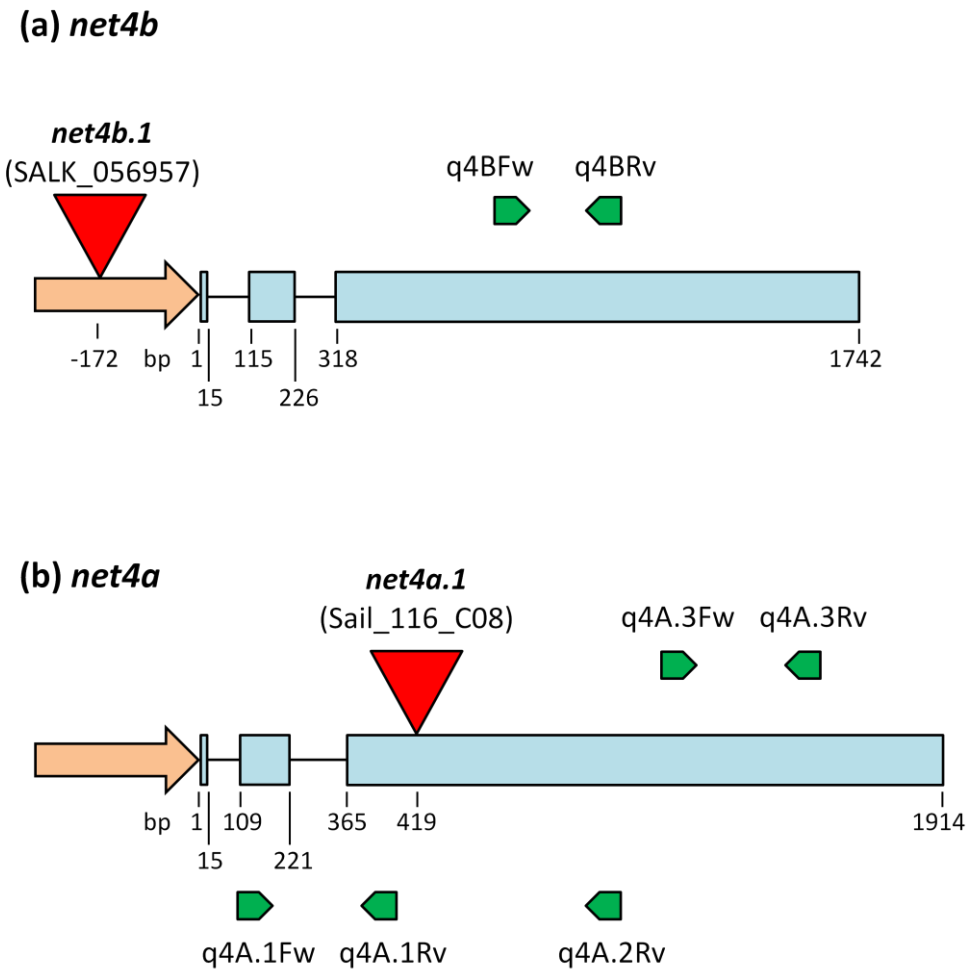

Figure 7.5: Designing primers to assess the transcript disruption in the T-DNA insertion lines. Diagram shows the position of the gene-specific primers that were used to analyse the disruption of the transcripts through RT-PCR. Exons are depicted in blue, introns in black, promoter in orange, T-DNA insertion with the red triangle, and the gene-specific primers with green arrows. (a) Only one primer pair was used for the *net4b.1* transcript as the insertion is in the promoter. (b) Several primer pairs were used to assess the transcript of *net4a.1*; q4A1 Fw + q4A.2 Rv were used to test whether a functional *NET4A* transcript could be made, q4A1 Fw/Rv amplified a fragment upstream of the T-DNA, q4A3 Fw/Rv amplified a fragment downstream of the insertion. The upstream and downstream fragments would show whether a truncated transcript could be made.

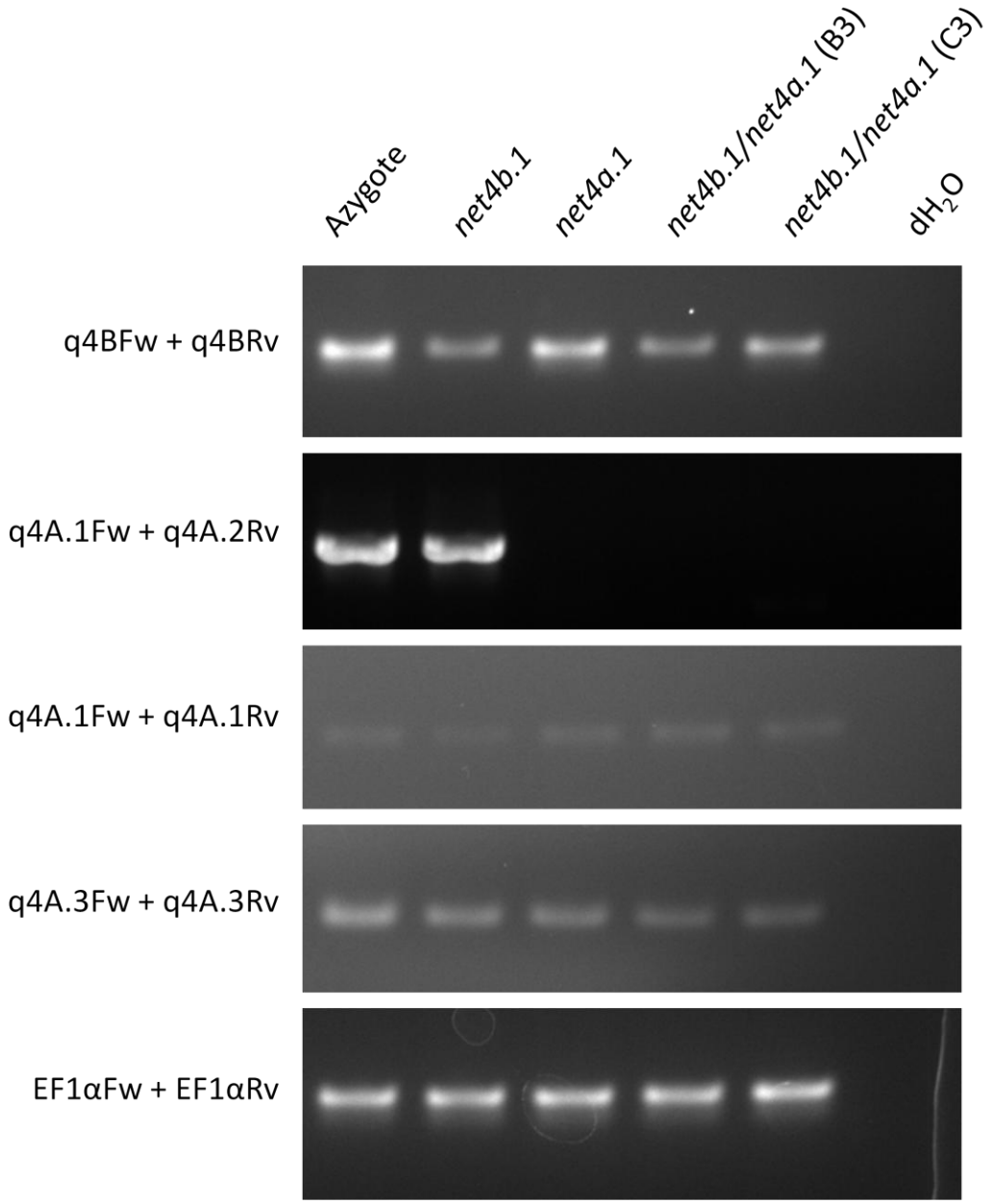

Figure 7.6: Analysis of the *NET4* transcripts in the mutant lines using RT-PCR. RNA extracted from the mutant lines was used to synthesis cDNA using a reverse-transcriptase enzyme (GoScript, Promega). The cDNA from each genotype was used in a PCR to amplify gene specific bands and therefore test the disruption caused by the T-DNA insertions. Two different double mutant parent plants (B3 and C3) were used to ensure they had been correctly genotyped. As a negative control dH_2O was used instead of a cDNA template. Using *NET4B* specific primers showed that the transcript levels could be reduced in the *net4b.1* and *net4b.1/net4a.1* mutants. Primers at either side of the *net4a.1* T-DNA insert could not be amplified in the *net4a.1* or *net4b.1/net4a.1* mutants, showing that the *NET4A* transcript was disrupted. However both upstream and downstream fragments were amplified, suggesting that *NET4A* transcription continues through the T-DNA insert. Primers amplifying the reference gene *EF1α* were used to ensure equal loading in all samples.

As the results of the RT-PCR were consistent between the two different double mutant lines, B3 and C3, only line B3 was used for further analysis.

7.2.5 Confirming the reduction of *NET4B* in the mutant lines using qPCR

The results of the RT-PCR showed that a fully functional *NET4A* transcript could not be produced in the *net4a.1* line. However, the *net4b.1* insertion caused a reduction in *NET4B* transcript levels and quantitative PCR (qPCR) was therefore used to accurately determine the expression level of *NET4B* in the mutant lines.

The cDNA that was previously used for the RT-PCR was used for a qPCR reaction using the SensiFAST SYBR No-ROX Kit (as described in 2.2.18). This kit allowed the determination of the *NET4B* transcript levels in the insertion lines through the use of the SYBR green dye which is incorporated into DNA during the PCR reaction. SYBR green is a fluorescent dye that changes conformation when bound to double-stranded DNA (dsDNA). This change in conformation allows the dye to absorb light at the excitation maxima of 491 nm and emit light at the maxima of 521 nm. As the PCR reaction proceeds, the level of the PCR product and therefore dsDNA exponentially increases, and this can be observed by an increase in SYBR green fluorescence. The time at which this increase occurs and the velocity to which it occurs can be monitored in real-time, therefore allowing the quantification of transcript levels. If the starting level of DNA is lower in a T-DNA insertion mutant than in an azygous sample, then this would lead to an increased amount of time before the SYBR green/dsDNA complex can be detected.

To quantify the level of *NET4B* transcripts in the different mutant lines, the q4BFw/Rv primers were used to amplify a band of 186 bp (as shown in Figure 7.5). The level of the *NET4B* transcript in all genotypes was determined by comparing the relative level of the q4BFw/Rv PCR product with the level of the reference gene *EF1α* PCR product, as was used in the RT-PCR. As well as using the cDNA as a template, a no template control (NTC) for the different primers, and a no primer control (NPC) for the different cDNA templates, were run to ensure the specificity of the qPCR.

RNA was extracted from three biological replicates of the different genetic lines, which was used to make cDNA for the qPCR reactions. Each biological replicate used three technical repeats for both primer pairs which increased the accuracy of the data produced. The cDNA abundance of *NET4B* was determined in the different genetic

backgrounds, relative to the *EF1α* reference gene and Table 7.3 and Figure 7.7 show the results of this qPCR analysis. There is sufficient evidence to suggest that the expression of *NET4B* is significantly different among the different genotypes (ANOVA; $F_{3,8}$ = 11.322, P = 0.003). Mean relative cDNA levels of *NET4B* are 3.93E-03 in the azygous lines, 9.31E-04 in *net4b.1,* 3.88E-03 in *net4a.1* and 1.06E-03 in the *net4b.1/net4a.1* double mutant. The *NET4B* transcript found in the *net4b.1* and *net4b.1/net4a.1* line was approximately a third of the level found in the azygous line.

The level of *NET4B* was significantly reduced when comparing the azygous level with the transcript level in *net4b.1* and the *net4b.1/net4a.1* double mutant (Tukey test; azygous and *net4b.1*, P = 0.012; azygous and *net4b.1/net4a.1*, P = 0.018). However there was no significant difference between the level of *NET4B* transcript in the single mutant and the double mutant (Tukey test; *net4b.1* and *net4b.1/net4a.1*, P = 0.989). This suggests that the transcription of *NET4B* does not increase to compensate for the disruption to *NET4A* in the double mutant.

7.2.6 Confirming the reduction of NET4B in the T-DNA insertion line through Western blot analysis

Having demonstrated that the *NET4B* transcript is reduced in the *net4b* mutants, the anti-NET4B antibody was then used in a Western blot to test whether there was a reduction of NET4B protein in the different mutant backgrounds.

Total protein was extracted from 15-day old vertically grown *net4b.1, net4a.1*, *net4b.1/net4a.1*, and azygous plants, and quantified using the Bio-Rad Detergent-Compatible (Dc) Bradford Assay kit (according to 2.4.7). Equal amounts of total protein (50 μg) from each genetic background were separated on a 10% SDS-PAGE gel and subsequently transferred to a nitrocellulose membrane. The membrane was probed with the anti-NET4B (1:500) and the mouse monoclonal C4 anti-actin (1:3000) antibody, which detects a single band at 42 kDa. The anti-actin antibody functions as a control to ensure equal loading amongst the samples. This Western blot was repeated in triplicate with three biological replicates.

Figure 7.8 (a) shows a representative Western blot using the anti-NET4B and anti-actin antibodies on total protein extracted from the mutant plants. The intensity of the band detected by anti-NET4B antibody shows a clear reduction in the *net4b.1* and

Genetic background	Relative cDNA abundance	Standard error	% of azygous level of transcript still present in the mutant
Azygous	2.52E-02	3.93E-03	100.00
net4b.1	8.06E-03	9.31E-04	31.94
net4a.1	2.53E-02	3.88E-03	100.26
net4b.1/net4a.1	9.31E-03	1.06E-03	36.88

Table 7.3: qPCR analysis to identify the extent of *NET4B* transcript reduction in the *net4* mutant lines. Results obtained from the qPCR analysis, showing the level of *NET4B* transcript relative to the *EF1α* reference gene.

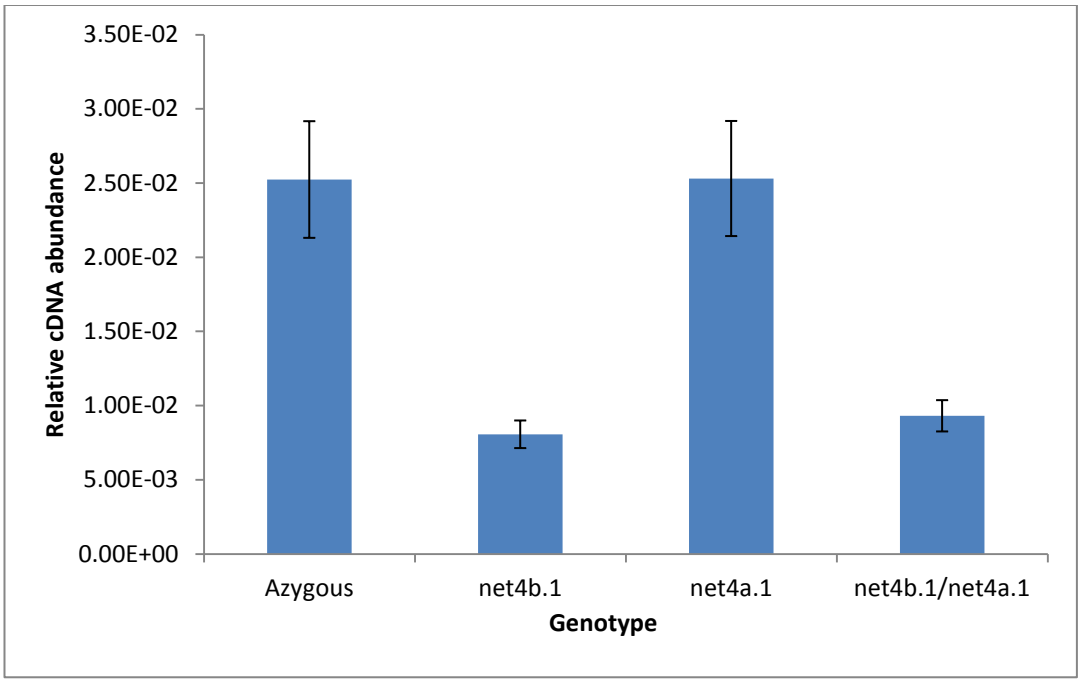

Figure 7.7: qPCR analysis of the *NET4B* transcript in the different genetic lines. Graphical representation of the qPCR data showing the average level of *NET4B* transcript relative to the *EF1α* reference gene. Transcript levels of *NET4B* are significantly reduced in the *net4b.1* and *net4b.1/net4a.1* mutants. Error bars represent standard error of the mean.

(a)

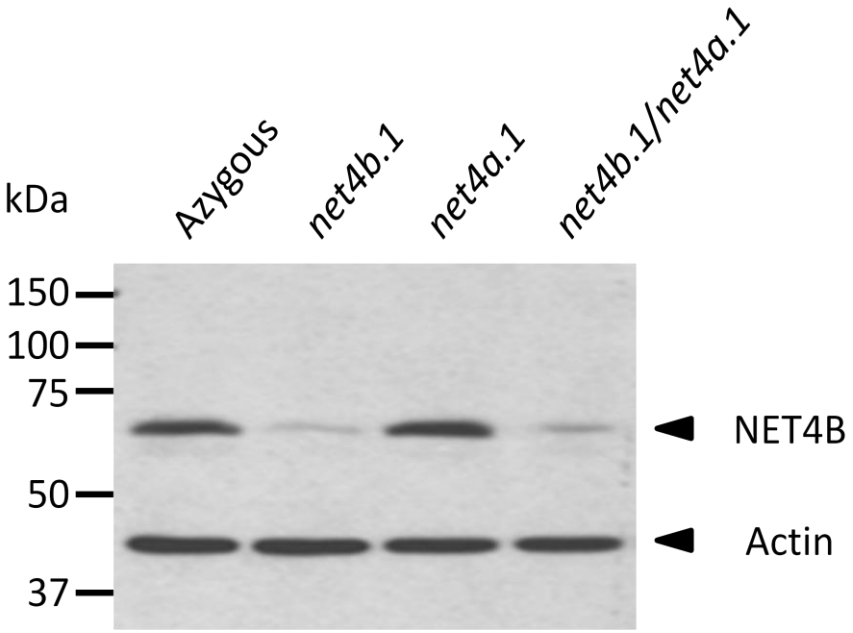

(b)

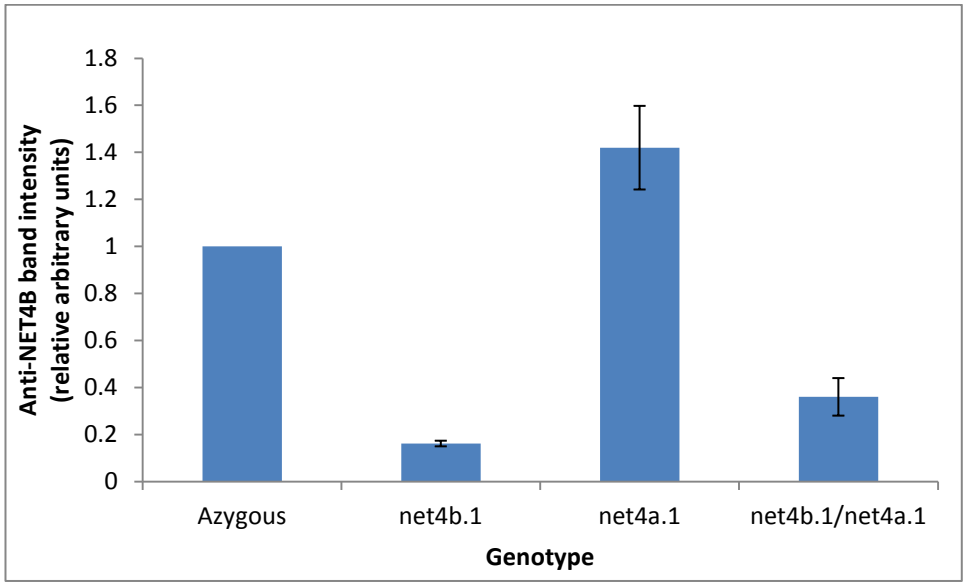

Figure 7.8: Analysis of the reduction of NET4B in the *net4* mutant lines using the anti-NET4B antibody. The reduction of NET4B in the mutant lines was confirmed through Western blot analysis on total protein extracted from the different genotypes. (a) Representative Western blot using the anti-NET4B antibody and anti-actin as a loading control. The intensity of the anti-NET4B band was decreased in the *net4b.1* and *net4b.1/net4a.1* mutant lines, suggesting the protein levels are reduced in the mutants. (b) The intensity of the anti-NET4B band was quantified through densitometry and shown here is a graphical representation of the data. The anti-NET4B band intensity, in relative arbitrary units, was first normalised to the loading control and then calculated as a proportion of the azygous level. Error bars represent standard error of the mean.

net4b.1/net4a.1 mutant lines, suggesting that the *net4b.1* T-DNA insertion affects both the transcript and protein levels of the *NET4B* gene.

The extent of the reduction in anti-NET4B band intensity was quantified through densitometry (as described in 2.7.2). Firstly, the intensity of the anti-NET4B and anti-actin band was measured for each genotype using the FIJI ImageJ software (Schindelin et al. 2012). The intensity of the NET4B bands were then normalised to the actin loading control, in that lane, to account for any differences in loading. Finally, the intensity of the anti-NET4B bands in the mutant lanes were determined relative to the azygous control. The results of this analysis are shown in Figure 7.8 (b) which depicts the average intensity of the anti-NET4B band in relative arbitrary units. This analysis showed that the anti-NET4B band in the *net4b.1* and *net4b.1/net4a.1* double mutant was 16% and 36%, respectively, of the total intensity seen in the azygous control. This therefore demonstrates that the NET4B protein level is greatly reduced in the single *net4b.1* and double *net4* mutant.

7.3 Analysis of root growth in the mutant lines

Both NET4B and NET4A have been shown to associate with the vacuole in the roots of Arabidopsis. Therefore, studying the roots of the single and double *net4* mutants could reveal whether the *NET4s* have a functional role in root growth. Three different experiments were performed to assess whether there was an observable phenotype in the roots of the mutant lines; root growth was measured under both unstressed and stress conditions, and finally the morphology of the lytic vacuole in the root was studied using a vacuolar dye.

7.3.1 Analysis of root growth under unstressed conditions

Seedlings from the F_3 generation *net4b.1*, *net4a.1*, *net4b.1/net4a.1*, and azygous plants were grown vertically on ½MS agar plates to assess whether there was a difference in root growth. All the seeds were sown on the same day and were stratified in the dark at +4 °C to ensure the seeds germinated at the same time. After stratification, the plates were moved into a growth chamber and the seedlings were allowed to grow vertically for 12 days. No difference in the rate of germination was detected between the different mutant lines. In addition, no obvious difference in the root architecture between the mutant lines could be observed, and all lines appeared to have a similar number and branching of lateral roots. Each genetic background also appeared to respond similarly

to gravity and grew vertically down the plates. Furthermore, there was no observable difference in cotyledon or true leaf development.

In order to assess the primary root length of the different mutants, the tip of the primary root was marked after 4, 6, 8, 10 and 12 days after germination. At day 12 the plates were scanned and the primary root length of each seedling was measured from the base of the hypocotyl to the marked point which equates to the primary root tip growth at the indicated time point. Figure 7.9 and Table 7.4 show the results of this root length assay. There was sufficient evidence to suggest that the average root length of the different genetic backgrounds differed at each monitoring time point (see ANOVA category of Table 7.4). Only the single *net4b.1* mutant showed a significant difference in root growth throughout the monitoring period, when compared to the azygous plants (Dunnett test, azygous and *net4b.1*, all time points, $P < 0.001$). Examining the first time point at day 4, revealed that the average root length of *net4b.1* was 4.2 mm, whereas the azygous root length average was 5.3 mm, which represents a 20.1% reduction in root growth compared to the azygous control. At day 12 the average root length of the *net4b.1* allele was 40.8 mm, compared to the azygous control average root length of 46.6 mm. This difference represents a reduction in growth of 12.4% in the *net4b.1* allele compared to azygous at this stage. This suggests that the shorter root length is not a cumulative phenotype, as the difference in average root length between the azygous and the *net4b.1* does not increase over time. Therefore, the mutant *net4b.1* could cause a phenotype at an earlier time point and the plant is able to recover after that.

The single *net4a.1* mutant allele showed a significant reduction in root growth at days 4 and 6, with an average root length of 13.4 mm at day 6 compared to the azygous control of 14.6 mm (Dunnett test, azygous and *net4a.1*, day 6, $P = 0.004$), which represents a reduction in growth of 8.5%. However at day 8, there was no significant difference between the average root length of the *net4a.1* and azygous plants, when using a threshold value of $P > 0.05$ (Dunnett test, azygous and *net4a.1*, day 8, $P = 0.089$). The mean root length at this stage for *net4a.1* and the azygous line was 24.1 mm and 25.5 mm respectively.

Interestingly, the *net4b.1/net4a.1* double mutant showed no significant difference in root growth at any of the monitoring stages when compared to the azygous control (Dunnett test, azygous and *net4b.1/net4a.1*, at all time points, $P > 0.7$). The result here

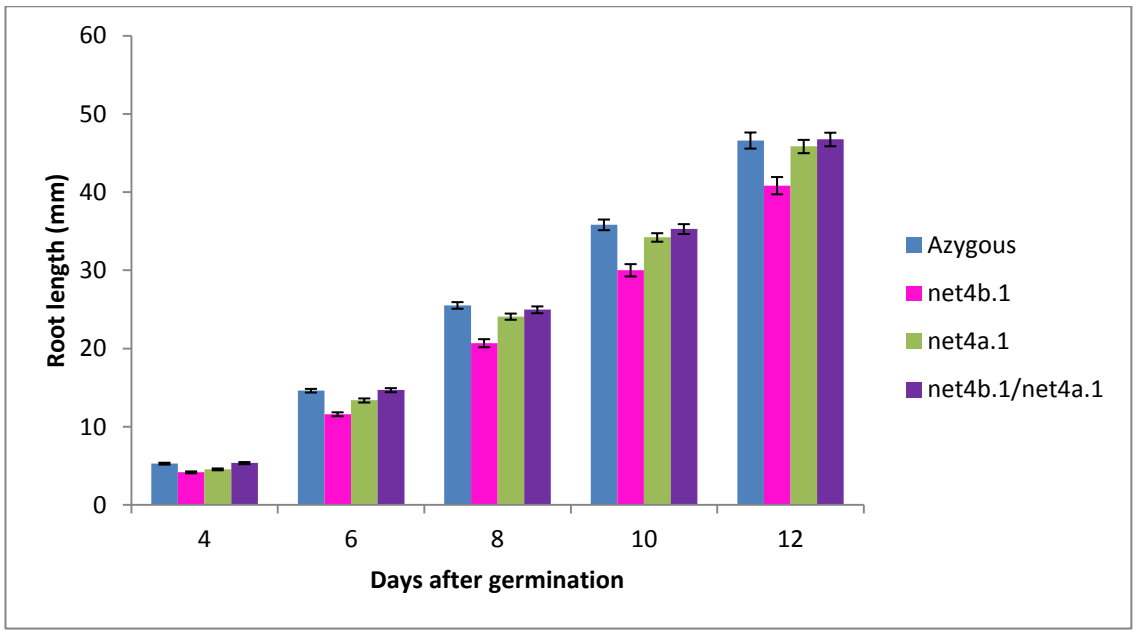

Figure 7.9: Primary root length measurements in the *net4* mutant lines, measured over 12 days. Seedlings of each line were grown vertically and measured at the different time point. Shown here is graphical representation of the mean average primary root lengths. Error bars represent standard error of the mean.

		Day 4	Day 6	Day 8	Day 10	Day 12
Azygous (n=29)	Average length (mm)	5.3	14.6	25.5	35.8	46.6
	Standard error	0.12	0.23	0.42	0.68	1.03
net4b.1 (n=35)	Average length (mm)	4.2	11.6	20.7	30.0	40.8
	Standard error	0.12	0.25	0.52	0.79	1.10
	Dunnett test (*P*)	<0.001	<0.001	<0.001	<0.001	<0.001
net4a.1 (n=30)	Average length (mm)	4.6	13.4	24.1	34.2	45.9
	Standard error	0.12	0.26	0.40	0.54	0.85
	Dunnett test (*P*)	0.001	0.004	0.089	0.255	0.91
net4b.1/net4a.1 (n=37)	Average length (mm)	5.4	14.7	25.0	35.3	46.8
	Standard error	0.14	0.26	0.44	0.63	0.87
	Dunnett test (*P*)	0.96	0.995	0.706	0.894	0.999
ANOVA	($F_{3,127}$, *P*)	(21.27, <0.001)	(33.66, <0.001)	(23.52, <0.001)	(15.79, <0.001)	(8.73, <0.001)

Table 7.4: Primary root length measurements of the *net4* mutants over 12 days vertical growth. Dunnett test was used to test for a significant difference in the mean root lengths between the azygous control and the mutant line.

were drawn from a single biological repeat, therefore in order to assess the reproducibility and significance of these results further biological repeats are needed.

7.3.2 Effect of salt and drought stress on root growth of the mutant lines

To test the possibility that the *NET4s* are an important factor in the plants ability to respond to stress, the *net4* mutants were grown under two different stress conditions: salt and drought stress. Both of these stresses cause osmotic stress to the plant but high salt can also cause additional stresses associated with sodium ion toxicity (Claeys et al. 2014). The vacuole has a major role in the plants ability to tolerate salt and drought stress and the vacuole has been shown to sequester ions which maintains the water balance of the cell and mediates the toxic effects caused by excess ions in the cytosol (Fukuda et al. 2004; Munns & Tester 2008; Gaxiola et al. 2001). Vacuolar membrane trafficking has also been implicated in the plants response to salt and drought stress as plants overexpressing a vacuolar Rab GTPase (RabG3e) in Arabidopsis showed an increased tolerance to these stresses (Mazel et al. 2004). Therefore it is possible that the NET4s, as actin-vacuole linkers, could participate in the plants response to salt and drought stress.

Two different growth conditions were used to test whether the *net4* mutants have a conditional phenotype; growth was tested on medium supplemented with 125 mM sodium chloride (NaCl) or 200 mM sorbitol. Both of these stresses are considered to cause severe stress in the plant (Claeys et al. 2014), as they reduce the water potential in the medium leading to osmotic stress. Sorbitol is a nonionic osmolyte which increases the solute concentration of the medium, and has been used in several studies looking at drought stress (Yuan et al. 2014; Mazel et al. 2004).

In this assay, the sample size was kept low in order to see whether a phenotype could be observed quickly. Post-germination growth was assessed in this assay, and seedlings were initially grown vertically on untreated ½MS agar plates for 5 days before being transferred to the stress treated plates and an untreated control plate. Transferred seedlings were all chosen to be at a similar developmental stage (approximately 1 cm in root length). Total root lengths were measured 6 days after transfer and the change in root length between day 5 and day 11 was calculated. The percentage reduction in root growth imposed by the stress was also calculated according to Baral et al. (2015) by inputting the initial root length (L) and the change in root length (ΔL; 11 days root

length - 5 days root length) into the following formula:

$$\%\ \text{reduction in growth} = [\ 1-\{\ (\Delta L/L)_{stress} / (\Delta L/L)_{control}\ \}] \times 100$$

Figure 7.10 and Table 7.5 show the results of this assay. Figure 7.9 shows the change in root growth and percentage reduction in growth (normalised to the ½MS control). The growth after transfer of all the genotypes exhibited variation on the ½MS agar control plate, and although the means differed (ANOVA; $F_{3,70} = 5.16$, $P = 0.003$), only the mean growth of the *net4b.1* and *net4a.1* mutant were significantly different from each other (Tukey test; *net4b.1* and *net4a.1*, $P = 0.001$). No significant difference was observed between the *net4* mutants and the azygous control (Tukey test, $P > 0.1$). The mean increase in root growth for the azygous, *net4b.1*, *net4a.1* and *net4b.1/net4a.1* lines were 36.5 mm, 32.7 mm, 38.8 mm and 36.0 mm respectively.

Transferring the seedlings onto plates treated with 125 mM NaCl resulted in a reduction of growth in each genotype, however it appeared that the *net4b.1/net4a.1* mutant plants were less sensitive to this stress. Under the salt stress the mean changes in growth of the azygous, *net4b.1*, *net4a.1* and *net4b.1/net4a.1* lines were 18.5 mm, 17.4 mm, 20.2 mm and 21.8 mm respectively. There was sufficient evidence to suggest that the mean increase in root growth after transfer differed between the different genotypes (ANOVA; $F_{3,7\,2} = 20.27$, $P < 0.001$), however only the *net4b.1/net4a.1* mutant differed significantly from the azygous control (Tukey test, $P < 0.001$). Even though the mean growth change was higher in the *net4a.1* than the azygous control, there was no significant difference between the two (Tukey test; azygous and *net4a.1*, $P = 0.075$). No significant difference was observed between the *net4a.1* and the *net4b.1/net4a.1* lines (Tukey test; *net4a.1* and *net4b.1/net4a.1*, $P = 0.056$). This suggests that perhaps the *net4a.1* mutation is responsible for making the plant more tolerant of salt and that this is accentuated when *NET4B* is knocked down as well. Although the actual percentage reduction in growth (normalised to the ½MS control) shows that only the *net4b.1/net4a.1* mutant is appreciably less inhibited by high salt, as growth was only reduced by 41% compared to between 51-56% for the single mutations and the azygous control.

Transferring the seedlings onto the drought stress plates similarly caused a reduction in growth in all genotypes, however the *net4a.1* single mutant was less affected by this

(a)

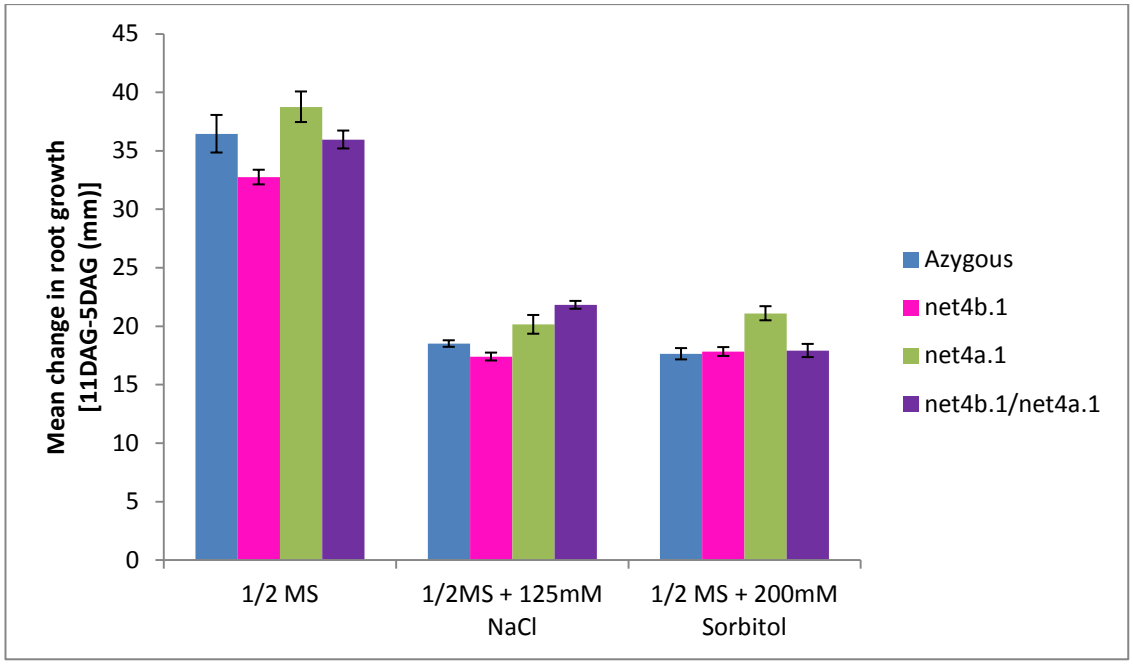

(b)

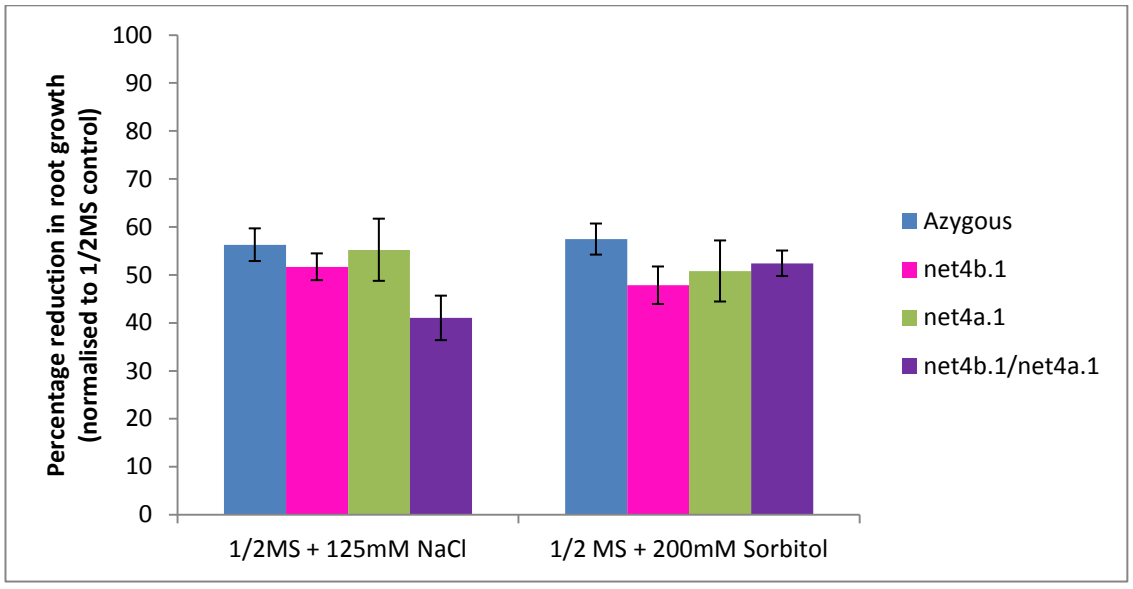

Figure 7.10: Response of the *net4* mutants to salt and drought stress treatments. Seedlings were vertically grown on untreated ½MS plates, and then 5 days after germination (DAG) they were transferred to plates containing either 125 mM NaCl, 200 mM sorbitol or an untreated ½MS control plate. Root lengths were measured 11 days after germination. (a) Graph showing the mean change in root growth (root length at 11DAG - root length at 5DAG). Error bars represent standard error of the mean. (b) Graph showing the percentage reduction in root growth on the stress treatment, normalised to the growth observed on the ½MS untreated plate, using the formula described in the text. Error bars represent standard error of the mean of (($\Delta L/L_{stress}$) x100).

	Azygous	*net4b.1*	*net4a.1*	*net4b.1/net4a.1*
½ MS				
Number of seedlings	17	20	20	17
5DAG (mm)	11.7	10.2	10.8	12.4
Standard error	0.29	0.20	0.24	0.32
11DAG (mm)	48.2	42.9	49.6	48.4
Standard error	1.62	0.71	1.43	0.80
11DAG-5DAG(mm)	**36.5**	**32.7**	**38.8**	**36.0**
Standard error	1.61	0.63	1.31	0.76
½ MS + 125 mM NaCl				
Number of seedlings	18	21	16	21
5DAG (mm)	13.6	11.2	12.6	12.8
Standard error	0.25	0.18	0.20	0.28
11DAG (mm)	32.1	28.6	32.7	34.6
Standard error	0.38	0.44	0.84	0.40
11DAG-5DAG (mm)	**18.5**	**17.4**	**20.2**	**21.8**
Standard error	0.28	0.34	0.80	0.33
% reduction in root growth (normalised to 1/2MS control)	56.3	51.7	55.2	41.0
½ MS + 200 mM Sorbitol				
Number of seedlings	22	20	17	19
5DAG (mm)	13.2	10.6	12.0	12.9
Standard error	0.19	0.20	0.30	0.34
11DAG (mm)	30.9	28.5	33.1	30.8
Standard error	0.60	0.49	0.71	0.85
11DAG-5DAG (mm)	**17.6**	**17.8**	**21.1**	**17.9**
Standard error	0.48	0.38	0.60	0.56
% reduction in root growth (normalised to 1/2MS control)	57.5	47.8	50.8	52.4

Table 7.5: Results of the *net4* mutants grown under salt and drought stress. Seedlings were grown on untreated ½MS plates and were transferred onto stress treatments or the ½MS control, 5 days after germination (DAG). Root growth after transfer was then recorded 11 days after germination. Shown in this table are the mean average root lengths at 5DAG and 11DAG as well as the mean change in root growth (11DAG-5DAG), and the percentage reduction in growth, on the stress treatment, when normalised to the ½MS control.

treatment. The mean changes in root growth for the azygous, *net4b.1*, *net4a.1* and *net4b.1/net4a.1* lines were 17.6 mm, 17.8 mm, 21.1 mm and 17.9 mm respectively. Although the means differed between the groups (ANOVA; $F_{3,74} = 9.8$, $P < 0.001$), only the *net4a.1* mutant showed a significant difference from the other genotypes (Tukey test; $P < 0.001$), and no difference was observed between the other groups, excluding *net4a.1* (Tukey test; $P > 0.9$). However it did appear that the percentage of reduction in root growth (normalised to the ½MS control), was lower in the *net4* mutants (47 to 52% reduction) compared with the azygous control (57% reduction in growth). This would suggest again that the *net4* mutants are better able to tolerate the drought stress.

As both NET4 proteins associate with the vacuole and the actin cytoskeleton, and as the vacuole is important in sequestering sodium ions during salt stress (Munns & Tester 2008), it would be expected that mutations of the *NET4s* would make the plants more sensitive to the stress rather than more tolerant. It is possible that the NET4s could negatively regulate the salt and drought stress responses, and therefore mutations of these genes could allow the plants to be more tolerant of the stress. However as this assay was only repeated once with a low sample size, it is hard to draw any clear conclusions. Repeating this experiment again using a larger sample size and a range of concentrations of salt/sorbitol would enable a more thorough understanding of the role of the *NET4s* in the response to stress.

7.3.3 Imaging the lytic vacuole of the *net4* unstressed roots

Both NET4 proteins localise to the tonoplast membrane, associate with actin filaments, and could potentially be effectors of vacuolar Rab GTPases. Previous studies have shown that overexpression of a dominant-negative RabG3f^{T22N} resulted in the disruption of vacuolar morphology in the root (Cui et al. 2014). Therefore it is a possible that the *net4* mutants could have a similar phenotype and the morphology of the lytic vacuole was studied in unstressed Arabidopsis roots.

The pH indicator 2',7'-Bis-(2-carboxyethyl)-5-(6)-carboxyfluorescein, acetoxymethyl ester (BCECF-AM) accumulates in acidic compartments of the cell and several studies have used this dye to image the lytic vacuole of plant cells (Swanson & Jones 1996; Viotti et al. 2013; Zheng et al. 2014; Kolb et al. 2015). BCECF is a ratiometric dye that can be used as a pH indicator as it has two excitation peaks. This dye can be excited at 440 nm (which is pH insensitive) and 495 nm (which is pH sensitive); comparing the ratios of these intensities gives a measurement of the intracellular pH (Boens et al.

2006). The acetoxymethyl ester (AM) makes the dye membrane permeable, and is cleaved off by cellular esterases, trapping the membrane impermeable dye inside the cell (Slayman et al. 1994). For the purpose of this experiment, BCECF was only excited at 488 nm as this efficiently highlighted the acidic lytic vacuole.

Five-day old seedlings of the F_3 generation *net4b.1*, *net4a.1*, *net4b.1/net4a.1*, and azygous lines were incubated for 1 hour in 10 μM BCECF-AM, and then briefly washed for 10 minutes before imaging using confocal laser scanning microscopy (CLSM). Figure 7.11 shows a representative maximum projection of a z-stack taken for each genotype.

The maximum projections clearly show the lytic vacuoles of the epidermis and no obvious phenotype could be observed between the different genotypes. The cells of the elongation zone of the root all have a lytic vacuole that appeared to occupy the majority of the cell in all genotypes and there was no noticeable fragmentation of the vacuole.

As this assay only effectively imaged the lytic vacuoles in the cells of the epidermis, it is possible that there is a phenotype associated with the vacuoles in deeper cell files that were not consistently penetrated by the dye. Transforming the *net4* mutant lines with a vacuolar-fluorescent fusion protein, for example the vacuolar SNARE protein YFP-VAMP711 (yellow fluorescent protein-VESICLE-ASSOCIATED MEMBRANE PROTEIN 711; Geldner et al. 2009), could provide a more detailed view on the vacuolar structures in these mutants.

7.4 Analysis of embryos in the *net4* mutant lines

As well as the large central acidic lytic vacuole, plants also contain protein storage vacuoles (PSV) which are found predominantly in the embryos and proteins stored there are used as a nitrogen source during germination (Krebbers et al. 1988). Several proteins associated with vacuolar trafficking have been shown to be crucial for maintaining the proper morphology of PSVs and also mitigating the proper trafficking of storage proteins. These include; MAIGO2 (Li et al. 2006), KATAMARI2/GRAVITROPISM DEFECTIVE 2 (KAM2/GRV2; Tamura et al. 2007), SNARE proteins (VAMP727/SYP22; VESICLE-ASSOCIATED MEMBRANE PROTEIN 727/Syntaxin22; Ebine et al. 2008) and RabG3 subfamily Rab GTPases (Ebine et al. 2014). As the NET4s interact with vacuolar Rab GTPases and *NET4B* was

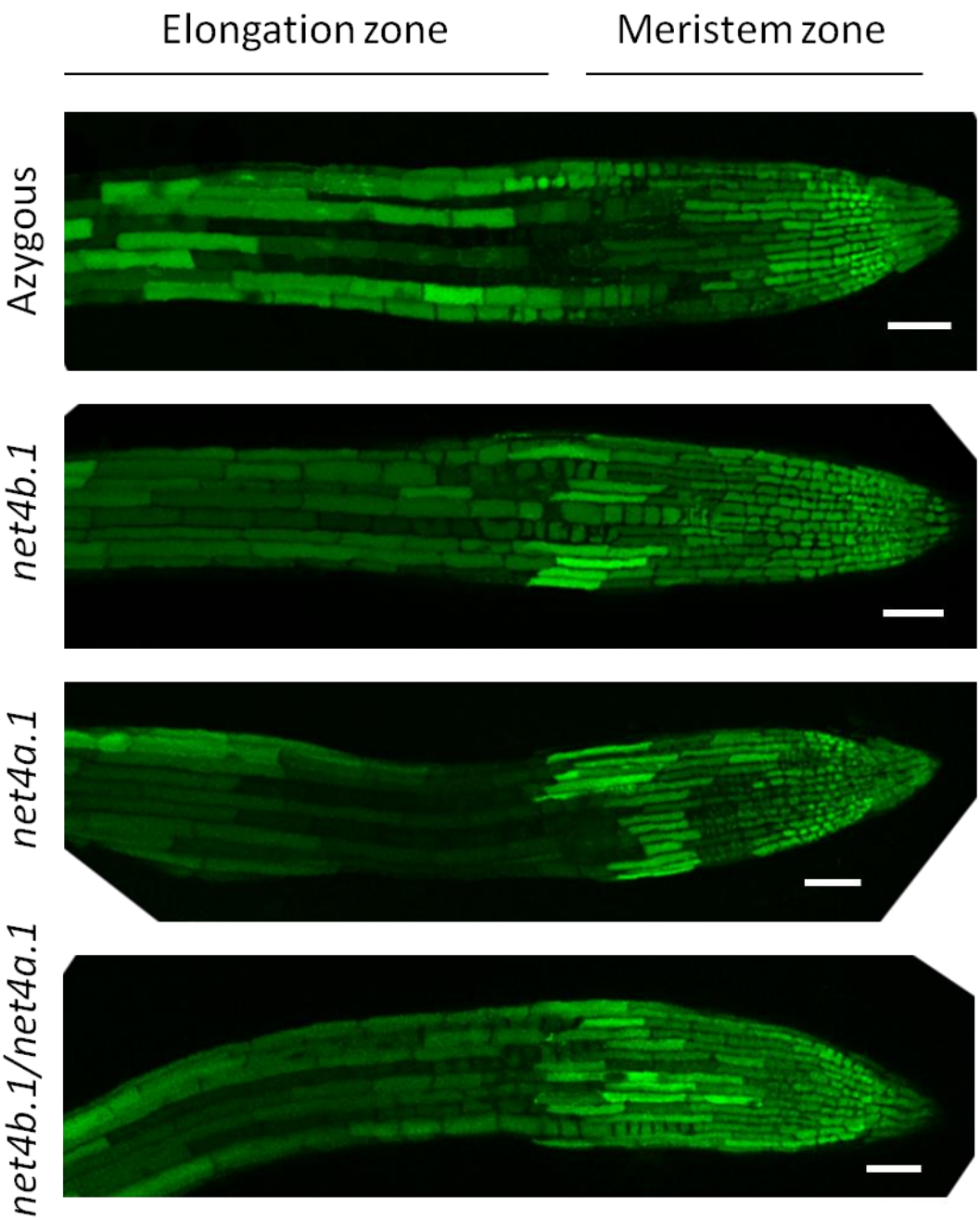

Figure 7.11: Imaging the lytic vacuole in roots of the different mutant backgrounds using BCECF-AM. BCECF-AM is a pH sensitive dye that accumulates in the lytic vacuole of plants. Five-day old seedlings of the F_3 generation *net4b.1*, *net4a.1*, *net4b.1/net4a.1*, and azygous lines were incubated in 10 μM BCECF-AM for one hour in the dark before being imaged using CLSM. BCECF-AM was excited at 488 nm and emission detected at 500-570 nm. Scale bars: 50 μm.

shown to be expressed in the embryos through *promoter*::GUS studies, the morphology of PSVs and the trafficking of seed storage proteins was studied in the *net4* mutants.

7.4.1 Imaging protein storage vacuole autofluorescence in the *net4* mutants

Previous studies looking at the role of the ARABIDOPSIS VACUOLAR SORTING RECEPTOR 1 (AtVSR1) in sorting storage proteins in the seed, revealed that the PSVs in seed embryos are autofluorescent and therefore provide an efficient way of studying their morphology (Shimada et al. 2003a). This study showed that mutants in *AtVSR1* had dramatically smaller and more distorted PSVs compared to wild-type plants. This phenotype has also been observed in other vacuolar proteins for example *MAIGO2*, the SNARE *VAMP727/SYP22* complex and a quintuple *rabg3b,c,d,e,f* mutant (Li et al. 2006; Ebine et al. 2008; Ebine et al. 2014).

To image the PSVs, dry seeds of the F_3 generation *net4b.1*, *net4a.1*, *net4b.1/net4a.1*, and azygous lines were imbibed on damp filter paper for one hour in the dark and were then mounted on a slide in glycerol. The embryos were then gently forced out of the seed by applying pressure on the coverslip. A minimum of five embryos were imaged for each genetic line using CLSM by exciting the PSV autofluorescence at 488 nm and detecting the emission at 500-630 nm. Figure 7.12 shows a representative image from each genetic background, showing both cotyledon and root PSVs. There was no apparent difference in the morphology of the PSVs in the *net4* mutants when compared with the azygous plants.

Previous studies looking at *MAIGO2* have shown a very dramatic alteration to PSV morphology with smaller, fragmented and more rounded PSVs. It could be that the *net4* mutants have a more subtle effect on the morphology of the PSVs which could be assessed through quantification of the size and shape of PSVs. However the signal to noise ratio from these images were insufficient to enable such quantification. Furthermore it could be that the NET4s have a role in the breakdown of the PSVs during germination rather than maintaining the PSV morphology in the seed, and future work could focus on studying this process in the *net4* mutants.

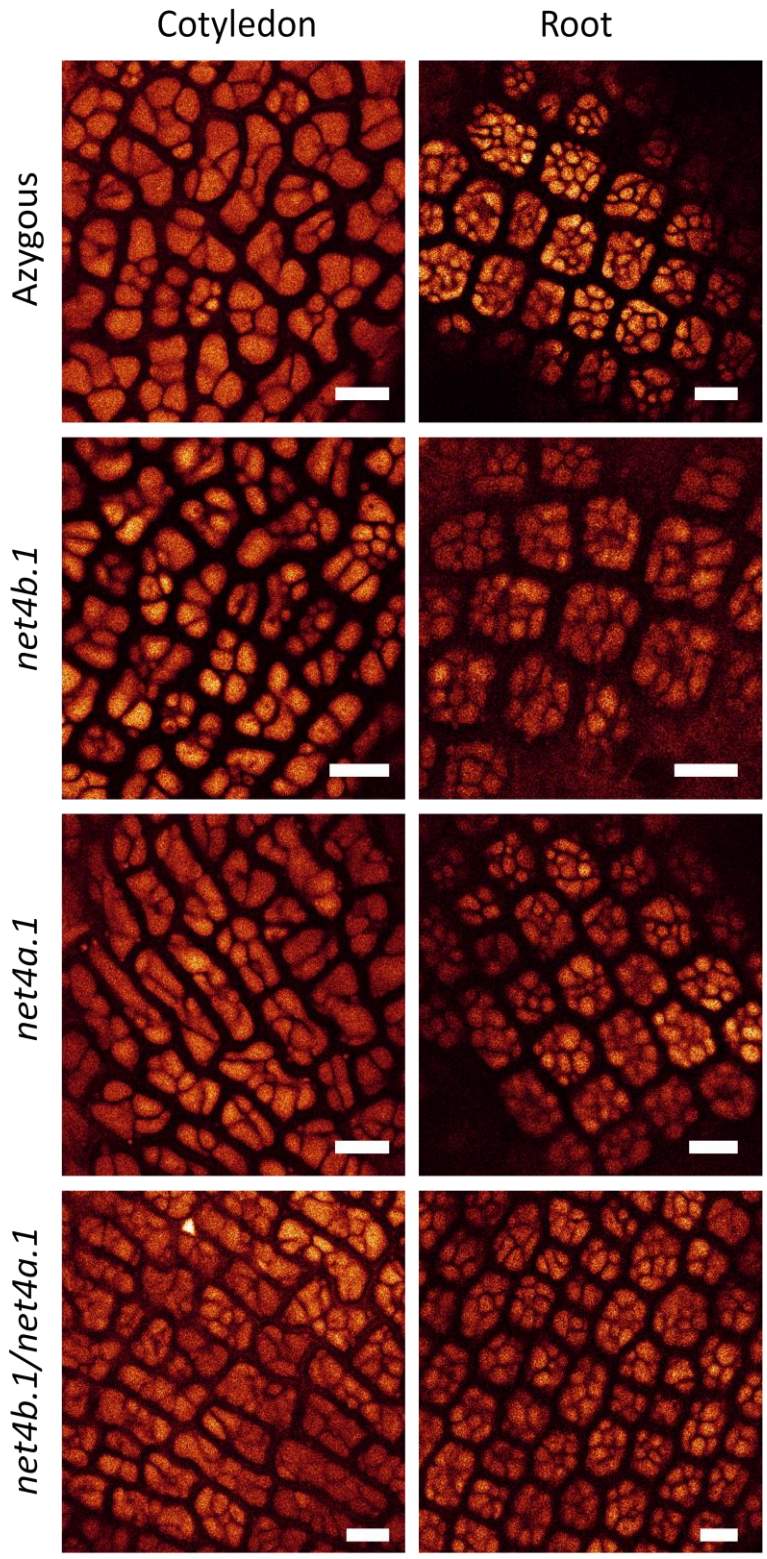

Figure 7.12: Analysis of protein storage vacuole morphology in embryos of the different *net4* mutant backgrounds. Dry seeds of the of the F_3 generation *net4b.1*, *net4a.1*, *net4b.1/net4a.1*, and azygous lines were imbibed for 1 hour at 4°C on damp filter paper in the dark. The seeds were then mounted on a side with glycerol and the embryos forced out of the seeds by applying pressure on the coverslip. The autofluorescence of PSVs was excited at 488 nm and detected between 500-630 nm. Scale bars: 10 μm.

7.4.2 Analysis of seed protein storage precursor trafficking in the *net4* mutants

Proteins are accumulated during seed development for use as a nitrogen source in the next generation. In Arabidopsis the majority of these proteins are 12S globulins and 2S albumins (Higashi et al. 2006). These proteins are synthesised as precursors in the endoplasmic reticulum and are targeted for storage in the PSV lumen where they undergo proteolytic cleavage by vacuolar processing enzymes (Shimada et al. 2003b). 12S globulins are synthesised as propeptide precursors that are cleaved to α and ß subunits (Heath et al. 1986). The maturation of 2S albumin involves the cleavage at four sites along the protein to produce a mature protein composed of large and small subunits (Krebbers et al. 1988). Improper trafficking of these propeptides to the vacuole leads to an accumulation of the precursors in the seed. Several proteins have been shown to be important for the proper trafficking of these proteins and this has been assessed by examining the total protein composition of Arabidopsis mutant seeds (Shimada et al. 2003a; Li et al. 2006; Ebine et al. 2008).

Total protein was extracted from ten dry seeds of the F_3 generation *net4b.1*, *net4a.1*, *net4b.1/net4a.1*, and azygous lines (as described in 2.4.8). The seeds were crushed and boiled in 20 µl 1x Laemmli sample buffer for 5 minutes at 95 °C before being separated on a 15% SDS-PAGE gel. Figure 7.13 shows the Coomassie Brilliant Blue (CBB) stained gel with the seed protein extracts from the different lines. The total protein extract composition from the *net4* mutant lines all appeared to be very similar to the azygous control. The α- and ß-subunits of 12S globulin and the large and small subunits of 2S albumin all accumulated to approximately equal levels in all the genetic backgrounds. Importantly, there was no accumulation of 54-, 51-, 49-, or 17- kDa proteins that correspond to 12S globulin (54, 51 and 49 kDa) and 2S albumin (17 kDa) precursor proteins, as has been seen in several mutants involved in seed protein storage trafficking (Shimada et al. 2003a; Li et al. 2006; Tamura et al. 2007; Ebine et al. 2008).

It could be possible that there is a subtle phenotype associated with the trafficking of these proteins and that the CBB stain is unable to detect this difference. Future work using antibodies for 12S globulin and 2S albumin could provide a more sensitive technique for assessing the trafficking of these proteins in the *net4* mutant backgrounds.

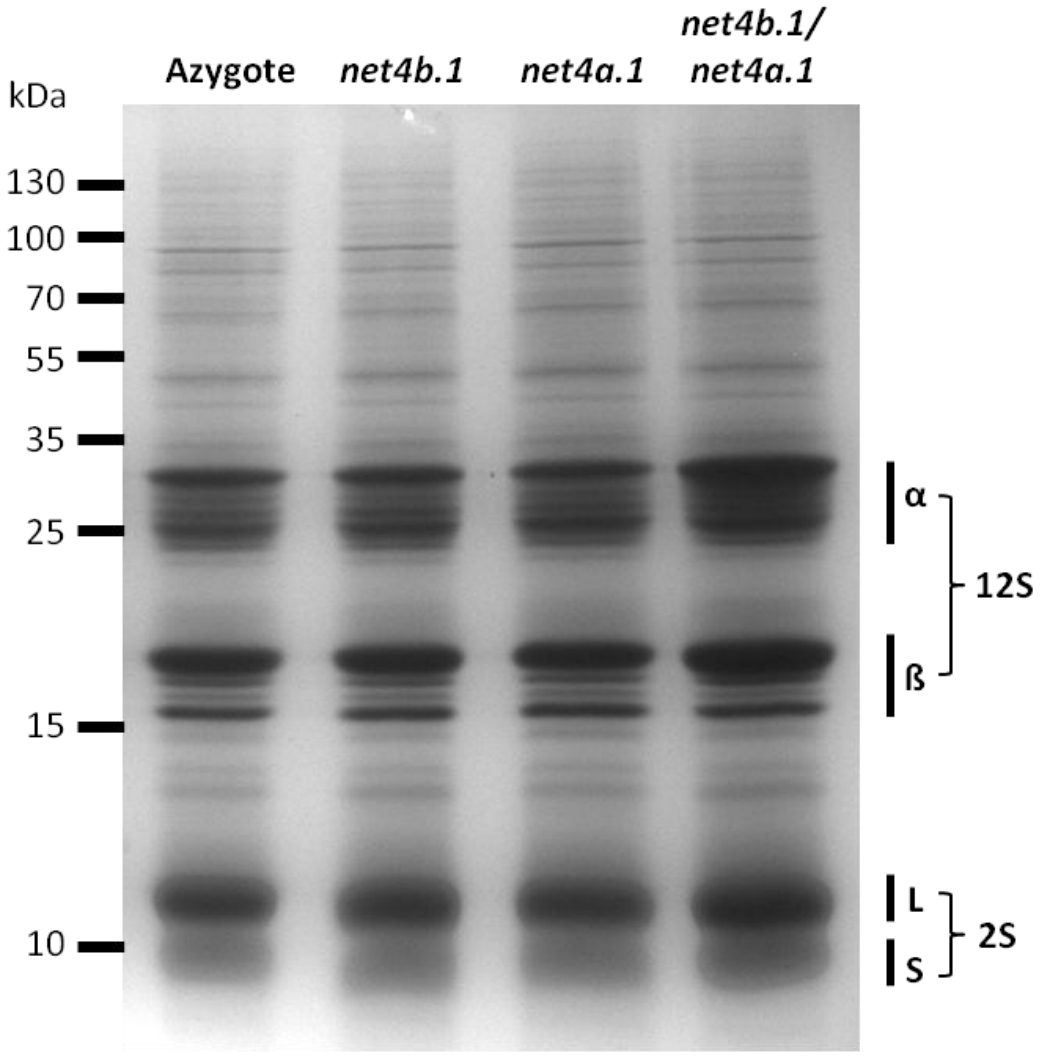

Figure 7.13: Analysis of seed storage protein trafficking in the *net4* mutant lines. Total protein was extracted from dry seeds of the F_3 generation *net4b.1*, *net4a.1*, *net4b.1/net4a.1*, and azygous lines and was separated on a 15% SDS-PAGE gel, followed by staining with Coomassie Brilliant Blue. All genotypes accumulated approximately equal amounts of α- and ß- subunits of 12S globulin and the large (L) and small (S) subunits of 2S albumin. No accumulation of 54-, 51-, 49-, or 17-kDa precursor proteins was observed in any of the genetic lines.

7.5 Analysis of transpirational water loss in detached leaves of the *net4* mutant lines

Although the expression pattern of both *NET4* genes was highest in the roots, *NET4B* is also highly expressed in the guard cells, as shown by publicly available microarray data (Chapter 3) and *promoter*::GUS analysis (Chapter 5). Therefore a transpirational water loss assay from detached leaves was performed to assess whether there was a potential guard cell phenotype associated with the *net4* mutant lines.

The regulated opening and closing of stomata is governed by changes in guard cell turgor pressure, and is an important feature of the plants ability to respond to the environment (Luan 2002). Numerous studies have demonstrated the importance of the actin cytoskeleton and vacuolar rearrangements in controlling the opening and closing of stomata (Higaki et al. 2010; Zhao et al. 2011; Jiang et al. 2012; Li et al. 2013; Bak et al. 2013; Andrés et al. 2014). However the molecular link between the actin cytoskeleton and the vacuole in guard cells is still unknown.

To assess whether the *NET4s* have an observable phenotype associated with guard cell control, a transpirational water loss assay from detached leaves was performed. This assay has been used previously to show the role of two actin binding proteins, STOMATAL CLOSURE-RELATED ACTIN BINDING PROTEIN1 (SCAB1) and ACTIN-RELATED PROTEIN C2/DISTORTED TRICHOMES2 (ARPC2; which encodes a subunit of the Arp2/3 complex) in regulating stomatal movements (Zhao et al. 2011, Jiang et al. 2012). Three leaves at a similar developmental stage were detached from 5-week old *net4b.1*, *net4a.1*, *net4b.1/net4a.1*, and azygous plants, and were placed in a plastic weighing boat and weighed immediately to give the fresh weight. Three plants from each genotype were used in this assay to give an average percentage of water loss. The detached leaves were incubated on the bench and weighed at the indicated time points to measure the water loss from the leaf. The leaves were weighed at 30, 60, 90, 120, 180, 240 and 300 minutes after detachment. After the final time point, the leaves were transferred to a 70 °C incubator overnight, and the leaves were weighed the following day to give the dry weight of the leaf. The total water content (TWC) of the leaf was calculated by subtracting the dry weight from the fresh weight. The water lost (ΔW) at each time point was calculated as a percentage loss of the total water content using the following formula:

$$\% \text{ Water loss} = 100 - [(TWC - \Delta W) / TWC) \times 100]$$

Figure 7.14 and Table 7.6 show the results of this experiment. The percentage of water loss appeared to be consistent between the different genotypes. The final time point, 300 minutes after detachment, was chosen for statistical analysis as differences in water loss would have accumulated over time. The results from this assay showed that there was not sufficient evidence to suggest a difference in transpirational water loss amongst the different genotypes (ANOVA; $F_{3,8}$, = 1.72, P = 0.24). The average percentage of water loss 300 minutes after detachment for the azygous, *net4b.1*, *net4a.1* and *net4b.1/net4a.1* lines was 45.84%, 41.52%, 39.77% and 37.94% respectively. Therefore it appears that in this assay, disrupting the *NET4* genes does not affect stomatal movements.

7.6 Conclusion

This chapter has described several different experimental approaches that were designed to determine the function of the *NET4s*. These experiments focused on the use of T-DNA insertion lines to disrupt the *NET4* gene transcripts and observe the effect this had on the plant. T-DNA insertion lines were identified for both *NET4* genes and these were crossed together to generate a double *net4b.1/net4a.1* homozygous mutant, as well as the single homozygous, and azygous control plants. RT-PCR was used to confirm the disruption to the *NET4* genes in these lines. The transcript and protein levels of NET4B were also shown to be reduced in the *net4b.1* mutant through qPCR and Western blot analysis.

Primary root growth was investigated in these mutant lines as both *NET4* genes are highly expressed in this tissue. Root length was measured on vertically grown seedlings over a period of four to twelve days. Only the single *net4b.1* mutant showed a significant reduction in root growth in comparison to the azygous control throughout the growth period. The single *net4a.1* mutant exhibited a significant reduction in root growth at earlier time points (day 4 and 6), however at day 8 there was no significant difference in root growth between the *net4a.1* mutant and the azygous plants. Throughout this experiment there was no significant difference between the double *net4b.1/net4a.1* mutant and the azygous plants.

It is possible that the NET4s function antagonistically to regulate root growth, with the loss of one gene altering the balance in this regulation leading to a reduced root length. Disruption to both genes could therefore effectively eliminate this competitive regulation and rescue the phenotypes associated with the single mutants. Indeed, such

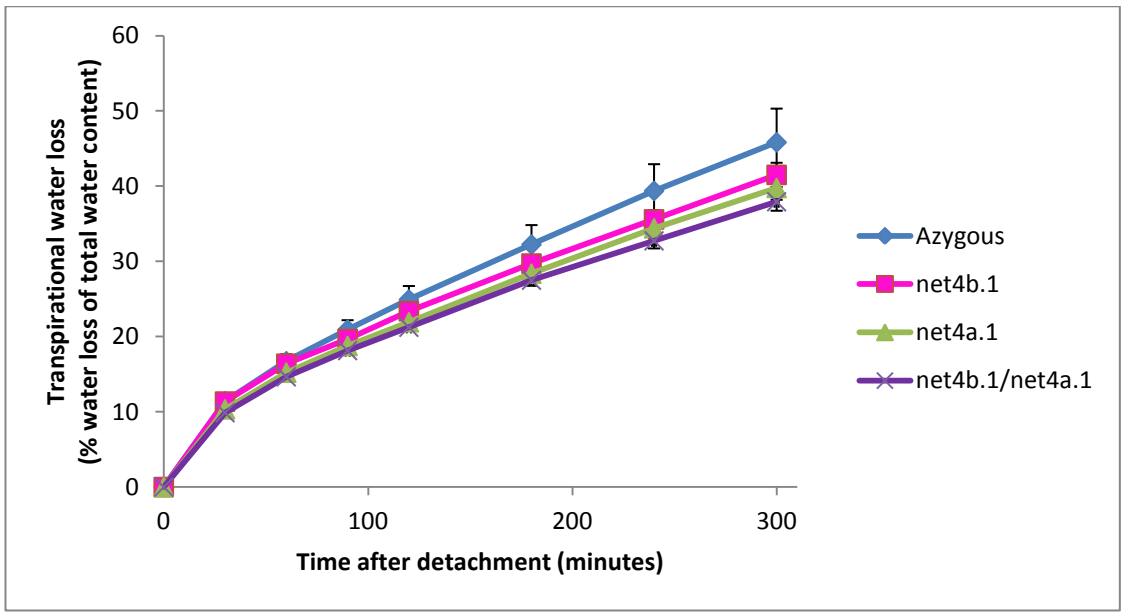

Figure 7.14: Transpirational water loss from detached leaves in the *net4* mtuant backgrounds. Leaves were detached from 5 week old plants from the F_3 generation *net4b.1*, *net4a.1*, *net4b.1/net4a.1*, and azygous lines and weighed at various time points over 300 minutes. Shown here is a graph showing the percentage of transpirational water loss as a function of the total leaf water content. Error bars represent the standard error of the mean.

		Time after detachment (minutes)						
		30	60	90	120	180	240	300
Azygous	Average % water loss	11.40	16.73	20.93	24.93	32.25	39.38	45.84
	Standard error	0.36	0.92	1.26	1.80	2.59	3.56	4.48
net4b.1	Average % water loss	11.37	16.41	19.69	23.38	29.72	35.60	41.52
	Standard error	0.21	0.26	0.51	0.67	0.91	1.24	1.61
net4a.1	Average % water loss	10.34	15.22	18.77	21.92	28.39	34.41	39.77
	Standard error	0.41	0.44	0.76	0.71	1.02	1.34	1.57
net4b.1/net4a.1	Average % water loss	9.89	14.66	18.14	21.25	27.50	32.75	37.94
	Standard error	0.46	0.14	0.35	0.42	0.74	1.01	1.20

Table 7.6: Results of the transpirational water loss assay from detached leaves of the *net4* mutants

an antagonistic relationship has been observed for two PIN auxin transporter proteins, *PIN5* and *PIN8* (Ding et al. 2012). Individual mutants of these genes results in defects in pollen morphology, and this phenotype is rescued in the double *pin5pin8* mutant. It is possible that such an antagonistic relationship exists between the *NET4s* however as this result was drawn from one biological replicate, further repeats with a larger sample size are needed to assess the significance and reproducibility of the results presented here.

In addition to analysing root growth under unstressed conditions, post-germination root growth was examined under salt and drought stress. This analysis demonstrated that the *net4b.1/net4a.1* double mutant was more tolerant than the ayzgous plants to growth on high salt plates, and the *net4a.1* single mutant was more tolerant to drought stress. It is possible that the *NET4s* are involved in the negative regulation of the plants response to these stresses, however more repeats with larger sample sizes are needed to confirm the results presented here.

As both NET4 proteins localise to the vacuole, the lytic vacuole was also imaged in the unstressed roots however there appeared to be no difference in epidermal vacuole morphology in the *net4* mutants. Further research could focus on studying the morphology of the lytic vacuole in cell files deeper in the root through stably transforming the *net4* mutant lines with a known vacuolar marker.

PSV morphology and trafficking of storage proteins to the PSV in the embryo were also investigated in the *net4* mutants. Several vacuolar trafficking proteins, including the RabG3 GTPases, have a role in protein trafficking to the PSV as well as maintaining PSV morphology (Ebine et al. 2014). From the analysis in this project, no difference in PSV morphology or vacuolar trafficking in the embryo could be discerned in the *net4* mutants. Future work could use antibodies against the seed storage proteins in a Western blot of *net4* seed protein extracts, as this would be a more sensitive method to detect subtle differences in precursor protein accumulation. In addition, it is possible that the NET4s might have a role in trafficking events to the lytic vacuole in the roots. The function of the NET4s in vacuolar trafficking could be examined through stably transforming the *net4* mutant lines with fluorescent lytic vacuolar cargo markers, for example the acidic cysteine protease aleurain-GFP (Di Sansebastiano et al. 2001).

Both vacuole and actin rearrangements have been shown to be important for guard cell opening and closing (Gao et al. 2009), however no direct linker between the two has

been described in guard cells. *NET4B* has been shown to be expressed in guard cells therefore a possible guard cell phenotype was investigated in the *net4* mutants using a transpirational water loss assay. Water loss was measured from detached leaves of the *net4* mutants however no significant difference was observed. Although a guard cell phenotype was not ascribed using this assay, it is possible that the *NET4s* are important in guard cell functioning in response to different stimuli for example ABA, drought or light/dark cycles.

The lack of a conclusive phenotype for the *NET4* genes could be the result of many different factors. The unstressed and stressed root length assays only used one biological repeat each with a relatively small sample size, which could cause the results to be more prone to error. Repeating these assays with a larger sample size could help us understand the role of the *NET4s* in root growth and the response to stress. Furthermore, it is possible that the mutations used in these assays were not severe enough to induce a phenotype. As the *net4b.1* was a knock-down mutation, there could still be sufficient *NET4B* transcript in the plant for it to function properly. Future work could use different genetic approaches to study the *net4s*, for example using RNAi to downregulate *NET4B* expression. Alternatively, overexpression of dominant-negative NET4 truncations, for example NET4 proteins lacking the NAB or IRQ domain, could induce a phenotype by interfering with the normal functioning of the NET4 proteins.

Chapter 8 - Wider presence of the IRQ domain

8.1 Introduction

Previous chapters have demonstrated that NET4B is a member of the NET family of actin-binding proteins, and can associate with actin filaments via the conserved N-terminal NAB domain. As well as containing this conserved actin-binding domain, previous bioinformatics analysis has also demonstrated that NET4B shares a conserved C-terminal domain with NET4A, NET3A and NET3C (as described in Chapter 3). This domain was termed the IRQ domain due to the conservation of three amino acids residues between the four NET proteins; isoleucine (I), arginine (R) and glutamine (Q). This domain is composed of a stretch of highly conserved central amino acids. As well as specific conserved amino acid residues flanking this central region. As this domain was conserved between these different NET proteins, it was hypothesised that it could be functionally important. Two different experimental approaches were used to ascribe a potential function for this domain; subcellular localisation studies and identification of interacting partners.

Firstly, the C-terminal 54 amino acid residues of NET4B, termed the IRQ + Ct truncation (IRQ domain to the C-terminal end), was fused to GFP and transiently expressed in *Nicotiana benthamiana* leaf epidermal cells (see Chapter 4). This domain localised to moving punctae within these cells and a similar localisation was also observed by Dr. Tim Hawkins for the homologues region in NET4A and NET3A (Dr. Tim Hawkins, personal communication). These punctae could represent vesicle bodies however this remains to be tested experimentally.

Secondly, evidence for the function of the IRQ domain came from yeast-2-hybrid (Y2H) studies on the interaction partners of NET4B (described in Chapter 6). Both NET4 proteins were shown to interact with two active GTP-bound Rab GTPases, RabG3f and RabG3a; which regulate membrane trafficking events at the vacuole (Rutherford & Moore 2002; Cui et al. 2014). After demonstrating that the full-length NET4B could interact with the activated RabG3a, it was then imperative to identify the NET4B Rab-binding domain. Various truncations of NET4B were used to test the interaction with the active RabG3a and from this experiment it was shown that the IRQ domain, including the less conserved amino acids flanking the highly conserved central region, were sufficient to mediate the interaction with the Rab. Therefore the IRQ

domain represents the Rab-binding domain of NET4B. Furthermore this result demonstrated it is not just the highly conserved central region of the IRQ domain that is functionally important, but also the conserved residues at either side.

This study has therefore assigned a potential function to the IRQ domain as a Rab-binding domain. Consequently further analysis of this domain was undertaken to assess whether it could be found in any other proteins outside of the NET family. This chapter will discuss the bioinformatics analysis used to characterise additional proteins containing the IRQ domain and the analysis described here was performed in collaboration with Dr. Tim Hawkins (Durham University).

8.2 Identification of the IRQ family in *Arabidopsis thaliana*

The highly conserved amino acid sequence in the IRQ domain of NET4B (EQKREAIRQLCMSLDHYRD) was used in a BLASTp (Basic Local Alignment Search Tool, using amino acid sequence) search against the Arabidopsis proteome to identify additional IRQ domain containing proteins. From this search, six additional proteins were identified that shared a high degree of conservation with these amino acids. These proteins were encoded at the following gene loci: At5g05180, At1g64330, At1g64320, At5g41790, At5g41780 and At3g10880. Figure 8.1 shows the alignment of the IRQ domain from these proteins and the four NET proteins, and was generated using ClustalX2.1 (Larkin et al. 2007). The alignment created in Figure 8.1 corresponds to the area equivalent to the Rab-binding domain of NET4B (NET4B$^{464\text{-}511}$). This alignment shows that these proteins all shared a high degree of conservation in the central region, but also conserved amino acids at either side. Together, the four NET proteins and the six proteins identified here were termed the IRQ family.

The majority of these proteins are uncharacterised apart from At5g41790 which is characterised as COP1-INTERACTING PROTEIN 1 (CIP1; Matsui et al. 1995). COP1 (CONSTITUTIVE PHOTOMORPHOGENIC 1) was one of the first identified repressors of the photomorphogenic response in plants, with *cop1* mutant plants having the appearance of light grown plants when grown in the dark (Deng et al. 1991). Recent developments have demonstrated that COP1 is a RING E3 ubiquitin ligase, that targets key photomorphogenic regulators for proteosomal degradation (Lau & Deng 2012).

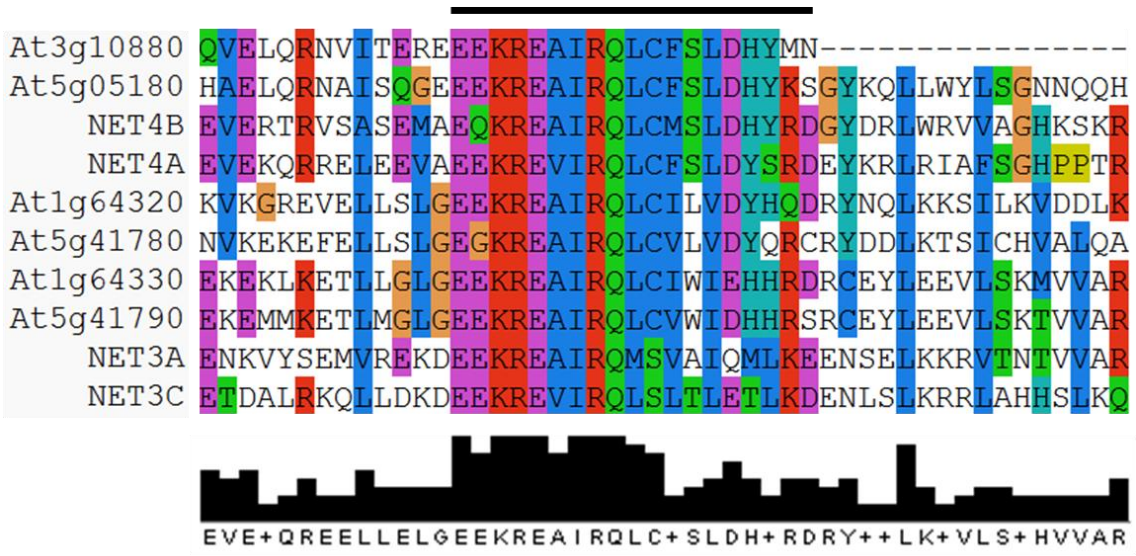

Colour	Residue at position	(Threshold, residue group)
BLUE	A, I, L, M, F, W, V	(60% WLVIMAFCHP)
	C	(60% WLVIMAFCHP)
RED	R, K	(60% KR) (85% K, R, Q)
GREEN	N	(50% N) (85% N, Y)
	Q	(60% KR) (50% QE) (85% Q, K, E, R)
	S, T	(60% WLVIMAFCHP) (50% TS) (85% S, T)
PINK	C	(100% C)
MAGENTA	E	(60% KR) (50% QE) (85% E, Q, D)
	D	(60% KR), (85% K,R,Q) (50% ED)
ORANGE	G	(0% G)
CYAN	H, Y	(60% WLVIMAFCHP) (85% W,Y,A,C,P,Q,F,H,I,L,M,V)
YELLOW	P	(0% P)

Figure 8.1: Alignment of the IRQ domains of the Arabidopsis IRQ family proteins. The homologous C-terminal regions of the newly discovered IRQ domain containing proteins and the four NET proteins were aligned using Clustal X2.1 (Larkin et al. 2007), and were coloured according to the default colour ClustalX colour scheme. The black line above the alignment represents the most highly conserved region within the domain and the consensus sequence is shown below. The ClustalX colour scheme key is shown below and denotes a colour according to the amino acid characteristics and conservation in the alignment. The key works as follows: the colour for the column is generated if the threshold value is met or exceeded. The minimum percentage is shown with the amino acids that must meet or exceed this threshold value. If the residues are grouped together such as 'KR' then the colour is applied if any combination of these residues meets or exceeds the threshold percentage. If the residues are separated by commas then the colour is applied when one of these residues individually meets or exceeds the threshold value.

COP1 localises to the nucleus in the dark and is able to target key transcription factors for degradation. However in the light, COP1 is exported from the nucleus and is present in the cytosol, which therefore allows specific transcription factors to promote photomorphogenesis (Lau & Deng 2012).

CIP1 was shown to interact with the predicted coiled-coil domain of COP1 *in vitro,* through a Far-Western blot of a recombinant CIP1 protein expressed from *Escherichia coli* and probed with biotin labelled COP1 (Matsui et al. 1995). Further analysis into the subcellular localisation of CIP1 in this study, using immunofluorescence with a CIP1 polyclonal antibody, revealed that it localised to a cytoskeleton-like filamentous array in Arabidopsis hypocotyl and cotyledon protoplasts and had a punctate localisation in root protoplasts. The authors of this paper hypothesised that the interaction between CIP1 and COP1 could be important in sequestering COP1 in the cytosol under light conditions, thereby preventing it from localising to the nucleus in the hypocotyl cells.

Although the other five proteins are currently uncharacterised, The Arabidopsis Information Resource (TAIR) database annotated At1g64330, At1g64320 and At5g41780 as myosin heavy chain-related proteins. At1g64330 and At1g64320 were also annotated as myosin heavy chain-related proteins in a study looking at putative Arabidopsis homologues of metazoan cytoskeletal coiled-coil proteins (Gardiner et al. 2011). This study used the PROPSEARCH algorithm to compare sequences on their amino acid compositions rather than working solely on sequence alignment. However, the authors noted that these two proteins are not true motor domain homologues.

Proteins containing outlier homologues of the IRQ domain were also detected in the Arabidopsis proteome. The most closely related outlier was ATATH8 (At2g39190.2), which is a member of the ABC (ATP-binding cassette) transporter family. The ATATH8 region of homology with the NET4B highly conserved IRQ region is shown in Figure 8.2, as well as the alignment of the NET4B and NET3A conserved IRQ region which show the least similarity out of all the nine other IRQ proteins.

This region of ATATH8 contained some identical amino acids with the NET4B IRQ domain, however, this region was distinctly different from the other 10 IRQ proteins. Figure 8.2 (c) shows an alignment of the IRQ domain of the IRQ proteins with the homologous region in ATATH8 and was generated using ClustalX2.1 (Larkin et al. 2007). This revealed that ATATH8 only shared partial conservation with the other

(a)

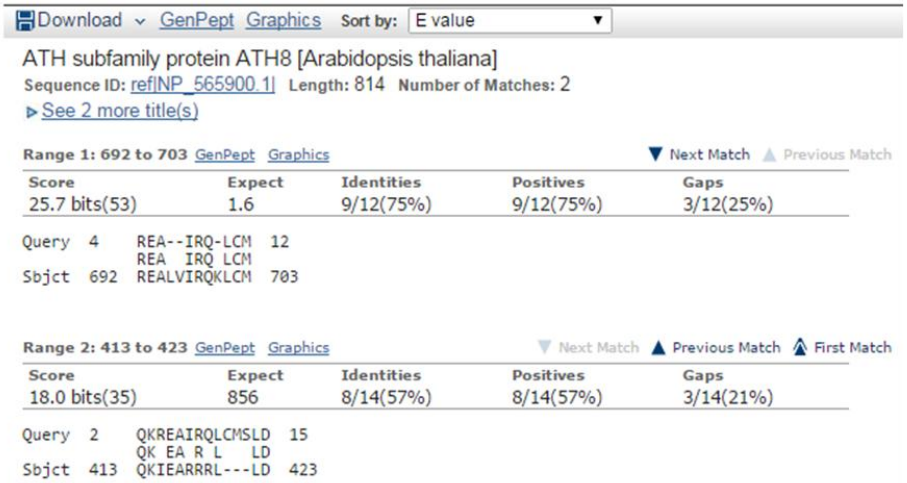

(b)

(c)

Figure 8.2: Identifying the outlier of the IRQ family. ATATH8 contains a region that is similar to the IRQ domain but is not as highly conserved as the other ten proteins. (a) and (b) screen shots from the initial BLASTp search using the conserved region of the NET4B IRQ domain, showing the alignment with (a) ATATH8 and (b) NET3A for comparison. (c) ClustalX2.1 was used to align ATATH8 with the IRQ proteins (Larkin et al. 2007), and was coloured using the ClustalX default colour scheme (as described in Figure 8.1).

proteins within the central highly conserved region, and was therefore not defined as an IRQ family member in this study.

8.3 Cladistic analysis of the Arabidopsis IRQ family

To better understand the relationship between the IRQ proteins, an IRQ family tree was generated. This approach was also used in the discovery of the NET proteins and was useful in defining different groups or subfamilies within the NET family (Calcutt 2009).

The full-length amino acid sequences of each IRQ protein was obtained from the TAIR database. Only At5g05180 had two different gene models, At5g05180.1 and At5g05180.2, with the former being annotated as the representative gene model. The second gene model is a splice variant that results in a reduction of 24 central amino acid residues (from amino acid residues 198-223 on At5g05180.1). The annotated representative gene model was used to generate the figures in this chapter for cladistic analysis and protein secondary structure predictions. Testing the alternative gene model in the aforementioned analysis did not lead to a dramatic change in the overall result and only changed the relative positions of the domains listed in the section below.

The relationship between the IRQ proteins was investigated by comparing the full-length amino acid sequences using ClustalX2.1 (Larkin et al. 2007), and a cladogram was generated through the bootstrapped neighbour-joining algorithm using 1000 iterations (Saitou & Nei 1987). The cladogram was then visualised in a radial format using the Hypertree programme and is shown in Figure 8.3 (Bingham & Sudarsanam 2000). This cladogram shows the bootstrap values at each branch node, and represents the number of times out of 1000 repetitions that the programme generated that particular branch node. These values represent the level of confidence in the specific branch node. Each branch node uses a different colour to represent the individual subfamilies within the IRQ family.

This cladogram shows that the 10 proteins form five different subfamilies, each composed of two proteins. The NET proteins could still be found in their previously classified groupings, with the NET3 proteins being distinct from the NET4s (Calcutt 2009, Deeks et al. 2012). The six newly identified IRQ domain proteins form three different groups; group 1 contained At3g10880 and At5g05180, group 2 contained At1g64320 and At5g41780, and group 3 contained At1g64330 and At5g41790 (CIP1).

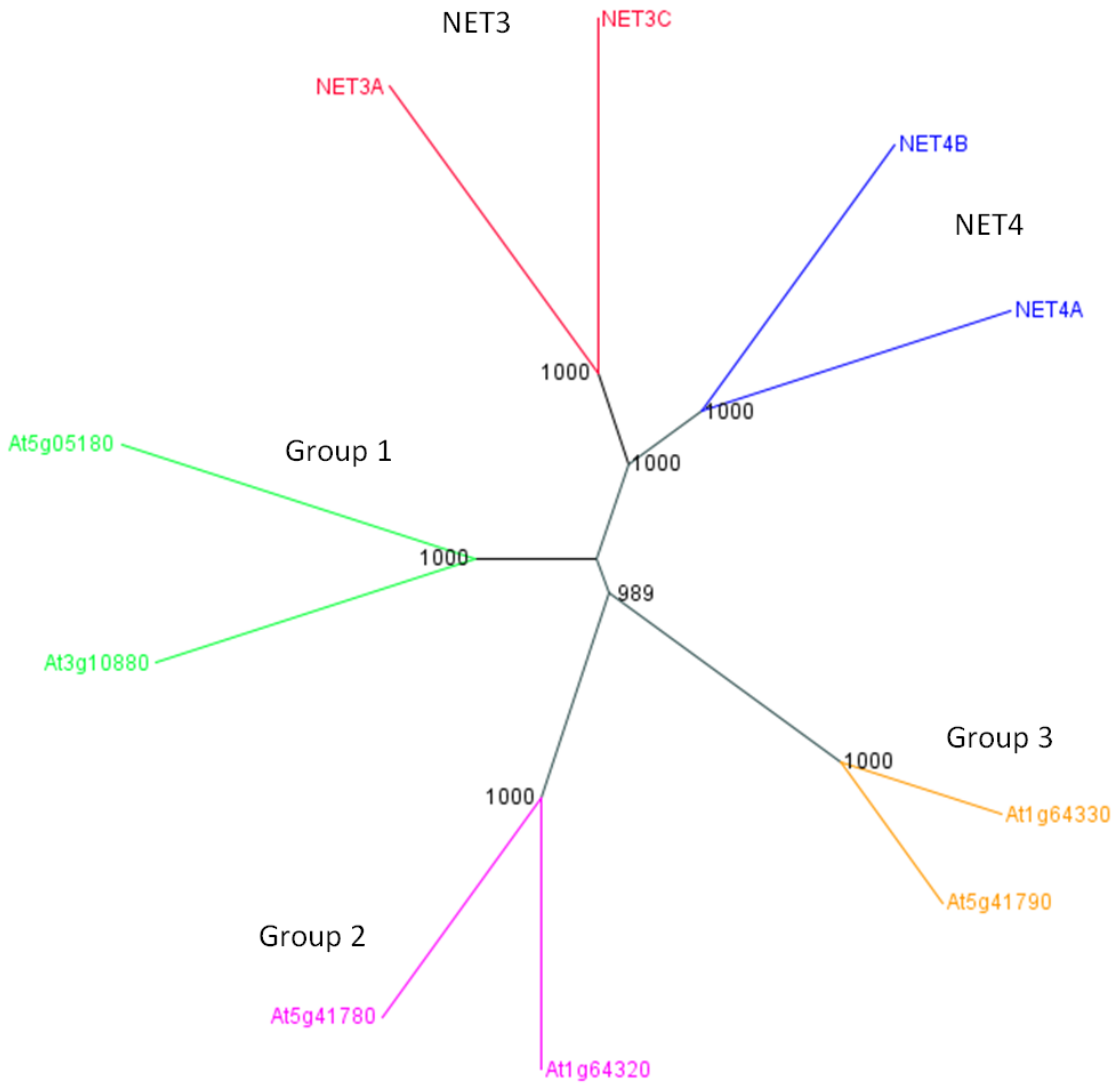

Figure 8.3: Cladogram of the Arabidopsis IRQ family. The full-length IRQ proteins were aligned using ClustalX2.1 (Larkin et al. 2007), and the bootstrap neighbour-joining algorithm was used to generate a family tree which was drawn in a radial format using the Hypertree programme (Bingham & Sudarsanam 2000). The bootstrap values are shown at the node of each branch and represent the number of times out of 1000 that the branch was generated by the programme. The different IRQ proteins group into 5 subfamilies, with two NET subfamilies and three novel groups, termed groups 1-3. Each subfamily branchnode is represented with a different colour.

This analysis has demonstrated that the Arabidopsis IRQ family divides into 5 different subgroups. Further analysis of the novel family members was performed through studying their predicted secondary structure, potential interacting partners, gene expression analysis and subcellular localisation predictions.

8.4 Predicted protein structures of the IRQ family

To further characterise these novel IRQ proteins it was important to study their predicted secondary structure. The SMART database and the Paircoil2 programme (Schultz et al. 1998; Letunic et al. 2014; McDonnell et al. 2006), were used to analyse the protein structure of the IRQ family members and the result of this analysis is shown in Figure 8.4, with the full breakdown of domains shown in Appendix 5.

Table 8.1 lists the amino acid lengths and predicted molecular weight of the IRQ proteins. Notably, At3g10880 is the smallest of the novel IRQ proteins with a molecular weight of 37 kDa and At5g41790 (CIP1) is the largest at 182 kDa. The remaining four proteins ranged in size from 50 to 65 kDa.

The IRQ proteins all share the conserved IRQ domain at their C-terminus (see Figure 8.1 for an alignment). All of these IRQ proteins shared a very highly conserved central region of this domain. Conserved residues could also be found outside of this central region, suggesting that this defined region is homologous between the proteins. Notably, the C-terminus of At3g10880 finished at the end of the central conserved region. This could have important implications as the results of the Y2H studies in Chapter 6.4 demonstrated that the central region of the NET4B IRQ domain alone was insufficient to mediate the Rab interaction. Therefore Figure 8.4 shows the distinction between the full IRQ domain and the highly conserved central region with two different shades of blue. This distinction could be important in future studies when considering the function of this domain in the IRQ family proteins.

The position of the IRQ domain was consistently at the C-terminus of the protein, although slight differences in the relative proximity to the C-terminus can be found between the different proteins. Significantly, the position of the IRQ domain in the NET3s is markedly different from the other IRQ family members, with the NET3 IRQ domain being more central than the other proteins.

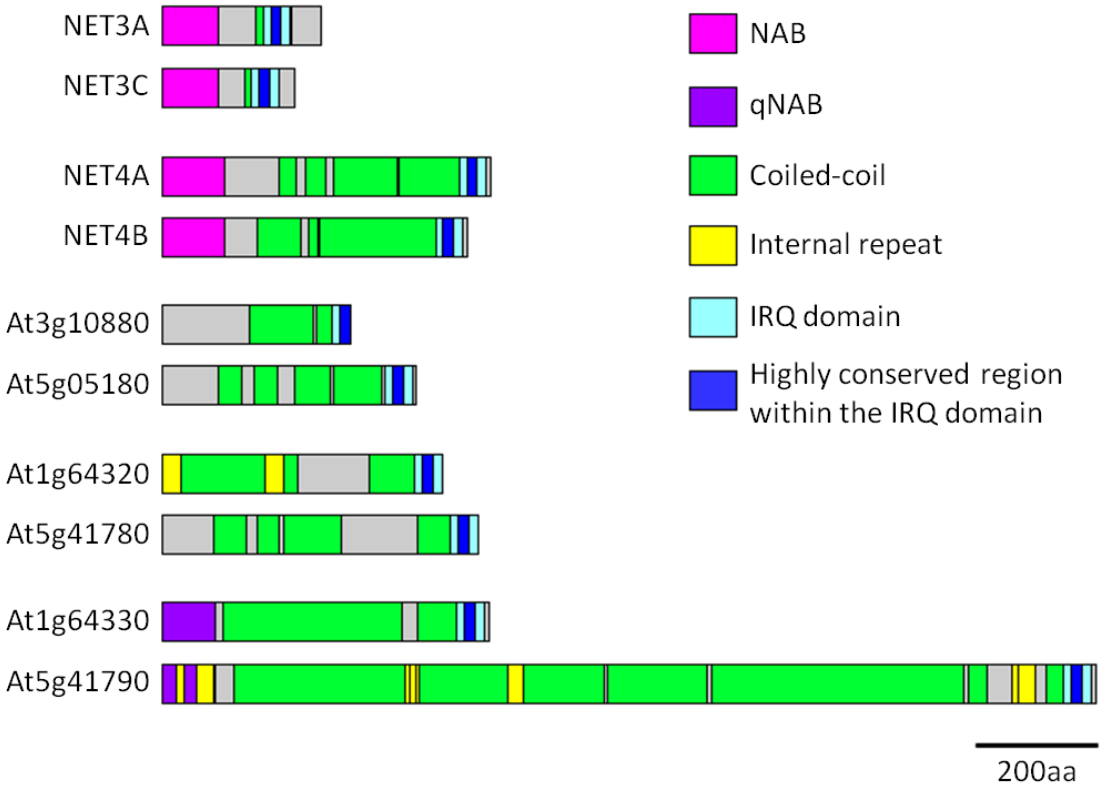

Figure 8.4 Predicted secondary structure of the IRQ proteins. Diagram representing the different domains of the IRQ proteins identified using the SMART and Paircoil2 programmes as well as protein sequence alignments. This diagram was created using the Illustrator of Biological Sequences (IBS) software (Liu et al. 2015).

Protein	Amino acid length	MW (kDa)
NET3A	269	31
NET3C	225	26
NET4A	558	64
NET4B	517	60
At3g10880	319	37
At5g05180	432	50
At1g64320	476	55
At5g41780	537	63
At1g64330	555	65
At5g41790	1586	182

Table 8.1: Amino acid lengths and predicted molecular weights (MW) of the IRQ proteins.

The SMART database did not detect any additional domains in the novel IRQ proteins. However this database did predict that At1g64330 and At5g41790 contained a NAB (KIP1; Pfam 07765) domain at the N-terminus of the proteins. The possibility of these proteins containing a NAB domain was analysed further by aligning the N-terminal 120 amino acids (aa) of the IRQ and NET proteins using ClustalX2.1 (Larkin et al. 2007), and the results of this are shown in Figure 8.5. This alignment shows the high degree of conservation in the NAB domain between the NET proteins. The N-terminus of the At1g64330 and At5g41790 proteins show some limited similarity with the NAB domain in terms of amino acid composition, however they do not contain the conserved triple tryptophan motif that is found in all the NAB domains (Hawkins et al. 2014). Therefore in the protein structure diagram in Figure 8.4 the N-terminus of these proteins is denoted as a quasi-NAB (qNAB) domain as it shares some similarity to the NAB domain.

Similar to the NET proteins, the IRQ proteins all contain predicted coiled-coil domains. The Paircoil2 programme was used to predict the coiled-coil domains shown in Figure 8.4, using a 28-residue window and a threshold probability of < 0.025 for a coiled coil domain. The presence of these coiled-coil domains in these proteins could indicate that they have the ability to oligomerise into higher order structures (Rose & Meier 2004).

Furthermore, the SMART database detected internal repeats within At1g64320 and At5g41790 (CIP1). At1g64320 contained one internal repeating region whereas At5g41790 contained four.

The results of this analysis demonstrated that the IRQ family all share a conserved C-terminal IRQ domain and are largely composed of predicted coiled-coil domains in the rest of the protein. Interestingly, the IRQ domain can be found in four NET proteins that contain a NAB domain and an IRQ domain, two proteins that contain a quasi-NAB domain and an IRQ domain, and four proteins that only contain an IRQ domain.

8.4.1 Predicted secondary structure of the IRQ domain

As well as studying the predicted secondary structure of the full-length IRQ proteins, it was also of interest to study the predicted secondary structure of the conserved IRQ domain. As this domain is highly conserved, it could form a conserved structure that is important to its function.

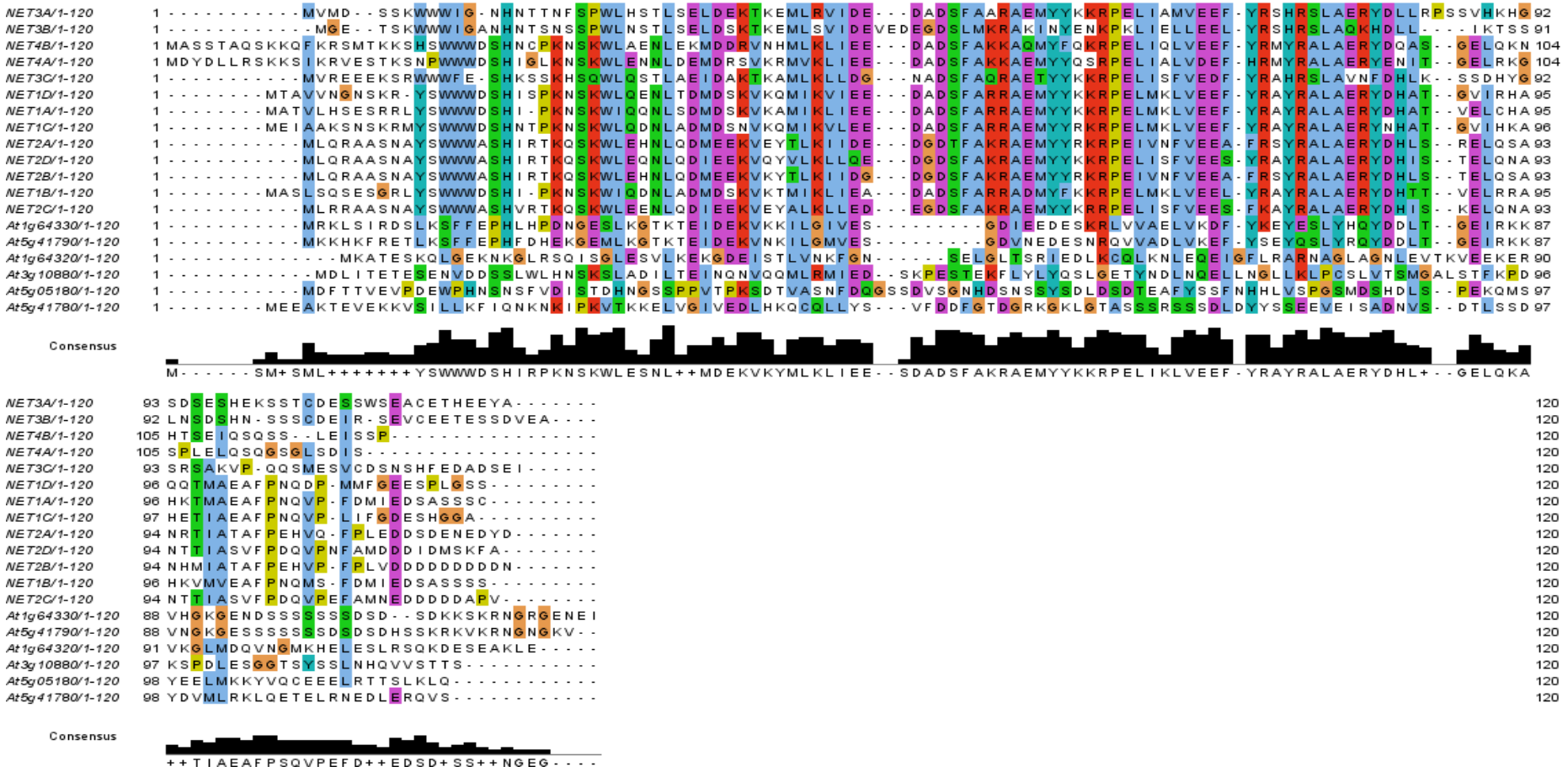

Figure 8.5: Alignment of the N-terminal regions of the NET and IRQ proteins. The N-terminal 120 aa of the NET and IRQ proteins were aligned using ClustalX2.1 (Larkin et al. 2007), and imaged using Jalview using the default ClustalX2.1 colour settings (Waterhouse et al. 2009). At1g64330 and At5g41790 showed some resemblance to the NAB domain, and the N-terminus of these two proteins was therefore termed a quasi-NAB domain (qNAB).

The secondary structure of the IRQ domain was predicted through the Jpred version 4 programme on Jalview (Waterhouse et al. 2009; Drozdetskiy et al. 2015), and the results are shown in Figure 8.6. This programme combines secondary structure predictions from different algorithms as well as using multiple sequence alignments to improve the accuracy in secondary structure predictions and provides an output in terms of α-helices, ß-sheets and coiled-coils (Cuff et al. 1998; Cole et al. 2008).

The Jpred version 4 was used to predict the secondary structure of the NET4B IRQ domain as the target sequence, using the alignment of the additional IRQ domains in the programme. This programme uses the Jnet algorithm for secondary structure prediction, and combines the predictions using position specific scoring matrixes (PSSM) and Hidden Markov Models (HMM). The output of this programme shows that the domain is predicted to form one α-helix, as shown by the jnetpred prediction. The confidence for this prediction is shown by JNETCONF, and demonstrates that only the central conserved region and a more C-terminal region has a high confidence of forming α-helices. It should be noted that this programme can also predict coiled-coil domain regions however this was not computed in this algorithm due to the small size of this domain.

When considering the significance of this secondary structure prediction, it is important to consider the NET4B IRQ domain as a Rab-binding domain. Most of the structurally characterised Rab effectors interact with their respective Rab via an interaction domain that consists of 1-2 α-helices or coiled-coil regions (Zhu et al. 2004; Wu et al. 2005; Eathiraj et al. 2005; Eathiraj et al. 2006; Jagoe et al. 2006; Kukimoto-Niino et al. 2008; Chavas et al. 2008; Schoebel et al. 2011; Lall et al. 2015). Therefore the confirmation of this domain could be important in providing a platform to interact with active Rab GTPases.

8.5 Gene expression analysis of the IRQ family

Having used bioinformatics analysis to predict the secondary structure of the six novel IRQ proteins, the next step in the analysis was to investigate their respective gene expression patterns. To perform this analysis, the Arabidopsis eFP browser was used to study the expression pattern of these genes, as was used previously for *NET4B* in Chapter 3. The Arabidopsis eFP browser visualises publicly available DNA microarray data that is generated for approximately 22,000 Arabidopsis genes represented on the

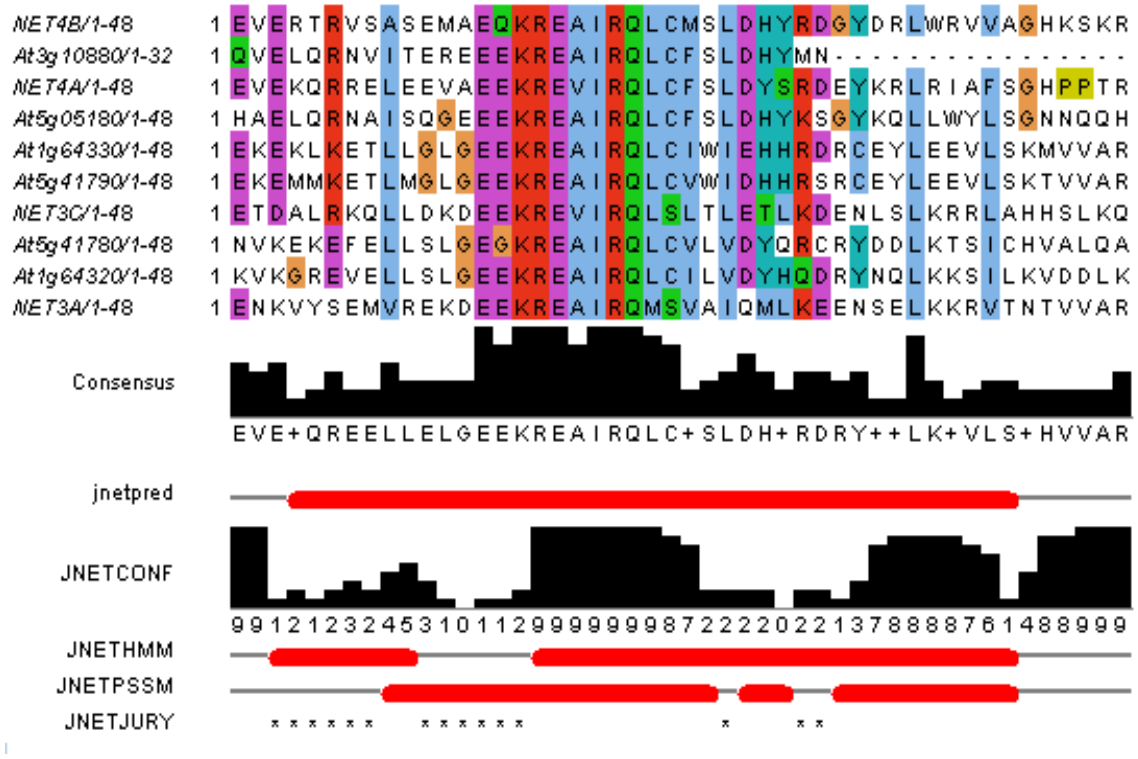

Figure 8.6: Predicted secondary structure of the IRQ domain. The predicted secondary structure of the NET4B IRQ domain was generated using the Jpred programme on Jalview. This programme combines various different secondary structure prediction algorithms as well as multiple sequence alignments to generate a predicted secondary structure. "jnetpred" represents the final prediction, showing one α-helix in red. "JNETCONF" represents the confidence in this prediction ranging from high (10) to low (0). "JNETHMM" and "JNETPSSM" represent two different algorithms (Hidden Markov Models and position specific scoring matrixes respectively). "JNETJURY" is used to denote positions of discrepancy between the two algorithm predictions.

Affymetrix ATH1 GeneChip (Winter et al. 2007). The developmental map of Arabidopsis tissue expression pattern was primarily used to study the gene expression pattern of the novel IRQ genes. This data was generated from a spatial map of Arabidopsis gene expression through the AtGenExpress project (Schmid et al. 2005). The tissue specific view from the Arabidopsis eFP browser was also consulted and the results were reported if any additional observations could be made.

Figure 8.7 (a) and (b) show the developmental map for the two group 1 members, At3g10880 and At5g05180. Both of these genes are weakly expressed in all tissues in terms of absolute expression levels, with peak expression value of 50 and 123 respectively. Both genes are relatively more abundant in the meristematic tissue of the shoot apex, as well as in the hypocotyl and early stages of floral development. In

addition, At5g05180 showed a relatively high abundance of expression in the petiole of the leaf, the stamen and in the siliques at a stage that corresponds to early embryo development (heart stage).

The gene expression profiles of the group 2 members are shown in Figures 8.7 (c) and (d). Both of these genes showed the highest level of expression in the mature pollen. Flowers and stamens also showed lower levels of expression of these genes, and relatively little expression could be found in the rest of the plant, suggesting that these two genes are pollen specific. Although both of these genes are expressed in the same tissue, the absolute levels of expression differed dramatically between the two, with At5g41780 showing a much higher level of expression than At1g64320. The absolute peak level of expression seen in the mature pollen in this study for At5g41780 and At1g64320 was 1439 and 183 respectively.

Figure 8.7 (e) and (f) show the gene expression profiles of the two group 3 members. At5g41790 had a relatively intermediate level of absolute expression levels with a peak value at 503. At1g64330 had a slightly lower level of absolute expression and had a peak value of 177. At1g64330 has a relatively uniform level of expression distributed across the different tissues, and the highest levels of expression could be seen in the dry seeds and the later stages of embryo development that corresponded to the curled to green cotyledons stage. Expression of At5g41790 was mostly observed in the leaf tissue, including both rosette and cauline leaves, as well as the sepals. The highest level of expression of this gene was found in the senescent leaves. Examining the tissue specific viewer also demonstrated that At1g64330 is highly expressed in trichomes (Marks et al. 2009), and At5g41790 is highly expressed in the xylem of the inflorescence stem (results provided by the Campbell lab).

8.6 Interacting partners of the novel IRQ family members

The potential interacting partners of the novel IRQ proteins was also investigated in an attempt to further our understanding of these proteins. Studying protein-protein interactions could determine whether these proteins function in a specific complex and could suggest a possible role for these proteins. The Biological General Repository for Interaction Datasets (BioGRID) database was used to search for interacting partners of the newly discovered IRQ proteins. This database curates publicly available protein interaction data from various model organisms and is a convenient tool to investigate

(a)

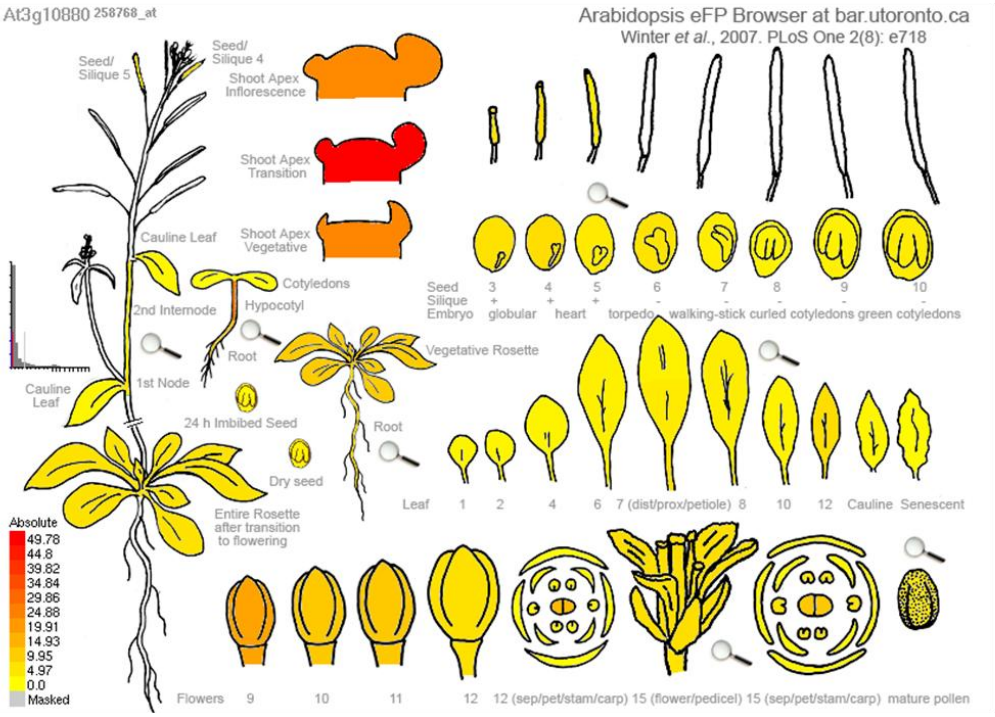

(b)

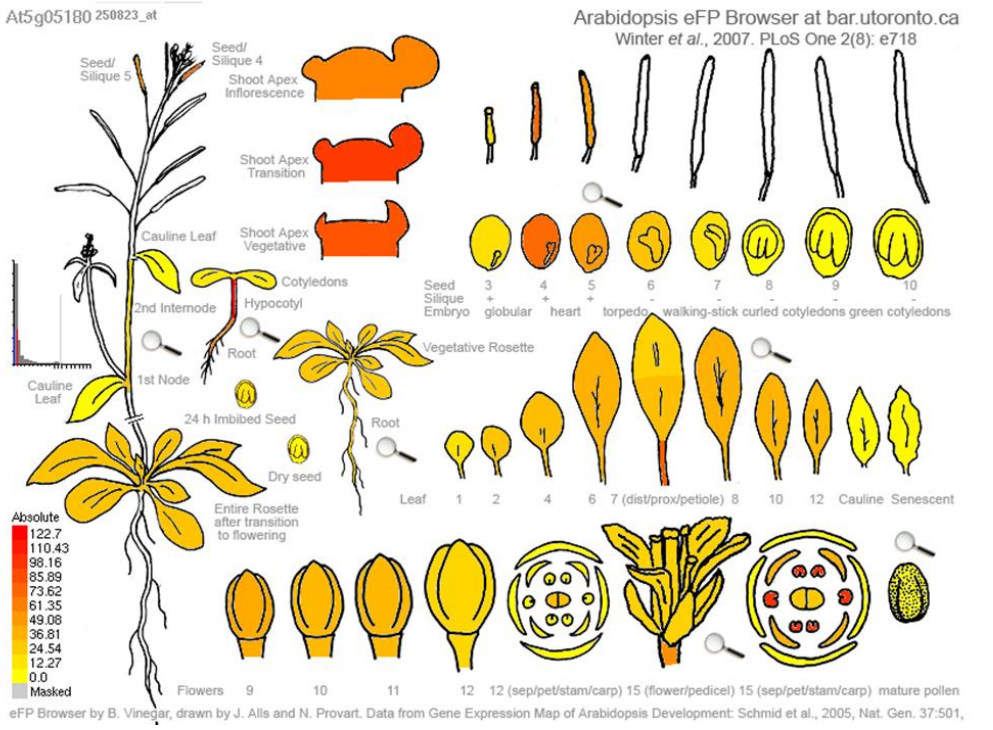

Figure 8.7: Gene expression patterns of the novel IRQ genes. The Arabidopsis eFP browser developmental map was used to visualised gene expression data relating to the tissue expression patterns of the IRQ genes (Winter et al. 2007). The browser shows expression levels on a gradient from low to high corresponding to a change in colour from yellow to red. (a) At3g10880, (b) At5g05180, (c) At1g64320, (d) At5g41780, (e) At1g64330, (f) At5g41790.

(c)

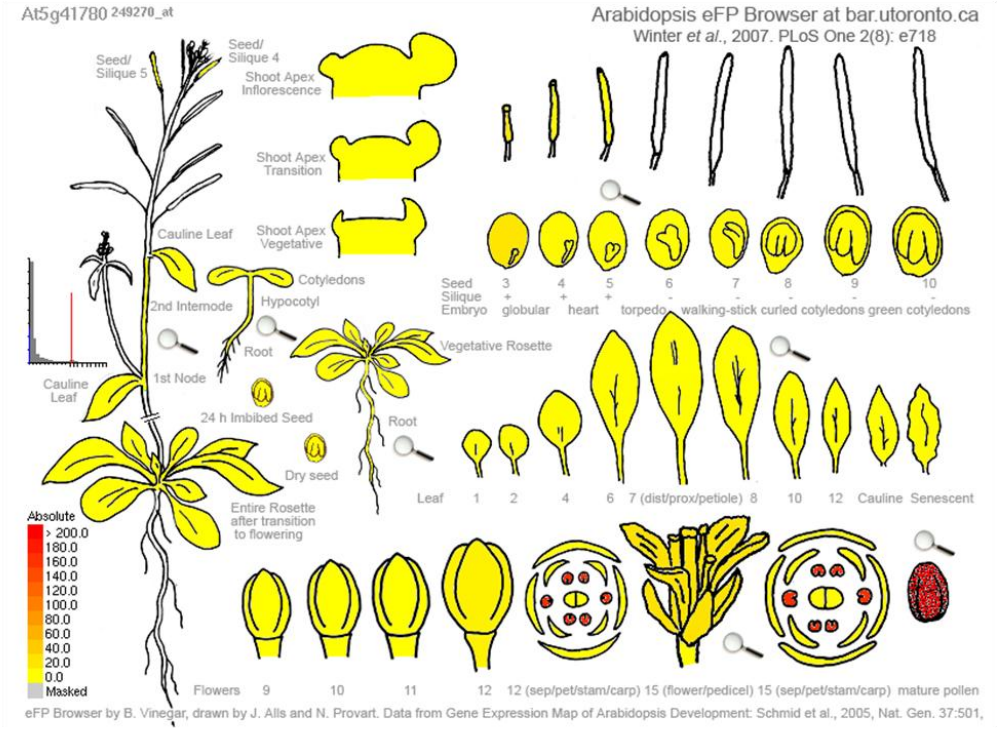
At5g41780 249270_at
Arabidopsis eFP Browser at bar.utoronto.ca
Winter et al., 2007. PLoS One 2(8): e718
Seed/ Silique 5
Seed/ Silique 4
Shoot Apex Inflorescence
Shoot Apex Transition
Shoot Apex Vegetative
Cauline Leaf
Cotyledons
Hypocotyl
2nd Internode
Root
1st Node
Cauline Leaf
24 h Imbibed Seed
Dry seed
Vegetative Rosette
Root
Entire Rosette after transition to flowering
Seed 3 4 5 6 7 8 9 10
Silique + + + - - - - -
Embryo globular heart torpedo walking-stick curled cotyledons green cotyledons
Leaf 1 2 4 6 7 (dist/prox/petiole) 8 10 12 Cauline Senescent
Absolute
> 200.0
180.0
160.0
140.0
120.0
100.0
80.0
60.0
40.0
20.0
0.0
Masked
Flowers 9 10 11 12 12 (sep/pet/stam/carp) 15 (flower/pedicel) 15 (sep/pet/stam/carp) mature pollen
eFP Browser by B. Vinegar, drawn by J. Alls and N. Provart. Data from Gene Expression Map of Arabidopsis Development: Schmid et al., 2005, Nat. Gen. 37:501,

(d)

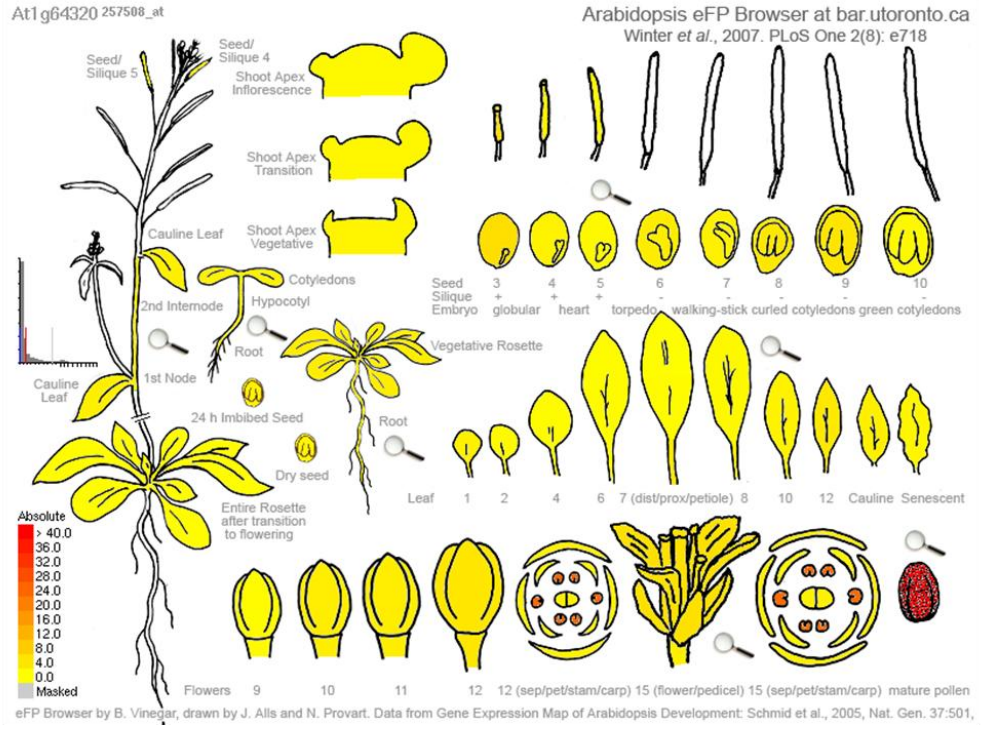
At1g64320 257508_at
Arabidopsis eFP Browser at bar.utoronto.ca
Winter et al., 2007. PLoS One 2(8): e718
Seed/ Silique 5
Seed/ Silique 4
Shoot Apex Inflorescence
Shoot Apex Transition
Shoot Apex Vegetative
Cauline Leaf
Cotyledons
Hypocotyl
2nd Internode
Root
1st Node
Cauline Leaf
24 h Imbibed Seed
Dry seed
Vegetative Rosette
Root
Entire Rosette after transition to flowering
Seed 3 4 5 6 7 8 9 10
Silique + + + - - - - -
Embryo globular heart torpedo walking-stick curled cotyledons green cotyledons
Leaf 1 2 4 6 7 (dist/prox/petiole) 8 10 12 Cauline Senescent
Absolute
> 40.0
36.0
32.0
28.0
24.0
20.0
16.0
12.0
8.0
4.0
0.0
Masked
Flowers 9 10 11 12 12 (sep/pet/stam/carp) 15 (flower/pedicel) 15 (sep/pet/stam/carp) mature pollen
eFP Browser by B. Vinegar, drawn by J. Alls and N. Provart. Data from Gene Expression Map of Arabidopsis Development: Schmid et al., 2005, Nat. Gen. 37:501,

(e)

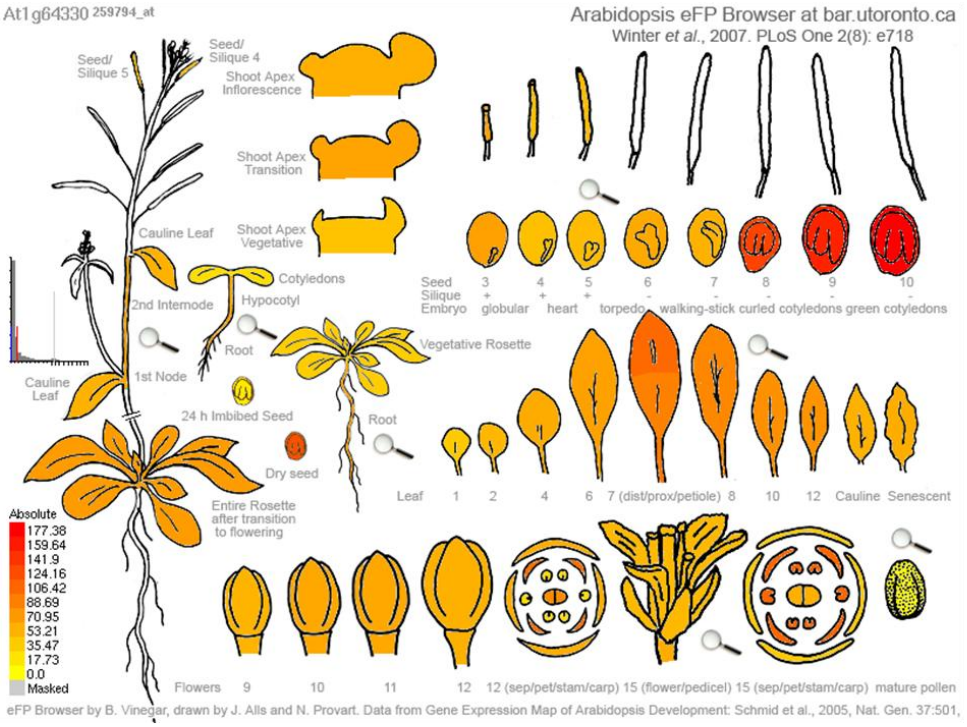
At1g64330 259794_at
Arabidopsis eFP Browser at bar.utoronto.ca
Winter et al., 2007. PLoS One 2(8): e718
Seed/ Silique 5
Seed/ Silique 4
Shoot Apex Inflorescence
Shoot Apex Transition
Shoot Apex Vegetative
Cauline Leaf
Cotyledons
Hypocotyl
2nd Internode
Root
1st Node
24 h Imbibed Seed
Dry seed
Entire Rosette after transition to flowering
Vegetative Rosette
Seed 3 4 5 6 7 8 9 10
Silique + + + - - - - -
Embryo globular heart torpedo walking-stick curled cotyledons green cotyledons
Leaf 1 2 4 6 7 (dist/prox/petiole) 8 10 12 Cauline Senescent
Absolute
177.38
159.64
141.9
124.16
106.42
88.69
70.95
53.21
35.47
17.73
0.0
Masked
Flowers 9 10 11 12 12 (sep/pet/stam/carp) 15 (flower/pedicel) 15 (sep/pet/stam/carp) mature pollen
eFP Browser by B. Vinegar, drawn by J. Alls and N. Provart. Data from Gene Expression Map of Arabidopsis Development: Schmid et al., 2005, Nat. Gen. 37:501,

(f)

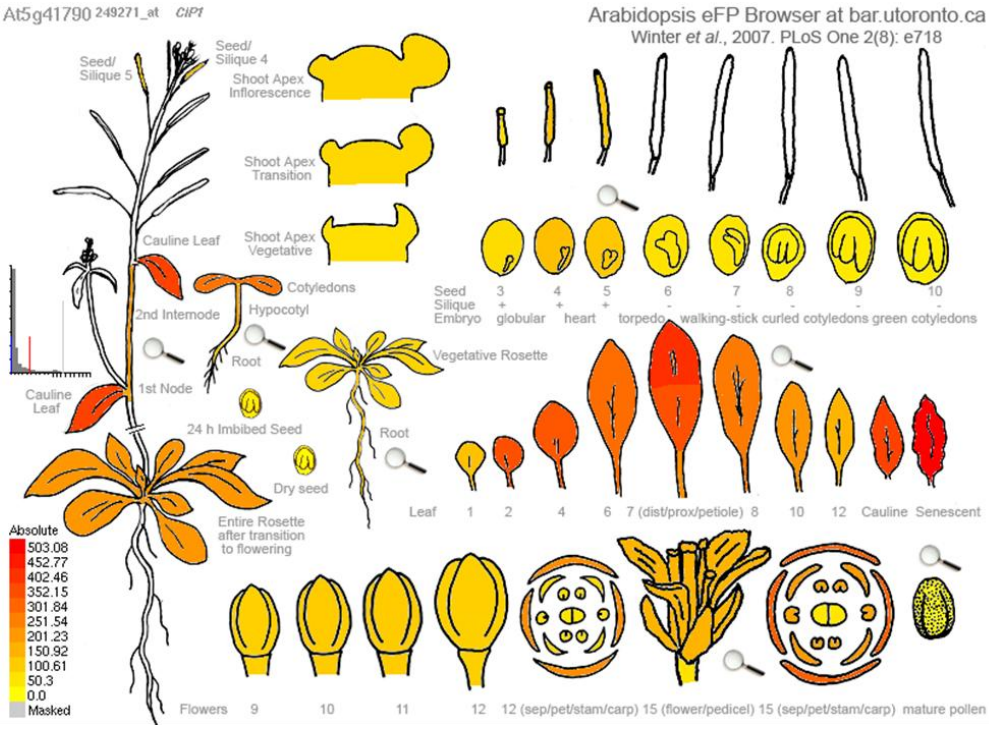
At5g41790 249271_at CIP1
Arabidopsis eFP Browser at bar.utoronto.ca
Winter et al., 2007. PLoS One 2(8): e718
Seed/ Silique 5
Seed/ Silique 4
Shoot Apex Inflorescence
Shoot Apex Transition
Shoot Apex Vegetative
Cauline Leaf
Cotyledons
Hypocotyl
2nd Internode
Root
1st Node
24 h Imbibed Seed
Dry seed
Entire Rosette after transition to flowering
Vegetative Rosette
Seed 3 4 5 6 7 8 9 10
Silique + + + - - - - -
Embryo globular heart torpedo walking-stick curled cotyledons green cotyledons
Leaf 1 2 4 6 7 (dist/prox/petiole) 8 10 12 Cauline Senescent
Absolute
503.08
452.77
402.46
352.15
301.84
251.54
201.23
150.92
100.61
50.3
0.0
Masked
Flowers 9 10 11 12 12 (sep/pet/stam/carp) 15 (flower/pedicel) 15 (sep/pet/stam/carp) mature pollen

protein-protein interactions (Stark et al. 2006; Chatr-Aryamontri et al. 2013). Protein-protein interactions could not be found for group 1 or group 2 members, however entries were found for At5g41790 (CIP1) and At1g64330.

The BioGRID database contained four entries for At5g41790 (CIP1). As previously discussed this protein was shown to interact with COP1 and was therefore termed the COP1 INTERACTING PROTEIN 1 (CIP1; Matsui et al. 1995). This database had also annotated that this protein could interact with CORONATINE INSENSTIVE 1 (COI1) and TRANSPORT INHIBITOR RESPONSE 1 (TIR1; Devoto et al. 2002). However this is an incorrect annotation as this paper used a Y2H screen to identify COI1 Interacting Partners which the authors termed CIP1-CIP7. The CIP1 found in this screen actually encoded ARABIDOPSIS SKP1 HOMOLOGUE 1 (ASK1; At1g75950). Finally, the database also revealed that At5g41790 could be conjugated to ubiquitin, in a high-throughput screen to identify ubiquitin targets in Arabidopsis (Kim et al. 2013). This could therefore suggest a possible method of posttranslational modification of this protein.

The potential interactor network for At1g64330, derived from BioGRID and additional co-immununoprecipitation (co-IP) data, is summarised in Figure 8.8. The BioGRID database has one annotated protein interaction entry for At1g64330 and that is an interaction with the cytoplasmic domain of ARABIDOPSIS HISTIDINE KINASE 2 (AHK2; Dortay et al. 2008). This interaction was found through a high-throughput Y2H screen using multiple components of the cytokinin signalling pathway as bait. AHK2 is a plasma membrane localised cytokinin receptor that is important for transmitting a phosphorylation cascade in response to cytokinin (To & Kieber 2008). The interaction between At1g64330 and AHK2 could implicate this protein in the signalling response to cytokinin and therefore in various plant developmental processes such as germination and shoot and root development (To & Kieber 2008).

In addition to At1g64330, 38 other proteins were shown to interact with AHK2 in the same screen. One of these proteins was DYNAMIN RELATED PROTEIN 1A (DRP1A, At5g42080), and analysing the protein-protein interactions of this protein has potentially identified another interactor of At1g64330.

Recently, the protein interactors of the PIN-FORMED 1 (PIN1, At1g73590) auxin efflux carrier was investigated through co-immunoprecipitation (co-IP) of GFP-PIN1

from Arabidopsis seedlings (Mravec et al. 2011). This study identified that DRP1A co-immunoprecipitated with PIN1 and that the interaction of these proteins was important in the localisation of PIN1 and consequently auxin-mediated development. Several additional proteins were also co-immunoprecipitated with PIN1 in this study and one of these proteins was annotated as a myosin heavy chain-related protein with a molecular weight of 64.494kDA. Although gene loci were not included, the protein description and molecular weight matches that of At1g64330. This protein could potentially represent a true interactor of PIN1 as it was recorded to have a high peak protein intensity as well as relatively high abundance in the experimental co-IP in comparison to the control. Therefore At1g64330 could potentially interact with PIN1 and could have an important role linked to this auxin efflux carrier.

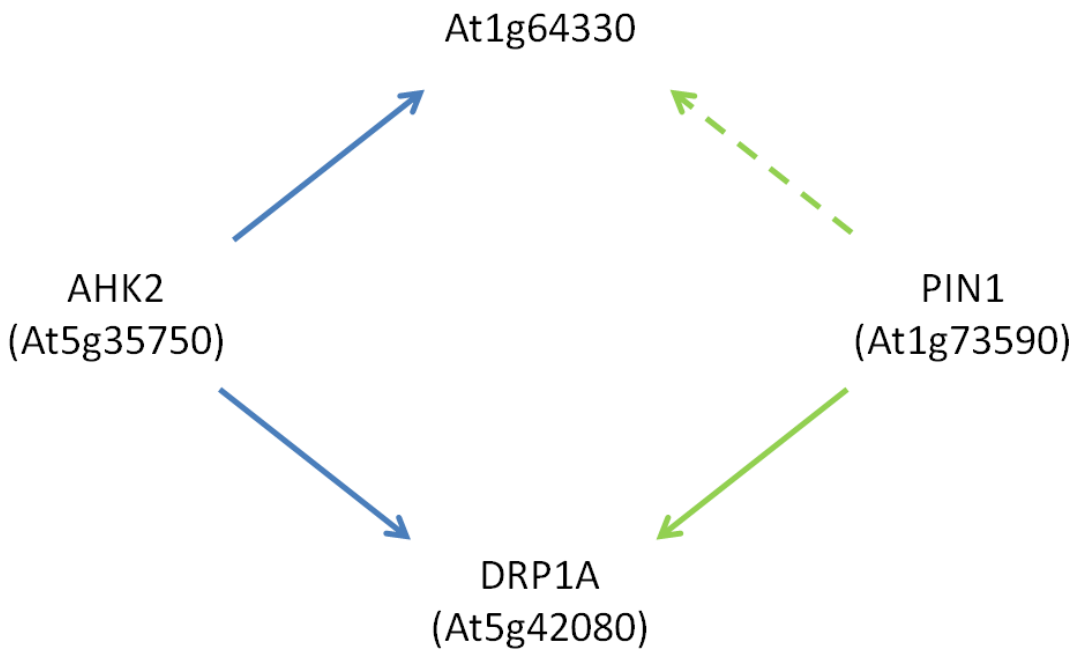

Figure 8.8: Schematic diagram of potential protein-protein interactions with At1g64330. Diagram shows the interaction data derived from two different data sets; a Y2H screen using AHK2 as bait (Dortay et al. 2008) and co-IP data using PIN1 as bait (Mravec et al. 2011). Blue arrow represents the Y2H study and the green arrow represents the co-IP data. The direction of arrow represents which protein was used as the bait (AHK2 and PIN1). The interaction between PIN1 and At1g64330 is represented by a dashed line as the exact gene locus was not stated in the results.

8.7 Subcellular localisation prediction using bioinformatics

Characterising a protein to a specific subcellular compartment can be useful when assigning a particular function to that protein. Therefore the final element of bioinformatics analysis for the novel IRQ family proteins involved analysing their subcellular localisation predictions.

The subcellular localisation database for Arabidopsis proteins (SUBA3) was used to analyse the bioinformatics data relating to the novel IRQ proteins. This database combines both manually curated subcellular proteomics, fluorescent protein visualisation and protein-protein interaction data with predictions from various different subcellular prediction programmes (Tanz et al. 2013). Eleven different subcellular prediction programmes were used during this analysis; SubLoc (Hua & Sun 2001), Wolf PSORT (Horton et al. 2007), MultiLoc2 (Blum et al. 2009), AdaBoost (Niu et al. 2008), BaCelLo (Pierleoni et al. 2006), Nucleo (Hawkins et al. 2007), Plant-mPloc (Chou & Shen 2010), PProwler (Hawkins & Bodén 2006), SLPFA (Tamura & Akutsu 2007), SLP-Local (Matsuda et al. 2005) and YLoc (Briesemeister et al. 2010). These computational prediction programmes use various different algorithms to predict subcellular compartmentalisation through analysing sequence features of a proteins amino acid sequence. The SUBA3 database combines these predictions with experimental data to show whether a protein can localise to 12 different subcellular compartments; cell plate, cytoskeleton, cytosol, endoplasmic reticulum, extracellular, Golgi, mitochondrion, nucleus, peroxisome, plasma membrane, plastid, and vacuole.

The Cell eFP browser was used to visualise the data from SUBA3 as it provides a confidence gradient associated with the predictions (Winter et al. 2007), and Figure 8.9 and Table 8.2 show the results of this analysis. The immunolocalisation data for At5g41790 was also added to this summary table as SUBA3 only curates fluorescent protein fusion data.

The SUBA3 data for six novel IRQ proteins demonstrate predicted localisation to the cytosol, nucleus and mitochondrion. In addition, At5g05180 is also predicted to localise to plastids, and At1g64320, At5g41780 and At1g64330 are predicted to localise to the cytoskeleton. However, the confidence in these predictions is relatively low for each of these proteins.

(a)

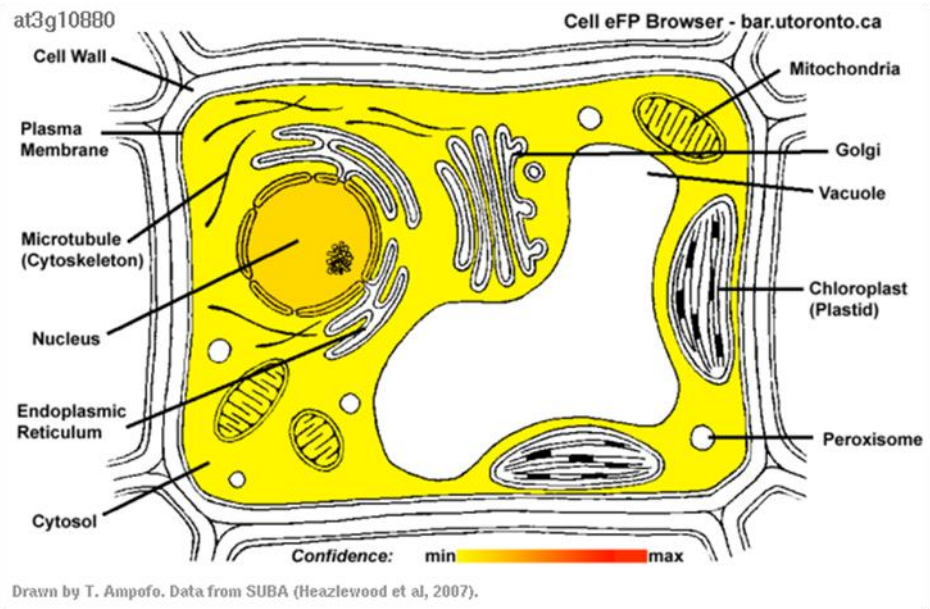

(b)

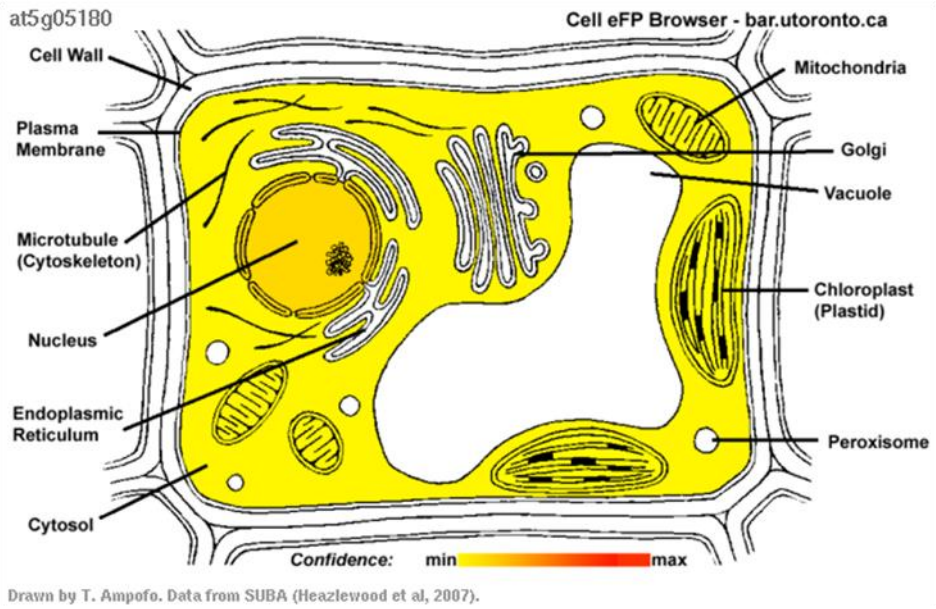

Figure 8.9: Subcellular localisation predictions for the IRQ proteins. The Cell eFP browser was used to visualise subcellular localisation prediction data compiled by the SUBA3 programme (Winter et al. 2007; Tanz et al. 2013). The confidence in these predictions is demonstrated by a gradient scale from yellow to red, with red representing high confidence. (a)-(f) Cell eFP browser diagrams for the novel IRQ proteins, (a) At3g10880, (b) At5g05180, (c) At1g6320, (d) At5g41790, (e) At1g64330, (f) At5g41790.

(c)

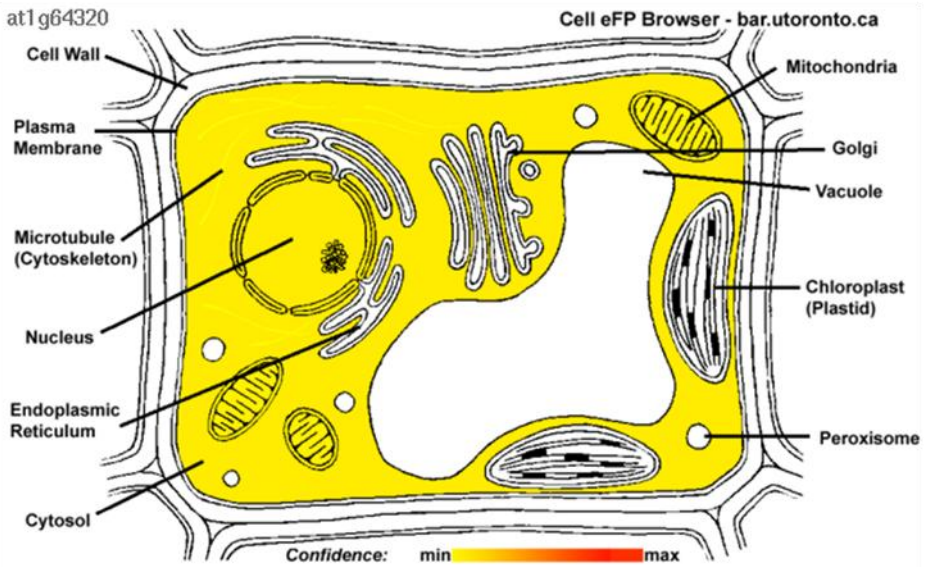
at1g64320
Cell eFP Browser - bar.utoronto.ca
Cell Wall
Plasma Membrane
Microtubule (Cytoskeleton)
Nucleus
Endoplasmic Reticulum
Cytosol
Mitochondria
Golgi
Vacuole
Chloroplast (Plastid)
Peroxisome
Confidence: min max
Drawn by T. Ampofo. Data from SUBA (Heazlewood et al, 2007).

(d)

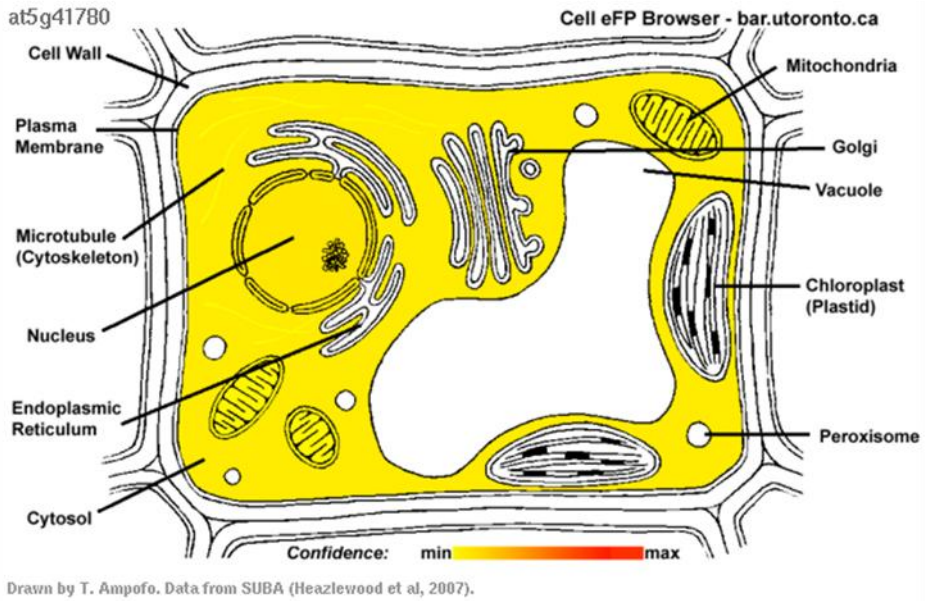
at5g41780
Cell eFP Browser - bar.utoronto.ca
Cell Wall
Plasma Membrane
Microtubule (Cytoskeleton)
Nucleus
Endoplasmic Reticulum
Cytosol
Mitochondria
Golgi
Vacuole
Chloroplast (Plastid)
Peroxisome
Confidence: min max
Drawn by T. Ampofo. Data from SUBA (Heazlewood et al, 2007).

(e)

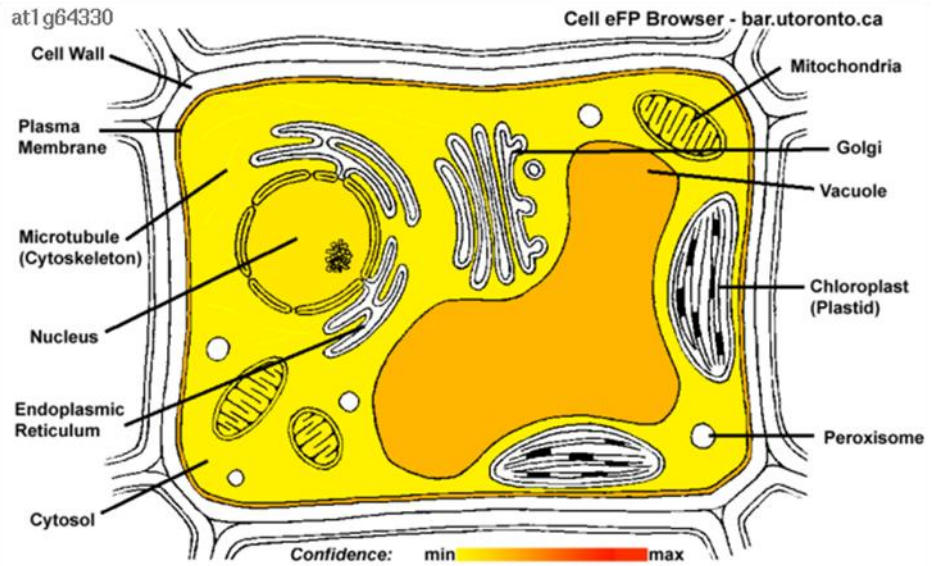
at1g64330
Cell eFP Browser - bar.utoronto.ca
Cell Wall
Plasma Membrane
Microtubule (Cytoskeleton)
Nucleus
Endoplasmic Reticulum
Cytosol
Mitochondria
Golgi
Vacuole
Chloroplast (Plastid)
Peroxisome
Confidence: min max
Drawn by T. Ampofo. Data from SUBA (Heazlewood et al, 2007).

(f)

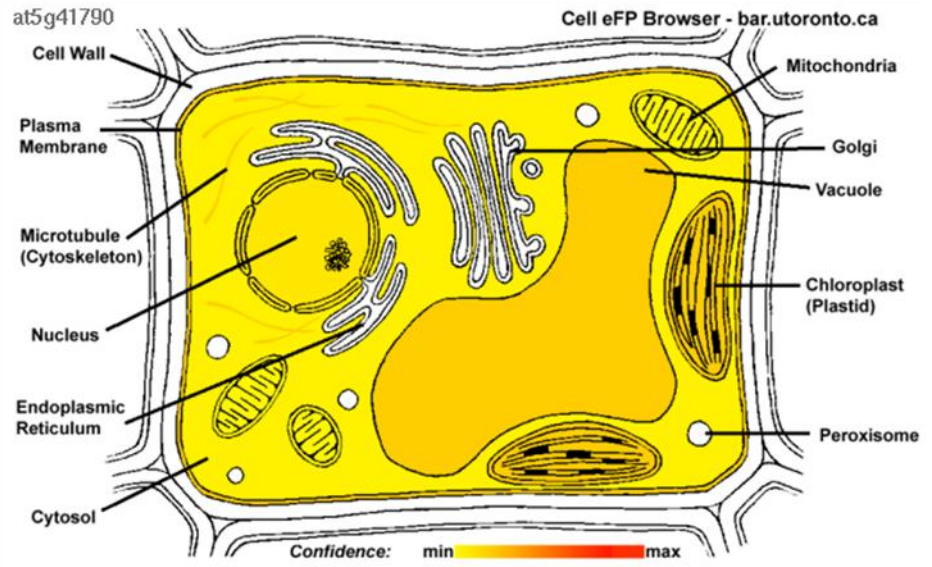
at5g41790
Cell eFP Browser - bar.utoronto.ca
Cell Wall
Plasma Membrane
Microtubule (Cytoskeleton)
Nucleus
Endoplasmic Reticulum
Cytosol
Mitochondria
Golgi
Vacuole
Chloroplast (Plastid)
Peroxisome
Confidence: min max
Drawn by T. Ampofo. Data from SUBA (Heazlewood et al, 2007).

Gene	Prediction	Imaging	MS
At3g10880	Cytosol Mitochondrion Nucleus		
At5g05180	Cytosol Mitochondrion Nucleus Plastid		
At1g64320	Cytosol Mitochondrion Nucleus Cytoskeleton		Cytoskeleton (Hamada et al. 2013)
At5g41780	Cytosol Mitochondrion Nucleus Cytoskeleton		
At1g64330	Cytosol Mitochondrion Nucleus Cytoskeleton		Vacuole (Yoshida et al. 2013; Nikolovski et al. 2012; Jaquinod et al. 2007; Carter et al. 2004) Plasma membrane (Elmore et al. 2012)
At5g41790 (CIP1)	Cytosol Mitochondrion Nucleus	Cytoskeleton and punctae (Matsui et al. 1995)	Vacuole (Yoshida et al. 2013; Jaquinod et al. 2007; Carter et al. 2004) Plasma membrane (Elmore et al. 2012) Plastid (Kong et al. 2011; Kleffmann et al. 2004)

Table 8.2: Summary subcellular prediction table for the novel IRQ proteins. Data obtained from the SUBA3 programme, which combines subcellular predictions, imaging studies and mass spectrometry (MS) data (Tanz et al. 2013).

SUBA3 also recorded experimental proteomics evidence for the subcellular localisation of At1g64320, At1g64330 and At5g41790 as shown in Table 8.2. At1g64320 was recorded to be associated with the cytoskeleton through a proteomics screen of microtubule associated proteins in Arabidopsis cell suspension cultures (Hamada et al. 2013). However examining the raw data revealed that At1g64320 was only recorded in low abundance once out of three technical replicates. The low frequency for this protein could suggest that it represents contamination during the screen.

At1g64330 and At5g41790 were both detected in proteomics screens investigating vacuolar and plasma membrane proteins. Both of these proteins were detected in three

screens studying vacuolar associated proteins (Yoshida et al. 2013; Jaquinod et al. 2007; Carter et al. 2004), and At1g64330 was detected in an additional fourth screen (Nikolovski et al. 2012). Two of these screens, Jaquinoid et al. (2013) and Carter et al. (2004), either recovered only a few peptides for each protein or gave the same score for each. As these proteins share a high degree of similarity, it could be that the latter screen failed to distinguish between the two proteins. Nonetheless, both proteins could be detected in multiple vacuole proteomic screens which suggests that this represents a true localisation.

In addition to these proteins being detected in screens for vacuole associated proteins, both At1g64330 and At5g41790 were also detected in a screen for proteins associated with the plasma membrane (Elmore et al. 2012). Furthermore, At5g41790 was also detected in two screen for chloroplast associated proteins (Kleffmann et al. 2004; Kong et al. 2011). However only one peptide was recorded once out of two repeats from the latter screen which therefore decreases the confidence in this localisation (raw data was not available from Kleffmann et al. (2004)).

Fluorescent protein visualisation data for these novel discovered proteins has not been previously published. However, as discussed previously, the subcellular localisation of At5g41790 (CIP1) has been characterised through immunofluorescence studies (Matsui et al. 1995), and showed localisation to a cytoskeleton-like fibrillar network in hypocotyl and cotyledon protoplasts, and an undefined punctate appearance in root protoplasts. The observed difference suggests that the function or regulation of this protein varies depending on the tissue it is expressed in.

8.8 IRQ-domain containing proteins in other plant species

In addition to identifying the IRQ domain containing proteins in the Arabidopsis proteome, it was also of interest to search for the presence of the IRQ domain in additional genome databases. This analysis would therefore elucidate the evolutionary history of this domain and could present hypotheses about when it first appeared in evolutionary terms.

The IRQ domain of NET4B (NET4B$^{464\text{-}511}$) was used in TBLASTN (translated nucleotide basic local alignment search) searches against several different genome databases. The presence of this domain in the plant kingdom was investigated from a range of species including; *Ostreococcus tauri* (Chlorophyta), *Physcomitrella patens*

(Bryophyta) and *Selaginella moellendorffi* (Spikemoss, Lycopodiophyta). In the angiosperms, genomes from both the monocots (*Brachypodium distachyon*, *Zea mays* and *Hordeum vulgare*) and eudicots (*Populus trichocarpa*, *Vitis vinifera* and *Solanum lycopersicum*) were searched.

Figure 8.10 shows an alignment of the IRQ domain of NET4B with the homologous region in examples proteins from other species. From this analysis it was shown that the IRQ domain could not be found in the Chlorophyte or Byrophyte. The IRQ domain could only be found in Tracheophytes (vascular plants) and a homologous region could be found in two proteins in the *S. moellendorffi* genome. These two identified proteins have been previously characterised as NET4 homologues (Hawkins et al. 2014), which implies that the IRQ family would have been derived from a protein that contained both a NAB and an IRQ domain.

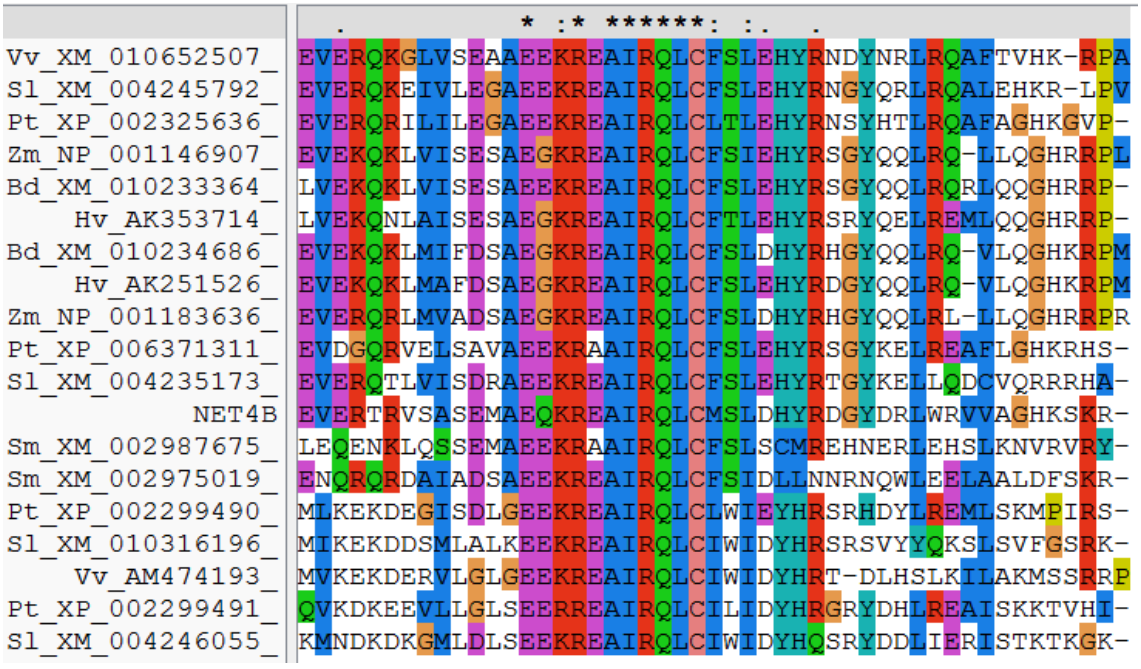

Figure 8.10: The IRQ domain in other plant species. Blasting the genomes with the NET4B IRQ domain revealed that this domain was also found outside of Arabidopsis. Shown here is an alignment of the IRQ domain from various different species, and was created using ClustalX2.1 and the default ClustalX colour scheme (Larkin et al. 2007). Vv = *Vitis vinifera*, Sl = *Solanum lycopersicum*, Zm = *Zea mays*, Bd = *Brachypodium distachyon*. Hv = *Hordeum vulgare*, Pt= *Populus trichorpha*, Sm = *Selegenilla moellendorffi*.

Examples of IRQ family proteins that lacked a NAB domain could be found in the genomes of the three eudicot species that were studied, however only proteins that contained a NAB and IRQ could be found in the monocot species. This could suggest that the IRQ proteins that lacked the NAB domain diversified in eudicot plants, however further phylogenetic analysis of this domain is needed to support this hypothesis.

As well as searching the genomes of species in the plant kingdom, three other genomes outside of this kingdom were also searched; *Saccharomyces cerevisiae*, *Drosophila melanogaster* and *Homo sapiens*. However no homologues of the IRQ domain could be found in these species, even when searching the genomes with just the most highly conserved region of the IRQ domain. This finding therefore suggests that the IRQ family represent a novel plant-specific family of proteins.

8.9 Conclusion

The IRQ domain was originally identified as a highly conserved C-terminal region between NET3A, NET3C, NET4A and NET4B. Further research into the function of the NET4B IRQ domain demonstrated that it could mediate the interaction with an active GTP-bound Rab GTPase (RabG3a). The results from this study prompted a wider search for the IRQ domain in additional proteins, and the results of this were described in this chapter.

Searching the Arabidopsis proteome revealed that six additional proteins outside of the NET family shared this conserved C-terminal domain, and together with the four NETs, these proteins were termed the IRQ family. Only one of these proteins, At5g41790 (CIP1) has been previously characterised, and this protein has been shown to interact with the RING E3 ubiquitin ligase COP1 (Matsui et al. 1995).

Cladistic analysis on the relationship of these proteins demonstrated that they group into five different subfamilies, two NET subfamilies and three novel IRQ groups. Further bioinformatics analysis on these novel proteins revealed that they are all predicted to be long coiled-coil domain proteins. No additional domains could be found in these proteins, although both group 3 members (At1g64330 and At5g41790) contain an N-terminal region that shares some resemblance to the NAB domain and was termed a quasi-NAB (qNAB) domain. This qNAB could potentially mediate the association with the cytoskeleton that has previously been observed with At5g41790 (CIP1) in hypocotyl

protoplasts (Matsui et al. 1995). In the same study, At5g41790 was shown to localise to a punctate pattern in root protoplasts. As the IRQ domain of NET4B has been shown to localise to moving punctae in *N. benthamiana* leaves, the punctate pattern of At5g41790 could represent the subcellular localisation caused by this homologous domain. The changing subcellular localisation could be due to specific regulation of the activity of these domains.

Additional secondary structure predictions were also made specifically for the IRQ domain in this chapter, which demonstrated that the IRQ domain of NET4B could form an α-helix. Most of the known structurally characterised effector/Rab complexes function through the interaction of one or two α-helices or coiled coil regions on the effector interacting with the switch/interswitch regions of the Rab (Gabe Lee et al. 2009). The α-helix that is formed by the IRQ domain could provide a similar platform for Rab interactions.

Analysis of the developmental expression patterns of the novel IRQ genes revealed that the different groups have specific tissue expression patterns. Group 1 and group 2 have the most specific expression patterns, with group 1 members being expressed in the meristematic tissue in the shoot apex, and group 2 members representing a pollen specific subfamily, whereas the genes in group 3 slightly differed from each other. At1g64330 is relatively uniformly expressed throughout the various Arabidopsis tissues, with high expression in the late stages of embryo development and in trichomes. At5g41790 is most highly expressed in leaf tissue, particularly in the senescent leaf, and high expression could also be found in the xylem. The expression pattern of the IRQ genes is similar to that of certain NET genes, with NET3 members being expressed in the shoot apex and NET2s being expressed in pollen (Hawkins et al. 2014).

Previously characterised interacting partners of these novel IRQ proteins were investigated in this chapter and protein interaction data could be found for At5g41790 and At1g64330. As mentioned previously, At5g41790 (CIP1) was shown to interact with COP1. Further data showed that it could also be conjugated to ubiquitin which could be mediated by COP1 and could represent a method of regulating the CIP1/COP1 interaction.

The interaction data for At1g64330 demonstrated that it could interact with an Arabidopsis cytokinin receptor; AHK2. In addition, a protein with the same molecular

weight and annotation as At1g64330 was pulled down in a co-IP with the auxin efflux carrier PIN1. This preliminary data suggests that At1g64330 could have an important role in plant cell growth and development linked to these two proteins.

The final bioinformatics analysis performed for these novel IRQ proteins involved investigated their subcellular localisation predictions. The SUBA3 programme was used as it compiles various subcellular prediction algorithms with curated proteomics and visualisation data. In general, this programme predicted that the novel IRQ proteins would localise to the cytosol, nucleus or mitochondria, however the confidence in these predictions was relatively low. Proteomics data could be found for both group 3 members, with both proteins being detected in multiple proteomic screens of vacuolar associated proteins and one proteomic screen of plasma membrane associated proteins. In addition, At5g41790 was also detected in proteomics data for the chloroplast. Neither of these proteins contain predicted transmembrane domains, therefore they are likely to associate peripherally with these membrane compartments.

Finally, the presence of the IRQ domain in additional species was also investigated through searching publicly available genomes. The IRQ domain was shown to be plant-specific and could only be found in the Tracheophytes. This domain is present in the two NET4 homologues in the clubmoss *S. moellendorffi*, which is an extant species of the earliest plants with a vascular system. This implies that the IRQ family evolved from a NET protein with both a NAB and IRQ domain.

The IRQ domain of NET4B represents the minimal binding site required for interaction with an active GTP-bound vacuolar Rab GTPase. Therefore the conservation of this domain in nine other proteins, suggests that they represent a family of plant specific Rab effector proteins. Currently there are very few characterised Rab effectors in plants and the discovery of this family could greatly increase our knowledge of plant-specific Rab mediated trafficking events. The significance of the IRQ family shall be explored further in the Discussion (Chapter 9).

Chapter 9 - Discussion

9.1 Context

The discovery of the NETWORKED (NET) superfamily originally began with the observation that the N-terminal fragment, of what was later termed NET1A, localised to a filamentous array in transformed *Nicotiana tabacum* leaf epidermal cells, through a high-throughput Arabidopsis cDNA-GFP expression library screen (Escobar et al. 2003). Further work on this fragment, revealed that it contained a highly conserved N-terminal region ($NET1A^{1-94}$) that was capable of associating with the actin cytoskeleton *in vivo* and could bind directly to actin filaments *in vitro* (Calcutt 2009). This region therefore represented a novel actin-binding domain and it was termed the NET actin-binding (NAB) domain. Bioinformatics analysis revealed that the NAB domain was plant-specific and could only be found in Tracheophyte genomes. Within Arabidopsis the NAB domain was found in 13 proteins, which were collectively termed the NETWORKED family (Calcutt 2009; Deeks et al. 2012; Hawkins et al. 2014). These proteins group into four phylogenetically distinct subclades that all share this conserved N-terminal NAB domain, with the C-terminus of these proteins containing stretches of predicted coiled-coil domains. Members of each subclade have been shown to associate with actin and different membrane structures in Arabidopsis (Deeks et al. 2012; Wang et al. 2014).

The aim of this project was to study NET4B, a previously uncharacterised member of the NET family. Through this project, it was established that NET4B can associate with actin filaments *in vivo* and bind directly to F-actin *in vitro*. The expression pattern of *NET4B* in Arabidopsis was studied using the GUS reporter system, revealing a high expression in the root tip and the guard cells. Using immunogold labelling and TEM with an anti-NET4B antibody, NET4B was shown to associate with the tonoplast in the Arabidopsis root tip. The interacting partners of the NET4s was also investigated which revealed that both NET4s interact with the RabG3 subclass of Rab GTPases, specifically when they are in their activated GTP-bound state. These Rabs are important signals in regulating vacuolar trafficking (Bottanelli et al. 2011; Cui et al. 2014; Ebine et al. 2014), and the NET4s could therefore potentially represent important effectors of these Rabs. Further experiments revealed that the C-terminal IRQ domain is the Rab-binding domain of NET4B. Bioinformatics analysis of this domain revealed that it was

conserved in six novel proteins in the Arabidopsis proteome, as well as being present in three other NET proteins (NET4A/3A/3C). Finally, the functional role of the NET4s in Arabidopsis was investigated through phenotypic analysis of *net4* mutant lines.

This chapter shall discuss the wider implications of the experimental work described in Chapters 3-8. The actin-binding properties of NET4B shall be discussed in relation to the NET family and other actin cross-linking proteins. The significance of the NET4s as actin-binding proteins (ABPs) at the tonoplast will be examined and potential roles will be attributed to these proteins in controlling vacuole dynamics. Models for the possible role of the NET4s as vacuolar Rab GTPase effectors shall also be presented. In addition, the results of the interactor screen for NET4B and the *net4* mutant analysis will be explored. Finally, the NET4 proteins shall be discussed in the wider context of the NET and IRQ families.

9.2 NET4B as an actin-binding protein

9.2.1 Association of NET4B with actin

NET4B was originally identified as a putative member of the NET family as it contained the conserved N-terminal NAB domain ($NET4B^{1-105}$). Initial studies on NET4B therefore focussed on characterising whether the putative NET4B-NAB domain and the full-length NET4B protein associate with the actin cytoskeleton.

To study the subcellular localisation of NET4B and the NAB domain, these proteins were fused to a C-terminal GFP tag and transiently expressed in *Nicotiana benthamiana* leaf epidermal cells. Both the full-length protein and the NAB domain highlighted a filamentous array in this ectopic overexpression system, however the nature of these arrays differed between the two fusion proteins. The full-length NET4B-GFP protein localised to a very dense and highly cross-linked array of filaments throughout the cell, whereas the NET4B-NAB-GFP fusion protein decorated a few highly bundled filaments within the cell, as well as displaying a strong signal throughout the nucleus.

The nature of the NET4B-NAB-GFP and NET4B-GFP decorated filaments was determined through applying cytoskeleton disrupting drugs to the transformed leaf sections, as well as colocalisation studies with known actin markers. Applying actin depolymerising drugs, Latrunculin B and Cytochalasin D, disrupted the NET4B-NAB-GFP and the NET4B-GFP decorated filaments, however disruption did not occur with

the application of the microtubule depolymerising drug, amiprophosmethyl. This therefore suggests that the minimal NET4B-NAB domain and the full-length NET4B associate with the actin cytoskeleton *in vivo*. Further evidence of this association was provided by colocalising the NET4B-NAB-GFP and NET4B-GFP decorated filaments with the known actin-binding marker, mCherry-FABD2, which encompasses the second actin-binding domain of AtFIMBRIN1 (Voigt et al. 2005). Taken together, these two studies established that NET4B and the NET4B-NAB domain are able to associate with F-actin *in vivo*.

Having established that the full-length NET4B and the NET4B-NAB domain can associate with actin, the subcellular localisations of various other NET4B regions were investigated in order to determine whether they contained any other functional domains. Confocal microscopy was used to image the localisation of various NET4B-GFP truncations that were transiently expressed in *N. benthamiana* leaf epidermal cells, and this resulted in two main findings. Firstly, NET4B without the NAB domain did not label a filamentous system, indicating that additional actin-binding domains cannot be found within this protein. This has also been observed with two other NET proteins, NET1A and NET3C (Cartwright 2011; Wang et al. 2014), which suggests that the NETs all have a structurally similar domain architecture containing one N-terminal actin-binding domain. Secondly, the most C-terminal 54 amino acids of NET4B, which contain the conserved IRQ domain, localises to moving punctae when transiently expressed in this system. Similar observations have been made with the C-terminus of NET3A and NET4A (Hawkins and Hussey, unpublished). As this domain represents the Rab-binding domain of NET4B, it is possible that this fusion construct was labelling RabG3 labelled vesicles in the *N. benthamiana* leaf epidermal cell, and further colocalisation studies could validate this hypothesis.

In addition to these *in vivo* studies, further *in vitro* characterisation was performed to assess whether the NET4B-NAB domain could bind directly to actin filaments. Initial work on the founding member of the NET family, NET1A, demonstrated that a recombinant NET1A-NAB domain co-sedimented with F-actin *in vitro* using a high-speed co-sedimentation assay, which therefore shows it can bind directly to actin filaments. Further research on the NET family members has primarily focussed on *in vivo* studies, and direct *in vitro* interaction of other NAB domains with F-actin has not been determined. Therefore to add further support that the conserved NAB domain is a universal actin-binding domain, a high-speed F-actin co-sedimentation assay was

performed using a recombinant NET4B-NAB domain, purified from *Escherichia coli*. The results of this assay demonstrated that the NET4B-NAB domain also bound directly to F-actin rather than through intermediary proteins as the soluble NET4B-NAB co-sedimented with the insoluble F-actin after ultracentrifugation. This study therefore confirms that the diverged NAB domains within the NET family are capable of binding directly to actin filaments.

9.2.2 Observed differences in actin association between the NET4 proteins

One of the most pertinent observations from the *in vivo* studies was the difference in actin association between NET4B and NET4A. These proteins share a high degree of homology, however when they are transiently expressed in *N. benthamiana* leaf epidermal cells they associate with markedly different arrangements of actin. These differences can be observed with the NAB domain alone and the full-length proteins.

The four subfamilies of the NET family can be grouped together based on their NAB domain sequence and organisation of the C-termini (Hawkins et al. 2014). Despite the similarities between the NAB domains of the two NET4 proteins, they label distinctly different actin arrays. Previous studies expressing NET4A-NAB-GFP in *N. benthamiana* leaf epidermal cells demonstrated that it labelled an extensive meshwork of actin filaments, similar to other members of the NET family (Chapter 4, Figure 4.1; Deeks et al. 2012). The NET4B-NAB-GFP construct expressed in this system labelled a distinctly different array of filaments to the NET4A-NAB, and localised to a few highly bundled actin filaments in the cell. This implies that there could be subtle differences in amino acid composition between the NAB domains of the NET4s, which could result in differences in their association with actin. Further *in vitro* studies, for example through F-actin co-sedimentation assays, could discern whether the NET4 NAB domains have different biochemical properties related to their association with actin.

In addition to differences in the nature of actin labelling of the NET4 NAB domains, the full-length proteins also exhibit variation in their subcellular localisation. Full-length NET4A-GFP has been shown to decorate both very fine actin filaments and thicker 'actin staples' that occur along the length of the filament (Chapter 4, Figure 4.1; Hawkins and Hussey, unpublished). These actin staples appear to be areas of discrete NET4A enrichment along the actin filament, and are similar to the immotile filamentous punctae, termed a 'beads on a string' arrangement, that has been observed for many NET members including; NET1A, NET2A, NET3A and NET3C (Deeks et al. 2012; Wang et

al. 2014). In contrast, the NET4B-GFP fusion protein decorated actin filaments alone when transiently expressed in *N. benthamiana* leaf epidermal cells, and discrete punctae could not be observed. It is possible that the overexpression of NET4B in this system, driven by the CaMV 35S promoter, could have masked the observation of distinct punctae along the actin filaments. Observations on the nature of the association between NET4B and actin under endogenous expression levels could not be made within this project as stable *NET4Bpro*::NET4B-GFP Arabidopsis lines only exhibited a cytosolic signal. The *in planta* association of NET4B and actin could be explored further through immunofluorescence studies using the anti-NET4B antibody.

In light of the interactor studies from this project, it is possible that the NET4A labelled punctae resemble specific Rab-labelled membrane domains. Two studies on mammalian Rab GTPases have revealed that distinct subpopulations of Rabs can be present on the same vesicle in separate microdomains. The first of these studies showed that Rab4, Rab5 and Rab11 GTPases appear segregated on the same endosomal membrane compartment (Sönnichsen et al. 2000). In addition, Rab7 and Rab9 have also been shown to localise to distinct late endosomal domains (Barbero et al. 2002). The formation of distinct Rab membrane domains could provide a localised signalling platform for downstream trafficking events (Pfeffer 2013). The nature of the NET4A 'actin staples' and their relation to the RabG3s is currently being explored through colocalisation studies in *N. benthamiana* and Arabidopsis.

9.2.3 Actin organisation of NET4B and the role of the coiled-coil domains

The *in vivo* studies with the full-length NET4B-GFP fusion protein revealed that it labelled a highly bundled and cross-linked array of actin filaments, which could suggest that it has a role in organising the actin cytoskeleton into higher-order structures. The NET4B-GFP labelled actin filaments were similar in appearance to those labelled by the known actin-marker GFP-FABD2. Both of these constructs labelled a dense network of filaments, however filaments labelled by NET4B appeared thicker and formed a more uniform meshwork across the cortex.

The ability of NET4B to create highly bundled and cross-linked filaments could be due to the structural properties of this protein. The C-terminus of NET4B, like the other members of the NET family, is predicted to form long coiled-coil domains. These domains are formed of α-helices that wrap around each other to form a supercoil

(Mason & Arndt 2004), and one of the key features of the coiled-coil domain is that it allows the dimerisation/oligomerisation of proteins (Rose & Meier 2004).

The presence of the coiled-coil domains in the NET proteins suggests that the NETs could oligomerise into higher-order complexes. Indeed, the *Petunia inflata* NET2 homologue, KIP1 (KINASE INTERACTING PROTEIN1) and NET3C have both been shown to physically interact with themselves and they could therefore form dimers/oligomers (Skirpan et al. 2001; Wang et al. 2014). During this study, the ability of the NET4s to oligomerise was tested using the yeast-2-hybrid (Y2H) system. Both NET4B and NET4A interacted with themselves and each other, and could therefore form homo- and hetero-oligomers. The ability of NET4A to oligomerise *in planta* was also demonstrated through the TAP-tagging screen as NET4A was consistently found in a complex with itself as well as RabG3a (Hawkins and Hussey, unpublished). NET4B was not detected to form hetero-oligomers with NET4A during this screen, however that could have been due to the increased abundance of NET4A relative to NET4B.

Protein dimerisation, through the coiled-coil domains, can form rod-like structures that contain functional domains at either end (Rose & Meier 2004). Therefore the ability of actin-binding proteins to oligomerise can create a protein complex with independent actin-binding domains at either end, which could bundle or cross-link actin filaments. The recently discovered plant specific STOMATAL CLOSURE-RELATED ACTIN BINDING1 (SCAB1) forms dimers and links two adjacent actin filaments creating actin bundles (Zhao et al. 2011; Zhang et al. 2012). In animals, the calponin-homology (CH) domain protein α-actinin forms anti-parallel homodimers which allows the formation of tight actin bundles (Matsudaira 1991). Filamin, another significantly larger CH domain protein, can dimerise and cross-link filaments into a loose mesh of orthogonal actin filaments (Matsudaira 1991). The ability of the NET4s to oligomerise, could allow them to link different actin filaments and therefore create the highly cross-linked and bundled actin array observed when expressed in *N. benthamiana* leaf epidermal cells (Figure 9.1).

As the Y2H data showed that the NET4 proteins could hetero-oligomerise, it opens up the possibility that different combinations of these NETs combine to create distinct actin-membrane platforms. The subtle differences in actin association between the NET4s (as discussed in 9.2.2), could therefore result in different biochemical properties of NET4 homo- and hetero-oligomers. These different combinations of NET4A/NET4B

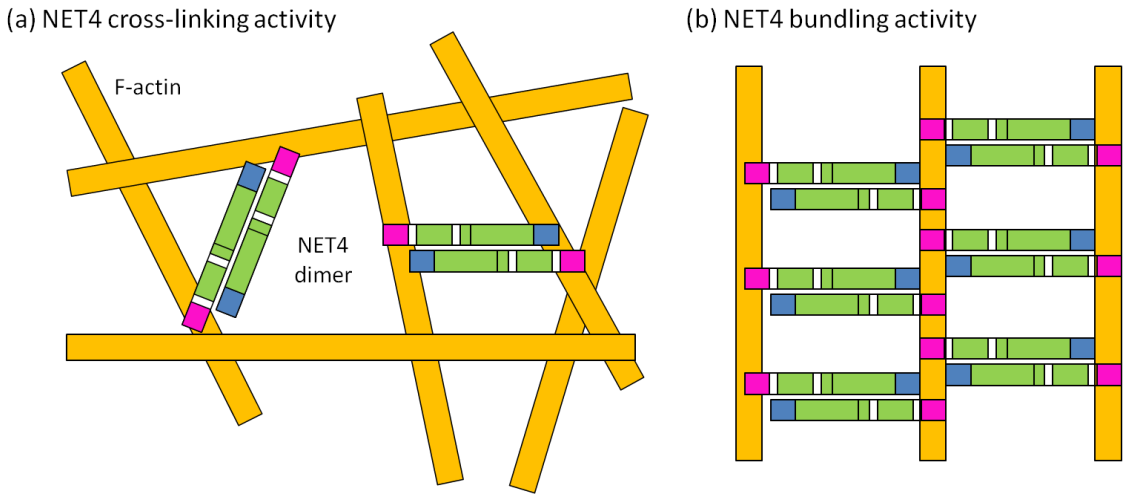

Figure 9.1: Model of NET4 actin cross-linking and bundling activity. The ability of the NET4s to dimerise would permit the joining of actin filaments either in cross linked arrays (a) or ordered bundled arrays (b). F-actin (orange), NET4 dimers with NAB domain (magenta), coiled-coil domains (green), IRQ domain (blue).

oligomers could therefore allow variation in the functional roles of the NET4s, and it will be interesting to observe the spatio-temporal colocalisation of these proteins in Arabidopsis throughout plant development.

Another important feature of coiled-coil proteins is that they can function as important adaptor proteins at actin-membrane interfaces. In metazoans, spectrins are large coiled-coil proteins that anchor the cytoskeleton to the plasma membrane through the adaptor proteins band 4.1 and ankyrin (De Matteis & Morrow 2000). In plants, CHUP1 (CHLOROPLAST OUTER ENVELOPE PROTEIN1) is an example of a coiled-coil protein that links the actin cytoskeleton to chloroplasts, and is important for their movement in response to blue light (Oikawa et al. 2003). Members of the NET family have been shown to associate with the actin cytoskeleton at distinct subcellular compartments and could therefore act as cytoskeletal-membrane anchors (Deeks et al. 2012; Wang et al. 2014).

Both NET4 proteins associate with the actin cytoskeleton and localise to the tonoplast in the Arabidopsis root tip, and they could therefore act as actin-vacuole adaptor proteins. As the NET4s do not contain transmembrane domains, they are likely to be peripherally associated with the vacuole. This connection could be mediated through interactions with membrane-bound proteins or membrane lipids, or alternatively the NET4s could be

post-translationally modified with lipid moieties (for example through S-acylation; Figure 9.2). Indeed, NET3C has been shown to interact with a transmembrane protein, VAP27, at the ER-PM interface, and also interact with the membrane through protein-lipid interactions (Wang et al. 2014). The results from this thesis have demonstrated that the NET4s associate with two Arabidopsis RabG3 vacuolar localised Rab GTPases through the C-terminal IRQ domain. The NET4s were shown to interact specifically with these Rabs in their active GTP-bound state, which only occurs when they are inserted in the target membrane (through their geranylgeranyl lipid moieties) and activated by their guanine exchange factor (GEF; Grosshans et al. 2006). This association could therefore link the NET4s to the vacuole membrane and implicate them in further downstream membrane trafficking processes. However, the NET4-Rab interaction could be spatio-temporally regulated and it is possible that other currently unknown mechanisms, as mentioned above, could link the NET4s to the vacuole.

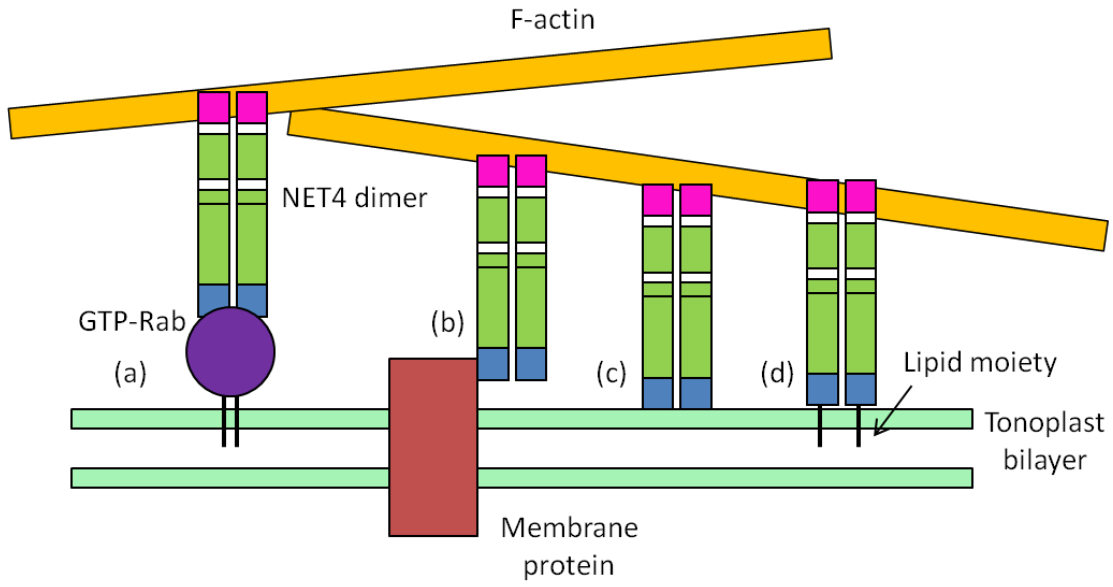

Figure 9.2: Models of NET4 association with the tonoplast. The NET proteins lack transmembrane domains and therefore are actin-membrane adaptors that peripherally associate with membranes. Shown here are four possible scenarios for NET4 membrane association. (a) NET4s are recruited by active RabG3s at the vacuole membrane. (b) NET4s interact with membrane proteins, either directly with transmembrane proteins or through additional peripheral membrane proteins. (c) NET4s could interact with specific lipids in the tonoplast membrane. (d) The NET4s are post-translationally modified with lipid moieties for example through S-acylation. In these models the NET4 dimers are depicted in the same orientation however, the membrane interaction sites is currently unknown. Only the IRQ domain (blue) is known to mediate an interaction with the active RabG3a.

9.3 Potential role of the NET4s at the tonoplast membrane

Plant vacuoles are large compartments within the cell and can occupy up to 90% of the total cellular volume (Taiz 1992). Water can flow into the vacuole, generating turgor pressure in concert with the plant cell wall, which drives cell wall expansion and growth at a low energetic cost (Zouhar & Rojo 2009; Zhang et al. 2014). The vacuole is not a static organelle, and its morphology changes during plant development and in response to the environment. The vacuole is also part of the biosynthetic and endocytic and pathways (Zouhar & Rojo 2009). The degradative function of the plant lytic vacuole is governed by the acidity of the lumen and the presence of hydrolytic enzymes (Marty 1999). In addition to the lytic vacuole (LV), plants also contain protein storage vacuoles (PSV) that serve as reserves for the germinating seed (Zouhar & Rojo 2009). Studying the factors that affect vacuole morphology and trafficking is crucially important for understanding how this multifunctional organelle functions in plant development and responses to the environment.

The actin cytoskeleton has been shown to be closely associated with the tonoplast membrane (Higaki et al. 2006). However, our current knowledge of the molecular adaptors linking the two structures is very limited and only two vacuole associated ABPs have been previously characterised; the vacuolar H^+-ATPase (V-ATPase) B subunits (Ma et al. 2012) and NET4A (Deeks et al. 2012). During this project, NET4B was also shown to preferentially localise to the tonoplast in Arabidopsis root tips using an anti-NET4B immunogold labelling and transmission electron microscopy. This discovery adds another element to the molecular framework linking the actin cytoskeleton and the vacuole in plants. This section will discuss the potential role of the NET4s as actin-vacuole adaptors.

9.3.1 Controlling vacuole morphology

The large central vacuole is not just a simple smooth shape like an inflated balloon, but can be highly convoluted, and contain distinct internal structures including transvacuolar strands, sheet-like structures and intravacuolar 'bulbs' (Verbelen & Tao 1998; Oda et al. 2009; Reisen et al. 2005; Hawes et al. 2001; Segami et al. 2014). In addition, the morphology of the vacuole is responsive to environmental cues such as abiotic and biotic stress (Reisen et al. 2005; Higaki et al. 2008).

Transvacuolar strands (TVS) are dynamic channels through the central vacuole that allow the movement of vesicles and organelles. Golgi bodies, mitochondria and endosomes have all been shown to move along TVS (Nebenführ et al. 1999; van Gestel et al. 2002; Ruthardt et al. 2005). Pharmacological disruption of the actin cytoskeleton in BY2 cells has been shown to disrupt TVS and can also lead to fragmented vacuole structures (van Gestel et al. 2002; Higaki et al. 2006; Sheahan et al. 2007). Disruption to the morphology of the central vacuole has also been observed in the trichomes of certain Arp2/3 complex mutants (Mathur et al. 2003). These results therefore suggest that the actin cytoskeleton is critical in maintaining vacuolar morphology in plants cells. Considering the ability of the NET4s to bind actin and associate the tonoplast, it is therefore possible that they are important in creating a scaffold of actin that supports these complex vacuolar structures.

The central lytic vacuole is a highly dynamic structure and undergoes major changes in response to environment signals including biotic stress. Disintegration of the vacuole, in response to biotic stress, has been proposed to be an important event in programmed cell death (PCD; Jones 2001). Disruption of the actin cytoskeleton during elicitor-induced PCD accelerates the changes to vacuole morphology, thus resulting in an earlier onset of cell death (Higaki et al. 2007). This suggests that the actin cytoskeleton regulates vacuole morphology in response to biotic stress. NET4B could be an important component of this response, as bioinformatics analysis in Chapter 3 revealed that *NET4B* expression increases when leaves are infiltrated with a bacterial pathogen that elicits the hypersensitive cell death response. It is tempting to speculate that NET4B provides a regulated link between the actin cytoskeleton and the vacuole during biotic stress.

9.3.2 Vacuole fusion in the root tip

Promoter::GUS studies revealed that *NET4B* is highly expressed in the root tip, and NET4B was subsequently shown to preferentially localise to the tonoplast in this tissue through immunogold labelling using the anti-NET4B antibodies. Previous studies, using stably transformed *NET4Apro*::NET4A-GFP plants, have also demonstrated that NET4A associates with actin surrounding the vacuole in the root tip (Deeks et al. 2012). The presence of both NET4 proteins at the tonoplast in the root tip could suggest that they have a role in vacuole formation in this tissue.

The Arabidopsis root is composed of several distinct zones of growth (Figure 9.3; Taiz & Zeiger 2000; Verbelen et al. 2006). At the apex of the root is the root cap that protects the root apical meristem from mechanical damage. The cells of the root cap are formed from the apical meristem and are sloughed away as the root grows. The meristematic zone lies under the root cap and is the zone of active cell division and defines the different cell files of the root. Behind the meristematic zone is the transition zone, which is an area of slow cell growth in length and width. The rate of cell division decreases in this zone and the cells undergo physiological changes required for rapid cell expansion. In the elongation zone, cells undergo rapid anisotropic cell elongation and can quadruple in size in two hours (Verbelen et al. 2006). Finally, the rate of cell elongation progressively starts to decrease as cells enter the growth termination zone, characterised by the onset of root hair initiation, and cells in this zone mature into their differential state (Le et al. 2004; Verbelen et al. 2006).

During the transition from the meristematic zone to the growth termination zone, there is a dramatic change in the morphology of the vacuole, from vacuole biogenesis to the formation of a large central lytic vacuole in the growth termination zone (Figure 9.3; Verbelen et al. 2006). The vacuole adopts a highly convoluted morphology in the meristematic and elongation zones of the root, which transitions to a large central vacuole in the differentiation zone (Viotti et al. 2013).

Homotypic vacuole fusion is critical in the formation of a large central vacuole. Recent studies using a weak mutant of the vacuolar SNARE *VTI11* (*VESICLE TRANSPORT V-SNARE 11*), showed that defects in this protein prevented the fusion of vacuoles in the root (Zheng et al. 2014a; Zheng et al. 2014b). Interestingly, the fragmented vacuole phenotype could be rescued through the application of wortmannin, a phosphatidylinositol 3-kinase (PI3K) inhibitor, however this rescue depended on an intact microtubule and actin cytoskeleton (Zheng et al. 2014a).

As both NET4s are expressed in the meristematic zone of the root and associate with actin and the tonoplast it is possible that they are involved in mediating vacuole fusion in the root tip. Previous studies have shown that NET4A-GFP can decorate the main central vacuole membrane in some cells, and in other cells NET4A labels smaller vacuoles and appears to form a 'bridge' between them (Figure 9.4 a). It is possible that this link between two vacuoles could be important in generating a contractile force that is necessary for vacuole fusion.

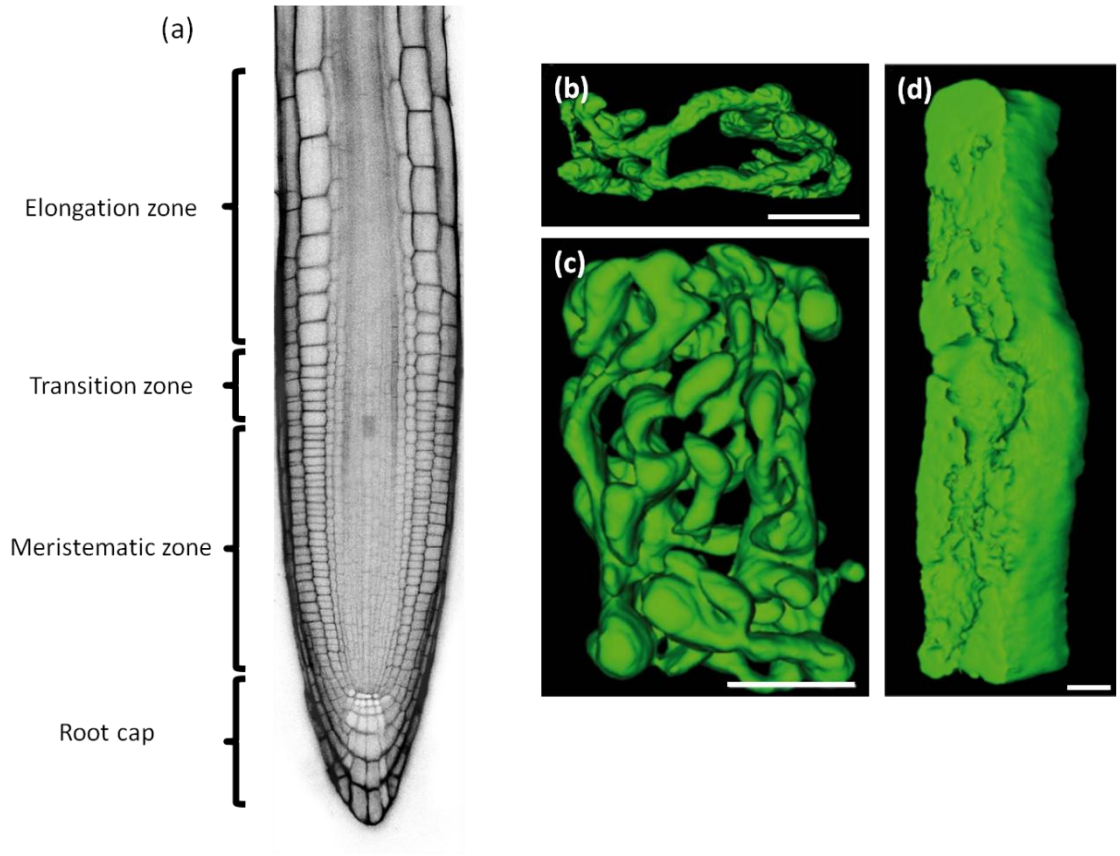

Figure 9.3: The Arabidopsis root. (a) Labelled micrograph of the Arabidopsis root showing the different zones; the growth termination zone occurs at the appearance of the first root hair (not shown on this micrograph). Labelled micrograph created by Mr. James Rowe (Durham University). (b-d) 3D surface renderings of the vacuole during development, as stained by the acidic dye BCECF (images from Viotti et al. (2013); www.plantcell.org, Copyright (2013) American Society of Plant Biologists). (b) = meristematic zone, (c) = elongation zone, (d) = differentiation zone. Cells of the vacuole are highly convoluted tubular structures during development that later form the large central vacuole. Scale bars: 5 μm.

The apparent formation of the vacuole bridges seen with the NET4A-GFP lines could be important in bringing vacuoles together via the actin cytoskeleton. It is possible that these bridges are formed of actin filaments that form between two vacuoles, allowing their contraction through the action of myosin motor proteins. The Arabidopsis genome does not contain "conventional" myosins (myosin II; Berg et al. 2001), that in metazoans form bipolar filaments, allowing for actin filament contraction (Mitchison & Cramer 1996). However, the actin cables between the vacuoles could provide 'tracks' for organelle associated myosins to bring the vacuoles in close proximity for fusion. Indeed, in yeast vacuole movement during cell division is driven by a myosin class V motor (Myo2p), moving the vacuole on actin cables (Hill et al. 1996).

Figure 9.4 (b) shows a speculative model for the role of the NET4s in homotypic vacuole fusion. The NET4s could be recruited to the tonoplast by the GTP-bound RabG3s, which could induce a change in actin morphology (as discussed in 9.5.3; model 4), allowing for actin cable formation between two opposing vacuoles. Myosin motors could then provide the contractile force required to bring the two vacuoles in close proximity to allow SNARE-mediated fusion. The NET4s could potentially serve as adaptor proteins for these myosins (as discussed in 9.5.3; model 1); alternatively the myosins could interact with additional tonoplast associated proteins.

In addition to homotypic vacuole fusion, the NET4s could also have a role in trafficking of vesicular compartments to the vacuole. Cargo can be targeted to the vacuole from both the biosynthetic pathway (for example vacuolar degradative enzymes produced in the ER) and the endocytic pathway (for example plasma membrane receptors targeted for degradation; Reyes et al. 2011). Pharmacological disruption of F-actin has been shown to disrupt the trafficking of two vacuolar reporter proteins, sporamin:GFP and aleurain-like:GFP, from the Golgi to the vacuole (Kim et al. 2005). It is possible that the NET4s could be an important actin-vacuole adaptor in the trafficking of vesicles to the vacuole. The role that NET4B/NET4A could play in this trafficking could be similar to the proposed homotypic vacuole fusion model described above, and could be linked to the potential models of the NET4s as a Rab effectors (as described in section 9.5.3). It should be noted that quantification of the anti-NET4B immunogold labelling did not reveal a preferential labelling to multivesicular bodies/prevacuolar compartments (MVBs/PVCs), or other vesicular compartments. However, if NET4B acts as a potential vesicle tethering factor (as described in 9.5.3; model 2), then it is possible that NET4B only labels vesicles in close proximity to the tonoplast.

The next stage of the NET4 project will be to confirm the function of the NET4A 'vacuole bridges' through colocalisation of these structures with vacuole and actin markers, as well as using time-lapse movies to visualise the dynamic changes in NET4A at the root tip during development. Although the native promoter driven NET4B-GFP lines generated in this project only showed a cytosolic signal, it will still be possible to image whether NET4B and NET4A colocalise at similar sites surrounding the vacuole through immunological techniques.

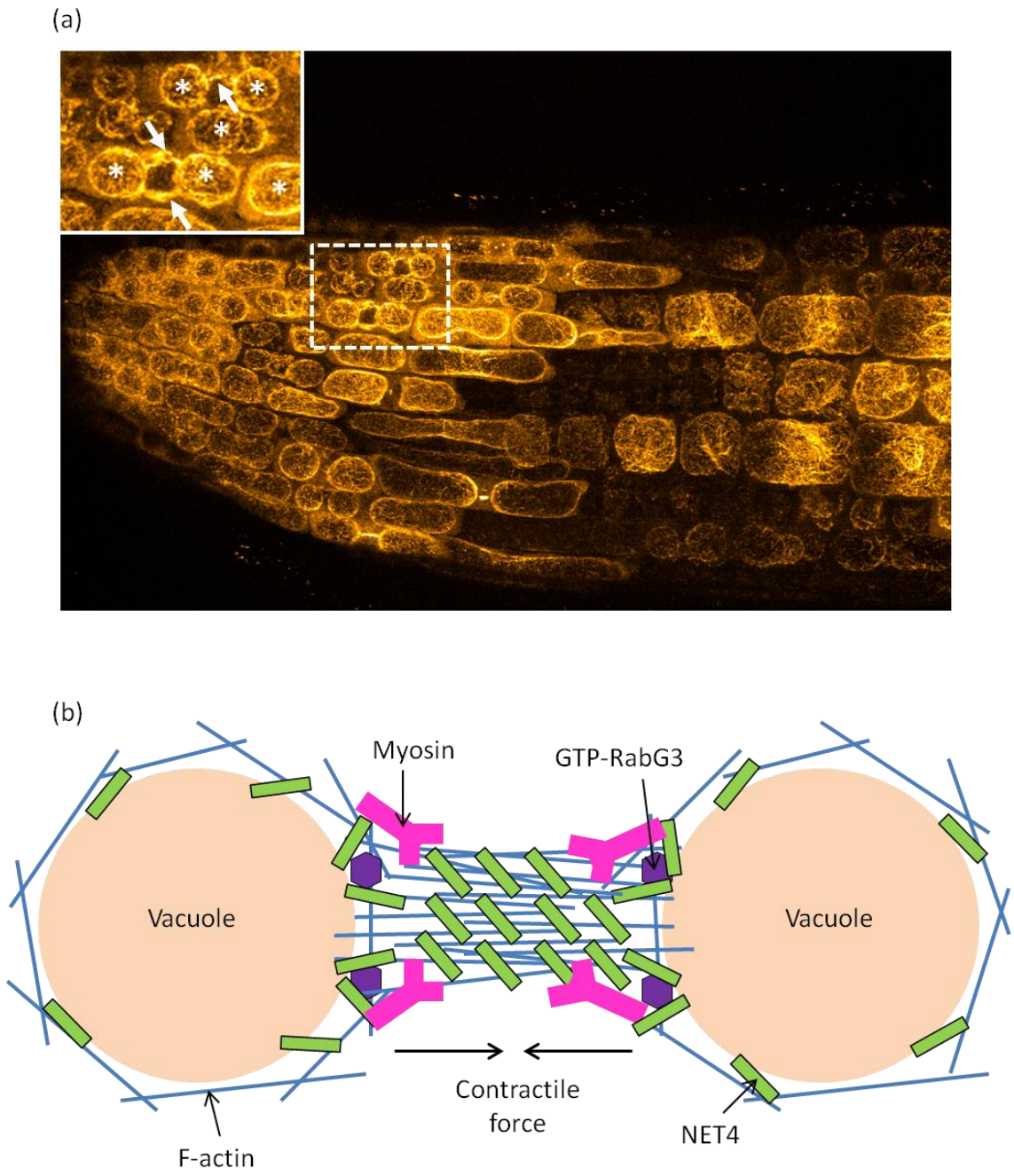

Figure 9.4: Speculative model for NET4 involvement in vacuole fusion. (a) Localisation of NET4A-GFP in the Arabidopsis root, visualised using the *NET4Apro*::NET4A-GFP lines (Hawkins and Hussey, unpublished). Inlet shows the labelling of NET4A-GFP surrounding the vacuole (white asterisks), as well as what appears to be NET4A labelled 'bridges' (white arrow) between vacuolar compartments in certain cells. (b) Schematic model for how the NET4s could function in vacuole fusion. NET4s could interact with active GTP-bound RabG3s at the vacuole. This could induce local changes to actin organisation creating actin bundles between the two vacuoles. Myosin motor proteins at the tonoplast could then use these cables as tracks, thus providing the contractile force needed to bring two vacuoles together. Blue = actin filaments, purple = GTP-RabG3, magenta = myosin, green = NET4.

9.3.3 A role for NET4B in guard cell functioning

As well as showing high expression in the root tips, the *NET4Bpro*::GUS analysis also showed that *NET4B* is highly expressed in guard cells. Microarray data has also demonstrated that *NET4B* is preferentially expressed in guard cells rather than mesophyll cells of the leaf (Leonhardt et al. 2004; Yang et al. 2008). Both changes to vacuole and actin dynamics have been shown to be important for the opening and closing of guard cells, and thus the regulation of gaseous exchange with the environment (Figure 9.5). As the results from this project have demonstrated that NET4B can bind actin and can associate with the tonoplast, it could play an important role in the dynamics of these two systems in guard cells.

Guard cells exhibit dramatic changes to the surface area and volume of the plasma membrane and vacuole during stomatal opening and closing (Tanaka et al. 2007). When guard cells are open, there are one or two large vacuoles that occupy the majority of the cell (Andrés et al. 2014). During guard cell closure, the vacuole decreases in volume and becomes highly convoluted (Gao et al. 2005; Tanaka et al. 2007; Andrés et al. 2014). Genetic manipulation of vacuole fusion proteins, for example the SNARE protein SYP22/AtVAM3 (SYNTAXIN OF PLANTS 22/VACUOLAR MORPHOLOGY 3), impacts upon vacuole dynamics in guard cells and reduces their ability to respond to external stimuli (Gao et al. 2005).

As well as changes to vacuolar architecture, dynamic changes to the actin cytoskeleton have also been observed during stomatal movements. Several studies have reported that guard cells exhibit a radial orientation of actin filaments in closed stomata and a randomly orientated longitudinal array in closed stomata (Hwang & Lee 2001; Gao et al. 2008; Higaki et al. 2010). Actin filaments have also been shown to depolymerise and repolymerise during guard cell changes (Hwang & Lee 2001; Gao et al. 2008), and it has been hypothesised that these dramatic rearrangements could lead to the rapid changes in stomatal closure (Gao et al. 2009). The regulation of the actin cytoskeleton through the action of ABPs is crucial for normal guard cell responses. Genetic manipulation of two ABPs, SCAB1 and ACTIN-RELATED PROTEIN C2/DISTORTED TRICHOMES 2 (ARPC2; a subunit of the Arp2/3 complex), impacts upon actin reorganisation in the guard cells and these mutants show delayed stomatal closure responses (Zhao et al. 2011; Jiang et al. 2012).

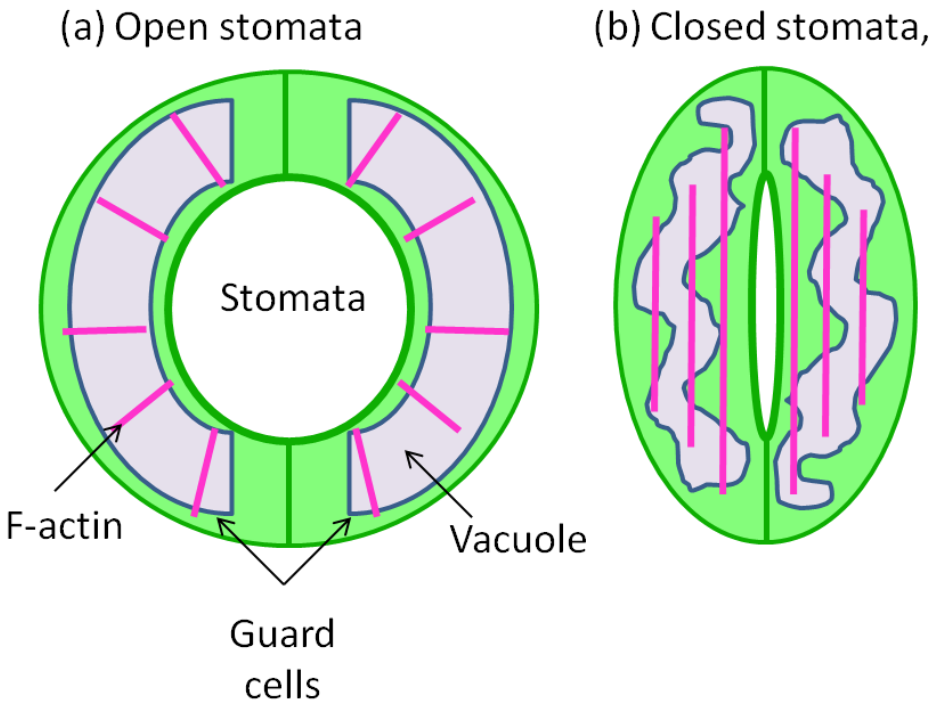

Figure 9.5: Diagram of actin and vacuole organisation during guard cell opening and closing. (a) When the stomata are open, the guard cells are turgid and have a large central vacuole (grey) with radially orientated actin filaments (magenta). (b) When the stomata are closed, the volume of the guard cells decreases and the vacuole becomes highly convoluted. F-actin also changes to a randomly orientated longitudinal array. During rapid guard cell changes, F-actin has been shown to depolymerise and repolymerise as it changes between the two arrays.

It is currently unclear whether changes in the actin cytoskeleton determine changes in vacuole morphology in stomatal responses, and there has only been one study on their relationship (Li et al. 2013). The authors of this work showed that pharmacologically depolymerising or stabilising actin filaments, through Cytochalasin-D and phalloidin respectively, resulted in an increased fragmentation of the vacuole during stomatal opening in comparison to wild-type plants. In addition, vacuole dynamics were studied in mutants of the Arp2/3 complex. In these mutants, guard cells contained a higher number of fragmented vacuoles during light-induced stomatal opening, compared with the wild-type plants, and this caused a delay in stomatal opening. However, longer exposure to light resulted in vacuole morphology that was similar to wild-type plants. Therefore it is possible that actin-dependent and independent pathways exist for vacuolar fusion during guard cell opening (Li et al. 2013).

If the actin-binding, tonoplast localisation and guard cell expression of NET4B is considered with the above findings, it is tempting to speculate that NET4B could potentially represent an important linker between the actin cytoskeleton and the vacuole in these highly specialised cells. It is possible that the actin-binding and vacuole association of NET4B is regulated during guard cell changes which could thus link these two structures and allow for their dynamic rearrangements. Furthermore the bundling and cross-linking activity of NET4B, observed during transient *N. benthamiana* expression, could be important for maintaining the different actin arrays observed in guard cells.

In addition to *NET4B* transcription in guard cells, as demonstrated by the *promoter*::GUS studies, it will be important to establish whether NET4B is also translated here, and if so what role it might have in these cells. During this project, a transpirational water loss assay (a measure of guard cell regulation) was performed with the *net4* mutant lines, however no discernible phenotype was observed. This does not necessarily eliminate a role for NET4B in the guard cells, as it could be involved in response to specific abiotic or biotic stresses.

9.4 Interactor results from the yeast-2-hybrid screen

One of the main aspects of this project was to study the potential interacting partners of NET4B. Initially, a yeast-2-hybrid (Y2H) screen was performed to identify interactors, using NET4B and the IRQ + Ct domain as bait, and from this screen a single potential interactor was identified; DEHYDRATASE-ENOLASE-PHOSPHATASE-COMPLEX 1 (DEP1). This trifunctional enzyme, is expressed in the phloem and is part of the Yang cycle that recycles 5-methylthioadenosine (MTA) to methionine, with MTA being a by-product created during ethylene, nicotianamine and polyamine synthesis (Pommerrenig et al. 2011).

The Y2H studies revealed that only a fragment of DEP1 (recovered from the screen) was shown to interact with NET4B and the IRQ + Ct domain (the last 54 amino acids of NET4B), and a positive interaction was not seen with the full-length DEP1 protein. It is possible that the full-length DEP1 is not compatible with the Y2H system, which could be the result of steric hindrance preventing an association of the binding/activation domains. The NET4B:DEP1 interaction could be explored further with additional

interaction techniques such as FRET-FLIM (fluorescence resonance energy transfer - fluorescence lifetime microscopy).

The potential association of DEP1 with NET4B could represent an important mechanism in which this enzyme is compartmentalised within the cell. The cytosol is a highly crowded space, and enzyme complexes are often localised to specific sites within the cell to ensure the channelling of intermediary substrates between enzymes (Luby-Phelps 2000; Araiza-Olivera et al. 2012). Several studies have reported that glycolytic enzymes, for example fructose-1,6-bisphosphate aldolase (aldolase), glyceraldehyde-3-phosphate dehydrogenase (GAPDH) and 6-phosphotfructo-1-kinase (PFK), associate with the actin cytoskeleton (Arnold & Pette 1970; Collin 1984; Waingeh et al. 2006; Real-Hohn et al. 2010). Associating with the cytoskeleton not only compartmentalises glycolytic enzymes, it can also stimulate their activity (Arnold & Pette 1970; Collin 1984; Real-Hohn et al. 2010). It is possible that DEP1 associates with NET4B as a similar compartmentalisation strategy, however the subcellular localisation of DEP1 currently remains uncharacterised. It will prove extremely useful to colocalise fluorescent fusion proteins of NET4B and DEP1, and therefore monitor their association *in planta*.

9.5 The NET4s as Rab GTPase effectors

9.5.1 Association of the NET4s with Rab GTPases

In an attempt to identify additional interacting partners of the NET proteins, various members, including NET4A, were sent for Tandem affinity purification (TAP)-tag analysis; a service provided by the Functional Interactomics Group at VIB, Ghent University. This screen revealed that NET4A interacted with RabG3a *in planta*. Furthermore, in collaboration with Dr. Ian Moore's group (University of Oxford), NET4B was identified as an interacting partner of RabG3f through a co-immunoprecipitation assay performed in Arabidopsis roots. Rab GTPases are molecular switches that govern different stages of membrane trafficking through interactions with specific effector proteins, and the Arabidopsis RabG3s control membrane trafficking events at the vacuole (Hutagalung & Novick 2011; Bottanelli et al. 2011; Cui et al. 2014).

The interaction between the NET4s and RabG3s was explored further using the Y2H system. Both NET4s were shown to interact specifically with constitutively-active (CA)

GTP-bound versions of these Rabs; which suggests that the NET4s could be effector proteins involved in mediating downstream membrane trafficking events. In addition, NET4B was shown to interact specifically with the RabG3 subfamily in the Y2H system, which implies that the NET4s could have a unique role in vacuole membrane dynamics controlled by these Rabs. The final experiment performed during this project identified the conserved C-terminal IRQ domain as the Rab-binding domain of NET4B. NET4B therefore has two functional domains at the N- and C-terminus; an actin-binding domain and a Rab-binding domain, respectively. Further discussion about the IRQ domain as a Rab-binding domain shall be explored in relation to the IRQ family in section 9.7.2.

Figure 9.6 shows a model of how the NET4s could interact with the Rabs at the tonoplast. Prenylated GDP-bound Rabs exist in the cytosol, in a complex with a Rab GDP dissociation inhibitor (GDI), which masks the lipid tails of the Rab (Barr 2013). GDI dissociation factors (GDFs) can recognise Rabs and catalyse the dissociation of the GDI, thus allowing Rab insertion into the membrane (Sivars et al. 2003; Hutagalung & Novick 2011). Rab GEFs then exchange GDP for GTP on the Rab which causes a change in conformation, allowing the interaction with effector proteins (Hutagalung & Novick 2011). The Rab GEF for Rab7 has recently been shown to be the conserved MON1-CCZ1 (MONENSIN SENSITIVITY1/CALCIUM CAFFEINE ZINC SENSITIVITY1) complex (Cui et al. 2014). The NET4s could either be recruited directly from the cytosol to interact with the GTP-RabG3 (option A) or they could already be peripherally associated with the tonoplast through membrane-bound protein interactions, interaction with lipids, or post-translational modification with lipid moieties, and then interact with the Rabs when they are activated at the membrane (option B). The interaction between the NET4s and the RabG3s could then stabilise this complex to enable it to perform various downstream functions (Grosshans et al. 2006). Several different models of how the NET4s could function as Rab effector proteins are presented in section 9.5.3. Finally, a Rab GTPase-activating protein (GAP) catalyses the hydrolysis of GTP for GDP on the Rab and thus inactivating the complex, and allowing Rab extraction from the membrane via GDI (Hutagalung & Novick 2011).

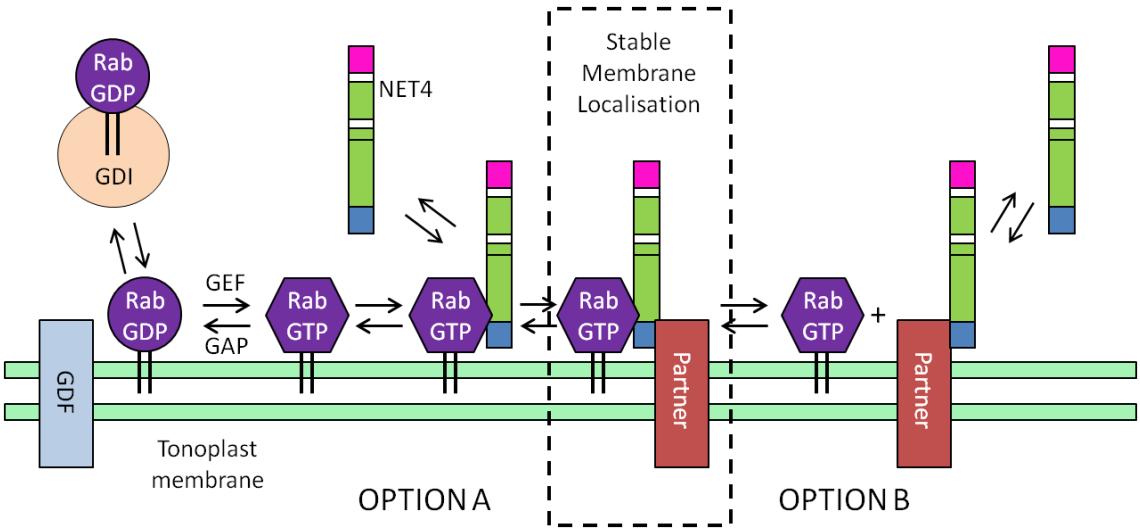

Figure 9.6: Possible models of NET4/Rab interaction. GDP-bound inactive RabG3s are present in the cytosol, in a complex with a GDP dissociation inhibitor (GDI). GDI dissociation factors (GDF) displaces the GDI and can enable Rab insertion into the membrane. Rab guanine exchange factors (GEF; MON1/CCZ1) exchange GDP for GTP and thus activate the Rab. (Option A), Active RabG3s recruit NET4s from the cytosol. (Option B) NET4s are already present at the tonoplast, through an interacting partner, that could be another protein, lipid or post-translational modification, and are then recruited by the active RabG3. The RabG3/NET4 interaction (in complex with other effectors) provides a stable membrane localisation. Rab GTPase activating proteins (GAP) inactivate the Rab by hydrolysing GTP to GDP, if not bound to an effector, therefore allowing for membrane extraction via GDI. Diagram modified from Aivazian et al. (2006).

9.5.2 Importance of Rab GTPases at the vacuole and implications for NET4 function

The association of the NET4s with Rab GTPases could implicate these proteins in membrane trafficking processes. Therefore in order to understand the function of the NET4/RabG3 interaction it is crucial to first consider the roles that the RabG3s have in the plant.

The Arabidopsis RabG3 subfamily, RabG3a-f, is most closely related to the mammalian Rab7 and yeast Ypt7p (Pereira-Leal & Seabra 2001; Rutherford & Moore 2002). Both Rab7 and Ypt7 have both been implicated in traffic to the lysosome/vacuole (Schimmöller & Riezman 1993; Méresse et al. 1995; Vitelli et al. 1997) and Ypt7 has also been shown to be important in homotypic vacuole fusion (Haas et al. 1995). Recent studies on the Arabidopsis RabG3 subfamily members have demonstrated that they localise to vacuolar compartments and are important for vacuolar trafficking. GFP-

fusion proteins of RabG3c revealed that it localised to the tonoplast membrane (Saito et al. 2002; Bottanelli et al. 2012; Bottanelli et al. 2011), whereas RabG3f has been shown to associate with the tonoplast membrane and PVCs (Ebine et al. 2014; Cui et al. 2014).

Overexpression of a nucleotide-free dominant-negative (DN) RabG3c in *N. benthamiana* epidermal cells prevents the trafficking of soluble and membrane cargo to the vacuole (Bottanelli et al. 2011; Bottanelli et al. 2012). Recent studies on RabG3f have also shown that overexpression of a DN-RabG3f (T22N mutation), under an inducible promoter in Arabidopsis, prevents trafficking of soluble proteins to the vacuole, and causes enlarged PVCs as well as fragmented vacuoles (Cui et al. 2014). The enlarged PVCs in this mutant demonstrate that this Rab is important in the trafficking of PVCs to the lytic vacuole (Cui et al. 2014). RabG3 members can also regulate specific trafficking events in response to stress; RabG3e is important in the response to salt stress (Mazel et al. 2004), and RabG3b is involved in PCD during senescence and in response to fungal pathogens (Kwon et al. 2009). Expression of the DN-RabG3f construct caused severe growth defects in seedlings (Cui et al. 2014), and studies using multiple genetic mutations of the RabG3s exhibited semi-dwarfism in early plant growth (Ebine et al. 2014), thus demonstrating the central importance of these membrane regulators in plant development. The results of these studies have demonstrated the importance of the RabG3s in controlling vacuole morphology and also specific trafficking events leading to the vacuole.

The conserved role of the RabG3 subfamily in mediating vacuolar trafficking events correlates with our knowledge of the NET4s. Both of the NET4s have been shown to associate with the tonoplast in the Arabidopsis root tip. Therefore it is likely that the Rabs recruit the NET4s at the vacuole membrane. Although the interaction of the NET4s with the RabG3s has been demonstrated *in planta* and through the Y2H system, we still do not know the spatial and temporal arrangement of this interaction.

The quantification of the anti-NET4B gold particles revealed that NET4B was preferentially localised to the tonoplast and relative labelling at the MVBs/PVCs was lower than expected for a random distribution of particles. It is possible that the interaction between NET4B and RabG3f is limited to the tonoplast membrane, or PVCs in close proximity with the tonoplast. Dual immunogold labelling using both the anti-NET4B antibody and an anti-RabG3f would distinguish the relationship between these two proteins at a subcellular level.

In addition to the role in vacuolar trafficking, this conserved subfamily of Rab GTPases is also involved in autophagy and the trafficking of autophagosomes to the vacuole. Autophagy is a eukaryotic process important in development and stress responses, where portions of the cytoplasm are engulfed by a double membrane structure and targeted to the vacuole for degradation (Bassham et al. 2015). Ypt7 and Rab7 have both been shown to be important for the normal progression of autophagosomes to the vacuole (Kim et al. 1999; Gutierrez et al. 2004; Jäger et al. 2004). One of the Arabidopsis RabG3 members, RabG3b, localises to autophagosomes and is involved in the activation of autophagy in tracheary element (TE) differentiation (Kwon et al. 2010). Initial observations of the anti-NET4B immunogold labelled samples suggested that NET4B localised to double membrane structures in the root tip, which could represent autophagosomes. Although further work needs to be done to confirm this localisation, it is possible that NET4B has a role in autophagy, which could be mediated through an interaction with RabG3b.

The yeast-2-hybrid data demonstrated that both NET4s could interact with RabG3a and RabG3f. Both NET4s contain the conserved IRQ domain which in NET4B was shown to interact with the CA-RabG3a, and it is possible that this domain is recognised by all RabG3 members. However the proteomics studies demonstrated specific RabG3/NET4 interactions; NET4A only showed an interaction with RabG3a and RabG3f only showed an interaction with NET4B. It is possible that only RabG3a co-purified with NET4A as it is the most prominently expressed RabG3 expressed in Arabidopsis cell culture. However Dr. Ian Moore's group co-immunoprecipitated the RabG3f-NET4B complex from Arabidopsis roots; a tissue in which both NET4s are expressed. This suggests that although the NET4s can interact with both RabG3s in the Y2H system, there may be some differences in their interaction affinities *in planta*.

Whether the NET4s exhibit preferential or specific binding to particular RabG3 members *in planta* remains to be investigated. The next section shall discuss possible ways in which the NET4s could represent effector proteins of the Rabs.

9.5.3 Model for the NET4s as Rab effectors

The yeast-two-hybrid studies performed in this study demonstrated that NET4B and NET4A could both interact with the constitutively-active GTP-bound versions of RabG3a and RabG3f. The specific association with the activated Rab would suggest that the NET4s could be recruited as effector proteins (see Figure 9.6) and mediate

downstream processes. Therefore this section shall discuss the possible mechanistic role of the NET4s as Rab effectors.

Effectors are generally defined as binding with the GTP-bound version of the Rab to mediate downstream processes (Hutagalung & Novick 2011). Activated Rabs are able to recruit specific sets of effector proteins to mediate key steps in membrane trafficking events, such as vesicle budding, transportation, uncoating/tethering and fusion with the destination membrane (Grosshans et al. 2006; Hutagalung & Novick 2011). Various different functional types of effectors have been characterised for example: tethering factors, molecular motors, kinases, phosphotases, sorting adaptors, and regulators of the SNARE assembly complex (Woollard & Moore 2008; Stenmark 2009). Considering the NET4s as actin-binding coiled-coil proteins, four models for their potential function as Rab effectors were developed in relation to other known effectors.

Model 1: NET4B as a motor adaptor protein

Membrane trafficking requires the delivery of vesicles from the site of formation to the site of delivery (Hammer & Wu 2002). The movement of vesicle systems within the cell relies on the use of molecular motors, such as kinesins and myosins, that use the microtubule and actin cytoskeleton respectively as 'tracks' (Vale 2003). Transport of vesicles in animal cells primarily relies upon the microtubule network for long-distance transport, and the actin cytoskeleton is utilised for short distance transportation and anchoring (Woolner & Bement 2009). In contrast, plant cells rely on the acto-myosin system for organelle and endomembrane trafficking (Boevink et al. 1998; van Gestel et al. 2002; Łangowski et al. 2010). The recruitment of both kinesin and myosin motors by Rab GTPases, either through direct or indirect interactions enables the direct targeting of membrane trafficking (Stenmark 2009). Currently our knowledge of Rab-molecular motor interactions in plants is very limited, however their associations have been fairly well characterised in yeast and mammalian systems.

Many Rab effectors can be found that act as adaptor proteins that bridge an active-Rab and a molecular motor. One of the most well characterised Rab-motor adaptors is the Rab27a effector, Melanophilin/Slac2a, that links myosin Va to the active Rab27a and is important for melanosome transport (Fukuda et al. 2002; Strom et al. 2002; Nagashima et al. 2002). Melanophilin has also been shown to bind directly to F-actin *in vitro* (Fukuda & Kuroda 2002), and overexpression of a dominant-negative Melanophilin,

that lacks an actin-binding domain, prevented the proper transportation of melanosomes (Kuroda et al. 2003).

It is possible that the NET4s are recruited as effector proteins of RabG3s and act as molecular motor adaptor proteins. The structural arrangement of the NET4s, with the actin-binding domain and Rab-binding domain at opposite ends of the protein, is similar to that of Melanophilin which interacts with myosin Va in the central region (Kuroda et al. 2003). The coiled-coil domains of NET4B could provide a platform for protein association with a molecular motor such as a myosin (Figure 9.7). Indeed, the myosin binding region of Melanophilin is mediated by a coiled-coil domain (Nagashima et al. 2002). The interaction between NET4s and motor proteins could be important in mediating vacuolar trafficking as previously discussed in section 9.3.2. In addition, as has been proposed for Melanophilin, the NET4 adaptor could be important for the transport of vacuolar compartments and also creating a stable anchor point with the actin cytoskeleton (Kuroda et al. 2003).

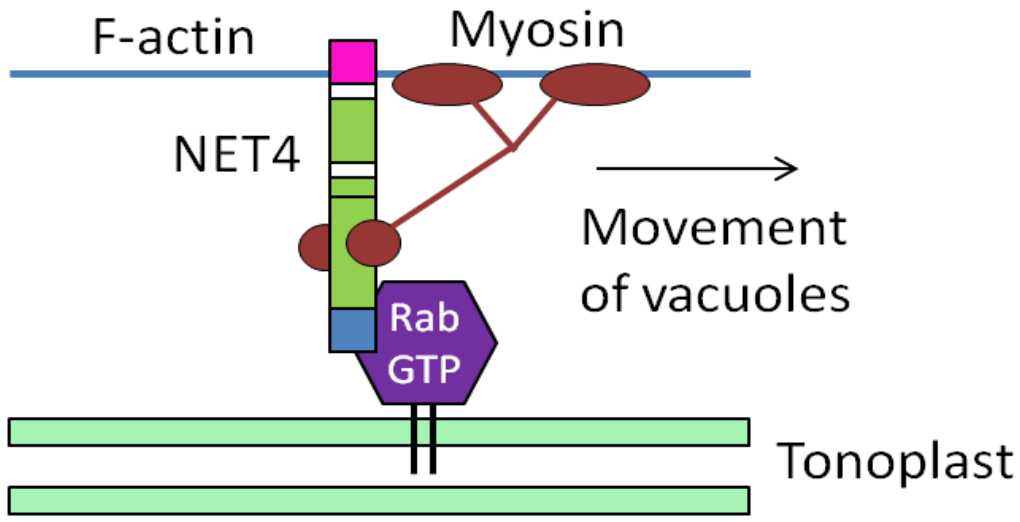

Figure 9.7: Model of NET4s as motor adaptor proteins. Schematic diagram showing how the NET4s could be adaptor proteins for myosin motor proteins. The NET4s could interact with the active GTP-RabG3 at the tonoplast via the IRQ domain (blue). NET4s could also bind actin with the NAB domain (magenta). Myosins could bind NET4s in the coiled-coil regions (green). Melanophilin is a motor adaptor protein that has a similar domain architecture to NET4B. The actin-binding domain of Melanophilin has been shown to be important for the proper positioning of melanosomes, however the precise mode of action has not been unequivocally proven (Kuroda et al. 2003).

Currently it is unknown whether NET4B interacts with a molecular motor. Analysis of the *in vivo* localisation of the GFP-fused NET4B truncations did not demonstrate any clear subcellular localisation for the central region between the NAB domain and the IRQ. However, the C-terminal IRQ + Ct domain did localise to moving punctae in the leaf epidermal cells which could resemble vesicle compartments. This domain was determined to be the Rab-binding domain of NET4B therefore it is possible that those punctae resemble Rab-labelled vesicles. These studies do not necessarily rule out the possibility of an interaction with a myosin motor, and it is possible that NET4B could form a RabG3-NET4B-Myosin complex.

Model 2: NET4B as a tethering factor

Tethering factors are Rab effectors that are considered to act prior to membrane fusion by forming a bridge between two opposing membranes (Pfeffer 1999; Whyte & Munro 2002; Kümmel & Ungermann 2014). In addition to catching vesicles, tethering factors have also been shown to proofread SNARE proteins prior to fusion and could therefore ensure the precise fusion of vesicle compartments (Starai et al. 2008).

Tethering factors belong to two main classes; multisubunit complexes and long-coiled coil proteins. The homotypic fusion and vacuole protein sorting (HOPS) complex is an example of a multisubunit tethering complex that mediates PVC to vacuole, and vacuole to vacuole trafficking (Bröcker et al. 2010). The HOPS complex is a Rab7/Ypt7 effector, and has Rab-binding sites at both ends of the complex that allow the tethering of opposing vacuoles prior to fusion (Bröcker et al. 2012). Coiled-coil tethers are another class of tethering factors and many different coiled-coil tethers that act as Rab effectors have been described, for example EARLY ENDOSOME ANTIGEN 1 (EEA1), Rabaptin-5, and the golgins (Stenmark et al. 1995; Lawe et al. 2002; Sinka et al. 2008). The coiled-coil domain enables dimerisation of the protein to form rod-like scaffolds that can tether oncoming vesicles (Munro 2011).

It is possible that the NET4s act as tethering factors as they could dimerise in an anti-parallel manner and thus be able to bind active RabG3 GTPases on opposing vesicles via the C-terminal IRQ domain. This interaction would then bring the vesicles in close proximity and enable the subsequent SNARE mediated fusion Figure 9.8 shows a schematic model of how the NET4 dimers could act as coiled-coil tethers linking two RabG3 labelled vesicles.

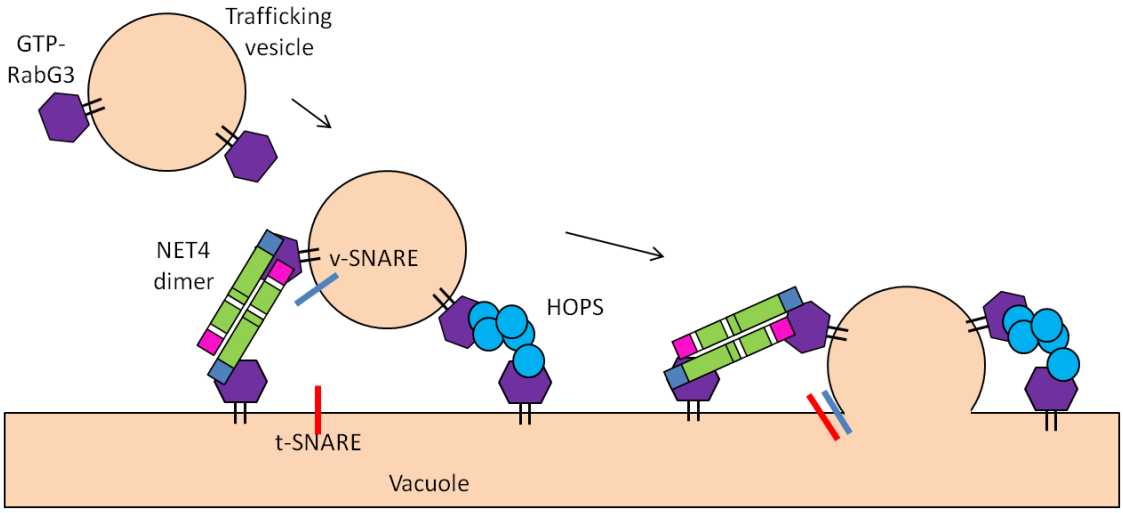

Figure 9.8: Model of the NET4s as tethering factors. Schematic diagram of how the NET4s could function as tethering factors in membrane trafficking. Shown here is a depiction of a RabG3 labelled vesicle transporting to the vacuole, however the same model could also apply to homotypic vacuole fusion. Anti-parallel NET4 dimers could tether oncoming vesicles through interactions with GTP-RabG3s on opposing membranes. This could then function to bring vesicles in close proximity for SNARE mediated fusion, in concert with the HOPS multisubunit tethering complex.

Coiled-coil tethers have not currently been identified at the lysosome/vacuole in animals or yeast, and vacuole tethering is performed efficiently by the HOPS complex (Kümmel & Ungermann 2014). It is possible that the NET4s could act in conjunction with the HOPS complex to tether vacuolar compartments which could represent a divergent method of vacuolar fusion specific to plants.

Model 3: NET4B as a scaffolding platform

Effectors of Rab GTPases often function as part of a complex of proteins to mediate downstream processes (Grosshans et al. 2006). Therefore one of the possibilities for NET4B as an effector could be to create a platform for further Rab-effector protein interactions. Active Rabs recruit several different types of effectors to the target membrane, and their subsequent interactions can cause positive feedback loops that stabilises the active Rabs, recruits further effectors and creates Rab specific membrane domains (Grosshans et al. 2006). The best example of this is comes from studies of the mammalian Rab5 that functions at the early endosome (Figure 9.9).

Rab5 is activated at the early endosome by its GEF, Rabex5 (Horiuchi et al. 1997), and the active GTP-Rab5 can then recruit its effector Rabaptin5 (Stenmark et al. 1995).

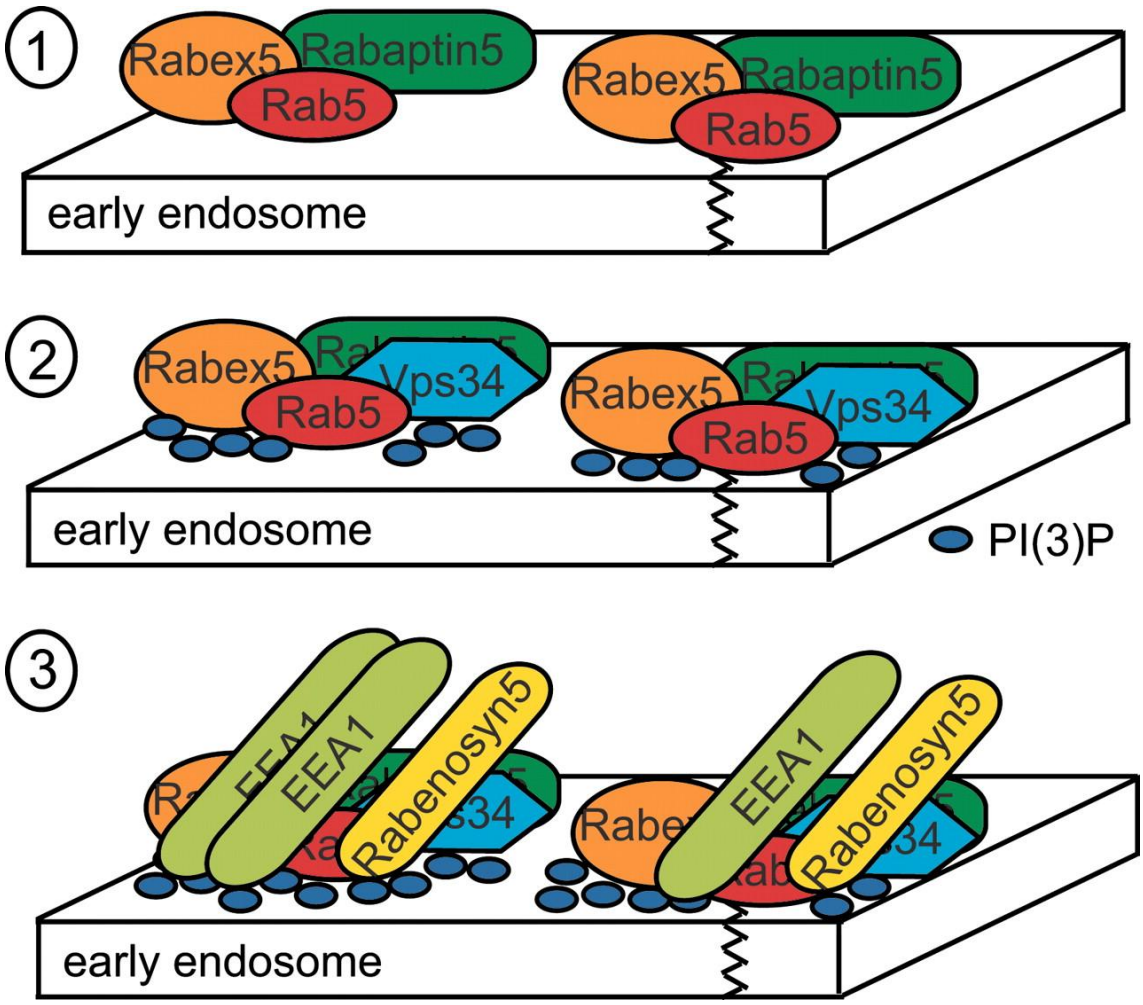

Figure 9.9: Model of how Rab effectors create scaffolds to stabilise Rab membrane domains. Example shown here is how Rab5 effector interactions can lead to Rab membrane domains, as explained in the text (Diagram from Grosshans et al. 2006, Copyright (2006) by the National Academy of Sciences, U.S.A.). (1) Rab5 is activated at the early endosome by its GEF, Rabex5 and can then recruit its effector Rabaptin5 which increases the Rabex5 activity. (2) Additional effectors are recruited to this protein complex platform, including the phosphatidylinositol-3-OH kinase VPS34, which generates lipid PI(3)P in the endosome membrane. (3) The presence of both PI(3)P and GTP-Rab5 recruits further effectors involved in membrane trafficking including EEA1 and Rabenosyn5.

Once bound, Rabaptin5 interacts with Rabex5 and increases its GEF activity (Lippé et al. 2001), and thus stabilises Rab5 in its active form, creating a positive feedback loop and preventing GAP-mediated inactivation. Additional effectors are then recruited to this protein complex platform, and include the phosphatidylinositol-3-OH kinase VPS34 (VACUOLAR PROTEIN SORTING 34; Murray et al. 2002). This protein then generates the lipid phosphatidylinositol-3-phosphate (PI(3)P) in the endosome

membrane (Gillooly et al. 2000), and the presence of both PI(3)P and GTP-Rab5 recruits further effectors involved in membrane trafficking including EEA1 and Rabenosyn5 (Simonsen et al. 1998; Christoforidis et al. 1999; Gaullier et al. 2000; Nielsen et al. 2000).

The NET4s could promote a similar positive feedback loop through an interaction with the RabG3f GEF, the Mon1-Ccz1 complex (Cui et al. 2014), and thus stabilise active RabG3f at the vacuole. The coiled-coil domains of the NET4s could also provide a scaffold for further effector interactions to occur at the tonoplast (Rose & Meier 2004). The association between the NET4s and actin could also be important in potentially stabilising the Rab-effector complex at a specific membrane domain. Further studies are therefore needed to identify additional RabG3 effector proteins and how they could function in a complex.

Model 4: RabG3-NET4B interaction as an actin modulator.

Another possibility, could be that the NET4s are recruited by the active RabG3s to modulate the actin cytoskeleton surrounding the tonoplast. Typically, the Rab subfamily of Ras GTPases regulate membrane trafficking events and the distinct Rho subfamily, which includes RhoA, Cdc42 and Rac1, regulate actin organisation (Wennerberg et al. 2005). However Rab35 and Rab13 are examples of Rab GTPases which are involved in both membrane trafficking and regulating actin organisation.

Rab35 is conserved in metazoans and has been shown to have a role in plasma membrane receptor recycling and cytokinesis (Kouranti et al. 2006), and has additional roles in actin dynamics (Zhang et al. 2009). Recently, fascin, an actin-bundling protein, has been shown to be an effector of Rab35 (Zhang et al. 2009). The recruitment of fascin by Rab35 leads to localised actin bundling and is important for filopodia formation in cultured cells and bristle formation in *Drosophila melanogaster*.

Another example of the link between membrane trafficking events and cytoskeleton regulation comes from studies on Rab13 and its effector JRAB (JUNCTIONAL RAB13 BINDING PROTEIN (JRAB)/MOLECULE INTERACTING WITH CasL-LIKE 2 (MICAL-L2)). Rab13 has been shown to be important in the trafficking of cell adhesion molecules to the sites of cell-cell contacts in epithelial cells (Marzesco et al. 2002; Morimoto et al. 2005). JRAB is an effector of Rab13 and is similarly involved in adhesion (Terai et al. 2006; Yamamura et al. 2008). JRAB can interact with two actin

cross-linking and bundling proteins, actinin-1 and actinin-4, and it also interacts directly with F-actin through a CH-domain (Nakatsuji et al. 2008; Sakane et al. 2012). The tertiary conformation of JRAB has been shown to change upon binding to GTP-Rab13 (Sakane et al. 2010), and this can affect its association with its interacting partners and F-actin (Sakane et al. 2012). When GTP-Rab13 interacts with JRAB, it causes the protein to unfold which subsequently exposes the CH domain, enabling F-actin binding, however this change also reduces the association with the actinin proteins (Sakane et al. 2012). Consequently, when GTP-Rab13 recruits JRAB at the plasma membrane near cell-cell contacts, it causes the stabilisation of F-actin through JRAB and maintains stationary cell-cell adhesion junctions (Sakane et al. 2012).

Rab35 and Rab13 are examples of Rab GTPases that influences membrane and actin dynamics through specific effector interactions. It is possible that GTP-bound RabG3s could recruit the NET4s to the tonoplast which could affect local actin organisation (Figure 9.10). Furthermore, the RabG3-NET4 interaction could create the filamentous cables seen between the two vacuoles with the NET4A-GFP lines, which could allow downstream processes in membrane trafficking to occur (as discussed in 9.3.2). This change could be due to intrinsic actin-binding properties of the NET4s, such as bundling and cross-linking activity, or through additional interacting partners as is observed with JRAB. Future work in the Hussey group will focus on imaging the actin cytoskeleton and NET4 rearrangements surrounding the tonoplast in cells overexpressing either dominant-negative or constitutively-active RabG3 mutations.

9.5.4 Concluding remarks on RabG3 interactions

The interaction between the NET4s and the RabG3s has been demonstrated both *in planta* and using the Y2H system. Through the Y2H system, it was demonstrated that the NET4s specifically interact with the GTP-bound active RabG3s, which suggests that they could be effector proteins of these Rabs. As both RabG3s and the NET4s are present at the tonoplast, it is likely that the NET4s are recruited for membrane trafficking events at the vacuole.

The models presented here consider various different scenarios for the role of the NET4s as RabG3 effectors. Although they were presented as distinct models, it is possible that the function of the NET4B/RabG3 interaction combines different aspects of each as Rab effectors could have multiple functions. Indeed, the golgins are described as multifunctional, having both roles in Rab mediated membrane trafficking

and providing a protein scaffold to support the Golgi structure (Munro 2011). It is possible that the NET4s have similar multifunctional roles, and that it could have a role in maintaining vacuole morphology as well as being specifically recruited by the Rabs at specific stages of membrane trafficking.

The interaction between the NET4s and the RabG3s suggests a signalling mechanism in which the NET4s could be recruited for downstream processes in membrane trafficking. The activation status of the Rabs is only temporary and is governed by the activation and deactivation by GEFs and GAPs respectively. Currently, little is known about the control of RabG3 activation and inactivation in vacuolar trafficking. This highlights the importance of future work that could include studying the spatio-temporal activation of the RabG3s and how this relates to NET4 localisation and function.

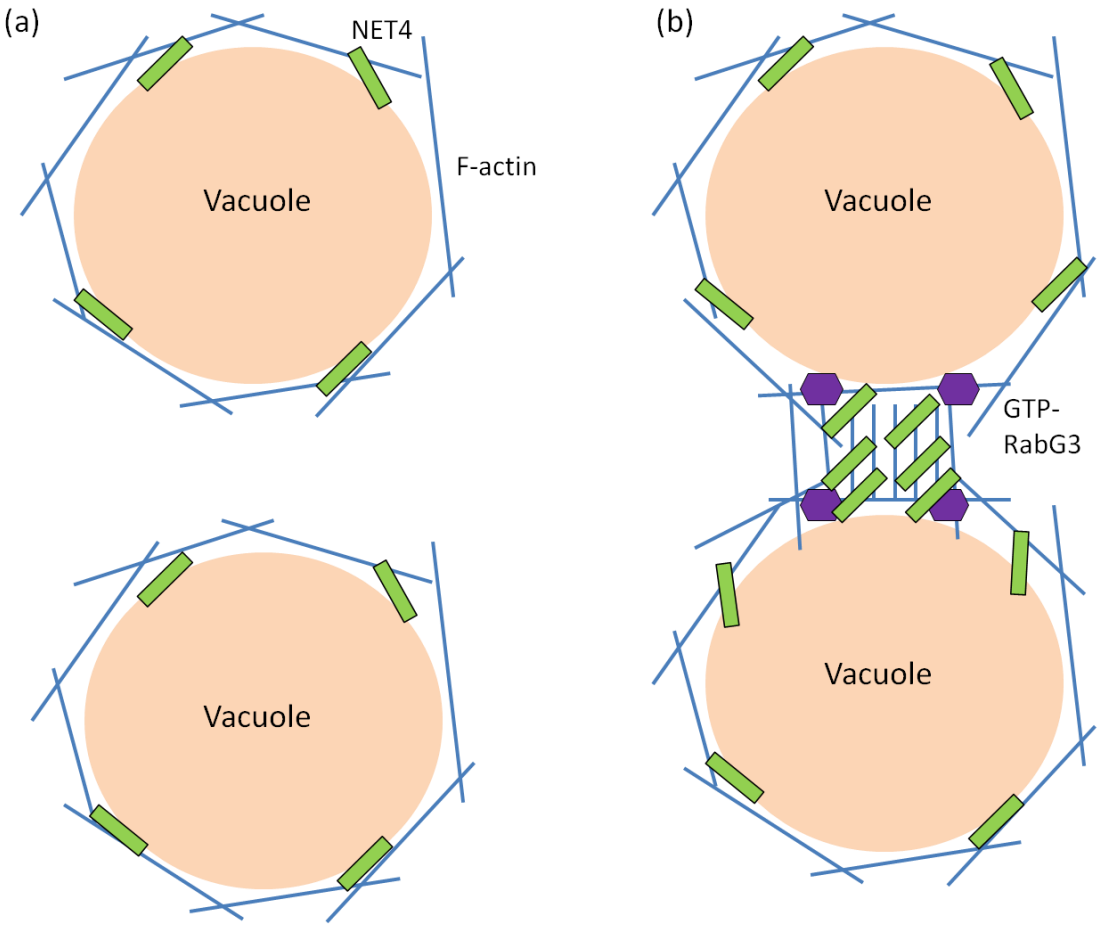

Figure 9.10: Model showing how the NET4-RabG3 interaction could mediate a change in actin organisation. (a) Under normal conditions, NET4s could link the actin cytoskeleton to the vacuole. (b) The activation of RabG3s at the tonoplast could induce a change in morphology of NET4B or affect additional interacting partners, leading to a change in actin morphology.

9.6 Implications for NET4 function derived from the *net4* mutant analysis

In order to ascribe a function for the NET4 proteins, phenotypic analysis was performed using T-DNA insertion lines that disrupted the *NET4* genes. Homozygous lines were identified for both *net4a* and *net4b*, and they were shown to disrupt and knock-down expression respectively. These two mutant lines were then crossed together to create a double-homozygous *net4* line that could be assessed for an observable phenotype.

As both NET4s localise to the tonoplast in the root, it was hypothesised that disruption of these genes could have a root length phenotype and a root length assay was performed. Only the single homozygous *net4b* mutant exhibited a statistically significant reduction in root growth compared to the azygous, at all growth time points. The single *net4a* mutant showed a significant reduction in root growth at earlier time points, although this was not apparent at later time points, and the double *net4* mutant showed no discernible phenotype in root length throughout the assay. It is possible that the *NET4s* could function antagonistically to regulate root growth, and therefore the loss of one gene could disrupt this balance and result in a reduced root length. In the double mutant, this antagonistic relationship between the NET4s would be lost and could therefore rescue this phenotype. Indeed, similar genetic relationships have been characterised in Arabidopsis; as is observed between *PIN5* and *PIN8* in the regulation of pollen morphology (Ding et al. 2012). Further biological repeats of this root length assay with a larger sample size are needed to assess the relationship of the *NET4s* in regulating root growth.

In addition, initial phenotypic analysis of root growth in the *net4* mutant lines was performed under salt and drought stress; using a fixed concentration of sodium chloride and sorbitol respectively. Interestingly the double *net4b*/*net4a* mutant showed an increased tolerance to salt stress and the single *net4a* mutant showed an increased tolerance to drought. It is possible that the *NET4s* act as a negative regulators during salt and drought stress, for example they could negatively regulate sodium ion transport into the vacuole, and therefore disrupting the *NET4s* could increase the plants tolerance to salt stress. However further work is needed to confirm the results found here as well as an investigation into the potential cause of these phenotypes.

Additional experiments were also performed to investigate the potential role of the *NET4s* in guard cell functioning, as well as protein storage vacuole and lytic vacuole

morphology, and protein trafficking in the embryos, however no discernible phenotype was observed.

The phenotypic analysis presented in this thesis has not currently provided a conclusive function for the *NET4s* in plant cell growth and development. In this study, only a knock-down mutant of *net4b* was used and it is possible that the residual expression of *NET4B* could prevent the appearance of a phenotype. Furthermore, it is possible that a phenotype could only be observed in response to additional stresses. For example, it is possible that the *NET4s* have a specific role in pathogen response as the bioinformatics analysis presented in Chapter 3 revealed that *NET4B* was upregulated in response to *Pseudomonas* infiltration.

9.7 The IRQ family

9.7.1 Overview of the IRQ family

One of the key aspects of this project was an investigation into the conserved IRQ domain of NET4B. This conserved domain, identified in NET4B/4A/3C/3A, contains three invariant residues: isoleucine (I), arginine (R), glutamine (Q), and was thus termed the IRQ domain. Interactor studies using the Y2H system, revealed that this C-terminal domain could interact with the constitutively-active GTP-bound RabG3a, and that the minimal fragment was encoded by NET4B$^{464\text{-}511}$. This domain therefore represents the Rab-binding domain of NET4B.

Searching the Arabidopsis proteome revealed that six other proteins, outside of the NET family, contained this conserved domain. These six proteins, as well as the four NET proteins, therefore comprise an IRQ domain family. The IRQ domain itself is composed primarily of a highly conserved central core domain, however conserved amino acids are found outside of this central region (see Chapter 8; Figure 8.1). As this stretch of amino acids in NET4B were shown to bind the active RabG3a this family of proteins could represent a family of putative Rab-effector proteins. Section 9.7.2 discusses further the implications of the conserved IRQ domain as a Rab-binding domain.

Further analysis of the evolutionary history of this domain revealed that it was plant-specific and was found only in the Tracheophyta, and was present in the genomes of the clubmoss *Selaginella moellendorffi*. Within the clubmoss genome, the IRQ domain was only found in two genes that had previously been characterised as containing NAB

domains, and resembling the NET4 proteins (Hawkins et al. 2014). Further discussion on the evolutionary nature of the IRQ family shall be discussed in section 9.7.3.

Bioinformatics analysis of the IRQ family showed that it is composed of 5 groups; the NET4s, NET3A and NET3C, and group 1-3 IRQs. All of these genes shared the C-terminal IRQ domain, as well as predicted coiled-coil domains. The NET proteins all share the conserved N-terminal NAB domain, and interestingly some similarity was observed between the NAB domain and the N-terminal regions of the group 3 proteins; this region was thus termed a quassi-NAB (qNAB) domain. The presence of the qNAB in the group 3 proteins could reflect that the founding NET/IRQ protein resembled a NET4 protein that had both the NAB and IRQ domain.

Bioinformatics analysis of the novel IRQ genes revealed that they all had differing expression patterns. The group 1 genes are mainly expressed in meristematic tissue, the group 2s are pollen specific and the two group three members showed differing expression profiles: At1g64330 showed highest expression in the embryo whereas At5g41790 (CIP1) was most highly expressed in leaf tissue. The expression profile of these proteins suggests that they are involved in different tissue-specific processes. Investigation of the IRQ proteins subcellular localisation predictions also revealed that both group 3 proteins have been found in vacuolar proteomes, suggesting that the IRQ family associate with membranes similar to the NETs.

Only one of the novel IRQ proteins has been previously characterised; At5g41790 was previously shown to interact with COP1 and was therefore termed COP1-INTERACTING PROTEIN 1 (CIP1; Matsui et al. 1995). COP1 (CONSTITUTIVE PHOTOMORPHOGENIC 1) is a RING E3 ubiquitin ligase that targets proteins key photomorphogeneic regulators for proteosomal degradation and was one of the first characterised repressors of the photomorphogenic response in plants (Deng et al. 1991; Lau & Deng 2012). Through immunofluorescence studies, CIP1 was shown to localise to the cytoskeleton in hypocotyl protoplasts and a punctate pattern in root protoplasts, and it was hypothesised that the CIP1-COP1 interaction in the hypocotyl would sequester COP1 in the cytosol and therefore allowing photomorphogenesis responses to occur (Matsui et al. 1995). From this study, it is tempting to speculate that the observed filamentous and punctate pattern could be mediated through the qNAB and the IRQ domain respectively.

Investigating characterised interactors of the other group 3 IRQ member, At1g64330, revealed that it was pulled back in a Y2H screen using ARABIDOPSIS HISTIDINE KINASE 2 (AHK2) as bait, and was pulled-down in a co-immunoprecipitation assay using PIN1 as bait (Dortay et al. 2008; Mravec et al. 2011). The interaction with PIN1 is uncertain as a gene locus was not provided, however the molecular weight and annotation matched that of At1g64330. These two interactions could implicate At1g64330 in hormonal regulation of plant growth and development.

PIN1 is an auxin efflux carrier at the basal plasma membrane in the root. This efflux carrier, as well as other PIN proteins, function to regulate the distribution of auxin, and therefore control cell division and expansion within the root (Blilou et al. 2005). Cytokinin functions antagonistically with auxin in the root meristem; cytokinin promotes cell differentiation and suppresses auxin activity, whereas auxin promotes cell division and maintains meristem activity (Moubayidin et al. 2009). There are three cytokinin receptors in Arabidopsis, AHK2, AHK3, and AHK4 (Higuchi et al. 2004). Recently it has been shown that perception of cytokinin by AHK4 affects the trafficking of PIN1 and leads to its vacuolar targeting and subsequent degradation (Marhavý et al. 2011). Although AHK2 was shown not to affect PIN1 trafficking (Marhavý et al. 2011), it is possible that At1g64330 could interact with AHK4 as well as AHK2, as this was not tested during the initial Y2H screen (Dortay et al. 2008). These results could therefore implicate At1g64330 in the trafficking events of PIN1 and further work is needed to confirm their functional relationships *in planta*.

9.7.2 The IRQ domain as the Rab-binding domain

Y2H studies demonstrated that the NET4B IRQ domain ($NET4B^{464\text{-}511}$) could interact with the constitutively-active RabG3a. Analysis of the predicted secondary structure of the IRQ domain of NET4B suggests that it could form an α-helix. Most structurally characterised effector-Rab complexes are mediated via an interaction domain that consisting of 1-2 α-helices or coiled-coil regions (Zhu et al. 2004; Wu et al. 2005; Eathiraj et al. 2005; Eathiraj et al. 2006; Jagoe et al. 2006; Kukimoto-Niino et al. 2008; Chavas et al. 2008; Schoebel et al. 2011; Lall et al. 2015). Consequently, it is possible that the whole IRQ domain is needed to form a structural motif that interacts with the Rab. Within this α-helix, the highly conserved central domain could form important interactions with the Rab, which could explain the higher conservation of this region.

The presence of this conserved domain throughout ten different proteins raises the question of whether these proteins could interact with specific Rab GTPases in different membrane trafficking events or whether they are a family of RabG3 effectors?

Rab effector proteins typically interact with Rab GTPases in their activated GTP-bound form (Stenmark 2009). The two switch regions of Rabs (switch I and II) interact with the γ-phosphate of GTP, and these regions change from a highly disordered to an ordered conformation upon GTP binding (Stroupe & Brunger 2000; Hutagalung & Novick 2011). This change in conformation creates an interface for effector binding specifically in the GTP-bound state (Behnia & Munro 2005). Alignment of Rab GTPase sequences revealed that there are four regions, termed Rab Subfamily Conserved regions, that vary among the Rab proteins and these regions define the various subfamilies (Pereira-Leal & Seabra 2000). Structural studies have shown that Rab effectors can interact with the switch and interswitch regions, as well as these variable regions, and structural differences in these regions achieve specific Rab-effector interactions (Ostermeier & Brunger 1999; Eathiraj et al. 2005; Hutagalung & Novick 2011; Khan & Ménétrey 2013).

The specific interfaces that different Rab GTPases create can allow for specific interactions with effector proteins (Hutagalung & Novick 2011). However, it is known that conserved Rab-binding domains can mediate interactions with multiple or specific Rabs. An excellent example of this comes from the eleven characterised Rab27 effectors in metazoans, which include Melanophilin and Rabphilin. These proteins share high homology in their N-terminal Rab27 binding domain (RBD27), which is composed of two subdomains (RBD27-1 and RBD27-2) separated by two zinc-finger motifs (Chavas et al. 2008). Although these effectors share high homology in the RBD27, they exhibit different Rab specificities. Some members, for example Melanophilin, exclusively interact with Rab27, and others like Rabphilin are able to additionally interact with Rab3 and Rab8 (Chavas et al. 2008). Structural studies have revealed that the different interactions of these effectors are not due to changes in their structure, but due to subtle differences in individual amino acids in the RBD27 that interact with the Rab (Ostermeier & Brunger 1999; Kukimoto-Niino et al. 2008; Chavas et al. 2008; Itzen & Goody 2008).

The Rab-binding domain of NET4B encompasses the highly conserved central core of the IRQ domain but also stretches of amino acids outside of this region. The IRQ family

share a great degree of conservation within this central domain as well as conserved outlying amino acids. Within the highly conserved region, there are some invariant amino acids (E_{478}, K_{480}, R_{481}, E_{482}, I_{484}, R_{485}, Q_{486}), however there is also a great degree of residue differences within the central region and in the full IRQ domain. Therefore, it would be of interest to test whether differences in the IRQ primary amino acid sequences could mediate distinct Rab interactions or whether they are all capable of interacting with RabG3s. The NET4s and possibly the group 3 IRQ members can associate with the vacuole, and it is likely that these proteins interact specifically with the RabG3 subfamily. However, NET3C and NET3A associate with the endoplasmic reticulum-plasma membrane (ER-PM) anchoring sites and the nuclear envelope respectively (Wang et al. 2014; Deeks et al. 2012); therefore it is likely that they interact with different subfamilies of Rab GTPases. The next stage of research will therefore be to examine whether the IRQ family members associate with different Rab GTPases.

9.7.3 The NET4s represent the founding member of the NET and IRQ families

Previous phylogenetic analysis of the NET family revealed that the NETs are a plant specific family, defined by the NAB domain and that they first emerged at the beginning of the vascular plant lineage (Deeks et al. 2012; Hawkins et al. 2014). The first NET, which resembled a NET4, could be found in the genome of the clubmoss (Lycophytes), *S. moellendorffii*, an extant species of the earliest vascular plant clade (Hawkins et al. 2014). The appearance of the NET family in the Lycophytes marks a critical point in land plant development, which signifies the onset of vascular plant development and dates back to the late Silurian/early Devonian period (Banks 2009). The development of vascular tissue (xylem and phloem) for transporting water and nutrients, as well as lignified cell walls to resist mechanical stresses, enabled these first vascular plants to grow taller and therefore disperse spores over a wider range (Banks 2009). The emergence of the NETs, specifically a NET4, at this evolutionary time point could have been crucial in supporting the vacuole against the increased turgor pressure associated with complex land plant structures (Hawkins et al. 2014).

The appearance of the NET4s at this stage in land plant evolution could also mark a change in the cytoskeletal network governing membrane dynamics. Spatial regulation of organelles and the endomembrane system, including the vacuole, is predominantly governed by actin filaments in higher plants (Boevink et al. 1998; Sheahan et al. 2004; Higaki et al. 2006). However studies on the Bryophyte, *Physcomitrella patens*,

demonstrated that microtubules are required for regulating their vacuolar structure and dynamics (Yoshihisa Oda et al. 2009). This therefore suggests that there was a possible divergence in the cytoskeletal system regulating vacuolar dynamics during land plant evolution. Both Arabidopsis NET4s have now been shown to associate with actin filaments *in vivo*, and associate with the tonoplast in the root. The emergence of the NET4s could have occurred at a critical point in land plant evolution, when the regulatory mechanism governing vacuole dynamics switched from microtubules to actin filaments.

Studies from this thesis suggest that if the first NET similarly localised to the vacuole, then this association could have been mediated through interaction with a vacuolar Rab GTPase. The conservation between the NAB and IRQ domains in the *S. moellendorffi* and Arabidopsis NET4 proteins would suggest that this could represent a conserved mechanism linking the actin cytoskeleton to the vacuole.

During land plant evolution, there has also been a divergence of proteins based on the functional NAB and IRQ domains. From the first NET4 proteins, with both a NAB and an IRQ, two interlinked protein families have diverged. Figure 9.11 shows how during land plant evolution, several proteins have evolved with different domain architectures: in Arabidopsis seven proteins only possess a NAB domain (NET1s, NET2s and NET3B), four proteins contain both a NAB and an IRQ domain (NET4s, NET3A and NET3C), and six proteins contain only an IRQ domain (groups 1-3 IRQ proteins).

Both the NET and IRQ proteins are predicted to contain coiled-coil domains and could therefore dimerise to form higher-order structures that could serve as scaffolds, adaptor proteins and signalling platforms (Rose & Meier 2004). The presence of the different domains could then effect the functioning of the proteins; with NAB only proteins linking the actin cytoskeleton to membranes independently of Rab GTPases, and the IRQ only proteins having an association with Rab GTPases independent of the actin cytoskeleton. However it is possible that the NAB only proteins could contain other uncharacterised Rab-binding domains, and that the IRQ only proteins could still associate with actin. Indeed, the group 3 IRQ proteins do possess the qNAB that is similar to the NAB, and CIP1 was shown to associate with a filamentous network in hypocotyl protoplasts (Matsui et al. 1995).

The discovery of the IRQ family, and it's relation to the NET family, could further our understanding of plant-specific membrane dynamics and further work is continuing in the Hussey group to characterise these putative Rab effector proteins.

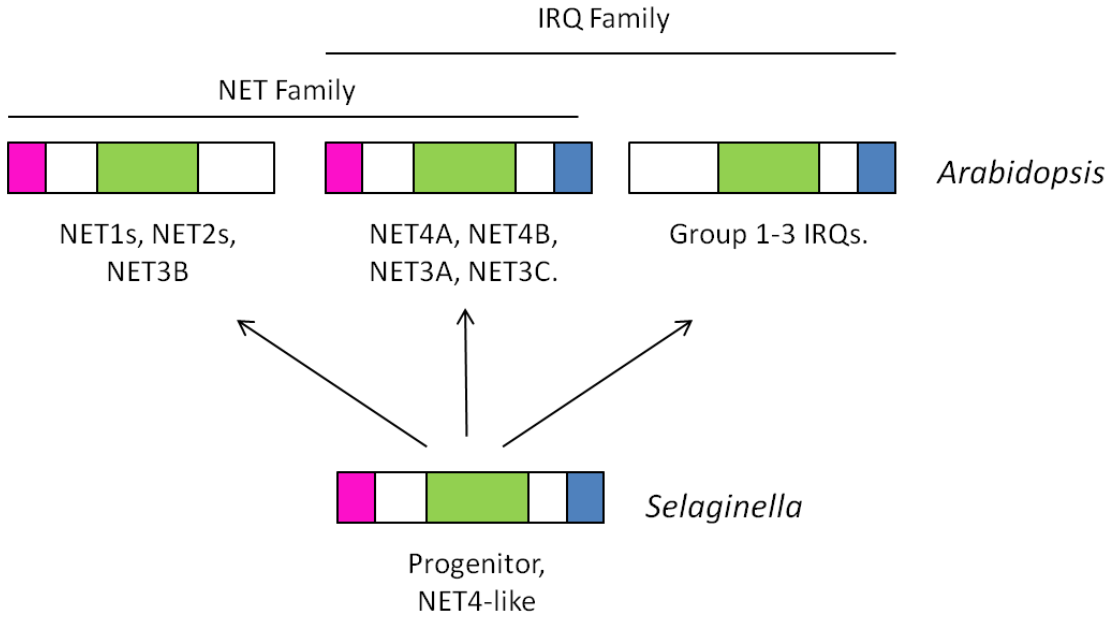

Figure 9.11: Diversification of the NET and IRQ families. The earliest NET gene would have represented a NET4-like gene, containing both a NAB and IRQ domain, as is present in the *Selaginella* genome. During land plant evolution, this gene diversified into both the NET and IRQ families which overlap with the NET4s and NET3A and NET3C. The NET families all contain a NAB domain (magenta), the IRQ proteins all contain a C-terminal IRQ domain (blue), and the NET4s/NET3A/NET3C contain both. All of these proteins contain predicted coiled-coil domains (green). Diagram created by Dr. Tim Hawkins (Durham University).

9.8 Future perspectives

The results from this thesis have demonstrated that NET4B can associate with actin and localises to the tonoplast in the root tips, as well as being expressed in the guard cells. These results therefore revealed that the NET4s are a tonoplast-associated subfamily of the NET proteins. In addition, both of these proteins were shown to associate with a vacuolar subclass of Rab GTPases and could potentially be involved in vacuolar trafficking. Several models have been proposed for the NET4s as Rab effectors and for their function at the vacuole. Further investigation into the function of the NET4s at the tonoplast would greatly increase our understanding of actin-vacuole dynamics in plants.

This study demonstrated that NET4B associates with the tonoplast, however, it did not provide evidence of how NET4B associates with actin surrounding the vacuole. Further work using immunofluorescence of whole Arabidopsis roots could therefore provide information on the array of actin that NET4B localises to. In addition, only a small section of the root tip was studied during this project, therefore further work would be required to study whether NET4B associates with the vacuole in particular cell files of the root, as is seen with the epidermal cell file restriction of NET4A (Deeks et al. 2012).

The expression of both NET4s in the root tip suggests that they could function together in actin-vacuole associated processes, for example vacuole fusion. The Y2H data also demonstrated that these proteins could form hetero-oligomers. Currently the cellular relationship between the two NET4 proteins in the root tip is unknown. Therefore it would be interesting to test whether these two proteins colocalise in the cell. This could be achieved through immunofluorescence studies of the *NET4Apro*::NET4A-GFP lines, using an anti-GFP antibody to detect NET4A and the anti-NET4B antibody to detect NET4B. This would indicate whether both proteins are expressed in the same cell and whether they localise to overlapping or distinct subdomains of the vacuole.

As well as being expressed in the root tip, *NET4B* was shown to be highly expressed in the guard cells through the GUS reporter system. NET4B could have a role in linking the vacuolar and actin systems in guard cells and further work is needed, through immunogold labelling, to ascertain whether NET4B is translated in these cells and whether there is an associated *net4b* phenotype.

Phenotypic analysis of the *net4* mutants suggested possible phenotypes associated with root growth under unstressed and stress conditions. However these studies were based on one experimental repeat each and further analysis is required to confirm these results. Further analysis of the *net4* mutant lines could focus on studying whether the actin cytoskeleton or vacuole morphology is disrupted in these mutant plants. This could be accomplished through dipping the mutant lines with fluorescently labelled actin and vacuole markers. However, as the *net4b* mutant was not a complete knock-out then it is possible that residual expression could still prevent an observable phenotype.

An alternative strategy for finding a phenotype for the *NET4s* could be to overexpress dominant-negative mutations of these proteins in Arabidopsis. Mutants of the NET4s could be generated, that lack either the NAB domain or the IRQ domain, and expressed in plants under an inducible promoter. By overexpressing these proteins, it could

prevent their normal processes, e.g. overexpressing a NET4 without an IRQ would prevent the normal Rab-mediated processes. The effect that these mutations have on plant growth and development as well as subcellular organisation could therefore attribute a possible function for the NET4s.

One of the key findings of this thesis was the interaction between the NET4s and the RabG3 GTPases. This interaction was shown to occur *in planta* with unmutated Rabs, and specifically with constitutively-active GTP-bound versions using the Y2H system. Currently it is uncertain how the NET4s function as effector proteins of these Rabs and several models have been presented here. One of the methods that could be used to study the role of the NET4s as Rab effectors would be to create stably transformed Arabidopsis plants expressing dominant-negative or constitutively-active RabG3s under an inducible promoter. These mutants could be created into both wild-type plants and the *NET4Apro*::NET4A-GFP lines. Inducing the expression of these Rab mutants in these lines would permit the visualisation of NET4 localisation changes; using GFP-fluorescence to visualise dynamic changes in NET4A localisation or immunological techniques to visualise NET4B. This would therefore reveal how the presence of an active RabG3 could affect the localisation or dynamics of the NET4 proteins. In addition, overexpressing the dominant-negative RabG3 could demonstrate whether the RabG3s govern the tonoplast localisation of the NET4s.

The experiment described above would be useful in showing how constitutively-active RabG3s could influence NET4 dynamics. However this would not indicate the endogenous regulation of RabG3 activation, through GEF and GAP activity, and how this relates to the NET4s. Recently, fluorescence resonance energy transfer (FRET) technology has been used to create FRET-biosensors that monitor the spatio-temporal activation of Rab GTPases (Aoki & Matsuda 2009). Figure 9.12 describes how these biosensors can be used to monitor the activation status of Rabs in living cells. Future work could create a FRET-biosensor that incorporates a RabG3 GTPase and the NET4B IRQ domain, and the different emission spectrums could be compared to determine where RabG3s are actively bound to GTP in the cell. Comparing this activation pattern to the subcellular localisation of the NET4s would indicate where the NET4s are specifically recruited by the active RabG3s, and therefore which membrane trafficking events they are involved in.

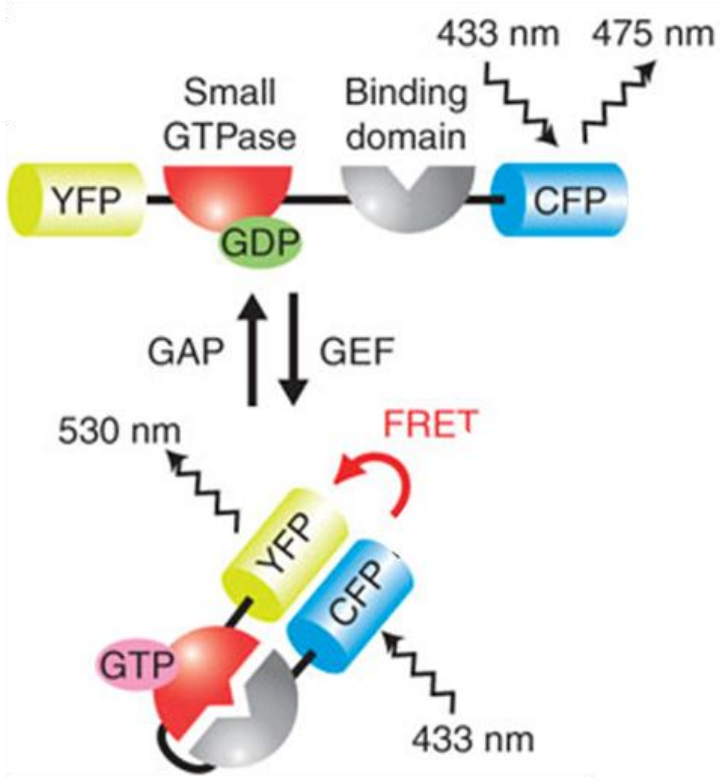

Figure 9.12: Fluorescence resonance energy transfer (FRET) biosensors to monitor RabG3 activation. Structure of a FRET probe is shown, consisting of yellow-emitting mutant of green fluorescent protein YFP (yellow), Rab GTPase (RabG3 GTPase; red), Rab-binding domain (the IRQ domain; grey), and cyan-fluorescent protein CFP (blue). When the Rab is inactive, and bound to GDP, the emission from CFP is at 473 nm when excited at 433 nm. When the Rab GTPase is bound to GTP through activation by the GEF, this will cause it to bind the IRQ domain and bring YFP in close proximity to CFP. This will then cause FRET and emission at 530 nm. Stably transforming Arabidopsis plants with this construct and comparing the two emission spectrums will therefore indicate where the RabG3s are activated. Diagram used with permission from Aoki & Matsuda (2009).

A final area of research is to examine the IRQ family proteins. These proteins all share the conserved IRQ domain, which in NET4B represents the Rab-binding domain. It is therefore of crucial importance to test whether this function of the IRQ domain is conserved across all the ten proteins that have been to shown to contain this domain. Furthermore it would be of interest to test whether the IRQ domain interacts specifically with the RabG3 subclass or different Rabs associated with different membrane systems. Additional experiments could also study the *in situ* localisation of these proteins

through creating stably transformed plants expressing these proteins as GFP fusions under their endogenous promoter. Previous proteomics studies have suggested that the group 3 IRQ proteins are found at the vacuole membrane, which could suggest they might form functional interactions with the NET4s. Furthermore, bioinformatics analysis revealed some potentially interesting interactions between At1g64330, PIN1 and an histidine kinase (AHK2), thus further research could focus on examining these interactions. In addition, further work is needed to study the function of the IRQ proteins through phenotypic analysis using T-DNA insertion mutant lines.

9.9 Conclusion

The link between the actin cytoskeleton and membranes is crucial in mediating membrane trafficking and organelle transport, as well as acting as platforms for signalling (Mathur et al. 2002; Peremyslov et al. 2008; Pleskot et al. 2014). Many of the mammalian proteins that produce specialised sites of interaction between the actin cytoskeleton and membranes, such as α-actinin, spectrin, filamin and the FERM domain proteins are absent in plants (Hussey et al. 2002). Recently, the plant-specific NET family of actin-binding proteins was discovered that all share a conserved N-terminal NET actin-binding (NAB) domain (Deeks et al. 2012). This family can only be found in the genomes of Tracheophyte plants, and members of each subfamily have been shown to associate with distinct membrane structures (Deeks et al. 2012; Wang et al. 2014). The association of this family with actin and membrane compartments thus increases our knowledge on how these two systems function in plant cells.

This thesis has focussed on studying one of the previously uncharacterised members of the NET family, NET4B. Throughout this project various different experimental techniques have been used to ascribe a potential function for this protein. Firstly, NET4B was shown to associate with actin filaments *in vivo* and can directly bind with F-actin *in vitro* via its conserved NAB domain. The expression of NET4B in transiently transformed *N. benthamiana* leaf epidermal cells highlighted a highly cross-linked and bundled actin array. NET4B could therefore function to create higher-order actin arrays *in planta*, and this could be due to the ability of this protein to oligomerise and associate with multiple actin filaments. Indeed, Y2H studies demonstrated that NET4B could form homo-oligomers and hetero-oligomers with NET4A. As these two closely related NET4 proteins could have differing affinities for actin, the formation of different

hetero- and homo-oligomers could provide a mechanism of modulating the organisation of actin in the cell.

This study also demonstrated that NET4B is highly expressed in the root tips and immunogold labelling revealed that this protein preferentially localises to the tonoplast. The NET4 proteins therefore represent a tonoplast-associated subfamily of the NETs, that could link the actin cytoskeleton to the vacuole. Several studies have demonstrated how the actin cytoskeleton is important in maintaining complex vacuole morphologies such as transvacuolar strands. In addition, the actin cytoskeleton has been shown to affect vacuole morphology during biotic stress and programmed cell death. Therefore the NET4s could serve as important adaptors in linking the actin cytoskeleton to the vacuole, and could support complex vacuole morphology as well as being responsive to dynamic changes to the vacuole and actin cytoskeleton observed during stress responses.

Both NET4 proteins are expressed in the Arabidopsis root tips and could therefore have a function in this plant tissue. During cell division and root maturation, the vacuole undergoes major morphological changes; from vacuole biogenesis at the root tip to the formation of the large central vacuole in the differentiation zone. Currently very little is known about the role of the actin cytoskeleton in vacuole fusion or controlling vacuole morphology during root development. However the expression of both NET4 proteins at this localisation suggests that they could have a functional role in vacuole fusion or development.

The expression of both proteins in the root suggested that they could have a role in root development. Therefore phenotypic analysis of *net4* mutants primarily focussed on root length. Only initial assessment of phenotypic analysis was examined during this project and the results of this analysis suggested that under unstressed conditions the single *net4b* mutants could cause a reduction in root length, and the single *net4a* mutant could cause a reduction in root growth during early seedling development. However a root length phenotype was not observed with the double *net4b/net4a* mutant. Under stress conditions, the double *net4* mutants exhibited an increased tolerance to salt stress, and the single *net4a* mutant were more tolerant to drought stress. However, these assays were only performed with one biological replicate and would require further work to substantiate these initial findings.

As well as being expressed in the root tip, *NET4B* was also shown to be highly expressed in the guard cells through the GUS reporter system. These specialised cells undergo major changes to the actin cytoskeleton and vacuole morphology during stomatal opening and closing. Our knowledge of how these systems are linked during guard cell changes is currently very limited. The discovery that *NET4B* is expressed in these cells opens up the possibility that it could be involved in guard cell responses, linking the actin cytoskeleton to the vacuole.

Interactor studies revealed that both NET4 proteins could interact *in planta* with two RabG3 GTPases, RabG3a and RabG3f. Y2H studies demonstrated that the NET4s interact specifically with the active GTP-bound versions of these vacuolar Rabs. This suggests that the NET4s are effector proteins of these Rabs and could function in mediating membrane trafficking events at the vacuole. Several models have been proposed for how the NET4s could function as effector proteins for these Rabs and include a function as molecular motor adaptors, tethering proteins, scaffolds for further interactions, and modulators of local actin organisation. Investigating how the NET4s function as effector proteins and how the actin cytoskeleton is recruited during vacuolar trafficking events will form the basis of future work in the Hussey group.

Finally, the conserved C-terminal IRQ domain of NET4B was shown to mediate the interaction with the active RabG3a. This domain was previously characterised as being conserved between NET4B, NET4A, NET3A and NET3C. Further bioinformatics analysis revealed that the IRQ domain is found in six novel proteins in the Arabidopsis proteome, and is only found in Tracheophyte genomes. Together these proteins were termed the IRQ family that could be considered as a plant-specific family of putative Rab effectors. Currently, our knowledge of Rab effectors in plants is very limited, therefore the discovery of this family could reveal how Rab GTPases mediate membrane trafficking events in plants.

Appendix 1: Primer list

1.1 Primers for amplifying truncations of NET4B for C-terminal fusions

Primer name	Sequence 5' - 3'	Tm (°C)
NET4B ATGFw	GGGGACAAGTTTGTACAAAAAAGCAGGCTTCACCATGGCTTCGTCTACGGCTCAGAG	69
NET4B NAB Rv	GGGGACCACTTTGTACAAGAAAGCTGGGTCATGGTTCTTCTGAAGTTCACCACTAGCTTG	73
NET4B -NAB ATGFw	GGGGACAAGTTTGTACAAAAAAGCAGGCTTCACCATGACATCTGAGATCCAGTCACAGAGCTCTCTTGAG	74
NET4B -IRQ Rv	GGGGACCACTTTGTACAAGAAAGCTGGGTCTTCCGTAAGCTCACTTGACCGTCTTC	71
NET4B IRQ ATG Fw	GGGGACAAGTTTGTACAAAAAAGCAGGCTTCACCATGGAAGTGGAAAGGACGAGAGTGTCTGC	71
NET4B IRQ Rv	GGGGACCACTTTGTACAAGAAAGCTGGGTCTCTCCAAAGTCTGTCGTACCCATCTCTG	72
NET4B Rv	GGGGACCACTTTGTACAAGAAAGCTGGGTCAGTTGATAAGACCACTACTCTCTTACTCTTATGTCC	70

1.2 Primers for amplifying truncations of NET4B for N-terminal fusions

Primer name	Sequence 5' - 3'	Tm (°C)
NET4B Fw	GGGGACAAGTTTGTACAAAAAAGCAGGCTTCATGGCTTCGTCTACGGCTCAGAG	69
NET4B NAB Stop Rv	GGGGACCACTTTGTACAAGAAAGCTGGGTCTCAATGGTTCTTCTGAAGTTCACCACTAGCTTG	73
NET4B Antigen frag Fw	GGGGACAAGTTTGTACAAAAAAGCAGGCTTCACCAAAGAGAAGTTGAGTCGCCG	70
NET4B Antigen frag STOP Rv	GGGGACCACTTTGTACAAGAAAGCTGGGTCTCAAATCTCGTCTTCGTGCATTCGC	73
NET4B -NAB Fw	GGGGACAAGTTTGTACAAAAAAGCAGGCTTCACATCTGAGATCCAGTCACAGAGCTCTCTTGAG	74
NET4B -IRQ Stop Rv	GGGGACCACTTTGTACAAGAAAGCTGGGTCTCATTCCGTAAGCTCACTTGACCGTCTTC	71
NET4B IRQ Fw	GGGGACAAGTTTGTACAAAAAAGCAGGCTTCGAAGTGGAAAGGACGAGAGTGTCTGC	71
NET4B IRQ Stop Rv	GGGGACCACTTTGTACAAGAAAGCTGGGTCTCATCTCCAAAGTCTGTCGTACCCATCTCTG	72
NET4B Stop Rv	GGGGACCACTTTGTACAAGAAAGCTGGGTCTCAAGTTGATAAGACCACTACTCTCTTACTCTTATGTCC	70

1.3 Primers for amplifying further truncations of the IRQ + Ct domain of NET4B for yeast-2-hybrid studies

Primer name	Sequence 5' - 3'	Tm (°C)
IRQ Truncation 1 Fw	GGGGACAAGTTTGTACAAAAAAGCAGGCTTCGAAATGGCTGAGCAGAAAAGAGAAGC	70
IRQ Truncation 2 Fw	GGGGACAAGTTTGTACAAAAAAGCAGGCTTCAGACAGCTTTGTATGTCTCTTGACCATTACAGAG	71
IRQ Truncation 3 Fw	GGGGACAAGTTTGTACAAAAAAGCAGGCTTCAGAGATGGGTACGACAGACTTTGGAGAG	70
IRQ Truncation 4 Stop Rv	GGGGACCACTTTGTACAAGAAAGCTGGGTCTCATCTCTTACTCTTATGTCCTGCAACAACTCTCC	73

1.4 Primer combinations used for cloning the NET4B truncations

Fragment	N- or C-terminal fusion	Forward primer	Reverse primer
NET4B	C	NET4B ATG Fw	NET4B Rv
NAB	C	NET4B ATG Fw	NET4B NAB Rv
-IRQ	C	NET4B ATG Fw	NET4B -IRQ Rv
-NAB-IRQ	C	NET4B -NAB ATG Fw	NET4B -IRQ Rv
-NAB	C	NET4B -NAB ATG Fw	NET4B Rv
IRQ	C	NET4B IRQ ATG Fw	NET4B IRQ Rv
IRQ + Ct	C	NET4B IRQ ATG Fw	NET4B Rv
NET4B	N	NET4B Fw	NET4B Stop Rv
NAB	N	NET4B Fw	NET4B NAB Stop Rv
-IRQ	N	NET4B Fw	NET4B -IRQ Stop Rv
-NAB-IRQ	N	NET4B -NAB Fw	NET4B -IRQ Stop Rv
-NAB	N	NET4B -NAB Fw	NET4B Stop Rv
IRQ	N	NET4B IRQ Fw	NET4B IRQ Stop Rv
IRQ + Ct	N	NET4B IRQ Fw	NET4B Stop Rv
$NET4B^{121-220}$	N	NET4B Antigen frag Fw	NET4B Antigen frag Rv
IRQ Δ1	N	IRQ Truncation 1 Fw	NET4B Stop Rv
IRQ Δ2	N	IRQ Truncation 2 Fw	NET4B Stop Rv
IRQ Δ3	N	IRQ Truncation 3 Fw	NET4B Stop Rv
IRQ Δ4	N	IRQ Truncation 3 Fw	IRQ Truncation 4 Rv
IRQ Δ5	N	IRQ Truncation 2 Fw	IRQ Truncation 4 Rv
IRQ Δ6	N	IRQ Truncation 1 Fw	IRQ Truncation 4 Rv
IRQ Δ7	N	NET4B IRQ Fw	IRQ Truncation 4 Rv

1.5 Cloning primers for yeast-2-hybrid interactor studies

Primer name	Sequence 5' - 3'	Tm (°C)	Target gene
DEP1 Fw	GGGGACAAGTTTGTACAAAAAAGCAGGCTTCAC CATGGCGGTGGCTGCAGC	71	DEP1 (At5g53850)
DEP1 fragment Fw	GGGGACAAGTTTGTACAAAAAAGCAGGCTTCGC AATGATAAGAGCTGATAGAAAGATCACTGC	70	
DEP1 Stop Rv	GGGGACCACTTTGTACAAGAAAGCTGGGTCCTA GATTTGGGAGAATGATGTGACAGTCTTG	71	
RFC Fw	GGGGACAAGTTTGTACAAAAAAGCAGGCTTCAC CATGGCGCCAGTTCTTCAGAGC	70	RFC4 (At1g21690)
RFC Stop Rv	GGGGACCACTTTGTACAAGAAAGCTGGGTCCTA CACTATGATAGTCTCATAAGTCTTAAGGCACAGG TC	70	
RabG3a Fw	GGGGACAAGTTTGTACAAAAAAGCAGGCTTCAT GGCGACGAGAAGACGTAC	70	RabG3a (At4g09720)
RabG3a Stop Rv	GGGGACCACTTTGTACAAGAAAGCTGGGTCTCA GCAAGCGCAACCAC	65	
RabG3f Fw	GGGGACAAGTTTGTACAAAAAAGCAGGCTTCAC CATGCCGTCCCGTAGACGTACC	69	RabG3f (At3g18820)
RabG3f Stop Rv	GGGGACCACTTTGTACAAGAAAGCTGGGTCTTA GCATTCACACCCTGTAGACCTCTG	69	
RabD2a Fw	GGGGACAAGTTTGTACAAAAAAGCAGGCTTCAC CATGAATCCTGAGTACGACTATCTTTTCAAGCTC	70	RabD2a (At1g02130)
RabD2a Stop Rv	GGGGACCACTTTGTACAAGAAAGCTGGGTCTCA AGTTGAGCAGCAGCCGTTC	71	
RabA5c Fw	GGGGACAAGTTTGTACAAAAAAGCAGGCTTCAC CATGGCTAGCTCTGGAAACAAGAACATC	69	Raba5c (At2g43130)
RabA5c Stop Rv	GGGGACCACTTTGTACAAGAAAGCTGGGTCCTA AGCACAACACGATGAACTCACTGC	70	
RabF2a Fw	GGGGACAAGTTTGTACAAAAAAGCAGGCTTCAC CATGGCTGCAGCTGGAAACAAGAG	71	RabF2a (At4g19640)
RabF2a Stop Rv	GGGGACCACTTTGTACAAGAAAGCTGGGTCCTA AGCACAACAAGATGAGCTCACTGC	70	

1.6 Site-directed mutagenesis primers

Primer name	Sequence 5' - 3'	Tm (°C)
RabG3a T22N Fw	GGTGACAGTGGGGTTGGAAAAAATTCCTTGATGAATCAATATGTGC	83
RabG3a T22N Rv	GCACATATTGATTCATCAAGGAATTTTTTCCAACCCCACTGTCACC	83
RabG3a Q67L Fw	GATTTGGGATACTGCTGGACTTGAGAGATTCCAGAGTCTTGGTG	82
RabG3a Q67L Rv	CACCAAGACTCTGGAATCTCTCAAGTCCAGCAGTATCCCAAATC	82
RabG3f T22N Fw	GATAGCGGGGTGGGAAAAACCTCTTTGATGAATCAGTATG	80
RabG3f T22N Rv	CATACTGATTCATCAAAGAGGTTTTTCCCACCCCGCTATC	80
RabG3f Q67L Fw	GGGATACAGCTGGACAGGAAAGGTTTCAGAGCCTTGG	81
RabG3f Q67L Rv	CCAAGGCTCTGAAACCTTTCCTGTCCAGCTGTATCCC	81

1.7 Genotyping primers

Primer name	Sequence 5' - 3'	Tm (°C)
957 Fw	CGAATCACGATAGAGCCACATGC	70
957 Rv	GTCTGCGTCTTCTTCAATCAGTTTTAACATG	70
C08 Fw	CCAGCTTTCCCATAGGGTCC	67
C08 Rv	CACCCTCGGCAACAAGCTC	68
604 Fw	ACAAAGATGGAGATGATTCTGCTTCC	68
604 Rv	GAAGCAAGAATGGATGATGGTCTTG	69
LBa1	TGGTTCACGTAGTGGGCCATCG	73
LB3	TAGCATCTGAATTTCATAACCAATCTCGATACAC	71
Mago Fw	ATTTGGACACGAGTTCCTGGAGTTCG	72
Mago Rv	GTAGGAATCCCGCATTGTGAGCCAC	74

1.8 RT-PCR and qPCR primers

Primer name	Sequence 5' - 3'	Tm (°C)
q4B Fw	CGGTGACGAGGCATTGATCCG	62
q4B Rv	CTCGTCTTCGTGCATTCGCA	70
q4A.1 Fw	ATGGATTATGATCTGCTTCGTTCCAAGAAG	71
q4A.1 Rv	CACCCTCGGCAACAAGCTCTC	70
q4A.2 Rv	GGTGGATGCCCTGAAAAGGC	70
q4A.3 Fw	CCCGGCAAAACTTGCTGCTTGT	73
q4A.3 Rv	AGCTGCCCCTTCGCTCTGTTC	71
EF1a Fw	CCCATTTGTGCCAATCTCT	63
EF1a Rv	CACCGTTCCAATACCACCAA	66

1.9 Sequencing primers

Primer name	**Sequence 5' - 3'**	**Tm (°C)**	Target
LB1	GCCTTTTCAGAAATGGATAAATAGCCTTGCTTCC	75	SAIL T-DNA insertions
LBb1	GCGTGGACCGCTTGCTGCAACT	76	SALK T-DNA insertions
GFP Fw	CCTTCTTGAGTTTGTAACAGCTGC	65	pMDC43 vectors
GFP Rv	CGTATGTTGCATCACCTTC	59	pMDC83 vectors and genotyping NET4B107
pDONR207 Fw	TCGCGTTAACGCTAGCATGGATCT	71	pDONR207 vectors
pDONR207 Rv	GTAACATCAGAGATTTTGAGACAC	58	
T7 promoter primer	CGAAATTAATACGACTCACTATAGG	59	pGADT7 and pGBKT7 vectors

Appendix 2: Summary of GUS histochemical staining using the transgenic *NET4Bpro*::GUS lines

2.1 GUS staining in floral tissue

	Guard cells					
Line	**Sepals**	**Anther**	**Stem**	**Filament**	**Papillae**	**Sepals**
1	X			X	X	X
2	X	X	X	X	X	X
3	X	X	X		X	X
4	X	X	X			X
5	X	X	X		X	X
6	X	X		X	X	X
7	X	X	X		X	X
8	X	X	X			X
9	X				X	X
10	X	X	X	X	X	X
11	X	X	X	X	X	X

2.2 GUS staining in embryos

Line	Whole embryo	Whole embryo particularly at the root tip	Root	Root tip	Cotyledons
1		X	X		X
5	X	X		X	
7		X			
10	X		X		
11				X	X

Appendix 3: Results of the yeast-2-hybrid screens

3.1 Results of the yeast-2-hybrid screen using NET4B as bait

Gene locus	Gene annotation	Number of colonies	Screen (1 or 2)
AT5G15650	ATRGP2, REVERSIBLY GLYCOSYLATED POLYPEPTIDE 2, RGP2	3	1,2
AT3G02230	ATRGP1, REVERSIBLY GLYCOSYLATED POLYPEPTIDE 1, RGP1	3	1,2
AT3G07195	RPM1-interacting protein 4 (RIN4) family protein, Defence response	2	1,2
AT3G47620	ATTCP14, TCP14, TEOSINTE BRANCHED, CYCLOIDEA AND PCF (TCP) 14,	2	1
AT5G64350	ARABIDOPSIS THALIANA FK506-BINDING PROTEIN 12, ATFKBP12	1	2
AT2G28550	RAP2.7, RELATED TO AP2.7, TARGET OF EARLY ACTIVATION TAGGED (EAT) 1, TOE1	1	2
AT4G27520	ATENODL2, EARLY NODULIN-LIKE PROTEIN 2, ENODL2	1	2
AT5G18255	Potential natural antisense gene	1	1
AT4G36980	Unknown	1	1
AT1G30230	EF1BB, ELONGATION FACTOR 1B BETA	1	2
AT5G62690	Tubulin Beta chain 2	1	2
AT1G12050	Fumarylacetoacetase	1	2
AT2G43130	RabA5c, ARABIDOPSIS RAB GTPASE HOMOLOG A5C,	1	2
AT5G18260	RING/U-box superfamily protein	1	1
AT5G66140	PAD2, PROTEASOME ALPHA SUBUNIT D2	1	1
AT5G08130	BIM1, Basic helix-loop-helix (bHLH) family protein BIM1 (BES1-INTERACTING MYC-LIKE 1)	1	2
AT1G03360	RRP4, Ribosomal RNA processing 4	1	2
AT3G12570	FYD	1	2
AT5G52552	CPUORF14, CONSERVED PEPTIDE UPSTREAM OPEN READING FRAME 14	1	1
AT3G17390	MAT4, METHIONINE ADENOSYLTRANSFERASE 4,	1	1

AT3G27830	RPL12, RIBOSOMAL PROTEIN L12	1	1
AT1G56280	ATDI19, DI19, DROUGHT-INDUCED 19	1	2
AT3G14240	Subtilase family protein	1	2
AT1G54850	HSP20-like chaperones superfamily protei	1	2
AT4G24690	NBR1, ARABIDOPSIS THALIANA NEXT TO BRCA1 GENE 1	1	1
AT2G36530	ENO2, ENOLASE 2, LOS2,	1	1
AT1G33140	PGY2, PIGGYBACK2	1	2
AT2G36410	Unknown	1	2
AT5G57160	ATLIG4, LIG4 | DNA ligase IV	1	1
AT1G70300	KUP6, K+ UPTAKE PERMEASE 6	1	2
AT2G36990	ATSIG6, RNAPOLYMERASE SIGMA-SUBUNIT F	1	1
AT1G72370	RP40, 40S RIBOSOMAL PROTEIN SA	1	1
AT5G03920	unknown	1	1

3.2 Results of the yeast-2-hybrid screen using the IRQ + Ct domain as bait

Gene locus	**Gene annotation**	**Number of colonies**	**Screen (1 or 2)**
AT1G21690	RFC4, REPLICATION FORK COMPLEX 4	5	1,2
AT5G53850	DEP1, DEHYDRATASE-ENOLASE-PHOSPHATASE-COMPLEX 1	4	1,2
AT1G05010	ACO4, EAT1, EFE, ETHYLENE FORMING ENZYME, ETHYLENE-FORMING ENZYME	2	1
AT1G30230	EF1BB, ELONGATION FACTOR 1B BETA	1	1
AT5G66140	PAD2, PROTEASOME ALPHA SUBUNIT D2	1	1
AT1G80010	FRS8, FAR1-related sequence 8	1	2

Appendix 4: Expression pattern of *RFC4* and *DEP1* as represented on the Arabidopsis eFP browser

Expression patterns of RFC4 and DEP1 were visualised using the Arabidopsis eFP browser (Winter et al. 2007).

4.1 *RFC4* - At1g21690

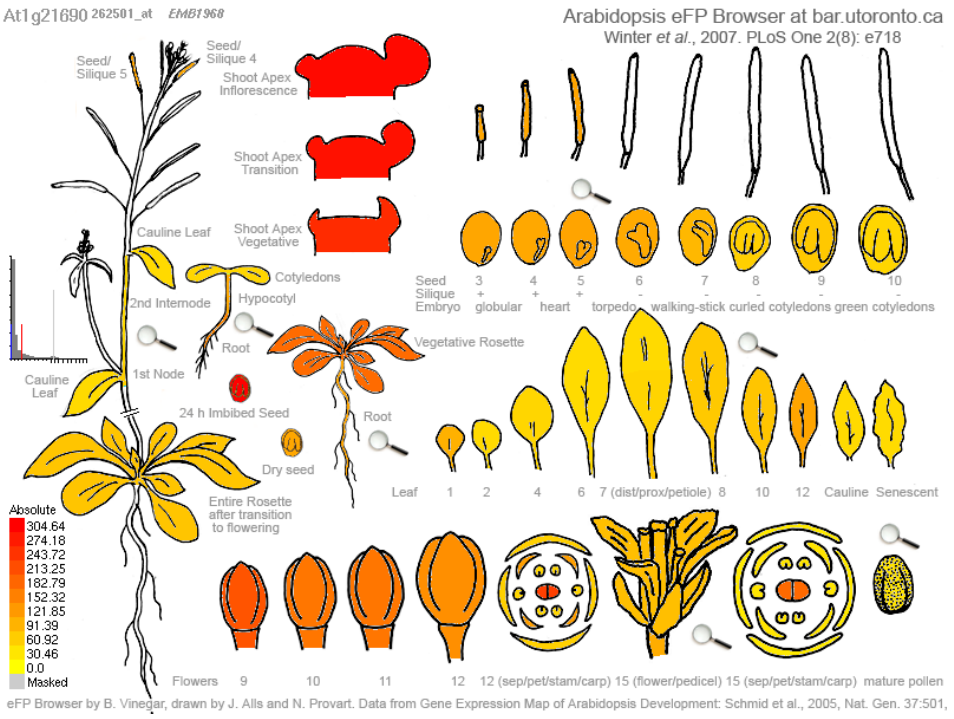

4.2 *DEP1*- At5g58350

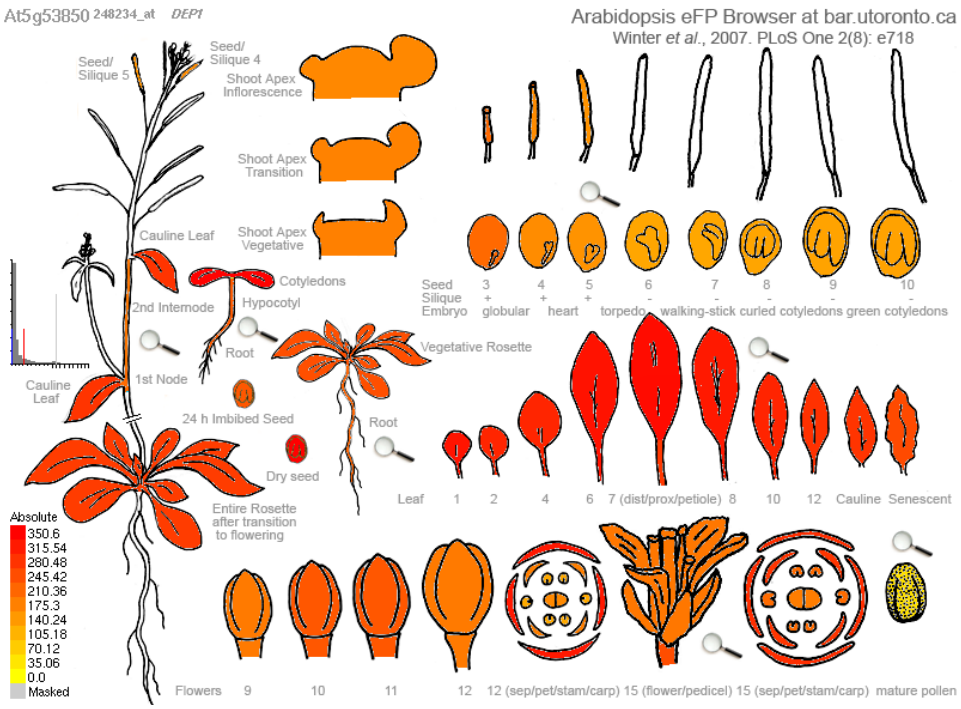

Appendix 5: Table showing the domain architecture of the IRQ proteins

Table shows the amino acid residues used to create the domain architecture of the IRQ proteins (Chapter 8, Figure 8.4). Coiled-coils and internal repeats were identified using the Paircoil2 and SMART database (McDonnell et al. 2006; Letunic et al. 2014). *Denotes a truncated IRQ domain.

Protein	Size	NAB	IRQ	Highly conserved section	Coiled-coil	Internal repeats
NET3A	269	1-94	171-218	184-202	(159-220)	-
NET3C	225	1-94	151-198	164-182	(140-193)	-
NET4A	558	1-105	504-511	517-535	(198-227, 244-278, 290-400, 402-527)	-
NET4B	517	1-105	464-511	477-495	(160-234, 248-264, 266-482)	-
At3g10880	319	-	288-319*	301-319	(147-257, 261-306)	-
At5g05180	432	-	379-426	392-410	(95-136, 155-196, 225-286, 291-372)	-
At1g64320	476	-	428-475	441-459	(4-231, 352-451)	(1-32, 175-206)
At5g41780	537	-	490-537	503-521	(87-143, 162-199, 207-304, 433-512)	-
At1g64330	555	1-89 (qNAB)	500-547	513-531	(104-408, 433-523)	-
At5g41790	1586	1-89 (qNAB)	1530-1577	1543-1561	(122-419, 426-591, 601-750, 757-926, 932-1361, 1368-1401, 1501-1538)	(412-436, 588-612), (1444-1458, 24-38), (59-88, 1453-1482), (194-204, 421-431)

References

Abdallah, A.M., Savage, N.D.L., van Zon, M., Wilson, L., Vandenbroucke-Grauls, C.M.J.E., van der Wel, N.N., Ottenhof, T.H.M., Bitter, W. (2008). The ESX-5 secretion system of *Mycobacterium marinum* modulates the macrophage response. *Journal of immunology,* **181**: 7166–7175.

Aivazian, D., Serrano, R. L., Pfeffer, S. (2006). TIP47 is a key effector for Rab9 localization. *Journal of Cell Biology,* **173***:* 917–926.

Allaire, P. D., Marat, A. L., Dall'Armi, C., Di Paolo, G., McPherson, P. S., Ritter, B. (2010). The connecdenn DENN Domain: a GEF for Rab35 mediating cargo-specific exit from early endosomes. *Molecular Cell,* **37**:, 370–382.

Alonso, J.M., Stepanova, A.N., Leisse, T.J., Kim, C.J., Chen, H., Shinn, P., Stevenson, D.K., Zimmerman, J., Barajas, P., Cheuk, R., Gadrinab, C., Heller, C., Jeske, A., Koesema, E., Meyers, C.C., Parker, H., Prednis, L., Ansari, Y., Choy, N., Deen, H., Geralt, M., Hazari, N., Hom, E., Karnes, M., Mulholland, C., Ndubaku, R., Schmidt, I., Guzman, P., Aguilar-Henonin, L., Schmid, M., Weigel, D., Carter, D.E., Marchand, T., Risseeuw, E., Brogden, D., Zeko, A., Crosby, W.L., Berry, C.C., Ecker, J.R. (2003). Genome-wide insertional mutagenesis of *Arabidopsis thaliana*. *Science,* **301**: 653–657.

Andrés, Z., Pérez-Hormaeche, J., Leidi, E.O., Schlücking, K., Steinhorst, L., McLachlan, D.H., Schumacher, K., Hetherington, A.M., Kudla, J., Cubero, B., Pardo, J.M. (2014). Control of vacuolar dynamics and regulation of stomatal aperture by tonoplast potassium uptake. *Proceedings of the National Academy of Sciences of the United States of America,* **111**: 1806–1814.

Antignani, V., Klocko, A. L., Bak, G., Chandrasekaran, S. D., Dunivin, T., Nielsen, E. (2015). Recruitment of PLANT U-BOX13 and the PI4Kb1/b2 phosphatidylinositol-4 kinases by the small GTPase RabA4B plays important roles during salicylic acid-mediated plant defense signaling in Arabidopsis. *The Plant Cell*, **27**:, 243–261.

Aoki, K., & Matsuda, M. (2009). Visualization of small GTPase activity with fluorescence resonance energy transfer-based biosensors. *Nature Protocols,* **4***:* 1623–1631.

Araiza-Olivera, D., Uribe-Carvajal, S., Chiquete-Félix, N., Rosas-Lemus, M., Ruíz-Granados, G., Sampedro, J.G., Mújica, A., Peña, A. (2012). Metabolic optimization by enzyme-enzyme and enzyme-cytoskeleton associations. In *Cell Metabolism - Cell Homeostasis and Stress Response. Edited by Bubulya P. InTech, Rijeka.* 101–114.

Arnold, H., & Pette, D. (1970). Binding of aldolase and triosephosphate dehydrogenase to F-actin and modification of catalytic properties of aldolase. *European Journal of Biochemistry,* **15**: 360–366.

Artimo, P., Jonnalagedda, M., Arnold, K., Baratin, D., Csardi, G., De Castro, E., Duvaud, S., Flegel, V., Fortier, A., Gasteiger, E., Grosdidier, A., Hernandez, C., Ioannidis, V., Kuznetsov, D., Liechti, R., Moretti, S., Mostaguir, K., Redaschi, N., Rossier, G., Xenarios, I., Stockinger, H. (2012). ExPASy: SIB bioinformatics resource portal. *Nucleic Acids Research*, **40**: W597–W603.

Asaoka, R., Uemura, T., Ito, J., Fujimoto, M., Ito, E., Ueda, T., Nakano, A. (2013). Arabidopsis RABA1 GTPases are involved in transport between the trans-Golgi network and the plasma membrane, and are required for salinity stress tolerance. *The Plant Journal*, **73**: 240–249.

Avisar, D., Abu-Abied, M., Belausov, E., Sadot, E., Hawes, C., Sparkes, I.A. (2009). A comparative study of the involvement of 17 Arabidopsis myosin family members on the motility of Golgi and other organelles. *Plant Physiology*, **150**: 700–709.

Bak, G., Lee, E., Lee, Y., Kato, M., Segami, S., Sze, H., Maeshima, M., Hwang, J., Lee, Y. (2013). Rapid structural changes and acidification of guard cell vacuoles during stomatal closure require phosphatidylinositol 3,5-bisphosphate. *The Plant Cell*, **25**: 2202–2016.

Banks, J. A. (2009). Selaginella and 400 million years of separation. *Annual Review of Plant Biology*, **60**: 223–238.

Bañuelos, S., Saraste, M., Carugo, D.K. (1998). Structural comparisons of calponin homology domains: implications for actin binding. *Structure*, **6**: 1419–1431.

Baral, A., Irani, N.G., Fujimoto, M., Nakano, A., Mayor, S., Mathew, M. K. (2015). Salt-induced remodeling of spatially restricted clathrin-independent endocytic pathways in Arabidopsis root. *The Plant Cell*, **27**: 1297-1315.

Barbero, P., Bittova, L., Pfeffer, S.R. (2002). Visualization of Rab9-mediated vesicle transport from endosomes to the trans-Golgi in living cells. *Journal of Cell Biology*, **156**: 511–518.

Barr, F.A. (2013). Rab GTPases and membrane identity: Causal or inconsequential? *The Journal of Cell Biology*, **202**: 191-199.

Barrero, R.A, Umeda, M., Yamamura, S., Uchimiya, H. (2002). Arabidopsis CAP regulates the actin cytoskeleton necessary for plant cell elongation and division. *The Plant Cell*, **14**: 149–163.

Bassham, D.C., Laporte, M., Marty, F., Moriyasu, Y., Ohsumi, Y., Olsen, L.J., Yoshimoto, K. (2015). Autophagy in development and stress responses of plants. *Autophagy*, **2**: 2–11.

Batoko, H., Zheng, H.Q., Hawes, C., Moore, I. (2000). A Rab1 GTPase is required for transport between the endoplasmic reticulum and golgi apparatus and for normal golgi movement in plants. *The Plant Cell*, **12**: 2201–2218.

Behnia, R., & Munro, S. (2005). Organelle identity and the signposts for membrane traffic. *Nature*, **438**: 597–604.

Bennett, V., & Lambert, S. (1991). The spectrin skeleton: From red cells to brain. *Journal of Clinical Investigation*, **87**: 1483–1489.

Berg, J.S., Powell, B.C., Cheney, R.E. (2001). A millennial myosin census. *Molecular Biology of the Cell*, **12**: 780–794.

Berger, B., Wilson, D.B., Wolf, E., Tonchev, T., Milla, M., Kim, P. S. (1995). Predicting coiled coils by use of pairwise residue correlations. *Proceedings of the National Academy of Sciences of the United States of America*, **92**: 8259–8263.

Berryman, M., Franck, Z., Bretscher, A. (1993). Ezrin is concentrated in the apical microvilli of a wide variety of epithelial cells whereas moesin is found primarily in endothelial cells. *Journal of Cell Science*, **105**: 1025–1043.

Bhatt, A.M., Page, T., Lawson, E.J., Lister, C., Dean, C. (1996). T-DNA as an insertional mutagen in Arabidopsis. *The Plant Cell*, **11**: 2283–2290.

Bingham, J., & Sudarsanam, S. (2000). Visualizing large hierarchical clusters in hyperbolic space. *Bioinformatics*, **16**: 660–661.

Blilou, I., Xu, J., Wildwater, M., Willemsen, V., Paponov, I., Friml, J., Heidstra, R., Aida, M., Palme, K., Scheres, B. (2005). The PIN auxin efflux facilitator network controls growth and patterning in Arabidopsis roots. *Nature*, **433**: 39–44.

Blum, T., Briesemeister, S., Kohlbacher, O. (2009). MultiLoc2: integrating phylogeny and Gene Ontology terms improves subcellular protein localization prediction. *BMC Bioinformatics*, **10**: 274.

Blümer, J., Rey, J., Dehmelt, L., Maze, T., Wu, Y., Bastiaens, P., Goody, R.S., Itzen, A. (2013). RabGEFs are a major determinant for specific Rab membrane targeting. *Journal of Cell Biology*, **200**: 287–300.

Boens, N., Qin, W., Basarić, N., Orte, A., Talavera, E.M., Alvarez-Pez, J.M. (2006). Photophysics of the fluorescent pH indicator BCECF. *Journal of Physical Chemistry A*, **110**: 9334–9343.

Boevink, P., Oparka, K., Cruz, S.S., Martin, B., Betteridge, A., Hawes, C. (1998). Stacks on tracks: The plant Golgi apparatus traffics on an actin/ER network. *The Plant Journal*, **15**: 441–447.

Bois, P.R.J., O'Hara, B.P., Nietlispach, D., Kirkpatrick, J., Izard, T. (2006). The vinculin binding sites of talin and alpha-actinin are sufficient to activate vinculin. *Journal of Biological Chemistry*, **281**: 7228–7236.

Bos, M.P., Robert, V., Tommassen, J. (2007). Functioning of outer membrane protein assembly factor Omp85 requires a single POTRA domain. *EMBO Reports*, **8**: 1149–1154.

Bottanelli, F., Foresti, O., Hanton, S., Denecke, J. (2011). Vacuolar transport in tobacco leaf epidermis cells involves a single route for soluble cargo and multiple routes for membrane cargo. *The Plant Cell*, **23**: 3007–3025.

Bottanelli, F., Gershlick, D.C., Denecke, J. (2012). Evidence for sequential action of Rab5 and Rab7 GTPases in prevacuolar organelle partitioning. *Traffic*, **13**: 338–354.

Brady, S. M., Orlando, D. A., Lee, J.Y., Wang, J.Y., Koch, J., Dinneny, J.R., Mace, D., Ohler, U., Benfey, P.N. (2007). A high-resolution root spatiotemporal map reveals dominant expression patterns. *Cell*, **318**: 801–806.

Bretscher, A., Edwards, K., Fehon, R.G. (2002). ERM proteins and merlin: integrators at the cell cortex. *Nature Reviews. Molecular Cell Biology*, **3**: 586–599.

Briesemeister, S., Rahnenführer, J., Kohlbacher, O. (2010). YLoc-an interpretable web server for predicting subcellular localization. *Nucleic Acids Research*, **38**: W497–W502.

Brückner, A., Polge, C., Lentze, N., Auerbach, D., Schlattner, U. (2009). Yeast two-hybrid, a powerful tool for systems biology. *International Journal of Molecular Sciences*, **10**: 2763-2788.

Bröcker, C., Engelbrecht-Vandré, S., Ungermann, C. (2010). Multisubunit tethering complexes and their role in membrane fusion. *Current Biology*, **20**: R943-R952

Bröcker, C., **Kuhlee, A.**, **Gatsogiannis, C.**, **Balderhaar, H.J.**, **Hönscher, C.**, **Engelbrecht-Vandré, S.**, **Ungermann, C.**, **Raunser, S.** (2012). Molecular architecture of the multisubunit homotypic fusion and vacuole protein sorting (HOPS) tethering complex. *Proceedings of the National Academy of Sciences of the United States of America*, **109**: 1991–1996.

Burkhard, P., Stetefeld, J., Strelkov, S.V. (2001). Coiled coils: A highly versatile protein folding motif. *Trends in Cell Biology*, **11:** 82–88

Calcutt, J.R. (2009). ABP195, a novel plant actin-binding protein. *PhD Thesis, University of Durham, Durham, UK.*

Camacho, L., Smertenko, A.P., Pérez-Gómez, J., Hussey, P. J., Moore, I. (2009). Arabidopsis Rab-E GTPases exhibit a novel interaction with a plasma-membrane phosphatidylinositol-4-phosphate 5-kinase. *Journal of Cell Science*, **122**: 4383–4392.

Carroll, K.S., Hanna, J., Simon, I., Krise, J., Barbero, P., Pfeffer, S.R. (2001). Role of Rab9 GTPase in facilitating receptor recruitment by TIP47. *Science*, **292**: 1373–1376.

Carter, C., Pan, S., Zouhar, J., Avila, E.L., Girke, T., Raikhel, N.V. (2004). The vegetative vacuole proteome of *Arabidopsis thaliana* reveals predicted and unexpected proteins. *The Plant Cell*, **16**: 3285–3303.

Cartwright, E.F. (2011). Investigating functional motifs within the N-terminal domain of novel actin binding proteins NET1A and NET2A. *MSc thesis, University of Durham, Durham, UK.*

Chatr-Aryamontri, A., Breitkreutz, B.J., Heinicke, S., Boucher, L., Winter, A., Stark, C., Nixon, J., Ramage, L., Kolas, N., O'Donnell, L., Reguly, T., Breitkreutz, A., Sellam, A., Chen, D., Chang, C., Rust, J., Livstone, M., Oughtred, R., Dolinski, K., Tyers, M. (2013). The BioGRID interaction database: 2013 Update. *Nucleic Acids Research*, **41**: D470–D478.

Chavas, L. M. G., Ihara, K., Kawasaki, M., Torii, S., Uejima, T., Kato, R., Izumi, T., Wakatsuki, S. (2008). Elucidation of Rab27 recruitment by its effectors: structure of Rab27a bound to Exophilin4/Slp2-a. *Structure*, **16**: 1468–1477.

Chen, Y.A, & Scheller, R.H. (2001). SNARE-mediated membrane fusion. *Nature Reviews. Molecular Cell Biology*, **2**: 98–106.

Cheung, A.Y., & Wu, H. (2004). Overexpression of an Arabidopsis formin stimulates supernumerary actin cable formation from pollen tube cell membrane. *The Plant Cell*, **16**: 257–269.

Chevalier, L., Bernard, S., Ramdani, Y., Lamour, R., Bardor, M., Lerouge, P., Follet-Gueye, M.L., Driouich, A. (2010). Subcompartment localization of the side chain xyloglucan-synthesizing enzymes within Golgi stacks of tobacco suspension-cultured cells. *The Plant Journal*, **64**: 977–989.

Choi, S., Tamaki, T., Ebine, K., Uemura, T., Ueda, T., Nakano, A. (2013). RABA members act in distinct steps of subcellular trafficking of the FLAGELLIN SENSING2 receptor. *The Plant Cell*, **25**: 1174–1187.

Chou, K.C., & Shen, H.B. (2010). Plant-mPLoc: A top-down strategy to augment the power for predicting plant protein subcellular localization. *PLoS ONE*, **5**: e11335.

Chow, C.M., Neto, H., Foucart, C., Moore, I. (2008). Rab-A2 and Rab-A3 GTPases define a trans-Golgi endosomal membrane domain in Arabidopsis that contributes substantially to the cell plate. *The Plant Cell*, **20**: 101–123.

Christoforidis, S., McBride, H.M., Burgoyne, R.D., Zerial, M. (1999). The Rab5 effector EEA1 is a core component of endosome docking. *Nature*, **397**: 621–625.

Claeys, H., van Landeghem, S., Dubois, M., Maleux, K., Inzé, D. (2014). What is stress? Dose-response effects in commonly used *in vitro* stress assays. *Plant Physiology*, **165**: 519–527.

Clough, S.J., & Bent, A.F. (1998). Floral dip: A simplified method for Agrobacterium-mediated transformation of *Arabidopsis thaliana*. *The Plant Journal*, **16**: 735–743.

Cole, C., Barber, J.D., Barton, G.J. (2008). The Jpred 3 secondary structure prediction server. *Nucleic Acids Research*, **36**: W197–W201.

Collin, M. (1984). Interaction between glycolytic enzymes and cytomatrix. *The Journal of Cell Biology*, **99**: 222–225.

Contento, A.L., & Bassham, D.C. (2012). Structure and function of endosomes in plant cells. *Journal of Cell Science*, **125**: 3511–3518.

van Criekinge, W., & Beyaert, R. (1999). Yeast two-hybrid: State of the art. *Biological Procedures Online*, **2**: 1–38.

Cuff, J. A., Clamp, M.E., Siddiqui, A.S., Finlay, M., Barton, G.J. (1998). JPred: A consensus secondary structure prediction server. *Bioinformatics*, **14**: 892–893.

Cui, Y., Zhao, Q., Gao, C., Ding, Y., Zeng, Y., Ueda, T., Nakano, A., Jiang, L. (2014). Activation of the Rab7 GTPase by the MON1-CCZ1 complex is essential for PVC-to-vacuole trafficking and plant growth in Arabidopsis. *The Plant Cell*, **26**: 2080-2097

Curtis, M.D., & Grossniklaus, U. (2003). A Gateway cloning vector set for high-throughput functional analysis of genes *in planta*. *Breakthrough Technologies*, **133**: 462–469.

Cvrčková, F. (2013). Formins and membranes: anchoring cortical actin to the cell wall and beyond. *Frontiers in Plant Science*, **4**: 436.

Czechowski, T., Stitt, M., Altmann, T., Udvardi, M.K. (2005). Genome-wide identification and testing of superior reference genes for transcript normalization. *Plant Physiology*, **139**: 5–17.

De Matteis, M.A, & Morrow, J.S. (2000). Spectrin tethers and mesh in the biosynthetic pathway. *Journal of Cell Science*, **113**: 2331–2343.

Deeks, M.J., Calcutt, J.R., Ingle, E.S., Hawkins, T.J., Chapman, S., Richardson, A.C., Mentlak, D.A., Dixon, M.R., Cartwright, F., Smertenko, A.P., Oparka, K. & Hussey, P.J. (2012). A superfamily of actin-binding proteins at the actin-membrane nexus of higher plants. *Current Biology*, **22**: 1595–600.

Deeks, M. J., Cvrcková, F., Machesky, L. M., Mikitová, V., Ketelaar, T., Zársky, V., Davies, B., Hussey, P.J. (2005). Arabidopsis group Ie formins localize to specific cell membrane domains, interact with actin-binding proteins and cause defects in cell expansion upon aberrant expression. *New Phytologist*, **168**: 529–540.

Deeks, M. J., Fendrych, M., Smertenko, A., Bell, K.S., Oparka, K., Cvrcková, F., Zársky, V., Hussey, P.J. (2010). The plant formin AtFH4 interacts with both actin and microtubules, and contains a newly identified microtubule-binding domain. *Journal of Cell Science*, **123**: 1209–1215.

Deeks, M.J., Hussey, P.J., Davies, B. (2002). Formins: Intermediates in signal-transduction cascades that affect cytoskeletal reorganization. *Trends in Plant Science*, **7**: 492–498.

Deeks, M.J., Rodrigues, C., Dimmock, S., Ketelaar, T., Maciver, S.K., Malhó,R., Hussey, P. J. (2007). Arabidopsis CAP1 - a key regulator of actin organisation and development. *Journal of Cell Science*, **120**: 2609–2618.

Delgado, I.J., Wang, Z., de Rocher, A, Keegstra, K., Raikhel, N.V. (1998). Cloning and characterization of AtRGP1. A reversibly autoglycosylated Arabidopsis protein implicated in cell wall biosynthesis. *Plant Physiology*, **116**: 1339–1350.

Deng, X.W., Caspar,T., Quail, P.H. (1991). cop1: a regulatory locus involved in light-controlled development and gene expression in Arabidopsis. *Genes & Development*, **5**: 1172–1182.

Dettmer, J., Hong-Hermesdorf, A., Stierhof, Y.D., Schumacher, K. (2006). Vacuolar H+-ATPase activity is required for endocytic and secretory trafficking in Arabidopsis. *The Plant Cell*, **18**: 715–730.

Devoto, A., Nieto-Rostro, M., Xie, D., Ellis, C., Harmston, R., Patrick, E., Davis, J.,Sherratt, L., Coleman, M., Turner, J. G. (2002). COI1 links jasmonate signalling and fertility to the SCF ubiquitin-ligase complex in Arabidopsis. *The Plant Journal*, **32**: 457–466.

Di Sansebastiano, G.P., Paris, N., Marc-Martin, S., Neuhaus, J.M. (2001). Regeneration of a lytic central vacuole and of neutral peripheral vacuoles can be visualized by green fluorescent proteins targeted to either type of vacuoles. *Plant Physiology*, **126**: 78–86.

Ding, Z., Wang, B., Moreno, I., Dupláková, N., Simon, S., Carraro, N., Reemmer, J., Pěnčík, A., Chen, X., Tejos, R., Skůpa, P., Pollmann, S., Mravec, J., Petrášek, J., Zažímalová, E., Honys, D., Rolčík, J., Murphy, A., Orellana, A., Geisler, M., Friml, J. (2012). ER-localized auxin transporter PIN8 regulates auxin homeostasis and male gametophyte development in Arabidopsis. *Nature Communications*, **3**: 941.

Dirac-Svejstrup, A.B., Sumizawa, T., Pfeffer, S.R. (1997). Identification of a GDI displacement factor that releases endosomal Rab GTPases from Rab-GDI. *The EMBO Journal*, **16**: 465–472.

Dixon, M.R. (2013). NET2A: bridging the gap in plant-specific actin-membrane intercations. *PhD thesis, University of Durham, Durham, UK*.

Djinovic-Carugo, K., Gautel, M., Ylänne, J., Young, P. (2002). The spectrin repeat: A structural platform for cytoskeletal protein assemblies. *FEBS Letters*, **513**: 119–123.

Dodds, P.N., & Rathjen, J.P. (2010). Plant immunity: towards an integrated view of plant-pathogen interactions. *Nature Reviews. Genetics*, **11**: 539–48.

Dortay, H., Gruhn, N., Pfeifer, A., Schwerdtner, M., Schmu, T., Heyl, A. (2008). Toward an interaction map of the two-component signaling pathway of *Arabidopsis thaliana* research articles. *Journal of Proteome Research*, **7**: 3649–3660.

Drakakaki, G., Zabotina, O., Delgado, I., Robert, S., Keegstra, K., Raikhel, N.V. (2006). Arabidopsis reversibly glycosylated polypeptides 1 and 2 are essential for pollen development. *Plant Physiology*, **142**: 1480–92.

Drøbak, B. K., Franklin-Tong, V.E., Staiger, C.J. (2004). The role of the actin cytoskeleton in plant cell signaling. *New Phytologist*, **163**: 13–30.

Drozdetskiy, A., Cole, C., Procter, J., Barton, G.J. (2015). JPred4: a protein secondary structure prediction server. *Nucleic Acids Research*, **43**: W389–W394.

Dumas, J.J., Zhu, Z., Connolly, J.L., Lambright, D.G. (1999). Structural basis of activation and GTP hydrolysis in Rab proteins. *Structure*, **7**: 413–423.

Dupree, P., & Sherrier, D.J. (1998). The plant Golgi apparatus. *Biochimica et Biophysica Acta - Molecular Cell Research*, **1404**: 259–270.

Eathiraj, S., Mishra, A., Prekeris, R., Lambright, D.G. (2006). Structural basis for Rab11-mediated recruitment of FIP3 to recycling endosomes. *Journal of Molecular Biology*, **364**: 121–135.

Eathiraj, S., Pan, X., Ritacco, C., Lambright, D.G. (2005). Structural basis of family-wide Rab GTPase recognition by rabenosyn-5. *Nature*, **436**: 415–419.

Ebine, K., Inoue, T., Ito, J., Ito, E., Uemura, T., Goh, T., Abe, H., Sato, K., Nakano, A., Ueda, T. (2014). Plant vacuolar trafficking occurs through distinctly regulated pathways. *Current Biology*, **24**: 1375–1382.

Ebine, K., Okatani, Y., Uemura, T., Goh, T., Shoda, K., Niihama, M., Morita, M.T., Spitzer, C., Otergui, M.S., Nakano, A., Ueda, T. (2008). A SNARE complex unique to seed plants is required for protein storage vacuole biogenesis and seed development of *Arabidopsis thaliana*. *The Plant Cell*, **20**: 3006–3021.

Echard, A., Jollivet, F., Martinez, O., Lacapère, J.J., Rousselet, A., Janoueix-Lerosey, I., Goud, B. (1998). Interaction of a Golgi-associated kinesin-like protein with Rab6. *Science* **279**: 580–585.

Edwards, K., Johnstone, C., Thompson, C. (1991). A simple and rapid method for the preparation of plant genomic DNA for PCR analysis. *Nucleic Acids Research*, **19**: 1349.

Ellinger, D., Glöckner, A., Koch, J., Naumann, M., Stürtz, V., Schütt, K., Manisseri, C., Somerville, S.C., Voigt, C.A. (2014). Interaction of the Arabidopsis GTPase RabA4c with its effector PMR4 results in complete penetration resistance to powdery mildew. *The Plant Cell*, **26**: 3185–3200.

Elmore, J.M., Liu, J., Smith, B., Phinney, B., Coaker, G. (2012). Quantitative proteomics reveals dynamic changes in the plasma membrane during Arabidopsis immune signaling. *Molecular & Cellular Proteomics*, **11**: 014555.

Escobar, N.M., Haupt, S., Thow, G., Boevnik, P., Chapman, S., Oparka, K. (2003). High-throughput viral expression of cDNA-green fluorescent protein fusions reveals novel subcellular addresses and identifies unique proteins that interact with plasmodesmata. *The Plant Cell*, **15**: 1507–1523.

Esseling-Ozdoba, A., Houtman, D., van Lammeren, A.A.M., Eiser, E., Emons, A.M.C. (2008). Hydrodynamic flow in the cytoplasm of plant cells. *Journal of Microscopy*, **231**: 274–283.

Favery, B., Chelysheva, L. a, Lebris, M., Jammes, F., Marmagne, A., De Almeida-Engler, J., Lecomte, P., Vaury, C., Arkowitz, R.A., Abad, P. (2004). Arabidopsis formin AtFH6 is a plasma membrane-associated protein upregulated in giant cells induced by parasitic nematodes. *The Plant Cell*, **16**: 2529–2540.

Feeney, M., Frigerio, L., Kohalmi, S.E., Cui, Y., Menassa, R. (2013). Reprogramming cells to study vacuolar development. *Frontiers in Plant Science*, **4**: 493.

Feig, L.A., & Cooper, G.M. (1988). Inhibition of NIH 3T3 cell proliferation by a mutant ras protein with preferential affinity for GDP. *Molecular and Cellular Biology*, **8**: 3235–3243.

Feraru, E., Paciorek, T., Feraru, M.I., Zwiewka, M., De Groodt, R., De Rycke, R., Kleine-Vehn, J., Friml, J. (2010). The AP-3 β adaptin mediates the biogenesis and function of lytic vacuoles in Arabidopsis. *The Plant Cell*, **22**: 2812–2824.

van der Flier, A., & Sonnenberg, A. (2001). Structural and functional aspects of filamins. *Biochimica et Biophysica Acta*, **1538**: 99–117.

Fields, S., & Song, O. (1989). A novel genetic system to detect protein-protein interactions. *Nature*, **340**: 245–246.

Finn, R.D., Bateman, A., Clements, J., Coggill, P., Eberhardt, R.Y., Eddy, S.R., Heger, A., Hetherington, K., Holm, L., Mistry, J., Sonnhammer, E.L.L., Tate, J., Punta, M. (2014). Pfam: The protein families database. *Nucleic Acids Research*, **42**: D222–D230.

Fontijn, R.D., Goud, B., Echard, A., Jollivet, F., van Marle, J., Pannekoek, H., Horrevoets, A.J.G. (2001). The human kinesin-like protein RB6K is under tight cell cycle control and is essential for cytokinesis. *Molecular and Cellular Biology*, **21**: 2944–2955.

Frigerio, L., Hinz, G., Robinson, D.G. (2008). Multiple vacuoles in plant cells: Rule or exception? *Traffic*, **9**: 1564–1570.

Fu, Y., Li, H., Yang, Z. (2002). The ROP2 GTPase controls the formation of cortical fine F-actin and the early phase of directional cell expansion during Arabidopsis organogenesis. *The Plant Cell*, **14**: 777–794.

Fukuda, A., Nakamura, A., Tagiri, A., Tanaka, H., Miyao, A., Hirochika, H., Tanaka, Y. (2004). Function, intracellular localization and the importance in salt tolerance of a vacuolar Na+/H+ antiporter from rice. *Plant and Cell Physiology*, **45**: 146–159.

Fukuda, M., & Kuroda, T.S. (2002). Slac2-c (synaptotagmin-like protein homologue lacking C2 domains-c), a novel linker protein that interacts with Rab27, myosin Va/VIIa, and actin. *Journal of Biological Chemistry*, **277**: 43096–43103.

Fukuda, M., Kuroda, T.S., Mikoshiba, K. (2002). Slac2-a/melanophilin, the missing link between Rab27 and myosin Va: Implications of a tripartite protein complex for melanosome transport. *Journal of Biological Chemistry*, **277**: 12432–12436.

Futai, M., Oka, T., Sun-Wada, G.H., Moriyama, Y., Kanazawa, H., Wada, Y. (2000). Luminal acidification of diverse organelles by V-ATPase in animal cells. *The Journal of Experimental Biology*, **203**: 107–116.

Gabe Lee, M.T., Mishra, A., Lambright, D.G. (2009). Structural mechanisms for regulation of membrane traffic by Rab GTPases. *Traffic*, **10**: 1377–1389.

Gao, C., Zhuang, X., Cui, Y., Fu, X., He, Y., Zhao, Q., Zeng, Y., Shen, J., Luo, M., Jiang, L. (2015). Dual roles of an Arabidopsis ESCRT component FREE1 in regulating vacuolar protein transport and autophagic degradation. *Proceedings of the National Academy of Sciences*, **112**: 1886–1891.

Gao, X.Q., Chen, J., Wei, P.C., Ren, F., Chen, J., Wang, X.C. (2008). Array and distribution of actin filaments in guard cells contribute to the determination of stomatal aperture. *Plant Cell Reports*, **27**: 1655–1665.

Gao, X.Q., Li, C.G., Wei, P.C., Zhang, X.Y., Chen, J., Wang, X.C. (2005). The dynamic changes of tonoplasts in guard cells are important for stomatal movement in Vicia faba. *Plant Physiology*, **139**: 1207–1216.

Gao, X.Q., Wang, X.L., Ren, F., Chen, J., Wang, X.C. (2009). Dynamics of vacuoles and actin filaments in guard cells and their roles in stomatal movement. *Plant, Cell & Environment*, **32**: 1108–16.

Gardiner, J., Overall, R., Marc, J. (2011). Putative Arabidopsis homologues of metazoan coiled-coil cytoskeletal proteins. *Cell Biology International*, **35**: 767–774.

Gaullier, J.M., Ronning, E., Gillooly, D.J., Stenmark, H. (2000). Interaction of the EEA1 FYVE finger with phosphatidylinositol 3-phosphate and early endosomes. Role of conserved Residues. *Journal of Biological Chemistry*, **275**: 24595–24600.

Gaxiola, R.A, Li, J., Undurraga, S., Dang, L.M., Allen, G.J., Alper, S.L., Fink, G.R. (2001). Drought- and salt-tolerant plants result from overexpression of the AVP1 H+-pump. *Proceedings of the National Academy of Sciences of the United States of America*, **98**: 11444–11449.

Geldner, N., Denervaud-Tendon, V., Hyman, D.L., Mayer, U., Stierhof, Y.D., Chory, J. (2009). Rapid, combinatorial analysis of membrane compartments in intact plants with a multicolor marker set. *The Plant Journal*, **59**: 169-178.

Gerondopoulos, A., Langemeyer, L., Liang, J.R., Linford, A., Barr, F.A. (2012). BLOC-3 mutated in Hermansky-Pudlak syndrome is a Rab32/38 guanine nucleotide exchange factor. *Current Biology*, **22**: 2135–2139.

van Gestel, K., Köhler, R.H., Verbelen, J.P. (2002). Plant mitochondria move on F-actin, but their positioning in the cortical cytoplasm depends on both F-actin and microtubules. *Journal of Experimental Botany*, **53**: 659–667.

Gillingham, A.K., & Munro, S. (2003). Long coiled-coil proteins and membrane traffic. *Biochimica et Biophysica Acta - Molecular Cell Research*, **1641**: 71–85.

Gillooly, D.J., Morrow, I.C., Lindsay, M., Gould, R., Bryant, N.J., Gaullier, J. M., Parton, R.G., Stenmark, H. (2000). Localization of phosphatidylinositol 3-phosphate in yeast and mammalian cells. *The EMBO Journal*, **19**: 4577–4588.

Gimona, M., Djinovic-Carugo, K., Kranewitter, W.J., Winder, S.J. (2002). Functional plasticity of CH domains. *FEBS Letters*, **513**: 98–106.

van Gisbergen, P.A.C., Li, M., Wu, S.Z., Bezanilla, M. (2012). Class II formin targeting to the cell cortex by binding PI(3,5)P 2 is essential for polarized growth. *Journal of Cell Biology*, **198**: 235–250.

Goda, H., Sasaki, E., Akiyama, K., Maruyama-Nakashita, A., Nakabayashi, K., Li, W., Ogawa, M., Yamauchi, Y., Preston, J., Aoki, K., Kiba, T., Takatsuto, S., Fujioka, S., Asami, T., Nakano, T., Kato, H., Mizuno, T., Sakakibara, H., Yamaguchi, S., Nambara, E., Kamiya, Y., Takahashi, H., Hirai, Masami Y., Sakurai, T., Shinozaki, K., Saito, K., Yoshida, S., Shimada, Y. (2008). The AtGenExpress hormone and chemical treatment data set: Experimental design, data evaluation, model data analysis and data access. *The Plant Journal*, **55**: 526–542.

Graumann, K., Runions, J., Evans, D.E. (2010). Characterization of SUN-domain proteins at the higher plant nuclear envelope. *The Plant Journal*, **61**: 134–144.

Grosshans, B.L., Ortiz, D., Novick, P. (2006). Rabs and their effectors: achieving specificity in membrane traffic. *Proceedings of the National Academy of Sciences of the United States of America*, **103**: 11821–11827.

Gucciardo, S., Wisniewski, J.P., Brewin, N.J., Bornemann, S. (2007). A germin-like protein with superoxide dismutase activity in pea nodules with high protein sequence identity to a putative rhicadhesin receptor. *Journal of Experimental Botany*, **58**: 1161–1171.

Gürkan, C., Stagg, S.M., Lapointe, P., Balch, W.E. (2006). The COPII cage: unifying principles of vesicle coat assembly. *Nature Reviews. Molecular Cell Biology*, **7**: 727–738.

Gutierrez, M.G., Munafó, D.B., Berón, W., & Colombo, M.I. (2004). Rab7 is required for the normal progression of the autophagic pathway in mammalian cells. *Journal of Cell Science*, **117**: 2687–2697.

Guyomarc'h, S., Leran, S., Auzon-Cape, M., Perrine-Walker, F., Lucas, M., Laplaze, L. (2012). Early development and gravitropic response of lateral roots in *Arabidopsis thaliana*. *Philosophical Transactions of the Royal Society B: Biological Sciences*, **367**:1509–1516.

Haas, A., Scheglmann, D., Lazar, T., Gallwitz, D., Wickner, W. (1995). The GTPase Ypt7p of *Saccharomyces cerevisiae* is required on both partner vacuoles for the homotypic fusion step of vacuole inheritance. *The EMBO Journal*, **14**: 5258–5270.

Haas, A.K., Fuchs, E., Kopajtich, R., Barr, F.A. (2005). A GTPase-activating protein controls Rab5 function in endocytic trafficking. *Nature Cell Biology*, **7**: 887–893.

Hamada, T., Nagasaki-Takeuchi, N., Kato, T., Fujiwara, M., Sonobe, S., Fukao, Y., Hashimoto, T. (2013). Purification and characterization of novel microtubule-associated proteins from Arabidopsis cell suspension cultures. *Plant Physiology*, **163**: 1804–16.

Hammer, J.A., & Sellers, J. R. (2012). Walking to work: roles for class V myosins as cargo transporters. *Nature Reviews. Molecular Cell Biology*, **13**: 13–26.

Hammer, J.A., & Wu, X.S. (2002). Rabs grab motors: Defining the connections between Rab GTPases and motor proteins. *Current Opinion in Cell Biology*, **14**: 69-75.

Hardham, A.R., Jones, D.A., Takemoto, D. (2007). Cytoskeleton and cell wall function in penetration resistance. *Current Opinion in Plant Biology*, **10**: 342–348.

Hashimoto, K., Igarashi, H., Mano, S., Nishimura, M., Shimmen, T., Yokota, E. (2005). Peroxisomal localization of a myosin XI isoform in *Arabidopsis thaliana*. *Plant and Cell Physiology*, **46**: 782–789.

Hawes, C., Saint-Jore, C.M., Brandizzi, F., Zheng, H., Andreeva, A.V., Boevink, P. (2001). Cytoplasmic illuminations: *In planta* targeting of fluorescent proteins to cellular organelles. *Protoplasma*, **215**: 77–88.

Hawkins, J., & Bodén, M. (2006). Detecting and sorting targeting peptides with neural networks and support vector machines. *Journal of Bioinformatics and Computational Biology*, **4**: 1–18.

Hawkins, J., Davis, L., Bode, M. (2007). Predicting Nuclear Localization. *Journal of Proteome Research*, **6**: 1402–1409.

Hawkins, T.J., Deeks, M.J., Wang, P., Hussey, P.J. (2014). The evolution of the actin binding NET superfamily. *Frontiers in Plant Science*, **5**: 254.

Hayes, G.L., Brown, F.C., Haas, A.K., Nottingham, R.M., Barr, F.A., Pfeffer, S.R. (2009). Multiple Rab GTPase binding sites in GCC185 suggest a model for vesicle tethering at the trans-Golgi. *Molecular Biology of the Cell*, **20**: 209–217.

Heath, J.D., Weldon, R., Monnot, C., Meinke, D.W. (1986). Analysis of storage proteins in normal and aborted seeds from embryo-lethal mutants of *Arabidopsis thaliana*. *Planta*, **169**: 304–312.

Henty-Ridilla, J.L., Li, J.J., Day, B., Staiger, C.J. (2014). ACTIN DEPOLYMERIZING FACTOR4 regulates actin dynamics during innate immune signaling in Arabidopsis. *The Plant Cell*, **26**: 340–352.

Henty-Ridilla, J.L., Shimono, M., Li, J., Chang, J.H., Day, B., Staiger, C.J. (2013). The plant actin cytoskeleton responds to signals from microbe-associated molecular patterns. *PLoS Pathogens*, **9**: e1003290

Higaki, T., Goh, T., Hayashi, T., Kutsuna, N., Kadota, Y., Hasezawa, S., Sano, T., Kuchitsu, K. (2007). Elicitor-induced cytoskeletal rearrangement relates to

vacuolar dynamics and execution of cell death: In vivo imaging of hypersensitive cell death in tobacco BY-2 cells. *Plant and Cell Physiology*, **48**: 1414–1425.

Higaki, T., Kadota, Y., Goh, T., Hayashi, T., Kutsuna, N., Sano, T., Hasezawa, S., Kuchitsu, K. (2008). Vacuolar and cytoskeletal dynamics during elicitor-induced programmed cell death in tobacco BY-2 cells. *Plant Signaling & Behavior*, **3**: 700–703.

Higaki, T., Kutsuna, N., Okubo, E., Sano, T., Hasezawa, S. (2006). Actin microfilaments regulate vacuolar structures and dynamics: Dual observation of actin microfilaments and vacuolar membrane in living tobacco BY-2 cells. *Plant and Cell Physiology*, **47**: 839–852.

Higaki, T., Kutsuna, N., Sano, T., Kondo, N., Hasezawa, S. (2010). Quantification and cluster analysis of actin cytoskeletal structures in plant cells : role of actin bundling in stomatal movement during diurnal cycles in Arabidopsis guard cells. *The Plant Journal*, **61**: 156–165.

Higashi, Y., Hirai, M.Y., Fujiwara, T., Naito, S., Noji, M., Saito, K. (2006). Proteomic and transcriptomic analysis of Arabidopsis seeds: Molecular evidence for successive processing of seed proteins and its implication in the stress response to sulfur nutrition. *The Plant Journal*, **48**: 557–571.

Higuchi, M., Pischke, M.S., Mähönen, A.P., Miyawaki, K., Hashimoto, Y., Seki, M., Kobayashi, M., Shinozaki, K., Kato, T., Tabata, S., Helariutta, Y., Sussman, M.R., Kakimoto, T. (2004). *In planta* functions of the Arabidopsis cytokinin receptor family. *Proceedings of the National Academy of Sciences of the United States of America*, **101**: 8821–8826.

Hill, K.L., Catlett, N.L., Weismann, L.S. (1996). Actin and myosin function in directed vacuole movement during cell division in Saccharomyces cerevisiae. *The Journal of Cell Biology*, **135**: 1535–1549.

Holliday, L.S., Lu, M., Lee, B.S., Nelson, R.D., Solivan, S., Zhang, L., Gluck, S.L. (2000). The amino-terminal domain of the B subunit of vacuolar H+-ATPase contains a filamentous actin binding site. *Journal of Biological Chemistry*, **275**: 32331–32337.

van der Honing, H. S., Kieft, H., Emons, A.M.C., Ketelaar, T. (2012). Arabidopsis VILLIN2 and VILLIN3 are required for the generation of thick actin filament bundles and for directional organ growth. *Plant Physiology*, **158**: 1426–1438.

Horiuchi, H., Lippé, R., McBride, H.M., Rubino, M., Woodman, P., Stenmark, H., Rybin, V., Wilm, M., Ashman, K., Mann, M., Zerial, M. (1997). A novel Rab5 GDP/GTP exchange factor complexed to Rabaptin-5 links nucleotide exchange to effector recruitment and function. *Cell*, **90**: 1149–1159.

Horton, P., Park, K J., Obayashi, T., Fujita, N., Harada, H., Adams-Collier, C.J., Nakai, K. (2007). WoLF PSORT: Protein localization predictor. *Nucleic Acids Research*, **35**: W585–W587.

Hoth, S., Morgante, M., Sanchez, J.P., Hanafey, M.K., Tingey, S.V, Chua, N.H. (2002). Genome-wide gene expression profiling in *Arabidopsis thaliana* reveals new targets of abscisic acid and largely impaired gene regulation in the abi1-1 mutant. *Journal of Cell Science*, **115**: 4891–4900.

Hruz, T., Laule, O., Szabo, G., Wessendorp, F., Bleuler, S., Oertle, L., Widmayer, P., Gruissem, W., Zimmermann, P. (2008). Genevestigator v3: a reference expression database for the meta-analysis of transcriptomes. *Advances in Bioinformatics*, **37**: D987-D991.

Hua, S., & Sun, Z. (2001). Support vector machine approach for protein subcellular localization prediction. *Bioinformatics*, **17**: 721–728.

Huala, E., Dickerman, A.W., Garcia-Hernandez, M., Weems, D., Reiser, L., LaFond, F., Hanley, D., Kiphart, D., Zhuang, M., Huang, W., Mueller, L.A., Bhattacharyya, D., Bhaya, D., Sobral, B.W., Beavis, W., Meinke, D.W., Town, C.D., Somerville, C., Rhee, S.Y. (2001). The Arabidopsis Information Resource (TAIR): a comprehensive database and web-based information retrieval, analysis, and visualization system for a model plant. *Nucleic Acids Research*, **29**: 102–105.

Huang, S., Blanchoin, L., Kovar, D.R., Staiger, C.J. (2003). Arabidopsis Capping Protein (AtCP) is a heterodimer that regulates assembly at the barbed ends of actin filaments. *Journal of Biological Chemistry*, **278**: 44832–44842.

Huang, S., Gao, L., Blanchoin, L., Staiger, C.J. (2006). Heterodimeric capping protein from Arabidopsis is regulated by phosphatidic acid. *Molecular Biology of the Cell*, **17**: 1946–1952.

Hussey, P.J., Allwood, E.G., Smertenko, A.P. (2002). Actin-binding proteins in the Arabidopsis genome database: properties of functionally distinct plant actin-depolymerizing factors/cofilins. *Philosophical Transactions of the Royal Society B: Biological Sciences*, **357**: 791–798.

Hussey, P.J., Ketelaar, T., Deeks, M.J. (2006). Control of the actin cytoskeleton in plant cell growth. *Annual Review of Plant Biology*, **57**: 109–125.

Hutagalung, A.H., & Novick, P.J. (2011). Role of Rab GTPases in membrane traffic and cell physiology. *Physiological Reviews*, **91**: 119-149.

Hutt, D. M., Da-Silva, L. F., Chang, L.H., Prosser, D.C., Ngsee, J.K. (2000). PRA1 inhibits the extraction of membrane-bound Rab GTPase by GDI1. *Journal of Biological Chemistry*, **275**: 18511–18519.

Hwang, J.U., & Lee, Y. (2001). Abscisic acid-induced actin reorganization in guard cells of dayflower is mediated by cytosolic calcium levels and by protein kinase and protein phosphatase activities. *Plant Physiology*, **125**: 2120–2128.

Ingle, E.K.S. (2011). An analysis of the NET1 proteins, a group of novel plant actin-binding proteins. *PhD thesis, University of Durham, Durham, UK.*

Itzen, A., & Goody, R.S. (2008). Key determinants of Rab specificity. *Structure*, **16**: 1437–1439.

Jäger, S., Bucci, C., Tanida, I., Ueno, T., Kominami, E., Saftig, P., Eskelinen, E.L. (2004). Role for Rab7 in maturation of late autophagic vacuoles. *Journal of Cell Science*, **117**: 4837–4848.

Jagoe, W.N., Lindsay, A.J., Read, R.J., McCoy, A.J., McCaffrey, M.W., Khan, A.R. (2006). Crystal structure of Rab11 in complex with Rab11 family interacting protein 2. *Structure*, **14**: 1273–1283.

Jaquinod, M., Villiers, F., Kieffer-Jaquinod, S., Hugouvieux, V., Bruley, C., Garin, J., Bourguignon, J. (2007). A proteomics dissection of *Arabidopsis thaliana* vacuoles isolated from cell culture. *Plant Signaling & Behavior*, **6**: 394–412.

Jefferson, R.A., Kavanagh, T.A., Bevan, M.W. (1987). GUS fusions: beta-glucuronidase as a sensitive and versatile gene fusion marker in higher plants. *The EMBO Journal*, **6**: 3901–3907.

Jia, H., Li, J., Zhu, J., Fan, T., Qian, D., Zhou, Y., Wang, J., Ren, H., Xiang, Y., An, L. (2013). Arabidopsis CROLIN1, a novel plant actin binding protein, functions in cross-linking and stabilizing actin filaments. *Journal of Biological Chemistry*, **288**: 32277-32288.

Jiang, K., Sorefan, K., Deeks, M.J., Bevan, M.W., Hussey, P.J., Hetherington, A.M. (2012). The ARP2/3 complex mediates guard cell actin reorganization and stomatal movement in Arabidopsis. *The Plant Cell*, **24**: 2031–2040.

Jimenez-Lopez, J.C., Wang, X., Kotchoni, S.O., Huang, S., Szymanski, D.B., Staiger, C.J. (2014). Heterodimeric capping protein from Arabidopsis is a membrane-associated, actin-binding protein. *Plant Physiology*, **166**: 1312–1328.

Jones, A.M. (2001). Programmed cell death in development and disease. *Plant Physiology*, **153**: 94–97.

Jürgens, G. (2004). Membrane trafficking in plants. *Annual Review of Cell and Developmental Biology*, **20**: 481–504.

Kadota, A., Yamada, N., Suetsugu, N., Hirose, M., Saito, C., Shoda, K., Ichikawa, S., Kagawa, T., Nakano, A., Wada, M. (2009). Short actin-based mechanism for light-directed chloroplast movement in Arabidopsis. *Proceedings of the National Academy of Sciences of the United States of America*, **106**: 13106–13111.

Kapila, J., De Rycke, R., van Montagu, M., Angenon, G. (1997). An Agrobacterium-mediated transient gene expression system for intact leaves. *Plant Science*, **122**: 101–108.

Katagiri, F., Thilmony, R., He, S.Y. (2002). The *Arabidopsis thaliana-Pseudomonas syringae* interaction. *The Arabidopsis Book, American Society of Plant Biologists, Rockville, MD, USA. Edited by Somerville C.R., Meyerowitz, E.M*

Keep, N. H. (2000). Structural comparison of actin binding in utrophin and dystrophin. *Neurological Sciences*, **21**: S929–S937.

Ketelaar, T., Allwood, E.G., Anthony, R., Voigt, B., Menzel, D., Hussey, P.J. (2004). The Actin-Interacting Protein AIP1 is essential for actin organization and plant development. *Current Biology*, **14**: 145–149.

Khan, A. R., & Ménétrey, J. (2013). Structural biology of arf and rab GTPases' effector recruitment and specificity. *Structure*, **21**: 1284–1297.

Kilian, J., Whitehead, D., Horak, J., Wanke, D., Weinl, S., Batistic, O., D'Angelo, C., Bornberg-Bauer, E., Kudla, J., Harter, K. (2007). The AtGenExpress global stress expression data set: Protocols, evaluation and model data analysis of UV-B light, drought and cold stress responses. *The Plant Journal*, **50**: 347–363.

Kim, D.Y., Scalf, M., Smith, L.M., Vierstra, R.D. (2013). Advanced proteomic analyses yield a deep catalog of ubiquitylation targets in Arabidopsis. *The Plant Cell*, **25**: 1523–1540.

Kim, H., Park, M., Kim, S.J., Hwang, I. (2005). Actin filaments play a critical role in vacuolar trafficking at the Golgi complex in plant cells. *The Plant Cell*, **17**: 888–902.

Kim, J., Dalton, V.M., Eggerton, K.P., Scott, S.V, Klionsky, D.J. (1999). Apg7p/Cvt2p is required for the cytoplasm-to-vacuole targeting, macroautophagy, and peroxisome degradation pathways. *Molecular Biology of the Cell*, **10**: 1337–1351.

Kinsella, B. T., & Maltese, W.A. (1992). Rab GTP-binding proteins with three different carboxyl-terminal cysteine motifs are modified *in vivo* by 20-carbon isoprenoids. *Journal of Biological Chemistry*, **267**: 3940–3945.

Kleffmann, T., Russenberger, D., von Zychlinski, A., Christopher, W., Sjölander, K., Gruissem, W., Baginsky, S. (2004). The *Arabidopsis thaliana* chloroplast proteome reveals pathway abundance and novel protein functions. *Current Biology*, **14**: 354–362.

Kolb, C., Nagel, M.K., Kalinowska, K., Hagmann, J., Ichikawa, M., Anzenberger, F., Alkofer, A., Sato, M.H., Braun, P., Isono, E. (2015). FYVE1 is essential for vacuole biogenesis and intracellular trafficking in *Arabidopsis thaliana*. *Plant Physiology*, **167**: 1361–1373.

Kong, R.P.W., Siu, S.O., Lee, S.S.M., Lo,C., Chu, I. K. (2011). Development of online high-/low-pH reversed-phase-reversed-phase two-dimensional liquid chromatography for shotgun proteomics: A reversed-phase-strong cation exchange-reversed-phase approach. *Journal of Chromatography A*, **1218**: 3681–3688.

Kouranti, I., Sachse, M., Arouche, N., Goud, B., Echard, A. (2006). Rab35 regulates an endocytic recycling pathway essential for the terminal steps of cytokinesis. *Current Biology*, **16**: 1719–1725.

Kovar, D.R., Staiger, C.J., Weaver, E.A., McCurdy, D.W. (2000). AtFim1 is an actin filament crosslinking protein from *Arabidopsis thaliana*. *The Plant Journal*, **24**: 625–636.

Krebbers, E., Herdies, L., De Clercq, A., Seurinck, J., Leemans, J., van Damme, J., Segura, M., Cheysen, G., van Montagu, M., Vandekerckhove, J. (1988). Determination of the processing sites of an Arabidopsis 2S albumin and characterization of the complete gene family. *Plant Physiology*, **87**: 859–866.

Kukimoto-Niino, M., Sakamoto, A., Kanno, E., Hanawa-Suetsugu, K., Terada, T., Shirouzu, M., Fukuda, M., Yokoyama, S. (2008). Structural basis for the exclusive specificity of Slac2-a/Melanophilin for the Rab27 GTPases. *Structure*, **16**: 1478–1490.

Kümmel, D., & Ungermann, C. (2014). Principles of membrane tethering and fusion in endosome and lysosome biogenesis. *Current Opinion in Cell Biology*, **29**: 61–66.

Kuroda, T.S., Ariga, H., Fukuda, M. (2003). The actin-binding domain of Slac2-a / Melanophilin is required for melanosome distribution in melanocytes. *Molecular Cellular Biology*, **23**: 5245-5255.

Kwon, S.I., Cho, H.J., Bae, K., Jung, J.H., Jin, H.C., Park, O.K. (2009). Role of an Arabidopsis rab GTPase RabG3b in pathogen response and leaf senescence. *Journal of Plant Biology*, **52**: 79–87.

Kwon, S.I, Cho, H.J., Jung, J.H., Yoshimoto, K., Shirasu, K., Park, O.K. (2010). The Rab GTPase RabG3b functions in autophagy and contributes to tracheary element differentiation in Arabidopsis. *Plant Journal*, **64**: 151–164.

Kyte, J., & Doolittle, R.F. (1982). A simple method for displaying the hydropathic character of a protein. *Journal of Molecular Biology*, **157**: 105–132.

Lall, P., Lindsay, A.J., Hanscom, S., Kecman, T., Taglauer, E.S., McVeigh, U.M., Franklin, E., McCaffrey, M.W., Khan, A.R. (2015). Structure-function analyses of the interactions between Rab11 and Rab14 small GTPases with their shared effector Rab Coupling Protein (RCP). *Journal of Biological Chemistry*, **290**: 18817–18832.

Lam, S.K., Siu, C.L., Hillmer, S., Jang, S., An, G., Robinson, D.G., Jiang, L. (2007). Rice SCAMP1 defines clathrin-coated, trans-Golgi-located tubular-vesicular structures as an early endosome in tobacco BY-2 cells. *The Plant Cell*, **19**: 296–319.

Langemeyer, L., Bastos, R.N., Cai, Y., Itzen, A., Reinisch, K.M., & Barr, F.A. (2014). Diversity and plasticity in Rab GTPase nucleotide release mechanism has consequences for Rab activation and inactivation. *eLife*, **3**: e02171.

Larkin, M.A., Blackshields, G., Brown, N.P., Chenna, R., Mcgettigan, P.A., McWilliam, H., Valentin, F., Wallace, I.M., Wilm, A., Lopez, R., Thompson, J.D., Gibson, T.J., Higgins, D.G. (2007). Clustal W and Clustal X version 2.0. *Bioinformatics*, **23**: 2947–2948.

Lau, O.S., & Deng, X.W. (2012). The photomorphogenic repressors COP1 and DET1: 20 years later. *Trends in Plant Science*, **17**: 584–593.

Laufman, O., Kedan, A., Hong, W., Lev, S. (2009). Direct interaction between the COG complex and the SM protein, Sly1, is required for Golgi SNARE pairing. *The EMBO Journal*, **28**: 2006–2017.

Lawe, D. C., Chawla, A., Merithew, E., Dumas, J., Carrington, W., Fogarty, K., Lifshitz, L., Tuft, R., Lambright, D., Corvera, S. (2002). Sequential roles for phosphatidylinositol 3-phosphate and Rab5 in tethering and fusion of early endosomes via their interaction with EEA1. *Journal of Biological Chemistry*, **277**: 8611–8617.

Lawe, D.C., Patki, V., Heller-Harrison, R., Lambright, D., Corvera, S. (2000). The FYVE domain of early endosome antigen 1 is required for both phosphatidylinositol 3-phosphate and Rab5 binding. Critical role of this dual interaction for endosomal localization. *Journal of Biological Chemistry*, **275**: 3699–3705.

Le, J., Vandenbussche, F., van Der Straeten, D., Verbelen, J.P. (2004). Position and cell type-dependent microtubule reorientation characterizes the early response of the Arabidopsis root epidermis to ethylene. *Physiologia Plantarum*, **121**: 513–519.

Lee, G.J., Sohn, E.J., Lee, M.H., Hwang, I. (2004). The Arabidopsis rab5 homologs rha1 and ara7 localize to the prevacuolar compartment. *Plant and cell physiology*, **45**: 1211–1220.

Leonhardt, N., Kwak, J.M., Robert, N., Waner, D., Leonhardt, G., Schroeder, J.I. (2004). Microarray expression analyses of Arabidopsis guard cells and isolation of a recessive abscisic acid hypersensitive protein phosphatase 2C mutant. *The Plant Cell*, **16**: 596–615.

Letunic, I., Doerks, T., Bork, P. (2014). SMART : recent updates , new developments and status in 2015. *Nucleic Acids Research*, **43**: D257–D260.

Lewis, J.D., Guttman, D.S., Desveaux, D. (2009). The targeting of plant cellular systems by injected type III effector proteins. *Seminars in Cell & Developmental Biology*, **20**: 1055–1063.

Li, J., Henty-Ridilla, J.L., Staiger, B.H., Day, B., Staiger, C.J. (2015). Capping protein integrates multiple MAMP signalling pathways to modulate actin dynamics during plant innate immunity. *Nature Communications*, **6**: 7206.

Li, J., Pleskot, R., Henty-Ridilla, J.L., Blanchoin, L., Potocký, M., Staiger, C.J. (2012). Arabidopsis capping protein senses cellular phosphatidic acid levels and transduces these into changes in actin cytoskeleton dynamics. *Plant Signaling & Behavior*, **7**: 1727–1730.

Li, L., Shimada, T., Takahashi, H., Ueda, H., Fukao, Y., Kondo, M., Nishimura, M., Hara-Nishimura, I. (2006). MAIGO2 is involved in exit of seed storage proteins from the endoplasmic reticulum in *Arabidopsis thaliana*. *The Plant Cell*, **18**: 3535–3547.

Li, L.J., Ren, F., Gao, X.Q., Wei, P.C., Wang, X.C. (2013). The reorganization of actin filaments is required for vacuolar fusion of guard cells during stomatal opening in Arabidopsis. *Plant, Cell & Environment*, **36**: 484–497.

Lippé, R., Miaczynska, M., Rybin, V., Runge, A., Zerial, M. (2001). Functional synergy between Rab5 effector Rabaptin-5 and exchange factor Rabex-5 when physically associated in a complex. *Molecular Biology of the Cell*, **12**: 2219–2228.

Liu, J., Elmore, J.M., Fuglsang, A.T., Palmgren, M.G., Staskawicz, B.J., Coaker, G. (2009). RIN4 functions with plasma membrane H+-ATPases to regulate stomatal apertures during pathogen attack. *PLoS Biology*, **7**: e1000139.

Liu, W., Xie, Y., Ma, J., Luo, X., Nie, P., Zuo, Z., Lahrman, U., Zhao, Q., Zheng, Y., Zhao, Y., Xue., Y., Ren, J. (2015). IBS : an illustrator for the presentation and visualization of biological sequences. *Bioinformatics*, **31**: 3359–3361.

Luan, S. (2002). Signalling drought in guard cells. *Plant, Cell and Environment*, **25**: 229–237.

Luby-Phelps, K. (2000). Cytoarchitecture and physical properties of cytoplasm: volume, viscosity, diffusion, intracellular surface area. *International Journal of Molecular Sciences*, **192**: 189–221.

Lupas, A., van Dyke, M., Stock, J. (1991). Predicting coiled coils from protein sequences. *Science*, **252**: 1162–1164.

Ma, B., Qian, D., Nan, Q., Tan, C., An, L., Xiang, Y. (2012). Arabidopsis vacuolar H+-ATPase (V-ATPase) B subunits are involved in actin cytoskeleton remodeling via binding to, bundling, and stabilizing F-actin. *Journal of Biological Chemistry*, **287**: 19008–19017.

Marhavý, P., Bielach, A., Abas, L., Abuzeineh, A., Duclercq, J., Tanaka, H., Pařezová, M., Petrášek, J., Friml, J., Kleine-Vehn, J., Benková, E. (2011). Cytokinin modulates endocytic trafficking of PIN1 auxin efflux carrier to control plant organogenesis. *Developmental Cell*, **21**: 796–804.

Marks, M.D., Wenger, J.P., Gilding, E., Jilk, R., Dixon, R.A. (2009). Transcriptome analysis of Arabidopsis wild-type and gl3-sst sim trichomes identifies four additional genes required for trichome development. *Molecular Plant*, **2**: 803–822.

Martinéz-García, J.F., Monte, E., Quail, P.H. (1999). A simple, rapid and quantitative method for preparing arabidopsis protein extracts for immunoloblot analysis. *The Plant Journal*, **20**: 251-257.

Martinière, A., Gayral, P., Hawes, C., Runions, J. (2011). Building bridges: Formin1 of Arabidopsis forms a connection between the cell wall and the actin cytoskeleton. *The Plant Journal*, **66**: 354–365.

Marty, F. (1999). Plant Vacuoles. *The Plant Cell*, **11**: 587–599.

Marzesco, A.M., Dunia, I., Pandjaitan, R., Recouvreur, M., Dauzonne, D., Benedetti, E. L., Louvard, D., Zahraoui, A. (2002). The small GTPase Rab13

regulates assembly of functional tight junctions in epithelial cells. *Molecular Biology of the Cell*, **13**: 189–1831.

Mason, J. M., & Arndt, K. M. (2004). Coiled coil domains: Stability, specificity, and biological implications. *ChemBioChem*, **5**: 170–176.

Mathur, J. (2006). Local interactions shape plant cells. *Current Opinion in Cell Biology*, **18**: 40–46.

Mathur, J., Mathur, N., Hülskamp, M. (2002). Simultaneous visualization of peroxisomes and cytoskeletal elements reveals actin and not microtubule-based peroxisome motility in plants. *Plant Physiology*, **128**: 1031–1045.

Mathur, J., Mathur, N., Kernebeck, B., Hülskamp, M. (2003). Mutations in actin-related proteins 2 and 3 affect cell shape development in Arabidopsis. *The Plant Cell*, **15**: 1632–1645.

Matsuda, S., Vert, J.P., Saigo, H., Ueda, N., Toh, H., Akutsu, T. (2005). A novel representation of protein sequences for prediction of subcellular location using support vector machines. *Protein Science*, **14**: 2804–2813.

Matsudaira, P. (1991). Modular organization of actin crosslinking proteins. *Trends in Biochemical Sciences*, **16**: 87–92.

Matsui, M., Stoop, C.D., von Arnim, A.G., Wei, N., Deng, X.W. (1995). Arabidopsis COP1 protein specifically interacts *in vitro* with a cytoskeleton-associated protein, CIP1. *Proceedings of the National Academy of Sciences of the United States of America*, **92**: 4239–4243.

Mayhew, T. M. (2011). Quantifying immunogold localization on electron microscopic thin sections: A compendium of new approaches for plant cell biologists. *Journal of Experimental Botany*, **62**: 4101–4113.

Mayhew, T.M., & Lucocq, J.M. (2008). Quantifying immunogold labelling patterns of cellular compartments when they comprise mixtures of membranes (surface-occupying) and organelles (volume-occupying). *Histochemistry and Cell Biology*, **129**: 367–378.

Mayhew, T.M., Lucocq, J.M., Griffiths, G. (2002). Relative labelling index: A novel stereological approach to test for non-random immunogold labelling of organelles and membranes on transmission electron microscopy thin sections. *Journal of Microscopy*, **205**: 153–164.

Mazel, A., Leshem, Y., Tiwari, B. S., Levine, A. (2004). Induction of salt and osmotic stress tolerance by overexpression of an intracellular vesicle trafficking protein AtRab7 (AtRabG3e). *Plant Physiology*, **134**: 118–128.

McClatchey, A.I., & Fehon, R.G. (2010). Merlin and the ERM proteins - regulators of receptor distribution and signalling at the cell cortex. *Cell*, **19**: 198–206.

McDonnell, A.V., Jiang, T., Keating, A.E., Berger, B. (2006). Paircoil2: improved prediction of coiled coils from sequence. *Bioinformatics* **22**: 356–358.

Meagher, R. B., & Fechheimer, M. (2003). The Arabidopsis cytoskeletal genome. *The Arabidopsis Book, American Society of Plant Biologists, Rockville MD. Edited by Somerville C.R. & Meyerowitz E.M.*.

Méresse, S., Gorvel, J. P., Chavrier, P. (1995). The Rab7 GTPase resides on a vesicular compartment connected to lysosomes. *Journal of Cell Science*, **108**: 3349–3358.

Michelot, A., Guerin, C., Huang, S., Ingouff, M., Richard, S., Rodiuc, N., Staiger, C.J., Blanchoin, L. (2005). The Formin homology 1 domain modulates the actin nucleation and bundling activity of Arabidopsis FORMIN1. *The Plant Cell*, **17**: 2296–2313.

Miller, L. (2010). ImageJ gel analysis. Available at http://www.lukemiller.org/ImageJ_gel_analysis.pdf. (Accessed July 2015).

Miller, V.J., Sharma, P., Kudlyk, T.A., Frost, L., Rofe, A.P., Watson, I.J., Duden, R., Lowe, M., Lupashin, V.V., Ungar, D. (2013). Molecular insights into vesicle tethering at the Golgi by the conserved oligomeric Golgi (COG) complex and the Golgin TATA element modulatory factor (TMF). *Journal of Biological Chemistry*, **288**: 4229–4240.

Mishina, T.E., & Zeier, J. (2007). Bacterial non-host resistance: interactions of Arabidopsis with non-adapted *Pseudomonas syringae* strains. *Physiologia Plantarum*, **131**: 448–461.

Mishra, A., Eathiraj, S., Corvera, S., Lambright, D.G. (2010). Structural basis for Rab GTPase recognition and endosome tethering by the C2H2 zinc finger of Early Endosomal Autoantigen 1 (EEA1). *Proceedings of the National Academy of Sciences of the United States of America*, **107**: 10866–10871.

Mitchison, T.J., & Cramer, L.P. (1996). Actin-based cell motility and cell locomotion. *Cell*, **84**: 371–379.

Moleirinho, S., Tilston-Lunel, A., Angus, L., Gunn-Moore, F., Reynolds, P.A. (2013). The expanding family of FERM proteins. *The Biochemical Journal*, **452**: 183–193.

Morejohn, L.C., & Fosket, D.E. (1984). Inhibition of plant microtubule polymerization *in vitro* by the phosphoric amide herbicide amiprophos-methyl. *Science*, **224**: 874–876.

Morimoto, S., Nishimura, N., Terai, T., Manabe, S., Yamamoto, Y., Shinahara, W., Miyake, H., Tashiro, S., Shimada, M., Sasaki, T. (2005). Rab13 mediates the continuous endocytic recycling of occludin to the cell surface. *Journal of Biological Chemistry*, **280**: 2220–2228.

Moubayidin, L., Di Mambro, R., Sabatini, S. (2009). Cytokinin-auxin crosstalk. *Trends in Plant Science*, **14**: 557–562.

Mravec, J., Petrášek, J., Li, N., Boeren, S., Karlova, R., Kitakura, S., Pařezová, M., Naramoto, S., Nodzyński, T., Dhonukshe, P., Bednarek, S.Y., Zažímalová, E.,

de Vries, S., Friml, J. (2011). Cell plate restricted association of DRP1A and PIN proteins is required for cell polarity establishment in Arabidopsis. *Current Biology*, **21**: 1055-1060.

Munns, R., & Tester, M. (2008). Mechanisms of salinity tolerance. *Annual Review of Plant Biology*, **59**: 651–681.

Munro, S. (2011). The golgin coiled-coil proteins of the Golgi apparatus. *Cold Spring Harbor Perspectives in Biology*, **3**: a005256

Murray, J. T., Panaretou, C., Stenmark, H., Miaczynska, M., Backer, J.M. (2002). Role of Rab5 in the recruitment of hVps34/p150 to the early endosome. *Traffic*, **3**: 416–427.

Murthy, J.V., Kim, H.H., Hanesworth, V.R., Hugdahl, J.D., Morejohn, L.C. (1994). Competitive inhibition of high-affinity oryzalin binding to plant tubulin by the phosphoric amide herbicide amiprophos-methyl. *Plant Physiology*, **105**: 309–320.

Nagashima, K., Torii, S., Yi, Z., Igarashi, M., Okamoto, K., Takeuchi, T., Izumi, T. (2002). Melanophilin directly links Rab27a and myosin Va through its distinct coiled-coil regions. *FEBS Letters*, **517**: 233–238.

Nakatsuji, H., Nishimura, N., Yamamura, R., Kanayama, H.O., Sasaki, T. (2008). Involvement of actinin-4 in the recruitment of JRAB/MICAL-L2 to cell-cell junctions and the formation of functional tight junctions. *Molecular and Cellular Biology*, **28**: 3324–3335.

Nassar, N., Singh, K., Garcia-Diaz, M. (2010). Structure of the dominant negative S17N mutant of Ras. *Biochemistry*, **49**: 1970–1974.

Nebenführ, A., Gallagher, L.A., Dunahay, T.G., Frohlick, J.A., Mazurkiewicz, A.M., Meehl, J.B., Staehelin, L.A. (1999). Stop-and-go movements of plant Golgi stacks are mediated by the acto-myosin system. *Plant Physiology*, **121**: 1127–1141.

Nick, P. (1999). Signals, motors, morphogenesis - the cytoskeleton in plant development. *Plant Biology*, **1**:, 169–179.

Nielsen, E., Christoforidis, S., Uttenweiler-Joseph, S., Miaczynska, M., Dewitte, F., Wilm, M., Hoflack, B., Zerial, M. (2000). Rabenosyn-5, a novel Rab5 effector, is complexed with hVPS45 and recruited to endosomes through a FYVE finger domain. *Journal of Cell Biology*, **151**: 601–612.

Nikolovski, N., Rubtsov, D., Segura, M.P., Miles, G.P., Stevens, T.J., Dunkley, T.P. J., Munro, S., Lilley, K.S., Dupree, P. (2012). Putative glycosyltransferases and other plant Golgi apparatus proteins are revealed by LOPIT proteomics. *Plant Physiology*, **160**: 1037–1051.

Niu, B., Jin, Y.H., Feng, K.Y., Lu, W.C., Cai, Y.D., Li, G.Z. (2008). Using AdaBoost for the prediction of subcellular location of prokaryotic and eukaryotic proteins. *Molecular Diversity*, **12**: 41–45.

Nordmann, M., Cabrera, M., Perz, A., Bröcker, C., Ostrowicz, C., Engelbrecht-Vandré, S., Ungermann, C. (2010). The Mon1-Ccz1 complex is the GEF of the late endosomal Rab7 homolog Ypt7. *Current Biology*, **20**: 1654–1659.

Nottingham, R.M., Ganley, I.G., Barr, F.A., Lambright, D.G., Pfeffer, S.R. (2011). RUTBC1 protein, a Rab9A effector that activates GTP hydrolysis by Rab32 and Rab33B proteins. *Journal of Biological Chemistry*, **286**: 33213–33222.

Nottingham, R.M., Pusapati, G.V., Ganley, I.G., Barr, F.A., Lambright, D.G., Pfeffer, S.R. (2012). RUTBC2 protein, a Rab9A effector and GTPase-activating protein for Rab36. *Journal of Biological Chemistry*, **287**: 22740–22748.

Oda, Y., Higaki, T., Hasezawa, S., Kutsuna, N. (2009). Chapter 3. New insights into plant vacuolar structure and dynamics. *International Review of Cell and Molecular Biology*, **277**: 103–135.

Oda, Y., Hirata, A., Sano, T., Fujita, T., Hiwatashi, Y., Sato, Y., Kadota, A., Hasebe, M., Hasezawa, S. (2009). Microtubules regulate dynamic organization of vacuoles in physcomitrella patens. *Plant and Cell Physiology*, **50**: 855–868.

Oikawa, K., Kasahara, M., Kiyosue, T., Kagawa, T., Suetsugu, N. (2003). CHLOROPLAST UNUSUAL POSITIONING1 is essential for proper chloroplast positioning. *The Plant Cell*, **15**: 2805–2815.

Oikawa, K., Yamasato, A., Kong, S.G., Kasahara, M., Nakai, M., Takahashi, F., Ogura, Y., Kagawa, T., Wada, M. (2008). Chloroplast outer envelope protein CHUP1 is essential for chloroplast anchorage to the plasma membrane and chloroplast movement. *Plant Physiology*, **148**: 829–842.

Orlova, A., & Egelman, E.H. (1992). Structural basis for the destabilization of F-actin by phosphate release following ATP hydrolysis. *Journal of Molecular Biology*, **227**: 1043–1053.

Ortiz, D., Medkova, M., Walch-solimena, C., Novick, P. (2002). Ypt32 recruits the Sec4p guanine nucleotide exchange factor, Sec2p, to secretory vesicles; evidence for a Rab cascade in yeast. *Cell*, **157**: 1005–1015.

Osakabe, Y., Arinaga, N., Umezawa, T., Katsura, S., Nagamachi, K., Tanaka, H., Ohiraki, H., Yamada, K., Seo., S.U., Abo, M., Yoshimura, E.,Shinozaki, K., Yamaguchi-Shinozaki, K. (2013). Osmotic stress responses and plant growth controlled by potassium transporters in Arabidopsis. *The Plant Cell*, **25**: 609–624.

Ostermeier, C., & Brunger, A.T. (1999). Structural basis of Rab effector specificity: Crystal structure of the small G protein Rab3A complexed with the effector domain of raBphilin-3A. *Cell*, **96**: 363–374.

Osterrieder, A. (2012). Tales of tethers and tentacles: golgins in plants. *Journal of Microscopy*, **247**: 68–77.

Osterrieder, A., Carvalho, C.M., Latijnhouwers, M., Johansen, J.N., Stubbs, C., Botchway, S., Hawes, C. (2009). Fluorescence lifetime imaging of interactions

between Golgi tethering factors and small GTPases in plants. *Traffic*, **10**: 1034–1046.

Otey, C.A, Pavalko, F.M., Burridge, K. (1990). An interaction between alpha-actinin and the beta 1 integrin subunit in vitro. *The Journal of Cell Biology*, **111**: 721–729.

Pantaloni, D., & Carlier, M.F. (1993). How profilin promotes actin filament assembly in the presence of thymosin β4. *Cell*, **75**: 1007–1014.

Pearson, M.A, Reczek, D., Bretscher, A., Karplus, P.A. (2000). Structure of the ERM protein moesin reveals the FERM domain fold masked by an extended actin binding tail domain. *Cell*, **101**: 259–270.

Pereira-Leal, J.B., & Seabra, M.C. (2000). The mammalian Rab family of small GTPases: definition of family and subfamily sequence motifs suggests a mechanism for functional specificity in the Ras superfamily. *Journal of Molecular Biology*, **301**: 1077–1087.

Pereira-Leal, J.B., & Seabra, M.C. (2001). Evolution of the Rab family of small GTP-binding proteins. *Journal of Molecular Biology*, **313**: 889–901.

Peremyslov, V.V., Mockler, T.C., Filichkin, S.A., Fox, S.E., Jaiswal, P., Makarova, K. S., Koonin, E.V., Dolja, V.V. (2011). Expression, splicing, and evolution of the myosin gene family in plants. *Plant Physiology*, **155**: 1191–1204.

Peremyslov, V.V, Prokhnevsky, A.I., Avisar, D., Dolja, V.V. (2008). Two class XI myosins function in organelle trafficking and root hair development in Arabidopsis. *Plant Physiology*, **146**: 1109–1116.

Peremyslov, V.V., Klocko, A.L., Fowler, J.E., Dolja, V.V. (2012). Arabidopsis myosin XI-K localizes to the motile endomembrane vesicles associated with F-actin. *Frontiers in Plant Science*, **3**: 184.

Peremyslov, V.V., Morgun, E.A., Kurth, E.G., Makarova, K.S., Koonin, E.V., Dolja, V.V. (2013). Identification of myosin XI receptors in Arabidopsis defines a distinct class of transport vesicles. *The Plant Cell*, **25**: 3022-3038.

Pfeffer, S.R. (1999). Transport-vesicle targeting: tethers before SNAREs. *Nature Cell Biology*, **1**: E17–E22.

Pfeffer, S.R. (2013). Rab GTPase regulation of membrane identity. *Current Opinion in Cell Biology*, **25**: 414–419.

Pierleoni, A., Martelli, P.L., Fariselli, P., Casadio, R. (2006). BaCelLo: A balanced subcellular localization predictor. *Bioinformatics*, **22**: E408–E416.

Pleskot, R., Pejchar, P., Staiger, C.J., Potocký, M. (2014). When fat is not bad: the regulation of actin dynamics by phospholipid signaling molecules. *Frontiers in Plant Science*, **5**: 5.

Pollard, T.D., & Borisy, G.G. (2003). Cellular motility driven by assembly and disassembly of actin filaments. *Cell*, **112**: 453–465.

Pommerrenig, B., Feussner, K., Zierer, W., Rabinovych, V., Klebl, F., Feussner, I., Sauer, N. (2011). Phloem-specific expression of Yang cycle genes and identification of novel Yang cycle enzymes in Plantago and Arabidopsis. *The Plant Cell*, **23**: 1904–1919.

Popowicz, G.M., Schleicher, M., Noegel, A.A., Holak, T.A. (2006). Filamins: promiscuous organizers of the cytoskeleton. *Trends in Biochemical Sciences*, **31**: 411–419.

Preuss, M.L., Schmitz, A.J., Thole, J.M., Bonner, H.K.S., Otegui, M.S., Nielsen, E. (2006). A role for the RabA4b effector protein PI-4Kβ1 in polarized expansion of root hair cells in *Arabidopsis thaliana*. *Journal of Cell Biology*, **172**: 991–998.

Rak, A., Pylypenko, O., Durek, T., Watzke, A., Kushnir, S., Brunsveld, L., Waldmann, H., Goody, R.S., Alexandrov, K. (2003). Structure of Rab GDP-dissociation inhibitor in complex with prenylated YPT1 GTPase. *Science*, **302**: 646–650.

Rautengarten, C., Ebert, B., Herter, T., Petzold, C.J., Ishii, T., Mukhopadhyay, A., Usadel, B., Scheller, H.V. (2011). The interconversion of UDP-arabinopyranose and UDP-arabinofuranose is indispensable for plant development in Arabidopsis. *The Plant Cell*, **23**: 1373–1390.

Real-Hohn, A., Zancan, P., Da Silva, D., Martins, E.R., Salgado, L.T., Mermelstein, C. S., Gomes, A.M.O., Sola-Penna, M. (2010). Filamentous actin and its associated binding proteins are the stimulatory site for 6-phosphofructo-1-kinase association within the membrane of human erythrocytes. *Biochimie*, **92**: 538–544.

Reddy, A.S., & Day, I.S. (2001). Analysis of the myosins encoded in the recently completed *Arabidopsis thaliana* genome sequence. *Genome Biology*, **2**: RESEARCH0024.1–0024.17

Reisen, D., Marty, F., Leborgne-Castel, N. (2005). New insights into the tonoplast architecture of plant vacuoles and vacuolar dynamics during osmotic stress. *BMC Plant Biology*, **5**: 13.

Reyes, F.C., Buono, R., Otegui, M.S. (2011). Plant endosomal trafficking pathways. *Current Opinion in Plant Biology*, **14**: 666–673.

Rice, P., Longden, I., Bleasby, A. (2000). EMBOSS: The European Molecular Biology Open Software Suite. *Trends in Genetics*, **16**: 276–277.

Rittig, M.G., Kaufmann, A., Robins, A., Shaw, B., Sprenger, H., Gemsa, D., Foulonge, V., Rouot, B., Dornand, J. (2003). Smooth and rough lipopolysaccharide phenotypes of Brucella induce different intracellular trafficking and cytokine/chemokine release in human monocytes. *Journal of Leukocyte Biology*, **74**: 1045–1055.

Rivera-Molina, F.E., & Novick, P.J. (2009). A Rab GAP cascade defines the boundary between two Rab GTPases on the secretory pathway. *Proceedings of the National Academy of Sciences of the United States of America*, **106**: 14408–14413.

Rose, A., & Meier, I. (2004). Scaffolds, levers, rods and springs: diverse cellular functions of long coiled-coil proteins. *Cellular and Molecular Life Sciences*, **61**: 1996–2009.

Rosquete, M.R., von Wangenheim, D., Marhavý, P., Barbez, E., Stelzer, E.H.K., Benková, E., Maizel, A., Kleine-Vehn, J. (2013). An auxin transport mechanism restricts positive orthogravitropism in lateral roots. *Current Biology*, **23**: 817–822.

Rounds, C.M., Hepler, P.K., Winship, L.J. (2014). The apical actin fringe contributes to localized cell wall deposition and polarized growth in the lily pollen tube. *Plant Physiology*, **166**: 139–151.

Ruthardt, N., Gulde, N., Spiegel, H., Fischer, R., Emans, N. (2005). Four-dimensional imaging of transvacuolar strand dynamics in tobacco BY-2 cells. *Protoplasma*, **225**: 205–215.

Rutherford, S., & Moore, I. (2002). The Arabidopsis Rab GTPase family: another enigma variation. *Current Opinion in Plant Biology*, **5**: 518–528.

Saito, C., Ueda, T., Abe, H., Wada, Y., Kuroiwa, T., Hisada, A., Furuya, M., Nakano, A. (2002). A complex and mobile structure forms a distinct subregion within the continuous vacuolar membrane in young cotyledons of Arabidopsis. *The Plant Journal*, **29**: 245–255.

Saitou, N., & Nei, M. (1987). The neighbor-joining method: A new method for reconstructing phylogenetic trees. *Molecular Biology Evolution*, **4**: 406–425.

Sakane, A., Abdallah, A. A. M., Nakano, K., Honda, K., Ikeda, W., Nishikawa, Y., Matsumoto, M., Matsushita, N., Kitamura, T., Sasaki, T. (2012). Rab13 small G protein and junctional Rab13-binding protein (JRAB) orchestrate actin cytoskeletal organization during epithelial junctional development. *Journal of Biological Chemistry*, **287**: 42455–42468.

Sakane, A., Honda, K., Sasaki, T. (2010). Rab13 regulates neurite outgrowth in PC12 cells through its effector protein, JRAB/MICAL-L2. *Molecular and Cellular Biology*, **30**: 1077–1087.

Sasaki, T., Kikuchi, A., Araki, S., Hata, Y., Isomura, M., Kuroda, S., Takai, Y. (1990). Purification and characterization from bovine Brain cytosol of a protein that inhibits the dissociation of GDP from and the subsequent binding of GTP to smg p25A, a ras p21-like GTP-binding protein. *Biological Chemistry*, **265**: 2333–2337.

Scheuring, D., Viotti, C., Kruger, F., Kunzl, F., Sturm, S., Bubeck, J., Hillmer, S., Frigerio, L., Robinson, D.G., Pimpl, P., Schumacher, K. (2011). Multivesicular bodies mature from the trans-Golgi network/early endosome in Arabidopsis. *The Plant Cell*, **23**: 3463–3481.

Schimmöller, F., & Riezman, H. (1993). Involvement of Ypt7p, a small GTPase, in traffic from late endosome to the vacuole in yeast. *Journal of Cell Science*, **106**: 823–830.

Schindelin, J., Arganda-Carreras, I., Frise, E., Kaynig, V., Longair, M., Pietzsch, T., Preibisch, S., Rueden, C., Saalfeld, S., Schmid, B., Tinevez, J.Y., White, D.J., Hartenstein, V., Eliceiri, K., Tomancak, P., Cardona, A. (2012). Fiji: an open-source platform for biological-image analysis. *Nature Methods*, **9**: 676–682.

Schliwa, M., & Woehlke, G. (2003). Molecular motors. *Nature*, **422**: 759–765.

Schmid, M., Davison, T.S., Henz, S.R., Pape, U.J., Demar, M., Vingron, M., Schölkopf, B., Weigel, D., Lohmann, J.U. (2005). A gene expression map of *Arabidopsis thaliana* development. *Nature Genetics*, **37**: 501–506.

Schoebel, S., Cichy, A.L., Goody, R.S., Itzen, A. (2011). Protein LidA from Legionella is a Rab GTPase supereffector. *Proceedings of the National Academy of Sciences of the United States of America*, **108**: 17945–17950.

Schultz, J., Milpetz, F., Bork, P., Ponting, C.P. (1998). SMART, a simple modular architecture research tool: identification of signaling domains. *Proceedings of the National Academy of Sciences of the United States of America*, **95**: 5857–5864.

Sechi, A.S., & Wehland, J. (2000). The actin cytoskeleton and plasma membrane connection: PtdIns(4,5)P(2) influences cytoskeletal protein activity at the plasma membrane. *Journal of Cell Science*, **113**: 3685–3695.

Segami, S., Makino, S., Miyake, A., Asaoka, M., Maeshima, M. (2014). Dynamics of vacuoles and H^+-pyrophosphatase visualized by monomeric green fluorescent protein in Arabidopsis : Artifactual bulbs and native intravacuolar spherical structures. *The Plant Cell*, **26**: 3416–3434.

Seibel, N.M., Eljouni, J., Nalaskowski, M.M., Hampe, W. (2007). Nuclear localization of enhanced green fluorescent protein homomultimers. *Analytical Biochemistry*, **368**: 95–99.

Sellers, J. R. (2000). Myosins: A diverse superfamily. *Biochimica et Biophysica Acta - Molecular Cell Research*, **1496**: 3–22.

Serebriiskii, I., Estojak, J., Berman, M., Golemis, E.A. (2000). Approaches to detecting false positives in yeast two-hybrid systems. *BioTechniques*, **28**: 328–336.

Sheahan, M.B., Rose, R.J., McCurdy, D.W. (2004). Organelle inheritance in plant cell division: The actin cytoskeleton is required for unbiased inheritance of chloroplasts, mitochondria and endoplasmic reticulum in dividing protoplasts. *The Plant Journal*, **37**: 379–390.

Sheahan, M.B., Rose, R.J., McCurdy, D.W. (2007). Actin-filament-dependent remodeling of the vacuole in cultured mesophyll protoplasts. *Protoplasma*, **230**: 141–152.

Shimada, T., Fuji, K., Tamura, K., Kondo, M., Nishimura, M., Hara-Nishimura, I. (2003a). Vacuolar sorting receptor for seed storage proteins in *Arabidopsis thaliana*. *Proceedings of the National Academy of Sciences of the United States of America*, **100**: 16095–16100.

Shimada, T., Yamada, K., Kataoka, M., Nakaune, S., Koumoto, Y., Kuroyanagi, M., Tabata, S., Kato, T., Shinozaki, K., Seki, M., Kobayashi, M., Kondo, M., Nishimura, M., Hara-Nishimura, I. (2003b). Vacuolar processing enzymes are essential for proper processing of seed storage proteins in *Arabidopsis thaliana*. *Journal of Biological Chemistry*, **278**: 32292–32299.

Shirane, M., & Nakayama, K.I. (2006). Protrudin induces neurite formation by directional membrane trafficking. *Science*, **314**: 818–821.

Shisheva, A., Chinni, S.R., & DeMarco, C. (1999). General role of GDP dissociation inhibitor 2 in membrane release of Rab proteins: Modulations of its functional interactions by in vitro and *in vivo* structural modifications. *Biochemistry*, **38**: 11711–11721.

Shultz, R.W., Tatineni, V.M., Hanley-Bowdoin, L., Thompson, W.F. (2007). Genome-wide analysis of the core DNA replication machinery in the higher plants Arabidopsis and rice. *Plant Physiology*, **144**: 1697–1714.

Sievers, F., Wilm, A., Dineen, D., Gibson, T.J., Karplus, K., Li, W., Lopez, R., McWilliam, H., Remmert, M., Söding, J., Thompson, J.D., Higgins, D.G. (2011). Fast, scalable generation of high-quality protein multiple sequence alignments using Clustal Omega. *Molecular Systems Biology*, **7**: 539.

Simonsen, a, Lippé, R., Christoforidis, S., Gaullier, J. M., Brech, a, Callaghan, J., Toh, B.H., Murphy, C., Zerial, M., Stenmark, H. (1998). EEA1 links PI(3)K function to Rab5 regulation of endosome fusion. *Nature*, **394**: 494–498.

Simonsen, A., Gaullier, J.M., D'Arrigo, A., Stenmark, H. (1999). The Rab5 effector EEA1 interacts directly with syntaxin-6. *Journal of Biological Chemistry*, **274**: 28857–28860.

Singh, M.K., Krüger, F., Beckmann, H., Brumm, S., Vermeer, J. E. M., Munnik, T., Mayer, U., Stierhof, Y.D., Grefen, C., Schumacher, K., Jürgens, G. (2014). Protein delivery to vacuole requires SAND protein-dependent Rab GTPase conversion for MVB-vacuole fusion. *Current Biology*, **24**: 1383–1389.

Sinka, R., Gillingham, A.K., Kondylis, V., Munro, S. (2008). Golgi coiled-coil proteins contain multiple binding sites for Rab family G proteins. *Journal of Cell Biology*, **183**: 607–615.

Sivars, U., Alvazian, D., Pfeffer, S.R. (2003). Yip3 catalyses the dissociation of endosomal Rab-GDI complexes. *Nature*, **425**: 856–859.

Sjöblom, B., Salmazo, A., Djinović-Carugo, K. (2008). α-Actinin structure and regulation. *Cellular and Molecular Life Sciences*, **65**: 2688–2701.

Skirpan, A.L., McCubbin, A.G., Ishimizu, T., Wang, X., Hu, Y., Dowd, P.E., Ma, H., Kao, T. (2001). Isolation and characterization of kinase interacting protein 1, a pollen protein that interacts with the kinase domain of PRK1, a receptor-like kinase of Petunia. *Plant Physiology*, **126**: 1480–92.

Slayman, C.L., Moussatos, V.V, Webb, W.W. (1994). Endosomal accumulation of pH indicator dyes delivered as acetoxymethyl esters. *The Journal of Experimental Biology*, **196**: 419–438.

Smertenko, A.P., Deeks, M J., Hussey, P.J. (2010). Strategies of actin reorganisation in plant cells. *Journal of Cell Science*, **123**: 3019–3028.

Snyers, L., Vlcek, S., Dechat, T., Skegro, D., Korbei, B., Gajewski, A., Mayans, O., Schöfer, C., Foisner, R. (2007). Lamina-associated polypeptide 2-α forms homo-trimers via its C terminus, and oligomerization is unaffected by a disease-causing mutation. *Journal of Biological Chemistry*, **282**: 6308–6315.

Sohn, E.J., Kim, E.S., Zhao, M., Kim, S J., Kim, H., Kim, Y.W., Lee, Y.J., Hillmer, S., Sohn, U., Jiang, L., Hwang, I. (2003). Rha1, an Arabidopsis Rab5 homolog, plays a critical role in the vacuolar trafficking of soluble cargo proteins. *The Plant Cell*, **15**: 1057–1070.

Sönnichsen, B., De Renzis, S., Nielsen, E., Rietdorf, J., Zerial, M. (2000). Distinct membrane domains on endosomes in the recycling pathway visualized by multicolor imaging of Rab4, Rab5, and Rab11. *Journal of Cell Biology*, **149**: 901–913.

Sparkes, I.A, Runions, J., Kearns, A., Hawes, C. (2006). Rapid, transient expression of fluorescent fusion proteins in tobacco plants and generation of stably transformed plants. *Nature Protocols*, **1**: 2019–2025.

Staiger, C.J., Gibbon, B.C., Kovar, D.R., Zonia, L.E. (1997). Profilin and actin-depolymerizing factor: Modulators of actin organization in plants. *Trends in Plant Science*, **2**: 275–281.

Staiger, C.J., Sheahan, M.B., Khurana, P., Wang, X., McCurdy, D.W., Blanchoin, L. (2009). Actin filament dynamics are dominated by rapid growth and severing activity in the Arabidopsis cortical array. *Journal of Cell Biology*, **184**: 269–280.

Starai, V.J., HIckey, C. M., Wickner, W. (2008). HOPS proofreads the trans-SNARE complex for yeast vacuole fusion. *Molecular Biology of the Cell*, **19**: 2500–2508.

Stark, C., Breitkreutz, B.J., Reguly, T., Boucher, L., Breitkreutz, A., Tyers, M. (2006). BioGRID: a general repository for interaction datasets. *Nucleic Acids Research*, **34**: D535–D539.

Steinmetz, M.O., Goldie, K.N., Aebi, U. (1997). A correlative analysis of actin filament assembly, structure, and dynamics. *Journal of Cell Biology*, **138**: 559–574.

Stenmark, H. (2009). Rab GTPases as coordinators of vesicle traffic. *Nature Reviews. Molecular Cell Biology*, **10**: 513–525.

Stenmark, H. (2012). The Rabs: A family at the root of metazoan evolution. *BMC Biology*, **10**: 68.

Stenmark, H., Vitale, G., Ullrich, O., Zerial, M. (1995). Rabaptin-5 is a direct effector of the small GTPase Rab5 in endocytic membrane fusion. *Cell*, **83**: 423–432.

Strom, M., Hume, A.N., Tarafder, A.K., Barkagianni, E., Seabra, M.C. (2002). A family of Rab27-binding proteins: Melanophilin links Rab27a and myosin Va function in melanosome transport. *Journal of Biological Chemistry*, **277**: 25423–25430.

Stroupe, C., & Brunger, A.T. (2000). Crystal structures of a Rab protein in its inactive and active conformations. *Journal of Molecular Biology*, **304**: 585–598.

Šubrtová, K., Panicucci, B., Zíková, A. (2015). ATPaseTb2, a unique membrane-bound FoF1-ATPase component, is essential in bloodstream and dyskinetoplastic trypanosomes. *PLOS Pathogens*, **11**: e1004660.

Swanson, S., & Jones, R. (1996). Gibberellic acid induces vacuolar acidification in barley aleurone. *The Plant Cell*, **8**: 2211–2221.

Taiz, L. (1992). The plant vacuole. *The Journal of Experimental Biology*, **172**: 113–122.

Taiz, L., & Zeiger, E. (2006). Plant Physiology. *Sinaur Associates, Sunderland MA.*

Takemoto, D., Jones, D.A., Hardham, A.R. (2003). GFP-tagging of cell components reveals the dynamics of subcellular re-organization in response to infection of Arabidopsis by oomycete pathogens. *The Plant Journal*, **33**: 775–792.

Tamura, K., Iwabuchi, K., Fukao, Y., Kondo, M., Okamoto, K., Ueda, H., Nishimura, M., Hara-Nishimura, I. (2013). Myosin XI-i links the nuclear membrane to the cytoskeleton to control nuclear movement and shape in Arabidopsis. *Current Biology*, **23**: 1776–1781.

Tamura, K., Takahashi, H., Kunieda, T., Fuji, K., Shimada, T., Hara-Nishimura, I. (2007). Arabidopsis KAM2/GRV2 is required for proper endosome formation and functions in vacuolar sorting and determination of the embryo growth axis. *The Plant Journal*, **19**: 320-332.

Tamura, T., & Akutsu, T. (2007). Subcellular location prediction of proteins using support vector machines with alignment of block sequences utilizing amino acid composition. *BMC Bioinformatics*, **8**: 466.

Tanaka, Y., Kutsuna, N., Kanazawa, Y., Kondo, N., Hasezawa, S., Sano, T. (2007). Intra-vacuolar reserves of membranes during stomatal closure: The possible role of guard cell vacuoles estimated by 3-D reconstruction. *Plant and Cell Physiology*, **48**: 1159–1169.

Tanz, S.K., Castleden, I., Hooper, C.M., Vacher, M., Small, I., Millar, H.A. (2013). SUBA3: A database for integrating experimentation and prediction to define the SUBcellular location of proteins in Arabidopsis. *Nucleic Acids Research*, **41**: D1185–D1191.

Terai, T., Nishimura, N., Kanda, I., Natsuo, Y., Sasaki, T. (2006). JRAB/MICAL-L2 is a junctional Rab-13 binding protein mediating the endocytic recycling of occludin. *Molecular Biology of the Cell*, **17**: 2465–2475.

Thompson, J.D., Gibson, T.J., Plewniak, F., Jeanmougin, F., Higgins, D.G. (1997). The CLUSTAL X windows interface: Flexible strategies for multiple sequence alignment aided by quality analysis tools. *Nucleic Acids Research*, **25**: 4876–4882.

Tian, H., Jia, Y., Niu, T., Yu, Q., Ding, Z. (2014). The key players of the primary root growth and development also function in lateral roots in Arabidopsis. *Plant Cell Reports*, **33**: 745–753.

To, J.P.C., & Kieber, J.J. (2008). Cytokinin signaling: two-components and more. *Trends in Plant Science*, **13**: 85–92.

Tse, Y.C., Mo, B., Hillmer, S., Zhao, M., Lo, S.W., Robinson, D.G., Jiang, L. (2004). Identification of multivesicular bodies as prevacuolar compartments in *Nicotiana tabacum* BY-2 cells. *The Plant Cell*, **16**: 672–693.

Ueda, T., Anai, T., Tsukaya, H., Hirata, A., Uchimiya, H. (1996). Characterization and subcellular localization of a small GTP-binding protein (Ara-4) from Arabidopsis: conditional expression under control of the promoter of the gene for heat-shock protein HSP81-1. *Molecular & General Genetics*, **250**: 533–539.

Vale, R. D. (2003). The molecular motor toolbox for intracellular transport. *Cell*, **112**: 467–480.

Valster, A., Pierson, E., Valenta, R., Hepler, P., Emons, A. (1997). Probing the plant actin cytoskeleton during cytokinesis and interphase by profilin microinjection. *The Plant Cell*, **9**: 1815–1824.

Verbelen, J.P., & Tao, W. (1998). Mobile arrays of vacuole ripples are common in plant cells. *Plant Cell Reports*, **17**: 917–920.

Verbelen, J.P., De Cnodder, T., Le, J., Vissenberg, K., Baluska, F. (2006). The Root apex of *Arabidopsis thaliana* consists of four distinct zones of growth activities: Meristematic zone, transition Zone, fast elongation zone and growth terminating zone. *Plant Signaling & Behavior*, **1**: 296–304.

Verchot-Lubicz, J., & Goldstein, R.E. (2010). Cytoplasmic streaming enables the distribution of molecules and vesicles in large plant cells. *Protoplasma*, **240**: 99–107.

Viotti, C., Bubeck, J., Stierhof, Y.D., Krebs, M., Langhans, M., van den Berg, W., van Dongen, W., Richter, S., Geldner, N., Takano, J., Jürgens, G., de Vries, S.C., Robinson, D.G., Schumacher, K. (2010). Endocytic and secretory traffic in Arabidopsis merge in the trans-Golgi network/early endosome, an independent and highly dynamic organelle. *The Plant Cell*, **22**: 1344–1357.

Viotti, C., Krüger, F., Krebs, M., Neubert, C., Fink, F., Lupanga, U., Scheuring, D., Boutté, Y., Frescatada-Rosa, M., Wolfenstetter, S., Sauer, N., Hillmer, S., Grebe, M., Schumacher, K. (2013). The endoplasmic reticulum is the main

membrane source for biogenesis of the lytic vacuole in Arabidopsis. *The Plant Cell*, **25**: 3434–3449.

Vitavska, O., Merzendorfer, H., Wieczorek, H. (2005). The V-ATPase subunit C binds to polymeric F-actin as well as to monomeric G-actin and induces cross-linking of actin filaments. *Journal of Biological Chemistry*, **280**: 1070–1076.

Vitelli, R., Santillo, M., Chiariello, M., Bifulco, M., Bruni, C.B., Bucci, C., Lattero, D. (1997). Cell biology and metabolism: Role of the small GTPase RAB7 in the late endocytic pathway. *Journal of Biological Chemistry*, **272**: 4391–4397.

Voigt, B., Timmers, A.C.J., Šamaj, J., Müller, J., Baluška, F., Menzel, D. (2005). GFP-FABD2 fusion construct allows *in vivo* visualization of the dynamic actin cytoskeleton in all cells of Arabidopsis seedlings. *European Journal of Cell Biology*, **84**: 595–608.

Voulhoux, R., Bos, M.P., Geurtsen, J., Mols, M., Tommassen, J. (2003). Role of a highly conserved bacterial protein in outer membrane protein assembly. *Science*, **299**: 262–265.

Waingeh, V.F., Gustafson, C.D., Kozliak, E.I., Lowe, S.L., Knull, H.R., Thomasson, K.A. (2006). Glycolytic enzyme interactions with yeast and skeletal muscle F-actin. *Biophysical Journal*, **90**: 1371–1384.

Wakatsuki, T., Schwab, B., Thompson, N.C., Elson, E.L. (2001). Effects of cytochalasin D and latrunculin B on mechanical properties of cells. *Journal of Cell Science*, **114**:1025–1036.

Walter, M., Clark, S.G., Levinson, A.D. (1986). The oncogenic activation of human p21ras by a novel mechanism. *Science*, **233**: 649–652.

Wang, P., Hawkins, T.J., Richardson, A.C., Cummins, I., Deeks, M.J., Sparkes, I.A., Hawes, C., Hussey, P.J. (2014). The plant cytoskeleton, NET3C, and VAP27 mediate the link between the plasma membrane and endoplasmic reticulum. *Current Biology*, **24**: 1397–1405.

Wang, P., & Hussey, P.J. (2015). Interactions between plant endomembrane systems and the actin cytoskeleton. *Frontiers in Plant Science*, **6**: 422.

Wang, Y.H. (2008). How effective is T-DNA insertional mutagenesis? *Journal of Biochemical Technology*, **1**: 11–20.

Waterhouse, A.M., Procter, J.B., Martin, D.M.A., Clamp, M., Barton, G.J. (2009). Jalview Version 2- A multiple sequence alignment editor and analysis workbench. *Bioinformatics*, **25**: 1189–1191.

Welch, M.D., Mallavarapu, A., Rosenblatt, J., Mitchison, T.J. (1997). Actin dynamics *in vivo*. *Current Opinion in Cell Biology*, **9**: 54–61.

Wennerberg, K., Rossman, K. L., Der, C.J. (2005). The Ras superfamily at a glance. *Journal of Cell Science*, **118**: 843–846.

Whyte, J.R.C., & Munro, S. (2002). Vesicle tethering complexes in membrane traffic. *Journal of Cell Science*, **115**: 2627-2637.

Wiederkehr, A., De Craene, J.O., Ferro-Novick, S., Novick, P. (2004). Functional specialization within a vesicle tethering complex: Bypass of a subset of exocyst deletion mutants by Sec1p or Sec4p. *Journal of Cell Biology*, **167**: 875–887.

Wilson, S.M., & Bacic, A. (2012). Preparation of plant cells for transmission electron microscopy to optimize immunogold labeling of carbohydrate and protein epitopes. *Nature Protocols*, **7**: 1716–1727.

Winder, S.J., & Ayscough, K.R. (2005). Actin-binding proteins. *Journal of Cell Science*, **118**: 651–654.

Winder, S.J., Jess, T., Ayscough, K.R. (2003). SCP1 encodes an actin-bundling protein in yeast. *The Biochemical Journal*, **375**: 287–295.

Winter, D., Vinegar, B., Nahal, H., Ammar, R., Wilson, G.V., Provart, N.J. (2007). An "electronic fluorescent pictograph" Browser for exploring and analyzing large-scale biological data sets. *PLoS ONE*, **2**: e178.

Woollard, A.A.D., & Moore, I. (2008). The functions of Rab GTPases in plant membrane traffic. *Current Opinion in Plant Biology*, **11**: 610–619.

Wu, M., Wang, T., Loh, E., Hong, W., Song, H. (2005). Structural basis for recruitment of RILP by small GTPase Rab7. *The EMBO Journal*, **24**: 1491–1501.

Xiao, G.H., Shoarinejad, F., Jin, F., Golemis, E.A., Yeung, R.S. (1997). The tuberous sclerosis 2 gene product, tuberin, functions as a Rab5 GTPase activating protein (GAP) in modulating endocytosis. *Journal of Biological Chemistry*, **272**: 6097–6100.

Xue, X.H., Guo, C.Q., Du, F., Lu, Q.L., Zhang, C.M., Ren, H.Y. (2011). AtFH8 is involved in root development under effect of low-dose latrunculin B in dividing cells. *Molecular Plant*, **4**: 264–278.

Yamamura, R., Nishimura, N., Nakatsuji, H., Arase, S., Sasaki, T. (2008). The interaction of JRAB/MICAL-L2 with Rab8 and Rab13 coordinates the assembly of tight junctions and adherens junctions. *Molecular Biology of the Cell*, **19**: 971–983.

Yang, Y., Costa, A., Leonhardt, N., Siegel, R.S., Schroeder, J.I. (2008). Isolation of a strong Arabidopsis guard cell promoter and its potential as a research tool. *Plant Methods*, **4**: 6.

Yoshida, K., Ohnishi, M., Fukao, Y., Okazaki, Y., Fujiwara, M., Song, C., Nakanishi, Y., Saito, K., Shimmen, T., Suzaki, T., Hayashi, F., Fukaki, H., Maeshima, M., Mimura, T. (2013). Studies on vacuolar membrane microdomains isolated from Arabidopsis suspension-cultured cells: Local distribution of vacuolar membrane proteins. *Plant and Cell Physiology*, **54**: 1571–1584.

Yu, M., Yuan, M., Ren, H. (2006). Visualization of actin cytoskeletal dynamics during the cell cycle in tobacco (*Nicotiana tabacum* L. cv Bright Yellow) cells. *Biology of the Cell*, **98**: 295–306.

Yuan, F., Yang, H., Xue, Y., Kong, D., Ye, R., Li, C., Zhang, J., Theprungsirikul, L. (2014). OSCA1 mediates osmotic-stress-evoked Ca2+ increases vital for osmosensing in Arabidopsis. *Nature*, **514**: 367–371.

Zerial, M., & McBride, H. (2001). Rab proteins as membrane organizers. *Nature Reviews. Molecular Cell Biology*, **2**: 107–117.

Zewert, T.E., & Harrington, M.G. (1993). Protein electrophoresis. *Current Opinion in Biotechnology*, **4**: 3–8.

Zhang, C., Hicks, G.R., Raikhel, N.V. (2014). Plant vacuole morphology and vacuolar trafficking. *Frontiers in Plant Science*, **5**: 476.

Zhang, J., Fonovic, M., Suyama, K., Bogyo, M., Scott, M.P. (2009). Rab35 controls actin bundling by recruiting fascin as an effector protein. *Science*, **325**: 1250–1254.

Zhang, W., Zhao, Y., Guo, Y., Ye, K. (2012). Plant actin-binding protein SCAB1 is dimeric actin cross-linker with atypical pleckstrin homology domain. *Journal of Biological Chemistry*, **287**: 11981–11990.

Zhao, Y., Zhao, S., Mao, T., Qu, X., Cao, W., Zhang, L., Zhang, W., He, L., Li, S., Ren, S., Zhao, J., Zhu, G., Huang, S., Ye, K., Yuan, M., Guo, Y. (2011). The plant-specific actin binding protein SCAB1 stabilizes actin filaments and regulates stomatal movement in Arabidopsis. *The Plant Cell*, **23**: 2314–2330.

Zheng, J., Han, S.W., Munnik, T., Rojas-Pierce, M. (2014a). Multiple vacuoles in impaired tonoplast trafficking3 mutants are independent organelles. *Plant Signaling & Behavior*, **9**: e29783.

Zheng, J., Won Han, S., Fernanda Rodriguez-Welsh, M., Rojas-Pierce, M. (2014b). Homotypic vacuole fusion requires VTI11 and is regulated by phosphoinositides. *Molecular Plant*, **7**: 1026–1040.

Zheng, Y., Xie, Y., Jiang, Y., Qu, X., Huang, S. (2013). Arabidopsis ACTIN-DEPOLYMERIZING FACTOR7 severs actin filaments and regulates actin cable turnover to promote normal pollen tube growth. *The Plant Cell*, **25**: 3405–3423.

Zhou, X., Graumann, K., Evans, D.E., Meier, I. (2012). Novel plant SUN-KASH bridges are involved in RanGAP anchoring and nuclear shape determination. *Journal of Cell Biology*, **196**: 203–211.

Zhou, X., Graumann, K., Wirthmueller, L., Jones, J.D.G., Meier, I. (2014). Identification of unique SUN-interacting nuclear envelope proteins with diverse functions in plants. *Journal of Cell Biology*, **205**: 677–692.

Zhou, X., & Meier, I. (2013). How plants LINC the SUN to KASH. *Nucleus*, **4**: 206–215.

Zhu, G., Zhai, P., Liu, J., Terzyan, S., Li, G., Zhang, X.C. (2004). Structural basis of Rab5-Rabaptin5 interaction in endocytosis. *Nature Structural & Molecular Biology*, **11**: 975–983.

Zhu, H., Liang, Z., Li, G. (2009). Rabex-5 is a Rab22 effector and mediates Rab22-Rab5 signaling cascade in endocytosis. *Molecular Biology of the Cell*, **20**: 4720–4729.

Zouhar, J., & Rojo, E. (2009). Plant vacuoles: Where did they come from and where are they heading? *Current Opinion in Plant Biology*, **12**: 677–84.

Zuo, J., Vergara, S., Kohno, S., Holliday, L.S. (2008). Biochemical and functional characterization of the actin-binding activity of the B subunit of yeast vacuolar H+-ATPase. *The Journal of Experimental Biology*, **211**: 1102–1108.